

Lecture Notes in Electrical Engineering 1125

Yonghong Zhang · Lianyong Qi · Qi Liu ·
Guangqiang Yin · Xiaodong Liu *Editors*

Proceedings of the 13th International Conference on Computer Engineering and Networks

Volume I

 Springer

Series Editors

Leopoldo Angrisani, *Department of Electrical and Information Technologies Engineering, University of Napoli Federico II, Napoli, Italy*

Marco Arteaga, *Departament de Control y Robótica, Universidad Nacional Autónoma de México, Coyoacán, Mexico*

Samarjit Chakraborty, *Fakultät für Elektrotechnik und Informationstechnik, TU München, München, Germany*

Jiming Chen, *Zhejiang University, Hangzhou, Zhejiang, China*

Shanben Chen, *School of Materials Science and Engineering, Shanghai Jiao Tong University, Shanghai, China*

Tan Kay Chen, *Department of Electrical and Computer Engineering, National University of Singapore, Singapore, Singapore*

Rüdiger Dillmann, *University of Karlsruhe (TH) IAIM, Karlsruhe, Baden-Württemberg, Germany*

Haibin Duan, *Beijing University of Aeronautics and Astronautics, Beijing, China*

Gianluigi Ferrari, *Dipartimento di Ingegneria dell'Informazione, Sede Scientifica Università degli Studi di Parma, Parma, Italy*

Manuel Ferre, *Centre for Automation and Robotics CAR (UPM-CSIC), Universidad Politécnica de Madrid, Madrid, Spain*

Faryar Jabbari, *Department of Mechanical and Aerospace Engineering, University of California, Irvine, CA, USA*

Limin Jia, *State Key Laboratory of Rail Traffic Control and Safety, Beijing Jiaotong University, Beijing, China*

Janusz Kacprzyk, *Intelligent Systems Laboratory, Systems Research Institute, Polish Academy of Sciences, Warsaw, Poland*

Alaa Khamis, *Department of Mechatronics Engineering, German University in Egypt El Tagamoa El Khames, New Cairo City, Egypt*

Torsten Kroeger, *Intrinsic Innovation, Mountain View, CA, USA*

Yong Li, *College of Electrical and Information Engineering, Hunan University, Changsha, Hunan, China*

Qilian Liang, *Department of Electrical Engineering, University of Texas at Arlington, Arlington, TX, USA*

Ferran Martín, *Departament d'Enginyeria Electrònica, Universitat Autònoma de Barcelona, Bellaterra, Barcelona, Spain*

Tan Cher Ming, *College of Engineering, Nanyang Technological University, Singapore, Singapore*

Wolfgang Minker, *Institute of Information Technology, University of Ulm, Ulm, Germany*

Pradeep Misra, *Department of Electrical Engineering, Wright State University, Dayton, OH, USA*

Subhas Mukhopadhyay, *School of Engineering, Macquarie University, Sydney, NSW, Australia*

Cun-Zheng Ning, *Department of Electrical Engineering, Arizona State University, Tempe, AZ, USA*

Toyoaki Nishida, *Department of Intelligence Science and Technology, Kyoto University, Kyoto, Japan*

Luca Oneto, *Department of Informatics, Bioengineering, Robotics and Systems Engineering, University of Genova, Genova, Italy*

Bijaya Ketan Panigrahi, *Department of Electrical Engineering, Indian Institute of Technology Delhi, New Delhi, Delhi, India*

Federica Pascucci, *Department di Ingegneria, Università degli Studi Roma Tre, Roma, Italy*

Yong Qin, *State Key Laboratory of Rail Traffic Control and Safety, Beijing Jiaotong University, Beijing, China*

Gan Woon Seng, *School of Electrical and Electronic Engineering, Nanyang Technological University, Singapore, Singapore*

Joachim Speidel, *Institute of Telecommunications, University of Stuttgart, Stuttgart, Germany*

Germano Veiga, *FEUP Campus, INESC Porto, Porto, Portugal*

Haictao Wu, *Academy of Opto-electronics, Chinese Academy of Sciences, Haidian District Beijing, China*

Walter Zamboni, *Department of Computer Engineering, Electrical Engineering and Applied Mathematics, DIEM—Università degli studi di Salerno, Fisciano, Salerno, Italy*

Junjie James Zhang, *Charlotte, NC, USA*

Kay Chen Tan, *Department of Computing, Hong Kong Polytechnic University, Kowloon Tong, Hong Kong*

The book series *Lecture Notes in Electrical Engineering* (LNEE) publishes the latest developments in Electrical Engineering—quickly, informally and in high quality. While original research reported in proceedings and monographs has traditionally formed the core of LNEE, we also encourage authors to submit books devoted to supporting student education and professional training in the various fields and applications areas of electrical engineering. The series cover classical and emerging topics concerning:

- Communication Engineering, Information Theory and Networks
- Electronics Engineering and Microelectronics
- Signal, Image and Speech Processing
- Wireless and Mobile Communication
- Circuits and Systems
- Energy Systems, Power Electronics and Electrical Machines
- Electro-optical Engineering
- Instrumentation Engineering
- Avionics Engineering
- Control Systems
- Internet-of-Things and Cybersecurity
- Biomedical Devices, MEMS and NEMS

For general information about this book series, comments or suggestions, please contact leontina.dicecco@springer.com.

To submit a proposal or request further information, please contact the Publishing Editor in your country:

China

Jasmine Dou, Editor (jasmine.dou@springer.com)

India, Japan, Rest of Asia

Swati Meherishi, Editorial Director (Swati.Meherishi@springer.com)

Southeast Asia, Australia, New Zealand

Ramesh Nath Premnath, Editor (ramesh.premnath@springernature.com)

USA, Canada

Michael Luby, Senior Editor (michael.luby@springer.com)

All other Countries

Leontina Di Cecco, Senior Editor (leontina.dicecco@springer.com)

**** This series is indexed by EI Compendex and Scopus databases. ****


Yonghong Zhang · Lianyong Qi · Qi Liu ·
Guangqiang Yin · Xiaodong Liu
Editors

Proceedings of the 13th International Conference on Computer Engineering and Networks

Volume I

Editors

Yonghong Zhang
Wuxi University
Wuxi, Jiangsu, China

Qi Liu 
School of Computer and Software
Nanjing University of Information Science
and Technology
Nanjing, Jiangsu, China

Xiaodong Liu
School of Computing
Edinburgh Napier University
Edinburgh, UK

Lianyong Qi
College of Computer Science and Technology
China University of Petroleum (East China)
Qingdao, Shandong, China

Guangqiang Yin
School of Information and Software
Engineering
University of Electronic Science
and Technology of China
Chengdu, Sichuan, China

ISSN 1876-1100

ISSN 1876-1119 (electronic)

Lecture Notes in Electrical Engineering

ISBN 978-981-99-9238-6

ISBN 978-981-99-9239-3 (eBook)

<https://doi.org/10.1007/978-981-99-9239-3>

© The Editor(s) (if applicable) and The Author(s), under exclusive license to Springer Nature Singapore Pte Ltd. 2024

This work is subject to copyright. All rights are solely and exclusively licensed by the Publisher, whether the whole or part of the material is concerned, specifically the rights of translation, reprinting, reuse of illustrations, recitation, broadcasting, reproduction on microfilms or in any other physical way, and transmission or information storage and retrieval, electronic adaptation, computer software, or by similar or dissimilar methodology now known or hereafter developed.

The use of general descriptive names, registered names, trademarks, service marks, etc. in this publication does not imply, even in the absence of a specific statement, that such names are exempt from the relevant protective laws and regulations and therefore free for general use.

The publisher, the authors, and the editors are safe to assume that the advice and information in this book are believed to be true and accurate at the date of publication. Neither the publisher nor the authors or the editors give a warranty, expressed or implied, with respect to the material contained herein or for any errors or omissions that may have been made. The publisher remains neutral with regard to jurisdictional claims in published maps and institutional affiliations.

This Springer imprint is published by the registered company Springer Nature Singapore Pte Ltd. The registered company address is: 152 Beach Road, #21-01/04 Gateway East, Singapore 189721, Singapore

Paper in this product is recyclable.

Preface

This conference proceeding is a collection of the papers accepted by the CENet 2023—the 13th International Conference on Computer Engineering and Networks held on November 3–5, 2023 in Wuxi, China.

This proceeding contains three volumes and covers four main topics: Internet of Things and Smart Systems (43 papers); Artificial Intelligence and Applications (72 papers); Communication System Detection, Analysis and Application (14 papers); Cloud Computing and Security (32 papers).

These parts serve as valuable references for industry practitioners, university faculties, research fellows, graduate students, and undergraduates seeking to stay abreast of the latest advancements and state-of-the-art practices in the respective fields covered by the conference proceedings. Utilizing this resource will enable them to develop, maintain, and manage systems with a high level of reliability and complexity.

We extend our gratitude to the authors for their outstanding contributions and dedication, as well as to the reviewers for ensuring the selection of high-quality papers, which made this conference proceeding possible.

Jiangsu, China
Qingdao, China
Nanjing, China
Chengdu, China
Edinburgh, UK

Yonghong Zhang
Lianyong Qi
Qi Liu
Guangqiang Yin
Xiaodong Liu

Contents

Research Status and Application of Water and Fertilizer Integrated Machine for Smart Mulberry Garden	1
<i>Dingjie Cen, Lei Lei, Zuojian Liu, Zhiling Chen, Yong Qin, and Yong Xu</i>	
A Review of the Research on Temperature and Humidity Control Systems in Silkworm Rooms	18
<i>Yuanji Chen, Sen Zheng, Danfeng Li, Yuna Tang, and Yong Xu</i>	
PassDiff: A New Approach for Password Guessing Using Diffusion Model	29
<i>Sheng Guo, Ming Duan, Yibin Du, Wei Wang, and Lulu Guo</i>	
Combining Image Caption and Aesthetic Description Using Siamese Network	41
<i>Xinghui Song and Peipei Zhu</i>	
Research on User Profile Analysis Method Based on LGIM Model	52
<i>Teng Zong, Fengsi Wang, Liang Guo, Yibo Liu, Xiaonan Feng, Zifu Qin, and Yinxiang Xia</i>	
Design and Implementation of Warning Signs for Vehicles Based on Automatic Navigation Algorithms	63
<i>Fangyan Wang, Ge Jiao, Jinjia Lu, and Yiping Yuan</i>	
Architecture of Integrated Resource System Based on Dataspace	74
<i>Hui Yan and Bo Chen</i>	
Task Allocation Method of Blockchain-Based Multi-robot System	86
<i>Fengbo Bao, Jiansheng Peng, and Jingsong Guo</i>	
Research on Improving TEB Algorithm for Mobile Robot Path Planning	93
<i>Hongyu Zhang, Jiansheng Peng, and Wei Qian</i>	
Research on Mobile Robot Path Planning Based on Improved A* and DWA Algorithms	105
<i>Wei Qian, Jiansheng Peng, and Hongyu Zhang</i>	
File System for Digital Signal Processing Equipment Based on FPGA	119
<i>Dong-cheng Chen</i>	

UAV-Assisted NOMA Network Power Allocation Under Offshore
Multi-energy Complementary Power Generation System 125
Wenyi Shao, Fei Lin, Ren Xu, Fanping Meng, and Haoran Wang

Bearings-Only Passive Localization in Unmanned Aerial Vehicle
Formation Based on Mathematical Model 137
Bingqian Meng, Xinqiao Hou, and Haiyan Wu

Design of Self-serve DUI Detection System Based on STM32 146
Yang Wu and Linxiang Zhao

Video Encryption Transmission in GCM Mode Based on SM4 Algorithm 153
Yiting Zhou, Jian Zhang, and Lin Liu

Target Spatial Positioning System Based on Dual Cameras 161
Yaqi Sun, Peng Tang, Jiayi Bu, and Mugang Lin

Controller Architecture and Performance Optimization for Intensive
Deployment Scenarios 170
Chuanming Zhu, Huiguang Chen, and Jingwen Li

A Text Sentiment Classification Method Enhanced by Bi-GRU
and Attention Mechanism 176
Dongdong Li, Xiaohou Shi, and Meiling Dai

An Improved Path Planning Algorithm Based on A* Algorithm 187
Dongdong Li, Xiaohou Shi, and Meiling Dai

Energy-Efficiency Resource Allocation for D2D Communications
Under-Laying UAV Networks 197
*Pan Zhao, Liuyuan Chen, Zhiliang Jiang, Ming Han, Fucui Yuan,
Aocheng Li, Xiangyuan Jia, Xinqi Fu, Jingqi Han, and Jiaqi Han*

Energy Efficient Multi-aerial Base Station Deployment Via DDPG-Mix
Algorithm 207
*Haoran He, Yikun Zhao, Jinli Zhang, Fanqin Zhou, Wenjing Li,
and Lei Feng*

Deep Learning-Based Beam Alignment and Tracking Mechanism
for mmWave Aerial Base Station 217
Yikun Zhao, Jinli Zhang, Fanqin Zhou, Wenjing Li, and Lei Feng

An Energy Saving Strategy for IoT Wristband Terminals Combined
with Human Activity Laws 227
Yu Chen, Shaojie Yang, Shaoyong Guo, Cai Zhi, Hui Yao, and Ao Xiong

Edge Caching Cooperation Method Based on Deep Reinforcement Learning	237
<i>Meng Zhu, Yuxiao Liu, Ao Xiong, Shaoyong Guo, Ke Yang, Nan Zhang, and Ke Chen</i>	
Edge-Oriented Resource Scheduling Algorithm Based on Deep Reinforcement Learning	247
<i>Longjun Zhao, Dandan Cui, Haipo Li, Ziyang Wang, Yating Sun, and Yang Yang</i>	
IMAP-GCG: Edge Container Resource Scheduling and Configuration Method Based on Improved MAPPO and GCN-GRU	258
<i>Xingle Gong, Yang Yang, Yating Sun, Zhipeng Gao, and Lanlan Rui</i>	
Small Object Detection Algorithm Combining Coordinate Attention Mechanism and P2-BiFPN Structure	268
<i>Zhou Juanjuan, Huang Xiaohan, Qin Zebang, and Yin Guangqiang</i>	
Domain Generalization for Multimodal Disaster Tweet Classification	278
<i>Chen Yu, Kangning Yin, and Zhiguo Wang</i>	
A Cooperative Edge Offloading Strategy for New Power System Services	288
<i>Fang Shen, Jiale Zhang, Yutong Ji, Chengyu Duan, and Zhen Wang</i>	
DVFS-Enabled Adaptive Offloading and Adjusting for High-Efficiency 5G Power MEC	298
<i>Zhenghao Li, Zhiwei Zhang, Gaofeng Zhang, Zhichang Feng, Qun Ma, Cong Chen, and Shuang Yang</i>	
Efficient Multi-dimensional Edge Resources Allocation for 5G Power MEC ...	311
<i>Baichao Ma, Tianyu Wang, Xiaomin Xie, Dan Chen, Kai Huang, Falei Ji, and Shuang Yang</i>	
Medical Image Segmentation Based on Improved Hunter Prey Optimization ...	323
<i>Shujing Li, Qinghe Li, Mingyu Zhang, and Linguo Li</i>	
Application of Improved Wild Horse Optimizer Based on Chaos Initialization in Medical Image Segmentation	334
<i>Linguo Li, Mingyu Zhang, Qinghe Li, and Shujing Li</i>	
Improved Northern Goshawk Optimization Algorithm for Medical Image Segmentation	344
<i>Tuo Zhou, Shunqiang Qian, Mingyu Zhang, and Linguo Li</i>	

Smart Home Camera Fall Detection System 355
Ziqi Ding, Hanwei Qian, Zechen Wu, and Wei Liu

Design and Implementation of an Automated APK Analysis System
for Practical Forensics 365
*Yicheng Li, Guangjun Liang, Keyan Tang, Yijia Teng, Haoran Ruan,
and Zixi Mo*

A Police UAV System Based on Target Recognition 378
*Zhenyu Qiu, Guangjun Liang, Hongtian Du, Bohan Yan, Jiahao Peng,
and Zexin Ju*

Design and Implementation of Public Opinion Safety Monitoring System
from the Perspective of Rumor Tracing Governance 388
Wenjie Tang, Lei Hong, Meng Yuan, and Yuyang Zheng

Design of Opinion Leader Identification System for Hot Public Opinion 400
Xinrong Cai, Lei Hong, Chengda Pan, and Yuxuan Han

Research on Deep Clustering Based on Image Data 411
*Xuanyu Li, Houqun Yang, Xiaoying Zhang, Dangui Yang,
Jianqiang Huang, and Lin Gan*

Exploring Cross-Chain Mechanisms and Projects in Blockchain:
A Comprehensive Summary 421
Yong Zhou, Yirui Bai, Zixuan Liu, Haoyu Gao, Chao Liu, and Hong Lei

A Data Processing and Analysis System for Fourier Transform Infrared
Spectrometer 432
Wanjie Ren, Qi Liu, Liang Li, Peng Wang, and Rui Tuo

A Method for Identifying Meat Quality Based on CNN-SVM 440
Peiyang Zhao, Yuhua Zhang, and Jianxi Zhang

Research on Asphalt Pavement Disease Detection Based on Object
Detection Algorithms 449
Wendang Cheng, Ke Hou, Wenjiang Liu, and Feng Liu

Research on Deep Learning-Based Concrete Bridge Crack Detection 459
Ke Hou, Wendang Cheng, Wenjiang Liu, and Feng Liu

Design of Automatic Brick Laying Machine Based on TRIZ Theory 468
Jinyang Zhao, Hongli Zhang, and Pengcheng Zhang

Design of Fuzzy Super-Twisting Sliding Mode Controller for Underwater Fishing Manipulator 479
Shanshan Yin, Zhiguang Guan, Chao Wang, and Mingxing Lin

Research on Remote Control System of Excavator Based on Industrial Internet of Things 492
Ran Liu, Zhenyuan Zhao, and Zhiguang Guan

Research on Underwater Positioning Based on Binocular Vision 501
Siqi Zhou, Yang Li, Zhiguang Guan, and Mingxing Lin

Simulation of Remote Control of Excavator Bucket Rod Hydraulic System Based on AMESim 509
Zhenyuan Zhao, Qin Sun, Baoping Wang, and Nan Zhang

Kinematics Study of Six-Axis Industrial Robots Based on Virtual Simulation Technology 520
Yuchen Liu, Lingyan Zhao, Maofei Liang, and Fayong Wang

FES Cycling System in Rehabilitation Engineering: A Survey 532
Wenyuan Wang, Yan Yan, Min Liu, Mingxu Sun, Tao Shen, Yiming Zhu, and Fangqiang Guo

Cooling Performance Elevation of a 3T Animal Gradient Assembly with Hollow Pipe Axial Gradient Coil 542
Zhaokun Lu and Yaohui Wang

Adaptive One-Step Prediction Enhanced Kalman Filter Algorithm for INS/Vision Integrated Mobile Robot Localization 552
Ronghao Shang, Yide Zhang, Tonghui Zhou, Tai Cheng, Kun Liang, Wuwen Zhang, Ting Wang, Zhongwei Shi, and Yuan Xu

Analysis of Abnormal Transmission Synchronous Belt of Industrial Robot Based on Visual Inspection 561
Han Jiang, Lanzhu Ren, Gandong Chen, and Lingyan Zhao

Author Index 573



Research Status and Application of Water and Fertilizer Integrated Machine for Smart Mulberry Garden

Dingjie Cen, Lei Lei, Zuojian Liu, Zhiling Chen, Yong Qin, and Yong Xu[✉]

Hechi University, Hechi 546300, Yizhou, China
xuyong@hcnu.edu.cn

Abstract. The water fertilizer integrated machine is a new agricultural technology equipment used for irrigation and fertilization in agricultural planting. Unlike traditional irrigation and fertilization, the water fertilizer integrated machine controls irrigation and fertilization based on artificial intelligence technology. Scientific water fertilizer replenishment can enable mulberry trees in mulberry gardens to obtain appropriate and sufficient nutrients at all stages of the growth process. This article discusses the research of mulberry garden water fertilizer integrated machine from the aspects of mulberry garden growth and water fertilizer integration technology, and analyzes and prospects the future development trend of mulberry garden water fertilizer integrated machine.

Keywords: Water fertilizer integrated machine · Artificial intelligence technology · Smart mulberry garden · Intelligent control · Scientific replenishment

1 Introduction

Since the 21st century, China's mulberry industry has launched the "East Mulberry to West" project. Guangxi has seized the opportunity to develop the mulberry industry as a key industry, comprehensively adjusting the agricultural industrial structure, and ultimately becoming an important province to undertake the mulberry industry. However, due to the increasingly scarce agricultural labor force, the development of the silkworm industry is hindered. In response to the situation of labor shortage, the development of mechanized mulberry planting and silkworm rearing is the best solution [1]. In the modern agricultural environment, crop cultivation techniques are continuously improving, and the utilization efficiency of water and nutrients has become the main factor in increasing production, increasing income, and reducing costs. In traditional agricultural cultivation, a large amount of water and fertilizer nutrients are wasted, and a large amount of waste of fertilizer can also cause environmental pollution to the soil and surrounding environment, which is not only detrimental to the efficiency of resource utilization but also has an impact on the ecological environment [2, 3]. At the same time, the indiscriminate use of fertilizers and pesticides, as well as the destruction of soil and soil erosion,

bring great contrast to the planting and life of farmers. Therefore, scientific guidance is advocated, and artificial intelligence technology is used for analysis and evaluation to achieve real-time monitoring and reasonable allocation of soil composition and fertility analysis, irrigation water, etc. This is also a hot spot in the research of water fertilizer integration technology in recent years.

Mulberry irrigation Based on years of experience, irrigated mulberry orchards increase mulberry leaves by 37.3–40.8% annually or in the current season compared to non irrigated mulberry orchards, with an average yield of more than 20%. Therefore, reasonable irrigation of mulberry orchards is one of the main technical measures to ensure high yield and quality of mulberry leaves. Especially in the southern or arid regions where there is little rain, if mulberry gardens in the spring and summer seasons are not irrigated properly, it is impossible to fertilize the mulberry gardens, let alone obtain high-quality mulberry leaves with high yield. Mulberry is a woody plant for leaves, and fertilization should be based on nitrogen fertilizer, combined with phosphorus and potassium fertilizers. Therefore, fertilization should be applied before the spring metabolism of the mulberry is vigorous, and sufficient nitrogen fertilizer should be applied before the accumulation and storage period of the mulberry in the autumn period. On the basis of fertilizer application, fertilizer should be increased to promote the transfer of sugar from branches and leaves to the root, which is conducive to the growth and nutrient accumulation of the mulberry tree, and enhance the cold resistance of the tree [4].

The integrated technology of water and fertilizer has the advantages of saving resources and increasing production, which is conducive to the sustainable development of agricultural production and reducing the degree of soil damage. At present, China's agricultural development is facing various development issues, including the lack of large-scale and scientific agricultural production, resource shortage, and other issues, indicating that agricultural production needs reform, and the application of water and fertilizer integration technology will also become a normalization in future agricultural production [5].

This article focuses on the current situation of mulberry plantation cultivation and the demand for water and fertilizer for mulberry trees, and introduces the research on water and fertilizer integration technology in recent years. Firstly, it introduces the research status of water and fertilizer integration technology, and then combines it with water and fertilizer integration technology based on the current situation of mulberry plantation and the water and fertilizer demand of mulberry trees. Then, it analyzes the application of mulberry water and fertilizer integration machines in mulberry plantations, and discusses and analyzes various water and fertilizer integration machine control systems and fertilization methods for mulberry plantations. Finally, it discusses and analyzes the future development trend of mulberry water and fertilizer integration machines, as shown in Fig. 1.

The mulberry garden water fertilizer integrated machine studied in this article can not only improve fertilization efficiency, reduce costs and save energy while meeting the requirements for normal growth of mulberry trees, but also reduce labor costs, improve labor efficiency, increase crop yield, provide an ideal growth environment for plants, improve equipment utilization, improve greenhouse climate, reduce mulberry pests, and

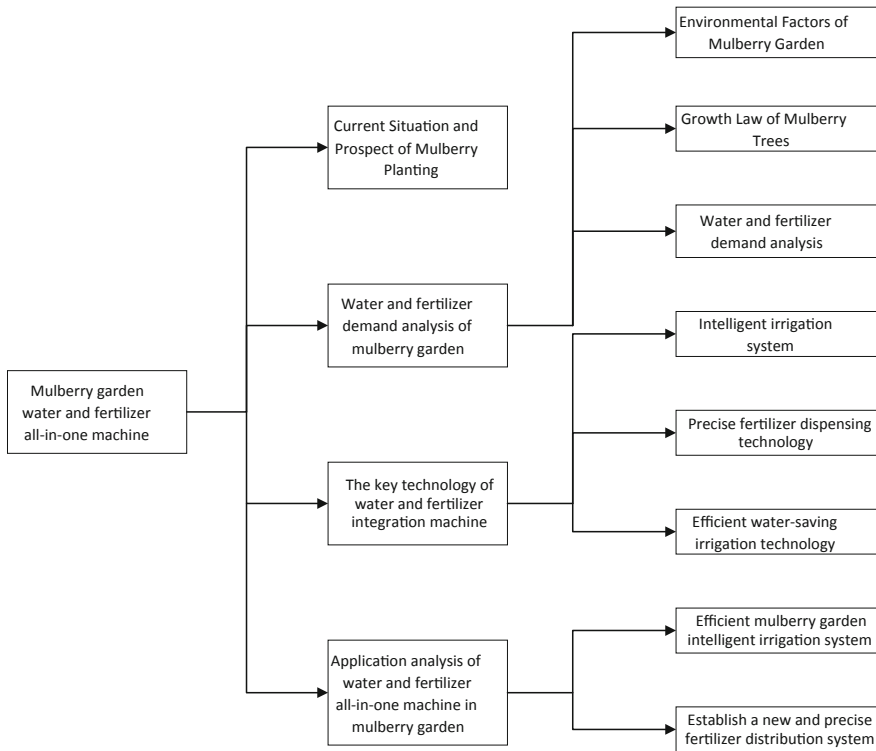


Fig. 1. Research structure diagram of mulberry garden water fertilizer integrated machine.

increase the growth rate of mulberry leaves, which has played a certain role in promoting agricultural development.

2 Current Situation and Prospect of Mulberry Planting

2.1 Current Situation of Mulberry Plantation

China is the birthplace of the silkworm industry and the world's largest producer and exporter of silk and silk. Since the reform and opening up, China has implemented the "the Belt and Road" economic strategy and jointly built the "Silk Road" economic circle and the "21st Century Maritime Silk Road", which have been endowed with Chinese characteristics in the new era. With the implementation of the "Western Development" and the industrial development strategy of "moving mulberry from the east to the west". Guangxi, which is located in the western region, has taken advantage of the above two opportunities and vigorously promoted the development of the silkworm industry. In just ten years, it has made rapid progress, taking two solid five years to take two major steps. That is, the output of mulberry cocoons at the end of the "Tenth Five Year Plan" in the first step jumped to the first place in the country, and the output of mulberry silk at the end of the "Tenth Five Year Plan" in the second step climbed to the first place in

the country, thus developing into the largest production and processing base of mulberry cocoons and silk in the country. In recent years, with the high attention of the Party committees and governments at all levels in Guangxi Zhuang Autonomous Region and the technical support of the national sericulture industry technology system project, the sericulture industry in Hechi City has achieved sustained and stable development. By the end of 2020 at the end of the “13th Five Year Plan”, the area of mulberry orchards in the city had developed to 62,100 hm², and the annual cocoon production had reached 141,300 tons. Compared to the end of the “12th Five Year Plan”, the mulberry orchards in 2015 had 53,800 hm², and the cocoon production had increased by 15.40% and 27.07%, respectively, accounting for 31.23% and 37.53% of the total area and cocoon production of mulberry orchards in Guangxi, and 7.69% and 19.44% of the total area and cocoon production of mulberry orchards in the country. Hechi City, with its mulberry garden scale and cocoon and silk processing capacity ranking first among prefecture-level cities in China for 16 consecutive years, is the largest mulberry cocoon and silk production base in Guangxi and the largest cocoon production base in China [6]. Yizhou District, located in the north-central part of Guangxi, is closely following the pace of the times, expanding its production scale, and bringing its people to prosperity. Among them, farmers planting mulberry and sericulture cover 202 villages (communities) in 16 townships and towns in the region, with 100,000 sericulture households and 456,000 people, accounting for 84.1% of the rural population. Among them, 8694 sericulture households are poor, accounting for 51.99% of the poverty households in the region. Currently, the area of mulberry gardens in Yizhou District has reached 382,000 mu, as shown in Fig. 2.



Fig. 2. Liu Sanjie silkworm industry core demonstration area, Yizhou District, Hechi City, Guangxi.

The planting mode of mulberry trees in Guangxi is basically close planting, and mainly involves sexual reproduction, namely seed sowing and seedling planting. The

main variety is Guangdong mulberry, which is densely planted in a garden. Generally, the number of trees planted per mu is between 5000 and 6000 (plant spacing: 15–20 cm, row spacing: 60–80 cm). This is significantly different from the sparse planting method of grafting mulberry with about 1000 plants per mu in Jiangsu and Zhejiang regions, Sichuan Basin, and northern regions of China, but it is based on the combination of their respective climatic conditions and the basic characteristics of mulberry varieties, using different planting methods suitable for the local area.

In recent years, although Guangxi has achieved preliminary results in the multipurpose development of mulberry resources, there are still many difficulties and problems. First, the ability to innovate in science and technology is not strong. Currently, there is a lack of specialized mulberry varieties for special purposes such as forage mulberry, medicinal mulberry, and ecological mulberry, and the supporting mulberry cultivation and management technology system for rocky desertification control, mining area reclamation, and heavy metal contaminated farmland restoration has not been established. Second, industrial development is still lagging behind. Due to the fact that the development of the mulberry industry in Guangxi has just started, the social recognition is not high, and the participation of leading industrialization enterprises in the development of mulberry resources is not sufficient, resulting in many mulberry resource products not yet entering large-scale production, especially the low technological content of the products, and the weak technological innovation ability of deep processing to improve the added value of products. The third is the shortage of capital investment and professional talents. Currently, the development of the mulberry industry has insufficient investment in basic research, construction of demonstration bases, and large-scale and high-value development of products. At the same time, there is a lack of professional and technical talents in interdisciplinary fields such as food processing, feed development, livestock and poultry breeding, and ecological and environmental protection, especially high-level top talents.

2.2 Development Prospect of Mulberry Garden

The reasons for the rapid growth of mulberry plantation scale in Guangxi are mainly driven by several factors: First, the strong government policy guidance and support. Entering the new century, the country has implemented the strategy of developing the western region, “moving mulberry trees from the east to the west”, promoting the conversion of farmland to forests, poverty alleviation, etc. The governments at all levels in Guangxi have increased their efforts to support the development of sericulture and mulberry production, and arranged special subsidy funds for planting mulberry seedlings in poverty-stricken areas. The second is that planting mulberry and raising silkworm yield fast and well. “The cash income from planting mulberry and raising silkworms has come quickly and the benefits are good. Although the prices of silkworm seedlings have fluctuated, they have generally improved, and the enthusiasm of mulberry farmers continues to rise”. The third is the strong support of improved mulberry varieties. The high-quality and high-yield hybrid mulberry varieties independently selected in Guangxi have been continuously promoted, ensuring the demand of sericulture farmers for expanding their varieties to mulberry orchards. Hybrid mulberry has a high breeding coefficient and fast growth rate. The cost of seed raising and seedling planting is low, and sericulture farmers

can achieve benefits from sericulture in the current year of planting [7]. Therefore, it is necessary to thoroughly implement the “Action Plan for the High Quality Development of the Sericulture and Silk Industry (2021–2025)”, improve the level of scientific and technological innovation, establish scientific research institutions, silkworm bases, etc., incorporate sericulture machinery into the development focus of agricultural machinery, and guide agricultural machinery research and manufacturing units to strengthen the research and development of key technical equipment around mulberry planting, mulberry garden management, mulberry leaf picking, silkworm seed production, intelligent sericulture, and other links, Develop labor-saving sericulture machinery and intelligent robots, and carry out demonstration applications.

3 Water and Fertilizer Demand Analysis of Mulberry Garden

3.1 Environmental Factors of Mulberry Garden

Mulberry is a deciduous tree or shrub, which is resistant to drought, barren soil, strong photosynthesis, good air purification effect Due to its strong soil fixation ability, sand is known as a “iron crop” [8]. Each plant has different environmental requirements. Mulberry is a deciduous tree that is suitable for growing in subtropical monsoon climate areas as a photophile, as shown in Fig. 3.



Fig. 3. Light loving mulberry trees.

The requirement of soil moisture for mulberry trees requires that the moisture content be relatively neutral. If excessive, it will cause mulberry roots to rot, making it unable to

absorb nutrients and water; If there is insufficient water, it will reduce the germination rate, and the mulberry leaves it grows will also appear withered, low water content, and poor quality. Therefore, it is necessary to detect the moisture content of the soil and supplement water or increase the concentration in a timely manner according to the situation.

The environmental temperature requirements for mulberry trees. The optimal growth temperature for mulberry trees is 20 °C. If the temperature is above 35 °C or below 10 °C, the growth of mulberry trees will be affected by printing. Therefore, it is necessary to detect the temperature of the mulberry garden environment and spray water to reduce temperature.

Mulberry trees can grow in a soil pH range of 4.5–9, but a neutral 6.5–7 growth environment is the most suitable. Soil pH is too acidic, affecting the absorption of roots, and prone to nutrient deficiencies such as phosphorus, potassium, magnesium, and calcium. Excessive alkali can lead to poor physical and chemical properties, which can easily lead to the failure of various nutrients. Mulberry trees are not easy to grow when the soil salt content exceeds 0.2%.

3.2 Growth Law of Mulberry Trees

In terms of time, mulberry trees begin to sprout in spring, and the period from the beginning of falling leaves in autumn and winter can be called the growth period of mulberry trees. During the germination stage, the leaves grow extremely rapidly, and the root system absorbs more nutrients, which also increases the need to absorb nutrients from the soil. Therefore, a large amount of fertilization is required at this time. However, due to the low temperature in spring and the slow decomposition of fertilizer, the mulberry tree cannot absorb nutrients in a timely manner. Therefore, fertilization needs to be carried out 15–20 days before the mulberry tree germinates, and fertilization must be completed one month before picking the leaves and feeding the silkworm.

In summer, due to spring silkworm rearing, mulberry trees need to undergo summer cutting after picking their leaves. Therefore, during this period, mulberry trees have entered a second rapid growth period. Moreover, in summer, the temperature is high, there is much rain, and the mulberry tree absorbs more water, so this is the most needed nutrient fertilizer.

3.3 Water and Fertilizer Demand Analysis

Soil is the foundation for the growth of mulberry trees. The content of soil nutrients directly affects the growth and development of mulberry trees. The types of fertilizer used in mulberry gardens are generally N, P, and K fertilizers, and the main organic fertilizers used are human manure, manure, and other manure. Xie Guiping et al. conducted research and diagnosis on N, P, and K fertilizers in mulberry orchards, and their soil nutrient content is shown in Table 1 [9]. The content of commonly used organic fertilizers in mulberry orchards is shown in Table 2 [9].

The amount of fertilizer applied in a mulberry garden is closely related to soil, climate, fertilizer types, and the growth status of the mulberry tree. It is generally based on the amount of nutrients required for the growth and development of the mulberry

Table 1. Nutrient content of mulberry garden soil.

Level	Organic matter (%)	Total nitrogen (%)	Hydrolyzed nitrogen (%)	Available phosphorus (%)	Abundance of nutrients
1	>4	>0.2	> 150	> 40	Ample
2	3–4	0.15–0.2	120–150	20–40	Ample
3	2–3	0.1–0.15	90–120	10–20	Ample
4	1–2	0.075–0.1	60–90	5–10	More adequate
5	0.6–1	0.05–0.075	30–60	3–5	Lack
6	<0.6	< 0.05	< 30	< 3	Less lacking

Table 2. N, P, K nutrient content of commonly used organic fertilizers in mulberry orchards.

Fertilizer name	N (%)	P (%)	K (%)	Remarks
Human feces and urine	0.5–0.8	0.13	0.21	Quick acting, slightly alkaline, can be used as base fertilizer or topdressing
Barnyard manure	0.5	0.11	0.5	Late-acting, slightly alkaline, used as base fertilizer or top dressing after rotting ripe
Silkworm excrement	0.93	0.9	0.27	Late-acting, slightly alkaline, applied after rotting is ripe
Soil miscellaneous fertilizer	0.20	0.08	0.58	Retarded, slightly alkaline, green manure composition changes greatly
Meju	6.3	0.40	0.10	Late-acting, high-efficiency, can be used as base fertilizer or top dressing
Wheat straw	5.0	0.09	0.50	Delayed effect, used as base fertilizer
Vegetation ash		1.29	8.33	Delayed and slightly alkaline, can be used as top dressing

tree. The nutrient content in the annual mulberry branch and leaf harvest, the natural fertilizer supply capacity of the soil, and the absorption and utilization rate of various fertilizers are used as the basis for determining the fertilizer amount. During the growth process of mulberry trees, they need to cut branches and pick leaves every year, which inevitably leads to the loss of a large amount of nutrients. Therefore, timely and effective supplementation of mulberry gardens can ensure the normal growth and development of mulberry trees. Fertilization in mulberry orchards is generally applied in four seasons:

spring fertilizer, summer fertilizer, autumn fertilizer, and winter fertilizer. Table 3 shows the yield and annual fertilization amount of mulberry orchards [10].

Table 3. Mulberry garden yield and annual fertilization amount.

Industrial volume (kg)	N	Urea	P	Ca(H ₂ PO ₄) ₂	K	K ₂ SO ₄
1000	15	33	6	40	8	16
1500	23	50	9	60	12	24
2000	40	87	16	107	20	40
2500	50	109	20	133	25	50
3000	60	130	24	160	30	60

Fertilization methods should be different depending on the type of fertilizer. For organic fertilizer, ditch and hole application are generally used, and it is required to be slightly away from the mulberry root system. As for ditch application, it is generally applied between rows. When applying fertilizer in a hole, it is also necessary to open the fertilizer hole between two trees and slant it between rows. Do not approach the root of the tree to avoid affecting the growth of the root system. Chemical fertilizers with high fertilizer content are generally applied in caves, located between two trees but at least 20 cm from the tree trunk [10].

4 The Key Technology of Water and Fertilizer Integration Machine

4.1 Intelligent Irrigation System

The main functions of an intelligent irrigation system are: first, to achieve intelligent control of the entire irrigation system; The second is to take water from the water source, and through the pressurization system, fertilization system, filtration system, measurement system, intelligent control system, intelligent management and Internet of Things system of the head hub, water and fertilizer will be poured into the field and transported to the root system of the crop through the transmission and distribution pipe network and irrigator; The third is to install a remote monitoring system in the mulberry garden for continuous monitoring around the clock; Fourth, real-time and dynamic observation of crop growth conditions and equipment [11].

With the wide application of computer technology, make full use of it to automatically monitor and control the agricultural environment, create a suitable crop growth environment, accurately and timely master environmental data, and predict crop growth and incidence rate of crop diseases based on real-time monitoring data to establish accurate Effective agricultural environmental monitoring and comprehensive management system has become a management technical problem to be solved in the current controllable environment agricultural production. The monitoring system designed by Lin Fengsheng et al. comprehensively uses sensor testing technology [3], RS-485 bus technology, GPRS wireless communication technology, TCP/IP network communication

technology, and effectively improves the operating performance of the intelligent irrigation system, but it does not consider the instability of the actual agricultural environment and cannot carry out precise irrigation. Bi Qianqian and other intelligent irrigation systems designed with ZigBee technology are low cost [12], simple to operate, and widely applicable, which can effectively improve the utilization rate of water resources in agricultural production, but they are only limited to the control of water flow and do not take into account fertilization concentration. The intelligent irrigation system based on NB-IoT designed by Cheng Zhangxiang and others uses NB-IoT and cloud communication to realize real-time monitoring of the irrigation site [13].

In response to the problems of rough management mode and low automation of intelligent irrigation control systems in the application of traditional water and fertilizer integration technology, Wang Xiaoli et al. developed an intelligent irrigation control system that integrates field information collection [14], remote automatic control, equipment operation status monitoring, and irrigation process regulation with modern technologies such as automatic control principles, sensors, and wireless communication technology, an irrigation decision model based on soil ET moisture was established, which effectively improved the automation of field irrigation management and improved the utilization rate of irrigation water, but did not combine the technology of precise fertilizer distribution. Qiu Yimin et al. designed an irrigation model based on image recognition and BP neural network [15], first using image recognition technology to determine whether crops are in a sick state, then using CWSI index to determine whether non-sick crops need irrigation, and finally combining the key factors affecting crop growth and BP neural network to construct an irrigation model, which has a certain accuracy for crops, but lacks research and analysis of irrigation needs of different species. Lu Xutao et al. designed a networked paddy crop precision irrigation system based on smart agricultural technology [16], and established an optimal deployment model of communication nodes, a crop water consumption prediction model, a precipitation prediction model, an optimal irrigation decision-making model, and a precise irrigation decision-making system based on fuzzy control theory. An optimal deployment method of irrigation network communication node based on the improved moth fire optimization algorithm improved by Vno Diagram is proposed, although it can be adaptively controlled by paddy irrigation equipment for precise irrigation through system decision-making, but the system relies too much on unstable weather forecast parameters, which may make the error too large and cannot achieve accurate irrigation.

At present, there are mainly several mainstream irrigation system controllers in the market: the first type uses the ST series microcontroller as the lower controller of the irrigation system. The system compares the soil moisture detected by the soil moisture sensor with the set soil moisture threshold to control the irrigation execution module. Zou Shengping et al. designed an intelligent irrigation system using the STC89C52 microcontroller as the core controller [17]. The system can collect real-time parameters such as temperature, humidity, and light intensity, with stable operation and simple operation. Liu Jun designed an intelligent irrigation system using the STM32 microcontroller as the core controller [18], achieving remote control of the irrigation process. The system can quickly respond to status and control commands, and accurately execute irrigation tasks. Lan Yu et al. designed an intelligent irrigation system based on STM32

microcontroller and raspberry pie that can intelligently detect plant species and provide scientific irrigation solutions [19]. The system can be used remotely with corresponding mobile apps, achieving the goal of scientific planting and water resource conservation. The second method is to use the Arduino microcontroller as the core controller of the irrigation system, which can play a role in automatic irrigation. Yang Zhiqin used the Arduino microcontroller as the core controller to design an intelligent irrigation system that controls irrigation based on the upper and lower limits of soil [20], and achieved automatic water renewal function of the water storage tank through a water level sensor. Fu Ning et al. designed an intelligent irrigation system using Arduino microcontroller as the core controller [21]. The system utilizes temperature sensors and soil humidity sensors to collect the temperature and humidity of crop growth, and automatically completes irrigation tasks based on crop growth habits. Sun Borui developed an intelligent irrigation system based on LSTM neural network using Raspberry Pi as the core controller [22], achieving real-time collection and monitoring of environmental data and remote control of irrigation switches. This ensures a good growth environment for crops while saving water resources.

4.2 Precise Fertilizer Dispensing Technology

If different fertilizers are simply mixed and fertilized at one time, this will directly affect the growth of mulberry trees, and excessive water and fertilizer can also cause environmental pollution issues such as soil acidification. Therefore, reasonable and accurate mixing of water and fertilizer is of paramount importance. The core lies in the precise control of EC and PH, which improves the water and fertilizer control rate and accuracy. Zhan Pan designed a fuzzy PID controller for water and fertilizer integration equipment [23], ensuring the accuracy of water and fertilizer application dosage, increasing crop yield, and saving water and fertilizer resources. Yuan Hongbo et al. studied an incremental PID fertilizer liquid regulation algorithm based on an improved Smith predictor [24]. The system has a high regulation speed and an error within the required range. Niu Yin et al. designed a mixed fertilizer control method based on variable universe fuzzy algorithm [25]. The system can better adapt to changes in formula and rotational irrigation conditions, and the control speed and accuracy have been improved. Shi Shi et al. designed an intelligent variable fertilizer allocation scheme based on fuzzy control algorithm [26], which can achieve high-precision dynamic adjustment of water and fertilizer. Wei Xianwen et al. studied the application of pH fuzzy control for water fertilizer integrated machines [27], reducing system overshoot and stability time, and improving anti-interference ability. Li Qi et al. designed a model reference adaptive conductivity regulation strategy [28], which allows the system to quickly stabilize under various disturbances and has high control accuracy. Li Qi et al. designed an accurate and intelligent control system capable of fully automatic online detection and real-time adjustment [29]. Wu Qi designed a water and fertilizer integrated control system based on particle swarm optimization and fuzzy PID algorithm [30], realizing automatic irrigation and fertilization and precise fertilizer allocation of the water and fertilizer integrated system. Wang Xiaolong designed a precise water and fertilizer ratio control system [16]. In this research method, two adjustable speed water pumps were used to respectively

absorb water and fertilizer, indirectly monitoring the concentration of water and fertilizer ratio, and achieving precise water and fertilizer ratio. In addition, the fuzzy PID control algorithm was also applied to the system. This study has certain limitations, as the error generated by the flow meter affects the concentration, Suitable EC sensors and pH sensors were not used to monitor the parameters of water fertilizer solutions. Liu Yangchun designed a variable rate fertilization mechanical device that can achieve the use of three different fertilizers [31], and based on this, developed a variable rate fertilization operation control system that can meet the needs of variable rate fertilization while meeting different fertilizers. However, this research plan has high cost and does not provide real-time monitoring of water and fertilizer concentration. A number of accurate studies make the development of water and fertilizer integrated machine have broad prospects.

In the process of transformation from traditional agricultural production mode to modern agriculture, a new technological mode has also been derived: “Internet plus” intelligent distribution technology mode. This mode is the result of the comprehensive integration of computer technology and intelligent fertilization, which fully conforms to the development trend of modern agricultural informatization. Zhang Qian elaborated and discussed the application of “Internet plus” intelligent fertilizer distribution technology model [32]. On the one hand, in order to promote the precision of fertilizer distribution by combining intelligent fertilizer distribution technology, intelligent technology and big data were introduced into the intelligent fertilizer distribution system to conduct real-time monitoring and analysis of soil water and fertilizer; On the other hand, it expands information collection and management to include crop varieties, crop cultivation, and environmental protection, making data analysis more convincing.

4.3 Efficient Water-Saving Irrigation Technology

In the current situation of water shortage, traditional water and fertilizer irrigation is no longer suitable for the development of the new mulberry industry. In the case of insufficient irrigation water, the mulberry leaves produced by mulberry trees are extremely susceptible to wilt and are not suitable for use as food for silkworm babies. Therefore, it is necessary to develop efficient water-saving irrigation technologies.

The most significant advantage of integrated water and fertilizer efficient water-saving irrigation technology is that crop irrigation and fertilization take effect quickly, and the full utilization rate of water and fertilizer is much higher than traditional water and fertilizer irrigation technology. The application of integrated water and fertilizer efficient water-saving irrigation technology can effectively avoid fertilizer application on excessively dry topsoil, resulting in problems such as volatilization loss of fertilizer nutrients and slow dissolution and absorption; In particular, it can effectively avoid the phenomenon of applying nitrogen fertilizer commonly used by fruit trees and crops to the ground, which not only saves nitrogen fertilizer, but also effectively protects the ecological environment [33]. Therefore, the integrated efficient water-saving irrigation technology of water and fertilizer has significant significance in significantly improving fertilizer utilization.

According to the relevant research by Professor Zhang Chenglin of South China Agricultural University [34], the integrated irrigation and fertilization system can save

up to 50–70% of fertilizer compared to traditional fertilization methods, effectively saving the planting cost of orchard crops; At the same time, the application of this agricultural irrigation technology has greatly reduced the water pollution and fertilizer damage caused by excessive fertilization in fruit tree planting.

The implementation of water and fertilizer integration technology in mulberry orchards has significant water and fertilizer saving effects, greatly improving the utilization rate of water and fertilizer; And can save labor; Compared to traditional flood irrigation, the integrated technology of water and fertilizer combines an appropriate amount of water and soluble fertilizer, and then delivers them to the soil near the root of the fruit tree accurately, quickly, and timely through the irrigation equipment system, reducing water evaporation and nutrient loss. Research by Lu and Wang [35], has shown that the water and fertilizer usage in apple orchards using integrated water and fertilizer technology is significantly lower than those using ordinary irrigation technology. The total irrigation and fertilization amount are significantly reduced compared to the control, with a decrease of 62.7% and 42.3%, respectively. Lu et al. [36], found that banana orchards using water and fertilizer integration technology save 49.6% water and 22.9% fertilizer compared to conventional irrigation methods. Zeng Zhi and other researchers have shown that the Shatian pomelo orchard using the integrated technology of water and fertilizer saves 395.2 yuan/mu of cost [37], 15.97% of fertilizer, and 27.73% of water compared to the conventional irrigation and fertilization orchard. Comprehensive analysis shows that the integrated technology of water and fertilizer can effectively save water and fertilizer resources, especially in areas with complex terrain, dry climate, and lack of water resources. It can save about 50% water and about 25% fertilizer.

5 Application Analysis of Water and Fertilizer All-In-One Machine in Mulberry Garden

The integrated technology of water and fertilizer is a black hole for ordinary mulberry farmers. Most mulberry farmers are unaware of new agricultural production methods and new technologies, and fail to understand their use value. Moreover, due to their relatively low educational background and lack of technical training, it is difficult to avoid encountering difficulties in the promotion process. In the process of planting mulberry, mulberry growers can only rely on their usual accumulated experience to irrigate by flooding, and are not aware of problems such as resource shortages.

Although the integrated technology of water and fertilizer has obvious advantages, it requires a large amount of funds to purchase professional equipment in the early stage, so most mulberry farmers cannot receive higher expenses. In addition, the technical development of water and fertilizer integration technology in China is not yet fully mature, coupled with large differences in local land, which cannot be fully implemented and promoted.

Due to multiple factors such as the adjustment of agricultural industrial structure and China's accession to the WTO, China's Congress has put forward higher requirements for agricultural irrigation automation technology, which indicates that the water fertilizer integrated machine will have a huge market in China. At the same time, from a long-term perspective, the integrated technology of water and fertilizer will develop towards full

functionality, simple operation, precise control, and low cost. In view of the booming trend of “precision agriculture” in recent years, the “precision control” of water and fertilizer integration has become particularly important and significant [38].

According to the current development status of water and fertilizer integration technology in China, Ma Yi discussed the development status and trend of water and fertilizer integration technology based on the development needs of agriculture in China [5]. The application area of water and fertilizer integration technology will further increase, which is an inevitable trend of agricultural development now; Water and fertilizer integration technology will also become the basic condition and inevitable requirement for the development of agricultural modernization. The national government will issue preferential policies and increase investment in technology research, making great contributions to the improvement and promotion of water and fertilizer integration, with significant results.

5.1 Efficient Water-Saving Irrigation Technology

After the above analysis, an efficient intelligent irrigation system for mulberry fields, water and fertilizer can be developed on the basis of existing intelligent irrigation systems, which can achieve precision, modernization, and informatization of mulberry gardens. The system uses ST series microcontrollers, raspberry pies, or Arduino microcontrollers as lower level controllers, servers as upper level computers, sensor technology, RS-485 bus technology, GPRS wireless communication technology TCP/IP network communication technology and other technologies are used to establish a network platform. ZigBee technology, neural network technology, and other technologies are used to improve water resource utilization. Irrigation decision-making based on soil ET moisture, image recognition, and BP neural network irrigation models are used to improve the automation of field irrigation management, achieving comprehensive and real-time management of mulberry orchard information, as well as integrated automatic control and allocation of water and fertilizer.

5.2 Efficient Mulberry Garden Intelligent Irrigation System

On the basis of the research on multiple precision fertilization techniques analyzed in Article 4.2, appropriate algorithms and controllers suitable for the mulberry garden water fertilizer integrated machine, such as fuzzy PID control algorithm and fuzzy PID controller, are selected and integrated into the control software of the water fertilizer ratio control system to achieve self adjustment during the water fertilizer ratio irrigation process and achieve the goal of water fertilizer integrated irrigation; Select appropriate EC sensors and pH sensors to monitor the parameters of water and fertilizer solutions, and improve the accuracy of the concentration of water and fertilizer solutions.

6 Summary

In summary, this article focuses on the demand for mulberry orchards and the key technologies of water and fertilizer integrated machines. Firstly, it analyzes and studies the current situation of mulberry plantation cultivation and the problems existing in the

development of mulberry orchards, mainly focusing on issues such as weak technological innovation ability and lagging industrial development. Secondly, it analyzes the water and fertilizer demand in mulberry orchards. Through reading various literature, it analyzes various methods and technologies, And it is proposed to adopt an efficient intelligent irrigation system for mulberry fields and establish a new and precise fertilizer distribution system to study the integrated machine for mulberry water and fertilizer. In recent years, there has been a large number of mature technological advancements in the research of integrated water and fertilizer technology, and the popularization of integrated water and fertilizer machines in various mulberry gardens is of utmost importance. Under the promotion of the “East Mulberry to West Movement” project in China, the integrated water and fertilizer machine in mulberry gardens has great potential for future development. Further, the flexible application of water and fertilizer integration technology in mulberry gardens can reduce the labor intensity of sericulture farmers and improve planting efficiency.

Through summary and analysis, the development trend of the integrated water and fertilizer machine in mulberry orchards is expected: the application of the integrated water and fertilizer machine in mulberry orchards will be an important research direction in the future mulberry industry, and how to more efficiently save water and fertilizer, improve the comprehensive production capacity of farmland will also be a research hotspot; Studying efficient intelligent irrigation systems and establishing new and precise fertilizer distribution systems will also be breakthroughs in maximizing agricultural benefits.

Acknowledgments. The authors are highly thankful to The College Students’ Innovative Entrepreneurial Training Plan Program for Program (No. S202210605092) for its financial support. This research was financially supported by First-class Discipline Construction Project of Hechi University, Guangxi Colleges and Universities Key Laboratory of AI and Information Processing (Hechi University), Education Department of Guangxi Zhuang Autonomous Region.

References

1. Tan, F., Peng, Y., Luo, J., et al.: Discussion on the selection and application of labor-saving machinery for management operation in Guangxi Mulberry Garden. *Guangdong Sericulture* **54**(11), 3–4 (2020)
2. Yi, Z.: Research on the application of drip irrigation water and fertilizer integration technology in agricultural irrigation. *J. Smart Agric.* **1**(22), 77–79 (2021)
3. Lin, F., Fu, X.: Research on Key technologies of wireless remote monitoring of agricultural environment. *Comput. Knowl. Technol.* **18**(11), 30–32 (2022)
4. Yang, X.: Water and fertilizer management measures of mulberry Garden in Chuxiong City. *Yunnan Agric. Sci. Technol.* **250**(S1), 90 (2010)
5. Ma, Y.: Discussion on the development status and trend of water and fertilizer integration technology. *J. Smart Agric.* **2**(13), 98–100 (2022)
6. Liao, X.: Hechi City of Guangxi actively promotes the development of 100 billion mulberry cocoon and silk industry. *News. Sericultural Sci.* **41**(03), 30 (2021)
7. Qi, G., Le, P., Wei, W., et al.: Current situation and development of mulberry industry in Guangxi. *Acta Sericologica Sinica.* **41**(06), 1115–1119 (2015)

8. Du, Z., Liu, J., Liu, G., et al.: Study on Mulberry as economic forest for soil and water protection. *Guangxi Sericulture* **03**, 10–12 (2001)
9. Xie, G., Xia, Y.: Application of N, P and K fertilizer and diagnosis of fertilizer deficiency in mulberry garden. *Yunnan Agric.* **373**(02), 66–68 (2020)
10. Zhao, P.: Optimal fertilization and management of mulberry garden. *Agric. Henan* **603**(07), 30 (2022)
11. Du, K.: Research and implementation of wireless remote monitoring system for agricultural environment. *Chin. Acad. Agric. Sci.* (2007)
12. Bi, Q., Fang, C.: Research on intelligent irrigation systems based on ZigBee and multiple sensors. *Internet Things Technol.* **13**(04), 34–36 (2023)
13. Lu, X., Zhang, L., Liu, H., et al.: Design of smart agriculture paddy field crop network precision irrigation system. *J. Agric. Eng.* **37**(17), 71–81 (2021)
14. Wang, X., An, S., Zhang, G., et al.: Intelligent irrigation control system based on cloud platform. *Agric. Eng. Inf.* **12**(06), 55–59 (2022)
15. Qiu, Y., Xing, L., Wu, P.: Research on irrigation model based on image recognition and BP neural network. *J. Xinyang Agric. College* **31**(02) (2021)
16. Wang, X.: Research and development of precise water and fertilizer ratio control system [D] Northwest A&F University, Shaanxi Province, Project 211 College, Project 985 College, directly under the Ministry of Education, (2018)
17. Zou, S., Chu, G: Design of intelligent irrigation system based on STC89C52. *Internet Things Technol.* **10**(09), 99–100+105 (2020)
18. Liu, J.: Design of intelligent irrigation control system based on STM32. *Agric. Mech. Res.* **44**(10), 181–184 (2022)
19. Lan, Y., Huang, Z., Zhu, Y., et al.: Design and implementation of intelligent irrigation system based on STM32 and Raspberry Pi. *Internet Things Technol.* **11**(07), 114–117 (2021)
20. Yang, Z.: Design and application of intelligent irrigation system based on Arduino microcontroller. *Mech. Electr. Eng. Technol.* **45**(11), 80–83 (2016)
21. Fu, N., Liu, H., Tang, Y., et al.: Design of intelligent irrigation system based on Arduino microcontroller. *Inf. Comput. (Theoretical Edition)* **08**, 76–77 (2019)
22. Sun, B.: Development of Intelligent Irrigation System Based on LSTM Neural Network. Tarim University, Xinjiang (2023)
23. Zhan, P.: Design and research of precise fertilizer distribution control system. Southwest University (2016)
24. Yuan, H., Li, L., Wang, J., et al.: Design and experiment of regulating equipment for integrated nutrient solution of water and fertilizer in greenhouse. *Agric. Eng. Inf.* **32**(08), 27–32 (2016)
25. Niu, Y., Zhang, K.: Variable domain fuzzy control of mixed fertilizer process in irrigation and fertilization system under wheel irrigation. *Trans. Chin. Soc. Agric. Mach.* **47**(03), 45–52 (2016)
26. Shi, S., Fen, T., Ji, X., et al.: Design of intelligent fertilizer dispensing terminal control system based on PLC. *J. Chin. Agric. Mech.* **37**(01), 191–196 (2016)
27. Wei, X., Sun, G., Wei, K., et al.: Application of fuzzy PID control in fertilizer stock mixing system of water and fertilizer integrated machine. *Technol. Innov. Appl.* **12**(06), 36–38 (2022)
28. Li, Q., Gao, Y., Wang, J., et al.: Adaptive control of conductivity of nutrient solution in hydroponic balcony vegetable machine. *J. Henan Agric. Sci.* **48**(01), 153–159 (2019)
29. Li, Q., Ma, L., Wang, K.: Integrated water and fertilizer applicator EC and pH improved active disturbance rejection decoupling control. *J. Chin. Agric. Mech.* **41**(02), 161–170 (2020)
30. Wu, Q.: Design of Water and Fertilizer Integrated Control System Based on Particle Swarm Optimization and Fuzzy PID Algorithm. Agricultural University of Hebei (2021)
31. Liu, Y.: Research on Key Technologies of Variable Rate Fertilization Precision Operation Equipment. China Academy of Mechanised agriculture Sciences, Beijing (2012)

32. Zhang, Q.: Application of “Internet +” intelligent fertilizer distribution technology mode. *Agric. Eng. Inf.* **42**(21), 14+40 (2022)
33. Mao, H.: Application of high efficiency Water-saving irrigation technology of integrated water and fertilizer in orchard. *J. Smart Agric.* **2**(14), 82–84 (2022)
34. Yu, L.: Discussion on integration of water and fertilizer in high efficient water-saving irrigation area. *Times Agricultural Machinery.* 45(06), 20+22 (2018)
35. Lu, C., Wang, J.: Water and fertilizer management in apple orchards under integrated water and fertilizer conditions. *Northern Fruit Trees* **03**, 35–36 (2020)
36. Lu, C., Li, H., Qin, Z.: Experiment on integrated drip irrigation technology for banana fertilizer and water. *Chin. Fruit Trees* **05**, 48–50 (2011)
37. Zeng, Z., Guo, C., Hu, X.: The demonstration application effect of integrated water and fertilizer for Shatian pomelo. *Agric. Technol.* **38**(08), 16–18 (2018)
38. Gao, X., Yao, P., Sun, Z.: Research on monitoring operation of water and fertilizer machine based on computer network. *J. Agric. Mech. Res.* **44**(03), 208–211+230 (2022)



A Review of the Research on Temperature and Humidity Control Systems in Silkworm Rooms

Yuanji Chen, Sen Zheng, Danfeng Li, Yuna Tang, and Yong Xu^(✉)

Hechi University, Hechi 546300, China
xuyong@hcnu.edu.cn

Abstract. With the continuous development of social progress, automatic control system has been widely used in temperature and humidity control. This paper first introduces the development status and prospect of silkworm houses, reviews the influence of silkworms under different temperature and humidity conditions, then discusses the research and development trend of temperature and humidity control system, and finally summarises the application of temperature and humidity control system in silkworm rooms.

Keywords: Temperature and humidity · Control system · Silkworm · Algorithm

1 Introduction

Temperature and humidity are one of the main factors affecting the normal growth and development of silkworms, so ensuring appropriate temperature and humidity is an important condition for improving cocoon yield and silkworm silk quality. The temperature and humidity required by silkworms at different ages are also different [1, 2], 1–3 years old 8 silkworms are generally called small silkworm stage, 4–5 years old silkworms are generally called large silkworm stage; Among them, the suitable temperature for the growth and development of silkworm stage was 26–27 °C, and the relative humidity was 85–90%; The suitable temperature for the growth and development of silkworm stage is 23–25 °C, and the relative humidity is 65–70%.

In recent years, simple silkworm houses have been widely promoted in Jiangnan region of China due to the advantages of low investment, good safety, separation of human settlements and sericulture sites, convenient auxiliary facilities and suitable for professional large-scale operation. Temperature and humidity regulation is a key technical measure for simple silkworm houses. Sericulture in spring, summer and autumn is widely practiced in southern China, but due to the large changes in temperature and humidity in southern China day and night and throughout the year, traditional room temperature breeding and artificial temperature regulation methods (such as ground fire dragon type and iron barrel type) have low efficiency, poor safety and poor effect, which greatly limits the benefits of sericulture [3]. The use of artificial intelligence to automatically regulate the indoor temperature and humidity of the silkworm room to

meet the growth needs of silkworms at different times, and realize artificial intelligence automation of the growth needs of silkworms, which can not only promote the complete development of silkworms and excellent physique; It can also increase sericulture production, reduce the labor force of silkworm farmers and increase income.

2 Development Status of Temperature and Humidity Control in Silkworm Rooms

At present, there are fewer devices on the market that can uniformly control the temperature and humidity of the silkworm room, and the heating of the silkworm room is mainly through brazier charcoal combustion, iron drum sawdust burning and household air conditioning control three heating methods, brazier charcoal combustion and iron drum sawdust burning. Although the equipment is simple and low cost, there will be the risk of carbon monoxide poisoning and fire, and the air conditioning temperature control is simple to operate, but its cost is too high and the heating is uneven. Cooling is controlled by household air conditioning, environmental protection air conditioning and water curtain + negative pressure fan, the cost of using household air conditioning is higher, although the cost of environmental protection air conditioning is lower, but the cost of water curtain + negative pressure fan is only slightly higher than that of environmental protection air conditioning. It can also moisturize. In terms of moisturization, most silkworm houses still use traditional artificial sprinkling through the ground or wet gauze to wrap small silkworm frames for humidification, although it can effectively improve the humidity of the silkworm room and is simple, but it will be difficult to grasp the humidity change, which is not good for small silkworms. In terms of dehumidification, mainly the use of dehumidifiers and air conditioners, dehumidifiers dehumidification will make the temperature rise, air conditioning dehumidification effect is better and do not need to purchase additional equipment, reduce infrastructure investment costs [4]. At present, the complete set of temperature and humidity intelligent control system has been applied to modern greenhouse, storage and animal husbandry industries, but its cost is too high and not targeted, and it is not suitable for sericulture [5]. Therefore, the design and research of silkworm house temperature and humidity control can reduce the cost of silkworm farming and improve the efficiency of silkworm farming.

2.1 Mulberry Silkworm Cocoon Industry Development Prospects

From the perspective of development status, with the improvement of sericulture technology, its output and economic benefits have gradually improved, and the production and cooperation mode have been innovated, which has promoted the diversification of income forms. From the perspective of technological development, farmers have developed from the original individual to large-scale breeding, and some townships have professionals to guide and effectively improve the quality of their technology. From the perspective of the macro development of mulberry sericulture, the extension of its products is not limited to the domestic market, at present, China's silk, mulberry wine and other related products have been exported abroad, and have a good market [6].

The silkworm industry has a broad market, which is mainly reflected in the increasing domestic market and the growing demand in the international market. As a traditional industry in China, sericulture has certain advantages, and the industries related to it for a long time are not only large in quantity, but also guaranteed in quality. High-quality silkworm products have been affirmed by the market and have a good reputation, which has laid a good foundation for silkworm products to compete in the market and promote the export of related products, especially silk products. From the current point of view, the silk produced in China has been exported to more than 100 countries, the product quality is recognized, and the market share is growing, which provides opportunities for the further development of China's silkworm industry, and the development prospects are very good.

2.2 Shortcomings in the Development of Silkworm Cocoon Industry

The labor-intensive characteristics of sericulture production determine sericulture production. Unlike other plantations and aquaculture, it can be operated on a large scale. The sericulture production cycle and dependence on natural conditions make sericulture production unable to be mechanized, and the production methods have hardly changed significantly in the past thousand years. At present, the actual situation of sericulture production in China is still quite far from the conceptual modern agriculture, mainly due to the scale of operation, the mode of production, and the low production efficiency, and has not fundamentally got rid of the traditional mode of small-scale peasant economy.

The labor-intensive characteristics of sericulture production determine that silkworm production, unlike other planting and breeding industries, can be operated on a large scale. The sericulture production cycle and dependence on natural conditions make sericulture production unable to be mechanized, and the production methods have hardly changed significantly in the past thousand years. At present, the actual situation of sericulture production in China is still quite far from the conceptual modern agriculture, mainly due to the small scale of operation, backward production methods, and low production efficiency, and has not fundamentally got rid of the traditional model of small-scale peasant economy [7–9].

3 The Importance of Temperature and Humidity for Sericulture

Ancient wild silkworms grow, develop and reproduce under natural conditions, and have great adaptability to changeable natural environmental factors. In order to obtain better economic results, people move silkworms into indoor breeding and cultivation, and after people purposefully and long-term cultivate and domesticate them into silkworms, their ability to adapt to the natural environmental conditions that vary greatly has also weakened, and gradually formed the habit of relying more and more on people's careful care and superior environmental conditions. Nowadays, silkworms can only grow and develop well under suitable environmental conditions, otherwise they will not only cause poor growth and development, significant differences between individuals, and the most serious will also endanger survival.

3.1 Effect of Temperature on Silkworms

Silkworms are ectothermic animals, the body temperature changes with the change of the environment, the ambient temperature is high, the body temperature of the silkworm is high, the ambient temperature is low, the body temperature of the silkworm is low, and the body temperature of the silkworm is basically close to the temperature. The starting point of silkworm development is 7.5 °C, below this temperature, the life activities of silkworms are weak or even stopped, and silkworms can grow and develop above 7.5 °C. The development temperature range of silkworms is 7.5–35 °C, in this temperature range, the higher the temperature, the more vigorous the life activities of silkworms, the faster they eat mulberry, and the growth and development are accelerated; The lower the temperature, the slower the life activity of silkworms, the slower it eats mulberry, and the slower its growth and development. Therefore, low temperature weather (15–20 °C, under natural temperature conditions without heating, silkworm seed puberty period (or incubation period) will be extended, some up to 15 days, or even more than 20 days; The age of silkworms will be extended by 1–4 days; The sleep time of silkworms will also be extended, each time extended by 2–3 days.

3.2 Effects of Humidity on Silkworms

Humidity mainly affects silkworm water metabolism and pathogen reproduction. Under humid conditions, the evaporation of silkworm water is slow. The body water rate rises rapidly after eating mulberry, which is prone to physiological disorders, and the pathogen multiplies rapidly, which is prone to stiff disease. In a dry environment, the mulberry leaves in the silkworm seat are easy to wither, causing hunger of silkworms, which is easy to cause weakness and viral diseases [10].

3.3 Suitable Temperature and Humidity for Silkworms at Various Ages

Silkworms of different ages have different metabolic rates and immunity, and the enzymes that affect metabolism and the reproduction of microorganisms are closely related to temperature and humidity, so the needs of silkworms of different ages for temperature and humidity are not the same. Moreover, silkworms are more sensitive to the temperature of the surrounding environment, and if the temperature is too high or low, it is not conducive to the growth and development of silkworms. Therefore, in the whole silkworm period, it is necessary to strictly control the temperature and humidity in the silkworm room, create a relatively good growth environment for the silkworm, avoid the phenomenon of sudden cold and hot, and the indoor temperature can only fluctuate in a small range. Therefore, mastering and adjusting the appropriate temperature and humidity of silkworms of all ages in the process of sericulture is the key to obtaining high yield and quality of silkworm cocoons. According to the data, in each age of silkworm growth and development, in order to meet its most suitable temperature and humidity, the environmental temperature and humidity should be regulated according to Table 1 [11].

Table 1. Suitable temperature and humidity range of silkworms at different ages

Age	Suitable temperature/°C	Relative humidity/%
1 instar	27.0–28.0	80.0–85.0
2 instars	26.0–27.0	85.0–90.0
3 instars	25.0–26.0	75.0–80.0
4 years old	24.0–25.0	70.0–75.0
5 years old	23.5–24.5	65.0–70.0

4 Research Status of Temperature and Humidity Control System in Silkworm Room

The temperature and humidity in the silkworm room are mostly controlled by manual attendance, which has problems such as inaccurate temperature and humidity control and high labor intensity. In order to solve these problems, several methods of intelligent control of temperature and humidity in silkworm rooms are introduced below.

4.1 The Single-Chip PID Algorithm Controls the Temperature and humidity of the Silkworm Room

At present, most of the silkworm room temperature and humidity control systems are composed of single-chip microcomputer control module, temperature and humidity acquisition module, keyboard input module, display module and control execution module. The modular design can reduce the interference of the outside microcomputer and improve the efficiency of program operation [12]. The overall structure diagram of the system is shown in Fig. 1.

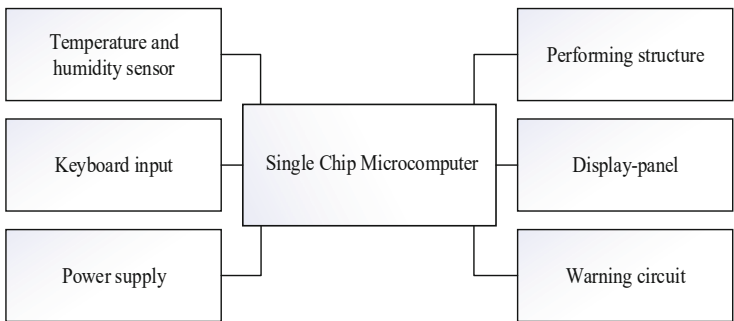


Fig. 1. Overall structure of the system

After the system starts, the single-chip microcomputer port is initialized, read the temperature and humidity of the silkworm room, and the read data is sent to the single-chip microcomputer, and the single-chip microcomputer determines whether it meets the

temperature and humidity set value range, if the read value is out of range, the single-chip microcomputer will send out the driving signal of the alarm circuit, so that the actuator, the corresponding fan, humidifier, etc. start.

Since the temperature and humidity control system is a closed-loop system, the PID control method is adopted, and the PID control method has the advantages of simple principle, convenient use and strong adaptability. The PID control subroutine is the core of the entire system software design, and its main role is to compare and calculate according to the preset basic parameters and measured values, and then control the work of various execution circuits. The overall flow chart of the temperature and humidity control system is shown in Fig. 2.

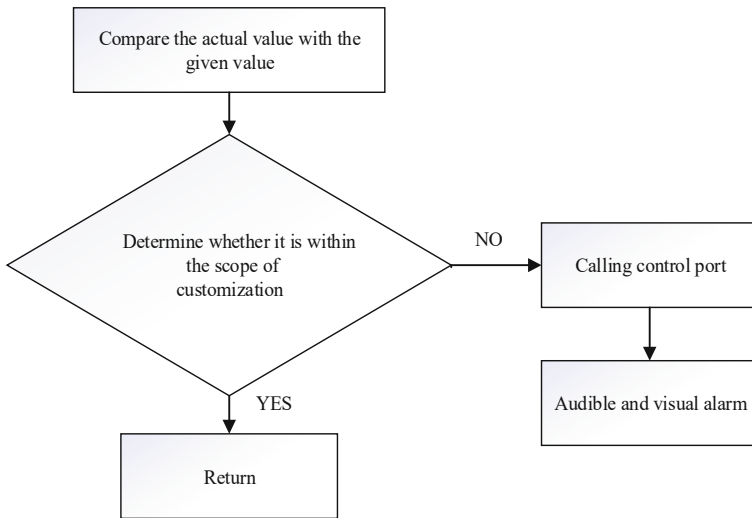


Fig. 2. Flow chart of temperature and humidity control system

The modular design of this scheme simplifies the connection between the peripheral circuit and the single-chip microcomputer, improves the operation efficiency of the program, is easy to use, and ensures that the accuracy of the system meets the requirements of the system design.

4.2 Application of Fuzzy Control in Silkworm Room Temperature and Humidity Control System

Because the temperature and humidity system of the silkworm room is a multivariate, large inertia nonlinear system, and there are coupling and delay and other phenomena, it is difficult to establish an accurate digital model and control, and the application of fuzzy control method can control the temperature and humidity parameters of the silkworm room without knowing the accurate mathematical model of the controlled object in advance, and the conditional statement summarized by human experience is used as the

control rule, which is suitable for the control of time-varying and hysteresis nonlinear systems.

Figure 3 is the general fuzzy control system structure diagram, its main core control part is the fuzzy controller in the system, and in the fuzzy control mentioned in the text, its mechanism is reflected by the fuzzy controller [13, 14].

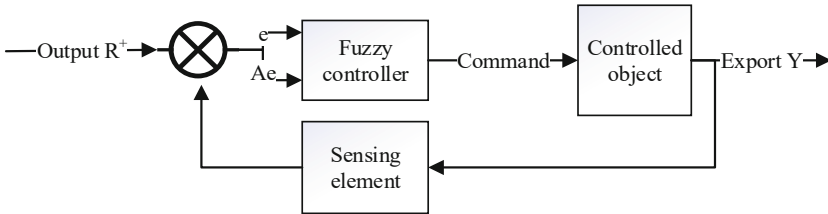


Fig. 3. Schematic diagram of the structure of the fuzzy control system

Therefore, the use of fuzzy control technology to control the temperature and humidity in the silkworm room can create suitable environmental conditions for silkworms, so that mulberry silkworms can grow and develop better, which is of great significance for improving the economic benefits of silkworm production.

4.3 Wireless Temperature and Humidity Silkworm Room Control System Based on Internet of Things Technology

The overall block diagram of this scheme is shown in Fig. 4, which is mainly composed of a control circuit and its external circuit, a temperature and humidity sensor circuit, a control circuit and a communication module circuit. As can be seen from Fig. 4, the STM32 chip computer is connected to a temperature and humidity sensor, a reset circuit, a clock circuit, a power indication circuit, a control circuit, and a WiFi module. Among them, the power supply circuit controls the WiFi module through the voltage conversion circuit, and the WiFi module controls the APP end. The STM32 microcontroller controls humidifiers, dehumidifiers, cooling devices and heating devices through control circuits [15].

The software design of this system includes two parts: the software design of the single-chip microcomputer and the software design of the mobile APP. The software design of the single-chip microcomputer mainly includes serial port initialization and ESP8266 initialization, reading temperature and humidity sub-function, serial port receiving interrupt handling function, serial port transmitting data function and delay function. The overall design of the APP software includes loading interface layout resources, obtaining interface elements, and setting up a connection server that listens to events.

In general, the temperature and humidity of each point in the silkworm room are different, and multiple sensors should be used to collect temperature and humidity more accurately, through the WiFi module, the temperature and humidity in the silkworm room can be monitored in real time and controlled, and more control objects can be added, such

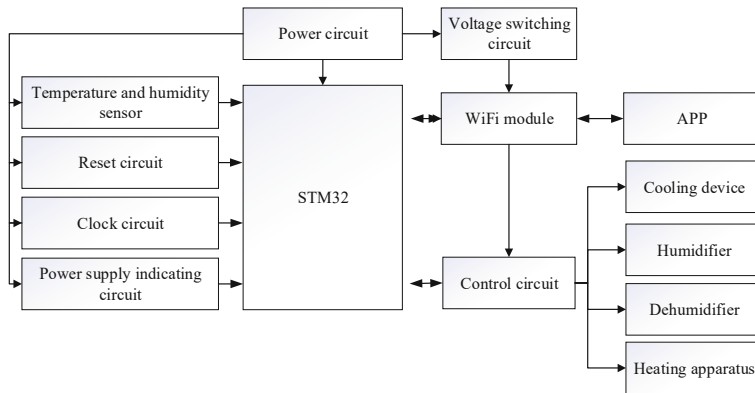


Fig. 4. Overall block diagram of temperature and humidity control of IoT

as light control and carbon dioxide concentration monitoring, etc., to further improve the application range of the system.

5 Development of Silkworm Room Temperature and Humidity Control System

With the continuous development of industrial control automation technology, many equipment have achieved unattended or uninterrupted operation, in order to ensure the normal operation of the equipment, the duty personnel need to check whether the parameters are normal. Temperature and humidity are commonly used controlled parameters of various equipment, if the single-chip microcomputer system can intelligently monitor and control the above parameters, it is of great significance for the normal and stable operation of the equipment.

5.1 Defects of the Temperature and Humidity Control System of the Silkworm Room

As early as the 18th century, human beings invented dry and wet bulbs and hair hygrometers, and the traditional method was to use test equipment such as humidity meters, hair hygrometers, bimetallic measuring meters and humidity paper, and then manual testing, artificial ventilation, humidification, cooling and other operations on substandard houses. Its operation mode is time-consuming and laborious, and the control effect can be imagined.

Generally, the temperature and humidity measurement in the temperature and humidity control system adopts thermistors and moisture sensitive capacitors, and this traditional analog temperature and humidity sensor generally needs to design signal conditioning circuits and go through complex calibration and calibration processes, so the measurement accuracy is difficult to guarantee, and there are certain problems in linearity, repeatability, interchangeability and other aspects. This sensor is only suitable for those occasions where the number of measuring points is small and the accuracy is not

required. Therefore, designing a temperature and humidity detection and control system with high precision, good stability and low cost will have a certain market.

The ordinary controller is an integral module, cannot replace a component with other parts with the same function and different interfaces, if you want to replace a local function only replace the entire controller, and this increases the cost of maintenance and upgrade. Inconvenient fault judgment. When troubleshooting some special faults, it is impossible to accurately judge the fault of the controller.

5.2 Development Trend of Silkworm Room Temperature and Humidity Control System

Intelligence

At present, a variety of intelligent temperature and humidity sensor series products have been developed internationally. These smart temperature sensors contain humidity and temperature sensors, A/D converters, signal processors, memories (or registers), and interface circuitry. Some products also come with multiplexing converters (MUX), central controllers (CPUs), random access memory (RAM), and read-only memory (ROM). Intelligent temperature and humidity sensor is characterized by the ability to output temperature and humidity data and related temperature and humidity control quantities, suitable for various microcontrollers (MCUs); Moreover, it is based on hardware to achieve testing functions through software, and its intelligence also depends on the level of development using software.

Miniaturization

New temperature and humidity sensors are developing rapidly from analog to digital, from integrated to intelligent and networked. Integrated temperature and humidity sensors mainly include analog integrated temperature and humidity sensors and intelligent temperature and humidity sensors (also known as digital temperature and humidity sensors). Analog integrated temperature and humidity sensor is a special IC that integrates temperature and humidity sensor on a small chip and can be used to complete temperature and humidity measurement and analog signal output functions. The characteristics of analog integrated temperature and humidity sensor have a single function (only measure temperature and humidity), small measurement error, low price, fast response speed, long transmission distance, small size, micro power consumption and many other advantages, suitable for long-distance measurement and control nonlinear calibration is not required, and peripheral circuitry is simple.

Modularity

In order to reduce costs, modular temperature and humidity controllers can be used, such as $Y = A + B + C + D$ mode. Each function is a separate module that can work independently of other modules, such as A is the module that collects temperature, and B is the module that collects humidity.... In addition, E is also a module for collecting temperature. If after purchase, the customer finds that the temperature sensor of module A is damaged or cannot operate normally due to the high pressure of the environment, and the temperature cannot be collected correctly. At this time, the temperature sensor

of the E module can withstand high voltage, and we can replace A with E to become $Y = E + B + C + D$ without the need for customers to completely purchase a new humidity and temperature controller [15].

6 Summary

Based on the traditional sericulture method and the environment required for sericulture, this paper compares the advantages, development status and development prospects of the temperature and humidity control system of silkworm house. It describes the development status of China's traditional sericulture industry, as well as the importance of environmental temperature and humidity to silkworm growth and development and silk quality, and also shows the basic framework, design ideas, basic principles and optimization schemes of temperature and humidity control system. Due to the inherent nonlinearity, large hysteresis and time variability of temperature and humidity, it is impossible to establish an accurate mathematical model, and the traditional control method is not effective. By improving sensor accuracy and reducing costs, combining the Internet of Things and intelligent control algorithms will be an important development trend of silkworm room temperature and humidity control system. Through the silkworm room temperature and humidity control system, the indoor temperature and humidity can be adjusted more effectively, which is conducive to the growth and development of silkworms, and all-weather monitoring can relieve the pressure of silkworm farmers.

Funding Statement. The authors are highly thankful to The College Students' Innovative Entrepreneurial Training Plan Program for Program (No. S202210605032) for its financial support. This research was financially supported by First-class Discipline Construction Project of Hechi University, Guangxi Colleges and Universities Key Laboratory of AI and Information Processing (Hechi University), Education Department of Guangxi Zhuang Autonomous Region.

References

1. Wan, F.: Sericulture pays attention to temperature and humidity. *Hunan Agric.* **11**, 17 (2004)
2. Zheng, G., He, Y.: Analysis on the industrialization development of mulberry and silkworm rearing. *Rural Pract. Technol.* **02**, 23–24 (2021)
3. Mahmood, M.H., Sultan, M., Miyazaki, T.: Significance of temperature and humidity control for agricultural products storage: overview of conventional and advanced options. *Int. J. Food Eng.* **15**(10) (2019)
4. Li, Y., Qin, Y., Wei, G., et al.: Effectiveness analysis of temperature and humidity regulation facilities for small silkworms in Guangxi. *Northern Sericulture* **35**(02), 36–38+40 (2014)
5. Zhang, Y., Dai, X.: Experimental study on all-weather automatic control system of temperature and humidity in silkworm room. *J. Agric. Mech. Res.* **12**, 128–130+149 (2008)
6. Lan, H.: Analysis of mulberry rearing technology and industry development trend. *Guangdong Sericulture* **55**(06), 9–10 (2021)
7. Xiang, Z., Gu, G., Li, J., et al.: Study on sustainable development Strategy of sericulture in China. In: *Chinese Sericulture Economic Management Seminar*. Hangzhou, Zhejiang, China, pp. 4–86+83 (2012)

8. Li, X.: Mulberry industry development and efficient breeding technology innovation. *Guangdong Sericulture* **56**(01), 1–3 (2022)
9. Huang, X.: Development prospect of mulberry industry and analysis of high efficiency mulberry rearing technology. *Guangdong Sericulture* **54**(10), 1–2 (2020)
10. Ramadiani, R., Widada, D., Widiastuti, M., et al.: Temperature and humidity control system for broiler chicken coops. *Indonesian J. Electr. Eng. Comput. Sci.* **22**(1327), 10.11591 (2021)
11. Chen, T., Peng, J., Lu, X.: Application of water curtain air conditioning in regulating temperature and humidity of silkworm house. *Guangxi Sericulture* **55**(03), 65–67 (2018)
12. Wan, K., Liu, Z.: Design of greenhouse temperature and humidity wireless control system. *Process Autom. Instrum.* **42**(12), 86–89+99 (2021)
13. Hu, R.: The principle and application of fuzzy control. *Sci. Technol. Trend.* **02**, 19–20 (2019)
14. Nguyen, A.-T., Taniguchi, T., Eciolaza, L., et al.: Fuzzy control systems: past, present and future. *IEEE Comput. Intell. Mag.* **14**(1), 56–68 (2019)
15. Purwanto, F.H., Utami, E., Pramono, E.: Design of server room temperature and humidity control system using fuzzy logic based on microcontroller. In: 2018 International Conference on Information and Communications Technology (ICOIACT), pp. 390–395. IEEE (2018)



PassDiff: A New Approach for Password Guessing Using Diffusion Model

Sheng Guo¹, Ming Duan^{1,2}(✉), Yibin Du¹, Wei Wang¹, and Lulu Guo¹

¹ College of Cyberspace Security, Information Engineering University, Zhengzhou 450001, China

mdscience@sina.com

² Henan Key Laboratory of Network Cryptography Technology, Zhengzhou 450001, China

Abstract. Password guessing models can be broadly divided into three classes: dictionary-based password guessing model, password guessing model based on probability statistics and password guessing model based on deep learning. Recurrent neural networks and generative adversarial networks are the main deep learning techniques used for password guessing in the past. In this paper, we propose a novel PassDiff method for password guessing using denoising diffusion probabilistic models (DDPMs). Considering the similarity between the password space and the text space, we incorporate a byte-level tokenizer in the input phase and optimize the sampling process by modifying the source code. We encode a special character, and it makes PassDiff can handle input of variable length and obtain variable output without manual truncation. The experimental results show that PassDiff produces high-quality passwords even with minimal denoising steps. We recommend setting the denoising steps to 5–50, which can increase the sampling speed by tens of times. Compared with PassGAN, the training process of PassDiff is more stable and the cracking rate is also significantly improved. Specifically, when the denoising steps is set to 10 and 10^8 passwords are generated, PassDiff increases the cracking rate by 3.17%, 6.33% and 13.22% on 12306, CSDN and RockYou datasets, respectively.

Keywords: Denoising diffusion probabilistic models · Passwords · Deep learning

1 Introduction

Password authentication, as a security mechanism to protect user privacy, has become the most popular authentication method for a long time because of its simplicity, practicality and efficiency. At the same time, attackers and researchers tried to apply various emerging technologies to the password guessing model. This promoted the development of cryptanalytic techniques.

Password guessing models can be broadly divided into three classes: dictionary-based password guessing model, password guessing model based on probability statistics and password guessing model based on deep learning.

The dictionary-based password guessing model usually converts the original password of the dictionary through predefined rules to generate a new extended set, that is, the guessing set. The quantity of the guessing set depends on the amount of the original dictionary and the number of rules. It is characterized by simplicity and speed, but the generation of rules depends on personal experience. HashCat [1] and John the Ripper (JTR) [2] both efficiently implement dictionary-based approaches.

The Markov model [3] and the Probabilistic Context Free Grammars (PCFG) model [4] are two classical representatives of the password guessing model based on probability statistics. The Markov model uses the statistical laws of the dictionary to calculate the probability of the next character according to the previous character or context, output to the guessing set in probability order, and guess as many passwords as possible with least small guessing set. The PCFG model firstly preprocesses the password structure, and divides the character types of the password into numbers D, letters L and special characters S, then it counts consecutive segments. For example, the password “abc@123456” will be recorded as L3S1D6. The PCFG model usually statistics the frequencies of all structures and strings, retains the high probability structures and then fills them with high probability strings, finally outputs the filled passwords as the guessing set.

In recent years, deep learning technology has made great progress, and password guessing models based on deep learning arise at the historic moment. Deep learning techniques such as Recurrent Neural Networks (RNNs), Generative Adversarial Networks (GANs), Variational Auto-Encoders (VAEs) have also been applied to password guessing models. In addition, many scholars have done a lot of research on the combination of deep learning and traditional password guessing techniques such as PCFG.

In 2016, Melicher et al. [5] proposed the FLA model. They firstly used RNN to extract and predict password features. Liu et al. [6] presented a PL model based on PCFG and Long Short-Term Memory network (LSTM). Wang et al. [7] constructed PR and PR+ models based on PCFG and RNN. In 2019, Hitaj et al. [8] proposed PassGAN, the first author to apply the generative adversarial network to the password guessing model. Nam et al. [8] proposed rPassGAN, which applied RNN to PassGAN and adopted a dual discriminator structure. Fu et al. [9] modified the generative and discriminant networks of PassGAN to DenseNet and named their model DenseGAN.

Unlike probability-based or rule-based password guessing models, models built on deep learning make no assumptions about the password structure. The guessing set generated by a deep learning method is not restricted to any specific subset of the password space. Inversely, neural networks can detect extensive password information beyond the power of traditional password guessing models.

Recently, diffusion model [10] has become one of the most popular generative models due to its powerful generative ability. In 2020, Ho et al. [11] published Denoising Diffusion Probabilistic Models (DDPMs), the first paper to give a rigorous mathematical derivation to prove that the diffusion model can produce high-quality images. Song et al. [12] accelerated the sampling and proposed DDIMs, which was a more efficient probabilistic model and had a same training process with DDPM. Peebles et al. [13] proposed Diffusion Transformers (DiTs), which replaced the commonly-used U-Net with Transformer. In addition to applications in computer vision, speech generation and

natural language processing, more applications of diffusion model are being explored by researchers [14].

1.1 Our Contribution

As far as we know, it is the first time to apply the diffusion model to the password guessing model. When generating 10^8 passwords, our model can increase the cracking rate by 13.22% on RockYou dataset. Through a lot of experiments, we prove the great potential of the diffusion model in the field of password guessing. Our works expand the application scope of the diffusion model.

We innovatively use the byte-level tokenizer embedding for encoding the password into the input vector of the diffusion model. By modifying the model interface, the passwords can be better input to the diffusion model.

By adjusting the parameters and modifying the source code, we optimize the denoising process to better fit the characteristics of the passwords. Additionally, we improve the sampling speed of the model.

1.2 Organization

The rest of our paper is organized as follows: We briefly introduce the basic knowledge of generative adversarial network and diffusion model in Chap. 2. In this chapter, we present our model: PassDiff. The fourth chapter is the description of our experimental settings. In Chap. 5, we introduce and discuss our experimental results. In Chap. 6, we draw the experimental conclusions and prospect our future work.

2 Background and Related Works

2.1 Generative Adversarial Networks

Generative adversarial networks (GANs) are made up of two parts: a generator (G) and a discriminator (D), both of which are constructed using neural networks. G usually takes random features or noise as its input. In the training process, G learns the distribution of the input data and makes its output gradually approach the distribution of the input. D estimates the conditional probability of the examples given a set of tagged inputs. Throughout the training process, D spares no effort to distinguish the real samples and fake ones. After hundreds of thousands of such games, G and D eventually reach an equilibrium, with G generating a sample that is consistent with the distribution of input data, and D having no advantage in guessing the source of the samples. The process can be express by the formula as follows:

$$\min_G \max_D \left(\sum_{i=1}^n \log D(x_i) + \sum_{j=1}^n \log(1 - D(G(z_j))) \right), \quad (1)$$

where G and D represent generator and discriminator, respectively.

2.2 Denoising Diffusion Probabilistic Models

The Denoising Diffusion Probabilistic Models (DDPMs) involve two Markov chains: a forward chain (diffusion process) for adding noise to the input data, and a backward chain (denoising process) for transforming the noise back into the original data. The diffusion process is often manually designed to convert any original distribution into a simple prior distribution such as standard Normal distribution, while the denoising process reverses this process using a parameterized transition kernel learned from a deep neural network. The denoising process continuously generate new data points in two steps: first sampling a random data from the prior distribution and then performing the original sampling.

Mathematically, given a data distribution $x_0 \sim q(x_0)$ and assuming that the transition kernel of the forward chain is $q(x_t|x_{t-1})$, the diffusion process will generate a sequence of random variables x_1, x_2, \dots, x_T . We use $q(x_1, \dots, x_T|x_0)$ to denote the joint distribution of x_1, x_2, \dots, x_T conditioned on x_0 . According to the chain rule of conditional probability, it can be decomposed into the following formula:

$$q(x_1, \dots, x_T|x_0) = \prod_{t=1}^T q(x_t|x_{t-1}). \quad (2)$$

In DDPM, the transition kernel $q(x_t|x_{t-1})$ is usually manual designed to gradually convert the data distribution $q(x_0)$ to a identifiable prior distribution. Gaussian perturbation is often used as the transition kernel, and the most typical design of transition kernel $q(x_t|x_{t-1})$ is

$$x_t \sim N\left(\sqrt{1 - \beta_t}x_{t-1}, \beta_t\right), \quad (3)$$

Among them, $\beta_t \in (0, 1)$ is a hyperparameter selected before training. We use this kind of transition kernel here to simplify our discussion. In addition, other types of transition kernels apply equally well. As we choose Gaussian perturbation as transition kernel, we can get expressions for the $q(x_t|x_0)$ of all $t \in \{0, 1, \dots, T\}$ by marginalizing the joint distribution in the equality (2). Specifically, let $\alpha_t = 1 - \beta_t$, $\bar{\alpha}_t = \prod_{s=0}^t \alpha_s$, we have

$$x_t \sim N\left(\sqrt{\bar{\alpha}_t}x_0, (1 - \bar{\alpha}_t)\right). \quad (4)$$

Given x_0 , by choosing a random vector, $\varepsilon \sim N(0, 1)$, and transforming it by the following formula

$$x_t = \sqrt{\bar{\alpha}_t}x_0 + (1 - \bar{\alpha}_t)\varepsilon, \quad (5)$$

we can easily obtain a sample of the x_t . When $\bar{\alpha}_T \approx 0$, the distribution of x_T is almost Gaussian, so we have

$$q(x_T) = \int q(x_T|x_0)q(x_0)dx_0 \approx x_T \sim N(0, 1). \quad (6)$$

The diffusion process consistently destroys the input data with noise until it loses all the features. To produce new data points, DDPM firstly samples a random noise point

that follows the prior distribution, and then conducts a regular reverse Markov chain to increasingly eliminates the noise. Concretely, we use a prior distribution $p(x_T)$ (where $x_T \sim N(0, 1)$) and a knowable transition kernel $p_\theta(x_{t-1}|x_t)$ to parameterize the reverse Markov chain. The construction of the diffusion process makes the $q(x_T)$. Approximately satisfy $x_T \sim N(0, 1)$. The knowable transition kernel $p_\theta(x_{t-1}|x_t)$ can be calculated by the following formula

$$x_{t-1} \sim N(\mu_\theta(x_t, t), \Sigma_\theta(x_t, t)), \quad (7)$$

where θ represents the model parameters, the mean $\mu_\theta(x_t, t)$ and the variance $\Sigma_\theta(x_t, t)$ are learned from deep neural networks, a very classical implementation is to learn using U-Net. Using the reverse Markov chain, we can firstly sample a noise point $x_T \sim p(x_T)$ and then iteratively calculate it from the knowable transition probability $p_\theta(x_{t-1}|x_t)$ until $t = 1$, and finally we will get a data point x_0 .

Training the reverse Markov chain to correspond to the forward Markov chain is very important to the denoising process. So, we need to select a proper parameter θ so that the reverse process joint distribution $p_\theta(x_0, x_1, \dots, x_T) = p(x_T) \prod_{t=1}^T p_\theta(x_{t-1}|x_t)$ is very close to the joint distribution $q(x_0, x_1, \dots, x_T) = q(x_0) \prod_{t=1}^T q(x_t|x_{t-1})$ of the forward process (Fig. 1).

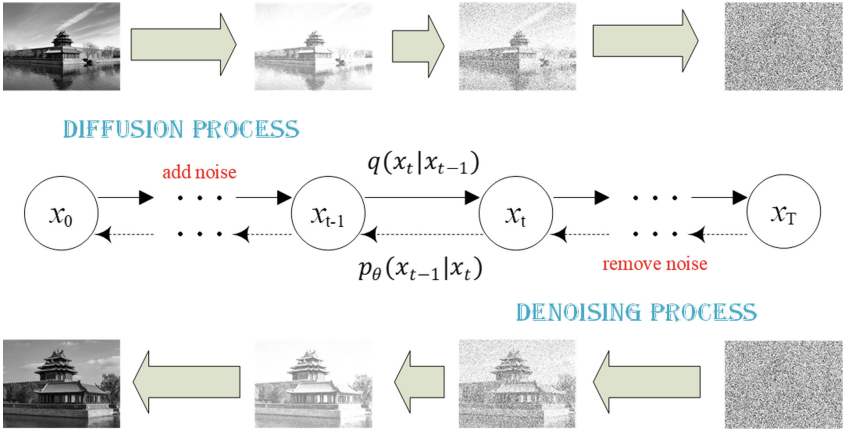


Fig. 1. Diffusion model architecture

3 Proposed Model: PassDiff

The standard diffusion model is mainly applied in the field of image generation, and both its input and output are 2D vectors. Li et al. [15] made some modifications on the standard diffusion model. They used Transformer to learn about noise distribution and added the text embedding step and rounding step. They named their model the Diffusion-LM model, which applies the diffusion model to the domain of controllable

text generation. Aman [16] simplified the source code of Diffusion-LM model to make it easier to use. The diffusion-LM model takes text as input and encodes the text into a 1D integral vector using word-level tokenizer embedding. In the diffusion process, the integral vector will be converted to a 1D floating vector. At the end of the denoising process, the rounding step converts a 1D floating vector back to a 1D integer vector and outputs semantically similar sentence text via the tokenizer. Diffusion-LM model, however, can only output fixed-length text, which needs to be truncated manually.

Word-level tokenizer embedding treats text as a sequence of words, typically divided by spaces or punctuation marks. Encoding each word or word with more than a certain frequency can preserve the semantic connection between words to a certain extent, but it is easy to cause the encoding range being too large.

Byte-level tokenizer embedding treats text as a sequence of bytes, encoding both a single byte and multiple bytes in a row. Single-byte encoding has poorer semantic connections, and multi-bytes encoding is a compromise between single-byte encoding and word-level encoding.

Considering the similarity between password space and text space, the semantic relationship between the preceding and following characters of the password is weaker than that in the corpus. Referring to the Diffusion-LM model, we encode the input password with character-level tokenizer, and propose a PassDiff password prediction model. In addition, we analyzed the code of the denoising process and found that it could only generate passwords of fixed length. We introduce a random factor so that users can generate passwords of any length within the required range according to their own needs, which makes the generated dictionary more close to the distribution characteristics of the training set and improves the password cracking rate to some extent.

We found no significant advantage of multi-bytes encoding over single-byte encoding. For simplicity, this article encodes only a single byte, i.e., only 1 special byte and 95 visible bytes. Our coding range is 0 to 95. The special byte is represented as 0, and the remaining visible bytes are represented in ASCII order from 1 to 95. The encoding of the special character can handle input of variable length and obtain variable output without manual truncation. We found that the PassDiff model produces high-quality passwords even with minimal denoising steps. We recommend setting the denoising steps to 5 to 50, which can increase the sampling speed by tens of times (Fig. 2).

4 Experiment Setup

Our experimental environment is a DELL Precision 5820 workstation with 128G memory, 10 CPU cores, and an NVIDIA GeForce RTX 3090 graphics card. All of our experiments were performed under Win10 and Ubuntu 22.04. We conducted PassGAN related experiments on Win10, using the source code of rnnPassGAN [8, 17]. Experiments related to diffusion model were carried out on Ubuntu 22.04, and the source code came from minimal-text-diffusion [16].

4.1 Dataset

We chose three classical datasets for the experiment: 12306, CSDN and RockYou. We start by suming up the amount of passwords in the three datasets. In the second step,

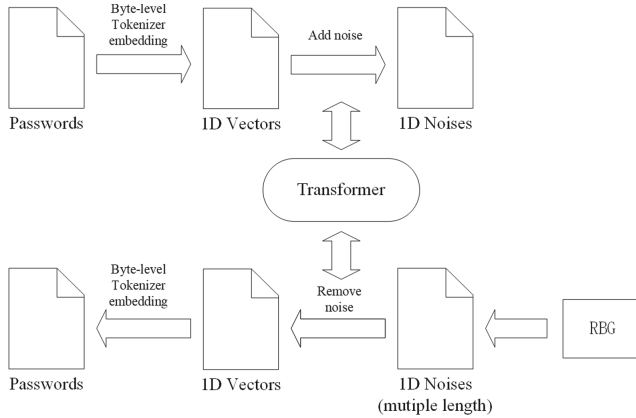


Fig. 2. PassDiff model architecture

we deleted passwords that contain invisible characters or are longer than 15 and marked them as Totals1. The number of unique passwords and the repetition rate were also recorded. We continued to divide the passwords in Totals1 into the train set and the test set at random ratios of 80% and 20%, respectively, and noted the count of unique passwords. The statistical results are as follows.

Table 1. Totals, unique totals and repetitive rate of 12306, CSDN and RockYou

Datasets	Totals	Totals1 (Uniques)	Repetition rate (%)	Train set (Uniques)	Test set (Uniques)
12306	131,653	131,652 (117,807)	10.5	105,321 (95,283)	26,331 (24,974)
CSDN	6,428,632	6358,467 (3973,939)	37.5	5086,773 (3256,919)	1271,694 (910,100)
RockYou	32,584,847	32,330,944 (12,350,913)	61.8	25,864,755 (10,562,791)	6466,189 (3498,440)

We counted the ratios of various length interval of the three datasets as follows.

It can be seen from Tables 1 and 2, 12306 dataset is small in scale with low repetition rate, while RockYou dataset has a large size with high repetition rate. The length intervals of the three datasets are all relatively concentrated.

4.2 Hyperparameters

The main hyperparameters of our PassDiff model include: training rounds, batch size, diffusion steps, denoising steps, input length, output length, learning rate and so on. At present, we set some parameters to the default values of the original diffusion

Table 2. The ratio of length intervals of 12306, CSDN and RockYou

Datasets	Totals1	Ratio of various length intervals				The primary length interval (ratio)
		1–5 (%)	6–10 (%)	11–15 (%)	> 15 (%)	
12306	131,652	0	94.11	5.89	0	6–10 (94.11%)
CSDN	6,358,467	0.62	76.56	21.72	1.1	8–12 (90.54%)
RockYou	32,330,944	4.32	86.54	8.36	0.78	5–11 (94.18%)

model. Moreover, we fixed the diffusion steps and the learning rate at 2000 and 0.0001, respectively.

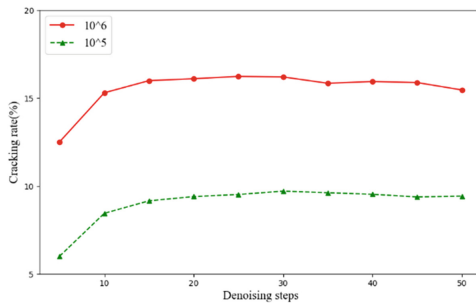
Using the PassDiff model, we generate 10^5 to 10^8 unique passwords, and calculated the cracking rate between the generated dictionary and the test set. Moreover, we compare our cracking rate with PassGAN’s dictionary of the same size. When calculating the cracking rate, the passwords in the generated dictionary are unique ones, while the train and the test sets contain duplicate passwords.

5 Evaluation

5.1 Experiments on the PassDiff Model

For the 12306 dataset, we conducted a lot of experiments of PassDiff model with different training rounds, batch sizes and denoising steps. Due to the slow sampling speed of the diffusion model, we mainly generated dictionaries of size of 10^5 and 10^6 for comparison.

The two dot plots below show how the cracking rate of the 12306 dataset varies with the number of denoising steps. The quantity of training rounds in both experiments was 200,000, and both generated 10^5 and 10^6 passwords, but their batch sizes were 1024 and 256, respectively (Figs. 3 and 4).

**Fig. 3.** Cracking rate of 12306 with batch size = 1024

The above plots show that the cracking rate is positively correlated with the batch size and the amount of the generated dictionary. As the number of denoising steps raises,

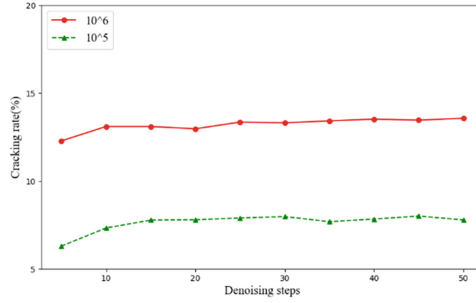


Fig. 4. Cracking rate of 12306 with batch size = 256

the cracking rate gradually increases and stabilizes around 20–25 steps, indicating that the PassDiff model requires only a small number of restore steps to produce a good dictionary.

Figure 5 illustrates the variation pattern of cracking rate with training rounds for the 12306 dataset. In this experiment, the batch size is 1024 and the number of denoising steps is 20. Respectively, we generated 10^5 and 10^6 passwords.

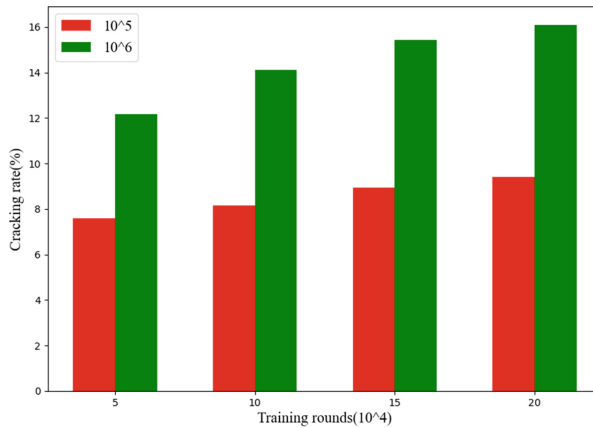


Fig. 5. Cracking rate of 12306 varies with the training rounds

As shown in the above graph that the cracking rate gradually increases with the increase of training rounds. Through other experiments, we found that the cracking rate had not reached the peak when training 200,000 rounds. If we increase the training rounds, we will acquire a higher cracking rate.

For CSDN and RockYou datasets, we also conducted experiments to generate dictionaries of different sizes under the conditions of different training rounds, different batch sizes and different denoising steps. The datasets showed roughly the same rule as 12306. Here, we present only our representative experiments. Figures 6 and 7 show the effect of the number of denoising steps on the cracking rate of CSDN and RockYou when

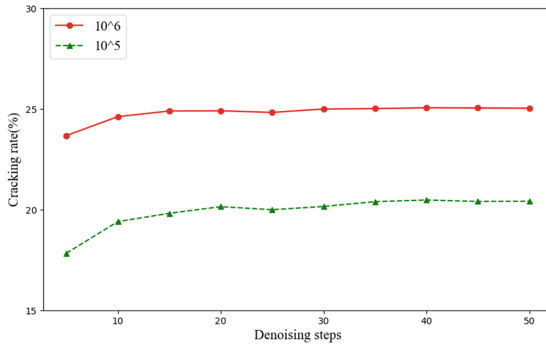


Fig. 6. Cracking rate of CSDN varies with the denoising steps

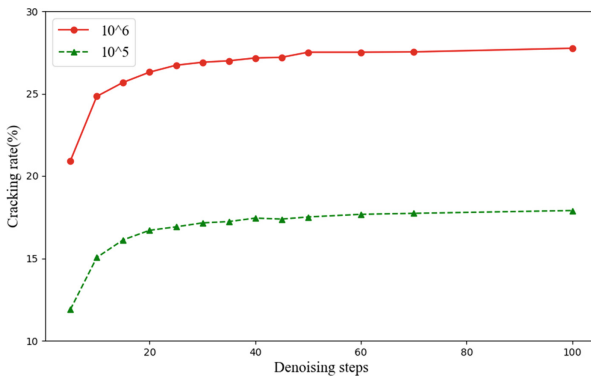


Fig. 7. Cracking rate of RockYou varies with the denoising steps

generating 10^5 and 10^6 passwords, respectively, under the condition that the quantity of training rounds is set to 200,000 and the batch size is 1024.

It is visible that the cracking rate of CSDN and RockYou is higher than 12306 on the whole. We think this is due to their repetition rate being higher than 12306. The cracking rates of CSDN and RockYou datasets gradually stabilized at about 40 denoising steps, exceeding the denoising steps required for 12306. Upon further analysis, we attributed it to inadequate training and larger data size.

From the experimental results of PassDiff model above, we analyze that increasing the quantity of both training rounds and batch size can improve the cracking rate. With the increase of the number of denoising steps, the crack first gradually rises to the maximum value and then tends to be stable.

Additionally, we explored the variation of repetition rate, training time and sampling time. We find that the repetition rate is positively correlated with the number of training rounds and denoising steps. The higher the repetition rate, the longer it takes to generate a unique password dictionary of the same size. The training time is proportional to the quantity of training rounds and batch size. Regardless of the repetition rate, the sampling time is proportional to the number of denoising steps and the amount of the generated

dictionary. Take the 12306 dataset as an example. When the batch size is 1024, it takes about 31 h to train 200,000 rounds. If the denoising step is set to 20, we will need about 11 h to generate 10^7 unique passwords.

5.2 Comparison with PassGAN

We tested the cracking rate of PassGAN under the same conditions for three datasets: 12306, CSDN, and RockYou. In the paper [7], the authors show that for the RockYou dataset, the model gets the best dictionary at 199,000 rounds of training. This is consistent with our experiment. Therefore, we trained 200,000 rounds on each of the three datasets for comparison. For our PassDiff model, we sacrifice some cracking rates to generate a larger dictionary, and the parameters of our model are 200,000 training rounds, 1024 batch size, and 10 denoising steps. Our results are shown in Table 3.

Table 3. Comparison of cracking rate of PassGAN and PassDiff for 12306, CSDN and RockYou

Dataset	Model	Size of dictionary (%)			
		10^5 (%)	10^6 (%)	10^7 (%)	10^8 (%)
12306	PassGAN	6.85	13.77	21.84	34.91
	PassDiff	8.45	15.30	24.70	38.08
CSDN	PassGAN	17.12	21.27	25.31	30.99
	PassDiff	19.41	24.61	30.03	37.32
RockYou	PassGAN	9.44	16.80	26.32	37.27
	PassDiff	15.45	24.83	37.36	50.49

From Table 3, we can clearly see that our PassDiff model has significant advantages over PassGAN. When generating 10^8 passwords, the cracking rate of our model is 3.17%, 6.33% and 13.22% higher than that of PassGAN on 12306, CSDN and RockYou data sets, respectively. In addition, it is not our best performance in cracking rate. However, there is still some gap between our model and the traditional password guessing model (such as PCFG). We will keep improving our model and try to combine it with traditional methods.

6 Conclusion

In this paper, by optimizing the diffusion model parameters and increasing the number of training rounds, we propose PassDiff model with shorter training time and more stable training process than PassGAN. However, due to the slow sampling speed of diffusion model, it is difficult for the model used in this paper to generate billion-level dictionaries. The diffusion model has great potential in constructing password guessing models, and can also make great breakthroughs in theory.

In future work, we will further optimize parameters and debug other parameters such as diffusion steps and learning rate. We plan to use other neural networks to learn from the noise to improve the cracking rate. We will also try other encoding methods, such as encoding more than two characters and trying to combine them with PCFG.

References

1. HashCat: <https://hashcat.net>. Last accessed 21 May 2023
2. John the Ripper: <https://www.openwall.com/john/>. Last accessed 15 Apr 2023
3. Narayanan, A., Shmatikov, V.: Fast dictionary attacks on passwords using time-space tradeoff. In: Proceedings of the 12th ACM Conference on Computer and Communications Security, pp. 364–372. ACM (2005)
4. Weir, M., Aggarwal, S., De Medeiros, B., Glodek, B.: Password cracking using probabilistic context-free grammars. In: 30th IEEE Symposium on Security and Privacy, pp. 391–405. IEEE (2009)
5. Liu, Y., Xia, Z., Yi, P., Yao, Y., Xie, T., Wang, W., Zhu, T.: Genpass: a general deep learning model for password guessing with PCFG rules and adversarial generation. In: Proceedings of the 2018 IEEE International Conference on Communications (ICC), pp. 1–6 (2018)
6. Wang, D., Zou, Y., Tao, Y., Wang, B.: Password guessing based on recurrent neural networks and generative adversarial networks. *Chin. J. Comput.*, 1519–1534 (2021)
7. Hitaj, B., Gasti, P., Ateniese, G., Perez-Cruz, F.: PassGAN: a deep learning approach for password guessing. In: Deng, R.H., Gauthier-Umaña, V., Ochoa, M., Yung, M. (eds.) ACNS 2019. LNCS, vol. 11464, pp. 217–237. Springer, Cham (2019)
8. Nam, S., Jeon, S., Moon, J.: Recurrent GANs password cracker for IoT password security enhancement. In: Proceedings of the International Workshop on Information Security Applications, pp. 247–258. Jeju Island, Korea (2019)
9. Fu, C., Duan, M., Dai, X., Wei, Q., Wu, Q., Zhou, R.: DenseGAN: A Password Guessing Model Based on DenseNet and PassGAN. In: Information Security Practice and Experience. ISPEC 2021. Lecture Notes in Computer Science, vol. 13107, pp. 296–305. Springer, Cham (2021)
10. Anderson, B.D.: Reverse-time diffusion equation models. *Stochast. Processes Appl.* **12**(3), 313–326 (1982)
11. Ho, J., Jain, A., Abbeel, P.: Denoising diffusion probabilistic models. *Adv. Neural. Inf. Process. Syst.* **33**, 6840–6851 (2020)
12. Song J, Meng C, Ermon S.: Denoising Diffusion Implicit Models. arXiv preprint [arXiv:2010.02502](https://arxiv.org/abs/2010.02502) (2020)
13. Peebles W, Xie S.: Scalable Diffusion Models with Transformers. arXiv preprint [arXiv:2212.09748](https://arxiv.org/abs/2212.09748) (2022)
14. Yang L, Zhang Z, Song Y, et al.: Diffusion Models: A Comprehensive Survey of Methods and Applications. arXiv preprint [arXiv:2209.00796](https://arxiv.org/abs/2209.00796) (2022)
15. Li, X., Thickstun, J., Gulrajani, I., et al.: Diffusion-lm improves controllable text generation. *Adv. Neural. Inf. Process. Syst.* **35**, 4328–4343 (2022)
16. Aman, M.: Minimal Text Diffusion. <https://github.com/madaan/minimal-text-diffusion>. Last accessed 10 Apr 2023
17. Peng, K.: GAN-Based Password Guessing. <https://github.com/ponedo/rnnPassGAN-password-cracking>. Last accessed 10 Apr 2023
18. Melicher, W., et al.: Fast, lean, and accurate: modeling password guessability using neural networks. In: USENIX Security Symposium, pp. 175–191 (2016)



Combining Image Caption and Aesthetic Description Using Siamese Network

Xinghui Song^(✉) and Peipei Zhu

School of Artificial Intelligence and Big Data, Guangdong Business and Technology University,
Zhaoqing 526000, Guangdong, China
songxinghui@tiangong.edu.cn

Abstract. In recent decades, the confluence of CV and NLP technologies has grown in popularity. Many researchers have focused their attention on Image caption task. In recent years, academics have been more interested in image aesthetic description because of image aesthetic indicative of the level. In this study, we present an aesthetic description technique that combines image description and aesthetic description at the same time. We use a Siamese network to acquire datasets for training from two data domains: Image caption task and Image aesthetic description task. The parameters gained from training were migrated back to the conventional Encoder-Decoder model for testing after training. On image caption task, we chose the flickr8k datasets to reduce computing cost. On aesthetic task, the PCCD datasets was used. The final findings indicate that our technique is capable of simultaneously training datasets from two data domains and producing both kinds of image descriptions.

Keywords: Image caption · Image quality evaluation · Aesthetic description · Siamese network · Transfer learning

1 Introduction

1.1 A Subsection Sample

Image captioning (IC) is a typical multi-modal task transition from image visual content to natural language text, involving related areas such as computer vision (CV) and natural language processing (NLP), and is frequently used in semantic image search and multi-modal image understanding. Traditional IC tasks primarily explain important information about images [1–4], such as the link between an entity’s attribute and the entity, Image aesthetic quality evaluation [5] is used to describe the aesthetic information and subjective feelings of images. Image aesthetic description is a small field of image quality assessment, which mainly describes image aesthetic information, such as color, lighting, composition. It was established by Taiwan researchers in 2017 [6]. In this paper, Image caption is referred as NIC (Natural Image Caption) and Aesthetic description is referred as AIC (Aesthetic Image Caption).

It is interesting to feed a computer a diagram that understands the content on the image and gives a description of image. On AIC, most researchers construct datasets

of different scene kinds based on their own knowledge of aesthetic description, using more Encoder-Decoder model framework to fulfill the goal of aesthetic description in the existing study [7–10]. However, the most critical step in most researchers’ methods is the construction of datasets, And because of copyright issues, can’t open source. At the same time, researchers have different understandings of beauty. Therefore, in this article species. We propose five criteria for aesthetic description of images, Use standard public datasets: NIC task flickr8k datasets, which has over 8000 pictures and over 40,000 linguistic descriptions, to minimize computing costs. More than 4000 pictures and 30,000 English descriptions are included in the AIC task PCCD datasets. The topology of Siamese networks is used to simultaneously train datasets from two data domains using the integrated learning concept. The model parameters were moved to the standard NIC task model [2] after training. The final experimental results demonstrate that our technique effectively learns data from both data domains and simultaneously produces both types of picture description. In Fig. 1, we compare and analyze the picture aesthetic description provided by the current IC and AIC tasks to better demonstrate these two difficulties.

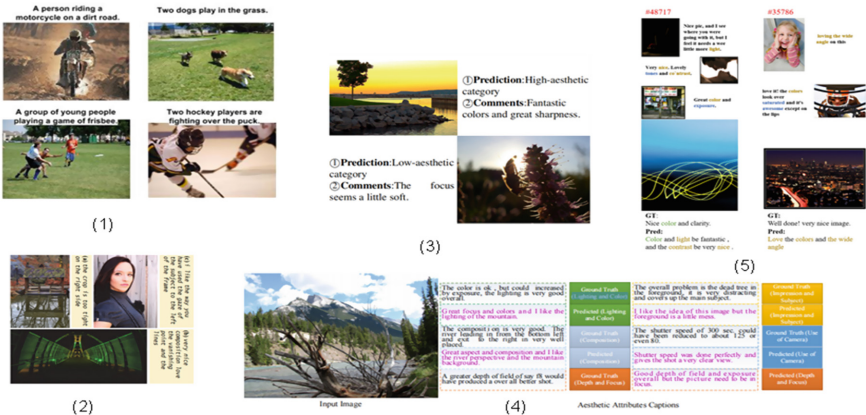


Fig. 1. Results of NIC task and AIC task at present

The image’s important information, such as the entity’s characteristics and the relationship between the entities, is depicted in Fig. 1 (1). The objective of (2) is to produce aesthetic remarks on the image, and the goal of (2–5) is to explain the evaluation of this image, sentiments, affection, and so on. (3) is tasked for perceiving visual aesthetics and generating human commentary and interpretations. The aim of (4) is to provide titles for each of the image’s attributes, including color and light, composition, depth, and focus. (5) The objective is to provide the title of tailored picture aesthetic duties for various consumers.

Figure 2 The experimental results of the present image description and aesthetic description



Fig. 2. Part of achievement display

Our main contributions include:

1. We present aesthetic description methods combining image descriptions and, to our knowledge, we are currently the first to do this work.
2. We use Siamese networks to effectively learn datasets from two data domains, the NIC and AIC tasks, and achieve image description Combining image caption and Aesthetic description results. In our tests, we had a good rate of over 65%.
3. We implemented image descriptions exporting both styles on the model.

2 Related Work

Because the aesthetic description encompasses a wider range of areas, the relevant work is divided into three categories.

2.1 Image Aesthetics Quality Evaluation

Researchers began using deep learning for automated picture feature extraction in 2014, when deep learning algorithms matured [11–16]. When compared to typical manual design characteristics, using deep learning has a far higher categorization accuracy. Google proposed the NIMA model [13] in 2018. The NIMA model produces a hierarchical distribution—from 1 to 10 for any given image, presenting better predictions of human preference, reaching 81.51% on the AVA datasets. 2019. Xin Jin et al., On the AVA aesthetic classification datasets, the suggested ILGNet obtains a classification accuracy of 85.53%. The researchers' emphasis is expanded to additional factors when they have developed a pretty sophisticated aesthetic judgment. Kong et al. [15] published a study

in 2016. A new image aesthetic datasets, AADB, comprises eight aesthetic variables, and some work has been built on AADB to assess the influence of aesthetic components on picture aesthetic quality, as well as related work on image aesthetics.

2.2 Image Caption

Image Caption, as the name implies, creates a descriptive text from a photograph, which is a difficult process. The areas of CV and NLP have made significant progress in producing text and comprehending pictures and video during the last two years. While both areas include techniques that are comparable to AI and machine learning, they have grown independently in the past and have had little contact in the scientific community. In Google CVPR2015 year papers [2], however, there has been a spike in problematic interest in the need to integrate linguistic and visual information in recent years. In natural language processing (NLP) machine translation, the Encoder-Decoder is used [17]. It connects better with recent breakthroughs in computer vision and machine translation by replacing the original Encoder RNN with the CNN structure utilized in the image. Deep learning techniques were used to turn images into text descriptions. In this new linguistic vision community, auto-description has become a key responsibility. Cho et al. [18] suggested an Attention method that does not employ unified semantic features and allows a Decoder to freely select the desired features in the in-put sequence. Xu and colleagues [3]. The Attention mechanism was used to improve the basic Encoder-Decoder system. Specifically, we employ CNN's spatial properties to extract a feature for each of the image's 196 positions, allowing Decoder to select these 196 position features during decoding [19]. The total number of labels for each image was first collected from the C words that appeared most frequently in all descriptions, and the training data for each image was obtained directly from its reported words. Chen and colleagues [20] Many improvements to Decoder RNN's structure, allowing the RNN network to not only translate picture features into text, but also to extract image features from text, all while boosting speed. 2019 [4] Starting with natural language, picture caption is proposed at the word level by predicting noun chunk sequences while carefully analyzing visual and linguistic variations, offering further grounding. External signals are in charge 2020 [1], Using abstract scene plots (Abstract Scene Graph, ASG), simultaneously controlling the desired expressed objects, properties, and relationships through the graph structure can not only reflect the user's fine-grained description intent, but also generate more diverse image descriptions.

2.3 Aesthetic Description Task

The image aesthetic task is divided into five tiers of tasks in the image aesthetic quality evaluation system, including aesthetic distribution, aesthetic score, aesthetic distribution, aesthetic components, and aesthetic description. The task was Image aesthetic/photography skills related titles for specific aesthetic aspects of color, clarity, and composition of images. The first datasets, PCCD. For the task was produced Image aesthetic/photography skills related titles for specific aesthetic aspects of color, clarity, and composition of images. Microsoft in 2018 [21] Poetically generated poetry from

images needs to satisfy both the correlation with the image and the rules of poetic language. Ghosal et al. [8] Following Chang’s work, we propose a title filtering strategy, which has compiled a cleaner, larger dataset AVA-Caption, and proposed a strategy for training convolutional neural networks that applies the LDA topic model to reviews and learns CNN parameters by fitting the topic distribution. In Jin [7], Kun et al. [6] used a larger datasets of DPC-caption; with change in their analysis. The paper comparison produced a description and score for the image aesthetic of 5 criteria (light/color, composition, depth of field/focus, theme/impression, camera use). According to Kun et al. [10], the network can simultaneously output a description of many dimensional features. A new personalized aesthetic image title (PAIC) approach for gathering and combining user preferences and improving aesthetic features for AIC tasks will be proposed in the study.

3 Methods

3.1 Training Stage

We chose to adopt [3] based on the CNN + LSTM + ATTENTION framework, with the caveat that it is generic and can be used for any framework-based Image Caption task in which visual features are extracted from ResNet101 networks trained with ImageNet and passed as input to LSTM, with the traditional image captioning dataset NIC captioning C1 and image aesthetic description captioning C2 to simultaneously at For our framework, we use a twin CNN network with shared parameters on the training visual model, trained on data from both datasets, trained training. Finally, our model training phase is shown in Fig. 3.

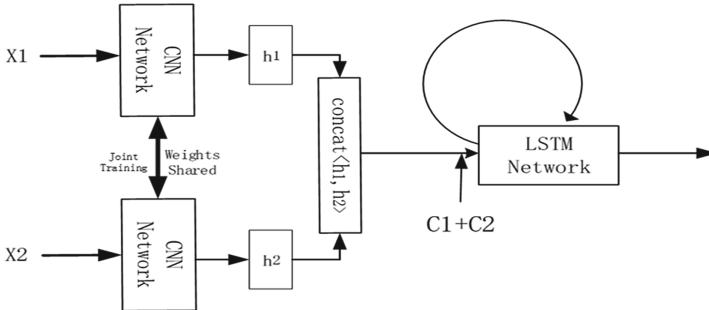


Fig. 3. Based on the twin network image description model

In Fig. 3, X1 represents the NIC image, X2 represents the AIC image, images from two datasets, after a shared parameter CNN feature extractor, yielding two eigenvectors h_1 , h_2 . The data splicing with the concat function yields an eigenvector h_0 . The h_0 contains information about the two images. C1 represents the description of image X1 of NIC and C2 represents the description of AIC image X2. The C1 and C2 data were spliced and sent to LSTM training along with h_0 . Training yielded shared CNN parameters, and LSTM parameters.

3.2 Test Phase

The used testing phase [3] for CNN + LSTM + ATTENTION, is shown in Fig. 4.

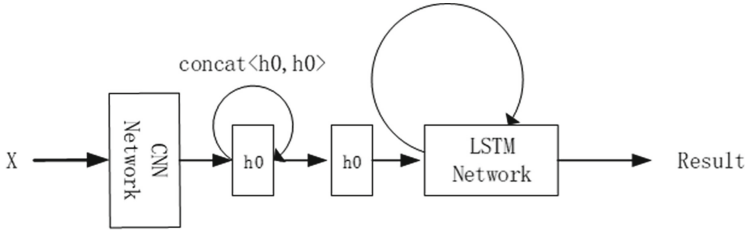


Fig. 4. The image caption generation model

We migrated the parameters trained by Fig. 3 model to model 4. In Fig. 4, X represents our test images, and the images passed via the CNN feature extractor to get the vector h_0 . In order to remain consistent with Fig. 3—1 model dimensions, we replicate h_0 . The h_0 was data stitched and then sent to the LSTM network to obtain the predicted results.

3.3 Training Details

The image feature extractor CNN was partially performed using the pre-trained Resnet101 network. The text generator uses the LSTM network. Increase the prediction effect using the Attention mechanism.

There are over 8000 photos and over 40,000 linguistic descriptions in the data from two datasets called flickr8k. More than 4,000 photos and 30,000 linguistic descriptions are included in the PCCD datasets. A json dictionary is used to store the first description of the two datasets. After doing embedding, C1 (which represents picture description) and C2 (which represents aesthetic description) were connected. The first problem encountered was the pairing problem of the two datasets. We provide two viable methods. The first, the few datasets replicate themselves. Mount data into datasets with loader and reload part of list, to data balance. The second, multiple datasets remove the excess. The balance parameter is set in the code. By True (means less copy itself), False means more removed excess. The model during tested, entering an image and then experiencing encoder, requires double at concat connection so that the data dimensions can be kept consistent before being sent to the decoder.

4 Experiments

4.1 Experimental Data

The NIC image captioning datasets uses the flickr8k datasets to reduce computational overhead. The data contained 8000 images, each paired with five descriptions. These descriptions provide a content description of the objects and events in the picture. The AIC image captioning datasets used PCCD (Photo Critique Captioning Datasets): This

datasets is generated from [6] Introduced, and is based on www.gurushots.com. Professional photographers have provided seven comments on the uploaded photos: general impression, composition and perspective, color and lighting, subject of photo, depth of field, focus and use of camera, exposure and speed.

4.2 Experiment Results and Analysis

Training indicators:

The `train_losses_step`: training set changes in the loss function with increasing step length.

The `train_accs_step`: training set changes accuracy with step length.

The `train_losses_epoch`: training sets change in the loss function with increasing epoch.

The `train_accs_epoch`: training set changes in accuracy with increasing epoch.

The `val_losses_step`: validation sets change in the loss function with increasing step length.

The `val_losses_epoch`: validation set changes in accuracy with increasing step size.

The `val_accs_step`: validation sets change in the loss function with increasing epoch.

The validation set of `val_accs_epoch`: changes in accuracy with increasing epoch (Figs. 5 and 6).

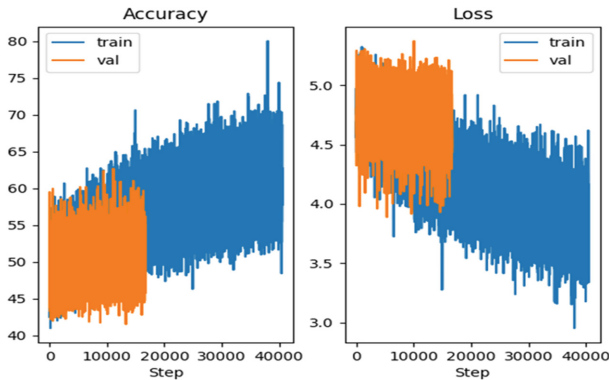


Fig. 5. Accuracy, loss curve with step

From the above two graph observations, the training set accuracy and loss are in oscillatory convergence, and the validation set accuracy and loss are also in oscillatory convergence. The accuracy is 62.5%, the main reason for this result is that the text we generated is first diverse and novel, and at training as a random combination of two datasets, the equivalent to each epoch is a brand new dataset in training.

Subjective evaluation results:

For the subjective evaluation, 200 images were randomly selected from the flickr8k datasets, and 100 images from the PCCD datasets were tested. The test results have been uploaded to <https://github.com/SongANIC/SampleANIC>.

We divided the evaluation results into three levels of perfect, good, general, poor.

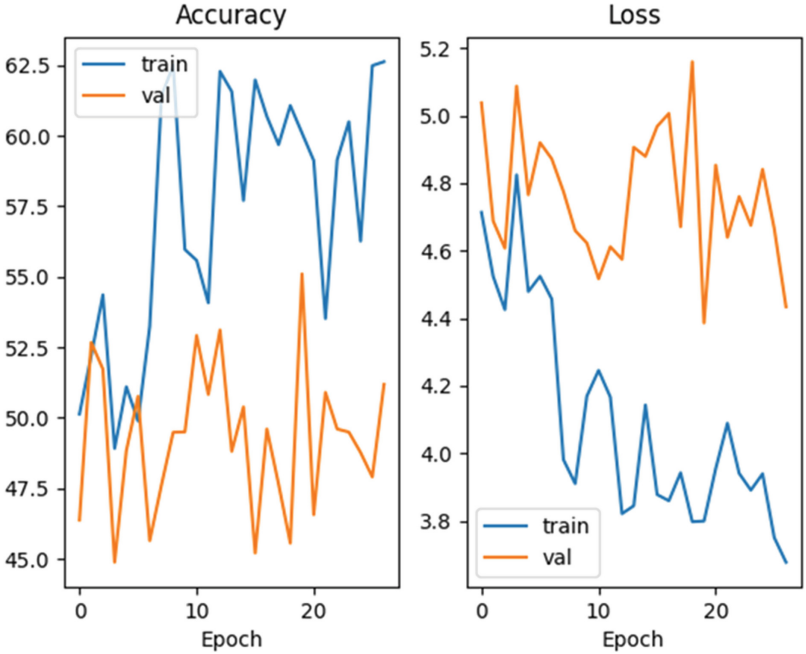


Fig. 6. Accuracy, loss curve with epoch

The standard of good (Good) is to accurately describe the image description and the aesthetic description.

The general (General) standard is, there are certain errors, but you can describe the image description more accurately, you can describe the aesthetic description.

Differential (Bad) criteria, poor statements, no sentence or generate only one style description.

The test result was generated with 300 images:

good images of 138, general 71, and bad 91.

Overall generated images meeting our requirements of $138 + 71 = 209$ bad 91 sheets.

The qualification rate is currently at 69.67%. There will be many flaws and unobjective elements in subjective judgment because of its subjectivity. The experimental results have been posted to <https://github.com/SongANIC/SampleANIC> to make future study and analysis easier.

First, there are four types of images:

Good standard: able to accurately express visual descriptions and smooth statements while also describing the aesthetic description (Fig. 7).

General (General) standard: there are certain errors, but you can more accurately describe the image description, can describe the aesthetic description (Fig. 8).

Bad standard: poor statements, no sentences or only one style description (Fig. 9).



Fig. 7. Generates a AIC aesthetic image describing the good classification



Fig. 8. Generates a AIC aesthetic image describing the general classification



Fig. 9. Generates a AIC aesthetic image describing the bad classification

5 Conclusions

For present aesthetic description informative challenges, we offer an aesthetic description strategy combining image description to create an end-to-end neural network system designed to combine the critical visual information of the image. In the picture feature extraction component of our system, we use a twin network. The concept of creating a twin CNN network with identical parameters. Allows it to receive picture features from

both datasets at the same time and learn how to extract the image's primary visual information as well as the aesthetic description's weakly supervised multi-level information. Our model is also nimble and light, equating to simultaneously extracting picture key and aesthetic information with a CNN feature extraction network, thanks to the same parameter characteristics. So when it comes to testing, all we need is a CNN network and an input image to get our results. We incorporate the language description of traditional image description from the NIC datasets and image aesthetic description from the AIC datasets into the text output model, and simultaneously input both styles of language description into the Language generation model LSTM for training, so that the computer realizes a network can output both styles of language description at the same time. If there are enough datasets and various styles of language descriptions, our model idea should be able to output more than two kinds of language descriptions at the same time. At the same time, as the datasets grows and the accuracy of the annotation data improves, our model's generalization performance and text output capability improve.

References

1. Chen, S., Jin, Q., Wang, P., Wu, Q.: Say as you wish: fine-grained control of image caption generation with abstract scene graphs. In: Proceedings of the IEEE/CVF Conference on Computer Vision and Pattern Recognition, pp. 9962–9971 (2020)
2. Vinyals, O., Toshev, A., Bengio, S., Erhan, D.: Show and tell: a neural image caption generator. In: Proceedings of the IEEE Conference on Computer Vision and Pattern Recognition, pp. 3156–3164 (2015)
3. Xu, K., Ba, J., Kiros, R., Cho, K., Courville, A., Salakhudinov, R., Zemel, R., Bengio, Y.: Show, attend and tell: Neural image caption generation with visual attention. In: International Conference on Machine Learning, pp. 2048–2057. PMLR (2015)
4. Cornia, M., Baraldi, L., Cucchiara, R.: Show, control and tell: a framework for generating controllable and grounded captions. In: Proceedings of the IEEE/CVF Conference on Computer Vision and Pattern Recognition, pp. 8307–8316 (2019)
5. Jin, X., Zhou, B., Zou, D., et al.: Image aesthetic quality evaluation technology development trend. *Sci. Technol. Guide* **9**, 36–45 (2018)
6. Chang, K.Y., Lu, K.H., Chen, C.S.: Aesthetic critiques generation for photos. In: Proceedings of the IEEE International Conference on Computer Vision, pp. 3514–3523 (2017)
7. Jin, X., Wu, L., Zhao, G., Li, X., Zhang, X., Ge, S., Zou, D., Zhou, B., Zhou, X.: Aesthetic attributes assessment of images. In: Proceedings of the 27th ACM International Conference on Multimedia, pp. 311–319 (2019)
8. Ghosal, K., Rana, A., Smolic, A.: Aesthetic image captioning from weakly-labelled photographs. In: Proceedings of the IEEE/CVF International Conference on Computer Vision Workshops, p. 0 (2019)
9. Wang W, Yang S, Zhang W, et al. Neural aesthetic image reviewer[J]. *IET Computer Vision*, 2019,13(8):749–758
10. Xiong, K., Jiang, L., Dang, X., Wang, G., Ye, W., Qin, Z.: Towards personalized aesthetic image caption. In: 2020 International Joint Conference on Neural Networks (IJCNN), pp. 1–8. IEEE (2020)
11. Mai, L., Jin, H., Liu, F.: Composition-preserving deep photo aesthetics assessment. In: Proceedings of the IEEE Conference on Computer Vision and Pattern Recognition, pp. 497–506 (2016)

12. Jin, X., Wu, L., Li, X., et al.: ILGNet: inception modules with connected local and global features for efficient image aesthetic quality classification using domain adaptation. *IET Comput. Vis.* **13**(2), 206–212 (2019)
13. Talebi, H., Milanfar, P.: NIMA: neural image assessment. *IEEE Trans. Image Process.* **27**(8), 3998–4011 (2018)
14. Lee, H., Hong, K., Kang, H., et al.: Photo aesthetics analysis via DCNN feature encoding. *IEEE Trans. Multimedia* **19**(8), 1921–1932 (2017)
15. Kong, S., Shen, X., Lin, Z., Mech, R., Fowlkes, C.: Photo aesthetics ranking network with attributes and content adaptation. In: *European Conference on Computer Vision*, pp. 662–679. Springer, Cham (2016)
16. Schwarz, K., Wieschollek, P., Lensch, H.P.: Will people like your image? Learning the aesthetic space. In: *2018 IEEE Winter Conference on Applications of Computer Vision (WACV)*, pp. 2048–2057. IEEE (2018)
17. Cho, K., Van Merriënboer, B., Gulcehre, C., Bahdanau, D., Bougares, F., Schwenk, H., Bengio, Y.: Learning Phrase Representations Using RNN Encoder-Decoder for Statistical Machine Translation (2014). arXiv preprint [arXiv:1406.1078](https://arxiv.org/abs/1406.1078)
18. Bahdanau, D., Cho, K., Bengio, Y.: Neural Machine Translation by Jointly Learning to Align and Translate (2014). arXiv preprint [arXiv:1409.0473](https://arxiv.org/abs/1409.0473)
19. Wu, Q., Shen, C., Liu, L., Dick, A., Van Den Hengel, A.: What value do explicit high level concepts have in vision to language problems?. In: *Proceedings of the IEEE Conference on Computer Vision and Pattern Recognition*, pp. 203–212 (2016)
20. Chen, X., Zitnick, C.L.: Learning a Recurrent Visual Representation for Image Caption Generation (2014). arXiv preprint [arXiv:1411.5654](https://arxiv.org/abs/1411.5654)
21. Liu, B., Fu, J., Kato, M.P., Yoshikawa, M.: Beyond narrative description: Generating poetry from images by multi-adversarial training. In *Proceedings of the 26th ACM International Conference on Multimedia*, pp. 783–791 (2018)

The Introduction of Author

22. Song Xinghui: Male, born in 1994, graduated from the School of Computer Science and Technology, TianGong University with a master's degree. Now working in Guangdong Business and Technology University: Once published the paper “CNTK communication optimization based on parameter server”, “Research on gene coexpression network based on RNA-seq data”, etc.
23. Zhu Peipei: Master degree, now working in Guangdong Business and Technology University.



Research on User Profile Analysis Method Based on LGIM Model

Teng Zong^{1,2(✉)}, Fengsi Wang³, Liang Guo¹, Yibo Liu¹, Xiaonan Feng², Zifu Qin²,
and Yinxiang Xia⁴

¹ National University of Defense Technology, Wuhan 430000, China
zt@nudt.edu.cn

² Information Engineering University, Zhengzhou 450000, China

³ Henan University, Zhengzhou 450000, China

⁴ Zhejiang Provincial Military Command, Hangzhou 310000, China

Abstract. Student profile analysis is a depiction of the characteristics of individual learning behavior and group learning development law of students during college. This study focused on 12,181 students surveyed between 2018 and 2021, and mainly based on the LGIM model. We tried to conduct in-depth research and analyze the characteristics of student profiles from multiple dimensions. Firstly, LGIM Model is tested for moderating effects based on categorical variables, and the models of management and engineering students are compared and analyzed. Then, the trend of students' learning gains was analyzed for different statistical years and student grades. Through the above analysis, this study scientifically summarizes the learning characteristics of college students in different disciplines during their studies, the development characteristics and transformation direction of school education concepts, and the general laws of students' learning and growth during college. The research results are helpful to improve the exploration and utilization of students' potential, improve the quality of university education, and provide some reference for teachers to teach according to their aptitude.

Keywords: User profile · Student characteristics · Moderating effects · LGIM model

1 Introduction

In the era of big data, information and knowledge play an increasingly important role in developing economies and societies. Effective access to and utilization of information resources has become the most important embodiment and guarantee for the development of individuals and organizations in this era. The value of information is reflected in all aspects of our lives and learning. According to the China Digital Economy Development Research Report (2023), the domestic digital economy continues to grow rapidly, and the scale of the digital economy exceeds 50 trillion yuan for the first time, accounting for 41.5% of GDP [1]. In the field of education, Ministry of Education of China formulated and released the Digital Literacy of Teachers in 2022 [2]. All kinds of education data also play an important role in effectively promoting the national education

digitalization strategic action, improving the education informatization standard system, and enhancing teachers' awareness, ability and responsibility to use digital technology to optimize, innovate and change education and teaching activities.

Data is the foundation of all information services. As big data enters a period of accelerated development around the world, data-based user services are getting closer to the personalized needs of users. Research on user profiling is attracting more and more researchers' attention. As a tool to achieve accurate information services, user profiles have been widely used in many fields in recent years [3]. Relevant studies have shown that constructing user profile models can help better understand user needs and achieve personalized and accurate information services.

The essence of user profile research is to extract the characteristics of users and classify users. Explore users' personalized needs based on their various behaviors, habits and preferences. The user profile analysis of student characteristics is essentially based on the potential characteristics of the student group to achieve scientific classification of the student group. The student profile analysis provides a basis for teachers to teach according to aptitude, and can also be used as a means of educational evaluation to test the characteristics of school development. At the same time, student profiles reflect the development trend and general law of students in the whole university stage. Through the profound analysis, this study provides a basis for students, teachers and education administrators to improve learning gains, and has important practical significance for giving full play to students' interests and characteristics, creating a good learning atmosphere, improving the quality of talent training, and promoting the benign development of university education.

2 Research

2.1 Review of Related Researches

User profiles were used in the field of product design and marketing in the early stage. Through user research, questionnaire interviews and other methods to explore user demands, outline target user profiles, so that product design does not depart from user and market demand, and then help enterprises achieve refined operation and marketing. With the emergence of various data mining technologies, it has brought new vitality to user profile research. In the big data environment, researchers analyze users' basic attributes, social attributes, behavioral habits, interests and hobbies from massive user behavior data through data mining and analysis methods, and refine user personalized labels to build more accurate user profiles. At the same time, the application field of user profiles is constantly expanding, from e-commerce, social networks to teaching practices [4].

From the perspective of user profile analysis technology, Zhuang Zhang (2020) proposed the idea of cross-modal learning and designed a user profile model based on multimodal fusion in view of the problem that the modal information in user profile work cannot be fully utilized [5]. Zhang (2020) aims at the problem of imperfect user preference acquisition in user-based collaborative filtering algorithms, and proposes a KNN classification recommendation algorithm based on dynamic user profile labels to solve the problems of ignoring users' potential preferences and changing trends of

user preferences in current mainstream recommendation algorithms [6]. Jiang (2016) studies the information ontology extraction method based on user profile by constructing a mathematical model of behavior-theme-vocabulary trinity, constructing user profiles, and realizing intelligent information push [7].

From the perspective of user profiles application, Lin (2018) aimed at social media applications, takes Weibo as an example to explore topics that users are interested in by collecting and analyzing the dynamics of users' Weibo, and to build Weibo user portraits, which plays a certain role in the personalized information service of social media and public opinion governance [8]. Wei (2021) proposed an accurate recommendation method of remote sensing information based on user profile for the accurate service of remote sensing information, which uses the theme model to construct the user profile by collecting and analyzing the explicit and implicit feedback behavior of the user, and completes the accurate recommendation of remote sensing information according to the profile model [9]. In the existing research, the application of user profiles in teaching practice is relatively rare. However, teaching according to aptitude has been an ideal teaching method in the field of education since ancient times, so this paper chooses this perspective as the research direction.

2.2 Research Data

The data used in this study are collected between 2018 and 2021 in the Chinese College Student Survey (CCSS) of X University. CCSS is an authoritative survey scale for studying the learning and development of college students in China, which was developed by Tsinghua University on the basis of the internationally influential National Survey of Student Engagement (NSSE) [10]. X University surveyed 12,181 students over four years. According to the discipline types, 7736 engineering students and 4445 management students were obtained. In the four years, 3566 students were surveyed in 2018, 2309 students in 2019, 3275 students in 2020, and 3031 students in 2021. Among all respondents, a total of 3588 first-graders participated in the survey, 3366 second-graders, 2883 third-graders and 2344 fourth-graders. Through the above classification, it lays a foundation for the subsequent potential profile analysis based on different student characteristics, which is convenient for studying the educational development law under different student characteristics.

3 Method

3.1 LGIM Model

On the basis of educational evaluation research over the years, Zong (2023) proposed Quality of Student Involvement (QSI), Quality of Teacher Involvement (QTI), and Supportive Campus Environment (SCE) has become the three key factors for universities to improve the quality of talent training, and is the main influence factor of Student Learning Gains (SLG). From the perspective of teachers, QTI is divided into Effective Teaching Practices (ETP) and Emotional Support of Teachers and Students (EST-S) [11]. Through data cleaning and confirmatory factor analysis, the evaluation indexes of

student learning and development with good reliability and validity are obtained. On this basis, the Learning Gains Influence Mechanism Model (LGIM Model) was explored by stepwise hypothesis testing (see Fig. 1). Through verification, the model fit indicators perform well. In the full sample analysis, the interpretable variance of LGIM Model reached 84%, which was significantly better than other models in similar studies [12]. Subsequent profiling of student characteristics is carried out on the basis of LGIM Model.

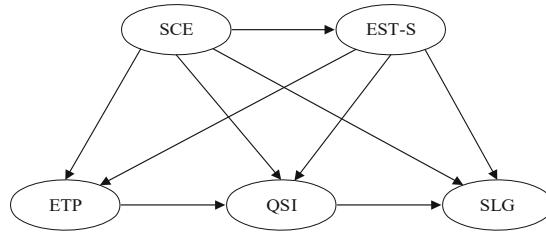


Fig. 1. Learning gains influence mechanism model (LGIM model).

3.2 The Basic Theory of Moderating Effect

As shown in Fig. 2, in model analysis, if the relationship between two variables (such as the relationship between X and Y) is a function of another variable M. In other words, the influence relationship between independent variable X and dependent variable Y is affected by another variable M, so we call M a moderating variable, and this effect is a moderating effect [13]. Among them, the moderating variable M can be categorical (e.g., gender, race, class, etc.) or continuous (e.g., height, age, years of education, etc.), which affects the direction (positive or negative) and strength of the relationship between the independent variable X and the dependent variable Y. The independent variable X can also be categorical or continuous; However, the dependent variable Y can only be continuous.

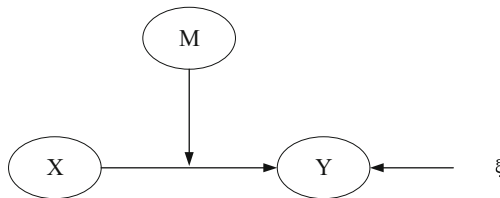


Fig. 2. Schematic diagram of moderating effect.

Baron et al. mentioned that the moderating effect affects the slope of the relationship between the independent variable X and the dependent variable Y [14]. In particular, Y and X have the following relationship:

$$Y = \beta_0 + \beta_1X + \beta_2M + \beta_3MX + e \tag{1}$$

As shown in Fig. 3, the path analysis diagram of the moderating effect is shown. Equivalently varying the above formula yields:

$$Y = (\beta_0 + \beta_2M) + (\beta_1 + \beta_3M)X + e \tag{2}$$

We can get that when M is a fixed value, this is a linear regression of Y to X. In general, the relationship between Y and X is characterized by the regression coefficient $(\beta_1 + \beta_3M)$. The regression coefficient is a linear function of M. If not 0, M is the regulating variable, which reflects the size of the regulating variable.

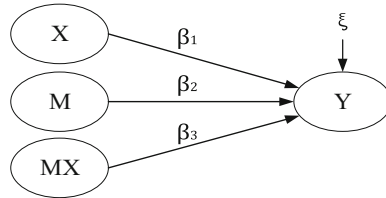


Fig. 3. Path analysis diagram of moderating effects.

3.3 Tests for Moderating Effects

Usually, different characteristics of students tend to show different atmosphere. Through group comparison of students, the characteristics of LGIM Model presented in different situations are discussed, and the development rules of students are summarized. In college, the major of the student is the main difference. Firstly, it is tested whether different disciplines have a moderating effect on the influence relationship of each path coefficient in the model. In this study, management students and engineering students were selected for comparative testing. According to the path order of LGIM Model, nine comparison models are constructed. From 1 to 9, it represents the difference comparison of path coefficients between the two variables. From this, the null hypothesis H_{01} to H_{09} is established (see Table 1). Taking H_{01} as an example, it means that the discipline type makes the impact factor between SCE and EST-S significantly different. The rest of the assumptions correspond to this.

P value is the probability of the null hypothesis misestimation. Usually, $P > 0.05$ indicates the rejection of the null hypothesis, and $P \leq 0.05$ indicates acceptance of the null hypothesis [15]. According to this judgment basis, we get that under different disciplines, except for the influence relationship of EST-S on QSI, the influence relationship of SCE on QSI and the influence relationship of ETP on QSI, the other influence relationships have significant differences. In other words, differences disciplines have significant differences on QTI and SLG, except that they have no significant differences on QSI.

Table 1. Test results of moderating effect.

Assumptions of comparison models	Representative path	Chi-square value (χ^2)	P-value
H ₀ 1	SCE → EST-S	26.115	0.000
H ₀ 2	EST-S → ETP	35.606	0.000
H ₀ 3	SCE → ETP	18.669	0.000
H ₀ 4	EST-S → QSI	0.032	0.857
H ₀ 5	SCE → QSI	0.320	0.571
H ₀ 6	EST-S → SLG	9.086	0.003
H ₀ 7	SCE → SLG	16.169	0.000
H ₀ 8	ETP → QSI	2.752	0.097
H ₀ 9	QSI → SLG	33.006	0.000

Note N_{Management} = 4445, N_{Engineering} = 7736

4 Results

4.1 Student Profiling for Different Disciplines

Through testing, we find that different disciplines have a moderating effect on the learning gains influence mechanism. The path represented by the bold lines in Fig. 4 is the path with the moderating effect verified above. This shows that management students and engineering students show significant differences in the process of learning gains. The analysis is mainly based on the following two points:

First, for the dependent variable SLG, the path coefficients of the three direct impact factors (SCE, EST-S and QSI) of management students were 0.31, 0.35 and 0.36, respectively, and the path coefficients of the three direct impact factors (SCE, EST-S and QSI) of engineering students were 0.24, 0.28 and 0.49, respectively. In contrast, it can be seen that the influence of engineering students QSI on SLG is significantly higher than that of the other two variables. The influence of management students on SLG in QSI, EST-S and SCE is basically the same.

Second, the influence relationship between the three factors of SCE, EST-S and ETP is a typical mediation model with moderating effect. Wherein, the independent variable is SCE, the dependent variable is ETP, the mediator variable is EST-S, and the moderator variable is discipline type. Among them, the moderator variable acts on both direct and indirect effects, which makes management students and engineering students show different characteristics. The direct impact effect of engineering students is more significant, while the indirect effect of management students is more significant. The most significant difference in impact is reflected in the path of EST-S on ETP. The path coefficient for management students is 0.35 and 0.19 for engineering students. In contrast, management students have a significantly stronger impact than engineering students.

After the above analysis, it shows that engineering students are more inclined to obtain learning gains through personal efforts to improve the quality of their learning input. Management students have relatively little personal investment, but they can make more effective use of the advantages of school resources and are better at handling the relationship between teachers and students. Moreover, the establishment of a good teacher-student relationship is more likely to affect the change of teaching behavior, so that teachers can make appropriate adjustments in a more timely manner in the classroom teaching process and improve the classroom teaching input.

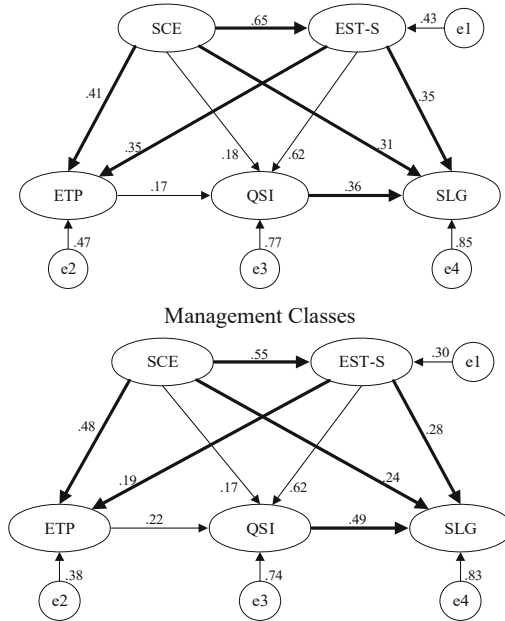


Fig. 4. Comparative analysis of LGIM Models for different disciplines.

4.2 Student Profiling for Different Statistical Years

Based on the CCSS data from 2018 to 2021, models of different statistical years can be compared. Analysis differed from follow-up studies for different statistical years. Because the follow-up study is a fixed sample, the sample measured in this study each year is a different group of students. The four-year data are stratified according to the discipline type, and the results can more generally reflect the overall change law.

Firstly, the data from 2018 to 2021 were tested sequentially by LGIM Model, and the explainable variances of SLG were 83%, 87%, 83%, and 82%, respectively. The difference of interpretability between statistical years is relatively small, and longitudinal comparison of explanatory proportion of each variable can be made for four consecutive years. For visual purposes, this study converted the path coefficients of influence variables in different statistical years into corresponding influence proportions, as shown in Table 2.

Table 2. Analysis of SLG impact in different statistical years.

The variable name	2018		2019		2020		2021	
	Path factor	Impact ratio (%)	Path factor	Impact ratio (%)	Path factor	Impact ratio (%)	Path factor	Impact ratio (%)
QSI	0.484	48.0	0.447	43.7	0.463	45.7	0.405	39.3
EST-S	0.286	28.4	0.271	26.5	0.286	28.2	0.352	34.1
SCE	0.238	23.6	0.306	29.9	0.264	26.1	0.274	26.6

Note $N_{2018} = 3566$, $N_{2019} = 2309$, $N_{2020} = 3275$, $N_{2021} = 3031$

The impact ratio of QSI, EST-S and SCE on SLG over four years is plotted as a line graph (see Fig. 5). We conclude that QSI has always been the variable with the greatest influence on SLG during the four years, but the explanation proportion of QSI decreases, the explanation proportion of EST-S increases, and the explanation proportion of SCE tends to be stable.

The above analysis shows that in recent years, with the change of educational philosophy from “teaching” to “learning”, teachers are paying more attention to emotional communication with students. In the process of learning gains, students gradually change from “independent learning” which is dominated by self-learning to “compound learning” which synchronously develops with self-learning and interactive learning. Students have a greater sense of participation and acquisition in the learning process, rather than just passively accepting knowledge.

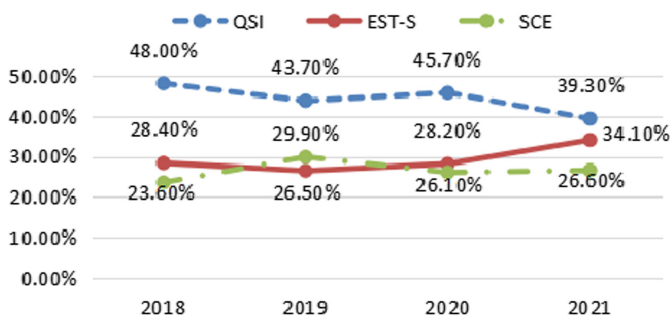


Fig. 5. Analysis of the trend of SLG influence in different statistical years.

4.3 Student Profiling for Different Grades

The student profiling for different grades reflects the law of students’ growth and development in four years. Firstly, LGIM model was used for the sequence test of data from freshmen to seniors. The explainable variances of SLG were 85%, 84%, 83% and 84%, respectively. It is also concluded that there is no significant difference in the interpretability of SLG among different grades, and horizontal comparison can be made on

the interpretability ratio of variables in the four grades. The path coefficients of each influence variable of SLG in different grades were converted into corresponding influence proportions, as shown in Table 3.

Table 3. SLG impact analysis by grade level.

The variable name	Freshman year		Sophomore year		Junior year		Senior year	
	Path factor	Impact ratio (%)	Path factor	Impact ratio (%)	Path factor	Impact ratio (%)	Path factor	Impact ratio (%)
QSI	0.461	45.2	0.492	48.6	0.413	40.6	0.472	46.7
EST-S	0.312	30.6	0.264	26.1	0.302	29.7	0.251	24.9
SCE	0.246	24.1	0.256	25.3	0.302	29.7	0.287	28.4

Note N_{Freshman} = 3588, N_{Sophomore} = 3366, N_{Junior} = 2883, N_{Senior} = 2344

In different grades, the impact ratio of QSI, EST-S and SCE on SLG is plotted as a line graph (see Fig. 6). We conclude that QSI has always been the most important direct impact on SLG in the whole college experience. From freshman to sophomore, the influence of QSI on SLG showed an upward trend and reached the highest value in the four years of college. From the sophomore year to the junior year, the influence strength continued to decline, reaching the lowest value in the whole university. From the junior to the senior year, the influence strength picked up again and reached the second peak. In addition, the explanatory strength of EST-S was significantly higher than that of SCE in the freshman year, but with the transition from freshman to senior year, the explanatory strength of SCE gradually improved and surpassed EST-S.

The above analysis shows that from freshman to sophomore year is the “adaptation period” for students to university life. From sophomore to junior year, students have a “slack period” of personal investment. At this stage, because many students have neither the enthusiasm for learning when they first enter college nor the pressure to graduate, the polarization is serious. On the whole, QSI has significantly declined in the interpretation of SLG. In the senior year, as graduation approaches, academic pressure increases, and QSI also increases significantly.

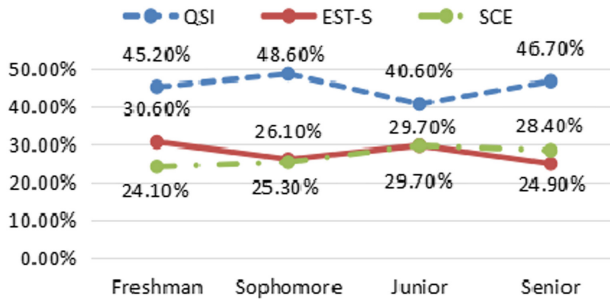


Fig. 6. Analysis of SLG influence trend in different grades.

5 Conclusion

This study mainly carried out a further study on the basis of LGIM Model, and analyzed the characteristics of student profiles from multiple dimensions. After testing the moderating effect of LGIM Model, we conclude that discipline type is a moderator variable of the learning gains influence mechanism. By comparing the study subjects in multiple categories, the following main conclusions were obtained. From the perspective of different disciplines, engineering students are more dependent on learning gains by improving the quality of individual learning input. Management students not only rely on individual efforts, but also focus on the support of the school environment and the emotional interaction between teachers and students. From the perspective of different statistical years, with the transformation of teaching philosophy from “teaching” to “learning”, teachers pay more attention to emotional communication with students. When students acquire learning gains, they gradually change from “independent learning” which is dominated by self-learning to “compound learning” which synchronously develops with self-learning and interactive learning. From the perspective of different grades, students have a “slack period” in personal input during the transition from sophomore to junior year. At this stage, the student’s own personal input has declined markedly in the interpretation of learning gains, reaching the lowest point throughout the university period. Through the analysis of the above student profiles, this study explains the learning characteristics of college students in different disciplines, the development directions of school education, and the general laws of students’ learning and growth in college.

References

1. China Digital Economy Development Research Report: http://www.caict.ac.cn/kxyj/qwfb/bs/202304/t20230427_419051.htm (2023). Last accessed 25 May 2023
2. Notice of the Ministry of Education on the release of Standards for the education industry called Digital Literacy of Teacher: http://www.moe.gov.cn/srcsite/A16/s3342/202302/t20230214_1044634.html. Last accessed 25 May 2023
3. Xu, F., Ying, J.R.: Overview of user profile research at home and abroad. *Res. Libr. Sci.* **479**(12), 7–16 (2020)

4. Renwu, W., Wenhui, Z.: Behavior and interest labeling construction and application of academic user profiles. *J. Mod. Inf.* **39**(09), 54–63 (2019)
5. Zhuang, Z., Xiaonian, F., et al.: User profiling based on multimodal fusion technology. *Acta Scientiarum Naturalium Universitatis Pekinensis* **56**(01), 105–111 (2020)
6. Zhang, Y., Zhang, C., et al.: KNN product recommendation algorithm based on dynamic user profile label. *Inf. Sci.* **38**(08), 11–15 (2020)
7. Jiang, J., Li, J., et al.: Intelligent information push method based on user profile. *Cyber Secur. Data Gov.* **35**(23), 86–89+92 (2016)
8. Lin, Y., et al.: User profile of diversified groups in micro-blog based on social identity theory. *Inf. Stud. Theory Appl.* **41**(03), 142–148 (2018)
9. Wei, E., Liu, D., et al.: Design of precise service system based on user profile for remote sensing information. *Radio Eng.* **51**(8), 720–724 (2021)
10. Construction of research project on Learning and Development of Chinese University Students: <https://www.ioe.tsinghua.edu.cn/info/1141/1046.htm>. Last accessed 26 May 2023
11. Zong, T., Wang, F., et al.: Mechanisms influencing learning gains under information security: structural equation modeling with mediating effect. *Intell. Autom. Soft Comput.* (6), 3447–3468 (2023)
12. Kwan, J.L.Y., Chan, W.: Comparing squared multiple correlation coefficients using structural equation modeling. *Struct. Equation Model.* **21**(2), 225–238 (2014)
13. Wen, Z., Liu, H: *Analyses of Mediating and Moderating Effects Methods and Applications*, 2nd edn. Educational Science Publishing House, Beijing (2020)
14. Hayes, A. F.: Beyond Baron and Kenny: statistical mediation analysis in the new millennium. *Commun. Monogr.* **76**(4), 408–420 (2009)
15. Bonovas, S., Piovani, D: On P-values and statistical significance. *J. Clin. Med.* **12**(3), 900 (2023)



Design and Implementation of Warning Signs for Vehicles Based on Automatic Navigation Algorithms

Fangyan Wang¹, Ge Jiao^{1,2(✉)}, Jinjia Lu¹, and Yiping Yuan¹

¹ College of Computer Science and Technology, Hengyang Normal University, Hengyang 421002, Hunan, China
jiaoge@126.com

² Hunan Provincial Key Laboratory of Intelligent Information Processing and Application, Hengyang 421002, Hunan, China

Abstract. Traditional warning signs use human retrograde placement; there are problems such as short warning distances, imprecise placement positions, and difficult positioning of accident points. According to statistics, the user's reaction time after facing a car accident is generally 1.05–1.28 s, and the reaction time to light is 0.225 s. The reaction time for the user to deal with a car accident independently is completely insufficient, and these reasons are the main reasons for secondary traffic accidents. In order to solve this social pain point, we designed a new intelligent triangle warning sign. The intelligent warning sign is installed with an intelligent base at the bottom, and it gets the traffic accident point precisely located when the intelligent warning sign is working, and the system gets the vehicle accident point and reminds the vehicles behind to pay attention to avoid, realizing the three-way interconnection of drivers and passengers, traffic control departments, and the personnel of the vehicles behind, and using the automatic navigation algorithm to realize the automatic navigation of the warning sign to protect the safety of drivers and passengers.

Keywords: Warning signs · Remote control · Precise positioning · Three-way alert · Automatic navigation

1 Introduction

With the rapid development of the transportation industry, the incidence of traffic accidents has increased. Traffic accidents not only cause a large number of casualties but also seriously affect economic development and social stability. In recent years, the rise in traffic accidents has become a serious problem faced by the traffic control department. When the vehicle breaks down or encounters an emergency, secondary accidents caused by the failure to place warning signs as required are common. At the same time, secondary accidents [1] have a high probability of being ignored by people due to the traditional warning signs artificially estimated distance error, incorrect placement, poor nighttime, rain, and other bad weather warning effects, the highway's artificially reversed

walk-to-place warning signs, and other problems caused by the highway's proneness to road traffic accidents.

Due to the limitations of traditional warning signs and potential road traffic hazards, in order to avoid the occurrence of secondary accidents, this paper designs a car warning sign based on an automatic navigation algorithm.

2 Domestic and International Overview

With the number of motor vehicles increasing year by year, when traffic accidents and vehicle failures occur, it is necessary to use warning signs to alert the vehicles behind. It is understood that in Beijing, where the largest number of cars are kept in China, various auto parts markets are selling triangular warning signs almost everywhere, which are cheap and confusing in style; drivers have poor safety awareness of warning signs [2], and warning signs have poor warning effect in fog, darkness, and other weather; and the application of intelligent warning signs is small and simple in function.

Europe is a major region for the development and application of smart triangle warning signs. The EU started a regulation in 2014 that required all new cars to carry triangular warning signs, and in 2018, the EU issued another regulation that required all new cars to carry smart triangular warning signs. Smart warning signs are also starting to be used in the market with some simple alarm or location functions [3]. In Australia, the development of smart warning signs is more mature; for example, after the launch of a pilot project of smart warning signs in 2019 [4], it is evident that road traffic accidents are significantly reduced due to the use of smart warning signs [5].

3 Overall Solution Design

The intelligent car warning sign is mainly composed of three parts: the hardware circuit, the client, and the management system. The intelligent warning sign is installed with an intelligent base at the bottom, and an intelligent cart and hardware module are set in the base for controlling the warning sign as well as realizing the related functions. The working principle is as follows:

- (1) A Beidou + GPS module is installed in the base of the intelligent warning sign to collect positioning data; the control of the intelligent warning sign is realized through an automatic navigation algorithm; A Bluetooth module and SIM card are used to realize multiple ways to connect the intelligent warning sign; a NBIOT wireless communication module is used to transmit data; and LED light strings are added to expand the warning range of the warning sign to avoid secondary accidents.
- (2) The Beidou + GPS module collects positioning data and transmits it to the server, which is used to manage system statistics and analyze data, as well as mark the accident point and accident danger range.
- (3) The management system acquires data from the server to make statistics on the accident points, which facilitates the traffic control department to deal with the accident, and uses SMS to ask the vehicle owner whether he needs help as well as to remind the rear vehicle personnel according to the danger range classified, so as to realize the three-way interconnection between the driver and passenger, the traffic control department, and the rear vehicle personnel.

- (4) When placing the warning sign, the driver and passenger can choose two placement methods—automatic navigation and remote control—instead of human placement to protect the safety of drivers and passengers.

To sum up, the intelligent triangle warning sign mainly realizes: precise positioning, accurate rescue, three-party interconnection, expanding the warning distance, and replacing the artificial placement of warning signs so that users can quickly and conveniently deal with road traffic problems.

4 Intelligent Triangle Warning Sign Function Design

4.1 Microcontroller

Traditional warning signs have simple functions and poor practicality, so considering the functionality and application scenarios of warning signs, the STM32 F103RET6 [6] is selected as the main control board, which effectively ensures real-time control and monitoring of the intelligent warning signs during their movement. Due to the high integration and low power consumption of the microcontroller, the warning sign works for a long time, which is convenient for users to deal with unexpected situations encountered during the journey.

4.2 Intelligent Warning Sign Automatic Navigation Algorithm

The Beidou + GPS module on the smart warning sign is positioned in real time, the Beidou satellite gets the data back to the server, and the management system gets the data from the server for parsing and processing, which is displayed in the map interface and analyzes and counts the specific location of the warning sign and vehicle information.

When drivers and passengers are using warning signs, they need to place them according to the requirements of different highways on the distance of warning sign placement. We use a search algorithm to plan the route. The algorithm ensures that the path found in the map is the shortest path and decides the direction of the search by evaluating the valuation function of each node to avoid useless routes as much as possible. The situation varies from road to road, so the warning signs are needed to ensure accuracy during the movement, so we plan an optimal path for the user based on the location of the start and end points.

The valuation function consists of two components: the heuristic function and the cost function.

$$f(n) = g(n) + h(n) \quad (1)$$

The above algorithm is used to implement the route planning of the warning signs, using the Beidou + GPS module to obtain the current position and update the data in real time to return it to the server. According to the positioning technology, to obtain the current information and route planning results, use the route tracking algorithm to calculate the current direction and speed that the warning sign needs to travel. Here, we use the PID control algorithm [7] to realize the route tracking of the warning sign. This

algorithm is a common feedback control algorithm that can minimize the error between the actual output and the desired output of the system by constantly adjusting the output so as to The PID algorithm has three main components: proportional control (P control), integral control (I control), and differential control (D control), which are implemented as follows:

P control, according to the current error, according to a certain proportion to adjust the output; the greater the error, the greater the output; the smaller the error, the smaller the output; The formula is as follows:

$$P = Kp * e(t) \quad (2)$$

P: proportional control output Kp: proportional coefficient e(t): current error.

The control adjusts the output proportionally according to the accumulated value of the error. Similarly, the larger the error, the larger the output, and the smaller the error, the smaller the output; the formula is as follows:

$$I = Ki * \int e(t)dt \quad (3)$$

I: integral control output; Ki: integration coefficient; $\int e(t)dt$: the cumulative value of the error.

D control adjusts the output according to the rate of error change in a certain proportion. The formula is as follows:

$$D = Kd * de(t)/dt \quad (4)$$

D: differential control output; Kd: differential coefficient; $de(t)/dt$: the rate of error change.

The final output control is the weighted sum of the three components:

$$Ut = P + I + D \quad (5)$$

U(t): the control output.

The above algorithm can realize the route planning, current moving position, and running speed of the warning sign, ensure the stability and accuracy of the system, and finally realize the automatic navigation function of the warning sign.

4.3 Communication Protocols

MQTT Protocol

Considering the diversity and wide use of smart warning signs and the reliability of positioning data, we use the MQTT message transmission protocol [8] in order to guarantee that smart warning signs can work properly and obtain precise positioning in remote areas or areas with weak signal coverage. The transmitted information is divided into topics and payloads. Topic requires both the client and the ONE NET server to subscribe to the same topic. After subscribing to the topic, the client uploads data from various

sensors, and the server sends commands to control the smart warning signs. The payload is the content of the message sent by both parties, i.e., various data and commands. The data from various sensors of the smart warning sign is uploaded to the client, and the server issues commands to control the smart warning sign.

By obtaining the data from the sensors, the server side obtains the latitude and longitude to display the information of the accident vehicle and the place where the accident occurred to achieve the function of three-end interconnection.

BLE V4.0 Protocol

The difference with the MQTT protocol is that it can realize direct communication between devices and is mainly used for remote control of smart warning signs by cell phone apps [10]. When dealing with traffic accidents or vehicle accidents on highways, placing warning signs on foot by humans is dangerous and prone to secondary accidents; therefore, we designed two methods of placing warning signs remotely to protect the safety of drivers and passengers.

First, when a traffic accident or malfunction occurs, the accident vehicle personnel can remotely control the intelligent warning sign through the cell phone terminal APP. After the cell phone end APP sends the control command, the Bluetooth layer by-layer analysis of data controls the warning sign forward and backward and other functions, without human placement, to ensure the safety of personnel.

The second, the client APP, sets up the function of automatic navigation on different highways. By clicking the button, the accident vehicle personnel use the automatic navigation algorithm to calculate the warning sign placement distance, running speed, and running direction and automatically run to the designated position without manual operation by personnel to achieve the effect of avoiding secondary accidents.

4.4 Wireless Remote Control

Two ways are used for wireless remote control: the first is the NB-IoT wireless communication module [11], which contains the SIM card and is characterized by low power consumption, long standby time, long connection distance, and wide coverage. The MQTT communication protocol was chosen; the main features of MQTT enable the use of a very small amount of writing and enough bandwidth to allow a fast and accurate transfer of the smart warning sign's positioning signal from the local device to the remote device and an efficient data exchange with the server.

The second way is the Bluetooth module, which uses the HC-08 Bluetooth serial communication module, which is a digital transmission module based on Bluetooth Specification V4.0 BLE Bluetooth protocol with GFSK modulation technology. It is able to reach ultra-long distance communication and can better link cell phone applications with data. Its working process: when the smart triangle warning sign is unfolded, the cell phone app connects to the smart cart to receive data or control the smart cart. The control process is shown in Fig. 1.

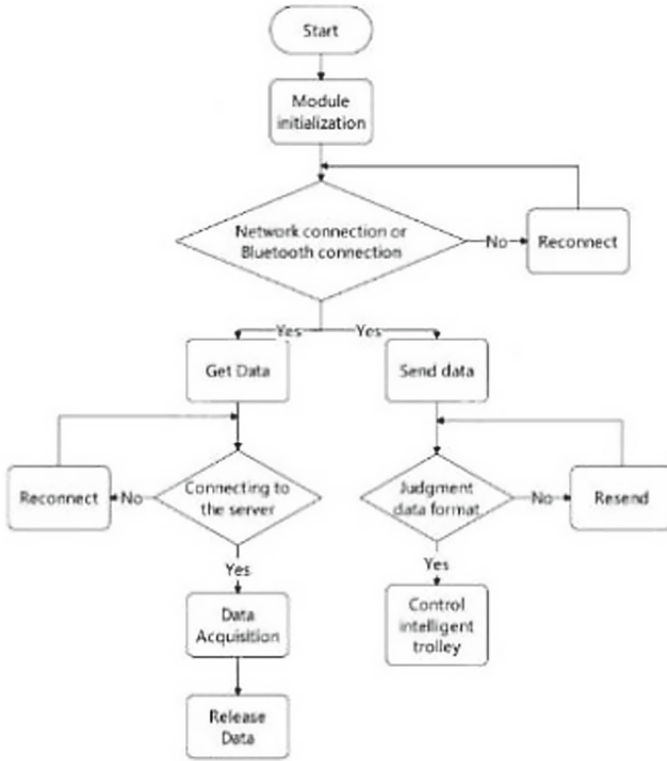


Fig. 1. Control process

4.5 Motor Drive Module

The motor drive module of the smart warning sign is used to control the motor’s operation; mainly, the control signal is converted into the voltage required by the motor through the motor drive chip, which has two start-up control terminals and an external detection resistor for high-precision logic control. It realizes real-time monitoring of the working condition of the motor and provides timely feedback to the control circuit to drive the intelligent warning sign and provide good power support for the intelligent warning sign.

PWM speed control technology uses a switching circuit to realize the switching operation of the circuit, in which the switching circuit generates pulses with different amplitudes, and the width of these pulses varies with the switching of the switching circuit, thus realizing the voltage change of the circuit and its frequency change and changing the driving speed of the intelligent warning sign. The signal frequency and duty cycle of the PWM output are determined by the values of the automatic reload register (ARR) and the comparison register (CCR). The resolutions are:

$$F = CK_PSC / (PSC + 1) / (ADD + 1) \tag{6}$$

$$DC = CCR / (ADD + 1) \tag{7}$$

$$RES = 1/(ADD + 1) \quad (8)$$

F: PWM frequency, DC: duty cycle.

Set two parameters, ENA and ENB, on L298N to adjust the PWM on it. When the enable signal is 0, the motor stops automatically. If the enable signal is 1, ENA, and ENB are 00 or 11, the motor will stop rotating.

4.6 Beidou + GPS Module

Beidou + GPS module [12] realizes double-precision positioning. The Beidou module mainly transmits signals through satellites, and the Beidou module on the intelligent warning sign receives the signals transmitted by satellites, measures the signal propagation time and the latitude and longitude positions of satellites, and can calculate the current position of the warning sign itself using the algorithm of triangulation, which covers a wide range.

4.7 LED Light-Emitting Module

LED light strings usually use LED chips, PVC material, and other components. LED lights are set on the front of the intelligent warning sign, and the warning distance grows, effectively reminding drivers to pay attention to safety and providing an effective reminder in case of traffic congestion to prevent secondary traffic incidents.

5 System Design

5.1 System Architecture Model

The vehicle backend management system uses the MVC model [13], which helps developers achieve separation of concerns. MVC is a three-tier structure consisting of a model, a view, and a controller. The model layer includes the business logic it executes with the state of the website; the view layer is responsible for interacting with the user, which presents the information in the database to the front-end through the server; the controller is the component that implements the core code of the website functionality, and the interaction with the user is handled and responded to by it.

5.2 Functional Design

Its function module is divided into four parts: vehicle distribution, user management, failure dangerous vehicle rescue SMS sending, and data analysis. The vehicle location information in vehicle distribution is obtained from the API provided by the ONE NET platform [14], extracted using regular expressions, and finally presented through the map API, with the faulty vehicle as the center and the danger range divided by a radius of 500 m. User management can add, delete, and check the owner's information; adding users to the database through the add method and deleting, changing, and checking all need to get the ID by clicking the event first and then calling different methods to operate on them. The SMS sent to the vehicle in danger of failure is realized by calling the API interface provided by SMS.com.

6 Mobile Software Design

6.1 Android Client Main Structure

The client is mainly divided into three major parts: the connection module, the control module, and the communication module, as shown in Fig. 2. The connection part can be divided into Bluetooth connection and Wi-Fi connection [15], which are used to remotely control the connection method of the smart warning sign; the control module is divided into automatic navigation placement of the smart warning sign and human remote control placement, which is used to place the warning sign at a specified distance when dealing with traffic accidents, replacing human walking. The reverse placement communication module uses a Bluetooth communication module [16], and the user sends commands to the smart warning sign to control the steering of the warning sign.

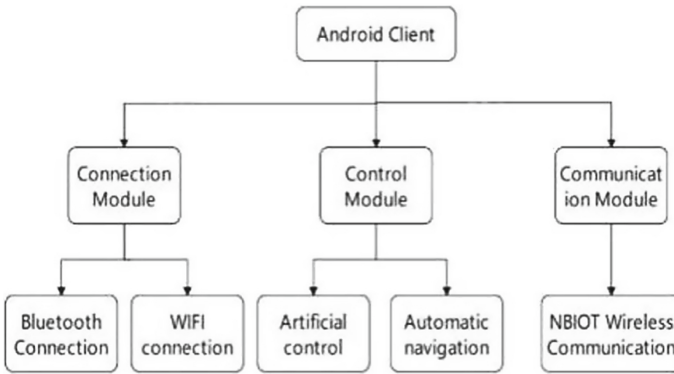


Fig. 2. Client general structure diagram

6.2 Main Interface Framework Design

The main page of the client contains connection setting and selection, an intelligent warning sign mobile control interface, automatic navigation, setting buttons, a power display, system information, etc.

7 Experimental Records

7.1 Experimental Method

- (1) Test the effective range of remote control; place the intelligent warning sign on the highway; remote control by the client APP; control its forward, backward, left turn, right turn, pause; test the delay time (the time from the client pressing the button to the intelligent warning sign giving a response); and the connection situation (the percentage of successful connection and failure).

- (2) Test the warning range of the intelligent warning sign, divided into daytime warning distance and night warning distance, i.e., how many meters the testers can still see the intelligent warning sign clearly in different environments.
- (3) Test the accuracy of the background management system in acquiring data and marking accident points, as well as the speed of data refresh and the completeness of information display.

7.2 Experimental Data

The following four distances were selected: 0–40 m, 40–80 m, 80–120 m, 120–160 m, and the delay time when the client APP controlled the intelligent warning sign, which was recorded as T. Through the data statistics, it was found that within the range of 40 m, T1s were negligible. With increasing distance, T increases proportionally, and the average delay time is close to 1.6 s when the distance reaches 160 m. The test results of accepting command T at different distances are shown in Fig. 3.

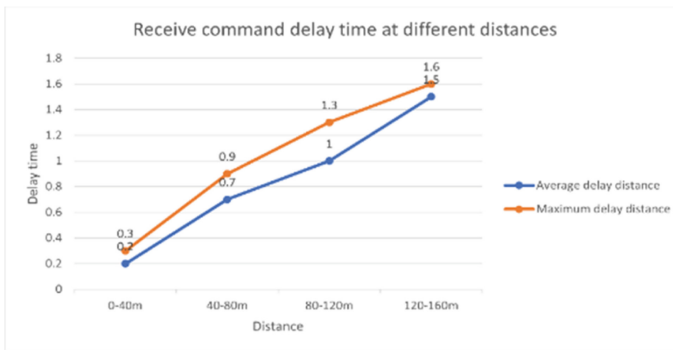


Fig. 3. Receive command delay time at different distances

According to the information, the user's reaction time after facing a car accident is generally 1.05 s to 1.28 s, while the reaction time to light is 0.225 s. When the user is exercising on the highway at 100 km/h, the reaction distance in the face of an emergency is 35.56 m, while the reaction distance to light is 6.25 m, which is a shorter reaction distance.

Through a number of testers to test the warning sign, according to the testers' feedback, during the driving process, the LED light of the warning sign can be clearly seen flashing at a distance of two hundred meters from the warning sign, and the warning distance grows compared with the ordinary warning sign, and the effect is more obvious, especially in the dark night fog and other bad weather effects.

Through the above test, the intelligent triangle warning sign designed in this paper can meet the needs of the vehicle in actual operation and cope with the unexpected situation, has achieved the design goal and the original intention, and will further improve its function in the future and continuously improve it to maximize its function and protect the safety of drivers and passengers.

8 Conclusion

Through continuous testing and debugging of the system, the design requirements can be completed. The innovative points and features of this design are reflected in: (1) real-time monitoring of accident point latitude and longitude through Beidou positioning and statistical accident points through the backend management system to achieve three-party interconnection, which is convenient for traffic control departments to deal with traffic accidents. (2) Through remote-controlled warning signs to protect the safety of drivers and passengers (3) Comparison of traditional warning signs to increase the LED light string: the warning effect is obvious, and the warning distance is extended. (4) Through an automatic navigation algorithm to achieve smooth operation and automatic navigation of intelligent warning signs placed without human personal placement to protect the safety of personnel.

Acknowledgement. This work is supported by the National innovation and entrepreneurship training program for college students (202210546004, cxcy2022004), the Hunan Provincial Natural Science Foundation of China (2021JJ50074), the Science and Technology Plan Project of Hunan Province (2016TP1020) and the 14th Five-Year Plan Key Disciplines and Application-oriented Special Disciplines of Hunan Province (Xiangjiaotong [2022] 351).

References

1. Zhang, B., Xu, W., Liu, G., Muhammad, A.: The early warning efficiency analysis of secondary accidents in expressway tunnels. *Adv. Mech. Eng.* **11**(4) (2019)
2. Anonymous: Warning light for night safety. *Commer. Motor* **231**(5821) (2019)
3. Sodikin: Mobile traffic warning signs, can it be applied?. *J. Phys. Conf. Ser.* **1376** (2019)
4. Frances, A.: A warning sign on the road to DSM-V: Beware of its unintended consequences. *Psychiatr. Times* **26**(8) (2009)
5. Zaw, K.P., Kyu, Z.M.: Character segmentation and recognition for Myanmar warning signboard images. *Int. J. Netw. Distrib. Comput. (IJNDC)* **7**(2) (2019)
6. Long, T.: Design of sweeping robot based on STM32 single chip microcomputer. *J. Phys. Conf. Ser.* **2456**(1) (2023)
7. Zhang, W., Lei, J., Lin, Z.: Research on improved PID control algorithm of a kind of high speed vehicle. In: *Proceedings of the 2nd International Conference on Electronics, Network and Computer Engineering (ICENCE 2016)* (2016)
8. Longo, E., Redondi, A.E.: Design and implementation of an advanced MQTT broker for distributed pub/sub scenarios. *Comput. Netw.* **224** (2023)
9. Held, G.: Moving IoT data with MQTT. *InfoWorld.com* (2022)
10. Wei, S., Zhang, Y., Li, J., et al.: Bluetooth remote control car based on app inventor. Information Engineering Research Institute (USA), Singapore Management and Sports Science Institute (Singapore). In: *Proceedings of 2018 7th ICEA International Conference on Information, Education and Social Sciences (ICEA-IESS 2018)*. Information Engineering Research Institute, pp. 134–138 (2018)
11. Guo, Z., Liu, Y. and Lu, F.: Embedded remote monitoring system based on NBIOT. *J. Phys. Conf. Ser.* **2384**(1) (2022)
12. Zhimin, S., Zhengjia, W., Zhijun, Z.: Research of ETC with GPS/BDS high-speed charging and navigation system. *Autom. Control Intell. Syst.* **9**(4) (2022)

13. Kanjilal, J.: How to Redirect a Request in ASP.NET Core MVC. InfoWorld.com (2020)
14. Jackson, L.: The Complete ASP.NET Core 3 API Tutorial. Apress, Berkeley, CA
15. Liu, J., Liu, J.: Design of embedded intelligent car control system based on android. J. Phys. Conf. Ser. **1651**(1) (2020)



Architecture of Integrated Resource System Based on Dataspace

Hui Yan¹(✉) and Bo Chen²

¹ China Telecom Research Institute, Beijing, China
yanhui@chinatelecom.cn

² China University of Political Science and Law, Beijing, China

Abstract. At present, there are some urgent problems in the process of data element circulation, which hinder the marketization process of data elements and block the circulation channel of data elements. It includes the difficulty of transforming original data into data resources, the difficulty of defining data ownership, the difficulty of standard governance of data assets, the difficulty of data element circulation pricing, and the difficulty of data application security and mutual trust. The emergence of these problems has brought great challenges to enterprises in large-scale distributed data governance and data mining. The architecture of this study loads the data space component of closed-loop management of data value circulation, and provides SaaS-level services, which users can subscribe to directly without considering the underlying resource deployment, network configuration and business system development and deployment. In addition, cloud, network, data are separated from each other, enterprises need to deploy these resources separately when perform business-oriented data services. That means to build a set of exclusive infrastructure services, involving cloud services, network services, privacy security services, etc. Such a format is cumbersome for enterprises, not only requires a lot of construction funds and also cause a lot of manpower and time costs. This study provides a custom PaaS-level service, the business system loaded on this architecture does not need to consider the underlying resource deployment and network configuration.

Keywords: Dataspace · Data flow · Resource scheduling · Resource allocation · Secure and trusted

1 Introduction

1.1 Background

With the continuous expansion of data scale, data assets have become a strategic resource that cannot be ignored by society and enterprises [1]. As a basic and strategic resource in the digital economy era, data has injected new momentum into economic development [2]. As a strategic requirement of national economic development, data governance has been widely concerned by countries around the world. The United States released the Federal Big Data Research and Development Strategic Plan, focusing on data assets

and developing data as strategic resources. The European Union has put forward the European Data Strategy, establishing a European data space and a single data market, and shaping the strategic plan for “Europe’s Digital Future”. China has launched the “Digital Computing from the East to the West” project, built a national computing power hub, planned a national data center cluster, and designed a national integrated big data center system.

The importance of data as a strategic resource is gradually increasing, but there are also some urgent problems in the circulation process of data elements. These problems include the difficulty of transforming original data into data resources, the difficulty of defining data ownership, the difficulty of standard governance of data assets, the difficulty of data element circulation and pricing, and the difficulty of data application security and mutual trust. These problems hinder the marketization process of data elements and block the circulation channel of data elements, which brings great challenges to the governance and data mining of large-scale distributed data for enterprises.

When enterprises conduct business-oriented data services, enterprises need to deploy these resources separately for the reason that cloud, network, data and business are separated from each other. Therefore, enterprises have to build a set of exclusive infrastructure services involving cloud services, network services, privacy security services, etc. Such a pattern is very heavy for enterprises, not only requires a lot of construction funds but also causes a lot of manpower and time costs.

In response to the above problems, this study proposes an integrated resource system architecture based on data space, which aims to provide integrated resources for large-scale distributed big data and artificial intelligence applications.

Existing data resource systems mostly provide a single data solution and are detached from real application scenarios, which can no longer meet the increasingly large data resource processing needs of enterprises. This research focuses on the whole process of data value circulation, while paying attention to the business needs of users, so as to achieve more efficient and comprehensive data resource processing by demand-driven data resource value circulation.

The European Union defines a data space as an ecosystem corresponding to any data model, data set, ontology, data sharing contract and professional management services, as well as soft capabilities such as governance, social interaction, business processes, etc. [3]. The data space proposed in this research architecture constitutes a closed loop of data value circulation with data fabric and governance, data trusted and secure computing, data identification and right confirmation, and data trading and accounting. By connecting data, cloud computing, network, computing power and other resources, the architecture helps to realize real-time and efficient resource allocation.

1.2 Related Work

In the context of the information age, the traditional architecture of separation of cloud and network cannot meet the large-scale cloud demand brought by the rapid development of digital economy. Cloud-network integration breaks the boundary between cloud and network, changes the traditional network organization mode, and has become

an important feature of information infrastructure [4]. At present, cloud-network integration presents six characteristics: cloud-network integration, element aggregation, capability openness, intelligence and agility, security and credibility, green and low carbon. It shows the trend of multi-technology aggregation and innovation, plays an important role in many fields, and has attracted wide attention of scholars.

Li Lingshu and Wu Jiangxing (2021) proposed a virtual network function mapping method based on SaaS security of cloud network integration, and established a mimic virtual network function mapping model and security optimization mechanism [5]. Qiao Aifeng (2022) summarizes the evolution goals and key technology applications of cloud-network integration, analyzes the innovation and development trend of cloud-network integration technology for full service scenarios, and expounds the application of key technologies such as cloud-native network and application, new network architecture, in-cloud and inter-cloud network interconnection [6]. Chen Kai (2022) proposed the technical scheme of 5G sliced private network based on cloud network integration, analyzed the difficulties encountered in the automatic opening of sliced private network under the new generation operation system, and helped operators move from traffic management to resource management era [7].

Based on the cloud and network integration technology, there are many researches focusing on the integration architecture of cloud and network, and proposing advanced and effective cloud and network integration architecture design schemes to provide solutions for data management applications in the industry.

Al-Fedaghi and Al-Qemlas (2020) selected the thinking (abstract) machine (TM) conceptual model to improve the design, analysis and documentation of the network architecture, modeled a real case study of cloud networks, and introduced the obtained model into the integrated representation of computer networks [8]. Zhu and Fang (2021) introduced three architecture models, four deployment models, five architectures and five key technologies of cloud computing, and expounded how to use cloud computing for network integration and sharing, flexible configuration and invocation of software and hardware resources [9]. Lu and Wu (2021) proposed an air traffic management system (ATM) integration architecture based on cloud computing and blockchain, clarified the overall design architecture and main functional module architecture of the solution, and analyzed and demonstrated the security of the solution from two aspects of process safety and system safety. This solution will help to improve the security, reliability and scalability of ATM services, and provide a reference for subsequent design research [10]. Liu et al. (2021) explore computer big data technology and cloud computing network technology to better store and make full use of data [11].

Based on the development of cloud and network integration, the concept of computing power network was proposed. Computing power network can effectively allocate basic resources such as computing and storage between “cloud-edge-end” by network means, which is the evolution from cloud-network integration to cloud-network end integration.

Pan et al. (2020) introduced the concept of edge-cloud computing (ECC) and reviewed the existing work on ECC-based Demand response (DR). According to the existing work of ECC-based Internet of Things (IoT) architecture, the DR Edge cloud collaborative control architecture is proposed to meet the requirements of ubiquitous

perception and intelligent control of power iot [12]. Wang et al. (2021) proposed a software-defined fine-grained multi-access architecture, which can fully control computing and communication resources, and then studied a two-stage resource allocation strategy based on Q-Learning to better meet heterogeneous radio environments and various user requirements, verifying the feasibility and effectiveness of the architecture [13].

Scholars pay more and more attention to exploring and developing new technologies and solutions to achieve high performance computing network integrated architecture, such as by means of machine learning.

In order to eliminate some of the existing security issues faced by cloud computing, Bahashwan et al. (2019) proposed a new architectural design A virtual security mechanism is established by integrating SDN (Software Defined Networking) and NFV (Network Function Virtualization) based on cloud computing [14]. Rocha et al. (2022) designed a service management system specifically for fog-to-cloud architecture and propose how to implement it using different machine learning solutions [15]. Zhang et al. (2021) used cloud computing, big data, mobile Internet and other technologies to build a smart management system for physical health, which consisted of data collection, transmission, query and analysis modules. Edge nodes were introduced into each data collection area for system deployment, and convolutional neural networks were used to learn features from unsupervised body measurement data [16].

With the accelerated evolution of business digitalization, technology integration and data value, big data and network are facing deep integration. The collaborative model of cloud, edge, network and computing is applied to various big data application scenarios, and provides positive solutions for data governance in multiple industries.

The open service platform for government affairs proposed by Zhou and Chen (2019) integrates information resources of distributed heterogeneous systems and eliminates the phenomenon of "information island". Through the four subsystems of open service platform, service background, e-government service management platform and monitoring platform, data exchange, information sharing and business collaboration based on different transmission protocols can be realized between different institutions, different application systems and databases, so as to provide a good data support environment for government and enterprise information construction [17]. Nimkar and Khanapurkar (2021) focus on the large amount of data in the Internet of Things (IoT), a dedicated scalable architecture for IoT as a Service to Governance (IoTaaS) using edge computing was proposed [18]. Lo et al. (2022) discussed the citizen-centric distributed data sharing model within the e-government architecture [19]. Based on big data and intelligent technology, Sun (2022) designed the system architecture of smart community composed of "infrastructure layer, resource provision layer, application support layer, business logic layer and presentation layer", and put forward strategies and suggestions for smart community governance [20]. To sum up, in the existing research at home and abroad, the cloud network integration architecture is widely used in the construction of government and enterprise data platform. On the basis of the integration of cloud and network, computing power has gradually become an important part of the future development of data governance platform, and various data processing methods, including machine learning have become an important means to support the construction of the platform. Based on

market demand and technology development status, this study proposes an integrated resource system architecture based on data space. On the basis of data space, it forms a closed loop of data value circulation, deeply integrates data and information, connects data, computing, cloud, network and edge to efficiently cooperate, and provides multiple factor integration services.

2 Integrated Resource System Architecture Based on Dataspace

This research aims to provide an integrated resource system architecture based on data space to facilitate the circulation of data value and the integrated invocation of resources. In this study, the data space formed by data fabric and governance, trusted and secure data computing, data identification and right confirmation, data trading and accounting constitutes a closed loop of data value circulation. By connecting data, cloud computing, network, computing power and other resources, it is called by business-driven integration to realize real-time and efficient resource allocation.

The technical scheme of the architecture is shown in Fig. 1, which is divided into four layers, including cloud network resource layer, data space layer, resource scheduling layer and business demand layer from bottom to top.

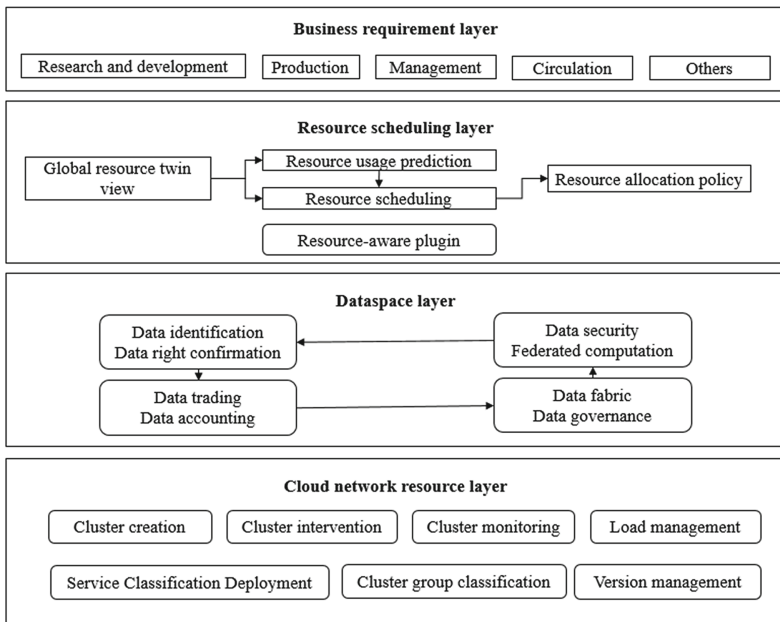


Fig. 1. Architecture of integrated resource system based on dataspace

2.1 Cloud Network Resource Layer

The cloud network resource layer takes nodes as units, and each node is a K8S cluster containing computing power, storage, network and data resources. This layer has

the characteristics of cross-domain, multi-cloud, cloud-edge collaboration and business diversification. It supports multi-regional deployment and forms a regional layout of “east data west calculation”. It supports cloud-native cluster deployment management and intelligent monitoring such as enterprise private cloud. According to the resource scale and service load of the data center, it is divided into three types of resource nodes: It hosts federated learning, cross-domain and cross-source database engines, distributed machine learning and other business subsystems.

The cloud network resource layer consists of multiple platform control subsystems:

(1) Cross-regional multi-cloud native environment management system

The system is responsible for resource cluster creation, cluster access, cluster monitoring and platform load management.

(2) Cross-domain deployment management system for business subsystems

The system groups and classifies clusters, deploys services according to classification, formulates multi-cluster deployment scheme of services and manages version.

(3) Cross-regional resource awareness monitoring system

The system is responsible for unified collection components, storage gateways, deployment of object storage clusters, and query components.

(4) Global resource scheduling management system

The system is responsible for unified resource view, unified management of resource prediction and scheduling.

(5) Global data management system

This system is responsible for unifying the full platform data view and relating the global data.

2.2 Data Space Layer

The data space layer mainly establishes a closed-loop management of data value circulation through core technologies such as active metadata, artificial intelligence, machine learning, blockchain, and privacy computing. The data space contains the following four technical components:

(1) Data Fabric and Data governance

Data fabric is a generic data architecture that enables fully integrated data management capabilities including discovery, governance, management, and orchestration, and uses AI capabilities for semantic exploration, analysis, and recommendation to move from a reactive to a proactive data strategy. Aiming at large-scale multi-source heterogeneous data in distributed, hybrid/multi-cloud environment, data fabric technology uses meta-data, artificial intelligence, machine learning and other algorithms and tools to connect

different data sources and the business relationship between the data, and realizes the distributed, automatic, and intelligent dynamic overall management of data.

(2) **Data security and Data federation**

The strategy of distributed federated data management can reduce the risk of data abuse, misunderstanding and leakage, and realize data protection and security. In order to protect privacy and ensure that the original sensitive data does not leave the local area, each data owner does not share the data directly, but calculates the data in each party first, and aggregates the intermediate calculation results to obtain the final calculation results.

(3) **Data right confirmation and Data identification**

For different sources of data, blockchain technology is used as a means to clarify the ownership of their data. Blockchain encapsulates data assets as data objects that can be uploaded to the chain, ensures the uniqueness of assets through the digital identity association mechanism, and registers and protects data ownership at different stages such as data ownership and intermediate data.

(4) **Data transaction and Data accounting**

In the process of data trading, with the transfer or grant of various tradable data rights of data products/services, through the automation and high credibility of blockchain-based smart contracts, automatic data trading is realized, the used data and resources are settled, and multi-party data value measurement based on contribution is carried out.

The data space constitutes a closed loop of data value circulation, and carries out data fabric and data governance for distributed data resources to realize the unified sorting, inventory, arrangement and governance of data, ensuring data security and privacy through data federation. For data from different sources, blockchain technology was used as a means to clarify the ownership of their data. In the process of data power transfer or grant, the used data and resources are settled, and the multi-party data value measurement based on contribution is carried out.

The four links constitute the closed loop of data value circulation, and finally constitute the data space layer of the architecture.

2.3 **Resource Scheduling Layer**

Resource scheduling constructs a global resource view based on resource probe data, and allocates suitable resource subsets for different types of computing tasks, so as to optimize the core resource scheduling index and form a scheduling closed loop.

The core functions of this layer include:

- (1) **resource data awareness.** The resource data awareness plug-in obtains cluster resource data by deploying cluster probes in each node.
- (2) **Resource twin view construction.** The global resource twin view is constructed based on the data object model, and the view is updated with real-time data.

- (3) **Resource usage prediction.** The resource usage prediction model is constructed, trained and updated based on historical resource data and machine learning algorithms.
- (4) **Resource scheduling.** Based on the resource data, prediction model and multi-objective optimization constraints, the resource allocation strategy is output.
- (5) **Resource allocation.** It allocates resources for tasks on the corresponding resource subset based on the allocation policy.

2.4 Business Requirement Layer

According to the business needs of data users, the business demand layer mobilizes data resources in the cloud network resource layer and the data space layer, drives the data resource value circulation with demand, and promotes the circulation of data value. The transmission of demand among the layers is shown in Fig. 2.

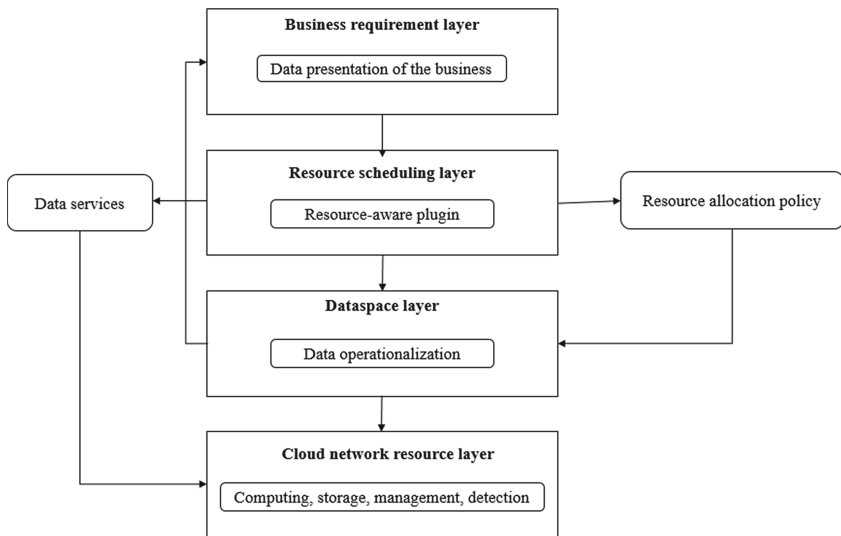


Fig. 2. Closed loop of business data flow

Aiming at the problems of independence of business units and weak data collaboration ability in the traditional government and enterprise informatization process, the business requirement layer digitizes the business processes involved in the user's operation and management process, including research and development, production, management, circulation and other businesses, and provides standardized data sources for the resource scheduling layer.

According to the digital twin model, the resource scheduling layer constructs a global resource twin view, uses historical resource data to train and update the resource usage prediction model, and then combines resource data, prediction model and multi-objective optimization constraints to output the resource allocation strategy. On the one hand, the resource scheduling layer schedules the cloud network resource layer, transmits the

resource data services such as the resource load of each cluster and the network load between clusters to the cloud network resource layer, and allocates computing power and network resources according to the load. On the other hand, the data space layer is scheduled to output the resource allocation strategy to the data space layer, so that it can allocate resources for tasks more efficiently. At the same time, the resource data awareness plug-in is used to sense the data in real time to realize the prediction and optimization of resource usage.

According to the allocation strategy calculated by the resource scheduling layer, the data space layer refines its value through artificial intelligence, machine learning and other methods. Firstly, the distributed business data resources are unified sorted, inventoried, arranged and governed, and data protection and security are realized through data federation. Then the ownership of different data sources is clarified through blockchain technology.

The cloud network resource layer provides virtual computing, storage, management, monitoring and other capabilities for the data space, and realizes the integrated supply of computing power, network, data and algorithm models. Through the global resource view and global data view, the global perception, prediction and resource optimization of data, computing and network are realized. The cloud network resource layer supports the business platform and data platform to form a closed loop to support enterprise decision-making, empower business processes, realize business agile development, and actively respond to user needs.

3 Business Case Introduction Under This Architecture

This section describes the process of implementing cross-cluster federated semantic retrieval of unstructured data. The data processing process of the architecture is described in detail, using the application of court document retrieval as an example.

3.1 Response from the Business Requirements Layer

When the system receives a task request for cross-cluster joint semantic retrieval, the requested content is as follows: Retrieve the court documents in Beijing, Shanghai and Nanjing, and find the court documents with more than 90% similarity to the target document.

The business requirement layer processed the task into data, transformed it into a standardized data source and passed it to the resource scheduling layer.

3.2 Response from the Resource Scheduling Layer

The resource scheduling layer constructs a global resource view based on resource probe data, allocates suitable resource subsets for different types of computing tasks, and optimizes the core resource scheduling index, forming a scheduling closed loop. Here are the steps:

- (1) The resource data perception plug-in obtains cluster resource data by deploying cluster probes on each node, that is, the perception plug-in obtains the business requirements of query document information.
- (2) Build a global resource twin view based on the data object model, and update the view with real-time data.
- (3) The resource usage prediction model is constructed, trained and updated based on historical resource data and machine learning algorithms, that is, the existing court documents in the system are used to train the prediction model.
- (4) Output resource allocation strategy based on resource data, prediction model and multi-objective optimization constraints.
- (5) Allocate resources for tasks on the corresponding resource subset based on the allocation policy. The existing court document resource collection is conveyed to the data space layer for comprehensive retrieval processing.

3.3 Response of the Dataspace Layer

According to the allocation strategy calculated by the resource scheduling layer, the data space layer refines its value through artificial intelligence, machine learning and other methods. Here are the steps:

(1) Data fabric and Data governance

For a large number of court documents, AI capabilities are used for semantic exploration, analysis and recommendation, so as to change from passive data strategy to active and responsive data strategy, and the relevant documents in Beijing, Shanghai and Nanjing are screened.

(2) Data security and Data federation

The strategy of distributed federated management is used to reduce the risk of data abuse, misunderstanding and leakage, and realize data protection and security. In order to protect privacy and ensure that the original sensitive data does not leave the local area, each data owner does not share the data directly, but calculates the data in each party first, and aggregates the intermediate calculation results to obtain the final calculation results.

(3) Data right confirmation and Data identification

For the data from different sources in the space, the blockchain technology is used as a means to clarify the ownership of the data. The data asset is encapsulated as a data object that can be linked to the chain, the uniqueness of the asset is ensured through the digital identity association mechanism, and the data ownership in different stages such as data ownership and intermediate data ownership are reliably registered and protected.

(4) Data transaction and Data accounting

Through the characteristics of automation and high reliability based on blockchain smart contract, automatic data trading is realized, the clerical data used in the system is settled,

the multi-party data value measurement based on contribution is carried out, and the most valuable data is judged and fed back.

3.4 Response of Cloud Network Resource Layer

The cloud network resource layer provides virtual computing, storage, management, monitoring and other capabilities for the data space, and realizes the integrated supply of computing power, network, data and algorithm models. Through the global resource view and global data view, the global perception, prediction and resource optimization of data, computing and network are realized, and the technical support is provided for the whole system.

4 Conclusion

Aiming to address the problems in enterprise data circulation and management, this study proposes an integrated resource system architecture based on data space. Compared to the traditional model, the architecture makes full use of edge nodes, builds a computing model closer to the data source, takes cloud network resources as the foundation, data space as the center, and performs platform-wide resource scheduling according to business requirements. Relying on the characteristics of wide distribution and inter-connection of the network, it assists the circulation and integration of data elements. The architecture provides SaaS and custom PaaS services, fully considers enterprise business, technology and management needs, provides a new idea and entry point for eliminating enterprise data islands and improving the efficiency of data platform, and reflects the value in innovation and practicability.

In order to further improve the efficacy of the government and enterprise data platform and make full use of data information resources, there are still a number of research problems to be explored in the next work. We should continue to promote the in-depth research of data space and computing power network technology, strengthen the deep integration of enterprise business and data, provide integrated services of multi-factor fusion, enhance the breadth and depth of the application scope of the architecture, and help various big data application scenarios to improve the efficiency and effectiveness of the use of emerging information technology. At the same time, it pays attention to the importance of data security and privacy computing in the application of data platform, which provides tighter privacy protection for the architecture, ensures the security of data information, and accelerates the development of digital industry.

References

1. Wang, J., Li, Y., Song, W., et al.: Research on the theory and method of grid data asset management. *Procedia Comput. Sci.* **139**, 440–447 (2018)
2. URL http://paper.cntheory.com/html/2020-06/05/nw.D110000xxsb_20200605_3-A2.htm (in Chinese). Last accessed 2020
3. European Commission website: https://ec.europa.eu/info/sites/default/files/communication-european-data-strategy-19feb2020_en.pdf

4. Ke, R.: Based on science and technology Self-reliance and self-strength to comprehensively promote cloud network integration. *People's Forum* (2021)
5. Li, L., Wu, J.: Virtual network function mapping method for saas security in cloud and network integration. *Comput. Eng.* (2021)
6. Joe loves Feng: Research on architecture and key technologies of cloud network integration. *Des. Technol. Posts Telecommun.* (2022)
7. Kai, C.: Technical scheme and application of 5G slice private network based on cloud network integration. *Telecommun. Sci.* **38**(7), 166–174 (2022)
8. Al-Fedaghi, S., Al-Qemlas, D.: Modeling network architecture: a cloud case study. *arXiv preprint arXiv:2004.10350* (2020)
9. Zhu, G., Fang, X.: Cloud computing technology for the network resource allocation on the research of application. In: *The 2020 International Conference on Machine Learning and Big Data Analytics for IoT Security and Privacy: SPIoT-2020*, vol. 2, pp. 740–744. Springer International Publishing, Cham (2020)
10. Lu, X., Wu, Z.: ATMCC: design of the integration architecture of cloud computing and blockchain for air traffic management. In: *2021 IEEE Intl Conf on Parallel & Distributed Processing with Applications, Big Data & Cloud Computing, Sustainable Computing & Communications, Social Computing & Networking (ISPA/BDCLOUD/SocialCom/SustainCom)*, pp. 37–43. IEEE (2021)
11. Liu, X., Liu, Y., Fei, Y.: Computer big data analysis and cloud computing network technology. In: *The 2021 International Conference on Machine Learning and Big Data Analytics for IoT Security and Privacy: SPIoT-2021 Volume 1*, pp. 517–522. Springer International Publishing (2022)
12. Pan, X., Jiang, A., Wang, H.: Edge-cloud computing application, architecture, and challenges in ubiquitous power Internet of Things demand response. *J. Renew. Sustain. Energy* **12**(6), 062702 (2020)
13. Wang, L., Zhang, J., Wang, T., Wu, K.: A fine-grained multi-access edge computing architecture for cloud-network integration. *Jisuanji Yanjiu yu Fazhan/Comput. Res. Dev.* **58**(6), 1275–1290. ISSN: 10001239 (2021). <https://doi.org/10.7544/issn1000-1239.2021.20201076>
14. Bahashwan, A.A., Anbar, M., Abdullah, N.: New architecture design of cloud computing using software defined networking and network function virtualization technology. In: *Emerging Trends in Intelligent Computing and Informatics: Data Science, Intelligent Information Systems and Smart Computing* vol. 4, pp.705–713. Springer International Publishing (2020)
15. Rocha, A.L.B., Cesila, C.H., Maciel, P.D., Jr., et al.: CNS-AOM: design, implementation and integration of an architecture for orchestration and management of cloud-network slices. *J. Netw. Syst. Manage.* **30**(2), 34 (2022)
16. Zhang, N., Zhang, C., Wu, D.: Construction of a smart management system for physical health based on IoT and cloud computing with big data. *Comput. Commun.* **179**, 183–194 (2021)
17. Zhou, G., Chen, K.: Use Big Data+ internet thinking to solve the problem of data governance. In: *Journal of Physics: Conference Series*, vol. 1302, no. 2, p. 022092. IOP Publishing (2019)
18. Nimkar, S., Khanapurkar, M.M.: Edge computing for IoT: a use case in smart city governance. In: *2021 International Conference on Computational Intelligence and Computing Applications (ICCCA)*, pp. 1–5. IEEE (2021)
19. Lo, O., Buchanan, W.J., Sayeed, S., et al.: GLASS: a citizen-centric distributed data-sharing model within an e-governance architecture. *Sensors* **22**(6), 2291 (2022)
20. Sun, X.: Smart community governance system and governance strategies in the big data era. In: *2021 International Conference on Big Data Analytics for Cyber-Physical System in Smart City: Volume 2*, pp. 343–349. Springer Singapore (2022)



Task Allocation Method of Blockchain-Based Multi-robot System

Fengbo Bao¹, Jiansheng Peng^{1,2}(✉), and Jingsong Guo¹

¹ College of Automation, Guangxi University of Science and Technology, Liuzhou 545000, China

sheng120410@163.com

² Department of Artificial Intelligence and Manufacturing, Hechi University, Hechi 547000, China

Abstract. With the continuous development of multi-robot systems, the main problems are task assignment and multi-robot task planning. This paper will combine blockchain technology with the design of multi-robot system task allocation architecture, and make use of the nature of blockchain information sharing to carry out multi-robot system task allocation. Firstly, the main problems faced by multi-robot systems in recent years are introduced. The application of blockchain technology should not be able to solve the problem of multi-robot task allocation, but also can solve the problem of multi-robot system node intrusion. Then describe the concept of dividing tasks and how individual blocks in a blockchain store information. Finally, the architecture of blockchain multi-robot system is designed, and the assumptions of application scenarios are made.

Keywords: Multi-robot system · Task allocation · Blockchain · System architecture

1 Introduction

With the continuous development of society, task coordination of multi-robot systems is one of the main challenges faced by multi-robot systems [1]. If there is no good coordination strategy of multi-robot system, the work efficiency of multi-robot system will be greatly reduced, and even the task of multi-robot can not be completed.

The most important problem in the coordination of multi-robot systems is the task assignment of a single robot [2]. The mechanism for assigning tasks to multiple robots should consider the performance of a single robot to determine whether the robot can efficiently complete the task. For example, in a flood disaster rescue mission, a multi-robot system is required to perform rescue operations. At this time, the multi-robot system performs a broad rescue task, and a single robot will perform its own tasks according to the specific task assignment, such as drawing maps and finding the victims. According to the performance of a single robot in a multi-robot system, a single robot role is set to improve the efficiency of the multi-robot system.

Inspired by the flood disaster, in a dynamic and decentralized task allocation architecture, we must consider setting the role of a single robot, dividing the multi-robot system into a single small execution unit, and assigning the specified task type according to the role set by a single robot.

In order to manage the information exchanged during the distribution process, the use of blockchain technology is proposed in the multi-robot system architecture [3], because blockchain has the nature of immutable messages, decentralized communication, sharing messages, etc., making blockchain as a technology to manage information is an innovative aspect of the proposed architecture. May be a promising approach to dealing with issues of consistency, integrity, security, etc. The approach builds on the idea of multi-machine communication and task coordination through a consortium blockchain in a multi-robot system architecture. The architecture should support a dynamic and decentralized task allocation mechanism, setting different roles in the multi-robot system, and assigning tasks according to different roles in task allocation.

2 Task Allocation and Blockchain for Multi-robot Systems

Task allocation between multiple robots refers to the need for individual robots to figure out which tasks to perform and to work together in the best way to achieve as many global goals as possible. Among them, the existing task allocation of multiple robots is a market-based method. One of the most common mechanisms is called auction mechanism [4]. When tasks are allocated through auction, a single robot provides a bid, which is usually calculated based on utility value. The robot with the highest utility value of each task will win the task, which requires individual robots to share the utility value of information when they receive task information in order to perform the task.

For tasks in different realistic scenarios, different types of task characteristics are used to describe the complexity of tasks. In this paper, the description types of tasks in literature [4] will be considered:

1. Atomic task: If a task cannot be broken down into subtasks, then it is an atomic task.
2. Simple tasks that can be decomposed into a set of atomic subtasks or other simple tasks that can be decomposed, as long as the different parts of the decomposition must be performed by the same robot.
3. Compound task: A task that can be broken down into a set of atoms or compound subtasks. When each subtask needs to be assigned to a different individual robot, we call it a CN task (N subtasks require exactly N robots). In the absence of constraints, subtasks can be assigned to a maximum of 1 robot, where M is the number of subtasks called CM tasks.

In 2009, Satoshi Nakamoto published a paper introducing an electronic peer-to-peer cash system called Bitratio [5]. His proposal makes it possible for any two nodes in a blockchain network to carry out transactions without the need for a third party's witness. Bitcoin is the first truly decentralized global monetary system based on an architecture constructed by hashing algorithms and asymmetric cryptographic algorithms. Figure 1 shows the contents stored in a block.

As can be seen from the figure, a block contains the size of the block, which is a value in bytes, the block header, is composed of the version number, the hash value of

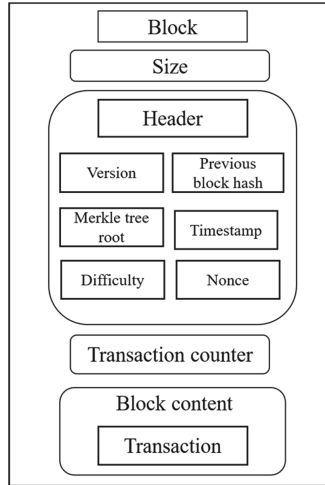


Fig. 1. Block storage content

the previous block, the hash value of the Merkle root, the time stamp, the difficulty value of mining, the nonce value, the transaction counter identifies the current block and how many transactions are stored in the content block storing all block transactions.

In the blockchain network, each node stores a copy of the ledger of all transactions, and they are all able to create new things, in order to avoid the malicious behavior of nodes to forge transactions, there is a consensus algorithm between nodes. Bitcoin uses proof-of-work algorithm [6], which is the most original consensus algorithm. Although it has high security, it consumes a lot of energy due to a large number of operations. Along with this shortcoming, a lot of consensus algorithms have been gradually derived, such as proof of equity [7], proof of importance [8], confidence measure [9], etc. Consensus algorithm is a kind of organization method for blockchain between nodes, which can choose the appropriate consensus algorithm according to the specific environment to reduce the energy consumption.

3 Task Allocation Architecture Based on Blockchain

In order to enable the blockchain to act as a decentralized database, the nodes of a single robot are allowed to share information. The next step is to construct an architecture for task allocation of multi-robot systems based on blockchain technology.

First consider that there is a multi-robot system that is responsible for announcing the tasks that need to be performed by a single robot in a given task, and the multi-robot system, as described in the literature [4], decomposes the task into subtasks that can be performed by a single robot. When a multi-robot system completes the assignment process and a single robot assigned to a task begins to perform the task, at the end of the assignment process, there may be a robot without an assigned task, or there may be a task that cannot be assigned to any suitable available robot. Such a result depends on the constraints indicated and the characteristics of the available agents.

This paper will consider the architecture based on reference [10], which is used because it is widely used in a variety of methods. Figure 2 shows the components of this architecture.

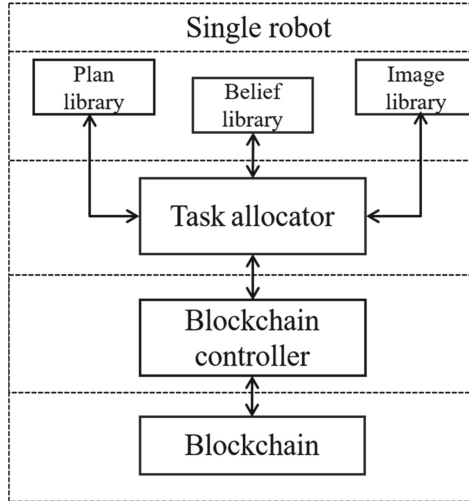


Fig. 2. Architecture of blockchain multi-robot system

The task assignment mechanism interacts with a single robot's plan library, belief library, and image library to provide input to the assignment process. In order to share information between multiple robot nodes, the task allocation mechanism also interacts with the blockchain controller component, which is responsible for managing the content to be added to the blockchain. The multi-robot system interacts with its own blockchain to add information related to tasks that need to be performed by a single robot, as well as the roles of the robots available in the multi-robot. Multi-robot systems use blockchain to share information about the tasks that need to be performed and the roles available to individual robots in the multi-robot and the functions they need to perform each role. Each robot initially senses the task it needs to perform via a blockchain controller. Perceptual tasks based on the recognition of a single robot, through the task assignment mechanism, based on the role it can play in a multi-robot system, the tasks it can perform, are also perceived through the blockchain. The individual robot then identifies the tasks it will attempt to assign itself and calculates its bid for those tasks. A single robot then goes through a blockchain controller and places its bid in the blockchain. The bids added to the blockchain will be perceived by all the other individual robots, which will then check if certain bids are better than the bids they have assigned to their own tasks. If this is the case, a single robot will withdraw that task from the pre-assigned task list and then check for the next task it will bid on to replace the one it abandoned. These steps are repeated until all individual robots have agreed to the assignment, that is, until the task assigned to all robots has not undergone any further modification.

4 Scene Analysis and Research

Suppose that in a flood disaster scenario, multiple robots are asked to perform the two tasks of graphic drawing and water quality detection in the disaster area. For these two tasks, a single robot must have the function of map drawing, water sample collection and navigation. In the multi-robot system, it is assumed that three robots can help complete these tasks, one is responsible for collecting water samples, referred to as USV1, and two are responsible for drawing maps, UAV1 and UAV2. Specific functions are as follows:

USV1: Capability ([surface navigation, collection of water samples])

UAV1: Ability ([take photos, drawmaps])

UAV2: Ability ([take photos, drawmaps])

Individual roles can be set according to the capabilities of individual robots, USV1 is the collector, UAV1 and UAV2 are the plotter. The tasks to be performed by the robot are sorted, named, delimited, and assigned to roles:

Task (Task 1, collecting water samples, Area A, Collector)

Task (Task 2, map making, Region A, Plotter)

Task (Task 3, map making, Region B, Plotter)

A multi-robot system distributes tasks through the blockchain, a single robot in the multi-robot system creates a blockchain network, and then starts to create a blockchain, and a single robot in the multi-robot system can share roles and task information through the blockchain. Figure 3 shows a schematic diagram of task allocation between a multi-robot system and a blockchain.

Block 1 represents a multi-robot system that adds information about a single robot role to the blockchain. Blockchain technology is responsible for synchronizing character information with a copy of the blockchain available in the robot. Once the robot's blockchain is updated with a new transaction, the blockchain controller in each robot will generate a perception to the robot about the new information. Each robot is now able to determine the role it can play in the organization. USV1 identifies itself as a collector, whereas UAV1 and UAV2 identify itself as a painter. Block 2 indicates that a multi-robot system uploads task information to the blockchain, and a single robot senses the task information through the blockchain. According to the role that a single robot can play, it determines the tasks that can be completed and bid for in a multi-robot system. For example, USV1 can only bid for task 1 based on its own capabilities, while UAV1 and UAV2 can only bid for task 2 and Task 3. Individual robots acquire tasks by inserting bidding information on tasks into their blockchain copy, and their bids reference the individual robot plan library as well as the input from the goal and image library. According to the nature of the blockchain, the transaction information between them will be recorded and synchronized in the blockchain, block 3 represents the bidding information of a single robot for a task. A single robot can recognize the high and low bids for the same task based on the blockchain, and if the bid is low, it will execute the next bid for the task. For example, when UAV1 and UAV2 bid for the same task, UAV2 bids lower for task 2

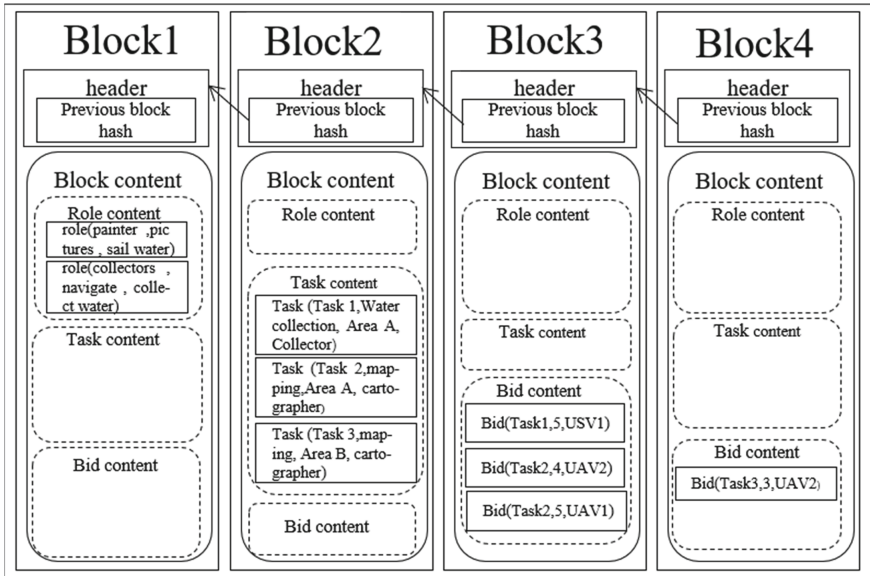


Fig. 3. A blockchain-based transaction for a multi-robot system

than UAV1, and UAV2 bids for task 3. Block 4 represents UAV2's bid information for task 3 until the final task assignment is completed.

5 Summary and Outlook

The use of blockchain technology in multi-robot systems for task distribution between robots ensures the advantages of multi-robot systems in terms of communication security, privacy and non-tampering. However, there are also various problems, such as a delay in receiving information from a single robot during the experiment, insufficient memory in the storage block, and an increased possibility of the block information being tampered with due to the number of robots. Although the use of blockchain technology in multi-robot systems is full of various challenges, from the current development trend, the combination of blockchain technology and multi-robot systems can solve many problems in multi-robot systems. On the one hand, according to the decentralized nature of blockchain technology, it can make up for the shortcomings of the centralization of multi-robot systems, so that the fault tolerance of multi-robot systems is improved, on the other hand, according to the distribution of blockchain storage data, the loss of data of multi-robot systems can be avoided.

Funding Statement. The authors are highly thankful to the Natural Science Foundation of Guangxi Province (NO. 2023GXNSFAA026025), the National Natural Science Foundation of China(NO. 62063006), to the Innovation Fund of Chinese Universities Industry-University-Research (ID: 2021RYC06005), to the Research Project for Young and Middle-aged Teachers in Guangxi Universities (ID: 2020KY15013), and to the Special research project of Hechi University (ID: 2021GCC028). This research was financially supported by the project of outstanding

thousand young teachers' training in higher education institutions of Guangxi, Guangxi Colleges and Universities Key Laboratory of AI and Information Processing (Hechi University), Education Department of Guangxi Zhuang Autonomous Region.

References

1. Feng, Z., Hu, G., Sun, Y., et al.: An overview of collaborative robotic manipulation in multi-robot systems. *Annu. Rev. Control. Rev. Control.* **49**, 113–127 (2020)
2. Farivarnejad, H., Berman, S.: Multirobot control strategies for collective transport. *Annu. Rev. Control Robot. Auton. Syst.* **5**, 205–219 (2022)
3. Castelló Ferrer, E.: The blockchain: a new framework for robotic swarm systems. In: *Proceedings of the Future Technologies Conference (FTC) 2018: Volume 2*, pp. 1037–1058. Springer International Publishing (2019)
4. Zlot, R.M.: *An Auction-Based Approach to Complex Task Allocation for Multirobot Teams*. Carnegie Mellon University, The Robotics Institute (2006)
5. Nakamoto, S.: Bitcoin: a peer-to-peer electronic cash system. *Decentralized Bus. Rev.* 21260 (2008)
6. Sleiman, M.D., Lauf, A.P., Yampolskiy, R.: Bitcoin message: data insertion on a proof-of-work cryptocurrency system. In: *2015 International Conference on Cyberworlds (CW)*, pp. 332–336. IEEE (2015)
7. Watanabe, H., Fujimura, S., Nakadaira, A., et al.: Blockchain contract: Securing a blockchain applied to smart contracts. In: *2016 IEEE International Conference on Consumer Electronics (ICCE)*, pp. 467–468. IEEE (2016)
8. Rao, A.S., Georgeff, M.P.: BDI agents: from theory to practice. In: *Icmas*, vol. 95, pp. 312–319 (1995)
9. Pohl, M., Nahhas, A., Bosse, S., et al.: Proof of provision: improving blockchain technology by cloud computing. In: *CLOSER*, pp. 523–527 (2019)
10. She, W., Liu, Q., Tian, Z., et al.: Blockchain trust model for malicious node detection in wireless sensor networks. *IEEE Access* **7**, 38947–38956 (2019)



Research on Improving TEB Algorithm for Mobile Robot Path Planning

Hongyu Zhang¹, Jiansheng Peng^{1,2}(✉), and Wei Qian¹

¹ College of Automation, Guangxi University of Science and Technology, Liuzhou 545000, China

sheng120410@163.com

² Department of Artificial Intelligence and Manufacturing, Hechi University, Hechi 547000, China

Abstract. To address the issue of unstable velocity output in the TEB algorithm during multi-point navigation, this paper introduces the TEB-confidence algorithm. This algorithm resolves the problem by incorporating buffer and expansion zones around the target points, which impose velocity constraints as the points are approached. Moreover, the Chebyshev series method is utilized to accurately fit the decay function, $\text{erf}(x)$, enhancing the precision of the fitting process. Experimental evaluations were conducted using the Robot Operating System (ROS) with an Ackermann motion model robot. The experiments involved navigating through seven target points using both the TEB-confidence algorithm and the classical TEB algorithm. The TEB-confidence algorithm successfully completed the multi-point navigation task in 22.5 s, whereas the classical TEB algorithm required 25.9 s. This demonstrates a significant 15.11% reduction in execution time when using the TEB-confidence algorithm compared to the classical TEB algorithm. Additionally, during the experiments, the classical TEB algorithm resulted in a collision, leading to a complete stop. The experimental results provide solid evidence that the enhanced TEB-confidence algorithm effectively prevents collisions resulting from velocity instability.

Keywords: Mobile robot · Path planning · ROS · TEB

1 Introduction

In the field of robot navigation, achieving precise navigation requires the integration of global path planning and local path planning. The global path planning algorithm determines the optimal route from the starting point to the target point, while the local path planning algorithm dynamically adjusts the robot's trajectory during travel to avoid obstacles and ensure safe navigation. This paper focuses on enhancing the multi-point navigation algorithm in the Robot Operating System (ROS) by optimizing global and local path planning and introducing innovative improvements to enhance navigation accuracy and precision.

Global path planning algorithms, such as A* [1], Dijkstra's algorithm [2], and graph search-based algorithms [3], analyze the environment map to find a path that minimizes

obstacles or distances. These algorithms commonly use discrete map representations and incorporate heuristics to efficiently search for feasible navigation paths.

Local path planning algorithms, such as the TEB algorithm [4] and DWA algorithm [5], dynamically generate obstacle-avoiding trajectories in real-time using sensor data and environment-aware information. These algorithms have low computational complexity and ensure the robot can respond quickly to changes in the environment, enabling safe navigation.

However, traditional multi-point navigation algorithms face challenges in controlling the robot's behavior around the target point [6]. Typically, the robot travels in a straight line at a constant speed and abruptly stops upon reaching the target point. This approach often results in overshooting the target point and navigation inaccuracies. To address this issue, this paper introduces the TEB-confidence algorithm, which defines an expansion region and a buffer region around each target point. This allows the robot to decelerate proactively when approaching the target point, preventing overshooting. The algorithm employs the erf(x) function as the decay function to achieve this control.

2 TEB Algorithm

Motion planning is of utmost importance in robotics as it aims to find the optimal path in a given map, ensuring collision avoidance. As a result, extensive research and application of motion planning algorithms have been carried out in the field of robotics. However, in real-world scenarios, robot navigation maps often include dynamic objects, rendering the reliance on a global path planner insufficient to effectively address this challenge. Therefore, it becomes crucial to incorporate local path planning components that can dynamically adapt and avoid obstacles in real-time, ensuring both efficiency and safety in navigation. In our specific case, the TEB algorithm has been employed for motion planning of our robot.

The TEB algorithm produces a sequence of local poses based on the trajectory planned by the global path planner [7] (Fig. 1).

$$X_i = (x_i, y_i, \beta_i) \quad (1)$$

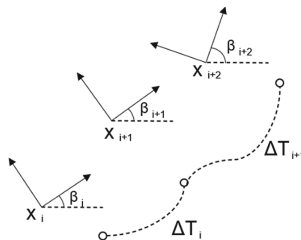


Fig. 1. TEB algorithm pose sequence and time series

X_i represents the pose of the robot at moment i , The coordinates of the robot in the corresponding coordinate system (or map coordinate system) are denoted by x_i and y_i .

Additionally, β_i represents the orientation angle of the robot. The adjacent poses of the robot are subject to constraints imposed by the adjacent time interval ΔT , which can be expressed as follows:

During the optimization process, the TEB algorithm utilizes the concept of graph optimization, employing g2o to optimize the pose and time series of multiple moments as nodes, while the constraint terms are represented as edges. This approach aims to find the optimal path using the B solver. Subsequently, the control quantity $V(v, w)$ is generated as the output, allowing for the control of the trolley speed.

The TEB optimization process can be mathematically represented by the following equation:

$$f(B) := \sum_k \gamma_k f_k(B) \quad (2)$$

$$B^* := \underset{B}{\operatorname{argmin}} f(B) \quad (3)$$

The TEB algorithm employs the concept of accumulating multiple constraints to define the objective function to be optimized. The variable $f_k(B)$ represents the collection of multiple path constraints, which can be categorized into the following four types:

(1) Wayfinding points and obstacle constraints

$$e_\Gamma(x, x_r, \epsilon, S, n) \simeq \begin{cases} \left(\frac{x - (x_r - \epsilon)}{S}\right)^n & \text{if } x > x_r - \epsilon \\ 0 & \text{otherwise} \end{cases} \quad (4)$$

$$f_{\text{path}} := e_\Gamma(d_{\min,j}, r_{p_{\max}}, \epsilon, S, n) \quad (5)$$

$$f_{\text{ob}} := e_\Gamma(-d_{\min,j}, -r_{o_{\min}}, \epsilon, S, n) \quad (6)$$

where x_r denotes the boundary, S denotes the scaling, n denotes the polynomial order, $d_{\min,j}$ denotes the minimum distance between the robot and the j th path point or obstacle, $r_{p_{\max}}$ denotes the maximum distance to the path point, and $r_{o_{\min}}$ denotes the minimum distance to the obstacle.

(2) Linear velocity and acceleration constraints

$$v_i := \frac{1}{\Delta T_i} \left\| \begin{pmatrix} x_{i+1} - x_i \\ y_{i+1} - y_i \end{pmatrix} \right\| \quad (7)$$

$$\omega_i := \frac{\beta_{i+1} - \beta_i}{\Delta T_i} \quad (8)$$

$$a_i = \frac{2(v_{i+1} - v_i)}{\Delta T_i + \Delta T_{i+1}} \quad (9)$$

(3) Non-holonomic kinematics constraints

The robot utilized in this paper adheres to AKM kinematics and is limited to two degrees of freedom. As a result, it is capable of motion solely in the direction aligned with the robot's current heading.

$$\vartheta_i := \vartheta_{i+1} \Leftrightarrow \begin{pmatrix} \cos \beta_i \\ \sin \beta_i \\ 0 \end{pmatrix} \times \mathbf{d}_{i,i+1} = \mathbf{d}_{i,i+1} \times \begin{pmatrix} \cos \beta_{i+1} \\ \sin \beta_{i+1} \\ 0 \end{pmatrix} \quad (10)$$

$$\mathbf{d}_{i,i+1} := \begin{pmatrix} x_{i+1} - x_i \\ y_{i+1} - y_i \\ 0 \end{pmatrix} \quad (11)$$

$$f_k(\mathbf{x}_i, \mathbf{x}_{i+1}) = \left\| \left[\begin{pmatrix} \cos \beta_i \\ \sin \beta_i \\ 0 \end{pmatrix} + \begin{pmatrix} \cos \beta_{i+1} \\ \sin \beta_{i+1} \\ 0 \end{pmatrix} \right] \times \mathbf{d}_{i,i+1} \right\|^2 \quad (12)$$

(4) Fastest path

$$f_k = \left(\sum_{i=1}^n \Delta T_i \right)^2 \quad (13)$$

3 Improved Algorithm Based on TEB

3.1 TEB-Confidence Algorithm

In the task of multi-point navigation, it is common to employ both a local path planner and a global path planner. The global path planner generates an initial path plan, while the local path planner is responsible for obstacle avoidance and fine-tuning during operation. However, the TEB algorithm, due to its combination of multiple condition constraints, may sometimes result in minor violations, particularly when the robot approaches the target point at high speed. This can lead to overshooting the target or even causing collisions, resulting in wasted time and posing a safety risk. To address this issue, this paper proposes an improved TEB algorithm based on elastic confidence. The elastic confidence algorithm conceptually divides the target point into confidence regions, and a speed decay penalty term is introduced when the robot enters the arrival region threshold. The TEB-confidence algorithm proposed in this paper introduces a secondary speed constraint when the robot is close to the target point, effectively reducing the likelihood of violations during the navigation process.

The TEB local path planner, in conjunction with the global path planning algorithm shown in Fig. 2, generates the corresponding control volume $V(v, w)$ for the robot within the time interval ΔT . As the robot enters the buffer zone of the target point (inside the blue circle), the control volume is further constrained to facilitate a gradual slowdown. Similarly, when the robot reaches the expansion zone of the target point (inside the black circle), the control volume $V(v, w)$ is constrained to prevent the robot from rushing past the target point. Additionally, upon reaching the expansion zone, the current target point

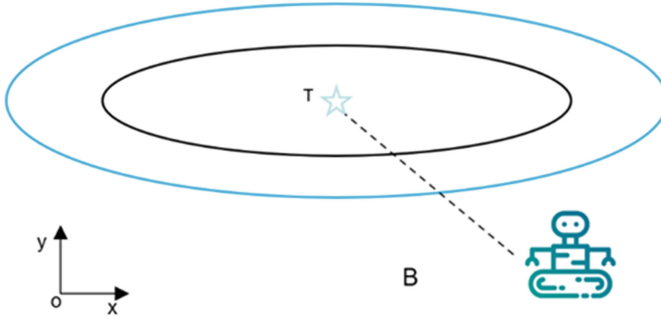


Fig. 2. Diagram of TEB-confidence algorithm

T is cancelled to fulfill the requirements of multi-point navigation, thereby allowing the next target point to be released.

The core algorithm of TEB-confidence focuses on determining whether the robot is within the buffer zone of the target point. If the robot enters this buffer zone, a velocity decay is applied to the control quantity $V(v, w)$, along with a penalty factor, to prevent the robot from rushing past the target point. In the figure, T and B represent the coordinates of the target point and the robot in the map coordinate system. During the navigation process $\|(T - B)\|_2$, the robot continuously measures the real-time distance between B (in the robot's body coordinate system) and T (in the target point coordinate system). This distance is denoted as t_{TB} and is used to determine if the robot has entered the expansion region. The expansion region has a radius of r_T , and the buffer region circle has a width of d . When the robot enters the buffer region, a penalty coefficient, represented by the $\text{erf}(x)$ function in this paper, is added to the control quantity $V(v, w)$ to induce velocity decay. This penalty coefficient is defined in Eq. (14). Once the robot enters the expansion region, the current target point T is canceled, and the coordinates of the next target point are assigned to complete the multi-point navigation task.

$$V(v, w)_{new} = \text{erf}(t_{TB})V(v, w), \text{ if } r_T < t_{TB} < r_T + d \quad (14)$$

To ensure both speed and safety during planning, the expansion area radius r_T is set to 0.2 m, and the buffer area circle width d is set to 0.3 m. The robot follows the execution flow chart of the TEB-confidence algorithm, as depicted in Fig. 3. This flow chart outlines the steps and decision-making process involved in implementing the TEB-confidence algorithm.

The concept of introducing a buffer zone to impose a secondary constraint on velocity proves to be effective in preventing the robot from overshooting the target point. This approach greatly enhances the robustness of navigation while maintaining a satisfactory velocity. By incorporating the buffer zone, the robot can navigate more reliably and securely, reducing the chances of collisions or other unwanted outcomes during the navigation process.

3.2 Numerical Solution of the erf(x) Function

In this paper, the velocity decay function erf(x) is chosen, and it is typically fitted using either Taylor’s method or Chebyshev’s polynomial approximation. Chebyshev’s method is preferred due to its superior fitting accuracy and faster convergence compared to Taylor’s method. Moreover, the Chebyshev polynomial requires fewer terms, resulting in a more efficient approximation. Additionally, the Clenshaw algorithm can be utilized to reduce rounding errors when calculating the partial sum of the series. This approach ensures improved accuracy and precision in evaluating the velocity decay function.

erf(x) is a full function defined as [8]

$$\text{erf}(x) := \frac{2}{\sqrt{\pi}} \int_0^x e^{-t^2} dt, x \in C \tag{15}$$

Before delving into the fitting of the erf(x) function using the Chebyshev series method, let’s discuss the general concept. If a function $f(x)$ is defined on the interval $[-1, 1]$ and possesses a continuous first-order derivative $f'(x)$, then the function $f(x)$ can be expressed using a convergent Chebyshev series expansion.

$$f(x) = \frac{\tau_0}{2} + \sum_{i=1}^{\infty} \tau_i T_i(x) \tag{16}$$

In the above equation τ_i is the i-th term coefficient of Chebyshev’s Chebyshev polynomial and $T_i(x)$ is the Chebyshev’s Chebyshev polynomial:

$$T_i(x) = \cos(i \arccos x) \tag{17}$$

$$\tau_i = \frac{2}{\pi} \int_0^{\pi} f(\cos \varphi) \cos(i\varphi) d\varphi \tag{18}$$

If we extend the definition domain from $[-1, 1]$ to $[a, b]$, the coefficient τ_i can be determined using the following equation:

$$\tau_i = \frac{2}{\pi} \int_{-1}^1 \frac{f((a+b)/2 + (b-a)x/2) T_i(x)}{\sqrt{1-x^2}} dx \tag{19}$$

If the Chebyshev series expansion of $f(x)$ on the interval $[-1, 1]$ is obtained, then the calculation of $f(y)$ $y \in [a, b]$ can be transformed into the following equation:

$$f\left(\frac{y - (a + b)/2}{(b - a)/2}\right) \tag{20}$$

The calculation of A can be obtained using the Clenshaw algorithm, as shown by the following equation: $f(x) f(x)$

$$f(x) = \sum_{i=0}^N \tau_i T_i(x) - \frac{\tau_0}{2} \tag{21}$$

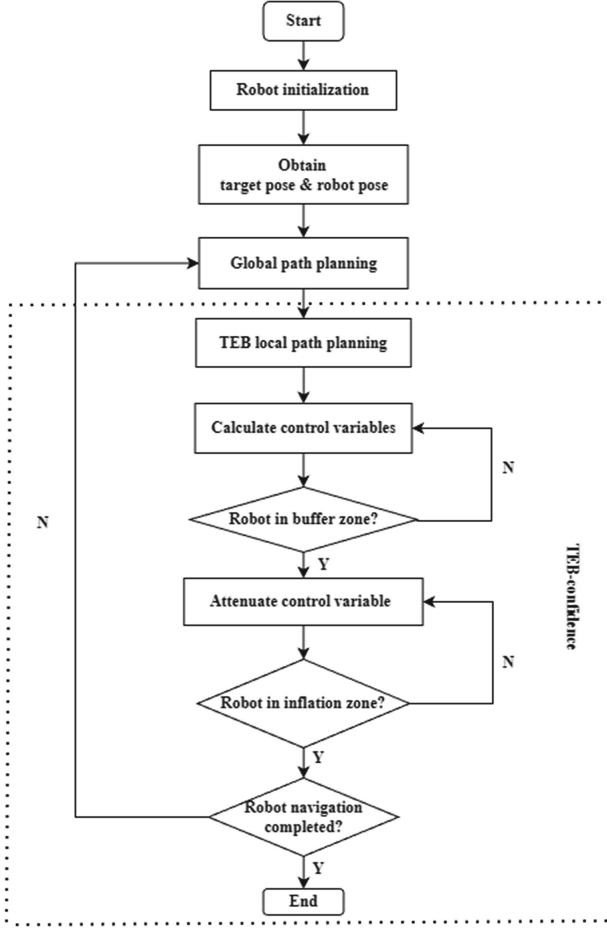


Fig. 3. TEB-confidence flow chart

By applying Clenshaw's algorithm [9], the equation $\sum_{i=0}^N \tau_i T_i(x)$ can be calculated, and it transforms $f(x)$ into the following equation.

$$f(x) = -T_0(x)y_2 + T_1(x)y_1 + T_0(x)\tau_0 - \frac{\tau_0}{2} \quad (22)$$

$$y_{N+2} = y_{N+1} = 0, \quad (23)$$

$$y = 2xy_{k+1} - y_{k+2} + \tau_k, \quad k = N, N-1, \dots, 1 \quad (24)$$

Substituting the values of τ_i and y_k into the equation, we can find $f(x)$ and consequently $\text{erf}(x)$.

4 Experimental Results

To assess the effectiveness of the algorithm, a multi-point navigation experiment for a wheeled robot with an AKM kinematic model was conducted, and its performance was compared to the traditional TEB algorithm. The experiment took place in a controlled environment with plastic barriers, and two cone obstacles were strategically placed in the middle. The specific parameters related to the experiment are provided in Table 1, while the setup of the experimental site and the appearance of the robot can be observed in Fig. 4. In this study, the evaluation criteria were selected as the navigation runtime and occurrence of collisions during navigation.

Table 1. Robot parameters

Sensors	Components
Radar	LeDong D300
Inertial sensors (IMU)	MPU6050
Master control	Jetson Nano



Fig. 4. Experimental robots and sites

The robot used in the experiment is equipped with the Robot Operating System (ROS) [10] version 18.04, which enables map building and multi-point navigation using the LiDAR map building algorithm (gmapping). In the ROS environment, the robot is initialized, and the gmapping map building node and the keyboard control node are started separately. The map building process is continuously monitored in real time using

RViz [11]. Figure 5a displays the trajectory of multi-point navigation using the classical TEB algorithm. It can be observed that the robot rushes through the target points after point 1, point 3, and point 6. Additionally, between point 3 and point 4, the robot even collides with an obstacle, resulting in parking. On the other hand, Fig. 5b illustrates the improved TEB-confidence algorithm. This algorithm applies velocity decay when approaching each target point, reducing the risk of collision on straight roads by reducing the speed. Moreover, it introduces velocity decay to allow for more steering space when navigating curves, thereby preventing collisions.

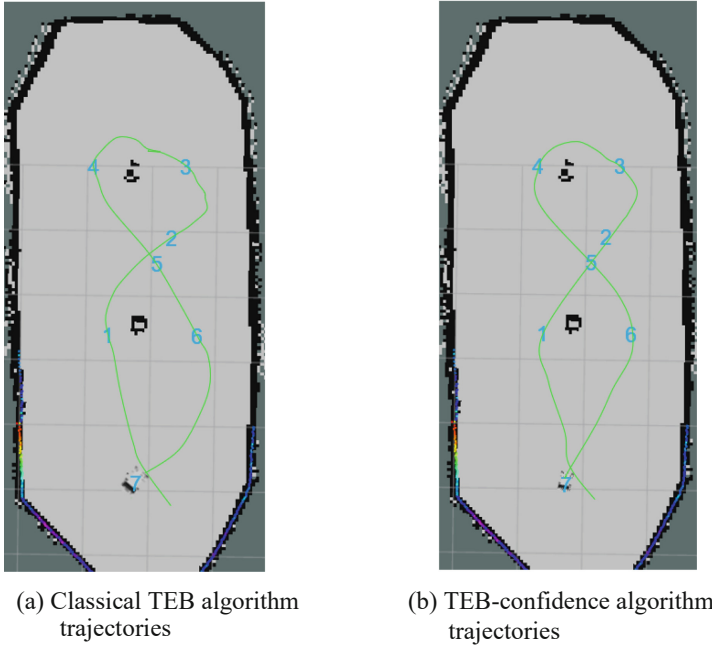


Fig. 5. Trajectory comparison between classical TEB algorithm and improved TEB-confidence algorithm in multi-point navigation task

During the navigation process, the linear velocity curve and angular velocity curve of the robot were recorded to quantitatively compare the effect of the algorithm before and after the improvement (Fig. 7). Figure 7a displays the velocity curve during the navigation using the classical TEB algorithm. The light blue curve represents the linear velocity, and the pink curve represents the angular velocity. It can be observed that the robot's velocity does not decay after reaching the target, resulting in the trolley overshooting at target point 4. On the other hand, Fig. 7b illustrates the velocity profile of the improved TEB-confidence algorithm. The blue curve represents the linear velocity profile, and the red curve represents the angular velocity profile. Combined with Fig. 6, it can be seen that velocity decay is applied at each target point. The improved TEB-confidence algorithm significantly reduces the risk of robot collision without excessively prolonging the entire navigation process.

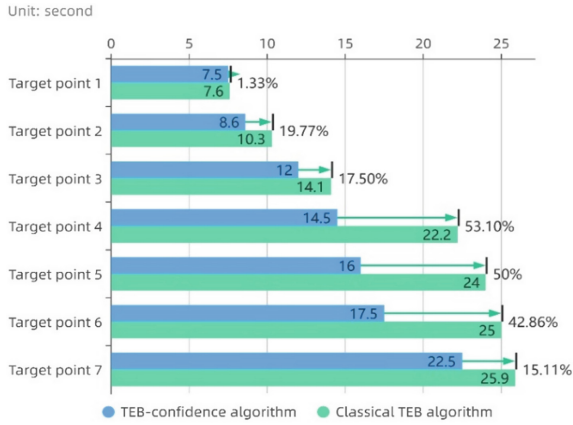
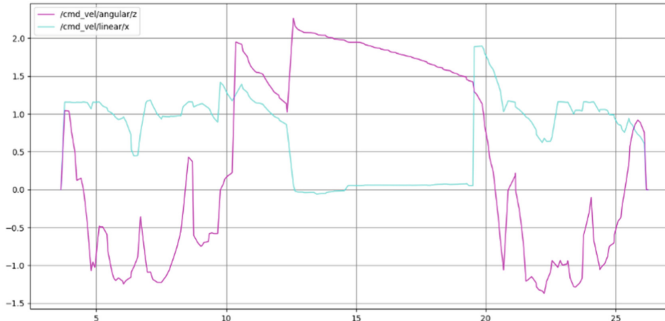
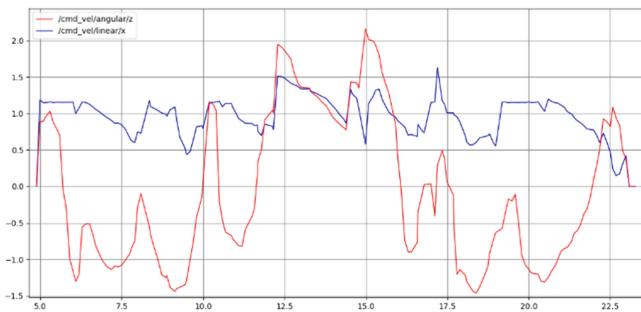


Fig. 6. Comparison of TEB-confidence algorithm and classical TEB algorithm in reaching target points: The figure demonstrates the time required to reach each target point using both algorithms.



(a) Classical TEB algorithm speed profile



(b) TEB-confidence algorithm speed profile

Fig. 7. Speed profile of classical TEB algorithm and TEB-confidence algorithm

This experiment provides a quantitative and qualitative analysis of the classical TEB algorithm and the improved TEB-confidence algorithm. The experimental data consistently demonstrate that the improved TEB-confidence algorithm exhibits greater robustness compared to the TEB algorithm, effectively avoiding the issue of rushing past the target point.

5 Conclusion

In this paper, the TEB algorithm is combined with the confidence algorithm, and the TEB-confidence algorithm is proposed to quadratically constrain the velocity output of the TEB algorithm to effectively prevent the robot from rushing past the target point or even causing collision problems in multi-point navigation; at the same time, the Chebyshev level method is used to fit the decay function, and more accurate fitting results are obtained. Finally, multi-point navigation experiments were conducted on a ROS vehicle to quantitatively and qualitatively compare the classical TEB algorithm with the improved TEB-confidence algorithm, and the obtained linear velocity curves and paths showed the superiority of the improved algorithm. Competition, industry, and life.

Acknowledgements. The authors are highly thankful to the National Natural Science Foundation of China(NO.62063006), the Natural Science Foundation of Guangxi Province (NO.2023GXNSFAA026025), to the Innovation Fund of Chinese Universities Industry-University-Research (ID:2021RYC06005), to the Research Project for Young and Middle-aged Teachers in Guangxi Universities (ID: 2020KY15013), and to the Special research project of Hechi University (ID:2021GCC028). This research was financially supported by the project of outstanding thousand young teachers' training in higher education institutions of Guangxi, Guangxi Colleges and Universities Key Laboratory of AI and Information Processing (Hechi University), Education Department of Guangxi Zhuang Autonomous Region.

References

1. Liu, X., Gong, D.: A comparative study of A-star algorithms for search and rescue in perfect maze. In: 2011 International Conference on Electric Information and Control Engineering, pp. 24–27 (2011)
2. Wang, H., Yu, Y., Yuan, Q.: Application of Dijkstra algorithm in robot path-planning. In: 2011 Second International Conference on Mechanic Automation and Control Engineering, pp. 1067–1069 (2011)
3. Chen, P.C., Hwang, Y.K.: SANDROS: a dynamic graph search algorithm for motion planning. *IEEE Trans. Robot. Autom.* **14**(3), 390–403 (1998)
4. Rösmann, C., Hoffmann, F., Bertram, T.: Timed-elastic-bands for time-optimal point-to-point nonlinear model predictive control. In: 2015 European Control Conference (ECC), pp. 3352–3357 (2015)
5. Li, X., Hu, X., Wang, Z., Du, Z.: Path planning based on combination of improved A-STAR algorithm and DWA algorithm. In: 2020 2nd International Conference on Artificial Intelligence and Advanced Manufacture (AIAM), pp. 99–103 (2020)

6. Aggarwal, S., Kumar, N.: Path planning techniques for unmanned aerial vehicles: a review, solutions, and challenges. *Comput. Commun.* **149**, 270–299 (2020)
7. Rösmann, C., Feiten, W., Wösch, T., et al.: Trajectory modification considering dynamic constraints of autonomous robots. In: *ROBOTIK 2012; 7th German Conference on Robotics. VDE*, pp. 1–6 (2012)
8. Lether, F.G.: Elementary approximation for erf (x). *J. Quant. Spectrosc. Radiat. Transfer* **49**(5), 573–577 (1993)
9. Smoktunowicz, A.: Backward stability of Clenshaw’s algorithm. *BIT Numer. Math.* **42**, 600–610 (2002)
10. Mittler, R.: ROS are good. *Trends Plant Sci.* **22**(1), 11–19 (2017)
11. Kam, H.R., et al.: RViz: a toolkit for real domain data visualization. *Telecommun. Syst.* **60**, 337–345 (2015)



Research on Mobile Robot Path Planning Based on Improved A* and DWA Algorithms

Wei Qian¹, Jiansheng Peng^{1,2}(✉), and Hongyu Zhang¹

¹ College of Automation, Guangxi University of Science and Technology, Liuzhou 545000, China

sheng120410@163.com

² Department of Artificial Intelligence and Manufacturing, Hechi University, Hechi 547000, China

Abstract. This paper explores the navigation of robots, which involves two key aspects: global path planning and local path planning. The current approach utilizes the A* algorithm for global planning and the DWA algorithm for local planning. However, the traditional A* algorithm often fails to consider obstacles, leading to impractical paths that robots struggle to navigate. As a result, success rates are narrow. To address these issues, we propose an enhanced A* algorithm that optimizes the search approach, heuristic function as well as path smoothing. This modification ensures that the generated paths align better with the robot's motion while still prioritizing the shortest distance. Additionally, we refine the evaluation function of the DWA algorithm to account for the robot's angular velocity at different linear velocities. This adjustment enables smoother steering through curves while maintaining a consistent linear velocity at the same time. The improved algorithm greatly improves the speed of the robot when cornering and has a more reasonable completion path, while the success rate of cornering is greatly improved. In our physical map, the robot with the improved algorithm consumes 33.95% less time than the robot with the traditional algorithm, and the robot's path is much better.

Keywords: DWA algorithm · A* algorithm · Mobile robot · ROS

1 Introduction

Robot navigation involves two main components: global path planning [1] and local path planning [2]. Global path planning determines the optimal path from the robot's starting point to its target point. It typically involves rasterizing and searching the map by using algorithms like A* [3] or Dijkstra [4] to find the best path. In this paper, we focus on improving the A* algorithm for global path planning and local path planning. On the other hand, it allows the robot to adjust its path based on its current state and surroundings while following the global path. This enhances the overall system's robustness. The robot collects information from its environment and itself to timely adjust its path and speed, ensuring that it stays on track and avoids disturbances. Common algorithms used for local path planning include DWA [5] and TEB [6], and in this paper, we aim to improve the DWA algorithm.

Traditional robot navigation algorithms have limitations when it comes to realistic and specific tasks. The four-wheel differential speed robot used in our experiment utilizes A* and DWA algorithms. However, the traditional A* algorithm doesn't fully align with the robot's motion principles. The DWA algorithm only calculates optimal routes for the next moment, resulting in sub-optimal performance during cornering. To address these issues, we propose modifications to the A* algorithm's neighborhood search strategy and heuristic function. These enhancements generate better curved paths for global planning. Additionally, we modify the evaluation function of the DWA algorithm to improve the robot's performance during bends. In summary, this paper focuses on improving global and local path planning algorithms for robot navigation. By adapting the A* algorithm and modifying the DWA algorithm, we aim to overcome the limitations of traditional approaches and achieve better performance in practical tasks.

2 Introduction to Traditional Algorithms

2.1 Traditional A* Algorithm

The traditional A* algorithm begins by searching for points in the surrounding area from the current point, as illustrated in Fig. 1. It completes this calculation through a systematic search process. Subsequently, the cost function evaluates the points reached by different search methods and selects the point with the lowest cost as the next target point. This iterative process continues until the final target point is reached [7].

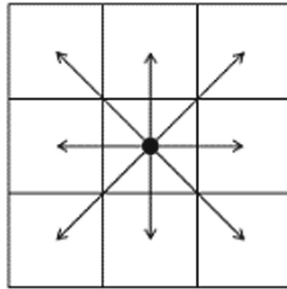


Fig. 1. Traditional A* algorithm search method

The A* algorithm uses heuristic search to get the best path to the destination, and it finds the optimal path by means of an estimation function, which is generally written as follows:

$$f(n) = g(n) + h(n) \quad (1)$$

where $g(n)$ represents the generation value from the starting node to the current node, using the Euclidean distance representation, and $h(n)$ represents the generation value from the current node to the target node. In simple terms $g(n)$ enables the robot to travel to the target point with a shorter path, and $h(n)$ enables the robot to plan the path faster while limiting the path deviation.

2.2 Traditional DWA Algorithm

The DWA algorithm samples multiple sets of velocity information in real-time local path planning (v, ω) , and based on this sampling the trajectory of the next moment of action is simulated. The optimal path is selected among the predicted trajectories for navigation. The robot is first modeled in motion, and considering that the robot used cannot move omni directionally, the kinematic model yields a trajectory at moment t as

$$x = x + v * \Delta t * \cos(\theta_t) \quad (2)$$

$$y = y + v * \Delta t * \sin(\theta_t) \quad (3)$$

$$\theta_t = \theta_t + \omega * \Delta t \quad (4)$$

Considering that this trajectory model will be limited by the robot's own structure, three constraints are added to its velocity sampling. One of the most-valued constraints is:

$$V = \{v \in [v_{\min}, v_{\max}], \omega \in [\omega_{\min}, \omega_{\max}]\} \quad (5)$$

Acceleration and deceleration constraints are:

$$V_d = \{(v, \omega) \in [v_c - v_b * \Delta t, v_c + v_a * \Delta t], \omega \in [\omega_c - \omega_b * \Delta t, \omega_c + \omega_a * \Delta t]\} \quad (6)$$

The safety distance constraint is:

$$V_\omega = \{(v, \omega) | (v \leq \sqrt{2dist(v, \omega) \cdot v_b}) \wedge (\omega \leq \sqrt{2dist(v, \omega) \cdot \omega_b})\} \quad (7)$$

After taking to multiple sets of speed information, the optimal path selection is performed by using the evaluation function as follows:

$$G(v, \omega) = f(\alpha * heading(v, \omega) + \beta * dist(v, \omega) + \gamma * vel(v, \omega)) \quad (8)$$

The heading term is the azimuth evaluation function. The dist term is the distance evaluation function and the velocity term is the speed evaluation function [8].

3 A* Algorithm Improvement and Simulation

In this project, the A* algorithm is employed for global path planning. However, the traditional A* algorithm solely focuses on finding the shortest path, disregarding the smoothness of the route. Although interpolation is commonly used to enhance the smoothness of the robot's motion trajectory, it often struggles to handle areas with significant curves effectively [9]. Furthermore, the traditional A* algorithm limits its search and calculation to the immediate vicinity, resulting in unnecessary distance wastage on obstacle-free, straight roads.

To overcome these limitations, this chapter introduces an improvement to the A* algorithm tailored specifically for this project. The enhanced algorithm aims to optimize the robot's motion trajectory by considering both the shortest path and the smoothness of the route. Additionally, it expands the search range beyond the immediate surroundings to minimize distance wastage on flat, obstacle-free roads. The effectiveness of the proposed improvement is validated through simulations.

3.1 A* Algorithm Improvement

To account for the limitations of the non-omnidirectional motion capability of the robot and the absence of obstacles in the experimental site, this paper presents an innovative algorithm for searching neighborhood points, as depicted in Fig. 2. The primary objective is to enhance speed and reduce computational effort. By specifically targeting the search in the surrounding neighborhood, the robot can efficiently obtain a shorter final path, which proves highly effective in obstacle-free, straight-line environments.

This algorithmic improvement optimizes the robot's path by reducing the distance traveled for corner points when no obstacles are present. Subsequent physical experiments revealed that this modification also provides the robot with an increased safety margin during curves. This finding underscores the significance of the proposed algorithm, as it allows the robot to navigate more effectively, ensuring a greater level of safety while maximizing efficiency.

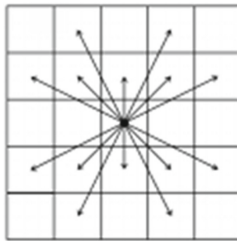


Fig. 2. Improved A* algorithm search method

Considering that the AKM chassis robot we utilize lacks direct lateral displacement capabilities, it bypasses the search for proximity points in the left and right directions. The conventional A* algorithm produces a path planning form as shown in Fig. 3. However, in practical scenarios, this trajectory fails to provide the robot with sufficient safety distance during sharp curves. Consequently, the robot is prone to getting stuck by obstacles, leading to navigation failures.

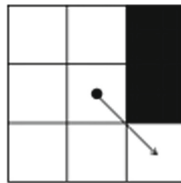


Fig. 3. Limitations of the traditional A* algorithm

To address this issue, we propose an alternative search method depicted in Fig. 4 when an obstacle is detected near the search point. In cases depicted in Fig. 5, only the search method shown in Fig. 4 is retained. This modified search method enables the robot to plan shorter paths in obstacle-free straight stretches and maintain an adequate safety distance

when approaching curves. Compared to the traditional A* algorithm, this approach only requires searching six neighbors, significantly reducing computational effort.

By implementing this search method, our robot can navigate more efficiently. It obtains shorter paths in straight sections without obstacles while ensuring increased safety margins during curved sections. This improvement proves crucial in avoiding obstacles and achieving successful navigation.

In addition, considering that in the actual navigation process, the robot's path will be offset to a certain extent, and the $h(n)$ term in the heuristic function is difficult to calculate accurately. Either using the Euclidean distance or the Manhattan distance will have unavoidable deviations, a compromise of the $h(n)$ term is considered as follows:

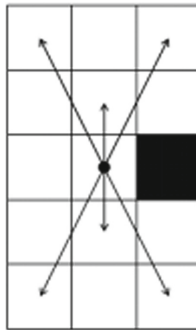


Fig. 4. Right neighborhood with obstacles

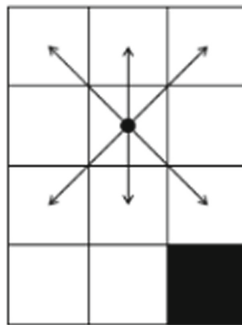


Fig. 5. Obstacles in the oblique front neighborhood

$$\begin{aligned}
 h(n) = & 0.5 * k * \left(\sqrt{(N_x - P_x)^2} + \sqrt{(N_y - P_y)^2} \right) \\
 & + 0.5 * (1 - k) * \left(\sqrt{(N_x - P_x)^2 + (N_y - P_y)^2} \right) \quad (0 \leq k \leq 1) \quad (9)
 \end{aligned}$$

where N represents the target point, P represents the current point, and k is the weight that can be chosen according to the different values of the robot's environment.

In practice, $h(n)$ and $g(N)$ are not well balanced, and the robot tends to have some extreme cases, such as when $h(n)$ is too large and $g(n)$ accounts for a smaller percentage, the robot will tend to choose the shortest path but the path direction will deviate more; in the opposite case the robot will consume more resources to plan more paths, wasting computational resources and computational time. We want these two items to be user-determined in the valuation function, and therefore add weights to these two items as follows:

$$f(n) = \frac{g(n) + e^{-\omega}h(n)}{1 + e^{-\omega}} \quad (10)$$

By choosing appropriate values for ω based on practical applications, the proportion of $g(n)$ and $h(n)$ in the pairwise valuation function is adjusted to achieve a balance between improving the computational efficiency of the algorithm and obtaining the shortest path.

In order to obtain a smoother path, consider three spline interpolations of the final generated global path for smoothing, assuming that a total of $n + 1$ folds and a total of h steps are known, we can obtain [10]:

$$a_i = y_i \quad (11)$$

$$b_i = \frac{y_{i+1} - y_i}{h_i} - \frac{h_i m_i}{2} - \frac{h_i(m_{i+1} - m_i)}{6} \quad (12)$$

$$c_i = \frac{m_i}{2} \quad (13)$$

$$d_i = \frac{m_{i+1} - m_i}{6h_i} \quad (14)$$

The final smoothed curve is obtained by bringing in the equation:

$$g_i(x) = a_i + b_i(x - x_i) + c_i(x - x_i)^2 + d_i(x - x_i)^3 \quad (15)$$

The flow chart of the improved algorithm is as followed in Fig. 6.

3.2 Simulation Results

To test the effectiveness of the algorithm, a simple map with large curves was created in Python. The focus was on comparing the improved algorithm's performance at the curves. The map consisted of squares, with black squares as obstacles, dark blue squares as starting points, and purple squares as ending points.

In Fig. 7, the yellow line represents the path planned by the traditional A* algorithm, while the blue line represents the path planned by the improved algorithm. The comparison mainly focused on the trajectory and distance traveled since the number of searched neighborhood points was similar. The improved algorithm showed better alignment with the robot's motion and provided a greater safety distance at the curves.

After smoothing, the improved algorithm had a slightly shorter overall distance traveled while maintaining better safety at the curves (red lines in Fig. 8). In open fields, the improved algorithm had significant advantages in terms of distance traveled. It prioritized allocating more paths for better safety at the curves, which is crucial in such environments (Table 1).

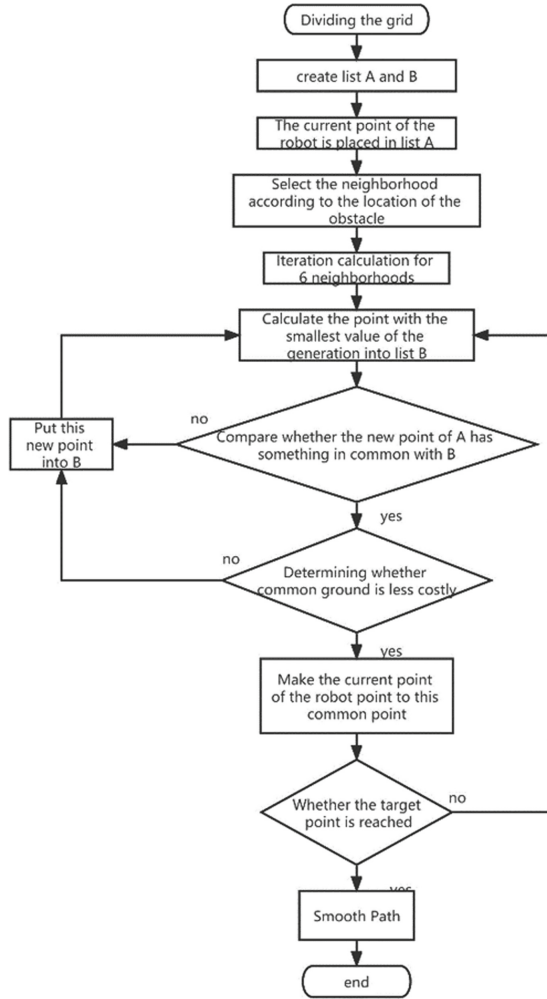


Fig. 6. Flow chart of the improved A* algorithm

Table 1. Comparison of the two algorithms

	Route	Curve safety
Traditional A* algorithm	32.48	Poor
Improved A* algorithm	32.26	Better

4 Improvement of DWA Algorithm

The traditional DWA algorithm has limitations that affect robot performance in curves and practical applications. It only predicts the next moment and calculates the next best path, which can lead to poor performance [11]. To address this issue, we made improvements for bending situations in this project. We adjusted the robot's velocity function to overcome the limitations of the DWA algorithm. By removing prediction planning, we ensured that the robot's actual direction aligns better with the planned path in curves. To enhance the evaluation function, we introduced constraints on the robot's angular velocity relative to its linear velocity. This ensures the robot has enough angular velocity for steering during deflection while preventing excessive steering on flat routes with high linear velocity. These modifications aim to improve the robot's performance in curves and enhance its steering capabilities in various scenarios.

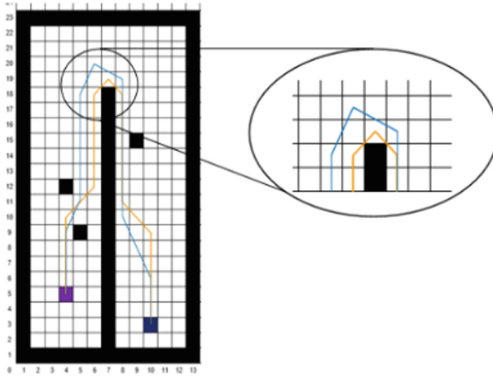


Fig. 7. Simulation results for improving A^*

$$r(v) = \kappa * \left(\frac{e^{|v|} - e^{-|v|}}{e^{|v|} + e^{-|v|}} \right) + b \quad (16)$$

This equation evolves from the hyperbolic tangent function (\tanh). This design holds a dual purpose: firstly, maximizing the robot's linear velocity to ensure sufficient speed, and secondly, preventing excessive velocities that could lead to instability during turns. The choice of this function brings forth unmistakable benefits. It allows for rapid growth in linear velocity when it is small, while still keeping it bounded within a desirable range. By adopting a linear function form, we gain greater control over its value range, providing us with more versatile means of regulation. And this function shows in Fig. 9.

By this means, the angular velocity of the robot during steering is proportional to the linear velocity, while the angular velocity of the robot is not too large due to the properties of the function (Fig. 9). Also add the angular velocity evaluation term for the evaluation function $anvel(v, \omega)$:

$$anvel(v, \omega) = \frac{r(v) * \omega}{v} \quad (17)$$

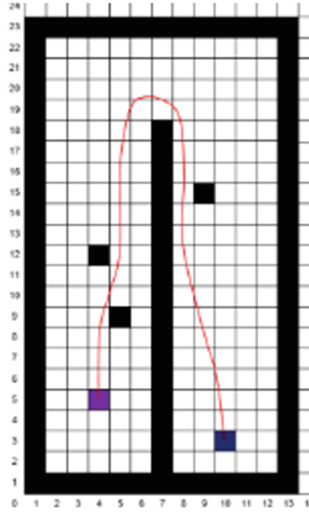


Fig. 8. Trajectory after smoothing process

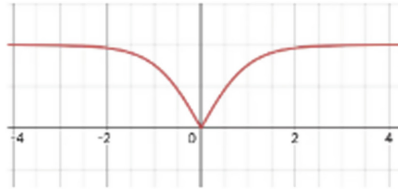


Fig. 9. $\tanh(|x|)$

By employing a linear function for the velocity-related component, we attain the ability to effortlessly manipulate its value range. Furthermore, our objective is to endow the robot with enhanced angular agility and reduced linear velocity. This entails not only capping the upper limit of linear speed to prevent unwieldy accelerations but also imposing penalties when linear velocity escalates, while offering generous rewards for heightened angular velocity. Thus, the resulting design embodies these thoughtful considerations.

This evaluation term will comprehensively evaluate the relationship between linear velocity and angular velocity, and the score of this term will be lower when the angular velocity is too small and the linear velocity is too large, which happens to be the case when the robot is out of control in a curve, and the improved evaluation function is

$$G(v, \omega) = f(\alpha * heading(v, \omega) + \beta * dist(v, \omega) + \gamma * vel(v, \omega) + \lambda * anvel(v, \omega)) \quad (18)$$

5 Experimental Results

The experimental robot is AKM robot, using two motors into the rear drive, the main control is Jetson nano, using ubuntu18.04 operating system, real-time map building and navigation using ROS (melodic) system to complete, radar using the Ledon D300, IMU using MPU6050. This experiment using LIDAR and using gmapping algorithm to complete the map construction. After getting the complete static map, the target point selection for navigation is performed in RViz. This experiment uses multi-point navigation to complete the pile wrapping test. Since the physical map is not empty and generates a lot of steering, a huge steering is generated at one side of the map end, which is a great challenge for the robot's navigation.

The experimental map and equipment are shown in Fig. 10. In the navigation process `rqt_plot` will record the indicators of the trolley in real time, we also wrote the same node file to listen to the robot map coordinates in real time and print on RViz to get the trajectory of the robot walking, so as to compare the trajectory performance and speed of the same robot under different algorithms, in the case of the same map and close to the starting and ending points. The maximum linear velocity of the robot was set to 2.5 m/s and the maximum angular velocity was set to 3 rad/s.



Fig. 10. Experimental environment and equipment

Comparing the trajectories in Figs. 11 and 12 reveals that the optimized algorithm outperformed the traditional algorithm, especially in the final sharp curve. Figure 14 illustrates that the optimized algorithm maintained a high angular speed throughout the curve, enabling the robot to take shorter paths and achieve higher linear speeds during cornering. In contrast, the common algorithm (Fig. 13) had limited adjustments in angular velocity, often resulting in delayed increases until the bend was nearly impossible to navigate. This led to wasted distance, and in practical use, the traditional algorithm had a low success rate in 180° bends.

In most situations, traditional algorithms struggle to navigate through this track successfully in the given experimental platform and environment. They often encounter difficulties, such as pausing or even colliding with walls during the challenging 180-degree turns. This observation is supported by monitoring the algorithm's output for

linear and angular velocities. It is commonly observed that these velocity values fluctuate around the zero point, causing the robot to move in a circular path and pause multiple times to adjust its direction before completing the turn. This behavior is visually reflected in the graph, where the angular velocity tends to follow the changes in linear velocity. The main reason behind this phenomenon is that the robot cannot fully execute the algorithm's commands, while the algorithm attempts to rectify the robot's motion. Consequently, the robot experiences frequent pauses and takes wider turns, resulting in significant time wastage. However, when the robot operates with the improved algorithm, these pauses are eliminated. The robot becomes more adept at following the algorithm's motion commands, particularly noticeable at the sharpest turn, where the commands exhibit minimal fluctuations. As a result, the robot smoothly completes the 180-degree turn with little to no deceleration in real-world scenarios. The difference between the two algorithms at the curve section is illustrated in Fig. 15 (Table 2).

Table 2. Comparison of the effects of the two algorithms

	Time consumption(s)	Success rate
Before improvement	40.62	Frequent failures
After improvement	26.83	Hardly ever fails

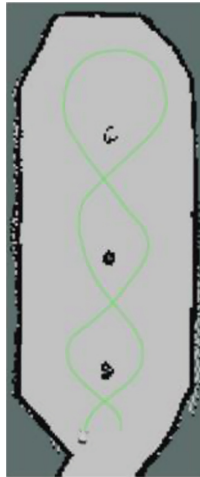


Fig. 11. Physical trajectory of the traditional algorithm

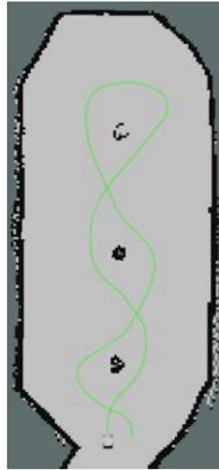


Fig. 12. Physical trajectory of the improved algorithm

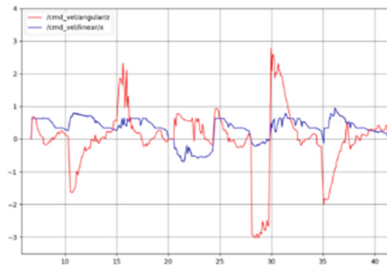


Fig. 13. Speed graph of traditional algorithm. Traditional algorithm speed graph: From 25 to 30 s, during the 180-degree turn, traditional algorithms decelerate, causing abrupt angular and linear velocity changes, and a lower overall cornering speed.

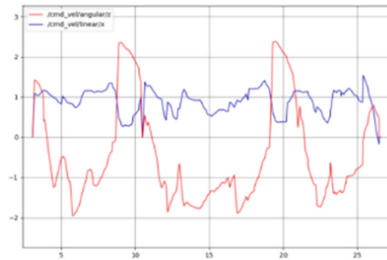


Fig. 14. Speed graph of improved algorithm. Between 25 and 30 s, the platform turns 180 degrees. The enhanced algorithm plans for a larger initial steering angle, leading to smoother angular and linear velocities, resulting in a higher overall cornering speed.

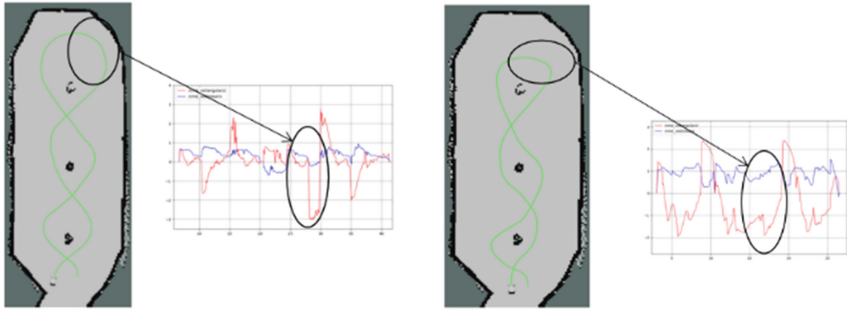


Fig. 15. Comparison of the two algorithms at the curve section. The improved algorithm has a clear advantage in trajectory and speed around curves.

6 Conclusion

In this paper, the traditional A* algorithm and DWA algorithm are optimized and improved for robot cornering. Firstly, an innovative 6-neighborhood A* algorithm is proposed, its heuristic function is optimized and its final trajectory is interpolated and smoothed, and finally the simulation verifies its effect so that its final cornering effect is better than that of the traditional A* algorithm. The evaluation function of the DWA algorithm is modified to allow the robot to obtain a larger angular speed and limit the linear speed in large bends, so that the robot can use a relatively faster speed to complete the bends safely. In the final physical experimental session, the robot's speed and operational stability were greatly improved. Such improvements can make the autonomous navigation mobile robot perform better in urban, logistics, industrial, and other map environments with multiple curves.

Acknowledgement. The authors are highly thankful to the National Natural Science Foundation of China (NO. 62063006), the Natural Science Foundation of Guangxi Province (NO. 2023GXNSFAA026025), to the Innovation Fund of Chinese Universities Industry-University-Research (ID: 2021RYC06005), to the Research Project for Young and Middle-aged Teachers in Guangxi Universities (ID: 2020KY15013), and to the Special research project of Hechi University (ID: 2021GCC028). This research was financially supported by the project of outstanding thousand young teachers' training in higher education institutions of Guangxi, Guangxi Colleges and Universities Key Laboratory of AI and Information Processing (Hechi University), Education Department of Guangxi Zhuang Autonomous Region.

References

1. Abdallaoui, S., Aglzim, E.H., Chaibet, A., et al.: Thorough review analysis of safe control of autonomous vehicles: path planning and navigation techniques. *Energies* **15**(4), 1358–1377 (2022)
2. Qin, H., Shao, S., Wang, T., et al.: Review of autonomous path planning algorithms for mobile robots. *Drones* **7**(3), 211–248 (2023)
3. Wu, B., Chi, X., Zhao, C., et al.: Dynamic path planning for forklift AGV based on smoothing A* and improved DWA hybrid algorithm. *Sensors* **22**(18), 7079–7098 (2022)

4. Luo, M., Hou, X., Yang, J.: Surface optimal path planning using an extended Dijkstra algorithm. *IEEE Access* **8**(1), 147827–147838 (2020)
5. Mohammadpour, M., Zeghmi, L., Kelouwani, S., et al.: An investigation into the energy-efficient motion of autonomous wheeled mobile robots. *Energies* **14**(12), 3517–3536 (2021)
6. Andreasson, H., Larsson, J., Lowry, S.: A local planner for accurate positioning for a multiple steer-and-drive unit vehicle using non-linear optimization. *Sensors* **22**(7), 2588–2606 (2022)
7. Tyagi, N., Singh, J., Singh, S.: A review of routing algorithms for intelligent route planning and path optimization in road navigation. *Rec. Trends Prod. Des. Intell. Manuf. Syst.* **16**(14), 851–860 (2022)
8. Öztürk, Ü., Akdağ, M., Ayabakan, T.: A review of path planning algorithms in maritime autonomous surface ships: navigation safety perspective. *Ocean Eng.* **251**(1), 111010–111031 (2022)
9. Sánchez-Ibáñez, J.R., Pérez-del-Pulgar, C.J., García-Cerezo, A.: Path planning for autonomous mobile robots: a review. *Sensors* **21**(23), 7898–7914 (2021)
10. Gul, F., Mir, I., Abualigah L., et al.: A consolidated review of path planning and optimization techniques: technical perspectives and future directions. *Electronics* **10**(18), 2250–2268 (2021)
11. Xiao, X., Liu, B., Warnell, G., et al.: Appld: Adaptive planner parameter learning from demonstration. *IEEE Robot. Autom. Lett.* **5**(3), 4541–4547 (2020)



File System for Digital Signal Processing Equipment Based on FPGA

Dong-cheng Chen(✉)

Jiangsu Automation Research Institute, Lianyungang, Jiangsu, China
chendongcheng8710@163.com

Abstract. A file system for digital signal processing equipment based on FPGA is designed. The ZYNQ-7000 FPGA is the processing center of the file system. An NVMe hard disk is connected to the GTx bank of FPGA as a PCIe device. FPGA and DSP chips interconnect through SRIO switch chip. Data which needs to be memorized comes from DSP through X4 SRIO interface. In FPGA, PL side receives command and data from DSP. PL buffers data to be memorized in different double port RAMs according to the command. PS reads data from buffer rams according to command data reading from command buffer rams and writes data to a responding subarea. Experiments show the designed file system memorizes data from DSP in real time. When data packet is 128 KB, writing data rate can be 550 MB/s.

Keywords: ZYNQ-7000 · NVMe hard disk · DSP · SRIO

1 Introduction

Digital signal processing system is a key device in equipment like radar, sonar and communication equipment. Data sampled and processed by digital signal processing system is very important and precious to the developer, especially in developing course. It is very important to save original data and some of processed data, for it's very useful for the developer to ameliorate the processing algorithm. Sonar digital signal processing system is the key device in the equipment. It is used to sample, transmit, process and memorize data. For the special experiment condition, equipment must do experiment in deep and large water like lake and ocean. Cost of experiment is quite large. Thus data is very precious in every experiment. A memorizing device is necessary in the digital signal processing system. For data needs to be memorized include the original data and processed data, the memorizing bandwidth will be high. For previous reasons, in this paper, a digital signal processing device file system based on FPGA is designed.

2 System Design

A file system based on FPGA is designed. Data transmitted by the processing unit needs to be memorized wrote to the hard disk by the FPGA. File system can memorize data from any processor in the processing system. The writing bandwidth can reach 500 MB/s. Data in disk can be accessed through the net.

Disk used in the system is an NVMe hard disk. The NVMe hard disk is connected to the GTx bank of the FPGA. The FPGA used in this system is a Xilinx ZYNQ7000 serial chip, XC7Z045. A PCIe hard core is integrated on the chip, the NVMe disk is connected to GTx bank through X4 PCIe. Processing center of the digital signal processing system is TMS320C6678, the DPS chip communicate with FPGA through Serial RapidIO(SRIO). For there are several DSP chips and one FPGA in the system communicate through SRIO, an SRIO switch chip is used. Any DSP core can communicate with FPGA through the SRIO switch. Data could be wrote to hard disk by any DSP core. What's more, DSP chips can be more according to the number of interface of SRIO switch. Data wrote to hard disk can be accessed through FPGA net. System design is shown in Fig. 1.

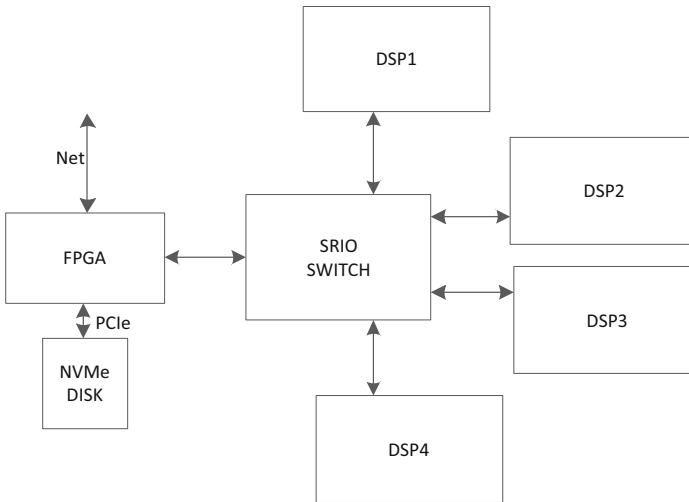


Fig. 1. System diagram of digital signal processing device file system

3 PL Program Design

In FPGA, command and data comes from DSP through SRIO. Command received is buffered in a double port RAM, the double port RAM is connected to PS core through Bram controller core. PS can access the data in double port RAM through the Bram controller. According to number of subarea data wrote to disk, every kind data will be wrote to a corresponding subarea. Each subarea has a double port RAM in PL of FPGA. The ARM core controls the PCIe core to write data to the corresponding subarea according to the commands reading from the command buffer double port RAM. Data in buffer ram is wrote to the DDR3 SDRAM on PS side through HP channel. When data in buffer rams wrote to DDR3, PL writes a data valid byte to a BRAM. PS checks the data valid byte, when the valid byte checked, PS starts to read command data from the command buffer RAM. PS core controls the PCIe core writing data to NVMe hard disk according to command data. PS core connects to the PCIe core through GP channel,

Which is used to communicate the command data with PCIe core. Data memorize flow is shown in Fig. 2.

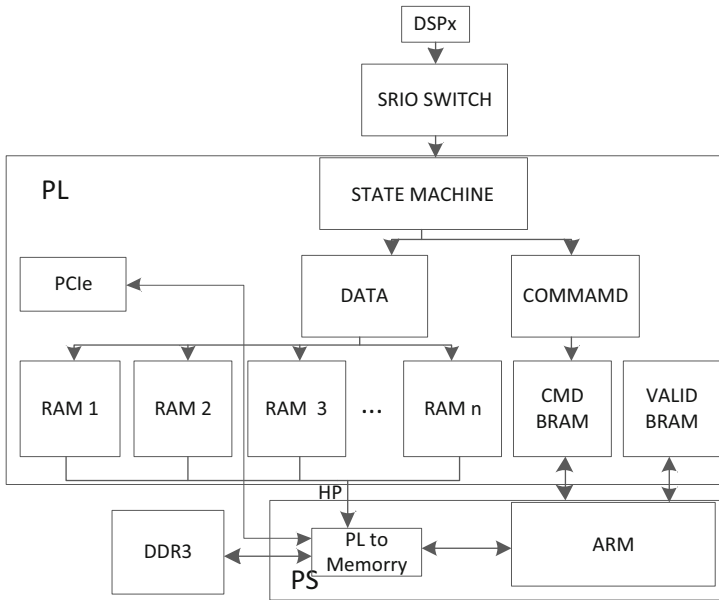


Fig. 2. Data memorize flow

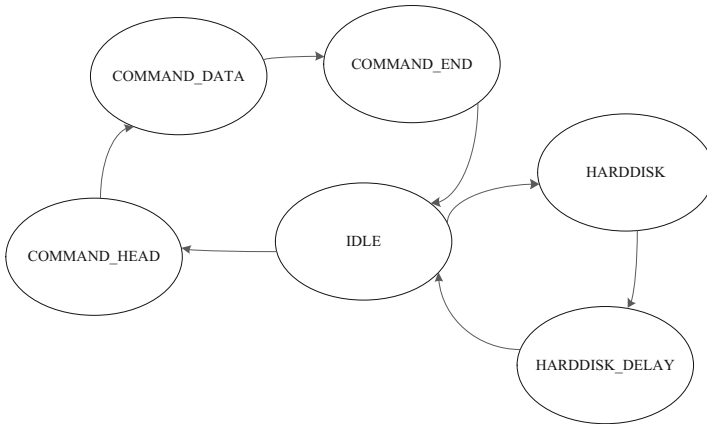


Fig. 3. File command data state machine

Command data state machine is shown in Fig. 3. Data received from DSP include command data and FR data. When command data head checked in the SRIO data packet, state machine runs to command branch. Command data from DSP includes FR initial, FR open, FR close, FR write, open file index, write file index and close file index.

Received file command is wrote to command buffer RAM and waits for PS reading. When a specific byte data received, state machine runs to HARDDISK branch. This brunch receive data to be wrote to the disk. FPGA operate data according to command received.

In HARDDISK brunch, received FR data is buffered in different RAMs according to command data. PL program check each double port RAM in sequence, when any RAM with data more than 128 bytes, program send data to the DDR3 on the PS side through HP channel. When all data according to command wrote to DDR3, PL write one given byte to a given DDR3 address. When PS checks the given byte, PS control the PCIe core to access data on the disk.

4 PS Program Design

Program for this system include PL program in FPGA hardware logic and PS program in ARM core. Hardware logic is the program in FPGA, as mentioned previously including data receiving, data state machine and data buffering. System software controlling center is on PS side. It is made up of one dual core Cortex-A9 processor, on chip memory and variety of interfaces. Which makes PS working independently with the PL.

4.1 Program Flow Design

PS can access data on PL side through BRAM controller. In this way, PS can control PL side and synchronize with the PS side. After system start up, PS sends a reset synchronization signal to PL side, which can ensure every module at the same beginning state. For PL will write data to the DDR3 on PS side, data in given address can be accessed by PL side through HP channel. DDR3 space accessed by the PL should be set to be uncached. Then program will initialize PCIe interface and NVMe hard disk. After initialization, program runs to a while(1), which process the FR data and command data. Software flow is shown in Fig. 4. The program checks the command valid byte, when checked, the program begin to do FR processing. Command processed include initialization, opening, closing, reading, writing, deleting, flushing, reparting and erasing. In each flow, the program do a responding operating.

5 Experiments and Discussing

The ZYNQ-7000 FPGA is processing center of the file system. Main processing task includes logic program and software. On PL side, logic communication with DSP through SRIO switch, parse command, data write to different buffer RAM, data writing to given address in DDR3, and communication of the PCIe core and NVMe hard disk. Software mainly deals with the file processing command comes from the DSP. PS reads command valid byte from PL side and dose the responding processing to the NVMe disk.

When debugging the program, integrated logic analyzer(ILA) is designed in the program. The key signal in the program can be watched from the Xilinx Chipscope tool,

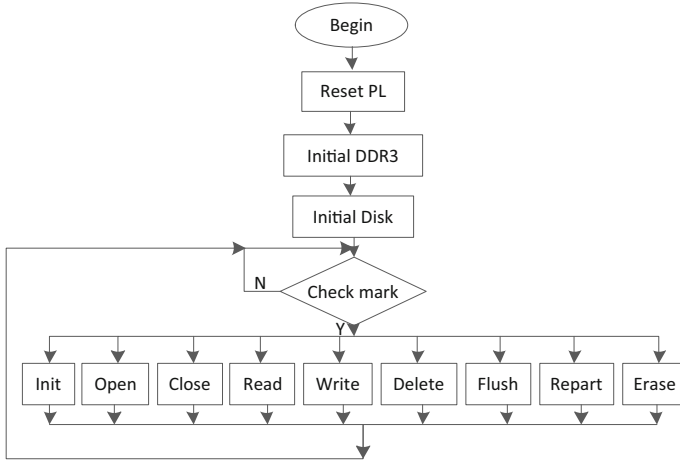


Fig. 4. Software flow

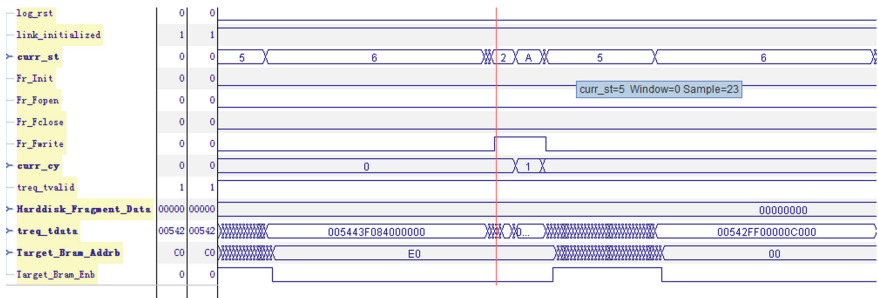


Fig. 5. Waveform from Chipscope

which will improve debugging efficiency. As shown in Fig. 5, when the PL received file command from SRIO, file initializing command is parsed. PL writes the command to BRAM, and responding command data was wrote to command data buffer BRAM.

According to data transmitted to ZYNQ from DSP, different data packets need to be memorized. There are some differences between different data packets in writing data rate. As shown in Table 1.

Table 1. Data rate between different packet

Packet size (KB)	Data rate (MB/s)
1	8
16	105
64	310
128	550
256	550

6 Conclusion

According to equipment in use, a digital signal processing device file system based on FPGA is designed. FR processing center is FPGA, NVMe hard disk is connected to a GTx bank of FPGA. FPGA receives command and data from DSP through SRIO. Command and data are pre-processed in FPGA, then wrote to given addresses in DDR3 on PS side. PS do processing according to command data. Experiments show when different data packets wrote to hard disk, the writing data rate is different. When data packets larger then 128 KB, writing data rate will be 550 MB/s.

References

1. Jian, L.: Implementation of a file system based on FPGA and Its application. Taiyuan university of technology (2013)
2. Jingzhang, L.: The design of PCI express transmission based on FPGA. Chongqing university (2012)
3. Zhiewei, Z.: SATA hard disk accessing technology based on FPGA. University of electronic science and technology of China (2012)
4. Siyang, C.: Design on the controller of NVMe interface based on FPGA. Xidian university (2015)



UAV-Assisted NOMA Network Power Allocation Under Offshore Multi-energy Complementary Power Generation System

Wenyi Shao, Fei Lin^(✉), Ren Xu, Fanping Meng, and Haoran Wang

School of Information and Automation, Qilu University of Technology (Shandong Academy of Sciences), Jinan 250300, China

linfei@qlu.edu.cn

Abstract. To solve the shortage of non-renewable energy sources, the development and utilization of abundant renewable energy sources at sea are gradually attracting attention. For the acquisition and analysis of offshore energy sources, we propose a new offloading framework for grid communication under offshore multi-energy power generation systems. This framework can enhance the performance of offshore communication and provide a good basis for command transmission of multi-energy complementary power generation systems. In this paper, we consider network offloading with the help of unmanned aerial vehicles (UAVs), while adopting non-orthogonal multiple access (NOMA) techniques on each UAV. The system hardware loss and incomplete successive interference cancellation (SIC) are jointly optimized for UAV trajectory and power allocation to minimize the system energy loss. To solve the non-convex problem, we use a two-step Deep Reinforcement Learning (DRL) based algorithm. Numerical results are based on the number of iterations and the variation of the signal-to-noise ratio magnitude to evaluate the effectiveness of the proposed algorithm in the system in terms of system energy consumption, transmission rate, interruption probability, and error rate. This research was funded by the National Natural Science Foundation of China, grant number U2006222 and Natural Science Foundation of Shandong Province, grant number ZR2020MF138.

Keywords: NOMA · Power allocation · Multi-agent · UAV

1 Introduction

After the 1950s, the global energy shortage gradually emerged, which has attracted continuous attention from all over the world [1]. The ocean covers about 71% of the earth's surface area, and the abundant ocean energy is very valuable for research in renewable energy.

In recent years 5G communication technology has been deeply integrated with land-based power IoT. Edge offloading technologies are widely used in it [2]. However, because renewable energy sources such as offshore wind and solar are too dispersed and

far from onshore power equipment and base stations, it is impossible to achieve edge offloading network coverage by relying only on terrestrial base stations [3].

The use of orthogonal multiple access (OMA) for land-based energy communication with UAVs has been widely used, and considering that the number of access terminals will grow immeasurably in the future 6G network with the integration of earth, sea, air, and sky, OMA is difficult to meet the maritime communication scenario with scarce spectrum resources [4]. Non-orthogonal multiple access (NOMA) allows multiple terminals to use the common resource block simultaneously, and the combination with the mobile UAV model can meet the problem of multi-node access to marine networks [5].

Therefore, based on the multi-agent DQN approach, we mainly make the following innovations:

- Considering the communication patterns under the offshore multi-energy complementary power generation system and using a three-path model that fits the characteristics of the sea, we propose a NOMA-based UAV-assisted offloading framework.
- We first invoke the K-means algorithm to classify user clusters. Then we use a multi-intelligent deep Q-network algorithm to reduce the system energy consumption by optimizing the action trajectory and power allocation of UAVs.
- Based on the optimal energy consumption, we analyze the outage probability and transmission rate of the system under different multi-access techniques and evaluate the effectiveness of the proposed framework.

2 System Model

2.1 System

We consider a maritime offload network consisting of U UAVs carrying mini-MEC servers and mobile ship users [6]. We assume that NOMA technology is used to support downlink communication, where each UAV can be associated with K users [7]. The collection of users and drones is denoted by $k \in \mathbb{K}$ and $u \in \mathbb{U}$. The considered UAV-assisted wireless network is shown in Fig. 1.

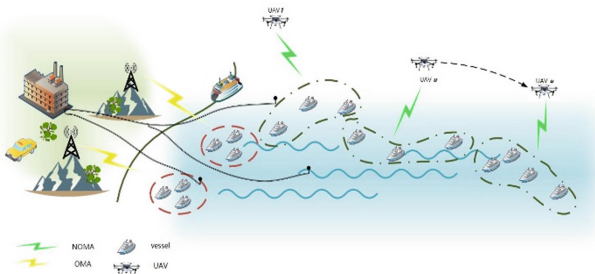


Fig. 1. NOMA-based framework for maritime UAV-assisted cellular networks

Considering the special atmospheric refractive index structure in the marine atmospheric environment easily forms evaporative waveguides, which provide conditions

for long-range communication. Assume that the evaporative duct layer is horizontally homogeneous. When reflected rays from the sea surface exist outside the LoS (Line of Sight) path, it is assumed that near-sweep incidence exists on the sea surface and, eventually, the reflection coefficient of the vertically polarized waves approaches -1 [8]. Using these assumptions, the 3-ray path loss model can be simplified to

$$L_k^u(t) = 10 \lg \left\{ \left(\frac{\lambda}{4\pi d_k^u(t)} \right)^2 [2 \times (1 + \Delta)]^2 \right\}$$

$$\Delta = 2 \times \sin \left(\frac{2\pi h_u h_k}{\lambda d_k^u(t)} \right) \times \sin \left(\frac{2\pi (h_e - h_u)(h_e - h_k)}{\lambda d_k^u(t)} \right) \quad (1)$$

where $d_k^u(t)$ is the distance between UAV and the user in the 3D model, $d_k^u(t) = \sqrt{h_u^2 + (x_u - x_k)^2 + (y_u - y_k)^2}$, h_u denotes the flight altitude of UAV u

It is assumed that the channel gain between the user and the UAV remains constant during each time slot t . Then the channel gain from the UAV u to the user k can be calculated as

$$g_k^u(t) = 10^{-\frac{L_k^u(t)}{10}} \quad (2)$$

2.2 UAV-User Group Association Problems

Assume that in the initial state, the users associated with the UAV are randomly distributed in the maritime cellular network. Let the location state of the UAV and users remain the same in each time slot. It is assumed that each user can be associated with only one UAV within a set of time slots, and the UAV also provides service only to the associated user.

Let $s_k^u(t)$ be the association between the UAV u and the user k . If UAV u is associated with user k , then denote $s_k^u(t) = 1$, otherwise $s_k^u(t) = 0$. Thus there is the following constraint:

$$\sum_{u=1}^U s_k^u(t) = 1, \forall k \in \mathbb{K}, u \in \mathbb{U} \quad (3)$$

Let P denotes the total power of the UAV u . Then the transmit power assigned to user k satisfies the constraint

$$P^u(t) = \sum_{k=1}^K P_k^u(t) s_k^u(t) \quad (4)$$

2.3 NOMA Downlink Communications

We assume that K users are in a cluster. Each user receives and decodes the data transmitted downlink from the associated UAV. Inter-cluster interference is generated when

different UAVs are offloaded to different users and reuse the same channel. If different users reusing the same channel under the same UAV association are considered, intra-cluster interference will occur. NOMA protocol applies SIC receiver at the receiving terminal to implement multi-user detection to eliminate the interference. The receiver first decodes the signal with large channel gain, subtracts the multi-access interference generated by that user's signal from the combined signal, and then judges the remaining users again, and so on, until all the interference is eliminated [9]. Therefore, the signal-to-noise ratio of user k :

$$SINR_k^u(t) = \frac{|g_k^u(t)|^2 P_k^u(t) s_k^u(t)}{I_{in\ k}^u(t) + I_{on\ k}^u(t) + z_k^u} \quad (5)$$

Here, " $I_{on\ k}^u(t) = \sum_{s=1, s \neq u}^U |g_k^s(t)|^2 P^s(t)$ " is the inter-cluster interference to user k from UAVs other than UAV u , where $g_k^s(t)$ denotes the channel gain between UAVs other than UAV u and user k , $s \neq u$. " $I_{in\ k}^u(t) = \sum_{i=k+1}^K |g_i^u(t)|^2 P_i^u(t) s_i^u(t)$ " is the intra-cluster interference generated within the same range served by the UAV. z_k^u is the additive white Gaussian noise (AWGN), $z_k^u \sim CN(0, \sigma^2)$.

With the above reasoning and Shannon's formula, the corresponding data rate can be calculated as

$$R_k^u(t) = \sum_{u=1}^U \sum_{k=1}^K B \log 2(1 + SINR_k^u(t)) \quad (6)$$

The time delay required for the UAV service at moment t is

$$T_k^u(t) = \frac{I_n}{R_k^u(t)} \quad (7)$$

The energy efficiency consumed is

$$E_k^u(t) = P_u(t) \cdot T_k^u(t) \quad (8)$$

2.4 System Outage Probability Analysis

To facilitate the discussion of system mid-range performance, it is necessary to define the system interrupt event first. If any user in the group does not decode successfully, the system is considered to be interrupted. Assuming that the target rate of transmission is r_k , the system interruption probability can be expressed as:

$$P^{out} = 1 - P^s \quad (9)$$

where denotes the probability of successful transmission and has

$$P^s = P^r \{ SINR_k^u \geq SINR_k^r, k \in \mathbb{K} \}$$

$$SINR_k^r = 2^{r_k} - 1 \quad (10)$$

Let $\alpha_k^u(t)$ be the power allocation factor for user k . Then the following relationship exists between user power and transmit power $P_k^u(t) = P^u(t)\alpha_k^u(t)$ and there is a constraint $\sum_{u=1}^U \sum_{k=1}^K \alpha_k^u(t) = 1$.

When $0 < \alpha_k^u(t) < \frac{1}{1+SINR'_k}$, the probability of successful transmission can be expressed as

$$P^s = \Pr \left\{ SINR_k^u(t) \geq \frac{SINR'_k(t)}{\alpha_k^u(t) - \sum_{i=0}^k \alpha_i^u(t) SINR'_k(t)} \right\}, \forall k \in \mathbb{K} \quad (11)$$

3 Question Formula

For the offshore renewable energy generation system, considering the different demands of communication users, we take minimizing the system energy consumption as the optimization objective, including jointly optimizing the trajectory and power allocation of UAVs. We express the positions of UAV u and user k in time slot t by L^u and L^k , respectively, and $L = \{x(t), y(t), h(t), 0 \leq t \leq T\}$. Assume that the UAV and user positions are fixed within each time slot t and that each UAV position is different.

Consequently, the optimization issue may be expressed as

$$\begin{aligned} & \min E(t) \\ & s.t. C1 : L_{\min} \leq L^u(t) \leq L_{\max}, \forall u \in \mathbb{U}, \\ & C2 : L_{\min} \leq L^k(t) \leq L_{\max}, \forall k \in \mathbb{K}, \\ & C3 : L_i^u \neq L_j^u, \quad i, j \in \mathbb{U}, \forall t, \\ & C4 : \sum_{k=1}^{\mathcal{K}} s_k^u(t) P_k^u(t) \leq P^u, \forall k \in \mathbb{K}, u \in \mathbb{U} \end{aligned} \quad (12)$$

C1 ~ C3 denote the location constraints of the UAV and the user in the stereoscopic space. According to C4, the entire amount of power provided to the user cannot be higher than the transmit power.

Since the class of problems in (11) was shown in [6] to be non-convex and NP-hard for this optimization problem, and due to high computational complexity and randomly varying channel conditions, it is difficult to obtain a globally optimal solution in practice. Therefore, this paper invokes an RL-based algorithm that interacts with the environment and learns from the interaction experience.

4 Solutions

This section focuses on the solution proposed to solve the above objective function, which is roughly divided into two steps. After the edge server calculates the offload, it first uses the K-means algorithm to cluster and associate users based on their location and the drones to determine each drone cluster and the users to be served. The multi-agent DQN method is then used to jointly optimize the trajectory and power allocation of the UAVs to accomplish the objective of minimizing system energy consumption [10]. Figure 2 shows a block diagram of joint optimization using a multi-agent DQN scheme. The solution will be described in detail in two areas next.

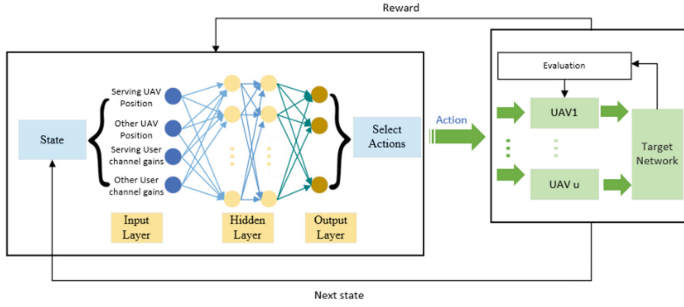


Fig. 2. Block diagram of the joint optimization of a multi-intelligent DQN scheme.

4.1 Clustering of User Based on K-Means

Spatial association of users using K-means clustering with an upper limit on cluster membership allows the offloaded users to be divided into multiple clusters to suppress inter-cluster interference. Within the system, we first divide, at random, the location of each user into U groups and randomly select U users as cluster centers for the clusters. The distance between the other users and each cluster center is calculated and these remaining users are assigned to the closest cluster of users. The number of users in each cluster is calculated, and if there are redundancies or vacancies, users are reassigned based on the nearest user cluster. The clustering center and the assigned users then represent a clustering cluster. For each user assigned, the position of the cluster center is recalculated based on the center distance of the existing users in the cluster. This process is repeated until all users have been allocated, or the cluster centers no longer change and the mean sum of squares of errors is minimized. Once users are allocated, the nearest UAV is selected for each user cluster to complete the clustering.

4.2 Deployment and Power Allocation of Multi-agent DQN Algorithm

In this subsection, we use a multi-intelligent DQN algorithm based on a user sub-clustering strategy to jointly optimize the UAV cluster trajectory and power allocation to minimize the system energy consumption. That is, multiple UAVs are deployed in the maritime cellular offload network, abstracting the scenario as intelligences that can choose their actions, and the UAVs exist independently of each other and do not know the choice of actions.

For each time t , the UAV as an agent decent to a state when it needs to select an action based on the state, receive a reward $r_t = r(s_t, a_t)$, and observe a new state s_{t+1} . Each intelligent body exists independently in the environment. Combined with the power allocation scenario, each part of the task is represented in the multi-intelligent body DQN framework as follows:

State: In the system multi-agent DQN model, each UAV and the cluster of users it serves is treated as an agent, and the state of the intelligent body consists of the cluster's location and channel gain [11]. Each agent interacts with the environment independently, allowing different agent to connect to the same neuron. As shown in Eq. (13):

$$S_t^u = \{L_u(t), L_s(t), g_k^u(t), g_k^s(t)\}, u, s \in \mathcal{U}, s \neq u, k \in \mathcal{K}$$

$$S_t = \{S_t^1, S_t^2, \dots, S_t^u\} \quad (13)$$

Actions: At time t , each agent $u \in U$ observes the current state of the environment $S_t \in S$ and chooses an action $A_t^u \in A^u$ based on a random policy π_u , and the actions of the intelligent agents form a joint action A_t . Each independent agent needs to choose the UAV flight action and the power allocation decision. The action usage is given by the following equation:

$$A_t = \begin{cases} A_L = \{\text{Left, right, front, back, up, down, stationary}\} \\ A_P = \{P_1, P_2, \dots, P_k\} \end{cases} \quad (14)$$

Reward: As a result of this joint action, all intelligences receive a reward signal $R_t = r(S_t, A_t)$ [12] and the environment is transferred to a new state $S_{t+1} \in S$ according to a transfer probability function $P(S_{t+1}|S_t, A_t)$ [13].

A natural approach to such a fully observable, cooperative multi-intelligence RL problem is to consider a “meta-intelligence” that chooses a joint action A_t based on π , π being a vector containing strategies $\pi_u, u \in U$, i.e. $\pi = (\pi_1, \dots, \pi_n)$. This meta-agent learns the Q function $Q(s, a) = E^\pi[G_t|S_t = s, A_t = a]$, which is conditional on the states and joint actions of all agents.

In summary, in a multi-intelligent DQN model, the intelligences can perform multiple discrete actions, and each network is trained independently without interfering with each other. The drone cluster feeds state information into the evaluation network after establishing appropriate connections with the neurons. After several iterations, the scheme results in higher reward values.

5 Analysis of Result

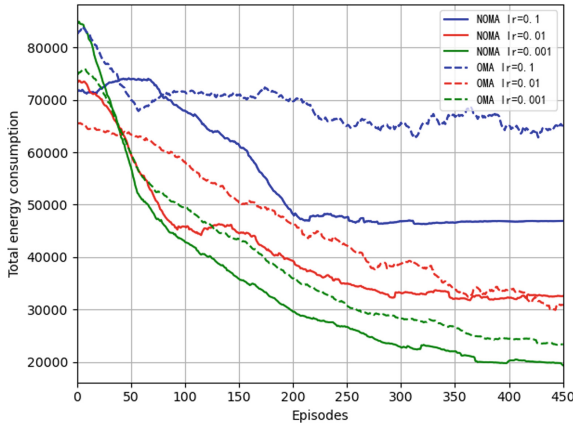
To determine the success of the suggested method and the gain of each component, numerical results are presented in this section. In the simulation scenario, we assume 3–20 UAVs and 10–60 sea vessel users distributed in a 3D space of $500 * 500 * 150$. Users are randomly distributed in the same horizontal plane in space. The hovering position of the UAV depends on the centroids of the user clusters and is optimized. Each UAV serves 2–10 users through NOMA. The neural network in use comprises three layers and a hidden layer with forty nodes. The mean square error is used as the loss function, while the activation function is a corrected linear unit. The neural network is trained using the Adam optimizer [14]. Table 1 includes a list of the additional default simulation parameters. Without a special justification, the simulation uses its default settings.

From Fig. 3, we can easily observe the convergence of the multi-agent model, with the increase of the number of algorithm iterations, the energy consumption decreases correspondingly, and the reduction of energy consumption is more significant for NOMA compared to OMA. However, we can see that as the learning rate increases it may cause the intelligences to update too quickly and not share information as quickly, therefore leading to a lower convergence of the curve.

Figure 4 shows the relationship between the number of errors in user association and the number of training sets, with NOMA also slightly outperforming OMA in terms of error rate.

Table 1. Simulation parameters

Parameter	Value
wavelength in meters λ	0.15
The height of evaporation duct layer h_e	20
Carrier frequency f_c	2 GHZ
Bandwidth	15 kHz
AWGN power	-100 dBm/Hz
Transmitting power of UAV	20 dBm

**Fig. 3.** Total energy consumption versus training episodes for OMA and NOMA.

It is assumed that a UAV can only serve two users. To facilitate the simulation of the degree of association in the 3D model, the UAV' is used to denote the projection of the UAV in the xy-axis plane, and a region of the same color is used to denote the cluster of UAVs and the users they serve under the same cluster. According to the above algorithm, and so that the multi-access method and energy consumption are selected differently, the UAV and user location state information is shown in Fig. 5. Any user under the same cluster with optimal and average energy consumption is selected for outage probability and transmission rate analysis. The analysis is shown below:

Figure 6 gives the outage probability performance of users within the same cluster for NOMA and OMA transmission methods with different energy consumptions. The decoding order of users under the same cluster within user 1 and 2 systems. to see that since each user needs to decode the interference of all previous users during the decoding process, user 2 can obtain a larger outage probability value for a suitable signal-to-noise ratio value. The reason for this is that since User 2 fails to adequately decode and remove the signal from User 1, the interfering signal from User 1 will gradually accumulate throughout the communication process, which will result in higher interference and thus higher outage probability performance for the highest-level user.

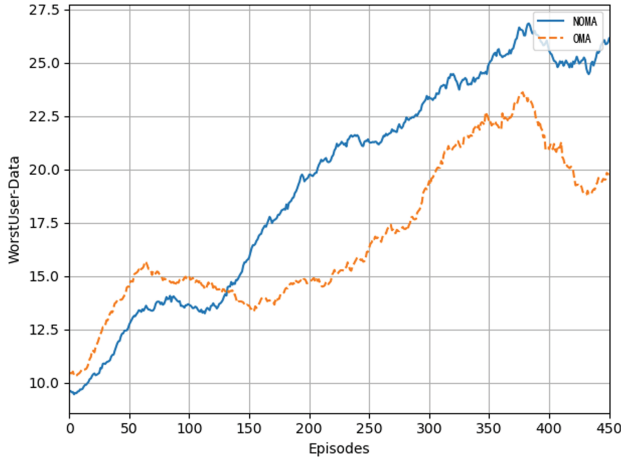


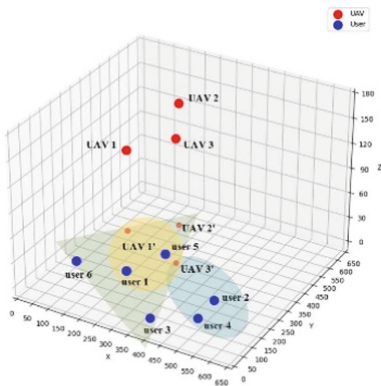
Fig. 4. Worst user-data rate in test episode with re-clustering.

And regardless of the user, the outage probability of interruption at optimal energy is lower than the outage probability at average energy consumption. This is due to the different co-power allocation at different energy consumptions, which results in different outage probabilities.

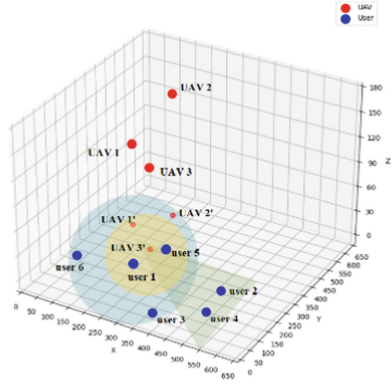
To verify the outage probability results in Fig. 6, the transmission rates of users within the same cluster are given in Fig. 7. As the signal-to-noise ratio increases, the transmission rate of the first user outperforms that of the second user, even if there are hardware defects and interference within the system. From the results, the user starts to have a more significant rate increase at a signal-to-noise ratio of 10dB under optimal energy consumption, while the user under average energy consumption has a change at around 15 dB. This indicates that the system is capable of accomplishing low-energy and high-rate transmissions in maritime communications.

6 Summary

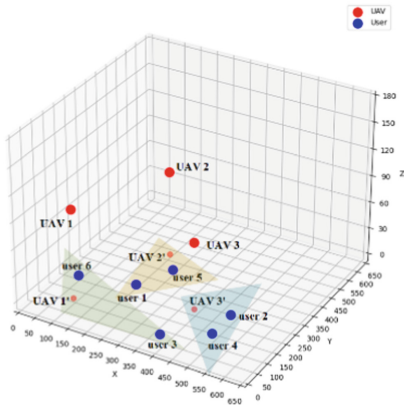
In order to improve the efficiency of offshore energy systems and ensure a tight connection and reliable operation of the sea-land grid. In this paper, a NOMA-based UAV-assisted offloading network is designed for optimizing communication performance under offshore multi-energy complementary power generation systems. The system uses UAVs equipped with edge servers and antennas to perform task offloading calculations and resource allocation tasks for offshore users. The system uses the K-means algorithm to make clustering associations between users and UAVs, and then uses a multi-intelligent deep Q-network algorithm to minimize system energy consumption by optimizing UAV cluster movement trajectories and user power allocation while considering system hardware loss and SIC incompleteness. The simulation results evaluate the performance of the proposed method through numerical results of energy consumption and error rate, comparing in terms of convergence, multi-access schemes, and learning rate. The cluster location analysis in the average energy consumption state in the selected



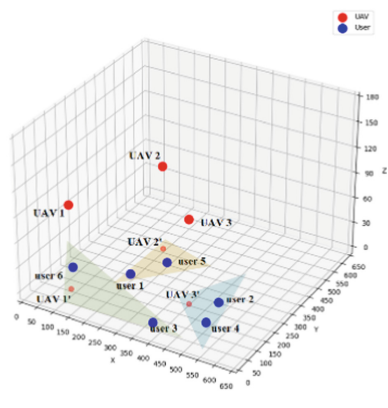
(a) The NOMA association case at optimal energy consumption.



(b) The OMA association case at optimal energy consumption.



(c) The NOMA association case at average energy consumption.



(d) The OMA association case at average energy consumption.

Fig. 5. Location and association information in the average state.

number of iterations and the simulation analysis of the interruption rate and transmission rate of users in this state for the same cluster and different multiple access techniques are given. These results demonstrate the superiority of the NOMA framework in the context of maritime UAV-assisted offload networks.

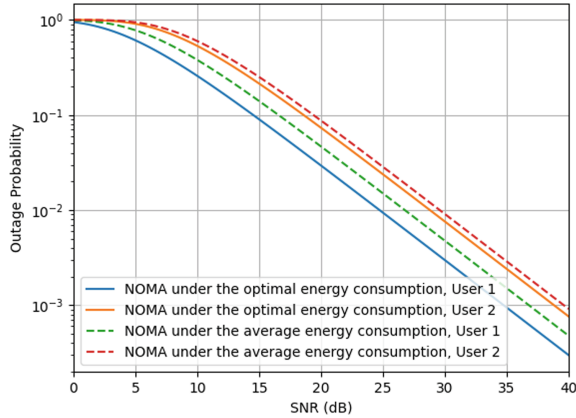


Fig. 6. Outage probability versus SNR.

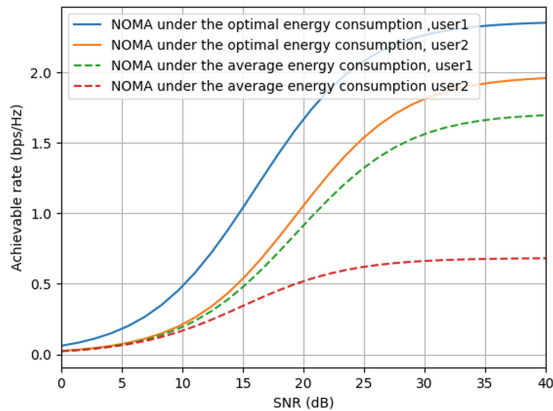


Fig. 7. Achieve rates within the same cluster.

Acknowledgment. This research was funded by the National Natural Science Foundation of China, grant number U2006222 and Natural Science Foundation of Shandong Province, grant number ZR2020MF138.

References

1. Gan, L., et al.: Balancing of supply and demand of renewable energy power system: a review and bibliometric analysis. *Sustain. Futures* **2**(100013), 100013 (2020). <https://doi.org/10.1016/j.sfr.2020.100013>. Accessed 23 May 2020
2. Shafi, M., Molisch, A.F., Smith, P.J., et al.: 5G: a tutorial overview of standards, trials, challenges, deployment, and practice. *IEEE J. Sel. Areas Commun.* **35**(6), 1201–1221 (2017)
3. Pei, H., Guo, S., He, Y., Wang, J.: Capacity optimization of concentrated solar power-photovoltaic wind Power combined generation system. *E3S Web Conf.* **118**, 02060 (2019)

4. Zhang, Y., Wang, X., Xu, Y.: Energy-efficient resource allocation in uplink NOMA systems with deep reinforcement learning. In: 2019 11th International Conference on Wireless Communications and Signal Processing (WCSP), Xi'an, China, pp. 1–6 (2019)
5. Zhong, R., et al.: Multi-agent reinforcement learning in NOMA-Aided UAV networks for cellular offloading. *IEEE Trans. Wireless Commun.* **1** (2021). <https://doi.org/10.1109/twc.2021.3104633>. Accessed 30 Sep 2021
6. Guo, S., Zhao, X.: Multi-agent deep reinforcement learning based transmission latency minimization for delay-sensitive cognitive satellite-UAV networks. *IEEE Trans. Commun.* **71**(1), 131–144 (2023)
7. Nguyen, M.: Interference and resource management techniques for wireless networks. *EspaceINRS*. <https://espace.inrs.ca/id/eprint/13131/> (1970)
8. Lee, Y.H., Dong, F., Meng, Y.S.: Near sea-surface mobile radio wave propagation at 5 GHz: measurements and modeling. *Radio Eng.* **23**, 824–830 (2014)
9. Li, Z.-H., Li, N.-N.: Unmanned aerial vehicle landing point recognition based on natural landmark image. *J. Comput. Appl.* **30**(4), 971–973 (2010). <https://doi.org/10.3724/sp.j.1087.2010.00971>. Accessed 22 Nov 2019
10. Zhang, S., Zhang, H., Di, B., Song, L.: Cellular UAV-to-X communications: design and optimization for multi-UAV networks. *IEEE Trans. Wirel. Commun.* **18**(2), 1346–1359 (2019)
11. Wang, R.Y., Xu, L.: Multi-agent dam management model based on improved reinforcement learning technology. *Appl. Mech. Mater.* **198–199**, 922–926 (2012). <https://doi.org/10.4028/www.scientific.net/amm.198-199.922>. Accessed 24 Sep 2019
12. Liu, W., He, Y., Zhang, J., Qiao, J.: Deep reinforcement learning-based MEC offloading and resource allocation in uplink NOMA heterogeneous network. In: 2021 Computing, Communications and IoT Applications (ComComAp), Shenzhen, China, pp. 144–149 (2021)
13. Melo, D.C., Máximo, M.R.O.A., da Cunha, A.M.: Push recovery strategies through deep reinforcement learning. In: 2020 Latin American Robotics Symposium (LARS), 2020 Brazilian Symposium on Robotics (SBR) and 2020 Workshop on Robotics in Education (WRE), Natal, Brazil, pp. 1–6 (2020)
14. Haworth, B., et al.: Deep integration of physical humanoid control and crowd navigation. *Motion, Interact. Games* (2020). <https://doi.org/10.1145/3424636.3426894>



Bearings-Only Passive Localization in Unmanned Aerial Vehicle Formation Based on Mathematical Model

Bingqian Meng, Xinqiao Hou, and Haiyan Wu^(✉)

Zhixing College of Hubei University, Wuhan, Hubei, China
haiyanshuxue@163.com

Abstract. In recent years, with the improvement of electronic technology, the maturity of satellite positioning system and the emergence of new UAVs, UAVs have entered a stage of rapid development. In order to ensure the concealment of UAVs and avoid external interference as much as possible, passive location and tracking system has gradually become a research hotspot when UAVs are flying in formation. The method of passive location has strong anti-interference ability and good concealment, which is a bridge between positioning technology and algorithm performance analysis. In this paper, aiming at the problem of how to maintain the formation of UAV cluster in the process of formation flight, the positioning coordinates of UAV are obtained by optimizing the particle swarm optimization algorithm, and the appropriate positioning model is constructed by using the bearing-only passive positioning algorithm. The position adjustment scheme of UAV is studied and extended to other formation scenarios.

Keywords: Bearings-only passive positioning · Mathematical model · Unmanned aerial vehicle

1 Introduction

With the improvement of electronic technology and the maturity of satellite positioning system, UAV has entered a stage of rapid development (see [1–4]). The method of passive location has strong anti-interference ability and good concealment, which is a bridge between location technology and algorithm performance analysis. In order to accurately locate the UAV and adjust the UAV to the ideal position, the passive location tracking system has gradually become a research hotspot. Reference [5] utilized geometric knowledge to locate unmanned aerial vehicles, and demonstrated the impact of positioning geometric parameters on estimation bias through analysis and numerical examples. References [6, 7] proposed an optimization algorithm for the distribution of positioning stations in the adaptive matching reconnaissance area, which effectively reduced the TDOA positioning error in the reconnaissance area and obtained more accurate positioning results. A new system supporting search and rescue activities was reported, and its performance was tested in on-site experiments simulating real search scenarios in [8].References [9, 10] provided a particle swarm optimization algorithm,

which accelerated the convergence speed of the algorithm, but the flexibility of the algorithm is low. This paper intends to use the method of bearing-only passive positioning to adjust the position of the UAV, that is, several UAVs in the formation transmit signals and the other UAVs passively receive signals, from which the direction information is extracted for positioning, so as to adjust the position of the UAV. Each UAV in the formation has a fixed number, and the relative position relationship with other UAVs in the formation remains unchanged.

2 Effective Localization of Unmanned Aerial Vehicles Under Symmetric Models

In the initial case of a slight deviation in the position of the drone, it is assumed that a drone is located at the center of the circle and up to three drones are around to transmit the signal. As shown in Fig. 1, the positions of FY00 (0) and FY01 (01) are fixed, and other UAVs are adjusted for azimuth. Calculate the angle between each drone site of the regular nine-sided based on 0 and 01 relative to the 0 and 01 drones. Because it is a regular nine-sided, it can be directly adjusted by using the relationship between the angle under the regular nine-sided and the current angle. Adjust from near to far, bundle the symmetry point, that is, when the drone 0 and 01 are fixed, first determine the orientation of the drone 02 to determine whether the drone 02 has a deviation. If the other drones have no deviation, we have the signal angle $\beta_1 = \frac{9}{2\pi}$.

When the drone 02 has deviation and the FY00 drone is at the center of the circle and the 01 drone is fixed, based on the drone number information, we can obtain $\beta'_1 = (b - a) * \frac{9}{2\pi}$, the arc length without deviation $L = r * \beta_1$ and the deviated arc length $L' = r' * \beta'_1$. Let $Q = \beta'_1 - \beta_1$.

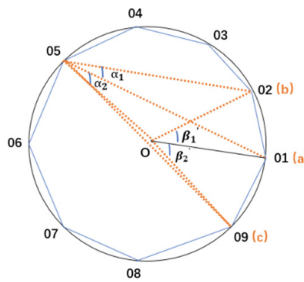


Fig. 1. Adjustment orientation of UAV

When $Q > 0(Q \neq 0)$, $D > 0$, it indicates that drone 02 has an upward angle deviation and a deviation from the center of the circle (drone FY00) radius deviation towards the outside of the track. At this time, it is necessary to send a signal to drone 02 to adjust it to the correct orientation;

When $Q > 0(Q \neq 0)$, $D < 0$., it indicates that drone 02 has an angle deviation upwards and a radius deviation towards the center of the circle (drone FY00) in the

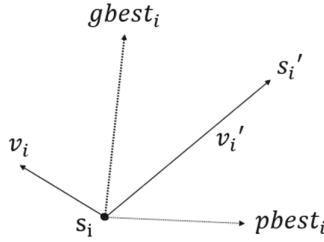


Fig. 2. The update position of particles

orbit. At this time, it is necessary to send a signal to drone 02 to adjust it to the correct orientation;

When $Q > 0 (Q \neq 0)$, $D = 0$, it indicates that drone 02 only has an upward angle deviation. At this time, it is necessary to send a signal to drone 02 to adjust it to the correct orientation;

When $Q < 0 (Q \neq 0)$, $D > 0$, it indicates that drone 02 has an angle deviation downwards and a radius deviation from the center of the circle (drone FY00) towards the outside of the track. At this time, it is necessary to send a signal to drone 02 to adjust it to the correct orientation;

When $Q < 0 (Q \neq 0)$, $D < 0$, it indicates that drone 02 has an angle deviation downwards and a radius deviation towards the center of the circle (drone FY00) in the orbit. At this time, it is necessary to send a signal to drone 02 to adjust it to the correct orientation;

When $Q < 0 (Q \neq 0)$, $D = 0$, it indicates that drone 02 only has downward angle deviation. At this time, it is necessary to send a signal to drone 02 to adjust it to the correct orientation.

At this time, the position of UAV 02 has been adjusted. Since UAV 09 should be in a symmetrical position with UAV 02, the position of UAV 09 should also be adjusted. In addition, since the positions of UAV 01 and UAV 02 have been determined and are symmetrical, the positions of UAV 0 and UAV 01 are fixed. Then, (the circumferential angle or central angle corresponding to the same arc is equal), that is, UAV 05 can also receive the signal of adjusting the position, and so on, the other UAVs with deviations will receive the signal of adjusting the position accordingly.

In summary, if the UAV position of the transmitted signal has no deviation, in addition to FY00 and FY01, at least one UAV is required to transmit the signal to achieve effective positioning of the UAV.

3 Particle Swarm Optimization Algorithm

The solution initialized by the particle swarm optimization algorithm is a random solution. The particles will update themselves according to the two values obtained by tracking to find the optimal solution. By optimizing the particle swarm optimization algorithm, the information data of each UAV is iteratively processed, that is, a massless particle is designed to simulate a UAV in the UAV cluster and extend to N-dimensional space. The UAV FY00 has only two parameters in the dimensional space: speed and

position, where the speed represents the speed of movement and the position represents the direction of movement. Let s_i and v_i ($i = 1, 2, \dots, N$) be the position system and the flight speed system, either.

The following is the updated speed and position formula:

$$v_i = v_i + k_1 * rand() \times (pbest_i - s_i) + k_2 * rand() \times (gbest_i - s_i) \quad (1)$$

$$s_i = s_i + v_i \quad (2)$$

The position of the particles is updated as shown in Fig. 2. The speed of a drone v_i is usually limited to the range of $[-v_{max}, v_{max}]$. $rand()$: Random numbers between 0 and 1. Let s_i be the current position of the particle. The learning factor (k_1, k_2) is usually 2, which can enable particles to possess self and social cognitive abilities. Since the dynamic can obtain better optimization results than the fixed value, the following formulas are obtained:

$$v_i = c * v_i + k_1 \cdot rand() \times (pbest_i - s_i) + k_2 \cdot rand() \times (gbest_i - s_i) \quad (3)$$

As an inertia factor, c takes a non negative value. When c is large, the global optimization ability is strong and the local optimization ability is weak; When c is small, the global optimization ability is weak and the local optimization ability is strong. Denote $pbest$ and $gbest$ the global and local optimal positions of the particle swarm, respectively.

When $k_1 = 0$, particles became models of only society.

$$v_i = c * v_i + k_2 \cdot rand() \times (gbest_i - s_i) \quad (4)$$

When $k_2 = 0$, particles became only a model of cognition.

$$v_i = c * v_i + k_1 \cdot rand() \times (pbest_i - s_i) \quad (5)$$

The dynamic changes linearly in the search process of the particle swarm optimization algorithm, and can be dynamically changed according to a measure function of its performance-linear decreasing weight strategy.

$$c^{(u)} = \frac{(c_{ini} - c_{end})(G_k - g)}{G_k} + c_{end} \quad (6)$$

In the Formula (6), G_k represents the maximum number of iterations, c_{ini} represents the initial inertia weight, and c_{end} represents the inertia weight when iterating to the maximum evolution algebra. Let $c_{ini} = 0.9$ and $c_{end} = 0.4$.

4 UAV Adjustment Scheme

By optimizing the particle swarm optimization algorithm, each UAV is iteratively processed, the UAV (particle) information is tracked to find, the distance between adjacent UAVs is fixed, and the design formation is adjusted. When the plane formation is known, the position of a part of the UAV is adjusted to complete the change of another formation (two-dimensional or three-dimensional).

Firstly, two vertices are determined. Let the vertices be FY00 and FY01, send signals to other UAVs, and other UAVs with slight deviation receive signals. Assuming that there are n UAVs, the distance between adjacent UAVs on the straight line is equal, and the formation diagram is shown in Fig. 3.

Using the idea of step-by-step following and greedy algorithm, the jump problem in the greedy algorithm is cited. Each element in the array is expressed as 1, and the update reaches the farthest distance to complete the coverage of all formations. Since the adjacent UAVs of the formation are equal in distance, three adjacent UAVs determine a regular triangle $\alpha_i = 60^\circ$.

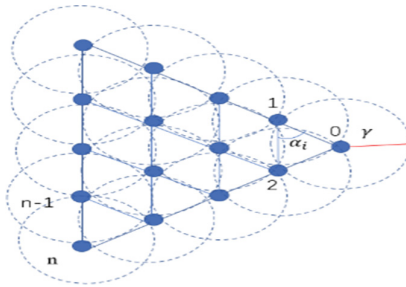


Fig. 3. UAV formation

Each UAV is positioned step by step, and the formation is completely covered when it is detected directly. There are two-dimensional formations into three-dimensional formation. Assuming that there are n UAVs, when n is odd, there is no UAV at the vertex, when n is even, there is a UAV at the vertex, and the serial number of the vertex UAV is FY00, which changes the serial number of the UAV in the counterclockwise direction.

In the case that the drone has been woven into a regular triangle (on the same plane), the interior is evenly distributed through an equilateral triangle (composed of 10 drones, which can be divided into three layers). The rising height is the first layer of the adjacent distance of the outermost UAV: composed of 6 UAVs with a spacing of 60, numbered FY0 (1–6). The second layer is composed of three UAVs with a spacing of 60, numbered FY0 (7–9). The third layer: the center position of the equilateral triangle composed of three UAVs in the second layer is numbered FY00. We can reach the shape of the pyramid by raising the same height layer by layer. The first step is to raise the drone number 7–9, taking No.1 and No.0 as the standard points, to test whether there is a deviation between 9 and the standard angle (connecting 0, 1 into a straight line, connecting 1 and 9 into a straight line, the angle between the two straight lines). The second step: Raise the drone number 0 at the same altitude as the first step. Connect drones 0 and 9, and connect drones 7 and 9. Compare whether the included angle is the standard 60° . If not, repeat the above steps to obtain an accurate position. The third step: The 10 drones will eventually form a pyramid shape.

Since the distance between adjacent UAVs is constant, the formation can form a regular triangular prism. The top view and elevation of the formation are shown in Figs. 4 and 5.

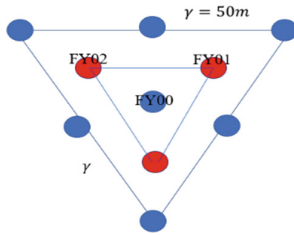


Fig.4. Top view of formation

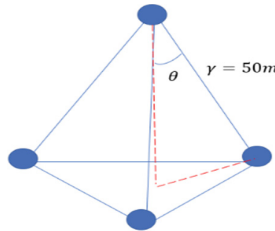


Fig. 5. Facade elevation diagram

The formation needs to determine the correct position of a surface of the UAV, by the correct position of the UAV to judge whether the next layer of aircraft adjacent layer UAV offset. Since the figure composed of the formation is a regular polygon, it is known that only the spatial angle between the position UAV and the upper layer is required.

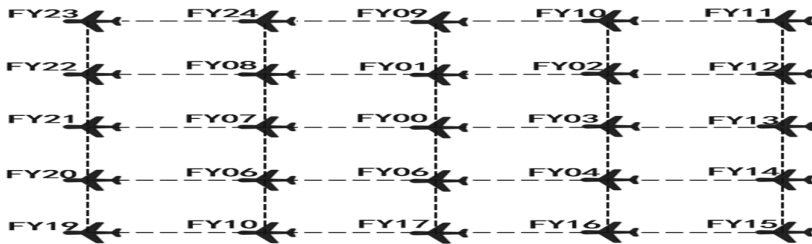


Fig. 6. Chessboard formation

5 Example of the Chessboard Model

It is assumed that the initial formation of the UAV formation is similar to the checkerboard shape (as shown in Fig. 6 above, taking 24 UAVs as an example, it can be more). The checkerboard is composed of countless squares. Set the side length of the square to 1, and the drone located in the center of the chessboard will still be FY00. Other drones will start from a length of 1 units directly above FY00 and form in a clockwise direction, returning to their original positions according to the drone number.

The UAV formation is adjusted by changing the radius of the trajectory circle of the UAV formation. The specific method strategy is shown in Fig. 7.

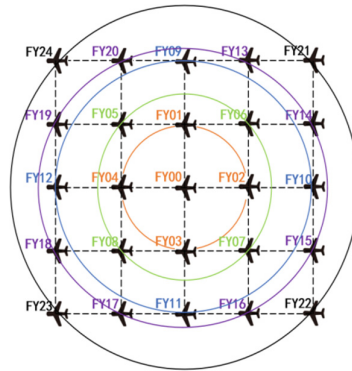


Fig. 7. UAV formation adjustment

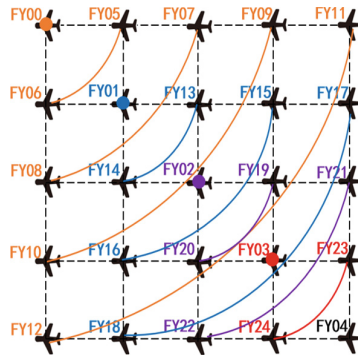


Fig. 8. Chessboard formation

Step 1: Draw a circle with l radius and the center of the circle is still the FY00 site. The intersection of the circle and the chessboard is the UAV site. Four intersections can be located to four UAVs. There is an intersection with the chessboard directly above FY00, which is recorded as FY01, and the other three intersections in the clockwise direction are recorded as FY02, FY03 and FY04;

Step 2: Set a circle with FY01 as the center and a radius of $\sqrt{2}l$. At this time, the circle has four intersection points with the chessboard. The starting position is still clockwise from the top of FY00 to determine other UAV sites. The numbers are FY05, FY06, FY07 and FY08;

Step 3: Set a circle with FY01 as the center and a radius of $2l$. At this time, the circle has four intersection points with the chessboard. The starting position is still clockwise from the top of FY00 to determine other UAV sites, numbered FY09, FY10, FY11, FY12;

Step 4: Set a circle with FY01 as the center and a radius of $\sqrt{5}l$. At this time, there are 8 intersections between the circle and the chessboard. The starting position is still clockwise from the top of FY00 to determine other UAV sites, numbered FY13, FY14, FY15, FY16, FY17, FY18, FY19, FY20;

Step 5: Then set a circle with FY01 as the center and radius of $2\sqrt{2}l$. At this time, the circle has four intersections with the chessboard. The starting position is still clockwise from the top of FY00 to determine other UAV sites, numbered FY21, FY22, FY23, FY24.

At this time, the chessboard-shaped formation mode is successfully adjusted into a layer-by-layer ring-shaped formation. Similarly, for the chessboard formation problem, if any point is selected as the location of FY00 (as shown in Fig. 8). The adjustment process is as follows:

Step 1: The chessboard is on a plane at this time, and the diagonal of the chessboard is numbered one by one from the upper left corner to the lower right corner, that is, FY00, FY01, FY02, FY03 and FY04. The FY01 is moved up a unit length in the direction of the reader, the FY02 is moved down a unit length in the opposite direction of the reader, and the FY03 is moved up a unit length in the direction of the reader;

Step 2: Firstly, a 1/4 arc is drawn for the radius with FY00 as the center of the circle. The intersection points of the arc and the chessboard are FY05 and FY06 from the top right to the bottom left. When the radius is doubled, the center of the circle is unchanged, and then the arc is drawn. At this time, the intersection points of the arc and the chessboard are FY07 and FY08; the radius is expanded again, the center of the circle is unchanged, and the arc is drawn again. At this time, the intersection points of the arc and the chessboard are FY09 and FY10; the radius is expanded again, the center of the circle is unchanged, and the arc is drawn again. At this time, the intersection points of the arc and the chessboard are FY11 and FY12;

Step 3: Taking FY01 as the center of the circle, quarter arc is drawn for the radius. The intersection points of the arc and the chessboard are FY13 and FY14 from the top right to the bottom left.

Step4: Taking FY02 as the center of the circle, quarter arc is drawn for the radius. The intersection of the arc and the chessboard is FY19 and FY20 from the upper right to the lower left.

Step 5: Finally, FY03 is used as the center of the circle, and quarter arc is drawn for the radius. The intersection of the arc and the chessboard is FY23 and FY24 from the upper right to the lower left.

Finally, the chessboard-shaped formation mode is successfully adjusted to a three-dimensional shape.


Acknowledgements. This work has been supported by the Hubei Province College Students' Innovation and Entrepreneurship Training Program (No. S202313234013 Research on Passive Location in Unmanned Aerial Vehicle Formation Based on Mathematical Modeling).

References

1. Masood, A., Scazzoli, D., Sharma, N.: Surveying pervasive public safety communication technologies in the context of terrorist attacks. *Phys. Commun.* **41** (2020). <https://doi.org/10.1016/j.phycom.2020.101109>
2. Xu, Z., Yang, J., Peng, C.: Development of an UAS for post-earthquake disaster surveying and its application in Ms7. 0 Lushan Earthquake, Sichuan, China. *Comput. Geosci.* **68**, 22–30(2014)
3. Li, X., Yao, H., Wang, J.: A near-optimal UAV-aided radio coverage strategy for dense urban areas. *IEEE Trans. Veh. Technol.* **68**(9), 9098–9109 (2019)
4. Pablo, F., Ahmed, R., Luna, M.A., Mohammad, S., et al.: WILD HOPPER: a heavy-duty UAV for day and night firefighting operations. *Heliyon* **8**(6) (2022). <https://doi.org/10.1016/j.heliyon.2022.e09588>
5. Kutluyıl, D.: On the bias of linear least squares algorithms for passive target localization. *Sig. Proc.* **84**(3), 475–486 (2004)
6. Ruhul, A., Nasir, S., Muhannad, A.: UAVs-assisted passive source localization using robust TDOA ranging for search and rescue (2022). <https://doi.org/10.1016/j.ict.2022.04.011>
7. Wang, G., Zhu, W., Ansari, N.: Robust TDOA-based localization for IOT via joint source position and NLOS error estimation. *IEEE Internet Things J.* **6**(5), 8529–8541 (2019)
8. Niedzielski, T., Jurecka, M., Miziński, B.: A real-time field experiment on search and rescue operations assisted by unmanned aerial vehicles. *J. Field* **35**(6), 906–920 (2018)
9. Wang, J., Gu, S., Zhang, S., Liu, S.: Research on indoor space positioning using improved particle swarm optimization algorithm based on visible light communication. *Opt. Commun.* **544** (2023). <https://doi.org/10.1016/j.optcom.2023.129616>
10. Zare, M., Akbari, M.-A.: A modified particle swarm optimization algorithm ith enhanced search quality and population using hummingbird flight patterns. *Decis. Anal. J.* **7** (2023). <https://doi.org/10.1016/j.dajour.2023.100251>



Design of Self-serve DUI Detection System Based on STM32

Yang Wu^(✉)  and Linxiang Zhao

School of Intelligent Equipment Engineering, Wuxi Taihu University, Wuxi, China
wuy1@wxu.edu.cn

Abstract. Drink driving accounts for a very large proportion of accidents arising from vehicle driving, which seriously threatens people's life safety. This question designs a DUI detection system based on STM32F103C6 microcontroller. Combine IOT technology with machine vision technology to contribute to social security. The MQ-3 alcohol concentration sensor is used to detect the concentration level of the driver's breath alcohol content, OpenMV is used to detect the closing of the driver's eyes, and the information is summarized by the STM32 microcontroller and a warning reminder is issued by voice to reduce DUI and reduce the risk of accidents.

Keywords: STM32 · DUI · OpenMV · Fatigue detection

1 Introduction

With the growing strength of the country, the quality of life of the people has been constantly improved and cars have become a necessity for almost every household. While vehicles bring us convenience, they also bring many accidents caused by vehicles, among which drink driving causes a large proportion of accidents, seriously threatening people's lives [1, 2]. In order to effectively stop the harm caused by drink driving, it is necessary to design an in-vehicle driver autonomous drink driving detection system [3, 4]. With the continuous development of computer and communication technology, Internet of Things (IoT) technology is also widely used in various fields of daily life and has become an important part of the National 12th Five-Year Plan [5, 6]. This paper is proposed in this context.

This paper designs a microcontroller-based self-service alcohol content detection system, which mainly consists of STM32F103C6 microcontroller, MQ-3 alcohol concentration sensor, LCD1602 liquid crystal, KT148A voice module and so on. The system is designed to detect whether those who have been drinking are in a drink-driving situation and whether the driver is fatigued. The system has the advantages of being convenient, fast and compact, and has a good market application prospect.

2 Overall System Design

There are two main types of DUI detection systems on the market, one is an automatic detection system [7] and the other is a handheld DUI detection system [8]. This design is a selfservice detection system based on the STM32, which is also a type of automatic detection system. An alcohol concentration sensor, infrared detection, and an OpenMV camera-based fatigue system are used to determine if a driver is driving under the influence of alcohol or fatigue. The alcohol concentration sensor is used to detect the alcohol concentration in the driver's breath to determine the driver's alcohol consumption, and the OpenMV is used to detect the closing of the driver's eyes to determine whether the driver is driving under the influence of alcohol and fatigue, and to issue an alarm to avoid dangerous driving.

The general framework of the design is shown in Fig. 1. The control chip is STM32F103C6 and its peripheral circuits, including power supply module, crystal module, key module, start module, filter module, program download module, reset module, and additionally contains PT333 infrared sensor, MQ-3 alcohol concentration sensor and OpenMV vision module, which will transmit these signals to the microcontroller, and after processing, issue an alarm message to remind the driver whether The driver is alerted to the fact that he or she is driving under the influence of alcohol.

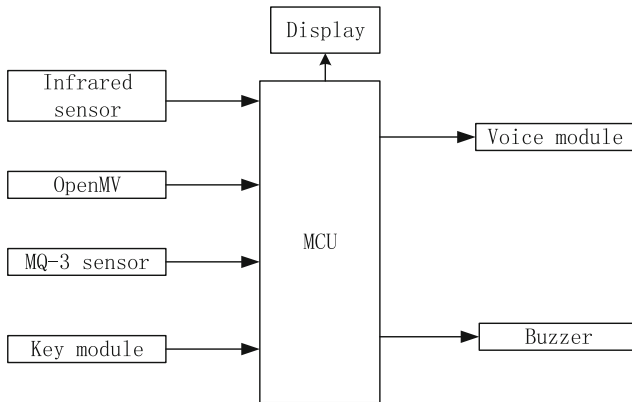


Fig. 1. General design framework

3 System Hardware Design

Figure 2 shows the overall circuit diagram for this design. According to the requirements of this design, a PT333 infrared sensor, an MQ-3 alcohol concentration sensor, and an OpenMV vision module were used.

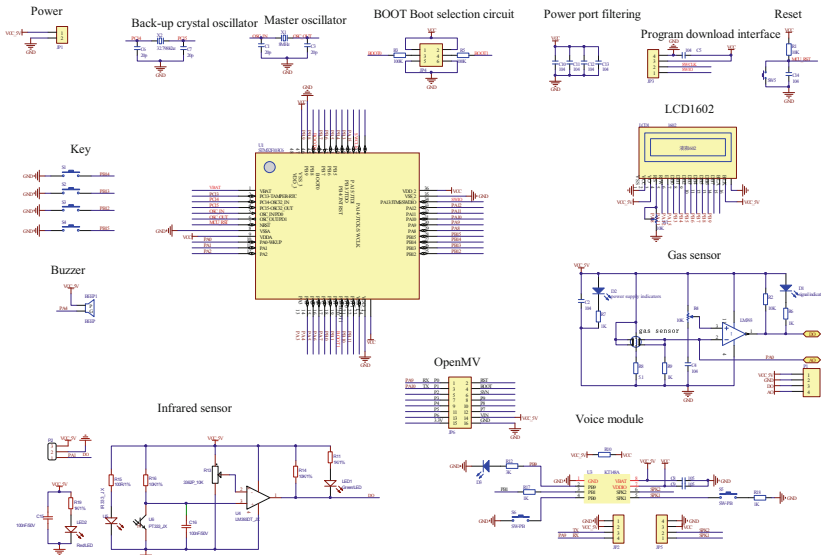


Fig. 2. Overall circuit design diagram

3.1 Main Control Chip

The STM32F103C6 is an embedded-microcontroller IC with a high-performance ARMCortex-M3 32-bit RISC core processor. Compared to the 51 microcontroller, it can bring out the functionality better.

3.2 Gas Sensors

The gas sensor used is the MQ-3 alcohol concentration sensor for the detection of alcohol gas concentrations. It is commonly used for drink driving detection and safety monitoring in drinking establishments [9]. The MQ-3 sensor works on the basis of an electrochemical reaction in the semiconductor sensitive element, when alcohol gas comes into contact with the sensitive element inside the sensor, it causes a series of chemical reactions that result in electrical signals. These signals are then amplified and processed so that they can be read and analysed by the microcontroller to determine the concentration level of the alcohol gas and, depending on the strength of the signal, the alcohol content of the driver's exhaled breath [10]. In addition to DUI detection and safety monitoring of drinking establishments, the MQ-3 sensor can also be used in areas such as gas leak detection in domestic and industrial environments. In this design, the MQ-3 sensor is used to detect the level of alcohol on a driver's breath to identify whether the driver is drink-driving or not [11, 12].

3.3 Infrared Sensors

Infrared sensors are devices that detect and respond to infrared radiation. They can be used to detect objects, ambient temperatures and other specific physical quantities

and are one of the most important components of modern electronics. Infrared sensors work by using the absorption and reflection properties of infrared light by a substance. When infrared light hits the surface of an object, part of it is reflected back and part is absorbed. By detecting the reflected or absorbed light signal, information about the object can be obtained. Common infrared sensors are passive infrared sensors (PIR infrared sensors) and active infrared sensors (e.g. infrared distance measurement modules). Passive infrared sensors can only detect infrared radiation from an object, while active infrared sensors can emit and receive infrared light for ranging, communication and other functions. This design uses the PT333 active IR sensor, which receives information via infrared light when the driver enters the driver's seat, transmits the information it receives to the microcontroller so that the microcontroller can give appropriate feedback and uses other expression modules to communicate to the driver that the DUI system wants the driver to perform a DUI test.

3.4 OpenMV

OpenMV is an open source machine vision system designed for low-power and real-time applications such as robotics, embedded devices and drones. It combines a microcontroller with a camera sensor to provide a corresponding platform for image processing and computer vision. OpenMV is an open source, low cost, powerful machine vision module. Using the STM32F427 CPU as the core and integrating the OV7725 camera chip, the core machine vision algorithm is efficiently implemented in C on a compact hardware module, providing a Python programming interface.

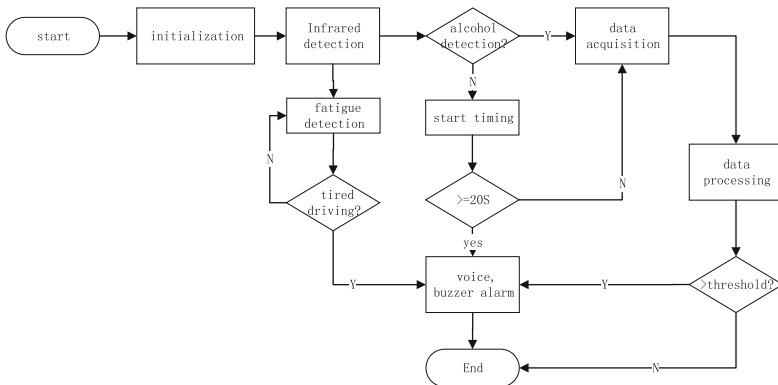


Fig. 3. System flow diagram

4 System Software Design

According to the design and requirements of the DUI detection system, the flow of this design is shown in Fig. 3.

When the driver enters the cockpit, the infrared sensor senses the driver and gives the microcontroller a feedback, after which the microcontroller will use the language announcement system to remind the driver to carry out the alcohol content test, if the driver has not carried out the alcohol content test after 20S, the microcontroller will make the buzzer sound a constant reminder to remind the driver to carry out the alcohol content test. If the driver conducts an alcohol test when the language is broadcast, the MQ-3 alcohol sensor will convert the alcohol concentration into an electrical signal, and if the result triggers the “1” threshold of the LM393, the output will be 0; if the “1” threshold of the LM393 is not triggered, the output will be 1. This is used to determine whether the driver has carried out a breath alcohol test, usually with a threshold value of 0. This means that if the driver’s breath alcohol content is detected as 0, everything is fine, but if the driver detects that the alcohol content is being carried out, the buzzer will alarm for a long time to remind the driver that the driver is driving under the influence. Also, using the OpenMV module for driver fatigue detection, when the driver closes his eyes for a long time, the driver is considered to be in fatigue detection and an alarm is issued.

5 System Testing

The hardware is shown in Fig. 4. When the power is switched on, the display starts to activate and the infrared sensors as well as the MQ-3 sensors start to work. The display lights for each sensor are red at this time. When the person approaches the infrared sensor, the infrared sensor displays a green light, indicating that the infrared sensor captures the driver in the driver’s seat, at this time, the infrared sensor will capture the driver’s information to the microcontroller. The first row of the display shows “Unmanned 01s” and then after a period of time it will change to “Please check **s” indicating the length of time the driver has passed the infrared sensor without being tested for drink driving. However, when the driver leaves the driver’s seat again, it will go into standby mode and will run again when the driver gets into the driver’s seat. When the driver performs an alcohol test, the MQ-3 module and the infrared sensor indicator both light up green. At this point, the first row of the display shows “Someone 00s”. This indicates that someone is in the driver’s seat and that an alcohol test has been carried out. When the detected alcohol concentration exceeds the threshold, the buzzer module in the lower right corner starts to alarm and the voice announcement module in the lower left corner starts to announce that drinking and driving is prohibited.

After passing the breath alcohol test, OpenMV is still used to detect if the driver is fatigued, enhancing the usability of the DUI detection system and protecting the driver in many ways. As long as the driver’s seat is occupied, OpenMV will detect the driver’s eye closure in real time, regardless of whether the driver has been drinking or not, and transmit the information to the microcontroller, which will start to alert the driver via verbal announcements when fatigue is determined.

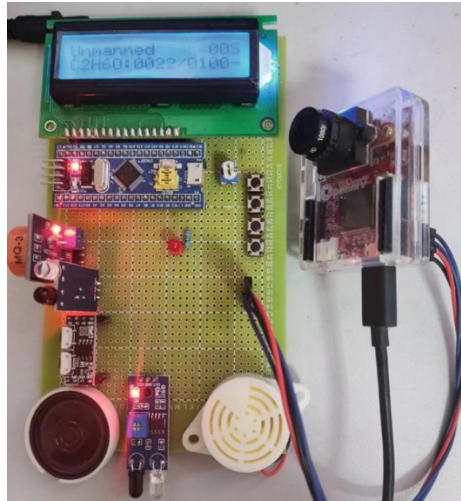


Fig. 4. Physical diagram of the hardware

6 Conclusion

This paper designs a microcontroller-based self-service alcohol content detection system to detect whether those who have been drinking are in a drink-driving situation and whether the driver is fatigued. The system is convenient, fast and compact, and has good market prospects. It can quickly and accurately detect the alcohol content of the person being tested, as well as determining whether the driver is fatigued. The drink-driving detection system is a useful technology that can reduce drink-driving behaviour on the road and provide safety for the public. In the future, with the continuous development of technology, there will be more development and innovation of this detection system to bring better experience for the public to use in order to protect public safety and reduce the occurrence of accidents.

Funding Statement. This research was funded by Outstanding Young Backbone Teacher Project of Jiangsu University “Qinglan Project” (Su Teacher [2021] No. 11).

Conflicts of Interest The authors declare that they have no conflicts of interest to report regarding the present study.

References

1. Jixian, L., Qing, Y., Ying, J.: Study on the correlation between drivers' blood alcohol concentration (BAC) and traffic accidents. *Mod. Traffic Technol.* **05**, 63–65 (2007)
2. Jia, K.Q., Fleiter, J., King, M., Sheehan, M., Ma, W.J., et al.: Alcohol-related driving in China: countermeasure implications of research conducted in two cities. *Accid. Anal. Prev.* **95**, 305–520 (2016)
3. Xinyue, Z., Yingqiong, M., Song, C.: Current status of development research on in-vehicle drink-driving monitoring. *Equip. Manuf. Technol.* **06**, 118–123 (2021)

4. Yang, K., Liu, Y., Zeng, Y.N.: Implementation of drink driving detection and control system. *J. Tianjin Agric. College* **24**(3), 85–87 (2017)
5. Boni, S., Xiyao, H.: Exploring the teaching of Internet of things application system design course. *Comput. Knowl. Technol.* **14**(11), 140–142 (2018)
6. Chen, K., Zhang, Z.C., Luo, X., Wang, J.R.: Pre-detection system for drink driving based on Internet of Things. *Sci. Technol. Perspect.* **21**, 116–118 (2021)
7. Meihua, L.: Design and implementation of a microcontroller-based vehicle alcohol content self-test system. *Mod. Ind. Econ. Inf.* **11**(10), 58–59 (2021)
8. Tao, W.: Trial analysis of breath alcohol detector wireless networking system. *Comput. Prog. Skills Mainten.* **05**, 57–58 (2021)
9. Jing, S.: Design of a microcontroller-based alcohol concentration detector. *J. Tonghua Normal College* **37**(06), 4–6 (2016)
10. Haihong, C.: A design of a car anti-drink driving monitoring and alarm system. *Autom. Instrum.* **07**, 233–234 (2016)
11. Weigang, R.: Design of gas alcohol concentration detection alarm. *Agric. Netw. Inf.* **10**, 24–26 (2011)
12. Xiaoying, L.: Design of an alcohol detection system based on MQ-3. *Sci. Technol. Perspect.* **21**, 31–32 (2019)



Video Encryption Transmission in GCM Mode Based on SM4 Algorithm

Yiting Zhou, Jian Zhang^(✉), and Lin Liu

College of Computer Science and Technology, Hengyang Normal University,
Hengyang 421002, China
zhangjian2100@126.com

Abstract. The leakage of Tesla vehicle camera video and image data seriously infringes on users' confidential information and personal privacy. Therefore, the security, reliability and privacy of video information in cameras have become one of the issues that all sectors of society pay more and more attention to, researchers mainly use AES encryption algorithm to encrypt video data. This paper takes the secure transmission of camera video data as the research object, and encrypts the original camera data by using Base64 coding and SM4 encryption algorithm, which can ensure the security and privacy of information data. The study compares six encryption modes of the SM4 algorithm and selects the GCM mode, which is more efficient and provides authentication functions. The encryption effect of the scheme was tested by using the microprocessor STM32F407 and OV2640 cameras, and the results showed that the encrypted transmission of video data and real-time decryption and playback could be completed, and the client video frame rate could reach 15fps, which effectively protected the user's video privacy.

Keywords: SM4 · GCM mode · Video · Encryp

1 Introduction

With the growth of national economy and the improvement of people's living standards, video has become one of the carriers of information dissemination in contemporary society. At present, most videos are stored and transmitted in plain text, which has a large security risk of information leakage [1]. However, not all videos can be shared with everyone. Therefore, in order to protect the information carried in the video from being stolen by criminals and protect personal privacy information, people's demand for video data encryption protection is becoming more and more urgent.

The encryption algorithms DES and AES spread and obfuscate the image data. It is converted into irregular and chaotic information, making it show the characteristics of white noise, thus completing the protection of image data [2]. Classical cryptographic algorithms such as DES and AES have various working modes such as ECB, CBC, CFB and OFB, among which CBC mode has higher security and encryption efficiency [3]. However, CBC mode does not guarantee the integrity of picture data in network transmission. The GCM working mode of the cryptographic algorithm can complete

the encryption operation and authentication operation at the same time, ensuring the security and integrity of the data [4]. SM4 encryption algorithm is a group symmetric cryptographic algorithm designed by Chinese scientists, which can be used for video data encryption/decryption operations to ensure the confidentiality of video data. Moreover, SM4 algorithm can support GCM working mode. Therefore, this paper chooses SM4 algorithm to encrypt and protect video data. The researchers also found that the encryption algorithm combined with other information processing techniques is conducive to the secure transmission of video data. For example, the combination of DES encryption algorithm and information hiding technology can not only complete the transformation of image data, but also change the statistical characteristics of data, which has higher security [5]. In addition, the Base64 encoding of video data before encryption can make video data more reliable in network transmission [6, 7]. Aiming at the security problem of video data in network transmission. This paper encodes video data into a unified data encoding format using Base64, and then encrypts it in GCM mode of SM4 encryption algorithm to ensure the security and reliability of data in network transmission.

2 System Design

The system is composed of STM32F407 microprocessor, OV2640 HD camera, router and PC, as shown in Fig. 1. In order to prevent attackers from stealing video data, the system implements Base64 encoding and SM4 encryption on the video data collected by the camera. The encrypted video information is transmitted to a PC over the network. Then, the client software on the PC obtains the encrypted video data, decodes the encrypted video data and plays it back in real time. The system can provide reliable security for video information captured by cameras with privacy and confidentiality.

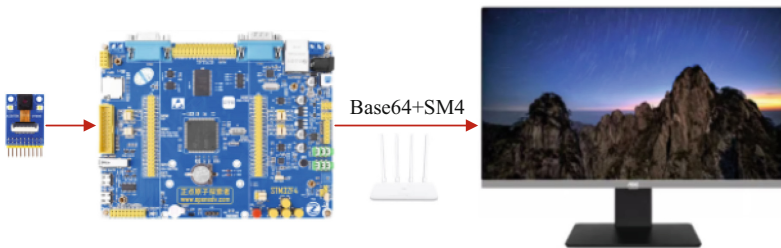


Fig. 1. The overall structure of the system.

3 Video Encryption Transmission Principle

3.1 Base64 Encoding

Base64 encoding uses 64 printable characters “A-Z”, “a-z”, “0-9”, “+”, “/” to represent binary data. It is an encoding that converts binary information data into printable ASCII characters. This encoding method is widely used in many aspects such as network transmission, data storage and data encryption. For example, MIME, SMTP, HTTP and other

protocols all use Base64 encoding for data transmission and storage. Base64 encoded data has a certain confidentiality, after the data encoded, it is difficult to be directly identified and understood, to ensure the privacy and security of the data. Moreover, the encoding and decoding of Base64 are relatively fast, and can be converted between various programming languages, so that the data is interactive and portable.

Base64 encoding can be divided into the following five steps:

- (1) Converts each byte of a string to its corresponding ASCII value against an ASCII table.
- (2) After converting the ASCII value obtained in the first step into binary data, determine whether the bits of binary data can be evenly divided by 6. If it is not divisible by 6, 0 is added to the lower part of the binary data.
- (3) Then divide the binary data into 6 bits, each 4 items into a group. If there are less than 4 items, fill the lower part with “ = ”.
- (4) Add two zeros in front of each item so that each item expands from 6 bits to 8 bits. Converts 8-bit binary numbers to decimal numbers, where the filled “ = ” does not need to be converted.
- (5) According to the obtained decimal number, find the corresponding encoding against the Base64 encoding table, where “ = ” is reserved.

Taking “SM4” as an example, the Base64 encoding example is shown in Table 1.

Table 1. Base64 encoding of “SM4”

Character	S	M	4	
ASCII value	83	77	52	
Binary	01010011	01001101	00110100	
Split into 6 bits	010100	110100	110100	110100
Expand to 8 bits	00010111	00110100	00110100	00110100
Base64 encoding	U	0	0	0

3.2 SM4 Encryption Algorithm

SM4 is a block cipher algorithm released by the National Cryptography Administration of China in 2012. It is commonly used in wireless Internet encryption and other fields. The block length of the SM4 cipher algorithm is 128 bits, that is, 16 bytes, and the key length is the same as its block length, which is also 128 bits. The SM4 encryption algorithm uses 32 rounds of operations. Each round of operation includes S-box substitution and synthetic substitution, nonlinear transformation and linear transformation. SM4 cryptographic algorithm repeatedly uses the substitution function with obfuscation function and the substitution function with diffusion function to process the plaintext data and realize the data encryption. Its decryption step is basically the same as the encryption step, only

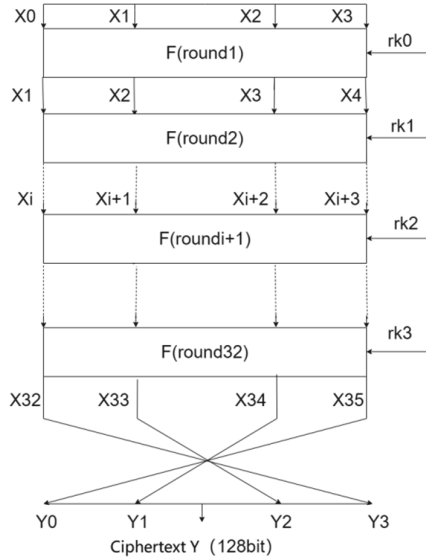


Fig. 2. The encryption process of the SM4 algorithm.

need to reverse the use order of the round key, can realize the decryption operation of the ciphertext.

The block length of the SM4 algorithm is 16 bytes, and the input is the plaintext of four words (X_0, X_1, X_2, X_3), where X_i is a word and the length is 4 bytes. After encryption, the output is a four words ciphertext (Y_0, Y_1, Y_2, Y_3). As shown in Fig. 2, the entire encryption process is divided into two steps. First, we need to perform 32 rounds of iterations on the plaintext. Each iteration involves a round function F , a synthetic permutation T , a nonlinear transformation τ , and a linear transformation L . Then, a simple reverse order transformation is performed to reverse order the last four words ($X_{32}, X_{33}, X_{34}, X_{35}$), and finally get the ciphertext. The SM4 encryption algorithm requires a round key for each round operation, so the total number of round keys required by the SM4 encryption algorithm is 32. The round key required for 32 rounds of operations is generated by key extension.

3.3 The GCM Mode

The GCM mode is a working mode of symmetric encryption algorithm block cipher, which is an advanced mode derived from MAC combination. Encryption mode, authentication mode and authentication encryption mode all belong to the block cipher working mode. The GCM mode is one of the authentication modes that belongs to the block cipher working mode, which uses a block size of 128bit. The GCM mode is very suitable for high-speed communication channels and is widely used in different standards. The GCM mode encryption process of SM4 algorithm is shown in Fig. 3.

The GCM encryption mode is designed based on parallelization, which can provide us with high throughput, low cost and low latency encryption functions. The essence

is that messages are encrypted in a variant counter mode. GHASH and GCTR are two functions that are often used in the GCM pattern. Assuming that P is plaintext, Key is initial key, IV is initial vector, and F is additional information, the encryption steps of GCM mode are as follows:

- (1) P is divided into P_1, P_2, \dots, P_n , and the packet length is 128 bits;
- (2) Generate accumulation counters $c_0, c_1, c_2, \dots, c_n$, and calculate a key named H from the key;
- (3) Operate IV and c_0 (join, add, XOR, etc.) to obtain the IV_{c_0} , and encrypt the IV_{c_0} with the key to obtain IVC_0 ;
- (4) Operate IV and c_1 (join, add, XOR, etc.) to obtain the IV_{c_1} , encrypt the IV_{c_1} with the Key to obtain IVC_1 , XOR IVC_1 and P_1 to obtain C_1 , use the key H to calculate F_1 by the additional message F through the GMAC algorithm, and F_1 and C_1 to OR to obtain FC_1 ;
- (5) Operate IV and c_2 (join, add, XOR, etc.) to obtain IV_{c_2} , encrypt IV_{c_2} with Key to obtain IVC_2 , XOR IVC_2 and P_2 to obtain C_2 , and use Key H to calculate F_2 by GMAC algorithm for additional messages FC_1 , and F_2 and C_2 to OR to obtain FC_2 ;
- (6) Repeat step (5) until IV and c_{n-1} are operated (join, add, XOR, etc.) to obtain $IV_{c_{n-1}}$, IVC_{n-1} and P_{n-1} are XOR operations to obtain C_{n-1} , and F_{n-1} is calculated F_{n-1} by the GMAC algorithm through the GMAC algorithm with key H, and F_{n-1} is ORED with C_{n-1} to obtain FC_{n-1} ;
- (7) Calculate IV and c_n (join, add, XOR, etc.) to obtain the IV_{c_n} , encrypt the IV_{c_n} with Key to obtain IVC_n , XOR the IVC_n and P_n to obtain C_n , and calculate F_n by the additional message FC_{n-1} through the GMAC algorithm with the key H, and F_n and C_n OR to obtain FC_n ;
- (8) Splicing C_1, C_2, \dots, C_n to obtain ciphertext C, using key H through GMAC algorithm combined FC_n and IVC_0 to finally calculate MAC.

4 System Test

SM4 encryption algorithm has 6 modes, namely ECB, CBC, CFB, OFB, CTR, GCM. This paper explores the encryption efficiency of different modes under SM4 algorithm and compares the effect of image encryption under each mode comprehensively. We selected Lena images with the size of $512 * 512$, the image format was BMP, the test platform was an ordinary PC, and the software running environment was Windows 10. The time and efficiency of SM4 algorithm's 6 modes of image encryption are shown in Table 2. As can be seen from Table 2, there is little difference in the time taken by the six modes of SM4 algorithm to encrypt images. However, GCM mode can complete the encryption operation and authentication operation at the same time, which is more suitable for the encryption of video data in the process of network transmission.

Since the video data consists of one frame image after another, the SM4 encryption and decryption function of the image data is tested separately in this paper. We select $512 * 512$ Lena image for encryption and decryption test in GCM mode of SM4 encryption algorithm. In this document, the selected key is "1234567891234567" and IV is "ccb5570ea53292e3". The effect of the original image and the encrypted image is

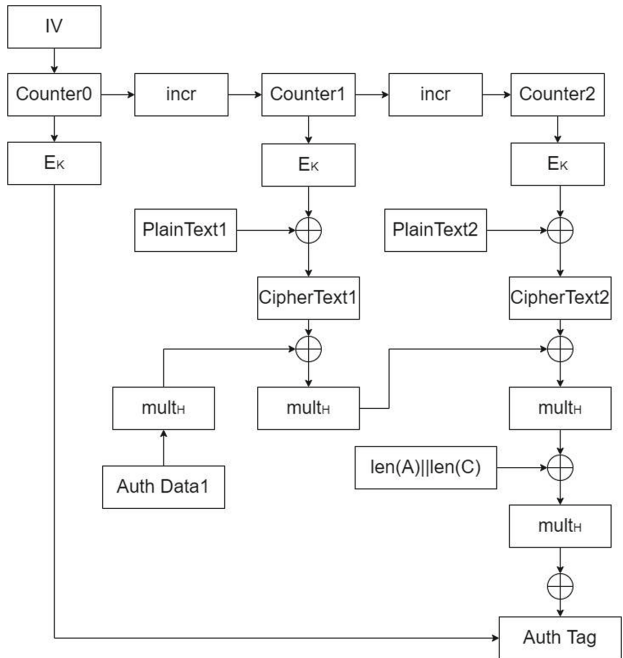


Fig. 3. SM4 encryption process in GCM mode.

Table 2. Speed and efficiency under 6 modes of SM4.

Operating mode	Time(s)	Efficiency (pix/s)	Operating mode	Time(s)	Efficiency (pix/s)
ECB	0.019	13797052.63	OFB	0.017	15420235.29
CBC	0.020	13107200.00	CTR	0.021	12483047.62
CFB	0.017	15420235.29	GCM	0.022	11915636.36

shown in Fig. 4. Figure 4a is the original image of Lena, and Fig. 4b is the image after Lena is encrypted. It is obvious that effective information can not be obtained from the encrypted image, which can effectively protect the user’s privacy and data security.

Finally, we use microprocessor STM32F407 and OV2640 camera to test the function of the whole system, as shown in Fig. 5. STM32F407 controls the OV2640 camera to output JPEG images with a resolution of 320 * 240. The original image is transmitted over the network after Base64 encoding and SM4 encryption. The client software of the PC receives the ciphertext data and decrypts and plays it in real time. The video frame rate can reach 15 fps, and the effect is good.

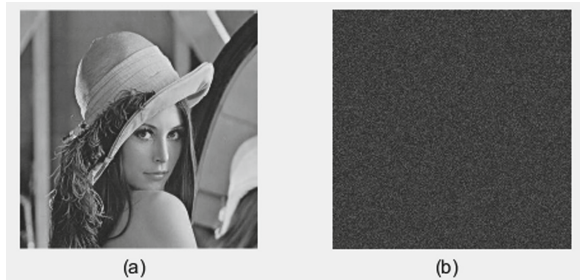


Fig. 4. Lena's original image and the encrypted image.

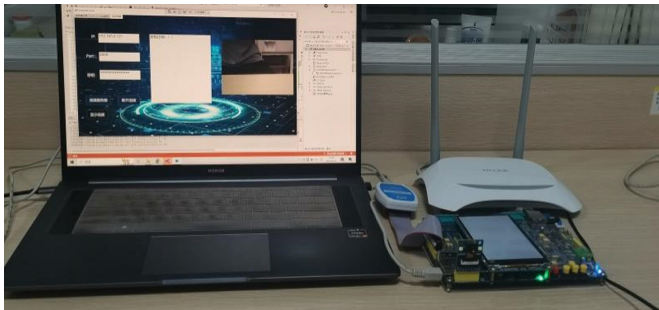


Fig. 5. Encrypt the video for network transmission and decryption before playing.

5 Conclusion

Aiming at the problem of information leakage of video data, this paper proposes a network transmission scheme of SM4 algorithm to encrypt video data. The scheme combines SM4 cryptographic algorithm and Base64 encoding to encrypt the original data, ensure the safe and reliable transmission of video data in the network, and protect the user's privacy data. In addition, we tested the efficiency of SM4 algorithm's 6 encryption modes to encrypt image data. The experimental results show that the six encryption modes of SM4 algorithm have little difference in the efficiency of image encryption. Because GCM mode can not only encrypt data, but also realize information authentication. Considering security and efficiency, we choose the GCM encryption mode of SM4 algorithm. Finally, we use the microprocessor STM32F407 and OV2640 camera to build a test platform. We have completed the test of encrypted video data for network transmission and client decryption data for real-time video playback. The client must enter the correct key to play the video properly. Otherwise, garbled characters will be displayed. Moreover, the video frame rate of the client can reach 15fps, which provides a solution for the safe transmission of video data.

Acknowledgements. This research is supported by the Scientific Research Fund of Hunan Provincial Education Department No. 19C0278, Double First-Class University Project of Hunan Province (Xiangjiaotong [2018] 469), Hunan Province Special Funds of Central Government for Guiding

Local Science and Technology Development No.2018CT5001, Hunan Provincial Natural Science Foundation of China with Grant No.2019JJ60004, Subject group construction project of Hengyang Normal University No.18XKQ02, Scientific Research Fund of Hunan Provincial Education Department No.18C0678, "the 14th Five-Year Plan" Key Disciplines and Application-oriented Special Disciplines of Hunan Province(Xiangjiaotong [2022] 351), College Students' Innovation and Entrepreneurship Training Program of Hunan Province (Xiangjiaotong [2022] 106) No.cxcy2022022.

References

1. Lixin, H., Bin, G.: Chaotic image encryption using double scrambling of pixel value and bit. *J. Jiamusi Univer. (Nat. Sci. Ed.)* **40**(06), 22–25+32 (2022)
2. Zhenjiao, C., Ze, H., Menghua, Z.: Research on digital image encryption based on AES in CBC mode. *Electron. Des. Eng.* **28**(19), 17–21 (2020)
3. Abhiram, K., Pulkit, S., Abhimanyu Kumar, P.K., Bibhudendra, A.: High-throughput and area-efficient architectures for image encryption using PRINCE cipher. *Integration* **90** (2023)
4. Jiaqi, Z., Bin, L., Qinglei, Z., Xiaojie, C.: Implementation of FPGA-based high-performance and scalable SM4-GCM algorithm. *Comput. Sci.* **49**(10), 74–82 (2022)
5. Fan, Z., Haiyang, D., Dingwu, Q., Guangya, M.: Image encryption domain information hiding based on block cipher. *J. Beijing Instit. Graphic Commun.* **31**(03), 1–7 (2023)
6. Jingjing, C., Fucheng, Y.: An image encryption algorithm based on SM4 and Base64. *J. Phys. Conf. Ser.* **1812**(1) (2021)
7. Yi, Z.: Image encryption algorithm mixed with Base64 and improved IDEA. *J. Zhejiang Wanli Univer.* **35**(05), 91–96 (2022)



Target Spatial Positioning System Based on Dual Cameras

Yaqi Sun, Peng Tang^(✉), Jiayi Bu, and Mugang Lin

College of Computer Science and Technology, Hengyang Normal University,
Hengyang 421008, Hunan, People's Republic of China
15115952633@163.com

Abstract. With the rapid development of computer graphics, binocular stereo vision technology has been widely used in robot navigation, autonomous driving, medicine and other fields. This paper focuses on the research and implementation of binocular positioning system using object tracking and binocular localization technology. Firstly, in order to obtain the image information of the target, a target tracking algorithm based on KCF kernel correlation filtering is used to track the target object. Then, OpenCV-based binocular positioning is applied to calculate the three-dimensional spatial coordinates of the target including camera calibration, stereo rectification, stereo matching and depth map calculation. Finally, this paper discusses practical applications and possible future research directions for binocular localization technology.

Keywords: Python programming language · OpenCv · KCF kernel correlation filtering · Binocular positioning system

1 Introduction

In recent years, the development of binocular vision has been increasingly rapid, providing people with more and more convenience in their daily lives. Binocular vision has made tremendous progress in various related fields such as military, medical, and security. In simple terms, binocular vision uses two cameras to work simultaneously and balance each other out. The process involves analyzing and processing the obtained image information to form a stereoscopic vision which greatly improves the degree of automation [1]. From classic tracking algorithms such as Meanshift, particle filtering, KCF kernel correlation filtering to research on tracking algorithms based on detection and recognition combined with deep learning applied to target tracking [2], these applications of target tracking in binocular vision can be combined with target positioning technology to solve practical problems while promoting the development, integration and innovation of computer vision. For example, in a vacuum environment or for underwater modeling using binocular vision techniques; highway vehicle speed measurement or distance measurement [3].

2 Related Works

This design mainly consists of target tracking and binocular positioning. Firstly, a binocular camera is used to obtain left and right images containing the target, and then the position information of the target is obtained through target tracking. Due to hardware reasons, images directly captured by cameras will have various distortions, so stereo calibration is needed to eliminate distortion. Here we use Professor Zhang Zhengyou's chessboard calibration method, which has simple operation and high accuracy, and is often applied in image correction processing for camera shooting. The selection of stereo matching algorithm has a direct impact on the accuracy of disparity map in images. In this paper, a semi-global matching algorithm between local matching and global matching is used. The depth map is an image where each pixel value represents the distance from the camera to the surface of objects in the scene. Depth maps are usually used to calculate positions and shapes of objects in 3D scenes by observing scenes with two cameras simultaneously and calculating depth by measuring their disparities [4].

3 Based on KCF Kernel Correlation Filtering for Object Tracking

This design uses the Kernelized Correlation Filter (KCF) algorithm, which is a target tracking algorithm based on kernel methods. It can achieve efficient real-time object tracking and has been widely used in practical scenarios. The algorithm trains a linear filter using obtained sample information and utilizes the Discrete Fourier Transform (DFT) acceleration algorithm for computation, making it highly efficient for real-time calculations. It can be used to search for targets in test frames [5].

3.1 Extracting Target Template Features

When performing target tracking, the first step is to obtain the template information of the target in the initial frame. We manually select the initial region of interest by boxing around the object and expand it 1.5 times to generate a target template T for subsequent tracking. The candidate region has the same size as the target template. After obtaining the target template, we can use feature mapping to transform it from spatial domain to frequency domain [6]. In frequency domain, features of templates are easier to analyze, which improves both speed and accuracy of template matching.

The mapping process introduces the Hanning window function for windowing, which can effectively reduce spectral leakage and improve spectral resolution [7]. The formula for the Hanning window is as follows:

$$w(n) = 0.5 * (1 - \cos(2\pi n / (N - 1))), 0 \leq n \leq N - 1 \quad (1)$$

$$T_w = T \cdot W_{hann} \quad (2)$$

$w(n)$ in the formula represents the Hann window coefficient at position n , N represents the length of the window function, and T_w represents the matrix obtained after applying the windowing operation.

Then perform discrete Fourier transform to convert the signal from time domain to frequency domain, obtaining its representation in the frequency domain for subsequent feature mapping and correlation filtering calculations.

$$T_f = DFT(T_w) \quad (3)$$

The DFT in Formula (3) represents the discrete fourier transform [8].

Performing the same operation on candidate regions yields I_f . Multiplying each element of I_f and T_f results in a feature map.

$$M_f = T_f \cdot I_f \quad (4)$$

3.2 Calculate Response Value

Matching the features of the target template and candidate regions for similarity can generate a response map. The peak values in the response map indicate possible locations of the target in the candidate regions, which is used for position prediction.

The formula for calculating the response value is as follows:

$$R = IDFT(H \odot I_f) \quad (5)$$

The IDFT in Formula (5) represents the inverse discrete Fourier transform, H represents the corresponding filter, I_f represents the feature mapping of the candidate region. The response value is obtained by element-wise multiplication of H and I_f followed by an inverse discrete Fourier transform.

3.3 Update Template

During actual tracking, the appearance of the target object will continuously change, so it is necessary to update the target template to adapt to these changes. Firstly, a learning rate is assigned to control the degree of target updating. Then, a weighted average is taken between the feature maps of the current candidate region and those of the old target template feature map in order to obtain a new target template feature map.

$$T_f^{(new)} = (1 - learning_rate) \cdot T_f^{(old)} + learning_rate \cdot I_f \quad (6)$$

$T_f^{(old)}$ is the old target template feature mapping, and I_f is the feature mapping of the current candidate region. By weighted averaging, the new target template can be matched with the candidate region's features while retaining previous target information.

Convert the new target template feature mapping back to the time domain to obtain the updated target template. The formula for calculating the updated target template is as follows.

$$T^{(new)} = IDFT(T_f^{(new)}) \quad (7)$$

Update the target template before calculating the response value and predicting the position of the target.

4 Dual-Eye Spatial Positioning Algorithm

4.1 Lens Distortion

Due to industrial production, cameras may produce lens distortion to a greater or lesser extent. Lens distortion refers to a phenomenon in the optical imaging process where the quality of the image is not ideal due to refraction or reflection of light when passing through optical components such as lenses or mirrors. In practical applications, distortion can cause problems such as image distortion and warping, affecting the accuracy and quality of imaging. Generally speaking, lens distortion can usually be divided into two types: radial distortion and tangential distortion.

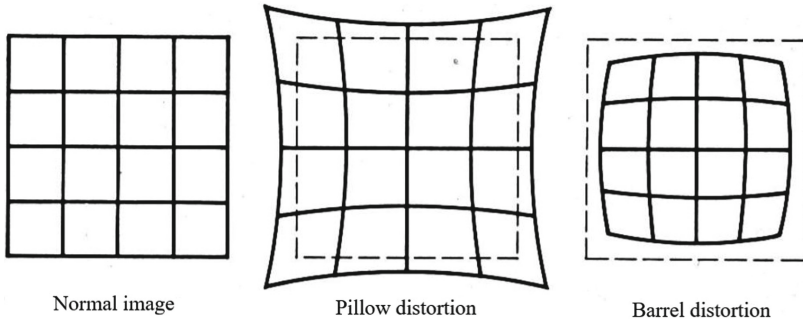


Fig. 1. Radial distortion comparison chart

As shown in Fig. 1, radial distortion is mainly manifested as a curved deformation appearing at the center and edge positions of the image. This is usually caused by the lens shape not being perfectly spherical. Because the refractive index of the lens to light is not uniform, different positions of light passing through the lens will result in different imaging positions. Radial distortion can produce two types which can be understood as barrel-shaped and pillow-shaped compared with normal images. As shown in the figure, barrel distortion will make the central part of an image relatively smaller while making its edges relatively larger, presenting a barrel-like shape for the entire image. Pillow distortion makes central part relatively larger while making its edges relatively smaller, presenting a pillow-like shape for entire image. Radial distortion can be eliminated by formulae.

$$[X_c y_c] = [X_d y_d] + [k_1 r^2 + k_2 r^4 + k_3 r^6 k_1 r^2 + k_2 r^4 + k_3 r^6] \quad (8)$$

In Formula (8), $(X_c y_c)$ represents the normal coordinates of the image after distortion correction, while $(X_d y_d)$ represents the original coordinates of the point with radial distortion. r is the distance from that point to the center of the image. k_1 , k_2 , and k_3 are three parameters in the model for correcting radial distortion.

The reason for tangential distortion is that the lens and image plane are not parallel, which causes deflection of light passing through the lens and leads to distortion. In images with tangential distortion, straight lines appear curved, presenting a form of

arc or S-shaped curve. This non-linear form has a significant impact on the use of cameras, reducing measurement or detection accuracy. The elimination of tangential distortion usually requires coordinate transformation of pixels in the image. We can introduce an additional transformation parameter between the lens and image plane to convert points in camera coordinates to distorted-corrected image coordinates using the following formula:

$$x_c = x_d + (2p_1y_d + p_2(r^2 + 2x_d^2)) \quad (9)$$

$$y_c = y_d + (p_1(r^2 + 2y_d^2) + 2p_2x_dy_d) \quad (10)$$

In the formula, (x_c, y_c) represents the normal coordinates of the image after distortion correction; (x_d, y_d) represents the original coordinates of radial distortion point; r is the distance from that point to the center of the image. The obtained p_1 and p_2 are parameters for correcting tangential distortion. A distortion correction model is constructed in a computer using five parameters (K1, K2, K3, P1, P2).

4.2 Stereo Vision Calculation

In binocular stereoscopic vision, ideally the two cameras should be perfectly parallel and at the same height. As shown in Fig. 2, O_{cL}, O_{cR} are the optical centers of the left and right cameras respectively, with $B = O_{cL}O_{cR}$ being the baseline length between them. Assuming there is a point $P(x, y, z)$ whose projections on the left and right views are $P_l(x_l, y_l), P_r(x_r, y_r)$, then the distance from camera center plane is focal length f .

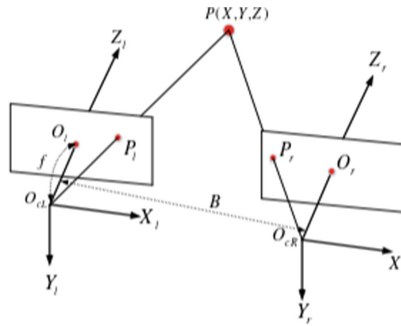


Fig. 2. Stereo disparity calculation model

The depth of Z can be calculated by the following formula:

$$\frac{B - (x_l - x_r)}{Z - f} = \frac{B}{Z} \quad (11)$$

$$Z = \frac{fB}{x_l - x_r} = \frac{fB}{d} \quad (12)$$

4.3 Polar Constraint

The purpose of stereo matching is to find the corresponding point (the same physical point in the world coordinate system) for each pixel in the left image in the right image, so that disparity can be calculated: (which are the column coordinates of two corresponding points in the images). Since under non-rational conditions, the imaging planes of two cameras are not completely parallel, this increases the computational complexity of stereo matching and easily leads to matching errors. Therefore, it is necessary to adopt epipolar constraint before matching.

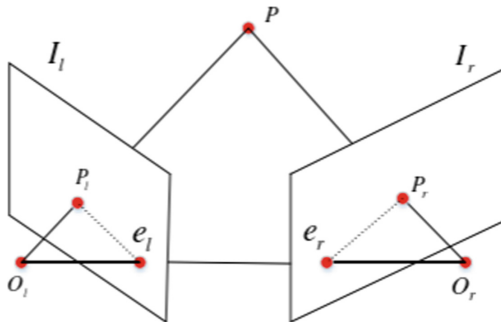


Fig. 3. Polar constraint diagram

As shown in Fig. 3, O_l and O_r are the optical centers of the camera, P is the detected point, I_l and I_r are the imaging planes of the camera. The plane formed by $P O_l O_r$ is called the epipolar plane. P_l and P_r are matching points. $P_l e_l$ is the projection of $P_l O_l$ on the epipolar plane, which can be matched with point P_l on this line. Similarly, point P_r also projects onto this line at position $P_l e_l$. Therefore, many incorrect matching points can be eliminated along the epipolar line.

5 Experimental Results and Analysis

5.1 Calibration Data

This article uses Zhang Zhengyou's method of using a black and white checkerboard as a calibration reference. In order to improve the accuracy of calibration, the angle between the checkerboard surface and the camera imaging plane must be less than 45° , and images of the checkerboard at various angles must be taken. Since Matlab has built-in stereo camera image processing tools that can perform well in measuring camera data, here we use Matlab's Stereo Camera Calibrator toolbox for calibrating camera data measurement.

5.2 Coordinate Calculation

Using the SGBM object to calculate the disparity map, passing in the scaled left and right images as parameters, an image disparity map can be obtained. Finally,

divide the obtained disparity map by 16 to obtain a real disparity map. Call `cv2.reprojectImageTo3D()` with the disparity map and reprojection matrix as input parameters to obtain the world's three-dimensional coordinates of objects (Fig. 4).



Fig. 4. Depth map

5.3 Experimental Results

After selecting the target object, the system will complete the calculation of the three-dimensional coordinates of the center point of the object relative to the left camera reference system. The experiment has achieved real-time coordinate calculation and tracking (Fig. 5).

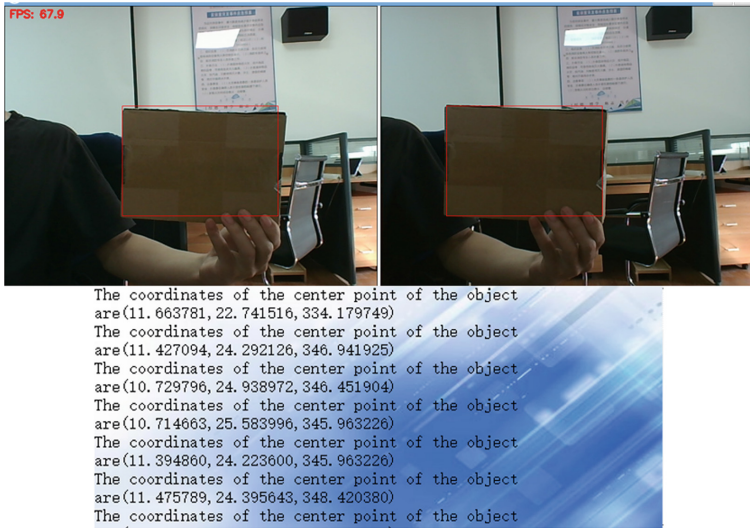


Fig. 5. Experimental results

6 Conclusion

As a hot topic in the field of binocular stereovision, binocular positioning has been widely applied in industries such as industrial manufacturing, robotics and autonomous driving. It can achieve high-precision positioning and tracking of targets, improve production efficiency and automation level, and has enormous market potential. This system uses target tracking based on KCF kernel correlation filtering and binocular positioning system to design a fusion system that realizes real-time measurement of spatial coordinates of targets while enhancing anti-interference ability against noise.

Acknowledgements. This work was supported by the National Natural Science Foundation of China (61772179), Hunan Provincial Natural Science Foundation of China (2020JJ4152, 2022JJ50016), and the Science and Technology Plan Project of Hunan Province (2016TP1020), Scientific Research Fund of Hunan Provincial Education Department (21B0649), the 14th Five-Year Plan Key Disciplines and Application-oriented Special Disciplines of Hunan Province (Xiangjiaotong [2022] 351), Postgraduate Scientific Research Innovation Project of Hunan Province (CX20221285), Foundation of Hengyang Normal University (KYZX21028), Industry University Research Innovation Foundation of Ministry of Education Science and Technology Development Center (2020QT09), and Science and Technology Innovation Project of Hengyang (No.202250045231).

References

1. Jinghui, Y., Dekang, L., Wanhe, D., et al.: Research on binocular ranging system based on image features. *J. Syst. Simul.* **34**(3), 624 (2022)

2. Xiang, H., Cheng, L., Wu, H., et al.: Mobile robot automatic aiming method based on binocular vision. In: 2021 40th Chinese Control Conference (CCC), pp. 4150–4156. IEEE (2021)
3. Sun, X., Jiang, Y., Ji, Y., et al.: Distance measurement system based on binocular stereo vision. In: IOP Conference Series: Earth and Environmental Science, vol. 252, no. 5, pp. 052051. IOP Publishing (2019)
4. Jiang, J., Liu, L., Fu, R., et al.: Non-horizontal binocular vision ranging method based on pixels. *Opt. Quant. Electron.* **52**, 1–10 (2020)
5. Fan, J., Yang, X., Lu, R., et al.: Long-term visual tracking algorithm for UAVs based on kernel correlation filtering and SURF features. *Vis. Comput.* **39**(1), 319–333 (2023)
6. Yang, X., Li, S., Yu, J., et al.: GF-KCF: aerial infrared target tracking algorithm based on kernel correlation filters under complex interference environment. *Infrared Phys. Technol.* **119**, 103958 (2021)
7. Yan, H., Xie, M., Wang, P., et al.: Kernel-correlated filtering target tracking algorithm based on multi-features fusion. *IEEE Access* **7**, 96079–96084 (2019)
8. Wu, D., Song, H., Fan, C.: Object tracking in satellite videos based on improved kernel correlation filter assisted by road information. *Remote Sens.* **14**(17), 4215 (2022)



Controller Architecture and Performance Optimization for Intensive Deployment Scenarios

Chuanming Zhu, Huiguang Chen, and Jingwen Li^(✉)

China Telecom Research Institute, Beijing, China
lijw21@chinatelecom.cn

Abstract. As the scale and complexity of the network increase, SDN controller in the intensive deployment scenario has problems in architecture and performance. Combined with the controller collection and control framework, the acquisition and control separation mode is designed by isolating the underlying protocols, and data collection and configuration delivery operations are performed on NE devices to improve the controller collection and control performance. Ensure that service delivery does not affect operation and maintenance; The controller acquisition and control architecture is optimized to ensure a balanced distribution of tasks within the framework and improve controller performance. Through key capability research and development, framework optimization and performance improvement, SDN controller technology is gradually mature, enabling intelligent operation of cloud network.

Keywords: Intensive deployment · SDN controller · SDN/NFV · Architecture optimization

1 Current Status and Problems of IP SDN Controller's Acquisition and Control Ability

IP SDN controller for IP network, based on the new network technology, through the NETCONF, SNMP, Telemetry, NETFLOW protocol intelligent collection control. By isolating the underlying protocols, the acquisition and control separation mode is designed to perform data collection and configuration delivery operations on NE devices, improving controller collection and control performance and ensuring that service delivery and operation, and maintenance do not affect each other. The controller acquisition and control architecture is optimized to ensure a balanced distribution of tasks within the framework and improve controller performance. Further optimize the acquisition and control capabilities to improve the overall controller performance, reliability, and stability to better cope with future intensive deployment scenarios.

SDN controller is the core capability of the new generation of cloud network operating systems. By optimizing the architecture and performance of the SDN controller and focusing on customers, the value of the controller is fully enhanced, and the operation

management capability for cross-domain, cross-vendor, and cross-professional services and networks is built, which is also the active exploration and practice of operators in the process of cloud network integration.

Although the NETCONF service layer of the IP SDN controller has the global connection pool capability, the underlying real connection does not distinguish between device configuration and NE data collection. In the intensive deployment scenario, the number of network elements is at least one order of magnitude higher than that in the privatized deployment. Frequent NE data collection blocks the delivery of normal service configurations and causes the upstream interconnection system to time out. Normal services are affected.

Currently, the controller collection module mainly includes NETCONF active pull collection, SNMP, Telemetry, and NETFLOW passive push collection. NETCONF collection is coarse and usually collected by NE function module. As a result, the CPU usage of routers in the collection period is too high, affecting the network processing capability of routers. Currently, only TeleDB is supported for collecting data stores. In intensive deployment scenarios, write bottlenecks may occur.

2 IP SDN Controller Key Technologies

2.1 SNMP Protocol

Simple Network Management Protocol (SNMP) is a standard network management protocol widely used on TCP/IP networks. SNMP provides a way to manage network elements (such as routers) from a central computer (i.e., a network management workstation) running network management software.

SNMP has the following operation modes:

- (1) The management workstation obtains network resource information through the GET, get-next, and GET-bulk operations.
- (2) The management workstation uses SET to set network resources.
- (3) The management agent reports traps and informs the management workstation so that the workstation can obtain the network status in a timely manner and the network administrator can take measures in a timely manner.

2.2 NETCONF Protocol

Network Configuration Protocol (NETCONF) is a network configuration and management protocol based on the Extensible Markup Language (XML). Communication between client and server is implemented using a simple RPC-based (Remote Procedure Call) mechanism.

NETCONF provides a way to remotely manage and monitor devices from a central computer (i.e., a network management workstation) running network management software. As the scale and complexity of networks increase, the traditional Simple Network Management Protocol (SNMP) cannot meet the requirements of complex network management, especially configuration management. In order to make up for the defects of SNMP, the NETCONF protocol came into being.

2.3 Telemetry Protocol

Telemetry is a network device monitoring technology that provides the ability to periodically sample statistics and status data within network devices. The traditional acquisition mechanism has some problems, such as poor real-time performance, low performance, no model definition, poor scalability, etc., which cannot meet the requirements of big data. Telemetry has the following advantages over traditional mechanisms:

By using pull mode to obtain device monitoring data, a large number of network nodes cannot be monitored, which limits network growth.

The sampling period accuracy of monitoring data is minute level. You can only increase the query frequency to improve the accuracy of data acquisition. However, this will cause high CPU utilization of network nodes and affect the normal functions of the device.

Because of the existence of network transmission delay, the monitored network node data is not accurate.

Therefore, in the face of large-scale and high-performance network monitoring requirements, users need a new network monitoring method. Telemetry technology can meet user requirements, support intelligent operation and maintenance systems to manage more devices, monitor data with higher accuracy and more real-time, and the monitoring process has less impact on device functions and performance. It provides the most important big data foundation for rapid network problem location and network quality optimization and converts network quality analysis into big data analysis. Strong support for intelligent operation and maintenance needs.

2.4 NETFLOW Protocol

NETFLOW technology is a statistical technology based on network traffic information. It can classify the communication traffic and resource usage in the network, and monitor and manage the network based on various services and resources. Because of the limitations of traditional traffic statistics, new technology is needed to better support the development of network services. NETFLOW technology comes into being. Data output through NETFLOW technology can be used for many purposes, network management and planning, business accounting and sub-department billing, ISP billing, data storage, and commercial data collection.

3 IP SDN Controller Optimization Scheme

It is planned to add a general tagging capability to virtual connections at the NETCONF service layer. Virtual connections and real connections use tag matching to optimize the device collection and device configuration connection allocation algorithms under the constraint of the global device connection number. In this way, live network service configurations are not affected when device collection operations peak. The maximum response time of service configuration can be increased from minutes to seconds when the peak value of the collection is expected (Fig. 1).

It is planned to separate configuration collection from performance status data collection. The former uses NETCONF and the latter uses lightweight Telemetry/NETFLOW to reduce the peak CPU usage from 90 to 70% in the collection period (Fig. 2).

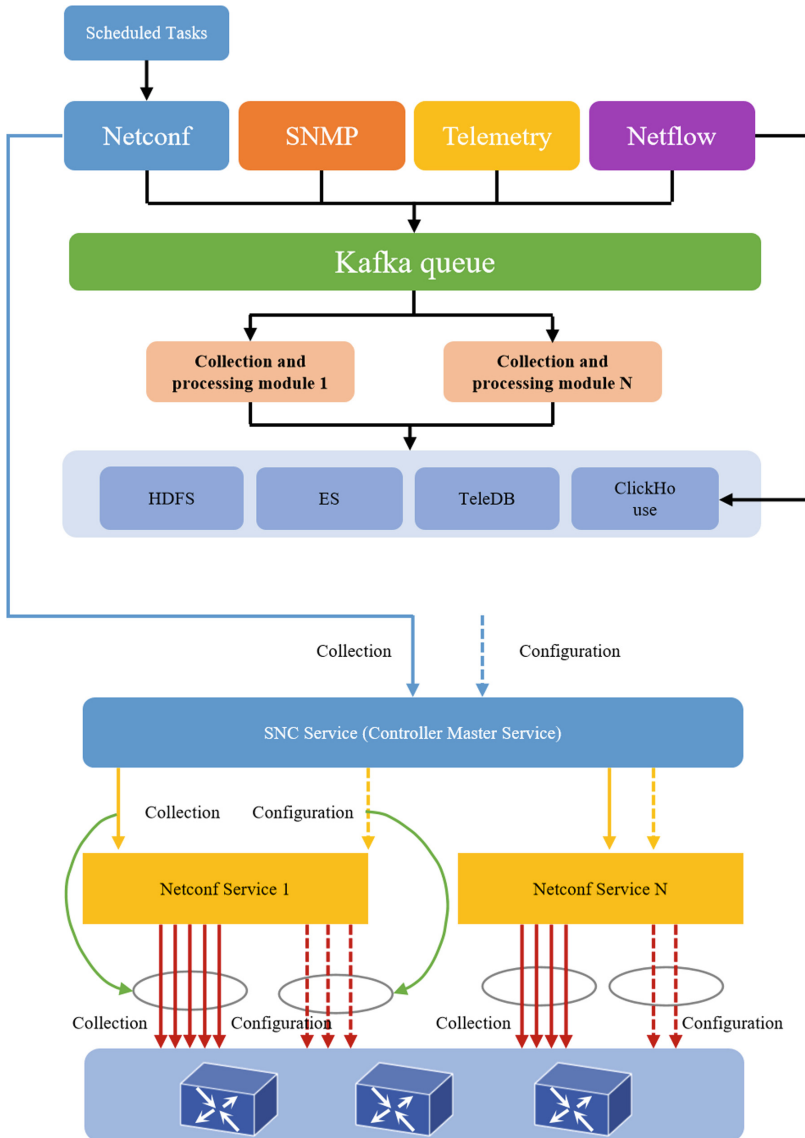


Fig. 1. The separation scheme of configuration collection and performance status data collection is implemented to reduce CPU utilization

4 IP SDN Controller Application

4.1 Configuration Data Delivery

Delivering NETCONF configuration data. NETCONF defines messages in XML format and uses the RPC mechanism to modify configuration information. In this way, the configuration information can be easily managed and interoperability between devices

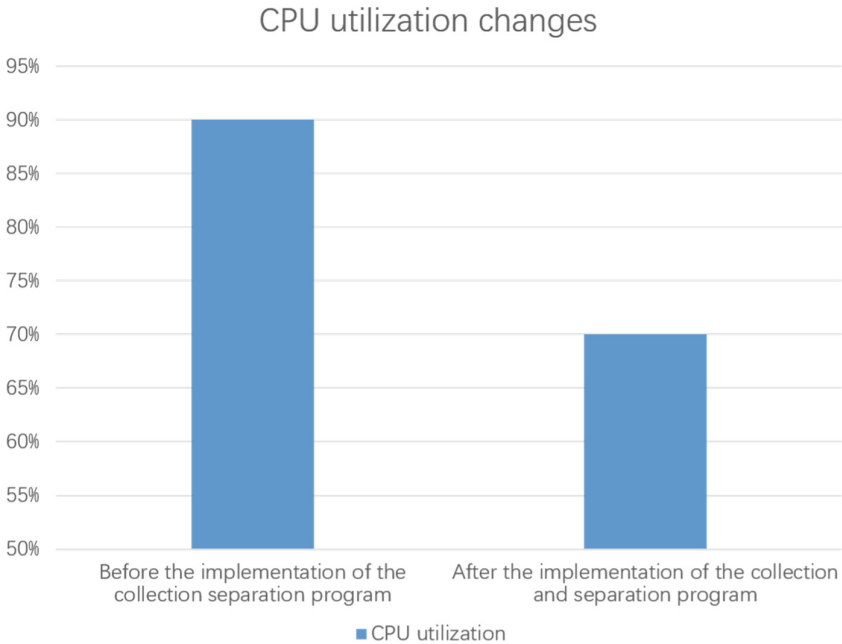


Fig. 2. Changes in CPU utilization before and after the separation of configuration collection and performance status data collection

from different manufacturers can be achieved. SDN control solves problems such as closed standards of heterogeneous vendors, difficult unification, and high operational complexity. NETCONF improves configuration efficiency and reduces network faults caused by manual configuration errors. NETCONF also provides security mechanisms such as authentication and authentication, ensuring the security of message transmission. The controller instantiates the network function model defined by YANG through the NETCONF protocol and obtains the corresponding data from the device or sends the corresponding data to the device for configuration. This module is based on the self-developed FAST YANG tool to complete YANG model compilation/code generation, model instantiation and verification, and interaction with device NETCONF protocol (including model and XML serialization/deserialization).

4.2 Performance Status Data Collection

Telemetry Collects performance data. Telemetry subscription means that the device as the client and the collector as the server connect to the collector for data collection and upload. After you configure the collection requirements, use the NE management micro-service to deliver static configurations of TWAMP and IFIT sampling tasks to devices through NETCONF, for example, to start the sampling tasks. The Telemetry micro-service subscribes to the device and sends the sampled data to the Telemetry micro-service process. The Telemetry micro-service pushes the received data to the corresponding Kafka Topic, enabling the data processing module that subscribes to

the Topic to receive Kafka messages. The data processing module calculates the link performance information such as delay, jitter, and packet loss rate based on the logical topology processed by IFIT, TWAMP, and other modules, and pushes messages to Kafka for other modules to use.

Monitoring and managing NETFLOW traffic. NETFLOW monitors and manages networks based on services and resources by collecting statistics on traffic and resource usage. You can configure a specified mode to sample service packets, create a NETFLOW flow based on the quintuple information, age the NETFLOW flow based on the specified mode, and output the NETFLOW flow based on the specified mode and packet version. The NETFLOW micro-service module pushes the received data to the corresponding Kafka topic so that the data processing module subscribed to the Topic receives the Kafka message. The data processing module parses information such as traffic and resource usage based on sampling and pushes messages to Kafka for other modules to use.

5 Conclusion

This paper proposes a framework based on the separation of acquisition and control of SDN controllers. By scheduling the acquisition module and configuration module, the acquisition module and control module schedule different protocols respectively to avoid the interaction between data acquisition and configuration delivery, and adopt multi-instance deployment mode to improve the overall performance of the controller. It provides a new way to improve the performance of SDN controllers for intensive deployment.

In the future, with the intensive deployment and application of SDN controllers, and the gradual optimization and improvement of architecture and performance, SDN controllers will be deployed more quickly and widely to meet complex and diverse service requirements and improve the level of network control.

References

1. Lv, H., Li, Q., Shen, G.: Belt network telemetry method review. *J. Software* 1–21 (2023)
2. Abdelaziz, A., Fong, A., Gani, A., Garba, U., Khan, S., Akhunzada, A.: Distributed controller clustering in software defined networks. *PLoS ONE* **12**(4), e0174715 (2017). <https://doi.org/10.1371/journal.pone.0174715>
3. Li, Z., Hu, H., Hu, H., Huang, B., Ge, J., Chang, V.: Security and energy-aware collaborative task offloading in D2D communication. *Future Gen. Comput. Syst.* **118**, 358–373 (2021)
4. Cui, Y., Hui, Zhang, H., Xu, H.: Network traffic statistics based on NetFlow technology. *Telecommun. Sci.* **6**, 62–64 (2003)
5. Xin, Z.: Design of a NetFlow flow analyzer. *Mod. Electron. Technol.* **21**, 80–83 (2006)
6. L.: Netflow technology principle and application. *J. Railway Commun. Sign.* **1**, 33–35 (2005)
7. Wang, Y., Ju, W., Cheng, Q.: Optimization of flow classification technology for large-scale high-speed network traffic analysis. *Commun. Inf. Technol.* **253**(05), 59–62 (2021)
8. Bjorklund, M.: RFC 6060: YANG—A data modeling language for the network configuration protocol (NETCONF). RFC Editor, USA (2010)
9. Li, Z., Hu, H., Hu, H., Huang, B., Ge, Chang, V.: Security and energy-aware collaborative task offloading in D2D communication. *Future Gen. Comput. Syst.* **118**, 358–373 (2021)



A Text Sentiment Classification Method Enhanced by Bi-GRU and Attention Mechanism

Dongdong Li^(✉), Xiaohou Shi, and Meiling Dai

China Telecom Corporation Research Institute Beijing, Beijing, China
{lidd4, daiml1}@chinatelecom.com

Abstract. Text sentiment analysis is a natural language processing technique designed to identify the emotional tendencies expressed in text. In recent years, this field has garnered significant attention and is widely used in practical applications. For example, sentiment analysis is employed for brand reputation management on social media, public opinion monitoring, and risk control in fields such as finance, medicine, and politics. Sentiment analysis is also utilized in tasks such as personalized recommendation and natural language generation. Despite the numerous methods and techniques proposed and applied in text sentiment analysis research, challenges and problems persist. During the sentiment classification process, text data exhibits problems such as uncertainty and semantic diversity, noise, and errors, leading to low accuracy and efficiency of sentiment analysis models. To enhance sentiment analysis accuracy and efficiency, this paper proposes an improved text sentiment classification method based on Bi-GRU and self-attention mechanism. The attention mechanism is initially fused with the update gate of the Bi-GRU gating unit to obtain important feature information in the text content. Subsequently, the Bi-GRU is followed by a self-attention mechanism to perform secondary screening on the text features, and the softmax function is applied to text vectors for sentiment classification, significantly enhancing the accuracy of sentiment classification. The proposed method is tested on the public dataset Yelp Dataset Challenge, and the experimental results indicate a considerable improvement in the accuracy of sentiment classification.

Keywords: Sentiment classification · Attention mechanism · Bi-GRU

1 Introduction

In recent years, significant progress has been made in sentiment analysis research. Deep learning methods have been widely applied in sentiment classification, including convolutional neural networks (CNNs), recurrent neural networks (RNNs), and attention mechanisms. For instance, Yoon Kim proposed a sentence-level sentiment classification approach based on CNNs [1]. This method transforms the text into a matrix and applies multiple convolution kernels to extract the feature representation. Pengfei Liu introduced a multi-task learning-based RNN method for text and sentiment classification [2], which optimizes multiple related tasks to enhance the model's ability to learn shared data characteristics. Zichao Yang proposed a hierarchical attention mechanism-based method for

text classification [3]. This method utilizes a two-level attention mechanism to learn text representation and better capture semantic information, thus improving sentiment classification performance. Richard Socher et al. proposed a semi-supervised recurrent autoencoder method for sentiment classification [4], which uses a recursive autoencoder to learn structural information and feature representation and semi-supervised learning to utilize unlabeled data. This approach has achieved promising results on sentiment classification tasks. Moreover, Bo Pang and Lillian Lee proposed a sentiment analysis method based on subjectivity summary [5], which separates the text into subjective and objective parts and summarizes the subjective part using the minimum cut algorithm for sentiment analysis. This method provides a significant idea for future sentiment analysis research.

This paper presents a novel Bi-GRU network model integrated with an attention update gate. The proposed model employs attention scores to regulate the update gate, thereby enhancing its performance. Moreover, the model is optimized and combined with a self-attention mechanism to boost the accuracy of sentiment classification. To mine information based on the similarity between words rather than their order, a self-attention mechanism is added after the Bi-GRU model. This approach avoids information loss for longer sentences during sentiment classification, and yields promising classification results.

1.1 Bi-GRU (Bidirectional Gated Recurrent Unit)

The development of Long Short-Term Memory (LSTM) [6] networks has led to the emergence of numerous network variants, including the widely adopted Gated Recurrent Unit (GRU) [7] network. GRUs have demonstrated comparable performance to LSTMs in addressing issues such as vanishing and exploding gradients, as well as capturing long-term dependencies.

Compared to LSTMs, the GRU network utilizes only two gate structures. The first gate combines the forget and input gates from LSTMs into a single update gate, denoted as z_t , which helps maintain a balance between input and forget operations. The second gate, referred to as the reset gate r_t , regulates the level of dependence on previous state information, with lower values indicating a reduced level of dependence.

The network structure diagram of GRU is illustrated in Fig. 1.

The calculation process of the recurrent unit in the GRU network can be outlined as follows: at time t , the input vector x_t and the hidden layer state h_{t-1} from the previous time step $t-1$ are taken as input. The reset gate and the update gate outputs, z_t and r_t , respectively, are computed using Eqs. (3)–(4). The candidate state, h'_t , is then updated using Eq. (5), and the hidden layer state, h_t , is updated using Eq. (6).

$$r_t = \sigma(W_{rx}x_t + W_{rh}h_{t-1} + b_r) \quad (1)$$

$$z_t = \sigma(W_{zx}x_t + W_{zh}h_{t-1} + b_z) \quad (2)$$

$$h'_t = \tanh(W_{hx}x_t + W_{hr}r_t h_{t-1} + b_h) \quad (3)$$

$$h_t = (1 - z_t)h_{t-1} + z_t h'_t \quad (4)$$

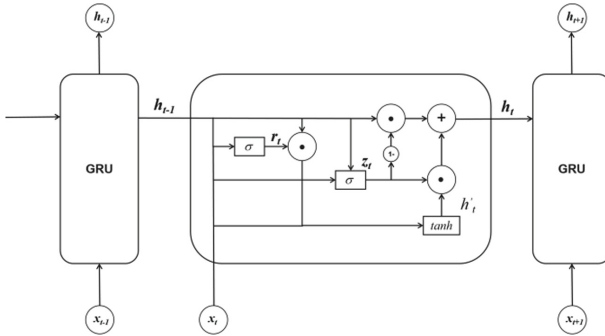


Fig. 1. GRU network structure diagram

In the formula, W_{rx} , W_{rh} , W_{zx} , W_{zh} , W_{hx} , and W_{hr} represent the weight matrix of the update gate, reset gate, and hidden layer, respectively, and b_r , b_z , and b_h are bias vectors.

The Bi-directional Gated Recurrent Unit (Bi-GRU) network comprises two GRU layers—the forward and the reverse layer. The forward propagation GRU calculates the sequence information of the current time step, while the backward propagation GRU reads the same sequence in reverse, introducing the reverse sequence information. The output layer of the network is interconnected with both layers of the GRU, with all neurons in the output layer incorporating both forward and reverse information during the network training process. Figure 3 depicts the specific architecture of the Bi-GRU network (Fig. 2).

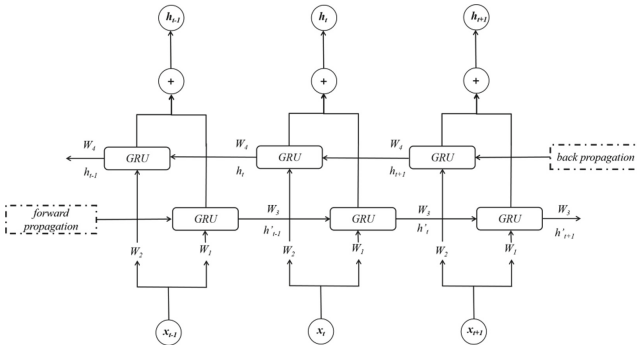


Fig. 2. Bi-GRU network structure diagram

The bidirectional recurrent network, as illustrated in Fig. 3, is constructed by combining two unidirectional recurrent networks. These networks share the same input and operate in opposing directions, with information flow proceeding in both directions.

Additionally, the two networks exhibit structural symmetry, independently performing computations using Eqs. (7) and (8), updating their states, generating outputs, and subsequently connecting the outputs in both directions according to Eq. (9).

$$h'_t = f(W_1x_t + W_3h'_t + b'_t) \quad (5)$$

$$h_t = f(W_2x_t + W_4h_{t-1} + b_t) \quad (6)$$

$$H_t = h'_t \oplus h_t \quad (7)$$

The formula presented includes the following variables: h'_t , h_t , x_t , and H_t . These variables respectively represent the state of the hidden layer for forward propagation, the state of the hidden layer for backpropagation, the input value of the input neuron, and the output value of the hidden layer state at the given moment. Additionally, h'_{t-1} and h_{t+1} represent the state of the forward propagation hidden layer at time $t-1$ and the back propagation hidden layer at time $t+1$, respectively. The activation function of the hidden layer is represented by f , while the vector splicing operation is denoted by the symbol \oplus . Furthermore, the variables b'_t and b_t respectively represent the bias vectors of the forward propagation hidden layer and the back propagation hidden layer. Finally, W_1 , W_2 , W_3 , and W_4 correspond to the weight matrix of different components.

2 Bi-GRU Based on Attention Mechanism

In this study, we propose a novel emotion classification model, Bi-GRU', which combines the BiGRU model and the Attention mechanism. The overall architecture of the model is illustrated in the Fig. 3, which can be divided into three main parts: text preprocessing, vectorization, and classifier. The first part, text preprocessing, involves preparing the input text data for further processing, including steps such as tokenization and stemming. In the second part, vectorization, the preprocessed text is transformed into numerical vectors, which can be effectively processed by the model. Finally, the classifier utilizes the Bi-GRU' architecture to classify the emotion expressed in the input text.

In the text preprocessing stage, the first step involves cleaning the text data by removing stop words and line breaks, unifying the case of English letters in the English data set, and serializing the data. Next, the processed data is vectorized using word2vector to convert the text data into a vector. Finally, the word vector is fed into the classifier for processing. In this stage, the BiGRU' model and the forced forward attention mechanism are used to learn the data and extract important features. The BiGRU' model filters the input information through the update gate and the reset gate, and extracts important features from longer input sequences. The attention mechanism is used to weight the key information in the input text, and assign different weight information to the words in the text to learn which words are more important, so that the model can better capture emotional information in classification tasks.

The GRU model uses the update gate to determine the influence degree of the output of the previous hidden layer on the output of the current hidden layer. However, traditional

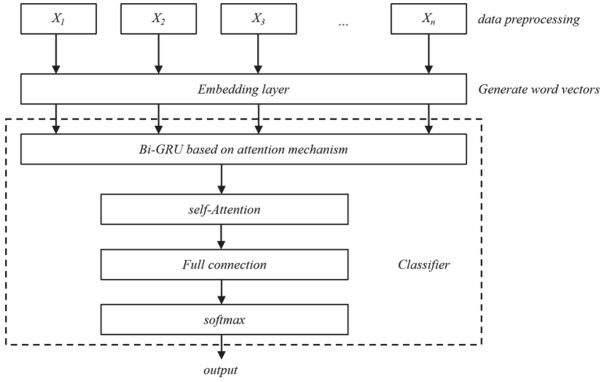


Fig. 3. Sentiment classification model architecture diagram

update gates mainly rely on historical information and newly received information, and may not effectively extract important information in longer input sequences. To address this issue, the attention mechanism is used to selectively focus on relevant input elements and improve the overall performance of the model. This paper proposes a sentiment classification model that combines the attention mechanism with Bi-GRU. To improve the ability of GRU to extract important feature information from text, an attention mechanism is added to the update gate of GRU. The attention score of the GRU update gate is calculated using the following formula:

$$u_i = \tanh(W_w x_i + b_w) \quad (8)$$

$$a_i = \text{soft max}(u_i) \quad (9)$$

In the above formula, W_w and b_w are the weight coefficients and offsets of the feature vectors, x_i is the currently input feature vector, and a_i is the attention score, which acts on the update gate in the GRU structure. Figure 5 is a structure diagram of the improved GRU model based on the attention mechanism (Fig. 4).

The calculation formula is as follows:

$$z_t = \sigma(w_r \cdot [h_{t-1}, x_t]) \quad (10)$$

$$z'_t = a_t * z_t \quad (11)$$

$$r_t = \sigma(w_r \cdot [h_{t-1}, x_t]) \quad (12)$$

$$\tilde{h}_t = \tanh(w_{\tilde{h}} \cdot [r_t * h_{t-1}, x_t]) \quad (13)$$

$$h'_t = (1 - z'_t) * h_{t-1} + z'_t * \tilde{h}_t \quad (14)$$

In the above formula, x_t represents the word vector of the t-th word segment, r_t is the reset gate, z_t is the original update gate of GRU, z'_t is the update gate with the

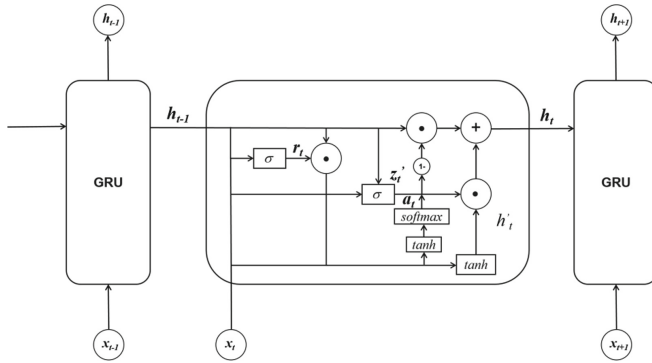


Fig. 4. Improved GRU structure diagram

attention mechanism added, h'_t and h_{t-1} are the hidden GRU state, a_t is the attention score in Formula (11), and σ is the sigmoid activation function. The enhanced update gate not only relies on the historical information of the previous moment and the newly received input information, but also on the attention score of the current information. The attention score reflects the importance of information and its impact on the current state. Information with higher attention scores are assigned larger weights, resulting in higher values for the update gate and are retained for further processing. Conversely, information with lower attention scores are assigned smaller weights, resulting in smaller values for the update gate and thus discarded. This mechanism improves the ability of the GRU model to extract essential information in the text and enhances its feature extraction ability (Fig. 5).

In this paper, the BiGRU' model is obtained by bidirectionalizing the GRU' model with the attention mechanism added to the update gate. BiGRU' is similar to the BiGRU model structure, as shown in Fig. 6.

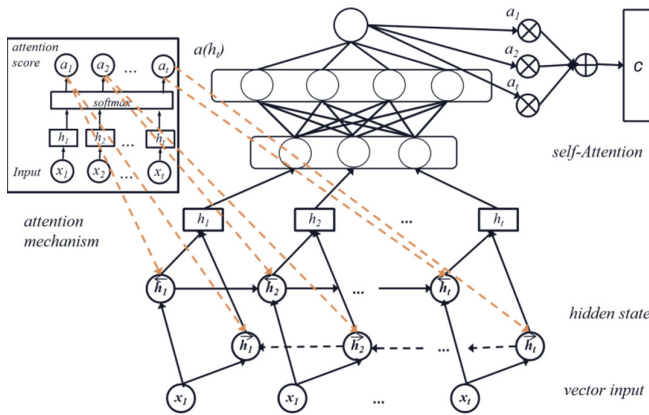


Fig. 5. BiGRU' network structure diagram

Given the word vector is x_t , $t \in [1, L]$, L is the length of the text, W_e is the weight matrix of BiGRU', then the word vectorization of the text is expressed as:

$$x_t = W_e w_t, t \in [1, L] \quad (15)$$

The calculation formula of BiGRU' is:

$$\vec{h}_t = AGRU(x_t), t \in [1, L] \quad (16)$$

$$\overleftarrow{h}_t = AGRU(x_t), t \in [1, L] \quad (17)$$

In this method, \vec{h} represents the hidden state of the word during forward propagation, and \overleftarrow{h} represents the hidden state of the word during backpropagation. Concatenating \vec{h} and \overleftarrow{h} , $h_i = [\vec{h}, \overleftarrow{h}]$, can obtain the bidirectional semantic information of the word vector.

This study also uses the self-attention mechanism after improving Bi-GRU to further integrate the important feature information of the text. The self-attention mechanism learns the hidden state weight at each moment t and extracts the feature information of the text by calculating the similarity between words. This mechanism does not depend on the order of words and retains important feature information. The specific calculation formula of self-attention is as follows:

$$e_t = u_{att}^T \tanh(W_{att} h_t + b_{att}) \quad (18)$$

$$\alpha_t = \frac{\exp(e_t)}{\sum_{k=1}^n \exp(e_k)} \quad (19)$$

$$c = \sum_{t=1}^n \alpha_t h_t \quad (20)$$

In the formula, u_{att}^T , W_{att} , and b_{att} are related parameter matrices of self-attention. h_t represents the hidden state at time t , and α_t represents the attention weight of the state hidden state at time t . The final weighted vector representation c of the text can be obtained by weighting and summing the hidden state h_t through Formula (22). Finally, c is passed through the softmax function to obtain the sentiment classification result.

3 Experiment and Analysis

3.1 Data Preprocessing

This paper employs the Twitter Tweet Comments Dataset to train and evaluate sentiment analysis algorithms. The Twitter Sentiment Analysis Dataset comprises tweets from the highly representative social media platform Twitter, which provides a rich source of freely expressed emotions and thoughts. The dataset consists of over 15,000 tweets

labeled with positive, negative, or neutral sentiment. The first step in the pre-processing of the dataset involves the removal or replacement of irrelevant information, noise, and unnecessary characters in the raw data with appropriate symbols. For instance, URLs, punctuation marks, numbers, and special characters in tweets are removed. Word2vector is then utilized to initialize the word embedding information of the comment text. Subsequently, the dataset is randomly partitioned into a training set and a test set in an 8: 2 ratio, which are employed for model training and performance evaluation, respectively. The training set comprises 12,000 instances, and the test set comprises 3000 instances.

3.2 Evaluation Index

This paper employs accuracy, recall, and F_1 as evaluation metrics, with the respective calculation formulas presented below:

$$accuracy = \frac{TP + TF}{TP + TF + FP + FN} \quad (21)$$

$$recall = \frac{TP}{TP + FN} \quad (22)$$

$$precision = \frac{TP}{TP + FP} \quad (23)$$

$$F1 = \frac{2 * recall * precision}{precision + recall} \quad (24)$$

Among these metrics, TP represents the number of samples that were correctly classified as positive samples, while TF represents the number of samples that were correctly classified as negative samples. In contrast, FP represents the number of samples that were actually negative but were misclassified, and FN represents the number of samples that were actually positive but were misclassified.

In this experiment, we compared the performance of the BiAGRU' model, which incorporates an attention mechanism, with the following four models: the word2vector-GRU model, which combines word2vector word vectors with a GRU text classifier, the Bi-GRU model, the Bi-LSTM model, and the GRU-Attention model. Notably, the GRU-Attention model only integrates the self-attention mechanism discussed in Chap. 2 after the Bi-GRU layer and does not apply attention to the update gate of the GRU layer.

The parameter configurations for the experimental model Bi-GRU' are presented in Table 1

3.3 Analysis of the Experimental Results of the Data Set

Table 2 presents the analysis outcomes of each model on the Twitter dataset, while the classification results for each category are displayed in Fig. 7.

As depicted in Fig. 7, the proposed implementation model exhibits superior performance in terms of accuracy, recall, and F1 score when compared with other models. Additionally, the analysis of Table 2 and Fig. 7 highlights that both BiGRU and BiLSTM models outperform the word2vector-GRU model, indicating that the bidirectional

Table 1. Model parameter setting table.

Parameter name	Parameter value
Word vector dimension	100
Learning rate	0.02
Loss function	Cross-entropy loss
Batch size	150
Dropout	0.1
Optimizer	SGD

Table 2. Sentiment analysis results of each model.

Models	Accuracy	Recall	F1
word2vector-GRU	0.846	0.839	0.841
Bi-GRU	0.873	0.871	0.874
Bi-LSTM	0.868	0.867	0.869
Bi-GRU-attention	0.883	0.884	0.886
Bi-GRU'	0.902	0.901	0.905

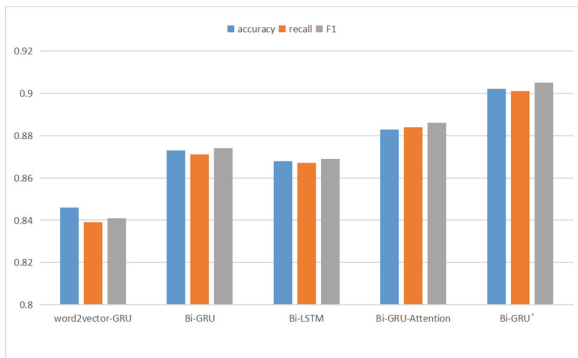


Fig. 6. Comparison of various model results

model performs better than the unidirectional model. Furthermore, the Bi-GRU' model, which utilizes a double-layer attention mechanism, surpasses the Bi-GRU-Attention model, despite both models using BiGRU and attention to extract text information. The difference in performance arises from the number of layers of attention, which suggests the effectiveness of the attention mechanism added to the update gate in Bi-GRU'. Additionally, while the performance of Bi-GRU and Bi-LSTM models is similar, the

double-layer attention mechanism incorporated in the Bi-GRU' model yields significantly better results than both Bi-GRU and Bi-LSTM models. The findings demonstrate that the proposed model, which builds on BiGRU, achieves outstanding performance in all aspects.

To further confirm the model's effectiveness, this study conducted additional experiments on the Amazon product review dataset, which contains millions of product reviews and ratings across different categories (e.g., books, electronics, household items, etc.). A test set of 76,537 items was randomly selected, and models including word2vector-GRU, Bi-GRU, Bi-LSTM, Bi-GRU-Attention, and Bi-GRU' were tested on the Amazon product review text in the test set. The experimental results are presented in Fig. 7.

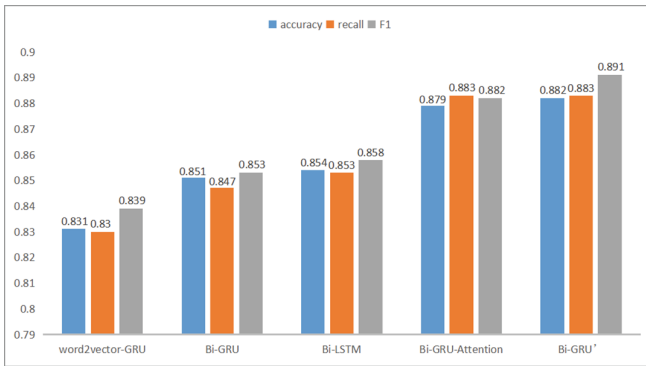


Fig. 7. Comparison of various model results

The results depicted in Fig. 8 show that the models with the added attention layer outperform the models without it in various performance indicators, confirming the effectiveness of the attention layer. Although the BiGRU-Attention model has a slightly higher recall rate and F1 value, its accuracy rate is lower. Overall, the performance of the Bi-GRU' model is better. The experimental results indicate that the Bi-GRU' model proposed in this paper, with the addition of a two-layer attention mechanism, can better capture the context and has a superior overall performance in sentiment analysis.

4 Conclusion

Traditional sentiment analysis models often overlook the context and the influence of crucial words on sentiment analysis. Most models rely on stacked neural network models and attention mechanisms. To overcome these limitations, this paper proposes a BiGRU network model with an attention update gate that utilizes the attention score to regulate the update gate. The model is optimized and combined with a forward attention mechanism to enhance its accuracy. Experimental results demonstrate the efficacy of the proposed model. In future studies, we aim to explore the integration of different attention mechanisms and GRU, optimize the loss function, and evaluate the model's effectiveness in various domains.

References

1. Yoon, K.: Convolutional neural networks for sentence classification. In: Proceedings of the 2014 Conference on Empirical Methods in Natural Language Processing (EMNLP) (2014)
2. Liu, P., Qiu, X., Huang, X.: Recurrent neural network for text classification with multi-task learning. In: Proceedings of the Twenty-Fifth International Joint Conference on Artificial Intelligence (IJCAI) (2016)
3. Yang, Z., Yang, D., Dyer, C., He, X., Smola, A., Hovy, E.: Hierarchical attention networks for document classification. In: Proceedings of the 2016 Conference of the North American Chapter of the Association for Computational Linguistics: Human Language Technologies (NAACL-HLT) (2016)
4. Socher, R., Perelygin, A., Wu, J., Chuang, J., Manning, C., YNg, A., Potts, C.: Recursive deep models for semantic compositionality over a sentiment treebank. In: Proceedings of the 2013 Conference on Empirical Methods in Natural Language Processing (EMNLP) (2013)
5. Pang, B., Lee, L.: A sentimental education: sentiment analysis using subjectivity summarization based on minimum cuts. In: Proceedings of the 42nd Annual Meeting of the Association for Computational Linguistics (ACL) (2004)
6. Hochreiter, S., Schmidhuber, J.: Long short-term memory. *Neural Comput.* **9**(8) (1997)
7. Cho, K., van Merriënboer, B., Gulcehre, C., Bahdanau, D., Bougares, F., Schwenk, H., Bengio, Y.: Learning phrase representations using RNN encoder-decoder for statistical machine translation. In: Proceedings of the 2014 Conference on Empirical Methods in Natural Language Processing (EMNLP) (2014)



An Improved Path Planning Algorithm Based on A* Algorithm

Dongdong Li^(✉), Xiaohou Shi, and Meiling Dai

China Telecom Corporation Research Institute Beijing, Beijing, China
{lidd4, daim11}@chinatelecom.com

Abstract. Path planning is a crucial aspect of vehicle navigation, and this paper presents an enhancement to the classic A* algorithm to address key challenges in this domain. The proposed method aims to improve both the efficiency and safety of path planning. In practical applications, path planning encounters various issues, such as an excessive number of unnecessary nodes during the search process, resulting in suboptimal planning efficiency. Additionally, obstacles may be present along the route between the starting point and the target node, requiring obstacle path search. Moreover, traditional cost functions often fail to fully account for vehicle safety, thereby increasing the risk of collisions. To overcome these challenges, the proposed method incorporates two key enhancements. Firstly, it employs a node marking technique on the grid map to identify key nodes and reduce the search process for unnecessary nodes, thus enhancing planning efficiency. Secondly, an incremental expansion of search nodes is utilized, employing an improved A* algorithm with a modified cost function. This enables the algorithm to plan collision-free paths from the starting point to the key nodes while considering the distance cost associated with potential collisions, thereby enhancing vehicle safety. Experimental results demonstrate that the proposed method significantly enhances path planning efficiency by reducing the search efforts for unnecessary nodes, resulting in accelerated path planning. Furthermore, the improved cost function enables the generation of safe and feasible paths, thereby enhancing vehicle safety.

Keywords: Path planning · A* algorithm · Vehicle navigation

1 Introduction

Path planning is a fundamental technology widely employed in the transportation field, playing a pivotal role in optimizing traffic flow, alleviating congestion, enhancing efficiency, and improving traffic safety. As urbanization accelerates and traffic demands grow, the need for efficient route planning becomes increasingly crucial to enable individuals to reach their destinations quickly and safely. This study aims to investigate enhancements to existing path planning methods, addressing limitations in terms of efficiency and safety.

Considerable research efforts have been devoted to improving the accuracy and efficiency of path planning. The classic A* algorithm [1], as a heuristic search algorithm, is extensively employed in path planning tasks. By evaluating the cost function and heuristic estimation function of nodes, the algorithm searches for the optimal path. However, when applied to large-scale maps and complex road networks, the A* algorithm encounters challenges such as excessive node searches and high computational complexity, leading to diminished efficiency.

To overcome these limitations, several studies have proposed enhanced methods. These methods incorporate techniques such as heuristic search strategies, pruning techniques, and map preprocessing [2] to improve path planning efficiency. Other approaches focus on vehicle safety and introduce technologies like collision risk assessment and traffic flow prediction [3] to plan safer and more reliable routes.

Nonetheless, these research methods possess certain drawbacks. Some enhancement methods may sacrifice path accuracy or struggle to handle complex traffic scenarios while improving efficiency. Although other methods prioritize security, they face challenges related to computational complexity and real-time performance, impeding their widespread practical implementation.

This paper proposes an improved path planning method that overcomes the limitations of traditional approaches while comprehensively considering both efficiency and safety aspects. The research methodology encompasses the following aspects: during node search, only the key nodes marked on the map are explored, reducing the search process for unnecessary nodes and improving path planning efficiency. Additionally, the cost function of the A* algorithm is enhanced by incorporating collision distance cost to enhance vehicle behavior.

2 Introduction to A* Algorithm

The A* algorithm, a renowned heuristic search algorithm, holds a significant position in the realm of path planning. By examining the node's cost function and heuristic estimation function, it efficiently determines the optimal path.

The fundamental principle underlying the A* algorithm involves a comprehensive consideration of both the actual cost of the node and the heuristic estimated value. This evaluation leads to the selection of the node with the minimum comprehensive cost for further exploration. Each node possesses a cost value that reflects the expense incurred along the path from the origin to that particular node. Typically, this value is expressed using a distance metric. Concurrently, the heuristic estimation function assesses the anticipated cost from the current node to the target node. Consequently, the A* algorithm assigns priority to nodes with lower comprehensive costs, facilitating the progression towards the ultimate goal during the search process.

During the planning process, the vehicle initiates its journey from the starting point and eventually reaches the target point by traversing an extended cycle. The specific steps of the conventional A* algorithm are depicted in Fig. 1.

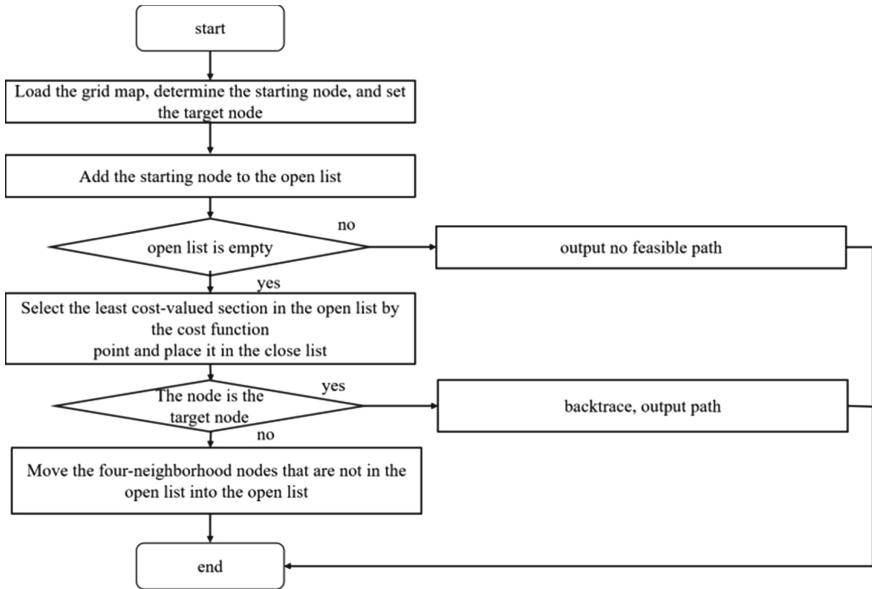


Fig. 1. Traditional A* algorithm process

3 Improved A* Algorithm

The proposed method begins by identifying essential nodes on the rasterized map. It then determines the target vector SG, which represents the connection line from the current node S to the target point G. Next, the method selects the key node N located closest to the target point G within the Manhattan distance around SG. In the event that obstacle nodes are present in the search area of N, the method applies an incremental expansion of the A* algorithm along with an enhanced cost function to search for a path from S to N that circumvents obstacles. This process is repeated iteratively, selecting key nodes N until N corresponds to the target point G, thus concluding the path planning phase. A visual representation of the overall process can be observed in Fig. 2.

The initial step involves rasterizing the map and subsequently identifying key nodes within the map. Marked path turning nodes and path dead-end nodes are added to the list of path key nodes. The process of identifying these key nodes is depicted in Fig. 3.

The next step involves generating the target vector SG, which extends from the current node S (initially set as the starting point) to the target node G. The target vector SG is represented in Fig. 4, providing a visual representation of its direction and orientation.

In Fig. 4, the key nodes A, B, C, and D are positioned around the target vector SG. Using the SG vector as a reference, the key node N closest to the target point G is selected. To determine this, the Manhattan distance [4] between each key node and the target point G is calculated, and the key node with the smallest distance is chosen. Taking Fig. 4 as an example, the distance between the current node S and the target point G can be computed as follows:

$$dM = |G_x - S_x| + |G_y - S_y| \quad (1)$$

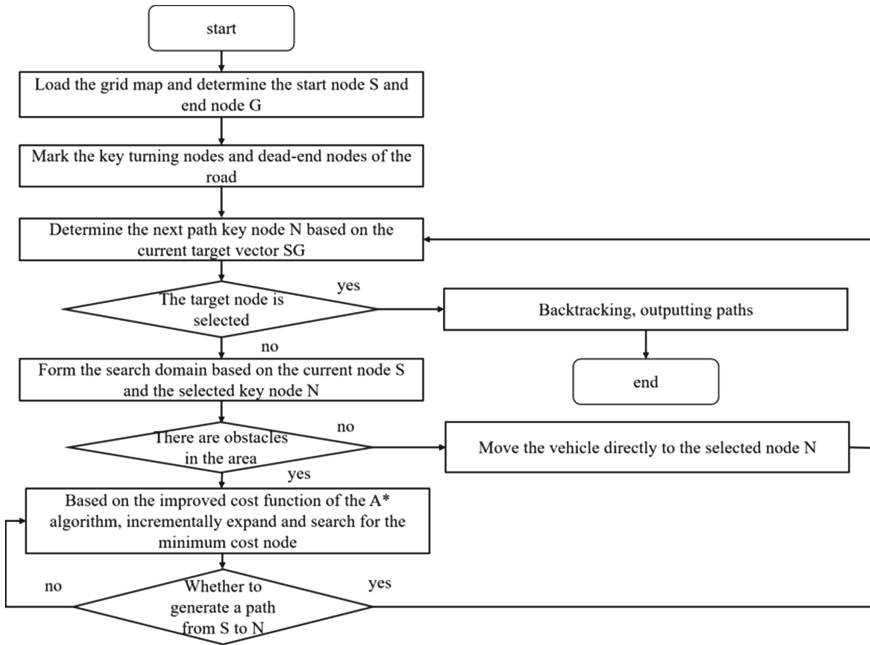


Fig. 2. The overall flow chart of the path planning algorithm

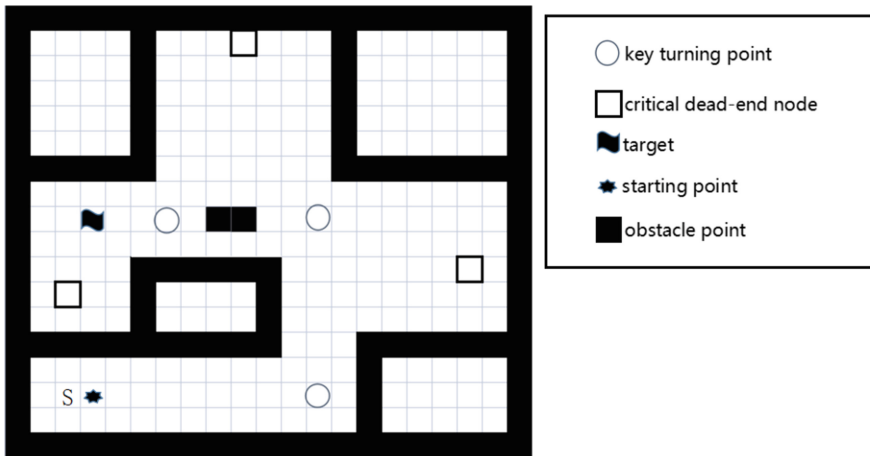


Fig. 3. Raster map with key nodes

The Manhattan distance d_M represents the distance between node S and node G. The coordinates of node S are denoted as (S_x, S_y) , while the coordinates of node G are denoted as (G_x, G_y) . Upon identifying the key node N with the smallest distance to the target point G, an assessment is made to determine if N is a path dead-end node. If it is indeed a dead-end node, a re-selection of the key node N is required. Conversely, if N is

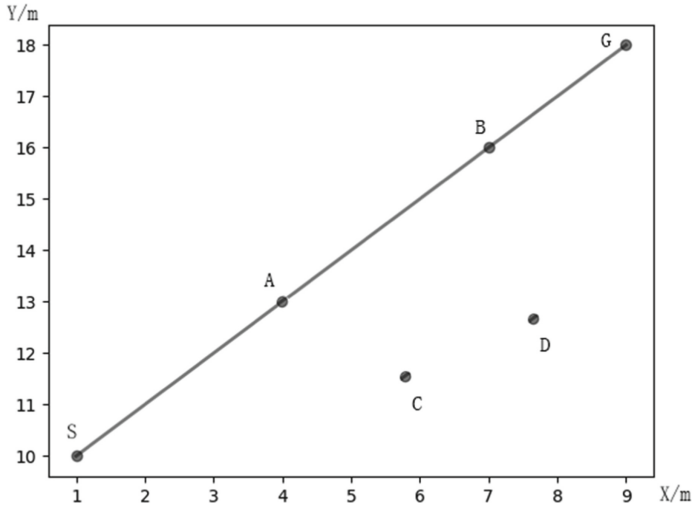


Fig. 4. Key node selection strategy based on target vector

not a dead-end node, the algorithm proceeds to evaluate the existence of obstacle points within the search area of the current node S and node N.

Referring to Fig. 5, the search area encompasses both node S and node N, with the length of the search area being $|N_x - S_x|$ and the width corresponding to the road length of 7 m. Here, N_x represents the x-axis coordinate of the selected node N. If no obstacle nodes are present within the search area, the vehicle can directly navigate to node N. However, in the presence of an obstacle point, the A* algorithm utilizes an incremental expansion technique to plan an obstacle-free path leading to node N. During the search process, the improved cost function, as outlined in step C, is employed for node evaluation and selection.

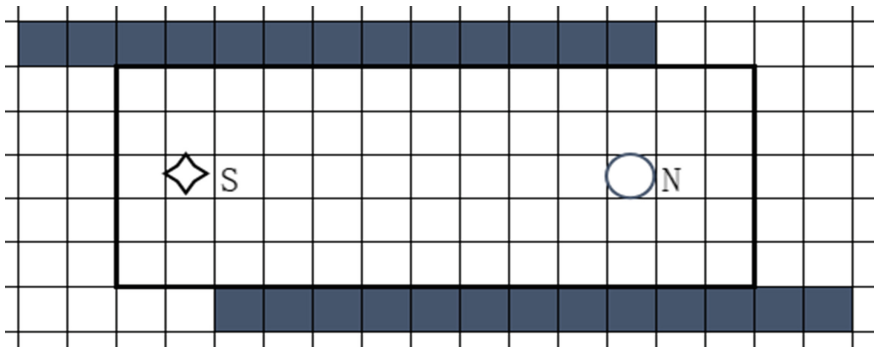


Fig. 5. Obstacle detection area indication

C. This method divides the obstacles in the search area into two types. The first type is obstacles with small size and high probability of movement, such as stationary

pedestrians beside the road, with a length $l \in (1, 2)$ m. the second type is Obstacles with low probability of movement but large size, such as parking next to the road, have length $l \in (3, 4)$ m.

Based on the vehicle speed, safe distance between vehicles and a large number of simulation test analysis, an anti-collision safety distance model is designed, in which the safety distance between the vehicle and obstacles is related to the vehicle speed and road friction coefficient, and the calculation formula is as follows:

$$ds = kv^2/(2\mu g) + (2 - \mu)du \tag{2}$$

Among them, ds is the safe distance between the vehicle and the obstacle, k is the weight of different types of obstacles, when the obstacle is large, $k = 1.5$, and when the obstacle is small, $k = 1.2$. v is the vehicle speed. μ is the vehicle The friction coefficient of the ground. g is the acceleration of gravity, the value is 10 m/S^2 . du is the unit distance, the value is 1 m .

Figure 6 shows the relationship model diagram of safe collision distance, road friction coefficient, and vehicle speed. This relationship model diagram is based on simulation tests of a large number of vehicle collision scenarios., the safe collision distance gradually increases, which is also in line with the driver’s collision avoidance habits during vehicle driving in the real world.

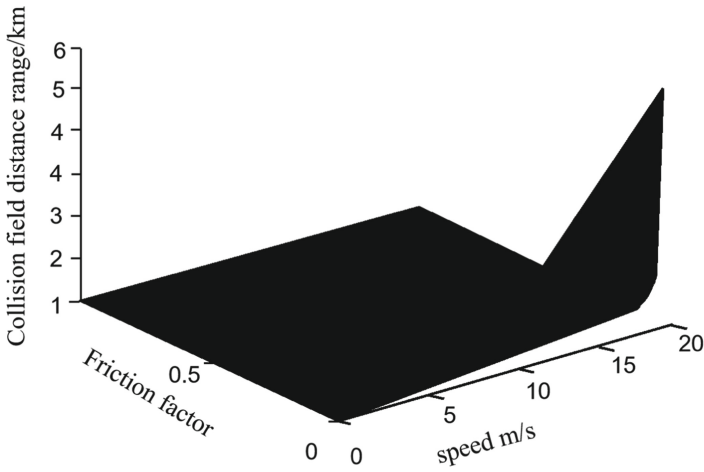


Fig. 6. Obstacle collision field model

The total number of layers c of the expanded grid can be obtained from ds as:

$$c = \lceil ds/10 \rceil \tag{3}$$

In the formula, $\lceil \rceil$ means round up. Re-assign the distance of the collision field to $10 \text{ m} \times c$, and use it as the cost value of the innermost grid of the extended grid, and then carry out decremental assignment in multiples of 10 m . If the extended grid of obstacles contains obstacle grids, It is not assigned a value. As shown in Fig. 6, when the vehicle

speed is 15 m/s and the road surface adhesion coefficient is 0.8, $d_s = 18.075$ m can be obtained from formula (3), and $c = 2$ can be obtained from formula (3), so directly $o(N) = 20$ m is assigned to the first layer grid outside the obstacle boundary, and the cost value $o(N) = 10$ m is assigned to the second layer grid outside the obstacle boundary (Fig. 7).

	10	10	10	10	10	10	10
	10	20	20	20	20	20	10
	10	20				20	10
	10	20				20	10
	10	20	20	20	20	20	10
	10	10	10	10	10	10	10

Fig. 7. Extend grid based on collision field distance

The overall cost function, the improved A* algorithm cost function is:

$$f(N) = g(N) + k_1h(N) + k_2o(N) \quad (4)$$

In formula (4), $f(N) = g(N) + h(N)$ is the cost function of the original A* algorithm, $o(N)$ is the collision field distance cost of different obstacles. k_1 and k_2 are different costs. The weight of the function. Among them, the larger k_1 is, the faster the path tends to the target point, and the shorter the calculation time is, but this will affect the optimality of the path, while the value of k_2 will directly affect the distance between the planned path and the obstacle boundary, and then affect the driving of the vehicle safety. After many simulations and verifications, this paper takes $k_1 = 2$ and $k_2 = 2$. For example, the A* algorithm gradually selects the key nodes with the smallest replacement value through repeated iterations, thereby generating an obstacle-free planning path from S to N. If N is not the target point, continue to execute step B, otherwise end the path planning.

4 Experiment and Analysis

To evaluate the performance of the improved A* algorithm, this study compares it with the traditional A* algorithm and the Weighted-A* algorithm on a regional grid map derived from real-world data. To validate the generalization ability and enhanced performance of the proposed algorithm, a simulation-based comparative analysis is conducted using a real scene map.

In this research, the same starting point and target point are set for all three algorithms, as depicted in Fig. 8. The grid map size is standardized at 30×30 m. Various parameters, including path length, average computation time, number of expanded nodes, number of turns, and minimum distance from road boundaries or other obstacle boundaries, are considered. It should be noted that the A* algorithm is classified as an optimal search algorithm, resulting in a unique output path. However, due to the influence of system test environment and hardware performance, the computation time may vary within a single iteration, leading to differences in time consumption across different test scenarios. To mitigate this variability, the algorithms are tested 50 times under identical conditions, and the average computation time for each algorithm is calculated, ensuring a comprehensive evaluation of the improved algorithm's computational efficiency. The final planning result for a specific scenario is presented in Fig. 8.

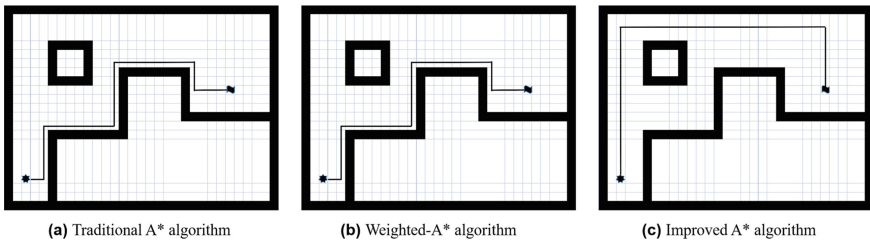


Fig. 8. Driving coverage trajectory of different algorithms under the real scene map

Figure 8 illustrates that the path results obtained by the traditional A* algorithm and the Weighted-A* algorithm exhibit similarity. However, their trajectories tend to hug the road edges with numerous turns, rendering them unsuitable for unmanned vehicles in this particular scene. In contrast, the path generated by the proposed improved algorithm not only maintains a safe distance from obstacles but also prioritizes straight trajectories to ensure the safety and feasibility of the planned path for unmanned vehicles.

The time-consuming results from 50 test calculations are presented in Fig. 9. It can be observed that the improved A* algorithm demonstrates significantly shorter computation times compared to the traditional A* algorithm. However, its computation time is comparable to that of the Weighted-A* algorithm in the real map scene. Furthermore, the fluctuation range of computation times for different algorithms remains within 20 ms, highlighting the improved algorithm's stable calculation performance.

The main parameters obtained from 50 test runs for different algorithms are recorded and presented in Table 1.

From Table 1, the number of expanded nodes significantly reduces with the improved A* algorithm compared to the traditional A* algorithm and the Weighted-A* algorithm. The algorithm improvement demonstrates a moderate enhancement of 8.3%. Furthermore, when compared to the traditional A* algorithm and the Weighted-A* algorithm, the improved A* algorithm showcased a decreased number of turns, ensuring a sufficient minimum distance between the path and various obstacle boundaries to guarantee driving safety. In conclusion, the proposed algorithm's effectiveness in this study is notably prominent.

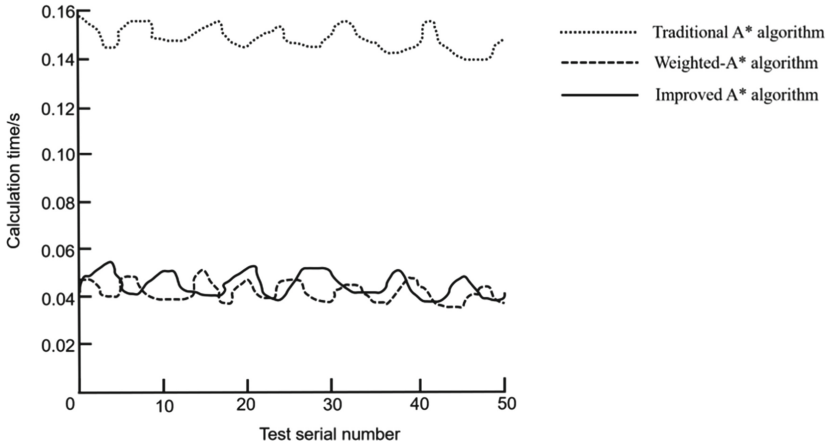


Fig. 9. Calculation time of different algorithms

Table 1. Test results of different algorithms.

Algorithm	Path length	Average time	Nodes number	Turns number
Traditional A* algorithm	58	102	913	8
Weighted-A* algorithm	58	30	325	8
Improved A* Algorithm	66	25	10	3

5 Conclusion

This study presents an improvement to the conventional A* algorithm for addressing the path planning problem, with the objective of enhancing both the efficiency of path planning and vehicle safety. The traditional A* algorithm encounters challenges, such as extensive node searches and high computational complexity, particularly when applied to large-scale maps and intricate road networks, resulting in suboptimal efficiency. To address these shortcomings, this paper proposes enhancements to the traditional A* algorithm by incorporating key node search techniques and introducing a collision field model based on a safe distance. Through experimental validation, the effectiveness and advantages of the proposed method are demonstrated, signifying its significance for practical applications. By leveraging key node identification and an improved cost function, the efficiency of path planning and the safety of vehicle navigation can be significantly improved. Nevertheless, there remain areas for further improvement and investigation, such as performance optimization when dealing with complex traffic scenarios and large-scale maps, as well as integration with real-world traffic environments. Advancements in these areas will contribute to enhancing the practicality and adaptability of path planning algorithms.

References

1. Hart, E., Nilsson J.: A formal basis for the heuristic determination of minimum cost paths. *IEEE Trans. Syst. Sci. Cyber.* **4**(2), 100–107
2. Sturtevant, N.: Benchmarks for grid-based pathfinding. *IEEE Trans. Comput. Intell. AI Games* **4**(2), 144–148
3. Wei, Z., Xia, F., Liu, Y., Xu, Y.: Safe path planning algorithm based on collision risk assessment for intelligent vehicles. *IEEE Trans. Intell. Transp. Syst.* **17**(8), 2164–2173
4. Zhao, Z., Meng Z.: Path planning of service mobile robot based on adding-weight A* algorithm. *J. Huazhong Univer. Sci. Technol. (Nat. Sci. Ed.)* **36**(S1), 196–198 (2008)



Energy-Efficiency Resource Allocation for D2D Communications Under-Laying UAV Networks

Pan Zhao^{1,2,3,4} , Liuyuan Chen^{2,3}, Zhiliang Jiang^{2,3}, Ming Han^{2,3}, Fucai Yuan^{2,3} (✉), Aocheng Li⁵, Xiangyuan Jia^{2,3}, Xinqi Fu^{2,3}, Jingqi Han^{2,3}, and Jiaqi Han^{2,3}

¹ College of Mechanical and Electrical Engineering, Henan University of Technology, Zhengzhou 450001, China

² Henan Aerospace Hydraulic and Pneumatic Technology Co., Ltd., Zhengzhou, China
136001315@qq.com

³ Key Laboratory of Grain Information Processing and Control, Ministry of Education, Henan University of Technology, Zhengzhou, China

⁴ Key Laboratory of Henan Province for Grain Photoelectric Detection and Control, Henan University of Technology, Zhengzhou, China

⁵ School of Applied Science, Taiyuan University of Science and Technology, Taiyuan, China

Abstract. Device-to-Device (D2D) communications under-laying Unmanned aerial vehicle (UAV) with its mobility extend the coverage and improve system capacity and flexible networking capabilities. However, the energy-efficiency are major challenge in UAV-assisted D2D networks. In this paper, the joint power and channel optimization problem has been investigated to maximize the system energy efficiency. Using the properties of objective function, the original optimization problem is transformed into two sub-problems. In the first step, the optimal power allocation problem is solved by using the Nash balance point of non-cooperative Game theory. In the second step, the channel allocation problem is constructed into a Bipartite graph, and then the Hungarian algorithm is used to find the best matching. The numerical simulation results show that the proposed scheme not only improves the energy efficiency of the system but also enhances the spectral efficiency.

Keywords: UAV · D2D communications · Resource allocation · Power control

1 Introduction

In recent times, there has been a widespread application of the Internet of Things (IoT) in smart cities, smart transportation, smart communities [1, 2], etc. Therefore, larger system capacity and flexible networking capabilities is required to support the development needs of IoT networks. However, deploying ground base stations in high mountains and remote areas is significant challenge due to the costs associated with huge construction and maintenance.

Then, unmanned aerial vehicle (UAV) communication has gained significant attention due to its portable advantages of convenient and flexible deployment options [3]. It

can not only provide support for the expansion of business capabilities in super hot areas such as major events and conference activities, but also serve as a mobile base station to timely convey rescue information [4]. Simultaneously, D2D communication as a pivotal component of 5G leverages direct communication between nearby users without relying on traditional network infrastructure. D2D communication enhances system throughput, spectrum utilization, transmission rate, energy efficiency and reduces latency [5, 6]. Therefore, D2D communication under-laying UAV networks receive widespread attention from both industry and academia, with great potential in improving network capabilities and capacity.

Designing a rational resource allocation scheme becomes critically important to fully leverage the benefits offered by UAV and D2D communications. The resource allocation of D2D under-laying UAV networks has been the subject of significant research, with numerous studies focusing on exploring and analyzing effective approaches in this area [7–13]. To optimize spectral efficiency in hybrid D2D and UAV networks, a novel 3D spectrum sharing scheme has been introduced in [7]. This scheme integrates machine learning techniques to effectively capture and model the random stochastic geometry framework, enabling efficient resource allocation and improving overall network performance. The paper [8] investigates the strategy of opportunistic UAV transmission in D2D communication networks. It focuses on selecting suitable transmission times and appropriate channels. The research in [9] investigates efficient approaches to select appropriate IRSs and optimize the beam-forming strategies for multiple IRS-UAV assisted D2D networks. The paper [10] introduces a low-complexity and robust link scheduling approach for D2D communications in UAV-assisted industrial IoT networks. Nevertheless, it is worth noting that the authors of the aforementioned studies did not explicitly address the energy consumption of system.

In [11], the research focuses on the energy-efficiency maximization problem with quality-of-service (QoS) constraints in interference-aware underlay D2D-enabled UAV systems. The study only tackles the optimization of power allocation to enhance energy efficiency. In [12], a new and innovative framework for energy-efficient D2D communication is proposed, which involves the allocation of power and bandwidth. It should be noted that in this study, the UAV is utilized as a relay rather than functioning as a traditional base station. The paper [13] focuses on studying a robust energy-efficiency maximization problem in an Energy Harvesting-based D2D communication framework within a UAV-assisted network. The study considers imperfect channel state information and coordinate information. Then, the air-to-ground links are designed only to account for line-of-sight (LoS) links. Driven by the aforementioned observations, the existing resource allocation approaches for energy efficiency either focus solely on optimizing a single dimension of resources or solely prioritize the performance optimization of D2D users. Take into account the overall system energy efficiency, a comprehensive and holistic approach is required. In this study, we adopt a comprehensive perspective by considering the total energy efficiency of the system, encompassing both D2D pairs and ground users (GUs), while ensuring the fulfillment of quality of service (QoS) requirements.

The remaining sections of the paper are structured as follows. Section II provides an introduction to the system model for D2D communication under-laying UAV network,

encompassing factors such as channel gain, interference and an analytical model of the system. In Section III, the optimization method employed in the study is discussed, focusing on power allocation and channel allocation strategies. Section IV presents a detailed analysis of the simulation results. Finally, Section V presents the conclusion with summarizing contributions of the research.

2 System Model

2.1 Network Model

A UAV-enabled network with device-to-device (D2D) communications is being considered, where UAV is stationed in the core of a cell with an altitude of h . As depicted in Fig. 1, the distribution of users is uniform within a circular cell of a radius R . The system users can be classified into two categories: ground users (GUs) and D2D pairs. The D2D pair is composed of transmitting users (DT) and receiving users (DR). OFDMA (Orthogonal Frequency Division Multiple Access) is specifically designed for GUs to communicate with the UAV. D2D pairs utilize the same spectrum as ground users (GUs) in an underlay manner, allowing for spectrum reuse.

Define $\mathcal{M} = \{D_m | m = 1, 2, \dots, M\}$ and $\mathcal{N} = \{U_n | n = 1, 2, \dots, N\}$ represent D2D pairs and GUs, where D_m represent the m th D2D pair, U_n represent the n th ground user. The n th ground user's horizontal position is denoted as (x_{U_n}, y_{U_n}) . The horizontal position of DT and DR are denoted as $(x_{D_m}^T, y_{D_m}^T)$ and $(x_{D_m}^R, y_{D_m}^R)$, respectively.

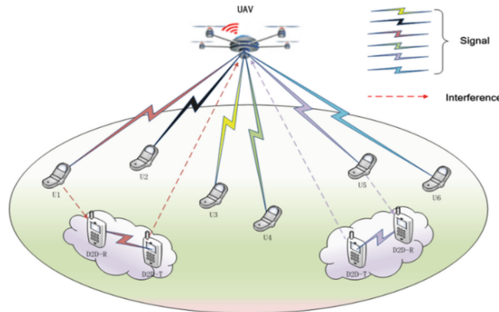


Fig. 1. System model for D2D and UAV networks.

2.2 Channel Model

The communication channels between the UAV and ground users, as well as between the UAV and D2D users, are classified as air-to-ground (ATG) channels. The communication channels encompass both Line-of-Sight (LoS) and Non-Line-of-Sight (NLoS) signals, each with varying probabilities of occurrence [14]. The channel gain between the UAV and the n th GU can be expressed as follows:

$$G_{U_n} = P_{LOS,U_n} g_{U_n}^{LOS} + P_{NLOS,U_n} g_{U_n}^{NLOS} \quad (1)$$

where $g_{U_n}^{LOS}$ represents the channel gain for the LoS link between the UAV and the n th ground user (GU). $g_{U_n}^{NLOS}$ represents the channel gain for the NLoS link between the UAV and the n th ground user (GU). They are expressed in the following:

$$\begin{cases} g_{U_n}^{LOS} = \sqrt{h^2 + x_{U_n}^2 + y_{U_n}^2}^{-\varphi_u}, LOS \\ g_{U_n}^{NLOS} = \eta \sqrt{h^2 + x_{U_n}^2 + y_{U_n}^2}^{-\varphi_u}, NLOS \end{cases} \quad (2)$$

where φ_u denotes the path loss exponent, and η represent an additional attenuation factor that accounts for the presence of a Non-Line-of-Sight (NLoS) link. Furthermore, the occurrence probability of a LoS link is determined by the geographical location of the user and the angle of elevation between the UAV and the ground user, which can be expressed as follows:

$$P_{LOS,U_n} = \frac{1}{1 + \alpha \exp(-\beta(\theta_{U_n} - \alpha))} \quad (3)$$

where $\theta_{U_n} = \frac{180}{\pi} \sin^{-1}\left(\frac{h}{\sqrt{h^2 + x_{U_n}^2 + y_{U_n}^2}}\right)$ is the elevation angle between the UAV and U_n . α and β are environmental variable parameters related to rural, urban or suburban. Therefore, the probability of U_n NLoS link generation can be expressed as $P_{NLOS,U_n} = 1 - P_{LOS,U_n}$.

Correspondingly, the interference gain between the transmitting user of D2D pair D_m and UAV is denoted as $G_{D_m,UAV}$. The channel gain of D2D pair D_m between the D2D transmitter and D2D receiver can be expressed as follows:

$$G_{D_m} = G\beta_{m,m}\gamma_{m,m}d_{m,m}^{-\delta} \quad (4)$$

where $\beta_{m,m}$ is fast fading which follows an exponential distribution, $\gamma_{m,m}$ is slow fading which is modeled as a log-normal distribution. $d_{m,m}$ is D2D pair distance. G and δ is the path loss constant and exponent. Similarly, the interfering gain from U_n to D_m is denoted as G_{U_n,D_m} .

Let $p = [p_{D_1}, p_{D_2}, \dots, p_{D_M}]^T$ denote as the power levels transmitted by the D2D transmitter to the D2D receiver, $p = [p_{U_1}, p_{U_2}, \dots, p_{U_N}]^T$ denote as the power levels transmitted by by ground users to UAV. Let a binary function $\lambda_{m,n} \in \{0, 1\}$ indicate whether the D2D pair D_m reuses the channel of ground user U_n . If the sub-channel of U_n is shared by the D2D link D_m , then $\lambda_{m,n} = 1$; otherwise, $\lambda_{m,n} = 0$.

Similarly, the SINR of users U_n and D2D pair D_m are represented as:

$$SINR_{U_n} = \frac{p_{U_n} G_{U_n,UAV}}{\sum_{m=1}^M \lambda_{m,n} p_{D_m} G_{D_m,UAV} + N_0^2}, SINR_{D_m} = \frac{p_{D_m} G_{D_m}}{\sum_{n=1}^N \lambda_{m,n} p_{U_n} G_{U_n,D_m} + N_0^2} \quad (5)$$

where N_0 is Gaussian noise.

2.3 Problem Formulation

Our objective is to maximize the Energy Efficiency (EE) of all users while ensuring satisfactory communication quality for both ground users (Gus) and D2D pairs. The Energy Efficiency (EE) is determined by dividing the total data rate of all users by the total power consumed by them. The energy efficiency can be calculated as follows:

$$EE = R/p = B \log_2(1 + SINR)/p \quad (6)$$

Therefore, the energy efficiency of U_n and D_m can be written as:

$$EE_{U_n} = \frac{B \log_2 \left(1 + \frac{p_{U_n} G_{U_n, UAV}}{\sum_{m=1}^M \lambda_{m,n} p_{D_m} G_{D_m, UAV} + \delta^2} \right)}{p_{U_n}},$$

$$EE_{D_m} = \frac{B \log_2 \left(1 + \frac{p_{D_m} G_{D_m}}{\sum_{n=1}^N \lambda_{m,n} p_{U_n} G_{U_n, D_m} + \delta^2} \right)}{p_{D_m}} \quad (7)$$

Hence, the optimization problem for maximizing system Energy Efficiency (EE) can be formulated in the following:

$$P1 : \max \left(\sum_{n=1}^N EE_{U_n} + \sum_{m=1}^M EE_{D_m} \right) \quad (8a)$$

$$s.t. \quad 0 \leq p_{U_n} \leq p_{U_n}^{\max} \quad 0 \leq p_{D_m} \leq p_{D_m}^{\max} \quad (8b)$$

$$SINR_{U_n} \geq SINR_{U_n}^{\min} \quad SINR_{D_m} \geq SINR_{D_m}^{\min} \quad (8c)$$

$$\sum_{n=1}^N \lambda_{m,n} \leq 1 \quad n \in [1, 2, \dots, N] \quad (8d)$$

$$\sum_{m=1}^M \lambda_{m,n} \leq 1 \quad m \in [1, 2, \dots, M] \quad (8e)$$

The maximum transmit power for ground user U_n and the D2D pair D_m is expressed as $p_{U_n}^{\max}$ and $p_{D_m}^{\max}$. The minimum Signal-to-Interference-plus-Noise Ratio (SINR) $SINR_{U_n}^{\min}$ and $SINR_{D_m}^{\min}$ are defined to ensure the Quality of Service (QoS) for ground user U_n and D2D pair D_m respectively. Constraint (8b) is designed to enforce that the assigned transmit power remains within the limits of the maximum allowable transmit power. Constraints (8d) is imposed to ensure that each D2D pair is allowed to utilize the channel of one ground user (GU) for transmission, ensuring channel reuse is limited to one GU. Constraints (8e) is imposed to ensure that the channel of a ground user (GU) can be shared by a maximum of one D2D pair, meaning that each GU's channel can only be used by one D2D pair at a time.

3 System Model

3.1 Power Strategy Based on Game Theory

Solving this problem directly is challenging due to its nature as a mixed integer linear optimization problem. Once the channel allocation is known, $P1$ can be reformulated as the optimal power allocation problem $P2$ for a single GU and a single D2D pair.

$$\begin{aligned}
 P2 : & \max(EE_{U_n} + EE_{D_m}) \\
 s.t. & 0 \leq p_{U_n} \leq p_{U_n}^{\max} \quad 0 \leq p_{D_m} \leq p_{D_m}^{\max} \\
 & SINR_{U_n} \geq SINR_{U_n}^{\min} \quad SINR_{D_m} \geq SINR_{D_m}^{\min}
 \end{aligned} \tag{9}$$

From the observation of $P2$, it is found that EE_{U_n} and EE_{D_m} is not only related to its own transmission power, but also to the transmission power of other users, and each user strives to maximize their own energy efficiency. Inspired by the above, Game theory can be applied to determine the optimal power allocation strategy in this context.

Therefore, the non-cooperative Game theory model can be used to characterize the relationship between them. Let a tuple $G = \{S, \{p_x\}, \{u_x(p)\}\}$ to represent game, where $S = \{x|U_n, D_m\}$ is a finite group of players and p_x is a collection of strategies or actions available to all players and $u_x(p)$ or $u_x(p_x, p_{-x})$ represents the EE utility function of each player. Each player selects its own power from the power space $p_x \in [0, p^{\max}]$, p_{-x} is the power selection of other players except x .

Each player x selects a power level from the power space with the objective of maximizing its utility function $u_x(p_x, p_{-x})$, i.e.

$$\max u_x(p_x, p_{-x}), \forall x \in W \tag{10}$$

Since the energy efficiency of each user is determined by its own power strategy and other user strategies. Nash equilibrium [15] offers a means to determine the most favorable power solution. Nash Equilibrium represents a stable strategic equilibrium where no player can improve their own payoff by unilaterally changing their strategy. For example, a point $p_x \in [0, p^{\max}]$ is an NE of the game $G = \{S, \{p_x\}, \{u_x(p)\}\}$ if $x \in S$ satisfies:

$$u_x(p_x, p_{-x}) \geq u_x(p'_x, p_{-x}), \forall x \in S \tag{11}$$

The optimal power of each player can be iterative calculated according to Nash equilibrium solution.

3.2 Channel Allocation Based on Hungarian

After obtaining power allocation solution $p_{U_n}^*, p_{D_m}^*$, $P1$ can be reformulated as the sub-problem $P3$, focusing on channel allocation.

$$P3 : \operatorname{argmax} \sum_{m=1}^M \sum_{n=1}^N \lambda_{m,n} EE_{D_m U_n}(p_{U_n}^*, p_{D_m}^*)$$

$$s.t. \sum_{m=1}^M \lambda_{m,n} \leq 1, \sum_{n=1}^N \lambda_{m,n} \leq 1 \quad (12)$$

Since the above problem is a combination optimization problem. The complexity of the algorithm can be reduced by employing the binary matching method to solve this problem. First, construct a bipartite graph $G(\mathcal{M}, \mathcal{N}, \omega)$ where \mathcal{M} and \mathcal{N} form the two sets of vertices of the bipartite graph, ω is weight of edge between $D_m \in \mathcal{M}$ and $U_n \in \mathcal{N}$, it is the energy efficiency of D2D pairs D_m sharing spectrum of U_n . It can be solved by the Hungarian algorithm. In view of absolute symmetry of the Hungarian algorithm, some virtual nodes are added to the original bipartite graph.

4 Simulation and Results

In this section, we present simulation results to demonstrate the effectiveness of the proposed algorithm for the system. We consider a target area characterized by a circular shape with a radius of 500. There are also some D2D communication pairs in the target area, which are random distributed. The simulation in this paper is based on MATLAB simulation platform. Some specific parameters are as follows.

Table 1. Parameters of system

Parameter	Value
UAV altitude h	200 m
Cell radius R	500 m
Noise power, N_0	-130 dBm
Maximum D2D pairs and GU transmit power	23 dBm
D2D Tx-Rx distance	40 m
Parameters for urban environment, α, β	11.95, 0.136
NLOS excessive loss factor, η	20 dB
Pathloss constant for D2D link G, δ	$10^{-2}, 3$
Minimum SINR for GUs and D2D, $SINR_{U_n, \min} SINR_{D_m, \min}$	2, 1.5 dBm

To demonstrate the performance of the proposed algorithm, We comprehensively compare the following benchmark schemes: (1) Random scheme: the channels are randomly allocated for D2D pairs with maximum transmit power. (2) Iterative scheme [11]: a resource allocation scheme to maximize D2D User Performance. (3) Robust Scheme [13]: its aim is to optimize the total capacity of cellular links with a joint spectrum and power allocation. These results are based on averaging over 1000 random instances of users' locations and channel conditions.

Figure 2 evaluates the total energy efficiency versus the D2D distance for all algorithm. Based on the observation of the figure, it can be noted that the system's energy efficiency declines as the D2D distance increases. The reason is that the longer distance offers worse SINR for D2D users, thus contributing to smaller energy efficiency.

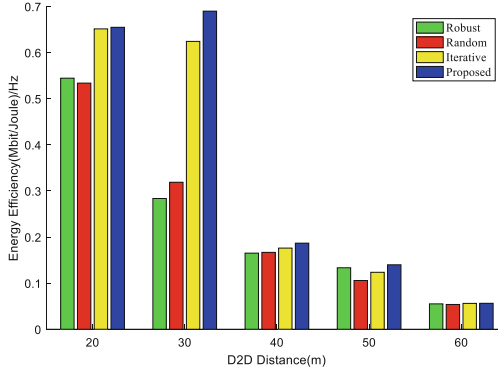


Fig. 2. Energy efficiency versus D2D distance

However, our proposed algorithm always remains optimal, this is because our algorithm not only optimizes power but also optimizes channel allocation. The Iterative algorithm only optimizes the power of D2D users rather than globally. The Robust algorithm only optimizes throughput, but neglects power optimization. The performance of random algorithms is the worst because their channel allocation has randomness, and the uncontrollable interference leads to deteriorating energy efficiency.

Figure 3 displays the performance of all algorithms in terms of Energy Efficiency (EE) across varying numbers of Device-to-Device (D2D) pairs. An observation from the figure reveals that the energy efficiency demonstrates an increasing trend as the number of D2D pairs increases. It is obvious that a larger number of D2D pairs corresponds to a higher energy efficiency (EE) of the system. This is attributed to the fact that D2D short-distance communication allows for higher transmission rates at the same transmission power. As a result, increasing the number of D2D pairs enhances the overall energy efficiency of the system. Upon comparing our proposed algorithm with other schemes, it is evident that our proposed algorithm outperforms the others in terms of performance. It achieves a 57, 60, 63% improvement over Iterative Robust Random algorithms, respectively.

5 Conclusions and Future Work

This paper presents a novel power allocation and resource allocation scheme for UAV-assisted Device-to-Device (D2D) communication. The proposed scheme aims to maximize energy efficiency of the system through effective power allocation and resource allocation strategies. In this scheme, the Nash equilibrium point of non-cooperative game is used to solve the optimum power allocation and resource allocation problems is modeling as a bipartite graph matching problem. In order to achieve maximum energy efficiency, Hungary algorithm is used to obtain the best match for channel multiplexing. From the simulation results, this scheme has great advantages and great feasibility compared with some other existing schemes.

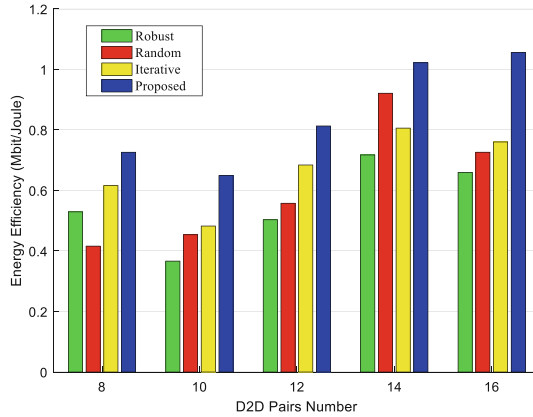


Fig. 3. Energy efficiency versus D2D pairs number

Acknowledgment. This work was supported in part by the National Natural Science Foundation of China (Grant No. 61973104, 62173127 and 61803146). The key Research Projects of Henan Higher Education Institutions(Grant No. 20B510003). Doctoral Foundation (Grant No. 2018BS074). Open Fund of Key Laboratory of Grain Information Processing and Control (Grant No. KFJJ-2020-114, KFJJ-2020-111 and Grant No. KFJJ-2020- 115). The Scientific and Technological Project in Henan Province of China (Grant No. 212102210169, 212102310296 and 212102210086).

References

1. Fang, T., Wu, D., Wang, M.: Multi-stage hierarchical channel allocation in UAV-assisted D2D networks: a stackelberg game approach. *China Commun.* **18**(2), 13–26 (2021)
2. Ghosh, S., Bhowmick, A., Roy, D.: UAVs-assisted multi-Hop D2D communication using Hybrid PTS for disaster management. In: 2023 5th International Conference on Recent Advances in Information Technology (RAIT), pp. 1–6 (2023)
3. Zhang, T., Wang, Y., Yi, W.: Joint optimization of caching placement and trajectory for UAV-D2D networks. *IEEE Trans. Commun.* **70**(8), 5514–5527 (2022)
4. Nguyen, T., Tuan, D., Duong, Q.: Joint D2D assignment, bandwidth and power allocation in cognitive UAV-enabled networks. *IEEE Trans. Cognit. Commun. Netw.* **6**(3), 1084–1095 (2020)
5. Budhiraja, I., Kumar, N., Tyagi, S.: Energy efficient mode selection scheme for wireless powered D2D communications with NOMA underlying UAV. In: IEEE INFOCOM 2020—IEEE Conference on Computer Communications Workshops (INFOCOM WKSHPS), pp. 877–882 (2020)
6. Zhong, X., Guo, Y., Li, N.: Joint optimization of relay deployment, channel allocation, and relay assignment for UAVs-aided D2D networks. *IEEE/ACM Trans. Netw.* **28**(2), 804–817 (2020)
7. Shang, B., Liu, L., Rao, M.: 3D spectrum sharing for hybrid D2D and UAV networks. *IEEE Trans. Commun.* **68**(9), 5375–5389 (2020)
8. Liu, D., Xu, Y., Wang, J.: Opportunistic utilization of dynamic multi-UAV in device-to-device communication networks. *IEEE Trans. Cognit. Commun. Netw.* **6**(3), 1069–1083 (2020)

9. Hou, Z., Huang, Y., Chen, J.: Joint IRS selection and passive beamforming in multiple IRS-UAV enhanced anti-jamming D2D communication networks. *IEEE Internet Things J.* 1–1 (2023)
10. Tuong, D., Noh, W., Cho, S.: Sparse CNN and deep reinforcement learning-based D2D scheduling in UAV-assisted industrial IoT networks. *IEEE Trans. Ind. Inf.* 1–11 (2023)
11. Alsharoa, A., Yuksel, M.: Energy efficient D2D communications using multiple UAV relays. *IEEE Trans. Commun.* **69**(8), 5337–5351 (2021)
12. Huq, S., Mumtaz, S., Zhou, Z.: Energy-efficiency maximization for D2D-enabled UAV-aided 5G networks. In: *ICC 2020—2020 IEEE International Conference on Communications (ICC)*, pp. 1–6 (2020)
13. Xu, Y., Liu, Z., Huang, C.: Robust resource allocation algorithm for energy-harvesting-based D2D communication underlying UAV-assisted networks. *IEEE Internet Things J.* **8**(23), 17161–17171 (2021)
14. Suman, S., Kumar, S., De, S.: Path loss model for UAV-assisted RFET. *IEEE Commun. Lett.* **22**, 2048–2051 (2018)
15. Jing, Y., Yang, M., Pan, W.: Pricing scheme based on the nash equilibrium point. In: *2006 6th World Congress on Intelligent Control and Automation*, pp. 7143–7146 (2006)



Energy Efficient Multi-aerial Base Station Deployment Via DDPG-Mix Algorithm

Haoran He, Yikun Zhao, Jinli Zhang, Fanqin Zhou, Wenjing Li^(✉),
and Lei Feng

State Key Laboratory of Networking and Switching Technology, Beijing University of
Posts and Telecommunications, Beijing, China
wjli@bupt.edu.cn

Abstract. Compared to ground base stations, aerial base stations (AeBSs) offer advantages in terms of overcoming limitations posed by complex terrain and transportation constraints, providing broader coverage and faster response speeds. In this paper, we investigate the problem of energy efficiency maximization in a multiple AeBSs network and adopt multi-agent deep reinforcement learning (MADRL) for the deployment of AeBSs. Specifically, considering the partial observation range of AeBSs, the multi-AeBS deployment problem is modeled as a decentralized partially observable markov decision process (Dec-POMDP) and a deep deterministic policy gradient mix (DDPG-MIX) algorithm is designed to solve the problem. The proposed algorithm uses the value decomposition framework to solve the lazy agent problem. Simulation results show that our proposed DDPG-MIX algorithm performs better than other baseline algorithms in the multi-AeBS deployment scenario.

Keywords: Aerial base station · Multi-agent deep reinforcement learning · Value decomposition

1 Introduction

The aerial base station (AeBS) is a mobile base station that installs communication equipment on the aerial platform, such as unmanned aerial vehicle (UAV), and plays an important role in the space-air-ground integrated network. Considering its limited energy support, maximizing system energy efficiency through the reasonable deployment of multi-AeBSs has become a prominent research topic [1]. In the deployment of AeBSs, the traditional heuristic algorithm needs repeated calculation, while deep reinforcement learning (DRL) provides a novel paradigm for decision systems to accumulate and utilize experience in the environment. With the increase in the number of AeBSs to be controlled, researchers use multi-agent deep reinforcement learning (MADRL) to deploy multi-AeBS. For the joint deployment of multi-AeBS, MADRL can solve the problem of large action space existing in centralized single-agent DRL. Considering the ability of AeBSs to observe the state of other AeBSs within a certain range, several recent

works have adopted the decentralized partially observable Markov decision process (Dec-POMDP) [2] to model the AeBSs deployment problem.

In a cooperative task scenario of partial observable reinforcement learning, the environment is typically non-stationary because the dynamics change as agents learn and update their policies. This non-stationarity makes it challenging to accurately estimate the value function or Q-function for each agent, as their actions affect the environment and the rewards received by other agents. Traditional value-based methods struggle to appropriately assign credit to individual agents for their contributions to collective behavior, which may lead to the training of lazy agents with poor performance [3]. Value decomposition algorithms are thus introduced to tackle these challenges. Value decomposition algorithms, such as QMIX [4] and VDN [5], mitigate the issue of lazy agents in multi-agent reinforcement learning by decomposing the global value function into individual value functions, encouraging active participation and optimizing contributions of each agent to the cooperative behavior. This improves coordination and cooperation, resulting in enhanced performance of the multi-agent system.

In this paper, we study the deployment problem of AeBSs, with the goal of maximizing the energy efficiency of the multi-AeBS system. Specifically, we model the multi-AeBS deployment problem as a Dec-POMDP and propose a Deep Deterministic Policy Gradient-MIX (DDPG-MIX) algorithm to solve the formulated problem. The main contributions of this paper can be concluded as follows:

1. Considering the limited observation range of AeBS, the energy efficiency maximization problem of AeBSs is modeled as Dec-POMDP and the DDPG-MIX algorithm is designed, in which the idea of value decomposition is introduced to clarify the contribution of each agent action to the total value function and address the lazy agent problem in the multi-agent cooperative task, and DDPG is adopted to handle the continuous action space associated with the AeBS deployment problem.
2. The simulation results show that the performance of our proposed DDPG-MIX algorithm is better than other baseline DRL algorithms, and the value decomposition can improve the deployment performance of multi-AeBS.

The rest of the paper is organized as follows. The system model and problem formulation are depicted in Sect. 2. Then, the DDPG-MIX algorithm for multi-AeBS deployment is specified in Sect. 3. Section 4 presents the discussions of simulation results. Finally, Sect. 5 concludes the paper.

2 System Model

2.1 Air-to-Ground Channel Model

AeBSs and UEs transmit data over an air-to-ground (A2G) channel. The signal transmitted by AeBS suffers from both free space path loss and excessive path loss. Therefore, the A2G mean path loss between UE u and AeBS m can be modeled as:

$$L_{LoS}^{m,u} = L_{FS}^{m,u} + \eta_{LoS}, \quad (1)$$

$$L_{NLoS}^{m,u} = L_{FS}^{m,u} + \eta_{NLoS}, \quad (2)$$

where $L_{FS}^{m,u}$ represents the free space path loss which can be expressed as $L_{FS}^{m,u} = 20 \log(4\pi f_c d_{m,u}/c)$, where c is the speed of light, f_c is the carrier frequency, and $d_{m,u}$ is the distance between AeBS m and UE u . η_{LoS} and η_{NLoS} refer to the mean value of the excessive path loss under the line-of-sight (LoS) environment and non-line-of-sight (NLoS) environment, respectively.

The probability of LoS is related to the communication environment constants α, β and elevation angle $\theta_{m,u}$ between AeBS m and UE u , which can be expressed as [6]:

$$P_{LoS}^{m,u} = \frac{1}{1 + \alpha \exp[-\beta(\theta_{m,u} - \alpha)]}. \quad (3)$$

And the probability of NLoS can be obtained as $P_{NLoS}^{m,u} = 1 - P_{LoS}^{m,u}$.

As a result, the average path loss between UE u and AeBS m is as follows:

$$L_{m,u} = P_{LoS}^{m,u} \times L_{LoS}^{m,u} + P_{NLoS}^{m,u} \times L_{NLoS}^{m,u}. \quad (4)$$

2.2 Beam Scheduling

Besides the A2G propagation path loss, the directional mmWave antenna gain is also an important factor in the AeBS channel. In this work, we suppose that a 3D beam has the same gain G_M within its beamwidth and a small constant sidelobe gain G_S outside the beamwidth, The main lobe gain G_M can be obtained as follows [7]:

$$G_M = \frac{2 - (2 - (1 - \cos \delta_u)) G_S}{1 - \cos \delta_u}. \quad (5)$$

In the procedure of 3D beam alignment, the time cost τ can be derived as [7]:

$$\tau = \frac{1 - \cos \delta_{T,s}}{1 - \cos \delta_{T,u}} \cdot \frac{1 - \cos \delta_{R,s}}{1 - \cos \delta_{R,u}} T_p, \quad (6)$$

where $\delta_{T,s}$ and $\delta_{R,s}$ depict the sector width at transmitter and receiver respectively, $\delta_{T,u}$ and $\delta_{R,u}$ represent the beamwidth of the beam link from AeBS m to UE u at both ends, T_p is the time when the beam traverses through the entire sector and sends a pilot signal at each position for alignment.

Due to the strong directivity of the narrow mmWave beam, it is required to conduct beam scanning to cover the whole considered area. When the number of associated UEs is higher than the beams of the AeBS, a round-robin scheme needs to be adopted for beam scheduling. The average ratio of time-frequency resources η_u occupied by UE u is approximated as:

$$\eta_u = \begin{cases} 1, & N_b \leq N_u, \\ \frac{N_b}{N_u}, & N_b > N_u, \end{cases} \quad (7)$$

where N_b is the number of mmWave beams of the AeBS and N_u is the number of UEs. In the following part, we take beam alignment time cost and resource utilization ratio into consideration when modeling the capacity.

2.3 Capacity Model

Each UE is associated with the unique AeBS with the strongest received signal, and the signal interference of other AeBSs to this UE is considered. If AeBS m and UE u are associated, the noise ratio (SINR) ξ_u of the signal received at UE u can be approximated as:

$$\xi_u = \frac{P_m G_{T,M} G_{R,M} L_{m,u}^{-1}}{I_{other} + \sigma^2}, u \in U, \quad (8)$$

where P_m is the transmit power of AeBS m , σ^2 denotes the power of thermal noise, $I_{other} = \sum_{i \in M(i \neq m)} P_i G_{T,M} G_{R,M} L_{i,u}^{-1}$ denotes the interference from other AeBSs, $G_{T,M}$ and $G_{R,M}$ are the main lobe antenna gain of transmitter and receiver. $G_{T,M}$ and $G_{R,M}$ are calculated from $G_{T,S}$ and $G_{R,S}$ according to (5), where $G_{T,S}$ and $G_{R,S}$ are the side lobe antenna gain of transmitter and receiver. In this paper, each UE selects the AeBS with the largest SINR for association.

Then the capacity of user u can be expressed as:

$$\varrho_u = \eta_u \left(1 - \frac{\tau}{T}\right) B \log_2(1 + \xi_u), \quad (9)$$

where B represents the channel bandwidth, τ is the beam alignment time in (6), T is the time slot and τ needs to be less than one slot T to ensure enough time for data transmission.

The system capacity can be expressed as:

$$\varrho = \sum_{i=1}^n \left[\sum_{u \in \mathcal{U}_i} \varrho_u \right]. \quad (10)$$

2.4 Energy Consumption Model

The energy consumption of the system is divided into two parts, the first part is the propulsion power consumption of the AeBSs, and the second part is the communication energy consumption of the AeBSs serving UEs.

The propulsion power consumption P_w [8] of the AeBS can be modeled as:

$$P_w = P_0 \left(1 + \frac{3V^2}{U_t^2}\right) + P_1 \left(\sqrt{1 + \frac{V^4}{4v_0^4}} - \frac{V^2}{2v_0^2}\right)^{1/2} + \frac{1}{2} d_0 \rho s A V^3, \quad (11)$$

where P_0 and P_1 are the blade profile power and induced power in the hovering status of AeBS, U_t denotes the tip speed of the rotor blade, v_0 is known as the mean rotor induced velocity in hover, d_0 is the fuselage drag ratio, s is the rotor solidity, ρ is the air density and A is the rotor disc area.

The communication power consumption P_c of the AeBS can be modeled as:

$$P_c = \sum_{u \in \mathcal{U}_m} P_{m,u}, \quad (12)$$

where $P_{m,u}$ is the transmitting power of AeBS m to UE u .

The total energy consumption definition of the system is modeled as follows:

$$P_{tot} = \sum_{i=1}^n [P_{w,i} + P_{c,i}]. \quad (13)$$

where $P_{w,i}$ and $P_{c,i}$ the propulsion power consumption and communication power consumption of the i -th AeBS, n is the number of AeBSs.

2.5 Problem Formulation

Our goal in this work is to maximize the energy efficiency of the entire system. The energy efficiency of the system J_m is defined as follows:

$$J_{tot} = \frac{Q}{P_{tot}}. \quad (14)$$

Consequently, the formulation of the optimization problem is as follows:

$$\begin{aligned} & \max_{(x_m, y_m, h_m)} J_{tot} \\ \text{s.t.} \quad & \text{C1 : } x_m \in [x_{\min}, x_{\max}], \forall m \in M, \\ & \text{C2 : } y_m \in [y_{\min}, y_{\max}], \forall m \in M, \\ & \text{C3 : } h_m \in [h_{\min}, h_{\max}], \forall m \in M, \\ & \text{C4 : } (x_m, y_m, h_m) \neq (x_l, y_l, h_l), \\ & \quad \forall m, l \in M, m \neq l, \\ & \text{C5 : } V_m \leq V_{max}, \forall m \in M, \end{aligned} \quad (15)$$

where J_{tot} energy efficiency in (14). C1–C3 constrain AeBSs from flying out of the considered region, and C4 is the collision restriction. C5 ensure that each AeBS does not move faster than the maximum speed V_{max} .

3 Deep Deterministic Policy Gradient-Mix Algorithm for AeBS Deployment

3.1 Reinforcement Learning Framework

First of all, we transform the multi-AeBS deployment optimization problem as a Dec-POMDP and each AeBS is regarded as an agent. The observation, action, and reward are defined as follows:

Observation: Each AeBS has an observation range, the observation of each AeBS is the current position of the AeBS and the position of other AeBSs within its observation range $o_m = (o_{1xm}, o_{1ym}, o_{2xm}, o_{2ym}, \dots, o_{n xm}, o_{n ym})$, $o_m \in O, m \in \{1, 2, \dots, n\}$, where o_{1xm}, o_{1ym} respectively represent the X-axis position and Y-axis position of the AeBS itself. Other observed values represent

the X-axis position and Y-axis position of other AeBSs. When other AeBSs are not in the observation range, the corresponding observation value is 0.

Action: The action of each agent is the distance traveled in the X-axis and Y-axis $a_m = \{(\Delta x_m, \Delta y_m)\}$, $a_m \in A, m \in \{1, 2, \dots, n\}$.

Reward: As a fully cooperative reinforcement learning scenario, reward is the system energy efficiency in Eq. (2.5).

3.2 DDPG-MIX

For a single agent in a cooperative multi-agent scenario, its reward is likely to be affected by the behavior of its teammates. In this situation, the issue of lazy agents may arise, referring to agents that overly rely on the decision-making of their counterparts and fail to actively contribute to cooperative behaviors. Value decomposition algorithms, such as QMIX, are introduced to tackle these challenges. In QMIX, the global value function is decomposed into individual value functions, allowing each agent to optimize its own value function while considering the influence of other agents. By decomposing the value function, QMIX enables better credit assignment and coordination among agents, facilitating more effective learning and decision-making in cooperative multi-agent scenarios.

Nevertheless, QMIX is an extension of deep Q-learning, which is mainly used to deal with the problem of discrete action space. Considering that the action space for the deployment of AeBSs is continuous, this paper proposes to integrate the idea of QMIX into the deep deterministic policy gradient (DDPG), which can deal with the continuous action space, and proposes DDPG-MIX algorithm to address the multi-AeBS deployment problem.

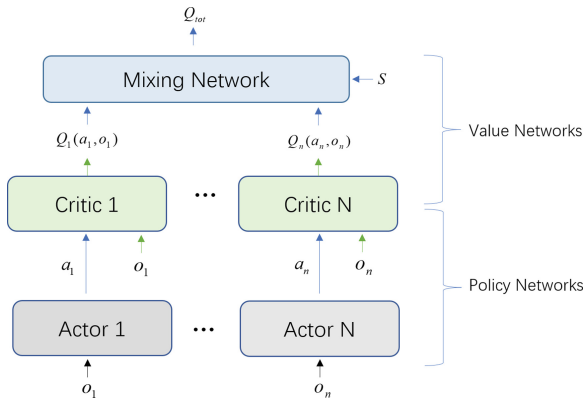


Fig. 1. The structure of DDPG-MIX.

The structure of DDPG-Mix is presented in Fig. 1. Specifically, each agent applies the DDPG to learn individual action value. DDPG is divided into two

networks, actor network and critic network, the actor network generates the actions of the agent, and the critic network evaluates the action and generation value of the action.

We employ value function decomposition in the multi-agent actor-critic framework [9]. The Q value of critic network Q_n and the multi-agent global state s_t are input into value mixing network, and the total value Q_{tot} of joint action is obtained. The value mixing network module uses a deep neural network to aggregate the values of each agent into a total value. Q_{tot} stands for total value of joint actions, which can be formulated as:

$$Q_{tot} = f_s(Q_1(a_1, o_1), \dots, Q_n(a_n, o_n)), \frac{\partial f_s}{\partial Q_n} \geq 0, \quad (16)$$

where s is the global state, a_n is the action of the n -th agent.

The distributed critic is optimized by minibatch gradient descent to minimize the following loss:

$$\begin{aligned} L(\theta_q) &= (y_t - Q_{tot})^2 \\ &= (y_t - f_s(Q_1(a_1, o_1), \dots, Q_n(a_n, o_n)))^2, \end{aligned} \quad (17)$$

where f_s denotes the mixing network and y_t is the target value.

4 Simulation Results and Discussions

Simulation is carried out in a 2 km \times 2 km environment, and the channel environment $(\alpha, \beta, \eta_{LoS}, \eta_{NLoS})$ is (9.61, 0.16, 1, 20). The maximum length of each step in the direction (x_m, y_m) is 100 m, the flight altitude of AeBSs is 20 m, and the observation range of AeBSs is 200 m. The layers of actor and critic are 4, the learning rate is set as 0.01, the layer type of actor and critic is fully connected, the neurons of hidden layers for each actor and critic is [64,64], the optimizer is Adam, the activation Function is ReLU, the soft updating rate is set as 0.5, the ϵ in ϵ -greedy is set as 0.1, the memory size is set as 10,000, and the batch size is set as 256. The simulation parameters of the environment are listed in Table 1.

We compare our proposed DDPG-MIX with the other DRL algorithms below:

1. VDN: VDN [5] is a classical value decomposition reinforcement learning framework, which uses a linear function to aggregate the values of each agent into a total value.
2. IDDPG [10]: IDDPG is a fully distributed algorithm. In IDDPG, each AeBS makes decisions based on its own observation.

Figure 2 shows the impact of the number of UEs on network performance. By comparing our proposed scheme with the other two DRL algorithms, it can be found that the IDDPG has the worst performance in energy efficiency. This is because IDDPG does not introduce the idea of value decomposition, which leads to the lazy agent problem, resulting in poor performance of the multi-AeBS

Table 1. The simulation parameters of the environment

Simulation parameters	Values
Speed of light c	3×10^8 m/s
Channel bandwidth B	150 MHz
Carrier frequency f_c	30 GHz
Sector width $\delta_{T,s}, \delta_{R,s}$	$\pi/2, \pi/2$
Beamwidth $\delta_{T,u}, \delta_{R,u}$	$\pi/6, \pi/6$
Pilot duration ratio T_p/T	2×10^{-4}
Side lobe gain $G_{T,S}, G_{R,S}$	0.1, 0.1
Thermal noise power density	-174 dBm/Hz
Tip speed of the blade U_t	60 m/s
Mean induced speed v_0	2.486 m/s
Lade profile power P_0	112.203 W
Induced power P_i	10.574 W
Fuselage drag proportion d_0	0.5
Air density ρ	1.225 kg/m^3
Rotor solidity s	0.0832
Rotor disc area A	0.2827 m^2

deployment algorithm. Simulation results show that the algorithm of DDPG-MIX has the best performance in energy efficiency. And by comparing DDPG-MIX and VDN, it can be found that the energy consumption of these two algorithms is similar, but DDPG-MIX improves the capacity and then improves the energy efficiency of the system.

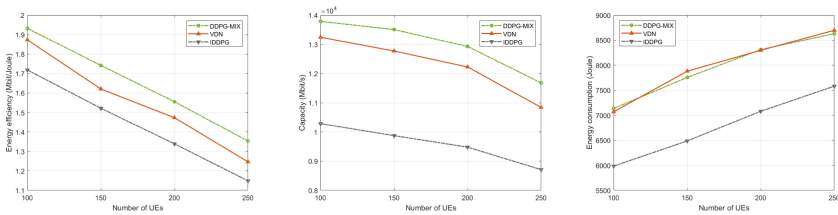


Fig. 2. Comparison of network performance metrics in different numbers of UEs. **a** Energy efficiency. **b** Capacity. **c** Energy consumption

Figure 3 shows the impact of the number of AeBSs on network performance. It can be found that with the increase of AeBSs, the energy efficiency, capacity, and energy consumption of the system show an increasing trend. Although the increase in the number of AeBS will indicate the total energy consumption of

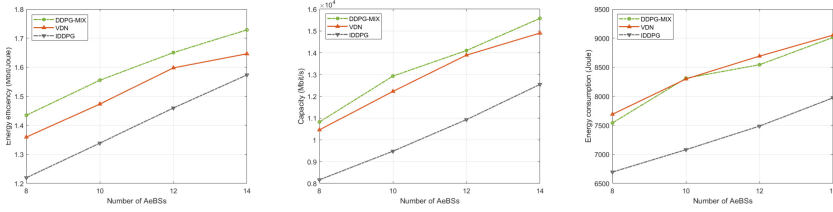


Fig. 3. Comparison of network performance metrics in different numbers of AeBSs. **a** Energy efficiency. **b** Capacity. **c** Energy consumption

the system, it can better serve the users within the system and improve the total system capacity, thus improving the energy efficiency of the system. By comparing Figs. 2 and 3, we can find that the algorithm performance of DDPG-MIX is better than that of other algorithms.

5 Conclusion

This paper models the deployment problem of multi-AeBS as a Dec-POMDP and adopts the MADRL framework to maximize the energy efficiency of the system. Especially, a novel algorithm called DDPG-MIX is designed to solve the optimization problem. The algorithm uses the value decomposition framework to solve the lazy agent problem. Simulation results show that the performance of our proposed DDPG-MIX algorithm is better than other algorithms, which can improve the energy efficiency of multi-AeBS system and enhance the efficiency of joint deployment of multi-AeBS.

Acknowledgments. This work was supported by the National Natural Science Foundation of China (Grant No. 61971053) and BUPT Innovation and Entrepreneurship Support Program (2023-YC-A131).

References

1. Dai, B., Niu, J., Ren, T., Hu, Z., Atiquzzaman, M.: Towards energy-efficient scheduling of UAV and base station hybrid enabled mobile edge computing. *IEEE Trans. Veh. Technol.* **71**(1), 915–930 (2021)
2. Yin, S., Yu, F.R.: Resource allocation and trajectory design in UAV-aided cellular networks based on multiagent reinforcement learning. *IEEE Internet Things J.* **9**(4), 2933–2943 (2021)
3. Sharma, P.K., Fernandez, R., Zaroukian, E., Dorothy, M., Basak, A., Asher, D.E.: Survey of recent multi-agent reinforcement learning algorithms utilizing centralized training. In: *Artificial Intelligence and Machine Learning for Multi-domain Operations Applications III*, vol. 11746, pp. 665–676. SPIE (2021)
4. Rashid, T., Samvelyan, M., De Witt, C.S., Farquhar, G., Foerster, J., Whiteson, S.: Monotonic value function factorisation for deep multi-agent reinforcement learning. *J. Mach. Learn. Res.* **21**(1), 7234–7284 (2020)

5. Li, J., Kuang, K., Wang, B., Liu, F., Chen, L., Fan, C., Wu, F., Xiao, J.: Deconfounded value decomposition for multi-agent reinforcement learning. In: International Conference on Machine Learning, pp. 12843–12856. PMLR (2022)
6. Al-Hourani, A., Kandeepan, S., Lardner, S.: Optimal LAP altitude for maximum coverage. *IEEE Wirel. Commun. Lett.* **3**(6), 569–572 (2014)
7. Zhu, L., Zhang, J., Xiao, Z., Cao, X., Wu, D.O., Xia, X.G.: 3D beamforming for flexible coverage in millimeter-wave UAV communications. *IEEE Wirel. Commun. Lett.* **PP**(3), 1–1 (2019)
8. Zeng, Y., Xu, J., Zhang, R.: Energy minimization for wireless communication with rotary-wing UAV. *IEEE Trans. Wireless Commun.* **18**(4), 2329–2345 (2019)
9. Su, J., Adams, S., Beling, P.: Value-decomposition multi-agent actor-critics. In: Proceedings of the AAAI Conference on Artificial Intelligence, vol. 35, no. 13, pp. 11 35–11360 (2021)
10. Ciftler, B.S., Alwarafy, A., Abdallah, M.: Distributed DRL-based downlink power allocation for hybrid RF/VLC networks. *IEEE Photonics J* (2021)



Deep Learning-Based Beam Alignment and Tracking Mechanism for mmWave Aerial Base Station

Yikun Zhao, Jinli Zhang, Fanqin Zhou, Wenjing Li^(✉), and Lei Feng

State Key Laboratory of Networking and Switching Technology, Beijing University of Posts and Telecommunications, Beijing, China
wjli@bupt.edu.cn

Abstract. Millimeter wave (mmWave) aerial base stations offer distinct advantages such as enhanced flexibility and mobility compared to ground base station communication. Additionally, the utilization of mmWave technology enables the provision of high-speed, directional services to ground users while mitigating interference with existing ground networks. To establish a good communication link between mmWave aerial base stations and terrestrial mobile users, it is essential for base stations to form directional beam to cover terrestrial users. However, the movement of users and the change of environmental factors will lead to the misalignment between the mmWave beam formed by the base stations and the users, resulting in the instability of the communication link, which will seriously affect the quality of communication service. Therefore, this paper proposes a deep learning-based beam tracking scheme for mmWave aerial base stations. Simulation results show that our proposed schemes achieve higher beamforming gain and require less beam training overhead compared to existing conventional and deep learning-based approaches.

Keywords: mmWave aerial base stations · Beam alignment · Beam tracking · Deep learning

1 Introduction

With the unmanned aerial vehicle (UAV) technology rapidly advances, UAVs as aerial base stations to assist wireless communication have become an important research field. However, the microwave bands in the sub-6 GHz band, which are already widely used in terrestrial communication networks, are becoming very crowded, facing serious spectrum scarcity and numerous interference problems. In contrast, mmWave communication offers abundant spectrum resources with bandwidths exceeding 150 GHz [1]. This enables mmWave communication to achieve higher transmission rates, as successfully demonstrated in satellite communication and short-range indoor field communication applications [2]. Relevant data show that the bidirectional data rate peak of an air-to-ground (A2G) E-band communication link has reached 40 Gbps [3]. Secondly, in mmWave communication, due to the short wavelength of mmWave signals, a compact

antenna array can be employed to effectively mitigate propagation loss and enhance array gain [4]. It is very suitable for UAV communication. mmWave can also achieve higher channel gain than full coverage by forming a flexible directional beam, so as to improve the spectral efficiency of mmWave aerial base station communication and increase the transmission distance. Furthermore, it will effectively reduce the high loss in the transmission process and greatly improve the performance and quality of mmWave aerial base station communication [5].

Consequently, the combination of UAVs and mmWave technology provides more opportunities for future communication networks, and also have high technical potential and wide application prospects. However, due to the mobility of both the user and the mmWave aerial base station, their relative positions constantly change, leading to potential variations in the channel between them, which poses great challenge on the performance of directional mmWave communication.

To address this problem, this paper proposes an effective scheme for beam alignment and beam prediction tracking between aerial base stations and mobile users. Considering the mobility of users and the complexity of the environment, deep learning algorithms are used in this paper for beam alignment and predictive tracking. Our main contributions can be summarized as follows:

- We utilize a Long Short-Term Memory (LSTM)-based beam training model to realize the beam prediction and tracking for mmWave aerial base stations. Specially, the cascade LSTMs structure is constructed to solve the problem that the beam training moment is not synchronized with the received information characteristics.
- We generate the data set for beam training of mmWave aerial base stations and conduct simulation verification of the proposed scheme. Results show that the proposed scheme can achieve higher beamforming gain and more stable performance than the baseline schemes, especially for the scenario of high-speed user movement.

2 System Model

The specific system model diagram is shown in Fig. 1. It is assumed that two mmWave aerial base stations are located directly above the vertical points A and B in the figure, respectively. They maintain a hovering state to provide services for mobile users distributed on the ground. We assume that user equipment (UE) moves in a straight line with velocity v m/s, and motion direction is from 0 to 2π . We consider that the mmWave aerial base station is equipped with $M = N_x \times N_y$ uniform linear array antenna and UE is equipped with a single antenna. It is simply considered that the BS side adopts a single RF chain, and all antennas are connected to it using an analog phase shifter. To precisely represent the beam variation resulting from UE movement and faithfully simulate the nonlinear correlation between UE motion and beam changes, DeepMIMO data set generated by accurate ray tracing based on SV channel model is adopted [6].

A2G Channel Model. The A2G channel model adopts the SV channel model [7], where the channel vector $\mathbf{h}_n \in C^{M \times 1}$ of the time slot N can be expressed as

$$\mathbf{h}_n = \sum_{l=1}^{L_n} \sqrt{\frac{1}{\rho_{n,l}}} \alpha_{n,l} \mathbf{a}^*(\phi_{n,l}); \quad (1)$$

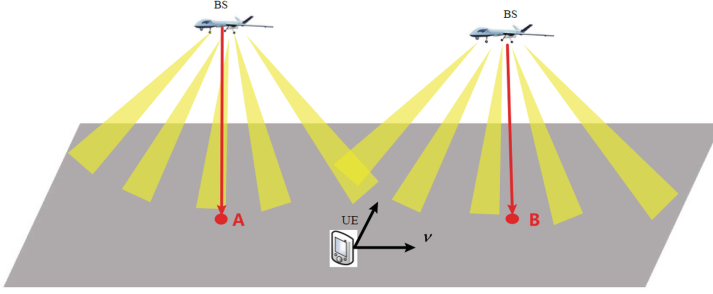


Fig. 1. System model

where L_n represents the number of paths at the time slot n , the path loss of the l -th path is represented by $\rho_{n,l}$, the complex gain is represented by $\alpha_{n,l}$, and the angle of departure (AoD) is represented by $\phi_{n,l}$. In addition, for the sake of simplicity, the model only considers the selection of the optimal beam of the transmitting base station. The UE is equipped with a single antenna, so the selection of the receiving beam is omitted. Meanwhile, the mmWave aerial base station is equipped with a uniform linear array. The base station's antenna response vector is represented by $\mathbf{a} \in \mathbb{C}^{M \times 1}$, which can be expressed as.

$$\mathbf{a}(\phi) = \left[1, e^{j2\pi d \sin \phi / \lambda}, \dots, e^{j2\pi (M-1) d \sin \phi / \lambda} \right]^T, \quad (2)$$

where d denotes the antenna size while λ represents the wavelength. And simply assuming that $d = \frac{\lambda}{2}$.

Beam Training Model. Analog beamforming technology based on phase shifters is considered and we use the Discrete Fourier Transform codebook [8] containing Q candidate beams. The mmWave aerial base station selects a transmitting beam $f_n \in \mathbb{C}^{M \times 1}$ from the codebook at the time slot N , then the q -th candidate transmitting beam $f^{(q)} \in \mathbb{C}^{M \times 1}$ ($q \in \{0, 1, 2, \dots, Q-1\}$) can be expressed as

$$f^{(q)} = \sqrt{\frac{1}{M}} \left[1, e^{j\frac{2\pi}{Q}q}, \dots, e^{j\frac{2\pi}{Q}(M-1)q} \right]^T. \quad (3)$$

Then the received signal y is

$$y = \sqrt{P} h^T f x + n_{AWGN}, \quad (4)$$

where P is the transmitted power, h^T represents the channel matrix, and n_{AWGN} represents the additional white Gaussian noise.

Beam training aims to find the optimal transmitting beam with the highest beamforming gain among the candidate beams, i.e.:

$$q^* = \underset{q \in \{1, 2, 3, \dots, Q\}}{\operatorname{argmax}} \left| h^T f^{(q)} \right|^2, f^{(q)} \in \mathbb{C}^{M \times 1}. \quad (5)$$

The normalized beamforming gain G_N was used for performance evaluation, defined as

$$G_N = \frac{|h^T f(\hat{q}^*)|^2}{|h^T f(q^*)|^2}, \quad (6)$$

where h^T represents the channel matrix, q^* represents the optimal beam in the beam training stage, and \hat{q}^* represents the optimal beam with the greatest prediction probability finally selected after processing by the deep learning model. The average result of three runs is used as the metric, considering that the performance of a deep learning model can be sensitive to its initialization during training.

The beam training period is defined as T , and the moment of the n -th beam training is t_n . For any prediction instant \bar{t} , the normalized prediction instant $\bar{\tau}$ related to T can be calculated as

$$\bar{\tau} = \frac{\bar{t} - t_n}{T}. \quad (7)$$

Using the received signal of the previous beam training as the prediction input, the received signal vector of the n -th beam training is $y_n = [y_n^{(1)}, y_n^{(2)}, y_n^{(3)}, \dots, y_n^{(Q)}]$. $y_n^{(Q)}$ is the received signal corresponding to the q -th beam. Considering the limited size of the candidate transmitting beam, the problem can be viewed as multiple classification tasks [9], i.e.:

$$q^*(\bar{t}) = g((y_1, y_2, y_3, \dots, y_n), \bar{\tau}), q^*(\bar{t}) \in \{1, 2, 3, \dots, Q\}, \quad (8)$$

where $q^*(\bar{t})$ is the optimal narrow beam index of moment \bar{t} , and $g(\cdot)$ is the classification function.

3 LSTM Assisted Beam Prediction Tracking and Alignment

Because of its excellent ability in time series learning [10], LSTM is utilized in the beam prediction model. The basic structure of the LSTM is depicted in Fig. 2. The input of the current time slot x_t along with the previous time slot's output $\{c_{t-1}, h_{t-1}\}$ are jointly taken into the LSTM module. This allows LSTM module to capture relevant features from the previous inputs.

In the periodic beam training process, the received signal of the t -th wide beam training is denoted as y_t . The received signals from the previous beam training $\{y_1, y_2, \dots, y_{t-1}\}$ are combined with the received signal from the current wide beam training y_t . The received wide beam training signal and its corresponding optimal narrow beam index are organized in chronological order to create a training sample for moving UE. LSTM module adjusts the narrow beam direction according to the received signal from the current beam training and prior beam training. The output module generates the prediction probability, allowing the selection of the beam with the highest probability as the optimal beam for prediction.

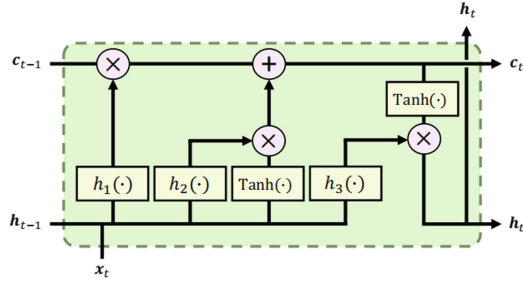


Fig. 2. Basic structure of LSTM.

Conventional LSTM Beam Prediction Model. The structure flow diagram of the proposed LSTM beam prediction model is given in Fig. 3. The model consists of four components: preprocessing layer, convolution module, LSTM module and output module.

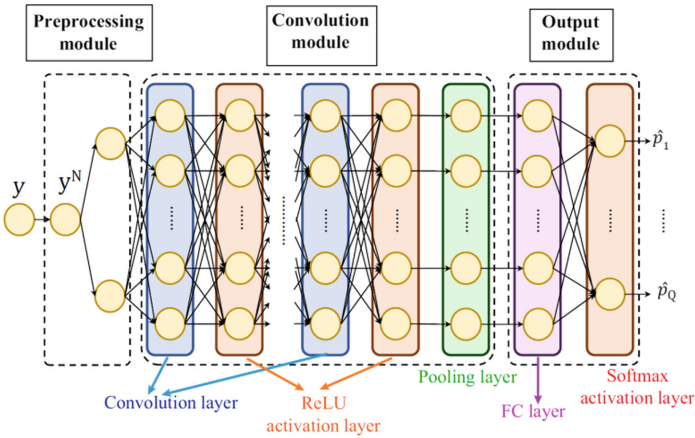


Fig. 3. LSTM beam prediction model structure flow diagram.

- (1) Preprocessing layer: After the t -th beam training, the received signal undergoes preprocessing before entering the convolution module. This preprocessing step is necessary because y is complex-valued and has a dynamic range, making it unsuitable for direct input into the convolution module. Therefore, the preprocessing layer first normalizes the received signal vector y through the maximum value of its elements. The normalized received signal vector y^N is divided into two real-valued feature channels and then it is fed to the convolution module respectively.
- (2) Convolution module: Initially, convolution layers are employed to extract hidden features from the received signal vector y . ReLU is applied for activation and a pooling layer is introduced to down-sample each feature channel into a scalar representation.
- (3) Output module: A fully-connected (FC) layer is subsequently utilized to convert the extracted features into predictions for each candidate beam. The Softmax activation

function is applied to normalize the outputs into probabilities, which can be expressed as follows:

$$\hat{p}_m = \text{softmax}\left(\mathbf{u}_m^T \mathbf{v} + b_m\right), m \in \{1, 2, 3, \dots, Q\}; \tag{9}$$

where \hat{p}_m represents the prediction probability of the m -th candidate beam being optimal; \mathbf{v} is the output vector of the pooled layer; \mathbf{u}_m and b_m are the weight vector and bias associated with the m -th output layer. Then, the optimal prediction beam is selected as the narrow beam with the highest predicted value \hat{m}^* , which can be expressed as follows:

$$\hat{m}^* = \underset{m \in \{1, 2, 3, \dots, Q\}}{\text{argmax}} \hat{p}_m. \tag{10}$$

Cascaded LSTM Beam Prediction Model. When the conventional LSTM model performs beam training, the moment of beam training may be out of sync with the information characteristics of the previously received wide beam training signals. To solve this problem, a cascade LSTMs is proposed. Multiple beam predictions are interpolated between the two previous LSTM learning features. Finally, the predicted beam with the shortest beam training interval is the optimal beam. The flow of the proposed beam prediction model based on the cascaded LSTMs is shown in Fig. 4. The preprocessing layer and convolution module are consistent with the structure in Fig. 3. The difference is the cascaded LSTMs. Γ interpolated beam predictions are inserted and homogeneous sampling is adopted, where Γ -th beam prediction instant is expressed as $t_n + \frac{2\gamma-1}{2\Gamma}T, 1 \leq \gamma \leq \Gamma$. Therefore, the prediction result that is closest to the beam training in time is used as the approximation of the optimal beam.

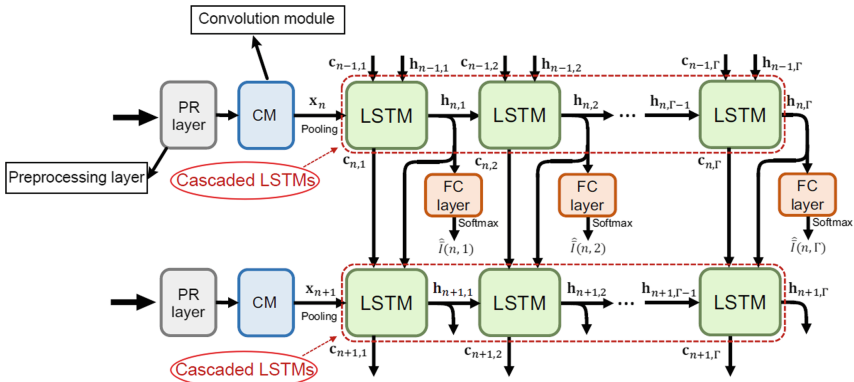


Fig. 4. Cascaded LSTM beam prediction model structure flow diagram.

4 Simulation Analysis

The DeepMIMO data set generator based on SV channel model is used to generate the air-to-ground data set. The specific parameters are listed in Table 1.

Table 1. Generated air-to-ground data set simulation parameters.

Parameters	Value
Scenario	Outdoor 2 ('O2_dyn_3p5')
Number of mAeBSs	2 ([1, 2])
UE location	Row 200 ~ 1000
Center frequency f_c	28 GHz
Bandwidth W	50 MHz
Number of mAeBS antennae M	64
Number of mAeBS beams Q	64
Beam training period T	160 ms
Beam prediction duration	1.6 s
Noise factor N_F	5 dB
Transmit power P	25 dBm
UE motion direction range	$[0, 2\pi]$
UE motion velocity v	$[5, 10, 15, 20, 25, 30]$ m/s
UE motion acceleration a	$[1-6]$ m/s ²

Table 2. LSTM deep learning model parameters.

Structure	Concrete layer	Value
Preprocessing layer	BN	$f_i = 2, f_o = 2$
Convolution module	CNN	$f_i = 2, f_o = 64$
	CNN	$f_i = 64, f_o = 256$
	Pooling layer	$f_i = 256, f_o = 256$
LSTM	LSTM	$f_i = 256, f_o = 256$
Output module	FC	$f_i = 256, f_o = 64, dropout = 0.3$
	<i>Softmax</i> layer	$f_i = 64, f_o = 64$

The specific network structure of the proposed model is shown in Table 2. f_i and f_o represents the number of input and output feature channels respectively.

In addition, the output FC layer utilizes dropout strategies to randomly drop some neurons and their connections during model training, preventing the interdependence of neurons and avoiding overfitting. The proposed deep learning model is fully trained with 60 epochs, and the model parameters are optimized using the Adam optimizer.

Figure 5 shows how the G_N of the EKF [11], the conventional LSTM and cascaded LSTMs schemes change with the instantaneous change of beam training under different UE moving speeds. EKF is a baseline scheme in which the extended Kalman filter is

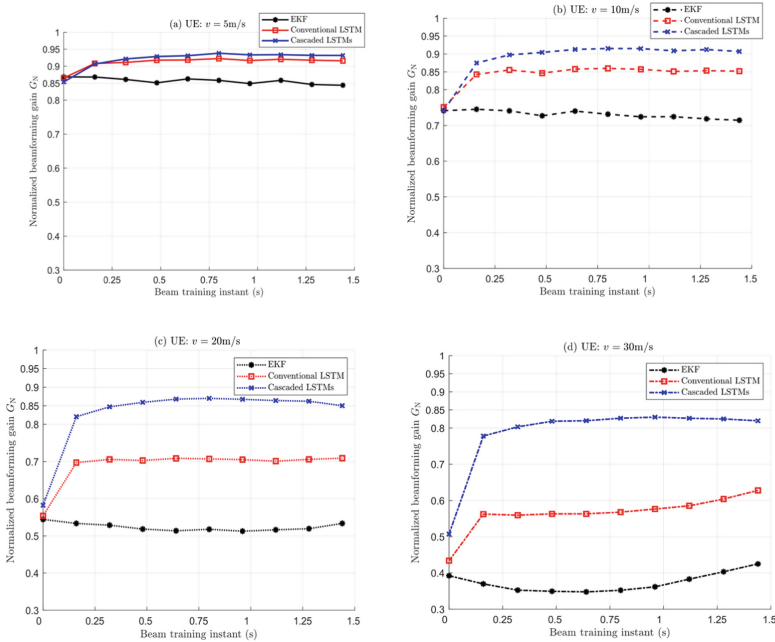


Fig. 5. The G_N of various schemes at different UE moving speeds changes with the beam training moment.

used to train only one beam pair to achieve predictive tracking of the beam. To ensure a fair comparison, the scheme of EKF incorporates angular velocity and acceleration to handle dynamic scenarios. As can be seen from the Fig. 5, the G_N of EKF scheme is the worst compared with the other three schemes. The G_N of conventional LSTM scheme and cascade LSTMs scheme all increase significantly over time and are superior to EKF at the beginning. This is because that the previous beam training received more signals and it could provide more adequate information. In addition, it can be found that the performance of cascaded LSTMs scheme is higher than baseline, and the performance gap is wider with the increase of UE speed.

Figure 6 further shows the G_N of these schemes for various UE movement speeds, focusing on the normalized prediction moment. It can be seen that due to the lack of sufficient ability to simulate the nonlinear relationship between UE motion and angle change, G_N of the EKF scheme decreases significantly at different speeds, especially at (d) from the beginning. Furthermore, in high-speed scenarios, the conventional LSTM scheme demonstrates performance characterized by a single peak, especially in (c) and (d). The peak value appears in the middle of the predicted instant. The conventional LSTM scheme focuses on predicting the optimal beam at a specific normalized moment. In order to minimize the overall performance decline, it tends to prioritize accurate predictions of the optimal beam at the middle moment. The cascade LSTMs scheme solves the single-peak problem of the conventional LSTM scheme by using multiple predictions to approximate the optimal beam of any instant.

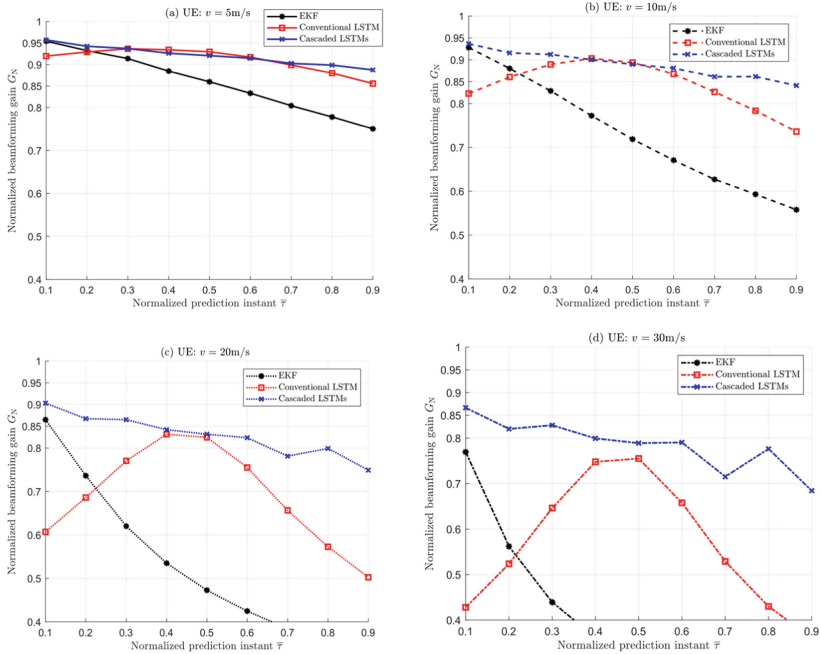


Fig. 6. The G_N of various schemes at different UE moving speeds changes with the normalized prediction moment.

5 Conclusion

This paper selects a suitable A2G channel model according to the specific scenario where aerial base stations apply directional mmWave beams to cover ground users. A beam alignment and predictive tracking scheme based on deep learning is proposed and the appropriate data set is generated for beam training. Results show that under the scenario of high-speed user movement, the proposed scheme can achieve higher beamforming gain and more stable performance than the existing schemes.

Acknowledgements. This work is supported by the National Natural Science Foundation of China (No. 61971053) and BUPT Innovation and Entrepreneurship Support Program (2023-YC-A131).

References

1. Xiao, M., et al.: Millimeter wave communications for future mobile networks. *IEEE J. Sel. Areas Commun.* **35**(9), 1909–1935 (2017)
2. Zhao, J., Gao, F., Wu, Q., Jin, S., Wu, Y., Jia, W.: Beam tracking for UAV mounted SatCom on-the-move with massive antenna array. *IEEE J. Sel. Areas Commun.* **36**(2), 363–375 (2018)
3. Xiao, Z., et al.: A survey on millimeter-wave beamforming enabled UAV communications and networking. *IEEE Commun. Surv. Tutor.* **24**(1), 557–610 (2022)

4. Xiao, Z., Zhu, L., Xia, X.-G.: UAV communications with millimeter-wave beamforming: potentials, scenarios, and challenges. *China Commun.* **17**(9), 147–166 (2020)
5. Wang, X., et al.: Millimeter wave communication: a comprehensive survey. *IEEE Commun. Surv. Tuts* **20**(3), 1616–1653 (2018)
6. Alkhateeb, A.: DeepMIMO: a generic deep learning dataset for millimeter wave and massive MIMO applications. *Proc. ITA*, 1–8 (2019)
7. Saleh, A.A.M., Valenzuela, R.: A statistical model for indoor multipath propagation. *IEEE J. Sel. Areas Commun.* **5**(2), 128–137 (1987)
8. Chen, K., Qi, C., Li, G.Y.: Two-step codeword design for millimeter wave massive MIMO systems with quantized phase shifters. *IEEE Trans. Signal Process.* **68**(1), 170–180 (2020)
9. Ma, K., et al.: Deep learning assisted calibrated beam training for millimeter-wave communication systems. *IEEE Trans. Commun.* **69**(10), 6706–6721 (2021)
10. Wang, T., Wen, C., Jin, S., Li, G.Y.: Deep learning-based CSI feedback approach for time-varying massive MIMO channels. *IEEE Wireless Commun.* **8**(2), 416–419 (2019)
11. Va, V., Vikalo, H., Heath, R.W.: Beam tracking for mobile millimeter wave communication systems. In: *Proceedings of 2016 IEEE Global Conference on Signal and Information Processing*, pp. 743–747 (2016)



An Energy Saving Strategy for IoT Wristband Terminals Combined with Human Activity Laws

Yu Chen¹ , Shaojie Yang¹, Shaoyong Guo¹, Cai Zhi², Hui Yao², and Ao Xiong¹

¹ State Key Laboratory of Networking and Switching Technology, Beijing University of Posts and Telecommunications, Beijing 1008764, China
cywhatme@bupt.edu.cn

² Xingyaoneng (Beijing) Technology Co., Ltd., Beijing 100036, China

Abstract. With the rapid development of 5G and Internet of Things (IoT), the objects connected by 5G have expanded from people to everything, and smaller and lighter IoT terminals are involved in people's production and life. The IoT wristband terminal is a kind of popular wearable devices with functions of monitoring human exercise intensity, sleep quality and daily health. The operating energy consumption of the heart rate sensor and global positioning system (GPS) in the IoT wristband terminal is the main source of energy consumption of the wristband terminal. The limited battery capacity leads to the problem of limited energy and short endurance of the IoT wristband terminal, which cannot realize long time human health monitoring. In order to achieve energy saving while ensuring the health monitoring functions and performance of the IoT wristband terminal, we research the user requirements and human daily activity laws, use the anomaly detection algorithm based on binary Gaussian distribution to fit the relationship between acceleration and heart rate in human activities and propose the energy-saving strategies for heart rate sensor, and then use the decision tree algorithm to obtain the human activity state classification model and the energy-saving strategies for GPS is then proposed. Simulation experiments show that the proposed energy-saving strategies can more intelligently adjust the sampling frequency and working mode of the heart rate sensor and GPS, reduce the power consumption of high-power sensors and improve the endurance of the IoT wristband terminal.

Keywords: Wearable devices · Energy-saving strategies · Human activity laws · Anomaly detection

1 Introduction

The Internet of Things (IoT) is a new intelligent network that enables the exchange and sharing of information between things through many sensor devices of various precision and types and with the help of communication technologies [1]. The IoT wristband terminal is a kind of wearable device which is highly popular among people. The built-in high-precision sensor of the terminal can collect human physiological characteristics signals such as heart rate, blood oxygen and ECG, including heart rate detection, motion recognition, etc. These functions greatly enrich people's life and provide users with health advice and record reports.

While the performance of IoT wristband terminal is improved in all aspects, the subsequent cost is the increase of power consumption. IoT wristband terminals need to consume a lot of power when collecting, processing and transmitting data. IoT wristband terminals basically contain acceleration sensors, heart rate sensor and GPS and the energy consumption of these sensors is the main energy consumption of the wristband terminal. The wristband terminal usually uses battery power and the battery capacity is limited due to the volume limitation, which leads to the problem of limited energy and short endurance of the terminal [2]. The short usage time will force users to charge frequently, which will produce poor user experience and cannot achieve long time human health monitoring. Therefore, in order to achieve energy saving while ensuring the health monitoring function of IoT wristband terminal, we start with the energy saving of sensors, study the users' needs and human daily activities, and use machine learning algorithms to design low-power consumption strategies and adjust the sampling frequency and working mode of large power consumption sensors more intelligently. Finally, the overall power consumption of the wristband terminal will be reduced and the endurance will be improved.

2 Related Work

Power (Battery)	Actuator	GPS Motion sensors Ambient light sensors Ambient temperature sensors	Wireless Communication (Bluetooth,LTE)
	Microcontroller		
	Bio-metrical sensors PPG, ECG, Skin temperature, GSR, Body fat		

Fig. 1. The hardware architecture of the smart wearables [5].

Reduced cost of sensors and recent advances in sensor technology have enabled the use of wearable sensors for health monitoring and human activity detection. Activity detection and classification using multiple sensors has become a revolutionary technology for activities of daily living, behavior analysis and rehabilitation care [3]. Smartphones and smart wearables are equipped with a variety of sensors for activity monitoring. The data from these sensors are pre-processed and different feature sets are combined with machine learning algorithms for human activity recognition [4]. Smart wearable devices are commonly used for health monitoring and the hardware structure of the smart wearable devices is shown in Fig. 1. Due to the size limitation of the wearable devices, battery capacity is often small. And as wearable devices become more functional, they need to collect, process and transmit large amounts of data, which consumes a lot of power. It is necessary to reduce the times of charges and extend usage time for wearable devices.

Combined with the characteristics of wearable devices, the existing wearable devices energy-saving technology mainly starts from three aspects: battery, data transmission and sensor. In terms of battery, in addition to maximizing the battery capacity within the limited space through existing battery technology, Ha et al. [6] proposed the dynamic

power management (DPM) technology, through which the operation mode and task scheduling of components in the system can be changed to reduce the recovery time and further save energy by extending the hibernation time. In terms of data transmission, researchers develop new communication protocols, optimize transmission algorithms or perform data compression to reduce the energy consumption. Li et al. [7] observed that the communication signals of wearable devices have a strong correlation with human motion and proposed a motion-based adaptive prediction mechanism (MAPM) to accurately fit and predict power. They demonstrated that MAPM can save more than 40% of energy compared with the state-of-the-art methods. In terms of sensor, it is mainly achieved by decreasing the sensor sampling frequency and operating time. Zhang et al. [8] proposed a dynamic sampling strategy DSI that can significantly reduce the energy consumption of wireless sensor nodes by analyzing the historical sampling data, and adopt a lower sampling frequency and data upload frequency to improve the sensor node endurance.

3 The Design of Energy-Saving Strategies

3.1 The Overall Energy-Saving Strategies

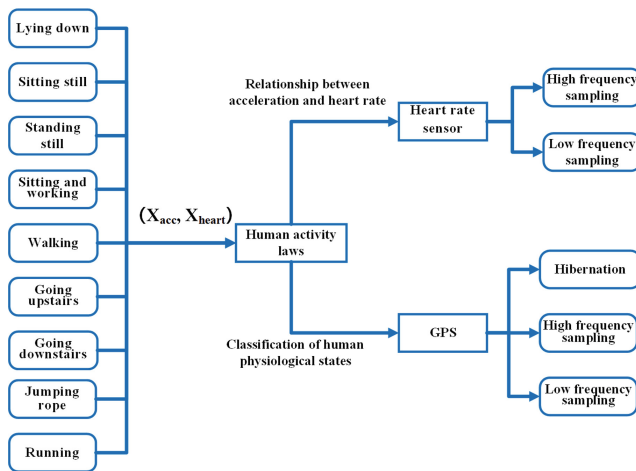


Fig. 2. A the overall energy-saving strategies for IoT wristband terminals.

In order to achieve energy saving while ensuring the health monitoring functions and performances of IoT wristband terminal, we propose an energy-saving strategies for wristband terminal combined with the human activity laws. We characterize the user’s motion intensity based on the data (X_{acc}, X_{heart}) collected by the acceleration sensor and heart rate sensor, and classify the human behavioral activities into nine types: lying down, sitting still, standing still, sitting and working, walking, going upstairs, going downstairs, jumping rope and running. The overall energy-saving strategies of the IoT

wristband terminal is shown in Fig. 2. By studying the needs of users and the human activity laws, the machine learning algorithms are used to design low-power consumption strategies and more intelligently adjust the sampling frequency of such large-power consumption sensors as heart rate sensor and GPS. Finally, the power consumption of the IoT wristband terminal is reduced by reducing the sensors' power consumption so as to achieve the maximum energy saving and endurance.

3.2 Energy-Saving Strategies for Heart Rate Sensor Based on Anomaly Detection

Anomaly detection is to learn a target class model from target class samples, and then use this model to determine whether the data samples conform to the model, and they are normal if they do, or anomalous if they don't [9]. The anomaly detection algorithm based on binary Gaussian distribution is the combination of binary Gaussian distribution and anomaly detection algorithm. Given an 2×2 dimensional training dataset, the binary Gaussian distribution function F is derived by analyzing the distribution of n training samples:

$$F(x|\mu, \Sigma) = \frac{1}{2\pi|\Sigma|^{\frac{1}{2}}} \exp\left\{-\frac{1}{2}(x - \mu)^T \Sigma^{-1}(x - \mu)\right\} \quad (1)$$

where the 2-dimensional vector μ is the mean, the 2×2 matrix Σ is the covariance, and $|\Sigma|$ is the determinant of Σ . The F is obtained through training and the probability threshold ϵ is determined based on the cross-validation set. When a new sample is given, its probability P is calculated based on FF. The sample is anomalous if P is less than ϵ , and it is normal if P is greater than ϵ . Heart rate is an important physiological indicator reflecting the blood circulation function of human body, which provides an important reference role in the field of human health monitoring. Human heart rate is generally 60~100 times/min, and the heart rate has individual differences [10].

In order to better fit the relationship between human heart rate and acceleration, it is need to collect data (X_{acc}, X_{heart}) covering 9 kinds of activities performed by healthy people of different ages and genders wearing IoT wristband terminal. After pre-processing the collected data, use the anomaly detection algorithm based on binary Gaussian distribution to fit the relationship between acceleration and heart rate. After deriving F through training, ϵ is then derived from the cross-validation set to determine whether the (X_{acc}, X_{heart}) is normal or not. The energy-saving strategies for the heart rate sensor are shown in Fig. 3 and described as follows:

- (1) The acceleration sensor and heart rate sensor collect the data $X_1 = (X_{acc'}, X_{heart'})$, and the probability P_1 of X_1 is calculated by F .
- (2) If P_1 is greater than ϵ , the heart rate value at the current exercise intensity is normal and the heart rate sensor works at low sampling frequency f_1 ; if P_1 is less than ϵ , the heart rate value at the current exercise intensity is anomalous and the heart rate sensor works at high sampling frequency f_2 , where f_2 is greater than f_1 .
- (3) The heart rate sensor will be converted to high sampling frequency immediately when the collected data $X_2 = (X_{acc}'', X_{heart}'')$ is anomalous, and it will maintain

the high sampling frequency state for a period of time T . The heart rate sensor will be converted to low sampling frequency only when the collected data $X_3 = (X'''_{acc}, X'''_{heart})$ is normal after T .

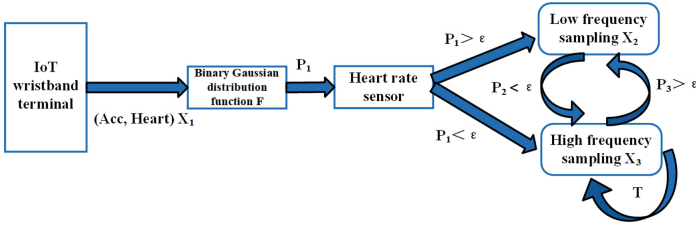


Fig. 3. Energy-saving strategies for heart rate sensor.

3.3 Energy-Saving Strategies for GPS Based on Decision Tree

Decision trees establish a mapping between values and attributes, and allows people to observe how the machine learning model performs decision analysis during the training process in a visual way [11]. There are three main generation algorithms for decision tree model: ID3, C4.5, and CART, each of which uses different criteria to measure the purity of split attributes. The information entropy is used to measure the purity of the sample in the decision tree. If p_k is used to represent the proportion of class k samples in the sample set D , the information entropy of D is defined as (2):

$$Ent(D) = - \sum_{k=1}^{|y|} p_k \log_2 p_k \tag{2}$$

The ID3 algorithm [12] uses the information gain as the splitting criterion. Assume that the discrete attribute a has \mathcal{V} possible values, and the samples set with value a_v on a is denoted as D^v . Then the information gain after the division of attribute a is:

$$Gain(D, a) = Ent(D) - \sum_{v=1}^{\mathcal{V}} \frac{|D^v|}{|D|} Ent(D^v) \tag{3}$$

The C4.5 algorithm [13], introduces the information gain rate as a measure of the sample attributes purity and assigns to each attribute a the intrinsic value $IV(a)$:

$$IV(a) = - \sum_{v=1}^{\mathcal{V}} \frac{|D^v|}{|D|} \log_2 \frac{|D^v|}{|D|} \tag{4}$$

The information gain rate of attribute a is obtained by dividing the information gain by the intrinsic value as (5):

$$Gain_{ratio}(D,a) = \frac{Gain(D, a)}{IV(a)} \tag{5}$$

The CART algorithm [14] response model impurity splitting criterion is Gini index defined as (6), where C_k denotes the number of class k .

$$Gini(D) = 1 - \sum_{k=1}^K \left(\frac{|C_k|}{|D|} \right)^2 \tag{6}$$

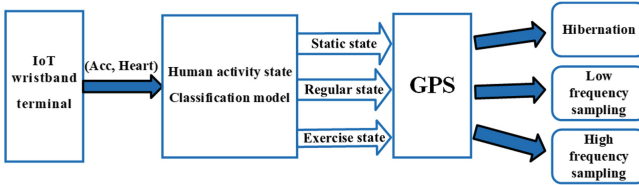


Fig. 4. Energy-saving strategies for GPS.

Human activity is a complex action process completed by the coordination of various joint parts of the body, and is the periodic repetition of a single action over a period of time. The main research direction of acceleration sensors for human activity recognition is to identify the steady state of continuous and periodic repetition of action over a period of time [10]. Based on the characteristics of frequency and amplitude of acceleration changes during human activity can achieve the recognition of human daily activities [15]. We use (X_{acc}, X_{heart}) to increase the reliability of activity recognition and achieve the classification of human activity states. According to the fact that people usually maintain stability for a period of time when performing a type of activity, we classify lying still, sitting still, and standing still as static activities, sitting and working, walking, going upstairs and downstairs as regular activities, and jumping rope and running as exercise activities. These three types of activities correspond to the three types of human activity states: static state, regular state and exercise state. The position change of these three states is different, for example, there is basically no position change in the static state, and the position change in the exercise state is greater than that in the regular state. Therefore, the working mode of GPS can be adjusted by the change of human state. The energy-saving strategies for GPS is shown in Fig. 4. The acceleration sensor and heart rate sensor collect data and determine the user’s current state through the human activity state classification model. If the user is in the static state, the GPS will hibernate; if in the regular state, the GPS works at low sampling frequency; if in the exercise state, the GPS works at high sampling frequency. Each activity state is judged to last for a period of time T' .

4 Experimental Simulation and Analysis

4.1 Data Pre-Processing

We use the human activity monitoring public dataset: Physical Activity Monitoring (2012) [16] in the experimental simulation, which was obtained from 9 testers, 8 males and 1 female aged 27.22 ± 3.31 years with BMI $25.11 \pm 2.62 \text{ kgm}^{-2}$. All testers wore

the experimental devices to perform activities. The experimental devices are three-axis inertial measurement units with sampling frequency of 100 Hz worn at three different locations of chest, wrist and ankle, and a heart rate sensor with sampling frequency of 9 Hz. We select the data collected by the three-axis accelerometer worn on the wrist and heart rate sensor. The tri-axial acceleration (m/s^2) and heart rate values (times/min) are obtained by cleaning the data of 9 testers under 9 activities, including lying down, sitting still, standing still, sitting and working, walking, going upstairs, going downstairs, jumping rope and running. Each activity is organized into 100 activity data by 9 testers, a total of 900 data (X_{acc}, X_{heart}).

4.2 Energy-Saving Strategies for Heart Rate Sensor Based on Anomaly Detection

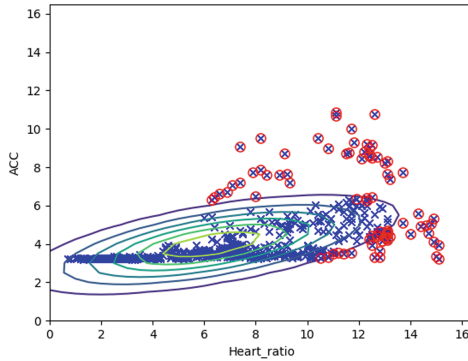


Fig. 5. Experimental effect of anomaly detection algorithm.

From the dataset in Sect. 4.1, 700 data were taken as the training set, and 200 normal data plus 10 anomalous data for a total of 210 data were taken as the cross-validation set. The Gaussian distribution function F with mathematical expectation $\mu = [6.30028571 \ 3.967639]$ and covariance $\Sigma = \begin{bmatrix} 13.63645706 & 2.9461896 \\ 2.9461896 & 1.72831636 \end{bmatrix}$ is learned from the training set, and then the optimal probability threshold ε is 0.007171. The recall rate is 80% and the accuracy rate is only 34.8%. The high recall rate indicates that the anomaly detection algorithm based on Gaussian distribution can detect most of the data identified as anomalous. The low precision rate is because the anomaly detection algorithm judges 15 normal data as anomalous while the ratio of normal data to anomalous data in the cross-validation set is 20:1. The effect of the anomaly detection algorithm in the training set is shown in Fig. 5, where “ACC” indicates acceleration and “Heart_ratio” indicates the heart rate value after maximum and minimum normalization. The blue mark is normal data, and the red mark is anomalous data. The farther from the middle of the concentric circles means the lower the probability of occurrence. There are 82 anomalous data are detected due to the interference of directional bias and arm sway during data collection. The energy-saving strategies for heart rate sensor are as follows:

- (1) Calculate the probability P of data (X_{acc}, X_{heart}) through F . If P is greater than ε , the heart rate value is normal and the heart rate sensor works at low sampling frequency, i.e., sampling once every 5 min; if P is less than ε , the heart rate value is anomalous and the heart rate sensor works at high sampling frequency, i.e., sampling once every 1 min.
- (2) When anomalous data is detected, the heart rate sensor will be converted to high sampling frequency immediately and maintain the high sampling frequency state for 15 min. The heart rate sensor will be converted to low sampling frequency when normal data is detected after 15 min.

4.3 Energy-Saving Strategies for GPS Based on Decision Tree

400 data are static activities labeled 0, 300 data are regular activities labeled 1, 200 data are exercise activities labeled 2, and the labeled dataset is divided into 630 training set and 270 cross-validation set in the human daily activity monitoring dataset. The classification accuracy of ID3, C4.5, and CART algorithms respectively are 79.3%, 85.9%, and 94.4%. Finally, the C4.5 decision tree classification algorithm was selected as the human activity state classification algorithm for its highest accuracy, and the decision tree is shown in Fig. 6, where “Acc” denotes the discretized acceleration (m/s^2) and “Heart” denotes the discretized heart rate value ($\times 10$ times/min). From the C4.5 decision tree classification model, the energy-saving strategies for GPS can be formulated: if user is in static state, the GPS hibernates; if in regular state, GPS updates positioning information every 5 min; if in exercise state, GPS updates positioning information every 30 s. The duration of each state is 15 min.

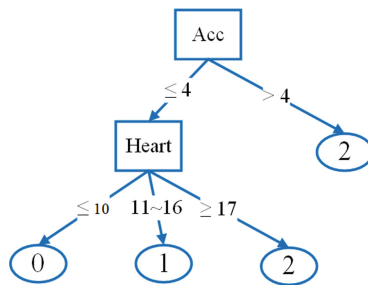


Fig. 6. Decision tree for human activity state classification based on C4.5.

4.4 Strategy Simulation and Analysis

In this paper, the energy-saving strategies for the heart rate sensor and GPS are applied to the one-day activity data of the fifth tester in the data set of Sect. 4.1 to verify the energy-saving effect. The fifth tester is a 26 years old male and his activity data collection is the most complete. Applying the anomaly detection algorithm to 24,728 data of the fifth tester, 2280 anomalies are detected. Compared with the energy consumption at high

frequency, the percentage of energy savings by the heart rate sensor operating with a mixture of high and low frequency sampling is (8):

$$1 - \frac{2280 \times 5 + (24728 - 2280) \times 1}{24728 \times 5} \approx 0.7262 = 72.62\% \quad (7)$$

where the multiplier “5” and “1” refers to the ratio of high to low frequency sampling of 5:1, and the heart rate sensor consumes the same amount of energy per sample. The energy-saving strategies of heart rate sensor can adjust the sampling frequency more intelligently, can collect and record heart rate changes in time, and make the heart rate sensor work at low frequency mode most of the time to reduce the energy consumption. In the activity data of the fifth tester, the classification model of human activity states yielded a ratio of 1833:589:323 for the static state, regular state and exercise state. Compared with the energy consumption at high frequency, the percentage of energy savings by GPS using the hibernation or mixed high and low frequency operation modes is (9):

$$1 - \frac{1833 \times 0 + 589 \times 1 + 323 \times 10}{2745 \times 10} \approx 0.8609 = 86.09\% \quad (8)$$

where the multiplier “10”, “1” and “0” refers to the ratio of 10:1:0 between high-frequency operation, low-frequency operation and hibernation, and the energy consumption of GPS is the same per sample. The energy-saving strategies for GPS is to determine the working mode of GPS by judging different human activity states more intelligently, which can significantly reduce the number of times of updates positioning information, and minimize the energy consumption of GPS.

5 Conclusion

In this paper, we have studied the IoT wristband terminal for human health monitoring and designed energy-saving strategies based on its application scenarios, business data processing and interaction links. Starting from the energy saving of sensors, we have first used the anomaly detection algorithm based on binary Gaussian distribution to fit the relationship between acceleration and heart rate in human activities. And we have proposed the energy-saving strategies for heart rate sensor combined with human activity laws to determine whether the heart rate value is anomalous under the corresponding human activity intensity, so that the sampling frequency can be adjusted more intelligently. Then, we have combined acceleration and heart rate to increase the reliability of human activity recognition, and used the decision tree algorithm to obtain the human activity state classification model. We have proposed the GPS energy-saving strategies combined with human activity state classification, so as to determine the working mode of GPS by judging the human activity state, which can more intelligently adjust the sampling frequency of GPS, significantly reduce the times of repeated acquisition of positioning information, and minimize the energy consumption. The energy-saving strategies proposed for the IoT wristband terminal achieve the reduction of overall device power consumption by reducing the power consumption of sensors, and improves the endurance of the IoT wristband terminal.

Funding Statement. This work was supported by the National Key R&D Program of China (2020AAA0140100) and the BUPT innovation and entrepreneurship support program (2023-YC-A120).

References

1. Afzal, M.K., Zikria, Y.B., Mumtaz, S., et al.: Unlocking 5G spectrum potential for intelligent IoT: opportunities, challenges, and solutions. *IEEE Commun. Mag.* **56**(10), 92–93 (2018)
2. Liang, Y., Meng, X., Hu, Y., et al.: Design and implementation of an ultra-low power wireless sensor network for indoor environment monitoring. In: 2017 IEEE 17th International Conference on Communication Technology (ICCT). IEEE, pp. 937–940 (2017)
3. Cao, L., Wang, Y., Zhang, B., Jin, Q., Vasilakos, A.V.: GCHAR: an efficient Group-based context—aware human activity recognition on smartphone. *J. Parallel Distrib. Comput.* **118**(Part 1), 67–80 (2017)
4. Nweke, H.F., Teh, Y.W., Mujtaba, G., Al-garadi, M.A.: Data fusion and multiple classifier systems for human activity detection and health monitoring: review and open research directions. *Inf. Fusion* **46**, 147–170 (2019)
5. Qiu, H., Wang, X., Xie, F.: A survey on smart wearables in the application of fitness. In: 2017 IEEE 15th International Conference on Dependable, Autonomic and Secure Computing, 15th International Conference on Pervasive Intelligence and Computing, 3rd International Conference on Big Data Intelligence and Computing and Cyber Science and Technology Congress, pp. 303–307 (2017). <https://doi.org/10.1109/DASC-PICom-DataCom-CyberSciTec.2017.64>
6. Ha, C., Wang, Y., Chang, C.: Dynamic power management for wearable devices with non-volatile memory. *Int. Conf. Appl. Syst. Innov. (ICASI)* **2017**, 37–39 (2017)
7. Li, Y., Kong, L., Wu, F., Zheng, Z., Chen, G.: MAPM: movement-based adaptive prediction mechanism for energy conservation in body sensor networks. *IEEE Glob. Commun. Conf. (GLOBECOM)* **2016**, 1–6 (2016)
8. Zhang, J., Chen, X., Zhao, Y.: Dynamic sampling control strategy for wireless sensor nodes. *J. Electron. Measur. Instrument.* **30**(02), 249–255 (2016)
9. Yu, B.: Anomaly detection algorithm based on Gaussian model. China University of Mining and Technology (2017)
10. Han, L.: Research on human multi physiological parameters monitoring fusion motion state recognition. Southeast University (2019)
11. Wang, X.: Decision Tree Based Attack Prediction and Analysis on Intelligent Traffic Signal System. Beijing Jiaotong University (2021)
12. Quinlan, R.J.: Induction of decision trees. *Mach. Learn.* **1**(1), 81–106 (1986)
13. Quinlan, R.J.: C4.5: Programs for Machine Learning. Morgan Kaufmann Publishers, pp. 235–240 1993
14. Breiman, L., et al.: Classification and regression trees. Wadsworth, 346–358 (1984)
15. Lee, M., Khan, A.M., Kim, T.: A single tri-axial accelerometer-based real-time personal life log system capable of human activity recognition and exercise information generation. *Pers. Ubiquit. Comput.* **15**(8), 887–898 (2011)
16. Available online, <http://www.pamap.org/demo.html>



Edge Caching Cooperation Method Based on Deep Reinforcement Learning

Meng Zhu¹, Yuxiao Liu²(✉), Ao Xiong², Shaoyong Guo², Ke Yang^{3,4}, Nan Zhang⁵, and Ke Chen¹

¹ State Grid Jiangsu Electric Power Company Marketing Service Center, Beijing, China

² State Key Laboratory of Networking and Switching Technology, Beijing University of Posts and Telecommunications, Beijing, China
liuyuxiao@bupt.edu.cn

³ State Grid Digital Technology Holding Co., Ltd., Beijing, China

⁴ State Grid Blockchain Technology (Beijing) Co., Ltd., Beijing, China

⁵ State Grid Corporation of China Customer Service Center, Beijing, China

Abstract. During the use of electronic licenses, IoT devices require access to data in the cloud. By introducing edge caching, we can reduce the latency and traffic consumption when massive IoT devices access data in the cloud. Cooperation between edge nodes can further improve system performance. However, how to manage edge caches effectively in cooperation scenarios remains a challenging problem. This article decomposes the cooperation problem in edge caching into two parts. Firstly, the Gate Recurrent Unit (GRU) is introduced into the Dueling Network to construct a local method for data evaluation. Then, the cooperation relationship between edge nodes is handled from two aspects: replica reduction and load balancing, and cooperation rules are designed. Experiments have shown that the approach proposed in this article can effectively improve the hit rate of edge caching systems and reduce average latency, and improve system performance.

Keywords: Reinforcement learning · Edge computing · Cooperative cache

1 Introduction

Electronic licenses have been widely used in various industries, including the power industry. The Internet of Things and cloud computing are two key technologies behind electronic licenses. We may issue or verify electronic licenses through IoT devices, while using cloud servers to store data related to electronic licenses.

The Internet of things technology refers to the use of various sensors, radio frequency identification technology, global positioning system, wireless communication technology to collect the information of things and realize the control and interaction of things. [1] Cloud computing mainly refers to obtaining dynamically scalable computing services on demand through the network [2]. Requests generated by massive IoT terminals will cause huge pressure on network bandwidth and cloud server computing resources, and there is a considerable time delay between the IoT terminal and the cloud server

[3]. Due to the capacity of the device, it is impossible for us to save all possible data. In this context, edge computing, especially edge caching technology, can mitigate the above problems. Edge computing refers to the deployment of devices with computing, storage and network communication capabilities on the side close to the end user to serve some terminal devices nearby, providing higher response speed for terminal devices and reducing the pressure on the cloud [4]. Caching data in the edge node close to the end user can reduce the delay of data access and the traffic of requesting data from the cloud. At the same time, in order to meet the needs of IoT devices distributed in different locations, we often need to set up a series of edge nodes, each of which serves the nearest device to further improve the response speed and share the pressure at the same time.

We need to design an effective scheme to select the appropriate cache management strategy for each edge node. In order to improve the utilization rate of cache space and reduce the delay of data accessing and external traffic consumption of devices, we can design strategies to encourage edge nodes to cooperate with each other and jointly manage the data that devices may use.

In this article, we decompose the cooperative caching algorithm into two parts: the local layer and the cooperative layer. The main contributions of this article are:

- This article proposes a two-layer method for the cooperation in edge caching, which analyzes and decomposes the cooperative cache problem, and turns it into two easier problems, so as to solve them one by one.
- The experimental results show that the edge cache cooperation method proposed in this paper can effectively reduce the device access data delay and improve the cache hit rate.

The following is the arrangement of this article: Sect. 2 reviews the existing related work and the motivation of this article, Sect. 3 describes the system model used in this paper and the problems to be solved, Sect. 4 introduces the propose method in detail, Sect. 5 shows the verification and evaluation of the proposed method, and finally Sect. 6 summarizes the article.

2 Related Work

2.1 Independent Edge Cache

Some methods proposed in these articles [5, 6] are closer to the recommendation algorithm rather than the caching algorithm, emphasizing unprompted caching and prefetching. The edge nodes have rich features about the cached data, even including some detailed user behavior data. However, these algorithms rely on the rich characteristics of the cached data, which also leads to the lack of generality of these algorithms. These algorithms can only be applied to data caching in specific types and scenarios.

Some articles [7] solve the caching problem of a single edge node through reinforcement learning. These methods do not rely on the complex features of the data to be cached, but relies on the features obtained from historical access records instead. The local layer of the method proposed in this paper belongs to this kind of algorithms, which has better versatility.

2.2 Cooperative Edge Cache

This kind of work [8–10] emphasizes the cooperation between different edge nodes. The main form of cooperation is that when an edge node receives a user request and does not cache the data, it can obtain the corresponding data from other nodes. Because the problem was not split, most of the work actually put the local layer and cooperation layer divided in this article into a single algorithm. These methods are based on Multi-Agent Reinforcement Learning and are closer to the traditional cache elimination strategy, that is, they will not prefetch, but only eliminate the cache when they need to make a choice. In these methods, the cooperative process is implicit, and the strategies learned by reinforcement learning include both independent cache replacement strategies and cooperative strategies.

3 System Model

3.1 System Architecture

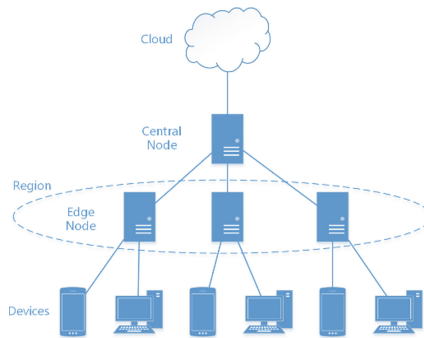


Fig. 1. System architecture

We assume that the whole system is composed of several regions, and each region has several edge nodes, which are used to accept the user's data access request and actually store the cached data. At the same time, there is a central node in each region, which is used to coordinate the work of edge nodes in the region and does not actually store cached data. The terminal device will request data through the nearest edge node, and the service scope of each edge node is relatively fixed. Since different regions will use the same caching method, we only need to consider the situation in one region, as shown in Fig. 1.

We divide time into time slots of the same length, and each time slot is divided into two stages. In the first stage, the terminal device sends data access requests to the edge node. If the edge node caches the data, it will directly return it to the terminal device. Otherwise, the edge node requests the data from the central node. The central node will check if other edge nodes in the region have cached the data. If so, it will obtain the data from the corresponding edge node and finally give it to the terminal device. If no edge

node caches the data requested by the terminal device, the central node will request the data from the cloud and return it to the terminal device. In the second stage, edge nodes replace the cache content. In the first stage, the new data obtained by the edge node from the center node and other edge nodes will be temporarily saved for the second stage to decide whether to reserve.

3.2 Problem Formulation

All data that may be accessed by terminal devices are divided into blocks of equal size. The size of each block is q and the total number of data blocks is N . The number of edge nodes in the region is M , and each edge node can store up to C_{max} data blocks.

There are three possible cases for each data request. The first case is the local hit with a delay of d_{edge} . The second case is the cooperative hit. In this case, the data needs to be retrieved from other edge nodes to the central node, and then returned to the terminal devices. The delay is $d_{edge} + 2d_{center}$, in which d_{center} represents the delay between the central node and the edge node. The third case is miss. In this case, the data needs to be retrieved from the cloud to the central node and then returned to the terminal device. The delay is $d_{edge} + d_{center} + d_{cloud}$, in which d_{cloud} indicates the delay of the central node retrieving data from the cloud.

For edge nodes m , we use $c_{m,1}^t, c_{m,2}^t, \dots, c_{m,n}^t, \dots, c_{m,N}^t$ to represent the cached data in time slot t . If the data block n is cached, the value of $c_{m,n}^t$ is 1. Otherwise, the value is 0. We use $p_{m,1}^t, p_{m,2}^t, \dots, p_{m,n}^t, \dots, p_{m,N}^t$ to represent the number of requests for each data block by the terminal device in the time slot t .

Therefore, in the time slot t , the total delay of all nodes is as follows.

$$d^t = \sum_{m=1}^M \sum_{n=1}^N p_{m,n}^t \left(d_{edge} + 2d_{center}(1 - c_{m,n}^t) + (d_{cloud} - d_{center}) \prod_{i=1}^M (1 - c_{i,n}^t) \right) \quad (1)$$

Therefore, the cache strategy with minimum delay is equivalent to solving the following integer programming problem.

$$\min_{c_{m,n}^t} d^t \quad (2)$$

$$s.t. c_{m,n}^t \in \{0, 1\}, \sum_{n=1}^N c_{m,n}^t \leq C_{max} \quad (3)$$

4 Proposed Approach

4.1 Motivation

For edge nodes, there are two main benefits of cooperation:

- For edge nodes, the access frequency of some candidate data is not very high, and other nodes have cached the data before, we may not cache the candidate data locally. This essentially reduces the number of replicas, reserving space for more frequent content.

- When the load of each node is unbalanced, the node with high load can borrow the space of the node with low load to cache data

So, it is not difficult for us to think of designing a two-layer method to design a conscious cooperative algorithm based on a local cache management strategy.

4.2 Local Layer

Definition of Reinforcement Learning Problem. We use deep reinforcement learning to build an independent edge node caching strategy that does not consider cooperation consciously. First, we need to define the state, action and reward function in the reinforcement learning process.

We define the state space as $S = \{s | s = (\text{cached}, \text{candidate})\}$, where cached represents the current cached data blocks of the edge node, specifically, including the feature vector of all cached data blocks. The other part, candidate, represents the state of the candidate data block, which is the feature vector of the candidate data block. The feature vector of the data block i $s_i = (f_{i1}, f_{i2}, f_{i3}, l_{i1}, l_{i2}, l_{i3})$ is generated according to log, which consists of the short-term access frequency f_{i1} , the medium-term access frequency f_{i2} and the long-term access frequency f_{i3} , the time slots that has passed since the last three visits.

The action space is defined as $A = \{1, 2, \dots, C_{max}, C_{max} + 1\}$. For $1 \leq c \leq C_{max}$, c means to replace the cached data block at position c with the candidate data block. $C_{max} + 1$ means that the candidate data block is not retained. In other words, the edge node can make two decisions, one is to retain the candidate data block to a certain location in the cache, and the other is to discard the candidate data block.

We want to minimize the total delay of requests processed by the edge node, so we can define the following reward function, and we can define the discount coefficient γ when calculating the cumulative reward. This reward function means that we will only reward when processing the last candidate data block in a time slot. The reward value is about the total delay of the request processed by the edge node in the time slot. See 3.2 for the definition of d^t , where $M = 1$.

$$r = \begin{cases} e^{-d^t}, & \text{When time slot } t \text{ ends} \\ 0, & \text{other} \end{cases} \quad (4)$$

Network Structure. Literature [11] first introduced recurrent neural networks into reinforcement learning. The original purpose of introducing recurrent neural networks into reinforcement learning was to solve decision problems under incomplete information (partially observable Markov decision process). Even for decision problems under complete information, the introduction of recurrent neural networks in reinforcement learning also helps to improve performance. Back to our problem, for a specific data block, we can think that the feature vector set at all times in history is the complete information, so we can use the recurrent neural network to retain more historical information for decision-making, and capture the temporal dependency. We introduce the Gate Recurrent Unit (GRU) into the dueling network to build the neural network as shown in Fig. 2.

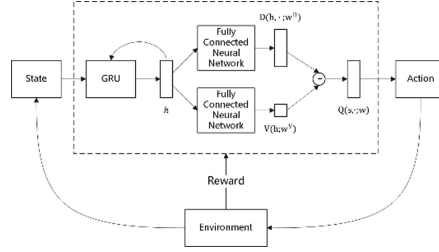


Fig. 2. Network structure of local layer

GRU [12] is a kind of recurrent neural network units that can capture the dependencies in time series data. We use GRU to remember past states. We put the state s into GRU to get the hidden states h .

As shown in Fig. 2, in the dueling network [13], we use two neural networks to estimate the optimal action-value function $Q(s, a)$, and finally output the value (Q value) of each action. The fully connected neural network, $V(h; w^V)$, is an estimate of the optimal state-value function, which can be regarded as the maximum cumulative reward that can be obtained in the current state. Its input is h , and its output is the value of the state. The output of another fully connected neural network $D(h, a; w^D)$ is a vector, which is the difference between the state value and the final output action value. Then we can add the two to get the estimated value of the Q value of each action. In the implementation, we also need to add the third item to make the neural network unique. The whole network can be represented by the following formula.

$$Q(s, a; w) = V(h; w^V) + D(h, a; w^D) - \text{mean}_a D(h, a; w^D) \quad (5)$$

Training. We apply the training method of double Q learning to the multi-agent scenario under the above network structure. We use the method of centralized training and distributed decision-making. Moreover, due to the introduction of GRU, the whole training process will be different from the conventional reinforcement learning.

In addition to saving the value network $Q(s, a; w)$, the central node will also save another neural network $Q(s, a; w_t)$, which we call the target network. Their structures are exactly the same, but only their parameters are different.

1. The parameters of the two neural networks are initialized with the same random value, and the target network is distributed to each edge node. And, set a fixed-size experience replay array in the central node.
2. Each edge node uses ϵ -greedy policy interacts with the environment. The edge node will send the collected experience quadruple (s, a, r, s') back to the central node, and the central node will store the quadruple in the experience replay array.
3. If the number of quadruples collected by the central node reaches the preset threshold, repeat step 4 and step 5 to update the neural network parameters. During this process, the edge node continues to perform step 2 to collect more experience.
4. Before each iteration, for the central node, we set the hidden state h_{-1} of GRU in the two neural networks to zero. Then an edge node is randomly selected, and a

quadruple is randomly selected as the starting quadruple from quadruple generated by the edge node.

5. Starting from the selected quadruple in the step 4, perform subsequent steps 6 to 13 on the quadruple (s, a, r, s') generated by the same edge node in sequence, until the number reaches the preset size or there are no more quadruple.
6. Use the current state s to conduct forward propagation on the network $Q(s, a; w)$, and get the estimated value \hat{q} of the current state-action tuple (s, a) .

$$\hat{q} = Q(s, a; w) \quad (6)$$

7. Use the next state s' to conduct forward propagation on the network $Q(s, a; w)$ forward and select the action a^* with the greatest value.

$$a^* = \operatorname{argmax}_{a' \in A} Q(s', a'; w) \quad (7)$$

8. Use the next state s' to conduct forward propagation on the target network $Q(s, a; w_t)$ instead of $Q(s, a; w)$ to obtain the estimated value \hat{q}' of (s', a^*) . And Calculate TD target.

$$\hat{q}' = Q(s', a^*; w_t) \quad (8)$$

$$\hat{y} = r + \gamma \hat{q}' \quad (9)$$

9. Define the loss function and use gradient descent or other optimization methods to update the parameters of the value network $Q(s, a; w)$.
10. The central node will periodically synchronize the parameters of the value network w to the target network, w_t and will also send the updated parameter w_t of the target network to the edge node. When the maximum number of iterations is reached, and the parameters of the value network are synchronized to the target network and edge nodes for the last time.

4.3 Cooperation Layer

For edge node m and data block i , we use the opposite number of Q value to represent the value $p_{m,i}$ of data block i , that is $p_{m,i} = -Q(s_m, i; w)$. s_m is the state of the edge node m . In this way, the action of the edge node is to eliminate the data block with the smallest value $p_{m,i}$. Starting from the two benefits of the cooperation layer mentioned in 4.1, we will introduce the specific rules of the cooperation layer.

Replica Reduction. At the edge node m , replica reduction will perform the following operations on each data block i reserved from the candidate data block location: compare $p_{m,i}$ with the threshold value p_{max} , and skip following steps if $p_{m,i} > p_{max}$. On the contrary, query whether other nodes have reserved this data block. If not, skip following steps. If yes, the data block will be marked, and its value will be calculated as $p_{m,i}' = \alpha p_{m,i}$ in the subsequent cache replacement until the data block is replaced or is the only replica of the data block in the region.

Load Balance. At the edge node m , load balance will perform the following operations for each data block i that is about to be eliminated from the cache (when the

candidate data block replaces its position): compare $p_{m,i}$ with the threshold value p_{min} , and skip if $p_{m,i} < p_{min}$. On the contrary, the central node issues a load balancing request to other nodes, including the number of data blocks and $p_{m,i}$. If the node k receives this request and does not cache the data block i , and there is still free space, it will directly cache the data block. If there is no free space, use the data block number in the request and its own log to generate the feature vector of this data block, and give the value $p_{k,i}$ like i is a candidate data block. Calculate $p_{k,i'} = (1 - \beta)p_{k,i} + \beta p_{m,i}$, where β is the scale factor. Compare $p_{k,i'}$ with the value of other data blocks. If it is not the lowest, replace the data block with the lowest value.

5 Experiment

5.1 Settings

This section will show the results of the experiment for the proposed approach to evaluate its performance. We used Python to build a simulated edge cache environment, which is composed of one central node and three edge nodes. We assume that the file request from the terminal device is random, and the access request arrival process of the three edge nodes is independent of each other. We assume that the total number of files in the system is 2000, and the size of each file is evenly and randomly distributed between 1 and 5 data blocks. The file access requests received by each edge node conform the Zipfian distribution. In the experiment, we assume that $d_{edge} = 5$ ms, $d_{center} = 5$ ms, $d_{cloud} = 25$ ms. Therefore, the delay in the three cases are 5ms, 15ms and 35ms respectively. We will compare the traditional cache replacement algorithms LRU and LFU, as well as the local-layer-only algorithm and the complete local layer and cooperation layer algorithm.

5.2 Results

The capacity of edge nodes is fixed at 30, and the parameters a of Zipfian distribution are 0.7, 0.9, 1.1 and 1.3, respectively. The changes of cache hit rate and average delay are observed. The results are shown in Fig. 3.

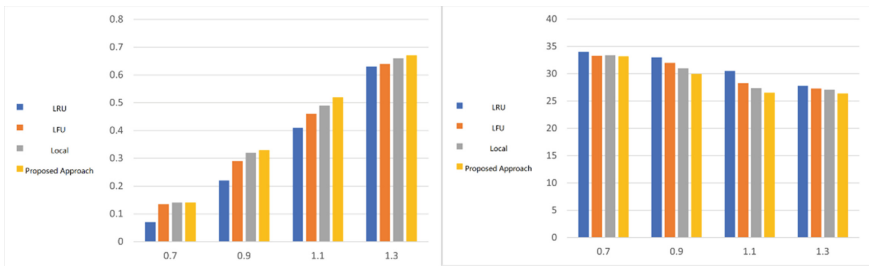


Fig. 3. Cache hit rate and average delay changes with the distribution parameter

We can find that that with the increase of parameters, the requested files tend to be centralized, the corresponding cache hit rate increases, and the average delay decreases.

From the perspective of the final effect, the effect of proposed approach is the best, which is better than that of the local layer only. This shows that the cooperation layer has played its due role, improving the cache hit rate and reducing the overall delay. Both algorithms are superior to the LRU and LFU algorithms that are not specially optimized for cooperation scenarios.

Fix the parameter a of Zipfian distribution to 1.1, adjust the cache capacity of each edge node to 20 blocks, 30 blocks, 40 blocks and 50 blocks respectively, and observe the change of system performance. The results are shown in Fig. 4.

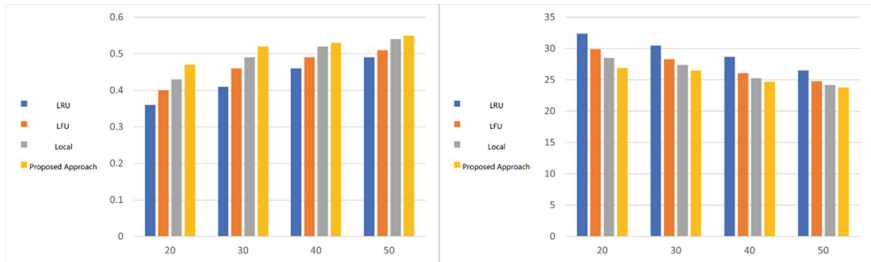


Fig. 4. Cache hit rate and average delay changes with node capacity

We can find that the proposed approach is superior to LRU algorithm and LFU algorithm in cache hit rate and average delay in the experimental cache capacity range. By comparing the local layer only approach and the proposed approach, we can find that when the cache capacity is low, the cooperation layer can give full play to its advantages, and the performance improvement is more obvious.

6 Summary

This article first analyzes the development status of the Internet of things and cloud computing, and points out the unique advantages of edge cache. Then, based on the analysis of the existing research on edge cache, a two-layer edge cache cooperation method is proposed. By introducing GRU into the dueling network, the cache management strategy of edge nodes is designed, and the cooperation rules between edge nodes are constructed, which reduces the average delay of the system and improves the cache hit rate.

Acknowledgments. This work has been supported by State Grid Corporation of China science and technology project “Research and Application of Key Technologies for Trusted Issuance and Security Control of Electronic Licenses for Power Business” (5700-202353318A-1-1-ZN).

References

1. Borgia, E.: The internet of things vision: key features, applications and open issues. *Comput. Commun.* **54**, 1–31 (2014)

2. Luo, J.Z., Jin, J.H., Song, A.B., Dong, F.: Cloud computing: architecture and key technologies. *J. Commun.* **32**(7), 3–21 (2011)
3. Chandra, S.R., Wang, Y.: Cloud things construction—the integration of internet of things and cloud computing. *Future Gener. Comp. Syst.* **56**(C), 684–700 (2016)
4. Peter, C.: Soumya, Kanti, Datta: mobile-edge computing and the internet of things for consumers: extending cloud computing and services to the edge of the network. *IEEE Consum. Electron. Magazine* **5**(4), 73–74 (2016)
5. Chen, G., Jing, W., Wen, X., Lu, Z., Zhao, S.: An edge caching strategy based on separated learning of user preference and content popularity. In: 2021 IEEE/CIC International Conference on Communications in China, ICC 2021, pp. 1018–1023 (2021)
6. Li, Z., Gao, X., Li, Q., Guo, J., Yang, B.: Edge caching enhancement for industrial internet: a recommendation-aided approach. *IEEE Internet Things J.* **9**(18), 16941–16952 (2022)
7. Zhou, Y., Wang, F., Shi, Z., Feng, D.: An end-to-end automatic cache replacement policy using deep reinforcement learning. *Proc. Int. Conf. Autom. Plann. Sched. ICAPS* **32**, 537–545 (2022)
8. Zhang, M., Jiang, Y., Zheng, F.-C., Bennis, M., You, X.: Cooperative edge caching via federated deep reinforcement learning in Fog-RANs. In: 2021 Proceedings of the IEEE International Conference on Communications Workshops, ICC Workshops (2021)
9. Zhang, Y., et al.: Cooperative edge caching: a multi-agent deep learning based approach. *IEEE Access* **8**, 133212–133224 (2020)
10. Radenkovic, M., Huynh, V.S.H.: Cognitive caching at the edges for mobile social community networks: a multi-agent deep reinforcement learning approach. *IEEE Access* **8**, 179561–179574 (2020)
11. Hausknecht, M., Stone, P.: Deep recurrent q-learning for partially observable MDPs. In: AAAI Fall Symposium—Technical Report FS-15-06, pp. 29–37 (2015)
12. Chung, J., Gulcehre, C., Cho, K.H., Bengio, Y.: Empirical evaluation of gated recurrent neural networks on sequence modeling. *Eprint Arxiv* (2014)
13. Wang, Z., Freitas, N.D., Lanctot, M.: Dueling network architectures for deep reinforcement learning. *JMLR.org* (2015)



Edge-Oriented Resource Scheduling Algorithm Based on Deep Reinforcement Learning

Longjun Zhao¹, Dandan Cui¹, Haipo Li¹, Ziyang Wang¹, Yating Sun²,
and Yang Yang²(✉)

¹ China Xiong'an Group Digital City Technology Co., Ltd., Xiong'an, China

² State Key Laboratory of Networking and Switching Technology, Beijing University of Posts
and Telecommunications, Beijing, China
yyang@bupt.edu.cn

Abstract. In the past few decades, the rapid development of information technology and the continuous innovation of computing paradigm have ushered people into a new era of edge computing. Compared to traditional cloud computing, edge computing provides better performance by bringing computing and storage capabilities to edge of network. As the scale of edge networks expands, the increasing number of latency-sensitive and compute-intensive tasks has led to a growing demand for computational power in terminal devices. Proper resource scheduling policies play a decisive role in improving the performance of edge networks. For the edge side resource scheduling scenario, this paper studies the multi-agent Counterfactual Soft self-Attention Actor-Critic algorithm (mCSAAC). To address the issue of credit assignment where global rewards during centralized training fail to reflect individual contributions, a counterfactual policy gradient is proposed to enhance the overall performance of the network. Furthermore, to tackle the short-sightedness problem introduced by fully decentralized execution, a self-attention communication mechanism is introduced between each agent, facilitating communication and reducing information loss in the environment. Through simulation experiments, the effectiveness of the proposed algorithm in reducing system energy consumption and task execution latency has been validated.

Keywords: Resource scheduling · Deep reinforcement learning · Self attention · Counterfactual baseline

1 Introduction

Mobile Edge Computing (MEC) enhances the capabilities of mobile cloud computing by deploying cloud computing and storage resources at the edge of wireless access networks [1]. In a distributed edge computing environment, resource scheduling refers to allocating reasonable computing resources (such as CPUs, memory, disks, etc.), network bandwidth, and transmission power to terminal devices with insufficient computing power to complete heavy computing tasks in the case of limited physical resources (such as servers and VMS).

In the past, researchers typically employed traditional resource scheduling methods, including approximation methods, heuristic methods, metaheuristic methods, and game theory methods, to optimize energy consumption or latency in edge-side resource scheduling [2]. However, these traditional methods often yield suboptimal solutions, lack scalability in dynamic environments, require recalculations when parameters change, and exhibit increased execution time proportional to the number of tasks, resulting in additional computational delays. The emergence of machine learning and reinforcement learning effectively addresses the limitations of traditional methods. However, machine learning-based resource allocation models often suffer from underfitting or overfitting issues and have strict requirements for training datasets. The trained model may fail to adapt to the full range of features and attributes in real-world testing data, while reinforcement learning tends to have slow convergence speed. In comparison, deep reinforcement learning offers fast convergence [3] and allows agents to approximate their policies and obtain optimal solutions without prior knowledge from training data.

Therefore, aiming to minimize the latency and energy consumption in edge-side resource scheduling, a multi-agent Soft Actor-Critic resource scheduling method based on self-attention mechanisms and counterfactual baselines, referred to as mCSAAC (multi-agent Counterfactual Soft self-Attention Actor-Critic), is proposed. Firstly, to address the issue of credit assignment where global rewards during centralized training fail to reflect individual contributions, a counterfactual multi-agent policy gradient is proposed. Secondly, a signature-based self-attention communication mechanism is added between each agent to tackle the short-sightedness problem introduced by fully decentralized execution. Finally, using the COSCO simulation platform and workload generated based on the Bitbrain dataset, the algorithm is evaluated through simulation experiments and compared with benchmark algorithms. The performance evaluation including energy consumption, response time, task completion and so on, demonstrates the effectiveness of the algorithm.

2 Related Work

Edge computing utilizes its powerful computational capabilities to enable real-time processing of tasks at user terminal nodes. However, due to the limitation of communication, computing and storage resources, how to effectively cooperate between multiple users and MEC servers to provide green, fast and high-quality services [4] is a hot and difficult point in the current edge resource scheduling research.

In order to solve the drawbacks of traditional methods, a group of more intelligent resource scheduling methods represented by machine learning and deep learning came into being. Machine learning has been widely employed to solve resource allocation problems in MEC networks. Liu et al. [5] introduced an algorithm grounded in machine learning for efficient resource allocation in edge and IoT networks. The algorithm leverages clustering techniques to categorize IoT users into distinct clusters. Xu et al. [6] presented a decision mechanism based on Q-learning that combines task offloading and scheduling. The primary objective of this mechanism is to minimize the energy consumption of applications while simultaneously ensuring the fulfillment of overall execution latency requirements. Resource allocation mechanisms based on

3.1 System Model

This paper models the collaborative resource scheduling problem for multiple users and multiple MEC servers as a fully cooperative multi-agent task. Each user with computational task demands is treated as an intelligent agent that needs to select the appropriate computing node to migrate its application container and occupy the corresponding computational resources to complete its computing tasks.

(1) Action

In the time slot I_t , the actions of each agent include the selection of the compute node (MEC server) and the migration of the application task container.

(2) Global state and local observation

In the time slot I_t , set the MEC server utilization indicator set as $U(h_i^i)$, including the MEC server RAM, CPU, disk and network bandwidth usage. In addition, the set of the maximum capacity of memory, CPU, disk and network bandwidth of the MEC server h_i and the average communication delay is recorded as $C(h_i)$, and the utilization index of the active task $j_t^m \in J_t$ is recorded as $U(j_t^m)$, when the agent makes action selection, the following constraints should be met:

$$U(h_i^i) + U(j_t^m) \leq C(h_i) \quad (1)$$

Thus, the agent action process can be described as:

$$\hat{D}(J_t) \times \left\{ U(j_t^m) \mid \forall j_t^m \in J_t \right\} \rightarrow \left\{ U(h_i^i) \mid \forall h_i \in H \right\} \times K \quad (2)$$

where K is a set of QoS parameters, including power consumption and response delay.

(3) Reward function

Since the optimization objectives are to minimize the average energy consumption and the average latency, this paper comprehensively considers the reward function in combination with the algorithm architecture and optimization goal, and adds additional auxiliary rewards to make the algorithm easier to get closer to the optimization goal [9].

The reward function consists of three parts, the formula is as follows:

$$r_t(s_t, a_t) = r_E(s_t, a_t) + r_T(s_t, a_t) + \sum_{h_i \in H} r_{\text{add}}(x_{h_i}) \quad (3)$$

$r_E(s_t, a_t)$ represents the average energy consumption reward in the time slot I_t , defined as follows:

$$r_E(s_t, a_t) = k_1 \cdot \frac{\sum_{h_i \in H} \int_{t_i^{\text{begin}}}^{t_{i+1}^{\text{begin}}} \text{Power}_{h_i}(t) dt}{|J_t| \sum_{h_i \in H} \text{Power}_{h_i}^{\text{max}} \times (t_{i+1} - t_i)} \quad (4)$$

where $\text{Power}_{h_i}(t)$ is the power function of the MEC server h_i at the moment, $\text{Power}_{h_i}^{\text{max}}$ is the maximum possible power of the MEC server h_i , k_1 is the weight of the current reward, $-1 < k_1 < 0$.

$r_T(s_t, a_t)$ represents the average delay reward in the time slot I_t , including the average response time of all completed tasks and the average migration time of all ongoing tasks, defined as follows:

$$r_T(s_t, a_t) = k_2 \cdot \left(\frac{\sum_{l_j^t \in L_t} \text{ResponseTime}(l_j^t)}{|L_t| \max_{\lambda \leq t} \max_{l_j^\lambda \in L_\lambda} \text{ResponseTime}(l_j^\lambda)} + \frac{\sum_{(j_k^t, h_k) \in \hat{D}(J_t)} \text{MigrationTime}(j_k^t, h_k)}{|\hat{D}(J_t)| \max_{\mu \leq t} \max_{j_k^\mu \in J_\mu} \text{MigrationTime}(j_k^\mu, h_k)} \right) \quad (5)$$

where $\text{ResponseTime}(l)$ is the response delay of the completed task l , $\text{MigrationTime}(j, h)$ is the migration time of the ongoing task j to the MEC server h , k_2 is the weight of the current reward, $-1 < k_2 < 0$, and the two reward weights follow $k_1 + k_2 = -1$.

According to the ratio x_{h_i} of the remaining CPU resources to the total CPU resources of the MEC server h_i , the auxiliary reward value is designed to improve the CPU resource utilization as much as possible while ensuring the low power consumption and latency. The auxiliary reward guide function is defined as follows:

$$r_{\text{add}}(x_{h_i}) = \begin{cases} \frac{1}{|\mathbb{H}|} \cdot (x_{h_i} - 0.6), & x_{h_i} \geq 0.6 \\ 0, & x_{h_i} < 0.6 \end{cases} \quad (6)$$

3.2 Counterfactual Credit Assignment

At each time step t , each agent independently makes scheduling decisions according to its policy network and obtains actions $a_t^i = \pi_i(z_t^i)$ based on the current local observation z_t^i . That is, each user needs to select appropriate edge computing nodes for task migration and calculation according to the attributes of the currently generated computing tasks. When action $a_t = (a_t^1, a_t^2, \dots, a_t^N)$ is performed, the evaluation network provides a common reward value for the joint action, and finally stores the experience (s_t, a_t, s_{t+1}, r_t) gained from the action in a replay buffer, s_t indicates the global status.

In the training process, the evaluation network adopts a dual network structure to reduce the evaluation network's overestimation of the action Q value. In each iteration, the smaller output Q value is selected from the two networks with the same structure for Q value iteration and gradient descent:

$$Q_{\theta_i, j}(s_t, a_t) = r_t(s_t, a_t) + \gamma E \left[\min_{j=1,2} Q_{\theta_i, j}(s_{t+1}, a_{t+1}) - \alpha \log(\pi_\phi(a_{t+1}|s_{t+1})) \right] \quad (7)$$

Then, the output of the dual objective network is used to calculate the target value of the agent's joint scheduling selection, which is defined as:

$$Q_{\theta_i, j, \text{tar}}(s_t, a') = r(a', s_t) + \gamma \left[\min_{j=1,2} Q_{\theta_i, j}(s_t, a') - \alpha \log(\pi_\phi(a'|s_{t+1})) \right] \quad (8)$$

where a' is the action made for the next time step state s_{t+1} .

In addition, the dual evaluation network needs to be updated by minimizing the loss function, which is

$$J_{Q(\theta_{i,j})} = E_{(s_k, a_k) \sim B} \left[\frac{1}{2} \left(Q_{\theta_{i,j}}(s_k, a_k) - Q_{\theta_{i,j}, \text{tar}}(s_k, a') \right)^2 \right], j = 1, 2 \quad (9)$$

The dual-objective network parameters are updated by soft update:

$$\theta_{i,j} \leftarrow \tau \cdot \theta_{i,j} + (1 - \tau) \cdot \theta_{i,j}, j = 1, 2 \quad (10)$$

Counterfactual baseline is the use of counterfactual thinking to infer how much each agent contributes to the completion of the overall task. In this paper, the concept of counterfactual baseline is introduced into the current algorithm, each agent is given a specific advantage function [10]. By comparing the expected return of an agent with the counterfactual baseline while keeping the actions of other agents unchanged, the contribution of the agent’s action to the overall task can be estimated, thereby improving the overall network performance. Therefore, the policy network is updated using the following gradient update strategy:

$$G = E_{\pi} \left[\sum_i \nabla_{\theta_k} \log \pi^i(a^i | \tau^i) A^i(s, a) \right] \quad (11)$$

In the formula, $A^i(\tau, a) = Q(s, a) - \sum_{a^i} \pi(a^i | \tau^i) Q(s, (a^{-i}, a^i))$ is the counterfactual advantage, calculating a separate benchmark for each agent to infer what would happen if only its own actions changed. s is the global state, τ^i is the action of all agents, τ^i is the historical sequence of actions of the agent i , a^{-i} is the actions of all other agents except the agent a .

3.3 Communication Mechanism

In this paper, the CTED architecture is used, which involves centralized training and decentralized execution. However, during decentralized execution, each agent can only take short-sighted actions based on its local observations, and agents cannot coordinate their actions. To address this limitation, a communication mechanism based on self-attention is proposed to enhance the algorithm presented in the previous section. This allows users to exchange messages among themselves, effectively reducing information loss and non-stationarity in the environment. By leveraging self-attention, users can share information and collaborate, enabling a more coordinated and effective resource scheduling process.

N agents perform a cooperative task together, and their policies $\{\pi_1, \dots, \pi_N\}$ correspond to the parameters $\{\theta_1, \dots, \theta_N\}$ respectively. At each time step t , the i th agent receives a local observation $\omega_i^t, i \in \{1, \dots, N\}$, and must select an environmental action $a_i^t \sim \pi_{\theta}$ and communication message m_i^t that will be received by other agents at the next time step, ultimately maximizing the global reward $r_t \sim R$.

Each agent serves as both a sender and a receiver. As a sender, it generates signatures and message values. As a receiver, it generates query vectors to focus on messages from other agents. The attention weight α_{ij} is obtained by using the standardized dot product between the sending end and the receiving end. When the value of α_{ij} is larger, it indicates that the agent i is more concerned about the information sent by the agent j . So the information of the agent i accounts for a significant proportion of the information collected by the agent j . In this framework, all agents are still fully connected. However, when processing information, each agent takes into account the weights for different intelligent agents' information, which is achieved through the attention mechanism.

The policy for each agent is π_{θ_i} . At each time step, local observations ω_i^t and a vector c_i^t that aggregates the messages sent by all agents in previous time steps are used to update the neural network's hidden state h_i^t , which encodes the complete information-action-observation history up to the current time period t . Based on this internal state representation, the agent policy $\pi_{\theta_i}(a_i^t|h_i^t)$ predicts the class distribution of the action space, and another output generates an outgoing output message vector m_i^t . In all experiments, the agents are symmetric and the policies are instantiated from the same set of shared parameters. This greatly speeds up learning.

The self-attention mechanism is used in the communication structure to achieve the goal, and each message m_i^t consists of two parts: a signature $k_i^t \in R^{d_k}$ and a value $v_i^t \in R^{d_v}$ sent to the target recipient. On the receiving side, each agent predicts a query vector $q_j^{t+1} \in R^{d_k}$ from its hidden state h_j^{t+1} and uses it to compute the dot product with N message signatures. This is done by adding $1/\sqrt{d_k}$ with softmax to get the attention weight of each message value vector:

$$\alpha_j = [\alpha_{j1} \cdots \alpha_{ji} \cdots \alpha_{jN}] = \text{softmax} \left[\frac{q_j^{t+1T} k_1^t}{\sqrt{d_k}} \cdots \frac{q_j^{t+1T} k_i^t}{\sqrt{d_k}} \cdots \frac{q_j^{t+1T} k_N^t}{\sqrt{d_k}} \right] \quad (12)$$

$$u_j^{t+1} = \sum_{i=1}^N \alpha_{ji} v_i^t \quad (13)$$

For multiple communication stages, the aggregated message vector u_j^{t+1} and internal state h_j^t are first used to predict the next internal state h_j^t , taking into account the first round of communication:

$$h_j^t = \text{sigmoid} \left(W_{h \rightarrow h'} \left[u_j^{t+1} \parallel h_j^t \right] \right) \quad (14)$$

Next, the signatures, values, and keys are predicted by h_j^t , and then the steps are repeated for multiple rounds until a new final aggregate message vector u_j^{t+1} is obtained as input for the next time step.

4 Experiment

4.1 Environment

The simulation environment used in this study is COSCO [11], which is a framework that enables coupled simulation and container orchestration in edge/fog environments. By employing COSCO, a platform that encompasses identical fundamental models of task migration, workload generation, and utilization metrics in both simulation and real testing, the resource scheduling process on the edge can be effectively simulated. In order to test the effectiveness of the proposed algorithm, experiments are carried out on the simulation platform. Moreover, the framework uses an open-source Bitbrain dataset based on the real world to generate dynamic workloads.

4.2 Results

In this paper, two multi-agent DRL algorithms, mSAC and MADDPG, are selected to test the edge side resource scheduling in the same environment. After running the specified number of rounds, the proposed model was evaluated overall using three indexes, namely, average response time, average migration time and average task energy consumption. The calculation results of these indexes were provided by the simulation framework.

Firstly, the setting of simulation parameters is introduced. A total of 300 rounds are run, and the interval of each round is 300 s. 50 servers are set in the edge network. The learning rate of the policy network is set to $1e-3$, the learning rate of the value network is set to $1e-2$, and the soft update parameter is set to 0.005. The overall performance of the algorithm is evaluated by using evaluation indexes.

Table 1. Overall experimental result.

Model	Average response time (s)	Average migration time (ms)	Average task energy consumption (KWH)
mSAC	1495.25	155.97	1109.91
MADDPG	1710.23	190.30	1121.93
mCSAAC	1441.73	69.77	1062.71

As can be seen from Table 1, the average response time of mCSAAC algorithm is reduced by 3.58 and 15.70% compared with mSAC and MADDPG. The average migration time is reduced by 55.27 and 63.34% compared with mSAC and MADDPG. The average task energy consumption decreased by 5.28 and 4.25% compared with mSAC and MADDPG.

Figure 2 shows the distribution of the average response time of each algorithm in each interval. The average response time of mCSAAC algorithm is concentrated in the range [0, 2170.14], with a median of 1098.45 and a maximum of 5425.36. The average response time of mSAC algorithm is concentrated in the range [0, 2218.22], the median is 1175.89, and the maximum is 5545.55. The average response time of MADDPG

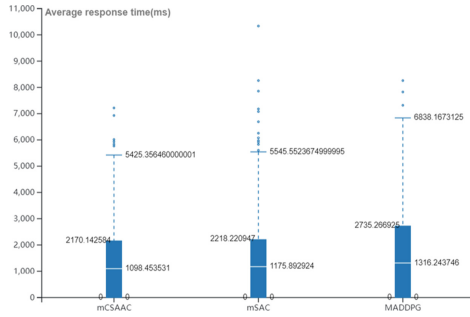


Fig. 2. Average response time

algorithm is concentrated in the interval of $[0, 2735.27]$, the median is 1316.24, and the maximum is 8838.17. From the perspective of the average response time of all intervals, mCSAAC algorithm is 3.58% and 15.70% lower than mSAC and MADDPG, respectively. Overall, mCSAAC outperforms other algorithms in terms of response time.

Figure 3 shows the average migration time, number of tasks completed and sum of wait time for each algorithm. In terms of average migration time, mCSAAC algorithm is 55.27 and 63.34% lower than mSAC and MADDPG. In terms of the number of tasks completed, mCSAAC algorithm is 22.30% and 3.34% higher than mSAC and MADDPG, respectively. In terms of wait time, mCSAAC algorithm is 6.08 and 3.01% lower than mSAC and MADDPG.

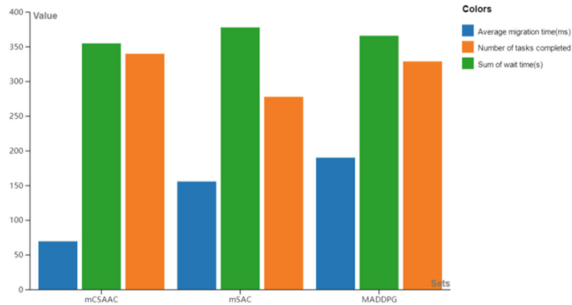


Fig. 3. Statistics of migration time, completed tasks and wait time

Figure 4 shows the distribution of per container interval energy consumption of each algorithm in each interval. The per container interval energy consumption of mCSAAC algorithm is concentrated in the range $[78.35, 132.76]$, with a median of 110.95 and a maximum of 182.71. The per container interval energy consumption of mSAC algorithm is concentrated in the range $[67.4, 147.56]$, the median is 119.95, and the maximum is 147.56. The per container interval energy consumption of MADDPG algorithm is concentrated in the interval of $[142.76, 193.82]$, the median is 165.73, and the maximum is 270.42. Overall, mCSAAC outperforms other algorithms in terms of energy consumption.

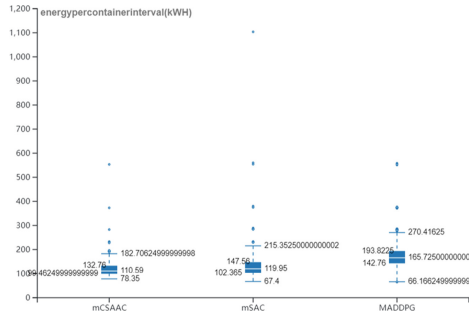


Fig. 4. Energy per container interval

5 Conclusion

In this paper, based on deep reinforcement learning algorithm, the multi-agent Counterfactual Soft self-Attention Actor-Critic algorithm(mCSAAC) is proposed to realize the resource scheduling of edge network, and to a certain extent the optimization goal of minimizing the delay and energy consumption of resource scheduling on edge side is achieved. In the future, indicators such as cost and mobility can be added. Then the attributes of various tasks can be more carefully considered and simulated to further improve the practicability of the algorithm.

Acknowledgement. This work is supported by National Key R&D Program of China (2019YFB2103202).

References

1. Khan, W.Z., Ahmed, E., Hakak, S., et al.: Edge computing: a survey. *Futur. Gener. Comput. Syst.* **97**, 219–235 (2019)
2. Djigal, H., Xu, J., Liu, L., et al.: Machine and deep learning for resource allocation in multi-access edge computing: a survey. *IEEE Commun. Surv. Tutor.* **24**(4), 2449–2494 (2022)
3. Fan, Y., Wang, L., Wu, W., et al.: Cloud/edge computing resource allocation and pricing for mobile blockchain: an iterative greedy and search approach. *IEEE Trans. Comput. Soc. Syst.* **99**, 1–13 (2021)
4. Karthiban, K., Raj, J.S.: An efficient green computing fair resource allocation in cloud computing using modified deep reinforcement learning algorithm. *Soft. Comput.* **24**(3), 14933–14942 (2020)
5. Liu, X., Yu, J., Wang, J., et al.: Resource allocation with edge computing in IoT networks via machine learning. *IEEE Internet Things J.* **7**(4), 3415–3426 (2020)
6. Xu, S., Liu, Q., Gong, B., et al.: RJCC: reinforcement-learning-based joint communicational-and- computational resource allocation mechanism for smart city IoT. *IEEE Internet Things J.* **7**(9), 8059–8076 (2020)
7. Yan, J., Bi, S., Zhang, Y.: Offloading and resource allocation with general task graph in mobile edge computing: a deep reinforcement learning approach. *IEEE Trans. Wireless Commun.* **19**(8), 5404–5419 (2020)

8. Feng, J., Yu, F.R., Pei, Q., et al.: Cooperative computation offloading and resource allocation for blockchain-enabled mobile-edge computing: a deep reinforcement learning approach. *IEEE Internet Things J.* **7**(7), 6214–6228 (2020)
9. Haarnoja, T., Zhou, A., Abbeel, P., et al.: Soft actor-critic: off-policy maximum entropy deep reinforcement learning with a stochastic actor. *Proc. Int. Conf. Mach. Learn.*, 1861–1870 (2018)
10. Foerster, J., Farquhar, G., Afouras, T., et al.: Counterfactual multi-agent policy gradients. *ArXiv, abs/1705.08926* (2017)
11. Tuli, S., Poojara, S., Srirama, S.N., et al.: COSCO: container orchestration using co-simulation and gradient based optimization for fog computing environments. *IEEE Trans. Parall. Distrib. Syst.* **33**(1), 101–116 (2022)



IMAP-GCG: Edge Container Resource Scheduling and Configuration Method Based on Improved MAPPO and GCN-GRU

Xingle Gong, Yang Yang^(✉), Yating Sun, Zhipeng Gao, and Lanlan Rui

State Key Laboratory of Networking and Switching Technology, Beijing University of Posts and Telecommunications, Beijing, China
yyang@bupt.edu.cn

Abstract. Container technology has been widely used in industrial development, including system deployment and program management, and has achieved very good results. However, in the current edge network environment, there are delay problems caused by container cold start and user terminal task changes, which need to be solved by designing a flexible and efficient edge container resource configuration method. In response to this problem, this paper proposes a method for dynamic container resource allocation called Improved Multi-Agent PPO with GCN-GRU (IMAP-GCG). This method mainly implements the prediction of terminal workload, container resource pre-configuration and container resource scheduling methods. First, we propose a timing prediction model with GCN and GRU as the encoder and LSTM as the decoder to predict the temporal periodicity of user requests, so as to deploy containers in advance. Then, a MAPPO algorithm based on trusted region policy optimization is proposed to schedule container resources, which improves the performance of container resource scheduling. Experiments on two workloads show that the IMAP-GCG model proposed in this paper is superior to the existing advanced multi-agent reinforcement learning model in terms of CPU utilization, bandwidth utilization, and task average delay. The task type forecasting accuracy on this indicator is due to the existing advanced time series forecasting models.

Keywords: Container resource scheduling · Edge network · Multi-agent reinforcement learning · Timing application category prediction

1 Introduction

In recent years, with the continuous development of information technology, virtualization technology has been widely used in the industry, among which container technology is gradually replacing virtual machine technology to become the most efficient and convenient method in the actual production environment.

Container technology also plays a key role in the current edge network environment. However, there are currently delays caused by container startup delays and user terminal task changes. For example, starting container processing after the task arrives. There

will be additional time loss in between, and the user's continuous request generates a large amount of time series data, and the user's request behavior has the potential time periodicity. For example, users only send latency-sensitive task requests to the edge network, including shopping, social and traffic application requests. Socially related task requests may increase significantly during the evening, when entertainment is often the norm. In addition, in container resource scheduling, there are also problems of inefficient resource scheduling and inability to cooperate effectively between containers. The CPU resources and bandwidth resources corresponding to the server cannot be effectively allocated. At present, the common method to solve the first problem is to use the time series model to predict the tasks in the period, such as traditional LSTM [1], GRU [2], or Transformer [3] application category prediction according to the amount of resources occupied by the task Level deploys the number of containers of the corresponding level. A common way to solve the second problem is to use a more advanced multi-agent deep reinforcement learning model, such as MADDPG [4] or MAPPO [5].

In order to solve the above two problems, this paper proposes a timing prediction model based on GCN and GRU as the encoder and LSTM as the decoder to predict the period of the task, so as to solve the problem of container startup delay, and the GCN module in the model matches The complex network structure of the edge network is further improved to further improve the accuracy of application category prediction; a MAPPO algorithm based on trust region policy optimization is proposed to schedule container resources, and to solve the problem that multiple containers cannot effectively cooperate with each other that may be caused by the MAPPO algorithm.

2 Related Work

At present, many researchers have studied task type prediction in the edge network environment. Miao et al. [6] proposed a computational offloading and task migration algorithm based on task prediction. Computing task prediction based on LSTM algorithm, mobile device computing offloading strategy based on task prediction, and task migration of edge cloud scheduling scheme are used to assist in optimizing the edge computing offloading model. Qin et al. [7] proposed an Application Prediction (AP) algorithm to minimize response delay. This problem has been proven to be an NP-hard problem. First, in applying the predictive model, a LSTM approach is proposed to predict future tasks for accessing the device. Su et al. [8] proposed an Edge-Cloud Collaborative Computing Framework and Resource Deployment Algorithm with Task Prediction (RDAP).

And many scholars are engaged in the research of multi-agent reinforcement learning resource scheduling in the edge network environment. Ju et al. [9] proposed a joint security offload and resource allocation (SORA) scheme based on deep reinforcement learning is proposed to improve the secrecy performance and resource efficiency of multi-user VEC networks. Li et al. [10] proposed TapFinger, a distributed scheduler for edge clusters that minimizes the total completion time of ML tasks by jointly optimizing task placement and fine-grained multi-resource allocation. Danino et al. [11] proposed Multi-agent environments for deep reinforcement learning-based decision-making mechanisms. High action space complexity is addressed by decentralizing the distribution of decisions among multiple agents.

3 Improved Multi-agent PPO with GCN-GRU

As shown in Fig. 1, this paper refers to the above ideas and proposes improved multi-agent PPO with GCN-GRU (IMAP-GCG) model. This model draws on the encoder and decoder architecture, combines the GCN, GRU and LSTM models, and uses the GCN-GRU as the encoder and the LSTM model as the decoder, and use GCN as the fitting function of MAPPO to fit the policy function and action value function.

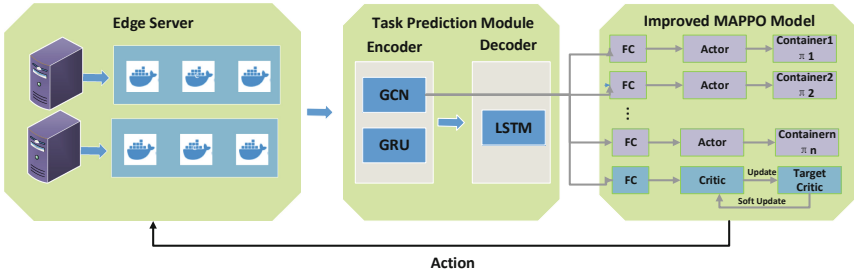


Fig. 1. IMAP-GCG model architecture

3.1 Application Category Prediction and Container Deployment via GCN-GRU

As shown in Fig. 2, this paper combines GCN and GRU to realize the encoder structure, and uses LSTM as the decoder to make predictions in time series, predict the types of tasks that will appear in the next period of time and the magnitude of occupied resources, according to the prediction result directs the server to dynamically configure the number of containers.

GRU is used as the main model for learning the temporal features of dynamic networks. GCN is applied to capture the local structural properties of network nodes and the relationships between them, and the GCN model is used to perform convolutional operations on the hidden layer h .

$$\bar{h}_{t-1} = GCN(A_{t-1}, h_{t-1}) \tag{1}$$

$$z_t = \sigma \left(W_z \cdot \left[\bar{h}_{t-1}, x_t \right] \right) \tag{2}$$

$$r_t = \sigma \left(W_r \cdot \left[\bar{h}_{t-1}, x_t \right] \right) \tag{3}$$

$$\tilde{h}_t = \tanh \left(W \cdot \left[r_t * \bar{h}_{t-1}, x_t \right] \right) \tag{4}$$

$$h_t = (1 - z_t) * \bar{h}_{t-1} + z_t * \tilde{h}_t \tag{5}$$

As shown in Fig. 2 and Eqs. (1)–(5): the hidden layer state h_{t-1} is obtained after GCN processing as \bar{h}_{t-1} , and \bar{h}_{t-1} is then calculated by Eq. to obtain the state h_t of the

next layer. In this paper, the output h_t of the encoder layer is used as the input of the attention layer, and the attention layer receives the input and then converts it into the decoder the input C_t of the LSTM model in the layer.

The attention mechanism used in this paper is Luong-Attention, and the formula is shown below:

$$a_t(s) = \frac{\exp(\text{score}(h'_t, h_s))}{\sum_{s'} \exp(\text{score}(h'_t, h_{s'}))} \tag{6}$$

First, calculate the decoder's hidden layer state h'_t at moment t for each hidden layer state h_s weight value $a_t(s)$ of Encoder, where score is the vector inner product (Dot), and then use the weights to calculate the context state vector S_t .

$$S_t = \sum_s a_t(s) \cdot \bar{h}_s \tag{7}$$

Next, the new state is obtained by splicing the generated state vector with the decoder state h'_{t+1} .

$$h'_{t+1} = \tanh(W_c \cdot \text{concat}(c_t, h'_t)) = \tanh(W_c \cdot [c_t; h'_t]) \tag{8}$$

After the decoder processing is completed, it is then processed by SoftMax function to do multi-classification processing and finally get the classification result. And according to the classification result, the server is guided to deploy the container of the corresponding application in advance, so as to solve the problem of container cold start delay.

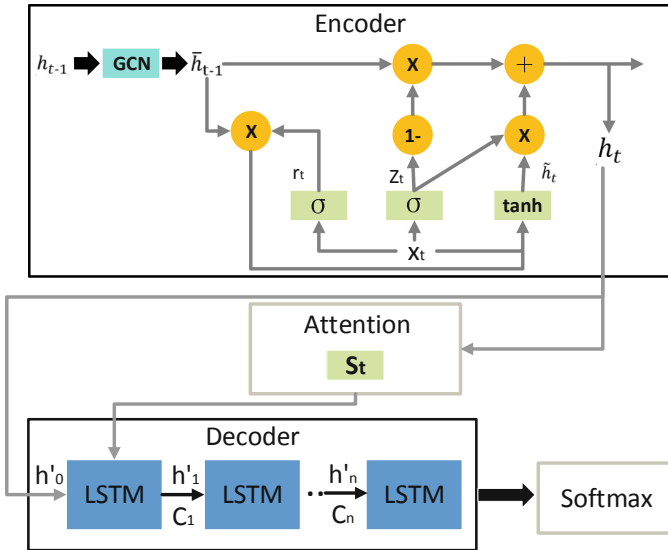


Fig. 2. Structure of application category prediction module

3.2 Container Resource Scheduling with Improved MAPPO

In the algorithm proposed in this paper, the intelligent body schedules resources based on the current state. The next network state obtained in the next time slot t depends only on the previous state and action, which is in accordance with the Markov property.

Status space. This state space refers to the network space state. It includes the computational resources, bandwidth resources, and node task latency occupied by all node tasks.

$$\begin{aligned} C_n(t) &= \frac{1}{|\sigma|} \sum_{l \in \sigma} C(t), \forall n \in N \\ B_n(t) &= \frac{1}{|\sigma|} \sum_{l \in \sigma} B(t), \forall n \in N \\ D_n(t) &= \frac{1}{|\sigma|} \sum_{l \in \sigma} D(t), \forall n \in N \end{aligned} \quad (9)$$

Action space. According to the definition of resource scheduling, the DRL action space in this paper is the container's request for computational resources RC as well as bandwidth RB resources and their recovery. Since resource allocation belongs to the action space that is continuous. In addition, the adjustment of the task maximum delay threshold D_{MAX} and the queue fluctuation length threshold U_{MAX} is included. Thus, the action can be expressed in the form of a quadruplet of $A = \{RC, QC, D_{MAX}, U_{MAX}\}$.

Reward function. The reward is the feedback given to the intelligence by the decision of resource scheduling. Thus, depending on the utilization of computational and bandwidth resources involved in the goal and the task latency set:

$$\mathcal{R}_t = \left[\alpha \cdot R_C(t) + \beta \cdot R_B(t) + \Omega \cdot \frac{1}{D(t)} \right] \quad (10)$$

α, β, Ω in the above equation are all weight parameters, which are artificially set according to different network environments.

Evaluation Metrics. Calculate resource utilization (CU) and bandwidth resource utilization (BU), representing the overall resource utilization of all containers over multiple runtimes t . Average task latency, including communication transfer time, task wait time and task execution time, $TAD = T_c + T_w + T_e$.

MAPPO adopts parameter sharing, which can well solve the cooperation problem of intelligences, but the current MAPPO model deals with the cooperation scenario of intelligences, where the direction of intelligence policy updates may conflict with each other, leading the algorithm into suboptimal solutions. To solve this problem, the idea of trust region policy learning is introduced into the multi-intelligent environment.

$$A_{\pi}^{a_1:n}(s, \mathbf{a}^{a_1:m}) = \sum_{a=1}^n A_{\pi}^{ax}(s, \mathbf{a}^{a_1:x-1}, a^{ax}) \quad (11)$$

where π denotes the joint strategy and $a_1 : n$ denotes an ordered subset of $[a_1, a_2, \dots, a_n]$.

In order to better improve the learning efficiency and help the intelligence to estimate the state and action values more accurately, a value function is designed in MAPPO to assist learning. The value function is shown below:

$$L(\phi) = \frac{1}{Bn} \sum_{i=1}^B \sum_{k=1}^n \left(\max \left[\left(Q_{\phi} \left(s_i^{(k)} \right) - Y \right)^2, \left(\text{clip} \left(Q_{\phi} \left(s_i^{(k)} \right), Q_{\phi_{\text{old}}} \left(s_i^{(k)} \right) - \varepsilon, Q_{\phi_{\text{old}}} \left(s_i^{(k)} \right) + \varepsilon \right) - Y \right)^2 \right] \right) \quad (12)$$

where y is the discounted reward, Bn denotes the size of batch-size and n denotes the number of intelligences.

MAPPO will have the problem of overestimation of the value function, in order to solve this problem, this paper uses a pair of independent neural networks to estimate Critic. But this treatment may carry high variance, in order to solve the problem of high variance, the method of clipped Double Q-learning is used, and the gradient is cropped when updating that is to take the smallest Q value. The formula is shown as follows:

$$Y = r + \gamma \min_{i=1,2} Q_{\theta_i}(s', \pi_{\phi_1}(s') + \varepsilon) \quad (13)$$

Since the learning target is susceptible to the error caused by the function approximation error, which increases the variance of the target This paper introduces a regularization strategy for value function learning. The formula is shown as follows:

$$\tilde{a} \leftarrow \pi_{\phi'}(s') + \varepsilon, \varepsilon \sim \text{clip}(N(0, \tilde{\sigma}), -c, c) \quad (14)$$

4 Simulation

First, we generate training data for the IMAP-GCG model by running a random scheduler with 500 intervals and a scheduling interval of 20 s in the simulation environment provided by [12]. The evaluation metrics in this paper are described in the algorithm section, including CPU utilization, bandwidth utilization, overall task latency, and application category prediction accuracy, which will be presented as a confusion matrix and a cross-entropy loss function.

4.1 Workload

In this paper, two workload cases, AZ2017 and AZ2019, are used to simulate realistic application task generation situations. In the above two workload cases, I train and test the IMAP-GCG algorithm as well as the comparison algorithm.

4.2 Baseline

We evaluate the performance of the proposed algorithms and compare them with excellent scheduling methods. We considered a total of four comparison algorithms.

MAPPO. This algorithm is used in this paper as a comparison of resource scheduling templates, MAPPO [5] is for multi-intelligent reinforcement learning that builds on the PPO (Proximal Policy Optimization).

IMP-MARL. This algorithm [13] is used in this paper as a comparison of resource scheduling templates, this algorithm is an open-source suite of MARL environments for large-scale infrastructure management planning (IMP) that uses decentralized execution of centralized training to better scale as the number of intelligences grows.

GC-LSTM. This algorithm [14] is used in this paper as a comparison of task prediction templates, this algorithm proposes a new end-to-end deep learning model that extracts the structural features of each snapshot network by GCN and learns the temporal structure by LSTM.

SPG. This algorithm [15] is used in this paper as a comparison of task prediction templates, this algorithm proposes a general scalable spatio-temporal time-series deep learning framework is proposed, which utilizes a novel coding method based on random cyclic components and scalable GNN architecture.

4.3 Simulation Results

Table 1 shows the comparison of the evaluation metrics of the IMAP-GCG model proposed in this paper with other baseline models under different workloads.

Table 1. Performance comparison of IMAP-GCG with other baseline models

Workload	Model	CU (%)	BU (%)	TAD (s)	Model	CE
AZ2017	IMAP-GCG	78.99	31.01	2.76	IMAP-GCG	0.0538
	MAPPO	78.23	31.25	2.87	GC-LSTM	0.0752
	IMP-MARL	76.52	29.83	2.96	SGP	0.1083
cAZ2019	IMAP-GCG	81.83	32.87	2.83	IMAP-GCG	0.0628
	MAPPO	81.28	32.97	2.96	GC-LSTM	0.0803
	IMP-MARL	80.75	30.52	3.05	SGP	0.1235

As can be seen from Fig. 3, the IMAP-GCG proposed in this paper is higher than MAPPO by 0.97% and higher than IMP-MARL by 3.23% in CPU utilization metrics on workload AZ2017, and higher than MAPPO by 0.68% and higher than IMP-MARL by 1.34% on workload AZ2019. The experimental results in two different workload environments indicate that the performance of the IMAP-GCG proposed in this paper is slightly better than MAPPO and better than IMP-MARL in balancing the CPU load. This indicates that IMAP-GCG has a greater advantage in resource scheduling, and the combination of the trust region policy mechanism and the clipped Double Q-learning approach can better balance the computational resource load and achieve a balanced state.

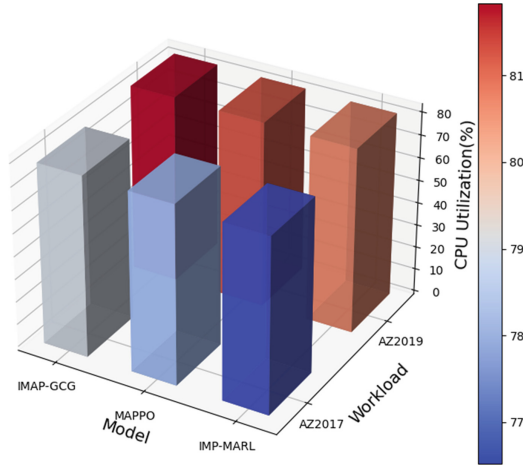


Fig. 3. Comparison of CPU utilization on different workloads

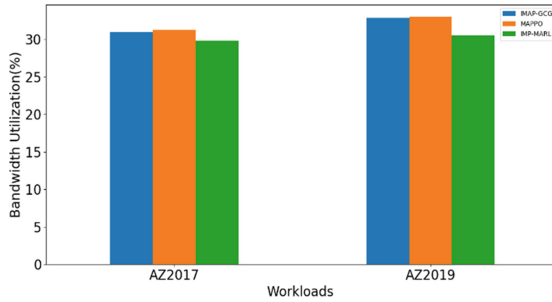


Fig. 4. Comparison of bandwidth utilization on different workloads

As can be seen from Fig. 4, the IMAP-GCG proposed in this paper is slightly lower than MAPPO by 0.79% and higher than IMP-MARL by 3.96% in terms of bandwidth utilization metric on workload AZ2017, and slightly lower than MAPPO by 0.30% and higher than IMP-MARL by 7.70% on workload AZ2019. The experimental results in two different workload environments indicate that the performance of the IMAP-GCG proposed in this paper is slightly lower than MAPPO and better than IMP-MARL in balancing the bandwidth load.

From Fig. 5, it can be seen that the IMAP-GCG proposed in this paper is higher than MAPPO by 3.83% and IMP-MARL by 6.76% on the task average delay metric of workload AZ2017, and higher than MAPPO by 4.39% and IMP-MARL by 7.21% on workload AZ2019. The experimental results in two different workload environments indicate that the performance of IMAP-GCG proposed in this paper is slightly higher than MAPPO and better than IMP-MARL in terms of task average delay, which indicates that IMP-MARL has a greater advantage in reducing task delay, using task type prediction and combining the trust region policy mechanism and clipped The double Q-learning



Fig. 5. Comparison of task average delay on different workloads

approach is better at reducing task latency, and the use of early deployment of containers greatly reduces task average delay.

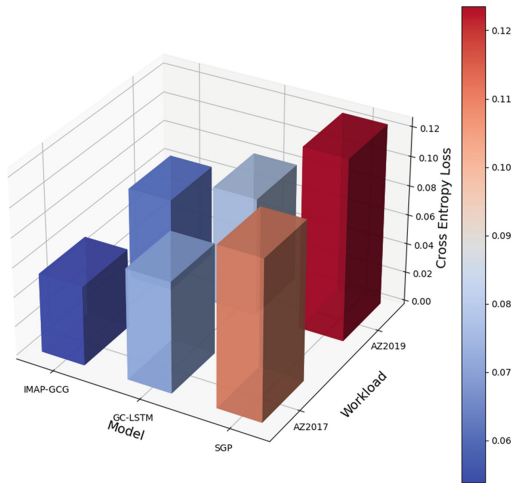


Fig. 6. Comparison of cross entropy on different models

From Fig. 6, it can be seen that the IMAP-GCG proposed in this paper is lower than MAPPO as well as IMP-MARL on Cross Entropy in workload AZ2017, and lower than MAPPO as well as IMP-MARL in workload AZ2019. Experimental results in two different workload environments indicate that the IMAP-GCG proposed in this paper This indicates that IMP-MARL has a greater advantage in task type prediction with high prediction accuracy, and the way of deploying containers in advance by using task type prediction in this paper greatly reduces task average delay.

5 Conclusion

This paper proposes a novel IMAP-GCG model for container resource scheduling and configuration in edge network environments. Aiming at the delay caused by container start-up delay and task request distribution, the model constructs a GCN-GRU structure to predict task types so as to deploy containers in advance to reduce task delay. Considering the problem that containers cannot cooperate effectively, a trusted region-based MAPPO is proposed to solve this problem. Experiments on two workloads show that our IMAP-GCG model outperforms existing multi-agent reinforcement learning models in container resource scheduling and outperforms existing time-series prediction models in application category prediction.

Acknowledgment. This work is supported by National Key R&D Program of China (2019YFB2103202).

References

1. Hochreiter, S., Schmidhuber, J.: Long short-term memory. *Neur. Comput.* **9**(8), 1735–1780 (1997)
2. Cho, K., et al.: Learning phrase representations using RNN encoder-decoder for statistical machine translation. arXiv preprint [arXiv:1406.1078](https://arxiv.org/abs/1406.1078) (2014)
3. Vaswani, A., et al.: Attention is all you need. *Adv. Neur. Inf. Process. Syst.* **30**, (2017)
4. Lowe, R., et al.: Multi-agent actor-critic for mixed cooperative-competitive environments. *Adv. Neur. Inform. Process. Syst.* **30**, (2017)
5. Yu, C., et al.: The surprising effectiveness of PPO in cooperative multi-agent games. *Adv. Neur. Inform. Process. Syst.* **35**, 24611–24624 (2022)
6. Miao, Y., et al.: Intelligent task prediction and computation offloading based on mobile-edge cloud computing. *Future Gener. Comp. Syst.* **102**, 925–931 (2020)
7. Qin, Z., et al.: Optimal workload allocation for edge computing network using application prediction. *Wireless Commun. Mobile Comput.*, 1–13 (2021)
8. Su, M., Wang, G., Raymond Choo, K.-K.: Prediction-based resource deployment and task scheduling in edge-cloud collaborative computing. *Wireless Commun. Mob. Comp.*, (2022)
9. Ju, Y., et al.: Joint secure offloading and resource allocation for vehicular edge computing network: a multi-agent deep reinforcement learning approach. *IEEE Trans. Intell. Transport. Syst.*, (2023)
10. Li, Y., et al.: Task placement and resource allocation for edge machine learning: a GNN-based multi-agent reinforcement learning paradigm. arXiv preprint [arXiv:2302.00571](https://arxiv.org/abs/2302.00571) (2023)
11. Danino, T., Yehuda, B.-S., Greenberg, S.: Container allocation in cloud environment using multi-agent deep reinforcement learning. *Electronics* **12**, 12 (2023)
12. Tuli, S., et al.: COSCO: container orchestration using co-simulation and gradient based optimization for fog computing environments. *IEEE Trans. Parallel Distrib. Syst.* **33**(1), 101–116 (2021)
13. Leroy, P., et al.: IMP-MARL: a suite of environments for large-scale infrastructure management planning via MARL. arXiv preprint [arXiv:2306.11551](https://arxiv.org/abs/2306.11551) (2023)
14. Chen, J., Wang, X., Xu, X.: GC-LSTM: graph convolution embedded LSTM for dynamic network link prediction. *Appl. Intell.*, 1–16 (2022)
15. Cini, A., et al.: Scalable spatiotemporal graph neural networks. arXiv preprint [arXiv:2209.06520](https://arxiv.org/abs/2209.06520) (2022)



Small Object Detection Algorithm Combining Coordinate Attention Mechanism and P2-BiFPN Structure

Zhou Juanjuan¹, Huang Xiaohan¹, Qin Zebang², and Yin Guangqiang²(✉)

¹ University of Electronic Science and Technology, Chengdu, China
{jjzhou, xhhuang}@std.uestc.edu.cn

² Shenzhen Institute for Advanced Study, UESTC, Shenzhen, China
zbqin@std.uestc.edu.cn, yingq@uestc.edu.cn

Abstract. Aiming at the difficulty of small object detection, a small object detection model combining coordinated attention mechanism and P2-BiFPN (P2 Bidirectional Feature Pyramid Network) structure is constructed based on YOLOv5. Firstly, we introduce the coordinated attention mechanism into the residual units of the backbone network to achieve more accurate localization of small objects. Secondly, to reduce the number of model parameters, we decompose the square convolution in the residual unit into parallel asymmetric convolutions. Then, the P2-BiFPN feature fusion network was constructed to enrich the information of small objects, so as to improve the small objects detection accuracy. Finally, we train and test the model on the WiderPerson dataset. The experimental results shows that compared with YOLOv5, our small object detection model has a 1.7% improvement in mAP and a 5.66 m reduction in the amount of parameters, with better detection performance for small-object pedestrians.

Keywords: Small object detection · YOLOv5 · Coordinated attention · BiFPN

1 Introduction

Object detection algorithm is mainly used to accurately locate and classify interested objects in pictures, which is widely used in industry [1], aeronautical sea surface [2], unmanned driving [3] and other fields. However, it has poor performance in small target detection. Due to the small scale of small targets, there will be problems such as low resolution, little effective information and easy to be affected by background interference, which make the feature expression ability of small targets poor, resulting in low detection accuracy of small targets.

Many researchers have focused on studying deep learning-based object detection algorithms and proposed improvements to comprehensively enhance the performance of small object detection. For instance, Song et al. [4] leveraged the concept of feature pyramid networks and devised a small object detection algorithm based on multiscale feature fusion, effectively integrating high-level and shallow-level features. However, with the increase of the number of network layers, the model parameters become larger

and the inference speed becomes slower. Liu et al. [5] introduced deconvolution layers at the output positions of convolution layers to enhance small object detection, but it slowed down the model's inference speed. Guo et al. [6] augmented the YOLOv5 model with a dedicated small object detection layer to improve detection precision, albeit at the cost of increased model complexity and computational requirements. Liu et al. [7] constructed a multi-branch parallel pyramid network and combined it with supervised spatial attention to suppress background interference, thus enhancing small object feature representation, but the detection precision remained low. Yi et al. [8] introduced the Efficient Channel Attention (ECA) mechanism in the detection model to enhance the representation of small objects. However, the disadvantage is that for smaller feature mappings, the computational overhead is increased.

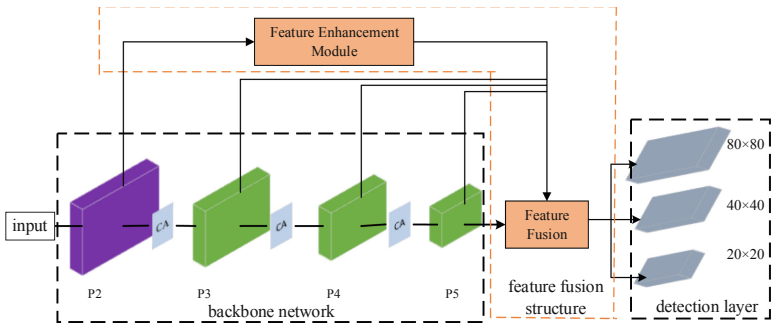


Fig. 1. The overall architecture of the proposed small object detection model

To overcome the aforementioned limitations, we construct a small object detection algorithm which combines coordinated Attention and P2-BiFPN Structure as shown in Fig. 1. Specifically, the contributions we have made are as follows:

- (1) Construction of a backbone network structure that incorporates asymmetric convolution and coordinated attention. The coordinated attention is introduced within the residual units of the backbone network to enhance the feature representation of small objects, and the square convolution in the residual units is replaced by parallel asymmetric convolution to improve model inference speed.
- (2) Construction of a Bidirectional weighted pyramid feature fusion structure that integrates the P2 layers. An edge is added between the input and output nodes of the same layer in the model to enhance feature fusion efficiency and the small target information of the shallow P2 layer is introduced into the high-level feature map to make full use of the shallow features.

2 Related Work

2.1 Combined Attention Mechanism Approach

Incorporating attention mechanisms in algorithmic models allows neural networks to focus more on object-relevant channels and regions by assigning appropriate weights to prioritize object information, thus enhancing model performance. Zhang et al. [9]

proposed a multi-scale feature fusion attention network that combines channel attention and feature fusion modules to enhance small object feature representation. Sun et al. [10] introduced a spatial attention module in the SSD network to enhance the preservation of small object detail features. Zhao et al. [11] incorporated a channel attention mechanism into the feature fusion network to adaptively learn the dependencies between channels and improve the network's feature extraction ability for small objects. Hou et al. [12] proposed an improved version of SENet called SRNet, whose attention mask integrates both local and global information descriptors. Wang et al. [13] added an attention module to sequentially capture feature information across channels and space, enhancing shallow feature extraction.

2.2 Multi-scale Feature Fusion Methods

Multi-scale feature fusion techniques could fuse spatial information from shallow layers with semantic information from higher-level features, resulting in a feature map that incorporates both spatial and semantic object information, thereby improving small object detection performance. Lin et al. [14] proposed feature pyramid networks (FPN) to enhance feature representation by laterally fusing shallow and high-level features. However, the one-way feature transfer in FPNs limits feature fusion capability. Liu et al. [15] introduced the PANet structure, which adds an additional bottom-up pathway to FPN to enhance feature fusion capability but increases the number of model parameters. Hou et al. [16] proposed a Dense Feature Pyramid Network (DFPN) that converges to good results without pre-training. Ghiasi et al. [17] proposed an FPN structure obtained through neural network search, enhancing network feature extraction capability at the cost of increased computational resources. The weighted Bidirectional Feature Pyramid Network (BiFPN) [18] overcomes the limitations of PANet by removing the single input node and adding edges between input and output nodes of the same layer, leading fuller feature fusion without significantly increasing computational overhead.

3 Method

3.1 Improving the YOLOv5 Model for Small Object Detection Algorithm

The YOLO series is a classic one-stage algorithm in object detection algorithms, which can directly return the class and location of the object in the output layer of the network. Among them, YOLOv5 is the fifth generation version with better performance in this series of iterative updates so far, and is also the benchmark model of our network structure. In this thesis, the YOLOv5 network model is improved by adding the coordinated attention, introducing asymmetric convolution and constructing the P2-BiFPN feature fusion structure. Its structure is shown in Fig. 2.

3.2 Introduction of CA and Asymmetric Convolutional Backbone Networks

Since the scale of small objects is relatively small, the effective information that can be extracted is limited. And the backbone network of YOLOv5 model itself has no

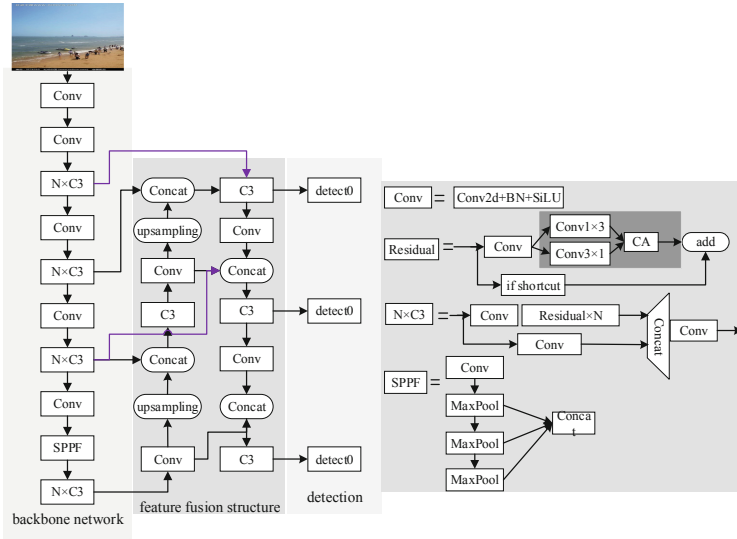


Fig. 2. The proposed network model

preference for object attention, which leads to poor small object feature expression, resulting in serious small object miss detection.

Applying attention mechanism in object detection model can make the network pay more attention to the information related to the object. In 2021, the Coordinate Attention (CA) mechanism [19] proposed a more effective method to capture channel and spatial information to enhance feature representation by embedding location information into channel attention. Compared with the commonly used SENet, CBAM and ECA attention. This method is more effective.

Aiming at the problem of poor feature expression ability of small objects, we added the CA method to the C3 module of the backbone network. The CA structure is shown in Fig. 3, which can acquire the attention on the width and height of the image to output a feature map that is more sensitive to direction and position, enabling the model to locate small objects more accurately.

The CSPDarknet53 backbone network is mainly a stack of ordinary convolutional layers composed of 1×1 and 3×3 convolutional kernels. The 1×1 convolutional layer is less sensitive to the width and height information of the feature map. The 3×3 ordinary convolutional layer is mainly used to learn the invariant features of the image, which has a high degree of nonlinearity and is mostly in the residual module. Therefore, we embed the CA method into the residual unit of the C3 module to enhance the feature representation of small objects. The feature map output by the residual unit is input into the CA structure to learn the weights, the output feature map has sensitive direction and position perception of the object to achieve more accurate localization, and improve the small object detection rate. The addition of the CA method leads to model complexity and larger model computation. The ENet network proposed by Paszke adopts an asymmetric convolution design [20], which reduces the model parameters by about 33% and the complexity of the network. Based on this approach, we decompose

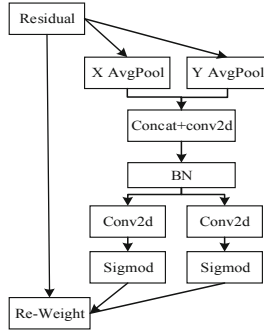


Fig. 3. Coordinate attention

the 3×3 square convolution of residual units in the C3 module into parallel 1×3 and 3×1 asymmetric convolutions, which are then subjected to batch normalization and nonlinear activation operations. This structure reduces the number of model parameters and improves the model inference speed. The structure of the improved C3 module network is shown in Fig. 4.

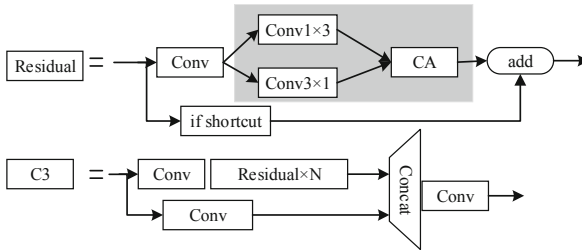


Fig. 4. Improved C3 module structure

3.3 P2-BiFPN Feature Fusion Structure

Since the introduction of FPN by Lin et al. [14], it has been widely used in neural networks for multi-scale feature fusion. The fusion of feature images between multiple layers can improve the effect of small object detection by fusing the shallow small object spatial information with the semantic information of high-level features, three typical multiscale feature fusion networks are FPN, PANet and BiFPN structure.

YOLOv5 network uses the PANet structure for multi-scale fusion, while the BiFPN structure has higher feature fusion efficiency. Therefore, we constructs the P2-BiFPN feature fusion network structure, which introduces an additional P2 layer feature map on the base of the BiFPN structure, because this feature map contains many small object detail information, it can be fused with the higher-level feature map to enrich the small object information. The P2-BiFPN structure is shown in Fig. 5, where a path is added between the P4 and P4_out nodes for feature fusion and the P2 layer is introduced to the

P3_out high-level feature map through the feature enhancement module, but the feature map perceptual field of this layer is small, so the features of the P2 layer are passed through the feature enhancement module to expand the perceptual field. This module introduces parallel asymmetric hole convolution to expand the perceptual field of the P2 feature map without changing the image size and increasing the model complexity. The P2 layer features are input into the three convolution layers successively, and the feature maps output from the 1×3 and 3×1 asymmetric convolutions are input into the convolution with a convolution kernel size of 2×2 void ratio of 2. Finally, the P2 shallow feature maps are obtained after expanding the perceptual field, and then they are fused with the high-level features to make full use of the shallow information of small objects, thus improving the detection accuracy of small objects.

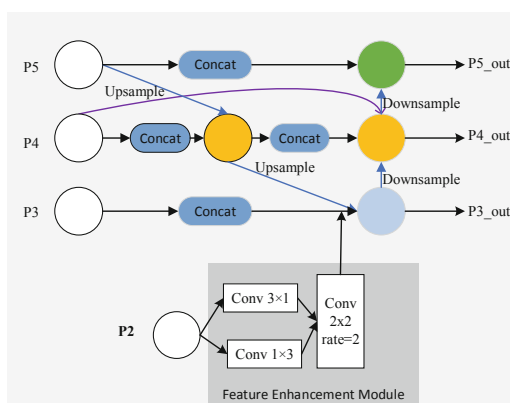


Fig. 5. P2-BiFPN network structure

4 Experiment

4.1 Dataset and Evaluation

(1) Pedestrian detection dataset

WiderPerson is a commonly used dataset for pedestrian detection. The dataset contains 13,382 images with 400,000 pedestrian objects of various degrees, including many small object. This dataset was randomly divided into 7000 images for training, 2000 images for validation, and 4382 images for testing. We cleaned the labels of this dataset to remove the labels of dumplings and dense crowds to obtain our desired pedestrian detection dataset.

(2) Evaluation Indicators

In order to verify the performance of the small object detection algorithm, Precision (P), Recall (R) and mean average precision (mAP) of each class are used as the evaluation indicators of the algorithm performance. The larger these three metrics are, the better the performance of the detection algorithm.

4.2 Implementation Details

The model in this thesis is implemented on the NVIDIA RTX3090 GPU computer platform based on the Pytorch1.11.0 framework. The CUDA version is 11.2 and the Python version is 3.8. This thesis uses the original YOLOv5 pretraining weights for training. The input images of the model were uniformly scaled to 640×640 , and the dataset was preprocessed by cropping, scaling and arranging. The batch size, initial learning rate, cosine learning rate and epoch values are set to 16, 0.01, 0.14 and 120, respectively, and Adam is used to update the parameters.

4.3 Ablation Studies

In order to verify the effectiveness of the improved strategy, we conducted ablation experiments on the WiderPerson pedestrian dataset, and the experimental results were shown in following Table 1.

(1) Compare with the benchmark model

As shown in Table 1, model 2 denotes the detection model we constructed. Compared with the baseline model YOLOv5, the mAP and R of model 2 are improved by 1.7% and 3.5%, respectively, and the P is also at a higher level, indicating that the detection effect of the model in this thesis is better. The introduction of asymmetric convolution significantly reduces the number of model parameters by 5.66M, indicating that our small object detection model is more lightweight.

Table 1. Performance comparison between the baseline model and our proposed small object detection model

Model	Method	mAP (%)	P (%)	R (%)	Parameters (M)	Layer
No. 1	Yolov5	75.7	80.5	64.9	44.44	392
No. 2	Ours	77.4	78.8	68.4	38.78	511

(2) The influence of CA method and asymmetric convolutions

As shown in Table 2, compared with the baseline model, the mAP and R of detection model 2 with the addition of CA attention mechanism improved to 76.9 and 69.1%, respectively, indicating that CA is effective in improving the model performance. Model 3 introduces asymmetric convolution to reduce the number of model parameters based on model 2. mAP and P improve by 0.2 and 1.8%, respectively, and the number of parameters is significantly reduced by 9.83 m. Compared with model 1, model 3 after two improvements, mAP and R were improved by 1.4 and 3%, respectively, and the number of parameters was significantly reduced by 6.51 m.

(3) The influence of P2-BiFPN feature fusion structure

We constructed the P2-BiFPN network by introducing the P2 shallow layer features into the BiFPN. There are two ways to increase the P2 layer perceptual field are model 2 with direct downsampling and model 3 with the introduction of null convolution. As shown in Table 3, compared with model 2, the mAP and R of model 3 were increased by 0.3 and 0.8% respectively, indicating that the downsampling method in this paper performs better in the detection model. The comparison between Model 3 and baseline model 1 shows that the introduction of P2-BiFPN structure improved the mAP and R of the model by 1.5% and 3.5%, respectively. It proves that the improvement strategy of the feature fusion network is effective.

Table 2. Comparison of experimental results of backbone network improvement

Model	Method	Map (%)	P (%)	R (%)	Parameters (M)	Layer
No. 1	Yolov5	75.7	80.5	64.9	44.44	392
No. 2	Yolov5 + CA	76.9	77.5	69.1	47.77	469
No. 3	Yolov5 + as-CA	77.1	79.3	67.9	37.93	511

Table 3. Comparison of experimental results of feature fusion network improvement

Model	Method	mAP (%)	P (%)	R (%)	Parameters (M)	Layer
No. 1	Yolov5	75.7	80.5	64.9	44.44	392
No. 2	Yolov5 + P2-Bifpn (upsampling)	76.9	79.1	67.6	47.77	392
No. 3	Yolov5 + P2-Bifp (dilated conv)	77.2	78.7	68.4	48.58	399

4.4 Comparisons Studies

In order to verify the superiority of the proposed model, the small object detection model constructed in this thesis is verified on the WiderPerson pedestrian detection dataset, and it is evaluated with the mainstream detection algorithm based on the indicator mAP. The experimental results are shown in Table 4.

Table 4 shows that compared with the baseline model YOLOv5, the mAP of the proposed model was 1.7% higher, which verifies the effectiveness of the improvement strategy. At the same time, compared with the object detection algorithm DETR based on Transformer self-attention mechanism and the one-stage detection algorithms SSD and YOLO-x, the proposed model has a higher mAP. Compared with the two-stage detection algorithm Faster-RCNN, our model has better performance compared with the existing mainstream detection algorithms, the performance of our detection model is better.

Table 4. Performance comparison of mainstream detection algorithms on the WiderPerson dataset

Method	mAP (%)
DETR [21]	49.8
SSD [22]	50.2
Faster-RCNN [23]	54.5
YOLO-x [24]	65.5
Cascade RCNN [25]	70.8
YOLOv5	75.7
Ours	77.4

5 Conclusion

Aiming at the difficult problem of small object detection, we uses YOLOv5 as the benchmark model and improves the backbone network and feature fusion structure, finally constructs a small object detection algorithm model combining the coordinate attention and P2-BiFPN structure. Firstly, the coordinated attention is incorporated into the residual units of the backbone network, and square convolution kernel of the residual unit is decomposed into two parallel asymmetric convolutions, enabling more precise object localization while reducing model parameters. Secondly, the P2-BiFPN feature fusion network structure is constructed. Since the feature map of P2 layer is rich in critical small object information, the feature map of this layer is introduced into the BiFPN structure and fused with the higher-level features. This fusion method enhances small object feature representation. Thus forming our small object detection model. Finally, our model is trained and evaluated on the WiderPerson dataset. Experimental results shows that compared to the YOLOv5 benchmark model, our model achieves a 1.7% improvement in mAP, demonstrating superior performance in small object detection.

Acknowledgements. This work was supported by the Shenzhen Science and Technology Program (No. JSGG20220301090405009).

References

1. Evo, I., Avramovi, A.: Convolutional neural network based automatic object detection on aerial images. *IEEE Geosci. Rem. Sens. Lett.* **13**(5), 740–744 (2017)
2. Erdelj, M., Natalizio, E., Chowdhury, K.R., et al.: Help from the sky: leveraging UAVs for disaster management. *IEEE Perv. Comput.* **16**(1), 24–32 (2017)
3. Joy, A., Jayanthi, V.S., Baskar, D.: Automatic object detection in car-driving sequence using neural network and optical flow analysis. In: *IEEE International Conference on Computational Intelligence and Computing Research*. IEEE (2014)
4. Song, Z., Zhang, Y., Liu, Y., et al.: MSFYOLO: feature fusion-based detection for small objects. *IEEE Lat. Am. Trans.* **20**(5), 823–830 (2022)

5. Liu, Z., Li, D., Ge, S.S., et al.: Small traffic sign detection from large image. *Appl. Intell.* **50**, 1–13 (2020)
6. Guo, L., Wang, Q., Xue, W., et al.: A small object detection algorithm based on improved YOLOv5. *Univ. Electron. Sci. Technol. J.* **51**(02), 251–258 (2022)
7. Liu, Y., Yang, F., Hu, P.: Small-object detection in UAV-captured images via multi-branch parallel feature pyramid networks. *IEEE Access* **8**, 145740–145750 (2020)
8. Yi, H., Song, W., Huang, J.: UAV small target detection based on improved YOLOv5. *Electromech. Eng. Technol.* **52**(02), 139–144 (2023)
9. Zhang, T., Chen, E., Xiao, W., et al.: Fast target detection method for improving MobileNet_YOLOv3 network. *Minicomp. Syst.* **42**(5), 1008–1014 (2021)
10. Sun, B., Zuo, Z., Wu, P., et al.: Object detection for environment perception of unmanned surface vehicles based on the improved SSD. *J. Instrument.* **42**(09), 52–61 (2021)
11. Zhao, P., Xie, L., Peng, L.: Deep small object detection algorithm integrating attention mechanism [J/OL]. *Comp. Sci. Explor.* (2021)
12. Hou, S., Wang, Z., Dong, Z., et al.: Self-supervised recalibration network for person re-identification. *Defence Technology* (2023)
13. Wei, W.A.N.G., Xiaogang, W.A.N.: A small target detection method combining attention mechanism and feature fusion. *J. Xi'an Eng. Univ.* **36**(06), 115–123 (2022)
14. Lin, T.Y., Dollár, P., Girshick, R., et al.: Feature pyramid networks for object detection. In: *Proceedings of the IEEE Conference on Computer Vision and Pattern Recognition*, pp. 2117–2125 (2017)
15. Liu, S., Qi, L., Qin, H., et al.: Path aggregation network for instance segmentation. In: *Proceedings of the IEEE Conference on Computer Vision and Pattern Recognition*, pp. 8759–8768 (2018)
16. Hou, S., Yin, K., Liang, J., et al.: Gradient-supervised person re-identification based on dense feature pyramid network. *Complex Intell. Syst.* **8**(6), 5329–5342
17. Ghiasi, G., Lin, T.Y., Le, Q.V.: NAS-FPN: learning scalable feature pyramid architecture for object detection. In: *2019 IEEE/CVF Conference on Computer Vision and Pattern Recognition (CVPR)*. IEEE (2019)
18. Tan, M., Pang, R., Le, Q.V.: Efficientdet: scalable and efficient object detection[C]. In: *Proceedings of the IEEE/CVF Conference on Computer Vision and Pattern Recognition*, pp. 10781–10790 (2020)
19. Hou, Q., Zhou, D., Feng, J.: Coordinate attention for efficient mobile network design. In: *Proceedings of the IEEE/CVF Conference on Computer Vision and Pattern Recognition*, pp. 13713–13722 (2021)
20. Paszke, A., Chaurasia, A., Kim, S., et al.: Enet: a deep neural network architecture for realtime semantic segmentation. *arXiv preprint arXiv:1606.02147* (2016)
21. Carion, N., Massa, F., Synnaeve, G., et al.: End-to-end object detection with transformers. In: *Computer Vision—ECCV 2020: 16th European Conference, Glasgow, UK, August 23–28, 2020, Proceedings, Part I 16*. Springer International Publishing, pp. 213–229 (2020)
22. Liu, W., Anguelov, D., Erhan, D., et al.: SSD: single shot multibox detector. In: *Proceedings of the 14th European Conference on Computer Vision—ECCV 2016, Amsterdam, The Netherlands, October 11–14, 2016, Part I 14*. Springer International Publishing, pp. 21–37 (2016)
23. Ren, S., He, K., Girshick, R., et al.: Faster R-CNN: towards real-time object detection with region proposal networks. *IEEE Trans. Patt. Anal. Mach. Intell.* **39**(6), 1137–1149 (2017)
24. Ge, Z., Liu, S., Wang, F., et al.: Yolox: Exceeding yolo series in 2021. *arXiv preprint arXiv:2107.08430* (2021)
25. Cai, Z., Vasconcelos, N.: Cascade R-CNN: Delving into high quality object detection. In: *Proceedings of the IEEE conference on computer vision and pattern recognition*, pp. 6154–6162 (2018)



Domain Generalization for Multimodal Disaster Tweet Classification

Chen Yu^{1,2}, Kangning Yin^{1,2}, and Zhiguo Wang^{1,2}(✉)

¹ University of Electronic Science and Technology of China, Chengdu 610054, China

zgwang@uestc.edu.cn

² Institute of Public Security, Kashi Institute of Electronics and Information Industry, Kashi 844000, China

Abstract. Disaster-related information on social media platforms facilitates situational awareness of disaster events. Benefiting from the development of multimodal deep learning, it has become easy to extract and fuse information from different modalities of social media data. However, existing multimodal models are developed on limited disaster datasets and have problems in generalization. The lack of generalization is mainly manifested by significant performance degradation on disaster events outside the dataset. One key reason for overfitting might be that the models combine class information too closely with specific disaster events during training. In multimodal social media applications, existing models are rarely optimized for the representation of event domains. In this paper, we treat different disaster events as separate domains and propose a new domain generalization method for multimodal representation learning. Our method takes multimodal features as the sum of domain-specific features and class-specific features. The proposed model obtains domain-invariant representations through feature separation and reconstruction. In addition, the multimodal information exchange is realized by the cross-modal interaction module, and highly generalized class representations are finally obtained. Experimental results show that the proposed method improves generalization performance on the CrisisMMD benchmark.

Keywords: Domain generalization · Disaster tweet classification · Multimodal fusion

1 Introduction

Multimodal disaster social media analysis techniques offer new approaches to situational awareness of disaster events. Considering that social media platforms have become important sources of real-time information, it is convenient to use social media applications to distribute emergency messages and gather feedback from users after a natural disaster. The relevant authorities and agencies can obtain first-hand data on casualties, traffic conditions, resource dispatch, and more by analyzing real-time posts shared by numerous users, which is essential for emergency relief and recovery. Various multimodal deep learning models [1–3] have been proposed to efficiently analyze multimodal

social media data. These models use deep neural networks as encoders to extract disaster-related information from the contents of social media posts in different modalities such as text, image, and video. Designed multimodal fusion modules are then used to fuse these features for classification. Existing studies have focused mainly on unimodal backbone networks and multimodal fusion approaches. Most of the unimodal backbone networks in the field of disaster social media analysis are efficient pre-trained models, such as BERT [4] and DenseNet [5]. As for the research on feature fusion modules, they have been extensively explored from simple score fusion to complex self-attention methods.

Although existing methods have good accuracy on known datasets, the generalization performance of multimodal models remains to be explored. A typical manifestation of the lack of generalization is the degradation of performance on out-of-domain data. The original data from different disaster events contain unique information associated with specific events. This event relevance makes it inevitable that the features of some disaster events will be confused with the disaster-related category representations. These impurities are not related to classification but can cause spurious correlations with specific classes, often causing deep neural networks to fail when applied to unseen events. Moreover, the limited amount of multimodal data in the experimental environment also constrains the generalization capability of multimodal models. This task of learning from multiple training domains and generalizing to unseen domains is called domain generalization [6]. Most existing domain generalization methods focus on CNN-based models and unimodal classification tasks. In this paper, we consider the problem of domain generalization in multimodal data. Compared to unimodal domain generalization, multimodal domain generalization requires consideration of both domain-invariant representations within each modality and semantic consistency across modalities. This challenge prompts us to develop new domain generalization methods.

Therefore, we propose a multimodal domain generalization method with domain feature disentanglement. Our motivation is to separate domain-invariant representations in each modality and use metric learning methods to align multimodal class distributions. First, we propose a domain separation module, which removes event domain information from the category representation by encoding domain features and category features separately. Second, we consider the presence of class centroids for each modal-class pair and propose a cross-modal interaction module. The module encourages the similarity between features of the same class and penalizes the similarity of different classes to facilitate cross-modal information exchange. Finally, we evaluate the cross-domain performance on the CrisisMMD benchmark [7], and the results show that the proposed method provides a significant improvement in the generalization ability.

2 Related Work

2.1 Multimodal Disaster Tweet Classification

Multimodal social media classification models often outperform unimodal models because they process information from both linguistic and visual inputs. Most studies use a late fusion strategy. In detail, this involves using separate unimodal backbones to process each modality separately and fusing the extracted representations with a multimodal fusion module. Commonly used backbone networks are those common in text

and image processing, such as BERT and DenseNet. Considering that multimodal disaster datasets are rare, using pre-trained backbones rather than training from scratch can reduce overfitting due to specific contexts. The multimodal fusion modules range from simple non-parametric methods such as feature concatenation and score fusion to popular attention methods. CIMHIM [8] uses DenseNet and BERT as the backbone network to consider fine-grained attention relationships between words and local regions of images. CBAN [1] employs a vision transformer (ViT) and BERT to simultaneously calculate positive and negative attentions to establish correlation and suppress irrelevance. The disadvantage of the late fusion strategy is that information interaction is only performed on the encoded features of each modality. This drawback has led some studies to adopt a mid-fusion approach. For instance, MI2P [2] enhances the mid-level features of unimodal models by bridging the heterogeneity between different modality features. However, mid-fusion methods can complicate the networks as the modality of input data increases. In general, the existing multimodal models have good classification performance, but the generalization capability of the models has not been fully explored.

2.2 Domain Generalization

Domain generalization aims to learn from multiple training domains and generalize to unseen domains. Most domain generalization methods can be broadly classified into three groups [6]: (1) representation learning is used to align features from different domains by reducing the domain-dependent information; (2) data augmentation is a common method to increase data diversity; (3) learning strategy uses specially designed learning processes to improve model generalization. While most domain generalization methods do enhance the generalization of models, they mostly address unimodal tasks. Our paper considers a new setting, the problem of multimodal domain generalization. This challenging task motivates us to develop new domain generalization methods to capture domain information in multimodal data.

3 Method

3.1 Problem Formulation

The multimodal domain generalization problem in this paper has an event domain space $\mathcal{D} = \{D_1, D_2, \dots, D_k\}$ and a discrete label space shared between domains $\mathcal{C} = \{1, 2, \dots, C\}$. Each sample data in each domain has two modalities, and we denote the samples from domain k by $D_k = \{(\mathbf{T}_i^k, \mathbf{I}_i^k, y_i^k)\}_{i=1}^{N_k}$, where \mathbf{T} denotes the text modality of the i -th sample, \mathbf{I} denotes the image modality, $y \in \mathcal{C}$ denotes the class label, and N_k denotes the size of domain D_k . For model training, we follow the leave-one-domain-out setting and divide the event space into two sets: source domain \mathcal{S} for training and target domain \mathcal{T} for testing, where $|\mathcal{S}| = |\mathcal{D}| - 1$ and $|\mathcal{T}| = 1$. In this way, the task aims to learn a parametric multimodal network from the source domain \mathcal{S} to make it perform well on the target domain \mathcal{T} .

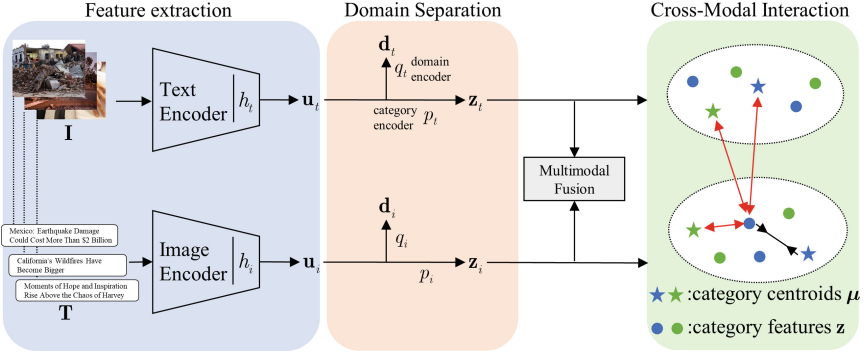


Fig. 1. Overview of the proposed framework. The blue shade represents the feature extraction pipelines. The pink shade represents the proposed domain separation module. The green shade represents the cross-modal interaction module, where different colors represent different categories.

3.2 Model Overview

The overall framework of the model is shown in Fig. 1. The first step is to encode the multimodal inputs by the multimodal feature extraction module. Specifically, we have separate encoders for each modality. These encoders encode the image and text information into the corresponding feature space, separately. The domain separation module is then used to separate the domain information in the text and image embeddings. To achieve efficient separation of domain information, four loss functions are used, including orthogonality loss, domain classification loss, reconstruction loss, and alignment loss. The orthogonality loss is used to reduce the correlation between the domain representation and the category representation. The domain classification loss maps the domain representation to the corresponding event label. The reconstruction loss is used to reduce information loss during feature separation. Moreover, the alignment loss is used to ensure that the distribution of the separated features is consistent with the original features. Next, the cross-modal interaction module is used to enable information exchange between modalities. Specifically, we use momentum-based category centroids to regulate the distance between modality-category representations. Finally, the multimodal fusion module fuses feature from different modalities and makes final predictions.

The multimodal feature extraction module consists of an image encoder and a text encoder. For an input image-text pair (\mathbf{I}, \mathbf{T}) , we have:

$$\mathbf{u}_i = h_i(\mathbf{I}), \mathbf{u}_t = h_t(\mathbf{T}), \tag{1}$$

where $h_i(\cdot)$ and $h_t(\cdot)$ can be arbitrary image and text models. The visual and text features have the same dimensions, i.e. $\mathbf{u}_i, \mathbf{u}_t \in \mathbb{R}^{768}$. We use the pre-trained BERT and DenseNet as the text and image backbone, respectively. Specifically, for each text input, the embedding of the [CLS] token of the BERT model is used as the global representation. For each image input, the output of the final pooling layer of DenseNet is projected as a 768-dimensional global representation. Moreover, we use feature concatenation as

the multimodal fusion method to get the final representation. A linear classification head is used to make predictions with fused features. The cross-entropy loss is used as the supervised loss function for the baseline model:

$$\mathcal{L}_{ce} = -\log p(y|\text{Concat}(\mathbf{u}_i, \mathbf{u}_t)) \quad (2)$$

3.3 Domain Separation Module

To separate the domain-specific information from each modality feature and obtain domain-invariant category representations, we disentangle the domain and category representations in the features. Related works use subspace orthogonal constraints to separate shared and private representations. ManyDG [9] uses parameter-free feature projection methods to obtain domain-invariant features. On this basis, we encode the features of each modality as domain features and class features, respectively. The orthogonality regularization constraint is used to ensure that domain features and class features are orthogonal so that domain-invariant category representations can be obtained. We used two three-layer MLPs, $q_t(\cdot)$ and $q_i(\cdot)$, as domain projection heads for text and image embeddings. Thus, the domain embedding representation of text and image modalities can be given by $\mathbf{d}_t = q_t(\mathbf{u}_t)$ and $\mathbf{d}_i = q_i(\mathbf{u}_i)$. Similarly, two three-layer MLPs, $p_t(\cdot)$ and $p_i(\cdot)$, are used to extract domain-invariant category embeddings. The category representations of text and image modalities can be given by $\mathbf{z}_t = p_t(\mathbf{u}_t)$ and $\mathbf{z}_i = p_i(\mathbf{u}_i)$. To make these projection heads achieve the designed function, the following constraints are used:

$$\mathcal{L}_{ds} = \mathcal{L}_{\text{orth}} + \mathcal{L}_{\text{cls}} + \mathcal{L}_{\text{rec}} + \mathcal{L}_{\text{align}} \quad (3)$$

Orthogonality Loss $\mathcal{L}_{\text{orth}}$. To achieve separation of domain information, each column in \mathbf{D} represents a domain-specific representation and each column in \mathbf{Z} represents a category-specific representation. We implement this property by applying a soft subspace orthogonality regularization between domain representation and class representation. This orthogonality loss acts on each modality and encourages \mathbf{D} and \mathbf{Z} to represent different aspects of the input features. Let \mathbf{H}_d and \mathbf{H}_z be the matrices whose rows denote \mathbf{D} and \mathbf{Z} . This orthogonality loss is calculated as:

$$\mathcal{L}_{\text{orth}} = \left\| \mathbf{H}_d^T \mathbf{H}_z \right\|_F^2 \quad (4)$$

Domain Classification Loss \mathcal{L}_{cls} . The Separated Domain Representations Should Have Distinguishable Semantic Information To Differentiate Samples From Different Domains. For this purpose, domain labels y_d are used to supervise the separated domain representations. We use a domain classification head to predict domain labels and bring them close to ground truth classes by cross-entropy loss:

$$\mathcal{L}_{\text{cls}} = - \sum_{m \in \{t, i\}} \log p(y_d | \mathbf{d}_m) \quad (5)$$

Reconstruction Loss \mathcal{L}_{rec} . The loss of information during the separation of domain and category representations can lead to overfitting of the model on the training domains.

Feature reconstruction is added to ensure that the separated domain representations and category representations still contain sufficient detail. Specifically, we use a three-layer MLP to obtain the reconstructed features $\tilde{\mathbf{u}}$. Reconstruction loss is used to bring the reconstructed features closer to the original features:

$$\mathcal{L}_{\text{rec}} = \sum_{m \in \{i, t\}} \|\mathbf{u}_m - \tilde{\mathbf{u}}_m\|_F^2 \quad (6)$$

Alignment Loss $\mathcal{L}_{\text{align}}$. To reduce the gap between distributions to facilitate the separation and reconstruction, we use the normalized Maximum Mean Discrepancy (MMD) to align the separated representations with the original representations. Intuitively, the MMD distance between two distributions reflects how similar the two distributions are in the same space:

$$\mathcal{L}_{\text{align}} = \sum_{m \in \{i, t\}} \left(\text{MMD}(\mathbf{u}_m, \mathbf{d}_m) \Big/ \underbrace{\|sg(\mathbf{u}_m)\|_F^2}_2 + \text{MMD}(\mathbf{u}_m, \mathbf{z}_m) \Big/ \underbrace{\|sg(\mathbf{u}_m)\|_F^2}_F \right) \quad (7)$$

where $sg(\cdot)$ means gradient truncation operation.

3.4 Cross-Modal Interaction Module

Proxy-based supervised loss functions, such as cross-entropy, enable supervised learning. However, for sample embeddings in multimodal spaces, considering only the sample-to-prototype relationship is not sufficient. TCL [10] maintains momentum-encoded category centroids for each modality for cross-modal alignment. MDLT [11] computes domain-class centroids on the training set to transfer domain features. Inspired by this, we use momentum-based category centroids as a consideration of the relationship between multimodal samples. Our intention is to modulate the distance between modality-category representations to learn better discriminative category representations. We maintain category centroids for all modality-category pairs and update them by moving averages. The model is first warmed up, and the category centroid features over the entire training set are $\boldsymbol{\mu}_{m,c}$, where m denotes the different modalities (i or t), and c denotes the target class. For image and text representations, we align them to their category centroids as follows:

$$L_{\text{cmi}} = -\frac{1}{|\mathcal{Z}|} \sum_{m \in \{i, t\}} \sum_{\mathbf{z}_m \in \mathcal{Z}} \log \frac{\exp(s(\mathbf{z}_m, \boldsymbol{\mu}_{m,c})/\tau)}{\sum_{(m', c') \in \mathcal{M} \setminus \{(m, c)\}} \exp(s(\mathbf{z}_m, \boldsymbol{\mu}_{m', c'})/\tau)} \quad (8)$$

where \mathcal{M} denotes all modality-category pairs. \mathcal{Z} is the feature set of \mathbf{z} . τ is the temperature factor. The distance function $s(\cdot)$ pulls the sample and the corresponding category centroid closer together, allowing higher similarity between representations from different modalities in the same category. The Euclidean distance is used as the distance function. This module performs cross-modal interactions directly and prevents the network from falling into overfitting of unimodal information.

4 Experiments

4.1 Datasets

We use the publicly accessible CrisisMMD [7] dataset as the benchmark to evaluate our approach. The samples in the dataset are collected from disaster-related posts uploaded by users on social media platforms. The content of these posts relates to seven specific disaster events, including Hurricane Irma (HI), Hurricane Harvey (HI), Hurricane Maria (HM), the Mexico earthquake (ME), California wildfires (CW), Iraq-Iran earthquakes (IIE) and Sri-Lanka floods (SLF). We have thus split the dataset into seven event domains. We use this dataset to perform two tasks, informativeness classification, and humanitarian classification. The informativeness classification task is to determine whether a post contains content related to a disaster. The humanitarian classification further subdivides disaster-related content into five categories: infrastructure and utility damage, vehicle damage, rescue volunteering or donation efforts, affected individuals, and other relevant information. All images are cropped to a size of 224×224 and common data enhancement methods such as random horizontal flips, crops of random size, and random grey scaling are applied. Noise in the text data is cleaned by removing URLs, removing stop words, removing all non-ASCII characters, and converting all letters to lowercase.

4.2 Implementation Details

We train the model on an NVIDIA 2080Ti GPU in PyTorch. We use the AdamW optimizer with an initial learning rate of $1e-4$. The experimental setup follows the leave-one-domain-out protocol [12]. During training, one domain is selected as the target domain for test and all remaining domains are used as source domains. The source domain samples are further split into train and validation by a ratio of 80%:20%. During training, the model is sampled on all source domains simultaneously, with a batch size of 8 on each domain. The models trained on different source domains use the same hyperparameter settings. We use classification accuracy as evaluation criterion.

4.3 Performance Comparison

The proposed method is compared to unimodal networks, common multimodal baseline models, and recently proposed image-text classification methods. The unimodal networks include the image backbone DenseNet [5] and the text backbone BERT [4]. The multimodal baseline models include Score Fusion, Feature Concatenation, and Gate Fusion. In addition, CIMHIM [8] uses attention mechanisms to establish fine-grained interactions across modalities. CBAN [1] considers both positive attention between relevant features and negative attention between irrelevant features. MI2P [2] designs a mid-fusion unit to exchange mid-level features of different backbones to provide more efficient cross-modal interactions. In fairness, we reproduce these models based on their open-source codes and compare them in the same experimental settings.

The comparison results on the CrisisMMD benchmark are shown in Table 1. First, the unimodal methods all perform significantly worse than the multimodal methods. This shows that multimodal information can facilitate cross-domain performance. Second,

Table 1. Comparisons on CrisisMMD in terms of out-of-domain classification accuracy (%).

Method	HI	HH	HM	ME	CW	IIE	SLF	Avg.
<i>Informativeness task</i>								
DenseNet	79.1	83.1	76.4	81.7	73.7	82.0	79.8	79.4
BERT	81.1	85.3	80.8	73.2	77.3	77.9	85.1	80.1
Score fusion	81.7	84.0	82.4	78.5	78.1	79.4	91.2	82.2
Feature concate	82.4	84.2	85.7	80.7	80.5	80.3	90.9	83.5
Gate fusion	82.8	84.7	81.2	83.5	80.9	81.6	92.6	83.9
CBAN	83.8	86.6	82.9	82.1	80.3	80.7	89.2	83.7
MI2P	82.5	85.8	83.4	81.9	80.6	82.0	92.1	84.0
CIMHIM	84.3	80.9	84.8	84.0	81.3	84.4	93.9	84.8
Ours	84.7	86.4	85.2	84.2	82.6	85.3	93.4	86.0
<i>Humanitarian task</i>								
DenseNet	85.9	80.2	87.1	74.4	67.5	58.2	77.9	75.9
BERT	85.9	84.2	86.0	90.8	69.3	80.4	87.8	83.5
Score fusion	88.2	86.3	88.6	87.2	77.1	63.7	87.6	82.7
Feature concat	86.5	86.9	87.4	89.8	78.7	72.9	86.5	84.1
Gate fusion	81.8	88.3	89.6	89.3	80.0	75.3	89.4	84.8
CBAN	88.0	88.5	88.7	88.3	66.2	87.7	85.6	84.7
MI2P	85.3	87.1	87.3	88.7	76.5	85.0	85.7	85.1
CIMHIM	84.7	86.5	88.3	90.1	77.2	83.5	82.2	84.6
Ours	88.4	88.6	89.9	89.9	78.8	82.0	85.7	86.2

even simple fusion strategies (e.g., Score Fusion, Feature Concatenation, Gate Fusion) exhibit significant domain generalization capabilities and their performance is comparable to that of complex attention methods (e.g., CBAN, CIMHIM, MI2P). This means that complex tensor-based strategies might be suboptimal for multimodal generalization. Finally, the proposed method achieves the best average accuracy among all models, with relative improvements of 1.2% and 1.1% compared to the best baseline on two tasks, respectively. In general, these results illustrate the effectiveness of the proposed method.

4.4 Ablation Study

To test the validity of the proposed model in improving multimodal generalization, we perform ablation studies on the informativeness task. The average out-of-domain classification results are shown in Table 2. The first row shows the performance of the baseline model, which uses the feature concatenation fusion with only \mathcal{L}_{ce} . We first analyze the impact of the domain separation module. There is a significant improvement in model performance with \mathcal{L}_{ds} . The 1.4% relative improvement indicates that separating

Table 2. Ablation study of each component.

Method	\mathcal{L}_{ds}	\mathcal{L}_{cmi}	Avg.
Baseline (\mathcal{L}_{ce})			83.5
+	✓		84.9
+		✓	84.5
+	✓	✓	86.0

out the domain features is effective, which is consistent with our motivation to build domain-independent representations. The \mathcal{L}_{cmi} loss is also effective and gives 1.0% relative improvements. It shows that establishing sample-to-proxy relationships across modalities enables more adequate inter-modal interactions. Finally, the model performs optimally when both modules are used. Relative to the baseline model, the proposed modules achieve significant improvements of 2.5%.

5 Conclusion

This paper explores the multimodal generalization problem and proposes a new multimodal generalization method. We reveal that disentangling the domain and category information in the sample features can effectively improve the generalization of multimodal models. The method consists of two main components: domain separation module and cross-modal interaction module. The domain separation module efficiently separates domain information from unimodal features through orthogonal constraints and feature reconstruction. The cross-modal interaction module enables cross-modal information interaction by pulling through the same class of different modalities while pushing away different classes. Experiment results show that the proposed method significantly enhances the generalization of multimodal models and outperforms state-of-the-art methods.

Acknowledgments. This work was supported in part by the Natural Science Foundation of Xinjiang Uygur Autonomous Region (No. 2022D01B187).

References

1. Cheung, T., Lam, K.: Crossmodal bipolar attention for multimodal classification on social media. *Neurocomputing* **514**, 1–12 (2022)
2. Liang, T., Lin, G., Wan, M.: Expanding large pre-trained unimodal models with multimodal information injection for image-text multimodal classification. In: *Proceedings of the IEEE/CVF Conference on Computer Vision and Pattern Recognition (CVPR)*, pp. 15492–15501 (2022)
3. Abavisani, M., Wu, L., Hu, S., et al.: Multimodal categorization of crisis events in social media. In: *Proceedings of the IEEE/CVF Conference on Computer Vision and Pattern Recognition (CVPR)*, pp. 14679–14689 (2020)

4. Devlin, J., Chang, M.W., Lee, K., Toutanova, K.: BERT: Pre-training of deep bidirectional transformers for language understanding. In: Proceedings of the 2019 Conference of the North American Chapter of the Association for Computational Linguistics: Human Language Technologies (NAACL-HLT), vol. 1, pp. 4171–4186 (2019)
5. Huang, G., Liu, Z., Van Der Maaten, L., Weinberger, K.Q.: Densely connected convolutional networks. In: Proceedings of the IEEE/CVF Conference on Computer Vision and Pattern Recognition (CVPR), pp. 4700–4708 (2017)
6. Zhou, K., Liu, Z., Qiao, Y., et al.: Domain generalization: a survey. *IEEE Trans. Pattern Anal. Mach. Intell.*, 1–20 (2022)
7. Alam, F., Ofli, F., Imran, M.: CrisisMMD: Multimodal twitter datasets from natural disasters. In: Proceedings of the International AAAI Conference on Web and Social Media (ICWSM), vol. 12, pp. 456–473 (2018)
8. Wu, X., Mao, J., Xie, H., Li, G.: Identifying humanitarian information for emergency response by modeling the correlation and independence between text and images. *Inf. Process. Manage.* **59**, 102977 (2022)
9. Yang, C., Westover, M.B., Sun, J.: ManyDG: Many-domain generalization for healthcare applications. In: Proceedings of the International Conference on Learning Representations (ICLR) (2023)
10. Yang, J., Duan, J., Tran, S., et al.: Vision-language pre-training with triple contrastive learning. In: Proceedings of the IEEE/CVF Conference on Computer Vision and Pattern Recognition (CVPR), pp. 15671–15680 (2022)
11. Yang, Y., Wang, H., Katabi, D.: On multi-domain long-tailed recognition, imbalanced domain generalization and beyond. In: Proceedings of the European Conference on Computer Vision (ECCV), pp. 57–75 (2022)
12. Gulrajani, I., Lopez-Paz, D.: In search of lost domain generalization. In: Proceedings of the International Conference on Learning Representations (ICLR) (2021)



A Cooperative Edge Offloading Strategy for New Power System Services

Fang Shen, Jiale Zhang, Yutong Ji^(✉), Chengyu Duan, and Zhen Wang

State Grid Jibei Electric Power Co., Ltd., Information and Communication Branch, Beijing, China

lunwenshenqing2023@163.com

Abstract. Multi-access edge computing (MEC) is a critical technology for 5G networks. Computing tasks can be processed in edge servers instead of cloud servers by deploying computing servers at the edge of integrated power communication networks. With the expanding scale of the power grid, the delay-sensitive and computation-intensive services are growing rapidly, and MEC-enabled base stations can meet the demand for low-delay and highly reliable power services. Because the capacity of base stations is limited, most existing schemes use queuing or retransmission to reduce the pressure of base stations. However, the quality of service (QoS) will deteriorate due to queuing and retransmission. In this paper, we study the cooperation between MEC base stations to improve the computing service capability by offloading computing tasks to other MEC base stations. An optimization strategy based on the Q-learning algorithm is proposed to reduce the total delay of power user equipment (UE) within the coverage of the base station. We consider the limitations of terminal battery capacity and the computing capacity of base stations. The simulation results show that the strategy effectively reduces the system delay and achieves the load balancing of the base station.

Keywords: Multi-access edge computing · Integrated power communication networks · Q-learning algorithm · Mixed integer nonlinear programming

1 Introduction

With the development of new power grid, many delay-sensitive and computation intensive applications have emerged such as fault detection, video monitoring, and distribution automation. These applications have caused an explosive growth of computing traffic, while UEs cannot handle a large number of tasks in a short time. In this case, the cloud computing model can no longer meet the demand for low delay and high reliability, and multi-access edge computing is considered as a solution to the challenge. MEC is a technology that provides service environment and computing capability at the edge of mobile networks, which can provide low delay services. By sinking the cache and computation resources, MEC reduces the delay caused by the long distance between terminals and servers and improve user service quality [1].

Task offloading decision is a key research problem in MEC systems, where UE will have high end-to-end delay in the case of a large number of users, and the MEC servers

may not be able to provide computing services to all UEs. Therefore, it is necessary to provide suitable task offloading decisions in multi-user scenarios based on system constraints and quality of service (QoS) of UEs. In [2] authors jointly optimize task offloading decisions, spectrum, transmission power and computing resource allocation of UEs to minimize the energy consumption in a densely deployed small cell network. But authors do not consider the QoS degradation of UEs. In [3], authors optimize the offloading decisions and resource allocation of UEs to minimize the end-to-end delay in TDMA MEC system, but authors do not consider the energy consumption of UEs. In [4] the authors propose a UE task offloading and multi-user scheduling method for NB-IoT edge computing systems, where the optimization goal is to minimize the long-term weighted sum of UE delay and energy consumption under random flow arrival and Markov decision process models. But authors do not consider the overloading of individual base stations.

The above work can effectively solve the computing offloading problem under different constraints and scenarios, but none of them considers the load of the base stations. In our work, base stations can handle the computing tasks and reduce the power UE's energy consumption by equipping the MEC server on the conventional power base station. Meanwhile, we can effectively reduce the original base stations' heavy load and increase the system capacity by further offloading tasks from the heavy-loaded edge base stations to the light-loaded edge base stations.

2 System Model

2.1 Network Model

In this paper, we consider the grid network scenario with M base stations (BS) and N users, where $\mathcal{M} = \{1, 2, \dots, M\}$ and $\mathcal{N} = \{1, 2, \dots, N\}$ denote the set of base stations and users, respectively. Each BS is equipped with a MEC server to process the offloading tasks of the users. The communication period is discretized in time and there is only one power computing task $A_i = \{D_i, X_i, T_i^{\max}\}$ for user equipment in a time slot t , where D_i denotes the size of the input computing task, X_i denotes the required CPU cycles to process the task, which varies significantly for different tasks; and T_i^{\max} denotes the maximum tolerated delay of the task (Fig. 1).

We consider the task as binary offload model, which means that the task cannot be divided. We use a binary variable $a_i \in \{0, 1\}$ to denotes whether the computing task A_i of the user i is processed locally, where $a_i = 1$ denotes that the computing task is processed locally. $b_{i,m} \in \{0, 1\}$, $b_{i,m} = 1$ denotes the task A_i is processed by the access base station. $c_{i,m} \in \{0, 1\}$, $c_{i,m} = 1$ denotes that the computing task is processed by the cooperative base station. Since each task has only one offloading decision, we can use $\chi_i = \{a_i, b_{i,m}, c_{i,m}\}$ to represent the vector of offloading decisions. Therefore, the following constraint need to be satisfied:

$$a_i + b_{i,m} + \sum_{k=1, k \neq m}^M c_{i,k} = 1, \quad i \in \mathcal{N} \quad (1)$$

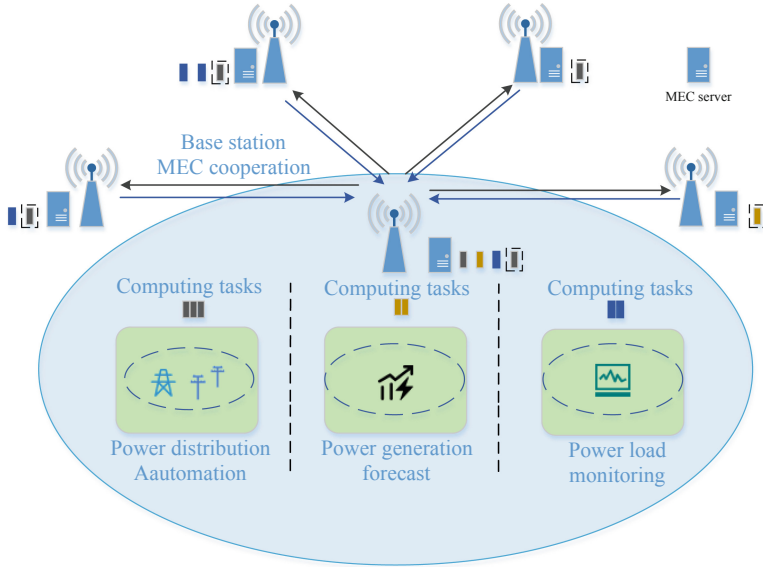


Fig. 1. Base station cooperative offloading model

2.2 Communication Model

Power system uses 230MHz wireless power private network for communication, the system uses orthogonal frequency division multiple access (OFDMA), where each base station allocates sub-carriers equally to its associated power UEs, so there is no inter-user interference between power UEs. The fiber optic network is used for data transmission between base stations, we assume the transmission rate is r_i^c , so the transmission delay of the base stations can be obtained by:

$$T_{i,m}^{coop} = \frac{D_i}{r_i^c} \tag{2}$$

We consider that the data transmission rate between the access base station and cooperative base station is high, and the offloading request data is extremely small, so we ignore the impact caused by parallel transmission between base stations.

2.3 Computing Model

A. Local Computing

The computing task is directly processed by the user equipment, f_i^L is the computing capacity (CPU cycles/s) of the user equipment. The processing delay can be expressed as:

$$T_i^{L,pro} = \frac{X_i}{f_i^L} \tag{3}$$

The energy consumption E_i^L can be expressed as:

$$E_i^L = \varepsilon X_i (f_i^L)^2 \quad (4)$$

where ε is the energy factor and its size depends on the chip architecture [5]. The device capacity f_i^L can be further improved by dynamic voltage regulation technology.

B. Base station MEC Computing

First the UE transmits the task to the base station through the radio access network, the MEC server allocates computing resources to process the task, and finally the MEC server returns the computation result. However, the data size of computation result is much smaller than the size of task data [6], and the downlink rate of the data is generally very high. Thus, we ignore the delay of the computation results back to UEs. We can obtain the UE uplink transmission delay under the base station calculation as, where r_i^s is the UE uplink transmission rate:

$$T_{i,m}^{trans} = \frac{D_i}{r_i^s} \quad (5)$$

The energy consumption $E_{i,m}$ can be expressed as:

$$E_{i,m} = P_t T_{i,m}^{trans} = P_t \frac{D_i}{r_i^s} \quad (6)$$

Further we can calculate the processing time delay:

$$T_{i,m}^{pro} = \frac{X_i}{f_m} \quad (7)$$

where f_m is the computing capacity of the base station B_m , so the total delay under the base station computing as:

$$T_i^m = T_{i,m}^{trans} + T_{i,m}^{pro} \quad (8)$$

If the task is processed at a cooperative base station, additional transmission delay between base stations is added:

$$T_i^c = T_{i,m}^{trans} + T_{i,m}^{coop} + T_{i,m}^{pro} \quad (9)$$

The computing capacity of each base station is limited, and the load of base station cannot exceed the maximum computing capacity of the base station, where Z_{\max}^m is the maximum computing capacity of base station B_m :

$$\sum_{i \in \mathcal{N}} (b_{i,m} X_i + c_{i,m} X_i) \leq Z_{\max}^m, \quad m \in \mathcal{M} \quad (10)$$

In summary, the delay and energy consumption of UE i can be expressed as:

$$\begin{aligned} T_i &= a_i T_i^L + b_{i,m} T_i^m + c_{i,m} T_i^c \\ E_i &= a_i E_i^L + b_{i,m} E_{i,m} + c_{i,m} E_{i,m}^c \end{aligned} \quad (11)$$

3 Reinforcement Learning-Based Solution

3.1 Base Station Cooperative Optimization Problem Formulation

With limited computing capacity of the base station, an edge computing offloading strategy with base station MEC cooperation is proposed to reduce the total delay of power UEs. In this strategy, $\chi_i = \{a_i, b_{i,m}, c_{i,m}\}$ denotes the offloading decision vector of UE i , $\chi = \{\chi_i, i \in \mathcal{N}\}$ denotes the offloading decision of all UEs, and the decision optimization problem can be formulated as:

$$\begin{aligned}
 & \min \sum_{i=1}^T \sum_{i=1}^N T_i \\
 & \text{s.t } C1 : a_i + b_{i,m} + \sum_{k=1, k \neq m}^M c_{i,k} = 1, i \in \mathcal{N} \\
 & \quad C2 : a_i, b_{i,m}, c_{i,m} \in \{0, 1\}, i \in \mathcal{N} \\
 & \quad C3 : \sum_{i \in \mathcal{N}} (b_{i,m} X_i + c_{i,m} X_i) \leq Z_{\max}^m, m \in \mathcal{M} \\
 & \quad C4 : a_i E_i^L + b_{i,m} E_{i,m} + c_{i,m} E_{i,m}^C \leq E_i^{\max}, i \in \mathcal{N} \\
 & \quad C5 : T_i \leq T_i^{\max}, i \in \mathcal{N}
 \end{aligned} \tag{12}$$

Here, C1 means each user only adopts one offloading decision to execute the task. C2 denotes that the offloading policy is binary offloading. C3 denotes the maximum base station computing capacity constraint. C4 means that the total energy consumption of UE cannot exceed the maximum battery capacity, where E_i^{\max} is the maximum battery capacity of the UE i . C5 means that the delay of task cannot exceed the maximum tolerable delay of the task.

3.2 Task Offloading Markov Decision Process (MDP) Model

We construct Markov Decision Process (MDP) including state space, offloading action and reward function.

- (1) The state space S_t in time slot t is composed of base stations and UEs, including the remaining battery capacity of all user equipment $E_t = \{e_1, e_2, \dots, e_i, \dots, e_N\}$, where e_i is the remaining battery capacity of equipment i . The computing tasks for all users $Task_t = \{A_1, A_2, \dots, A_i, \dots, A_N\}$, and the current computing capacity of all base stations $C_t = \{c_1, c_2, \dots, c_m, \dots, c_M\}$. The state space of the system can be expressed as follows.

$$S_t = \{E_t, Task_t, C_t\} \tag{13}$$

- (2) Decision action: In each episode, the agent executes an action $\chi_t \in \psi$ in the current state S_t to obtain an offloading decision $\chi_t = [\chi_1, \chi_2, \dots, \chi_i, \dots, \chi_N]$, where χ_i denotes the offloading decision of UE i and ψ denotes the set of all offloading choices in the current state.

- (3) The goal is to minimize the sum of the user's delay. However, reinforcement learning focuses on maximizing the reward, so the objective function is set to be negatively related with the reward function. When the generated offload action does not satisfy the system constraint, we give a punishment of $-X$ and regenerate the offload action.

$$r_t = \begin{cases} -\sum_{i=1}^N T_i, & \text{if } s.t \text{ satisfied} \\ -X, & \text{otherwise} \end{cases} \quad (14)$$

3.3 Q-learning Based Offloading Decision Algorithm

Q-learning is a value iteration reinforcement learning algorithm whose goal is to maximize the long-term expected reward $\sum_{k=0}^{\infty} \gamma^k r_{t+k+1}$, Where r_{t+1} is the reward when moving from state s_t to s_{t+1} . The discount factor $\gamma \in [0, 1]$ [0, 1] is a measure of future reward, the value close to 0 means that the agent tends to maximize the immediate reward. Therefore, after taking action x_t under state s_t according to strategy π , the Q function can be expressed as:

$$Q^\pi(s_t, x_t) = E^\pi(R_t | S = s_t, X = x_t) = E^\pi \left\{ \sum_{k=0}^{\infty} \gamma^k r_{t+k+1} | S = s_t, X = x_t \right\} \quad (15)$$

The Q function is an evaluation function of the state-action pair and refers to the cumulative reward expectation value obtained by taking the action x_t with the environment s_t , and continuing the interaction with the environment. And the value iterative estimation is used to approximate $Q^*(s_t, x_t)$ in Q-learning algorithm:

$$Q(s_t, x_t) = Q(s_t, x_t) + \alpha_k \left[r_{t+1} + \gamma \max_{s_{t+1} \in S} Q'(s_{t+1}, x_{t+1}) - Q(s_t, x_t) \right] \quad (16)$$

where α_k is the learning rate, it means the effect of current knowledge on the previous learning knowledge. However, the optimal policy of the algorithm may converge to a local region. To overcome this situation, a ε greedy strategy is adopted to improve the search performance. Thus, agent has the probability to choose a random action.

$$X_t = \begin{cases} \text{random}, & 1 - \varepsilon \\ \arg \max_{X_k \in \psi} Q(s_t, X_k), & \varepsilon \end{cases} \quad (17)$$

4 Simulation Results and Discussion

In this section, in order to evaluate the performance of proposed task offloading strategy, the following two baseline methods are proposed for comparison:

- (1) Base station offloading: the user processes all tasks at the base station.

(2) Random offloading: the user offloads randomly under the system constraints.

The simulation environment is based on Python 3.7. We consider five power base stations that communicate via fiber optic networking. The transmit power of UE is 0.5w, the channel bandwidth is 20 MHz, 802.11ac specifies that there are 52 data subcarriers in the 20 MHz channel, the protection time interval is 0.8 μ s, according to the TS 36.101 communication protocol of 3GPP LTE, the communication between the base station and the users adopts 16 QAM, the coding rate is 1/2. Therefore, the transmission rate between UE and base station is 26 Mbps.

The size of the computing task is between 200 and 400 KB, and the required CPU cycle is 2500 M–3000 Mcycles, both are changing dynamically in each time slot. We discretize the action space and state to integer type. The number of users is set to 10, the maximum tolerated delay of the task is 400 ms, the local computing capacity is 1 Gcycles/s, and the base station computing capacity is 2.5 Gcycles/s, the maximum computing capacity of base station is 23.5 Gcycles, the effective switching capacitance of the chip architecture is 10^{-27} .

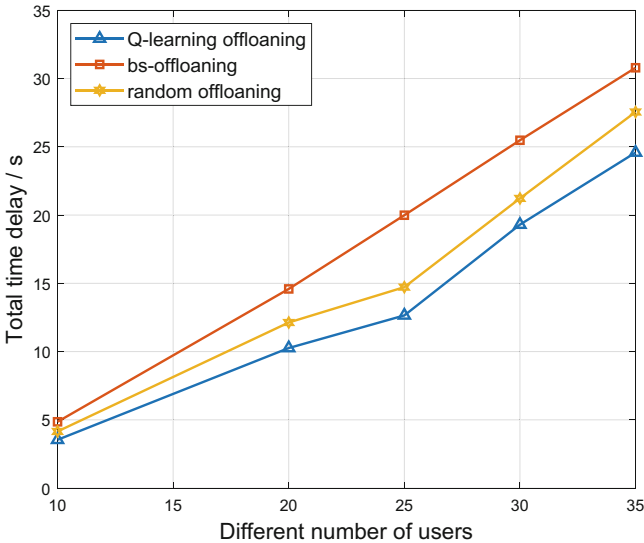


Fig. 2. Time delay comparison with different number of users

Figure 2 shows the time delay curves with different number of users. It can be seen that the delay of all three strategies increases with the increase of UEs, and our proposed strategy has the best performance. The total delay tends to increase linearly before 25 users, because the user tasks are offloaded to the access base station and the cooperative base station in similar proportions. The delay increases more significantly after 25 users, because the access base station load is in a heavy load situation and excess tasks will be transmitted over the fiber to the cooperative base station for processing, which causes additional delay.

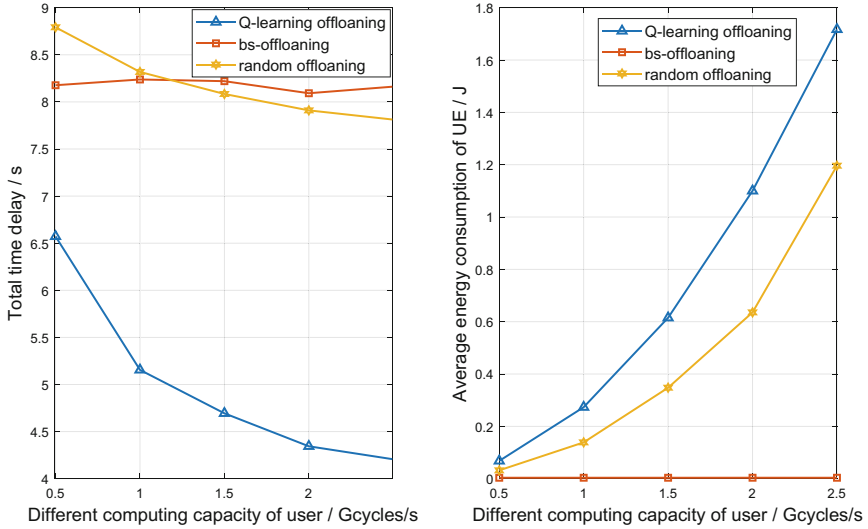


Fig. 3. Comparison of time delay and average energy consumption of user equipment under different computing capacity of users

Figure 3 shows the change of delay and average energy consumption of UE with different computing capacity of the user. It can be seen that increasing the local computing capacity reduces the task delay, which is more significant in the proposed Q-learning based strategy. This is because the algorithm will process tasks locally as much as possible within the system constraints, meanwhile the energy consumption is only slightly increased compared to random offloading. In the base station offloading strategy the equipment only needs to send the task to the base station, and the energy consumption is low. However, its delay is high and the base station cannot handle tasks of all users.

Figure 4 shows the change of base station available computing capacity under our proposed Q-learning strategy, where No. 1 base station is the access base station and others are the cooperative base stations. It can be seen that the load of all base stations increases as the number of users increases, because load balancing is achieved through cooperation between base stations to mitigate packet loss and retransmission caused by overloading of access base stations. While the load of the access base station increases most significantly, because the access base station has the smallest processing delay among the base stations, so the algorithm tends to process tasks at the access base station first. It can be seen that our strategy can effectively reduce the load of access base stations and improve the system capacity.

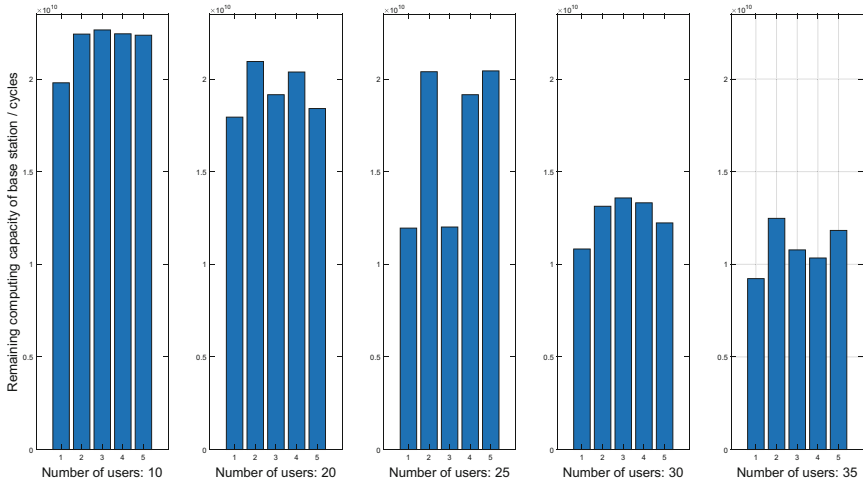


Fig. 4. Comparison of the base station's available computing capacity with different number of users

5 Conclusion

In order to reduce the delay and energy consumption of power equipment in integrated power communication networks, this paper proposed a computing offloading strategy based on base station cooperation. In our proposed scheme, the base station is equipped with an MEC server that can handle power tasks offloaded from the UE. Meanwhile, the access base station can schedule extra tasks to the cooperative base station, reducing the load on the access base station. The offloading decision process is modeled as MDP model, and the total power equipment delay is formulated as a minimization problem. A Q-learning based cooperative computing offloading algorithm is proposed to solve the optimization problem. Simulation results show that the Q-learning strategy proposed in this paper can significantly reduce the system delay and achieve load balance among base stations to guarantee the service quality of power services.

Acknowledgement. This work is supported by State Grid Jibei Electric Power Co., LTD. Science and Technology Project (No. SGJBXT00TJJS2200267).

References

1. Wang, F., Xu, J., Wang, X., Cui, S.: Joint offloading and computing optimization in wireless powered mobile-edge computing systems. *IEEE Trans. Wireless Commun.* **17**(3), 1784–1797 (2018). <https://doi.org/10.1109/TWC.2017.2785305>
2. Guo, F., Zhang, H., Ji, H., Li, X., Leung, V.C.M.: An efficient computation offloading management scheme in the densely deployed small cell networks with mobile edge computing. *IEEE/ACM Trans. Netw.* **26**(6), 2651–2664 (2018). <https://doi.org/10.1109/TNET.2018.2873002>

3. Ren, J., Yu, G., Cai, Y., He, Y.: Latency optimization for resource allocation in mobile-edge computation offloading. *IEEE Trans. Wireless Commun.* **17**(8), 5506–5519 (2018). <https://doi.org/10.1109/TWC.2018.2845360>
4. Lei, L., Xu, H., Xiong, X., Zheng, K., Xiang, W.: Joint computation offloading and multiuser scheduling using approximate dynamic programming in NB-IoT edge computing system. *IEEE Internet Things J.* **6**(3), 5345–5362 (2019). <https://doi.org/10.1109/JIOT.2019.2900550>
5. Hu, X., Wong, K.-K., Yang, K.: Wireless powered cooperation-assisted mobile edge computing. *IEEE Trans. Wireless Commun.* **17**(4), 2375–2388 (2018). <https://doi.org/10.1109/TWC.2018.2794345>
6. Zhou, C., et al.: Delay-aware IoT task scheduling in space-air-ground integrated network. *IEEE Glob. Commun. Conf. (GLOBECOM)* **2019**, 1–6 (2019). <https://doi.org/10.1109/GLOBECOM38437.2019.9013393>



DVFS-Enabled Adaptive Offloading and Adjusting for High-Efficiency 5G Power MEC

Zhenghao Li¹, Zhiwei Zhang², Gaofeng Zhang², Zhichang Feng², Qun Ma²,
Cong Chen², and Shuang Yang²(✉)

¹ State Grid Shandong Electric Power Company, Jinan, China

² State Grid Heze Power Supply Company, Heze, China

winnie.ys@163.com

Abstract. 5G Mobile edge computing (MEC) is a promising computing method to meet the low latency requirements of emerging power applications. By offloading computing intensive power applications from mobile devices to edge cloud servers, computing experience can be further improved in 5G power MEC systems. Based on 5G MEC, this paper proposes an adaptive offloading and allocating scheme (AOAS), which minimizes the response cost when the power application is constrained by the expected response delay. Specifically, this paper proposes a minimum consumption application offloading problem with corresponding delay, local CPU computing speed and other network resource constraints. Combined with variable replacement technology, this paper designs and proposes a resource control strategy integrating offload rate, local CPU computing speed and transmit power. Finally, the simulation results show that the system appearance of this scheme is better than that of local computing, full offloading and partial offloading with fixed computing speed.

Keywords: 5G MEC · Power applications · Dynamic voltage and frequency regulation · Adaptive offloading

1 Introduction

According to the survey of Cisco visual network index (VNI), the amount of the 5G mobile devices (MDs) in the world will exceed 12 billion by 2022 (far more than 9 billion in 2017) [1], which shows the strong demands of the 5G users for the MD to achieve convenient lifestyle. However, the existing MD with limited battery lifetime is not yet able to support sustaining response for the newly complex applications which requires fast response and high energy consumption [2, 3]. In recent years, the emergence of high-speed and highly reliable air interface technologies has prompted MD to offload the newly complex power applications (application offloading, the process of transmitting part or all of the compute-intensive power applications from 5G power MD to resource-rich power cloud servers [4]) to the edge cloud provided by the 5G power mobile edge computing (MEC) for short-distance IT services [5–7]. Under the practical

5G power MEC system, besides the complicated competition of the limited computing and communication resources, other key factors like the MD's execution (i.e., the local CPU computing state), the data transmitting and the charging of the computing resource would bring significant impact on application offloading, which cannot take full advantage of 5G power MEC.

So far, many academic works have been devoted to the power application offloading under 5G MEC systems. Authors in [8–11] considered dual time-scale and the heterogeneous application requests (i.e., different applications requirements for the computing resources, storage resources, etc.) to minimize the application response latency and ensure the robustness of offloading and scheduling. Besides, based on the Gilbert-Elliott model and monomial energy-consumption model, authors in [12, 13] optimized the application response energy consumption by joint radio and computing resources management, which helps to prolong the 5G MD's battery lifetime. Further, authors in [14] proposed low-complexity and adaptive application offloading scheme to minimize the response latency and energy consumption simultaneously, where the Lyapunov optimization and imitation learning are used.

However, above researches didn't involve the capability of 5G MD's local computing adjustment for further energy-efficient application offloading. Actually, dynamic voltage and frequency scaling (DVFS) technology is increasingly integrated into the general multi-core processors, by which more and more MD can flexibly adjust the local CPU computing speed based on the power application request (i.e., the local CPU computing speed adjustment) [15, 16]. The authors in [18–20] based on the DVFS technology, the application offloading decision, the local CPU computing speed and the transmit power were joint optimized for energy consumption reduction. Authors in [21–23] revealed the interaction between the MEC operator's pricing of the edge computing resources and the application offloading scheme of the network-wide mobile users, and they aimed to maximize the system profits. The important factors including the local CPU computing speed as well as the transmit power were not considered. As for the 5G power application response services, the local CPU computing speed and the transmit power control are interactive and should be reasonable adjusted to achieve high-quality user experience and promote green internet services, which has not been fully studied yet in existing 5G power networks.

In this paper, considering the heterogeneous power application requests, the DVFS-enabled 5G MD and operators charging conditions, a composite network-wide service benefit adjustment model constrained by application response latency is developed, which aims to minimize system response cost (i.e., minimizing the weighted sum of application response expense and energy consumption). Then, based on the variable substitution technique, an adaptive offloading and adjusting scheme (AOAS) including application partial offloading, local CPU computing speed and transmit power joint management is proposed. Our AOAS helps the 5G MD to adaptively adjust the power application response scheme, and comprehensively consider local computing energy consumption and the cost of acquiring power MEC computing resources to achieve low-consumption and green Internet services.

2 System Model and Problem Formulation

2.1 System Architecture

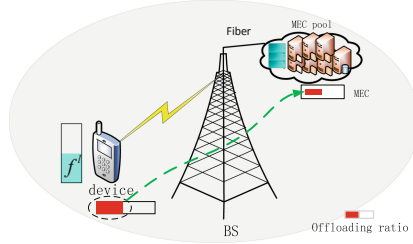


Fig. 1. MEC with adaptive offloading and allocation

The DVFS-enabled multi-user MEC network is shown in Fig. 1, which contains the base station (BS), the edge cloud pool and mobile devices (MD). Specifically, the BS is in charge of all uplink and downlink communications. The edge cloud pool is deployed around the base station and connected with the base station via short-haul fiber (e.g., telecom cloud), which can provide powerful computing capacities for MD to process the complex applications. The MD supports DVFS technology, which enables the embedded CPU to be adjusted adaptively based on its computing loads for optimizing the computing power consumption and extending the battery life. In practice, when the complex application arrives, the MD makes the offloading decide, the local CPU speed and the transmit power joint scheme to achieve minimum response cost, which also should satisfy system application response latency demands. This paper focuses on the data partitioned oriented applications.

2.2 System Component Models

In this section, the DVFS-enabled MEC system benefit is formulated, which incorporates offloading decision, DVFS-enabled CPU speed adjustment and the transmit power control simultaneously.

(1) Mobile device model

Considering the data partitioned oriented application, which is allowed to make full granularity partitioning (such as data compression and virus scanning) [19]. Specifically, the amount of data to be processed is known beforehand for this kind of application and can be divided into several independent subsets. That is, the application can be processed in parallel by the MEC and the mobile device simultaneously [19].

Application request: Vector $\{b, c, T^{\max}\}$ is used to abstract the application arriving at mobile device. b represents the amount of data bits. c is the complexity coefficient (i.e., the number of CPU cycles per bit). T^{\max} denotes the maximum allowable response latency.

DVFS-enabled adjustment: The capability of DVFS allows the embedded CPU in mobile device to adjust its voltage and its operating frequency adaptively according to the application request load, which helps to reduce the energy consumption of the mobile device as much as possible. And the computing power consumption of the CPU can be expressed as follows:

$$P = k(f^l)^3 \quad (1)$$

where k is a coefficient depending on the chip of the mobile device. f^l is the CPU computing speed of the mobile device (i.e., the computing cycles per second) and $f^l \in [0, f_{\max}^l]$. Obviously, the linear decrease in CPU computing speed results in cubic decreasing in the power consumption, which indicates the effectiveness of DVFS for energy conservation.

Local execution cost: When the application data bits $b(1 - \beta)$ needs to be executed locally by mobile device, then the local execution latency can be given as:

$$T^{local} = \frac{cb(1 - \beta)}{f^l} \quad (2)$$

where β is the offloading ratio and satisfies $\beta \in [0, 1]$ [0, 1].

Based on (1) and (2), the energy consumption to executing $b(1 - \beta)$ data bits is given by

$$E^{local} = (1 - \beta)bck(f^l)^2 \quad (3)$$

(2) Offloading model

The offloaded application data bits should be transmitted to the MEC through uplink for processing, then the results are sent back to the mobile device through the downlink. Thus, the transmission cost and the edge cloud execution latency should be considered for the application offloading.

Wireless Communication: The frequency-flat block-fading Rayleigh channel is used to model the wireless transmission links. The channel gain h mainly depends on the path loss and the channel fading coefficients. The uplink rate of mobile device can be expressed as:

$$R = B \log_2(1 + \gamma p^t) \quad (4)$$

where B is channels bandwidth for uplink, and N_0 is the while Gaussian noise power, $\gamma = h^2 / N_0$. p^t is the transmitting power and satisfies $0 \leq p^t \leq P^{\max}$.

Offloading cost: As mentioned above, the data bits $b\beta$ is transmitted to the MEC, then the latency of uplink can be given by

$$T^{trans} = \frac{b\beta}{R}. \quad (5)$$

Accordingly, the uplink energy consumption is expressed as

$$E^{trans} = T^{trans}(p^{ED} + k^t p^t), \quad (6)$$

where k^l denotes the efficient factor of power amplifier, and p^{ED} static power consumption of device.

In practice, the data amount of the application processing result is far less than the initial size, and the downlink transmission rate is usually much higher than the uplink transmission rate, and thus the downlink transmission delay and energy consumption can be ignored for simplifying the offloading model.

(3) Edge cloud model

As for the mobile device, the computing latency caused by MEC’s server can be expressed as:

$$T^C = \kappa cb\beta, \tag{7}$$

where κ is a coefficient factor, which depends on relevant operation protocol (i.e., the agreement between the user and the edge cloud operator). Based on (6) and (7), the latency spent on the offloaded application is given by

$$T^{MEC} = T^{trans} + T^C, \tag{8}$$

And the cloud service operator could charge fees from the mobile device

$$\xi = \rho cb\beta, \tag{9}$$

where ρ (\$/cycle) is the price of the edge computing resource (i.e., the price per computing cycle) charged by MEC operator.

(4) Application response cost

Focusing on the data partitioned oriented application (i.e., divided into several independent sub-applications), the response latency of mobile devices can be given by

$$T = \max\{T^{local}, T^{MEC}\}, \tag{10}$$

For achieving green and low-payment Internet service, a composite offloading utility function for mobile device is designed as follows:

$$u(f^l, \beta, p^t) = w^E(E^{local} + E^{trans}) + \xi, \tag{11}$$

where w^E is monetized earnings coefficient, which represents the benefit resulting from the energy consumption reduction, which decided by device or user.

In order to ensure high quality of system user experience, the network-wide application response cost function $u(f^l, \beta, p^t)$ is reformulated as follows:

$$u(f^l, \beta, p^t) = w^E(1 - \beta)v(f^l) + w^E\beta bg(p^t) + \rho\beta cb, \tag{12}$$

where $v(f^l) = cbk(f^l)^2$, and $g(p^t)$ is expressed as:

$$g(p^t) = \frac{(k^l p^t + p^{ED})}{B \log_2(1 + p^t \gamma)}, \tag{13}$$

2.3 Problem Formulation

In conclusion, the target problem in this paper can be formulated as the following objective, which involves the joint optimizing of the partial offloading decision, the local CPU speed and the transmit power. And our goal is to minimize the user cost, and further achieves green Internet service.

$$\begin{aligned} \mathbf{P1}: \min & u(f^l, \beta, p^t) \\ \text{s.t. } & C1 : 0 \leq \beta \leq 1, \\ & C2 : 0 \leq f^l \leq f_{\max}^l, \\ & C3 : 0 \leq p^t \leq p^{\max}, \end{aligned}$$

where C1 denotes the feasible region of the offloading ratio, C2 and C3 are the maximum CPU speed and transmit power constraints.

3 Adaptive OFFLOADING Based on DVFS

The centralized problem **P1** includes the offloading decision vector β , the local CPU speed decision f^l and the transmit power decision vector p^t , which are all coupled and make **P1** to be non-smooth and non-convex. In this paper, we propose an adaptive offloading and allocating scheme (AOAS), which finally transforms the **P1** into one-dimensional convex problem for easy solving.

3.1 Feasibility Analysis

To ensure application response latency demand of system users, there should satisfy $T \leq T^{\max}$, **P1** reformulated as follows.

$$\begin{aligned} \mathbf{P2}: \min & u(f^l, \beta, p^t) \\ \text{s.t. } & C1, C2, C3, \\ & C4 : T \leq T^{\max}, \end{aligned}$$

The latency constraint C4 in **P2** indicates that $T^{local} \leq T^{\max}$ and $T^{MEC} \leq T^{\max}$ should be hold simultaneously for mobile devices. Specifically, because $\beta \in [0, 1]$ is exiting, we can get

$$\beta^{\min} \triangleq \max\left(0, 1 - \frac{f_{\max}^l T^{\max}}{cb}\right) \quad (14)$$

$$\beta^{\max} \triangleq \min\left(1, \frac{T^{\max}}{T_{\min}^{off}}\right) \quad (15)$$

where $R^{\max} = B \log_2(1 + \gamma P^{\max})$ is the maximum transmit rate, and $T_{\min}^{\text{off}} = \kappa cb + b/R^{\max}$ is the minimum delay to transport full offloading. Obviously, $\beta^{\max} \geq \beta^{\min}$ must hold for feasible region of β , then we have

$$T^{\max} \geq \frac{1}{\frac{1}{T_{\min}^{\text{off}}} + \frac{1}{T_{\min}^{\text{local}}}} \triangleq T^{\min} \tag{16}$$

where $T_{\min}^{\text{local}} = cb/f_{\max}^l$ hold. And (16) also indicates the mobile user’s feasible response latency demand for supporting partial offloading.

3.2 Optimal Solution

In order to simplify P2, the mathematics lemma that $\inf_{X,Y} f(X, Y) = \inf_X \tilde{f}(X)$ where $\inf_X \tilde{f}(X) = \inf_Y f(X, Y)$ is used to decouple **P1** into sub-problems for effective solving. In the following, the **P1** can be solved by minimizing over f^l, p^t and β , sequentially.

(1) Local CPU Speed Decision: Fix p^t and β in **P2**, the local CPU speed decision problem is given as:

$$\begin{aligned} \mathbf{P3}: \quad & \min v(f^l) \\ & \text{s.t. } C2, C4. \end{aligned}$$

Here, we omit the items in **P2** which has nothing to do with the decision f^l , and $v(f^l) = cbk(f^l)^2$ indicates that $v(f^l)$ increases monotonically with the increases of f^l , which means low CPU speed results in low energy consumption. Besides, from C2 and C4, we have $f^l \geq cb(1 - \beta)/T^{\max}$. Hence, the optimal f^l can be derived in closed-form as follows:

$$f^{l*} = \frac{cb(1 - \beta)}{T^{\max}}, \tag{17}$$

Then based on (17), the original **P2** can be simplified into following **P4** with two decision vectors β and p^t :

$$\begin{aligned} \mathbf{P4}: \quad & \min u(\beta, p^t) \\ & \text{s.t. } C1, C3, C4, C5, \end{aligned}$$

where $u(\beta, p^t) = w^E C(1 - \beta)^3 + w^E \beta bg(p^t) + \rho \beta cb$, and $C = k(cb)^3 / (T^{\max})^2$.

(2) Transmit Power Decision: Fix β in P4, the transmit power decision problem can be expressed as:

$$\begin{aligned} \mathbf{P5}: \quad & \min_{f^l} g(p^t) \\ & \text{s.t. } C3, C4. \end{aligned}$$

The time spent for offloading should satisfy $T^{MEC} \leq T^{\max}$, then

$$p^f \geq \frac{2 \frac{b\beta}{BT^{\max} - B\kappa cb\beta}}{\gamma} - \frac{1}{\gamma} \triangleq p^{\min}(\beta)$$

Then based on C3, the feasible region of decision p^f can be expressed as $p^{\min}(\beta) \leq p^f \leq p^{\max}$.

Based on the lemma in [19], we know that function $g(p^f)$ is a unimodal. That is, the optimal p^f in closed-form can be expressed as:

$$p^*(\beta) = \begin{cases} p^{\min}(\beta), & p^o < p^{\min}(\beta), \\ p^o, & p^{\min}(\beta) \leq p^o \leq p^{\max}, \\ p^{\max}, & p^{\max} < p^o. \end{cases} \quad (18)$$

where p^o is the extreme point. Substituting (18) into P4 and considering the feasible region of β , the original problem can be rewritten as:

$$\begin{aligned} \mathbf{P6}: \quad & \min u(\beta) \\ & \text{s.t. } C5, \\ & C6 : \beta^{\min} \leq \beta \leq \beta^{\max}, \end{aligned}$$

where $u(\beta) = w^E C(1 - \beta)^3 + w^E \beta b g(p^*(\beta)) + \rho \beta c b$

(3) Partial Offloading Decision: The original problem P1 is simplified into one-dimensional P6, but the convexity of $u(\beta)$ is difficult to estimate directly due to the item $w^E \beta b g(p^*(\beta))$. In order to prove the convexity of $u(\beta)$, the following lemma should be used in this paper.

Lemma 1. *If function f is convex in (x, y) , and C is a convex nonempty set, then the function*

$$g(x) = \inf_{y \in C} f(x, y)$$

is convex in x , provided $g(x) > -\infty$ for some x . The domain of $g(x)$ is the projection of domain of f on its x -coordinates.

Based on lemma 1, the following efforts is made to prove problem **P6**. Specifically, **P4** is considered again. Let $x = 1 / \log_2(1 + p^f \gamma)$, then **P4** is reformulated into following compact form as:

$$\begin{aligned} \mathbf{P7}: \quad & \min_{\beta, x} u(\beta, x) \\ & \text{s.t. } C1, C5, \\ & C7 : T^{MEC}(\beta, x) \leq T^{\max}, \\ & C8 : x \geq \frac{1}{\log_2(1 + p^{\max} \gamma)}, \end{aligned}$$

And the objective $u(\beta, \mathbf{x})$ is

$$u(\beta, \mathbf{x}) = w^E C(1 - \beta)^3 + \frac{w^E \beta b}{B} x \left[p^{ED} + \frac{k^t}{\gamma} \left(2^{\frac{1}{x}} - 1 \right) \right] + \rho \beta c b,$$

where $T^{MEC}(\beta, \mathbf{x}) = b\beta x / B + \kappa c b \beta$,

Since the Hessian matrix of $u(\beta, \mathbf{x})$ is positive semi-definite, $u(\beta, \mathbf{x})$ is convex in (β, \mathbf{x}) . Also, the feasible region \mathcal{C} specified by the constraints C1, C5, C7 and C8 is also convex nonempty set. Therefore, **P7** is a convex optimization problem, which minimizes a convex function $u(\beta, \mathbf{x})$ over a convex set \mathcal{C} . Obviously, $u(\beta)$ in **P6** results from the operation $u(\beta) = \inf_{\mathbf{x} \in \mathcal{C}} u(\beta, \mathbf{x})$. Hence, based on lemma 1, $u(\beta)$ is convex w. r. t. β , and thus **P6** is also a convex problem.

Next, we need to obtain the optimal offloading decision β , and **P6** can be simplified to the separable structure for mobile user as follows:

$$\begin{aligned} \mathbf{P8}: \quad & \min_{\beta} f(\beta) \\ & s.t. \quad C6. \end{aligned}$$

where

$$f(\beta) = w^E c(1 - \beta)^3 + w^E \beta b g(p^*(\beta)) + \rho \beta c b \tag{19}$$

As **P8** is a one-dimensional convex problem, so, the bisection algorithm is considered here.

4 Simulation Results and Analysis

Extensive simulation results are presented in this section. We first show that the AOAS can adapt the joint partial offloading, local CPU computing speed and variable MEC pricing. Then, the advantages of our AOAS are presented from two key aspects. On one hand, the AOAS exploiting partial offloading aims at fit data change (i.e., reduce response cost). On the other hand, our AOAS with adaptive offloading management have a well performance in price fluctuations.

Figure 2 demonstrates the adaptive adjustment of MD local CPU assisted by DVFS technique under various user demands scenarios (i.e., b and T^{\max}). As shown in Fig. 2, the MD does adjust its local CPU speed properly for satisfying various user demands. Specifically, along with the increase of T^{\max} , the local CPU computing speed f^l decreases, and achieving very low energy consumption. When given the allowable latency, the CPU speed f^l increases with application data bits b (i.e., heavy application response load). Sometimes the local CPU should operate at maximum speed f_{\max}^l to execute the compute-intensive and delay-sensitive application, or even can't complete it.

Figure 3 shows the impact of user demand and MEC pricing on the system consumption, where the application data bits is set to $b = 10^6$ bits. As we can see that severe response latency demand $T^{\max} \leq 0.8s$ would make application request response failed, since the limited local CPU speed, the transmission rate and the edge computing

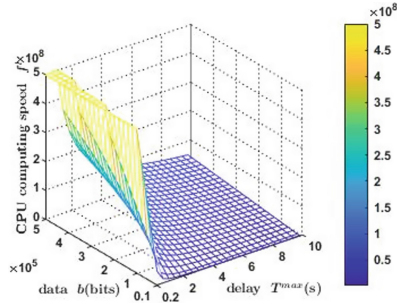


Fig. 2. Adaptive adjustment of local CPU speed.

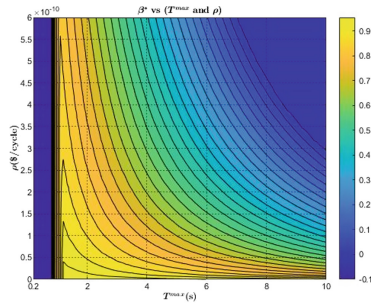
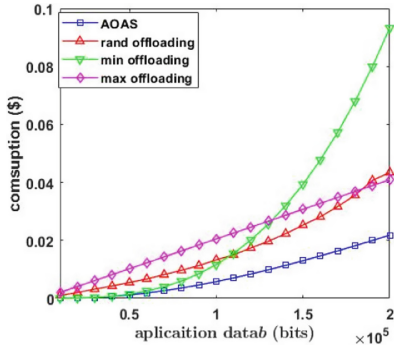


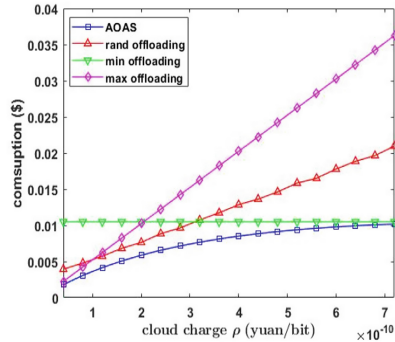
Fig. 3. Optimal offloading and system consumption under various user demands and MEC pricing.

resource are not enough for this demand. For good demonstration purposes, here let $\beta^* = -0.1$ represent the failed application request. When MD under the smaller T^{\max} and lower ρ case would prefer to offload the whole application (i.e., big) to the edge cloud for achieving minimum response cost, and under the higher T^{\max} and expensive ρ case would prefer to computing local for achieving minimum response cost.

Figure 4 compares several key MEC system performances under different methods (including AOAS, Rand offloading, Local computing, Full offloading). Figure 4a analyzes the changes of user response cost with application requests under AOAS, local computing, full offloading and random offloading. With the increase of data, the computing cost of the four offloading algorithms increases, and the computing cost of AOAS offloading algorithm is lower than that of the other three offloading methods. When the application data is small, the user prefers all local computing, and the computing cost of AOAS and local computing is lower than that of full offloading and random offloading. According to P8, the energy consumption of local computing has an exponential relationship with the application data, and the computing cost of local computing is higher than that of other offloading methods. Figure 4b analyzes the changes of user computing cost with MEC computing resource price under AOAS, local computing, full offloading and random unloading. With the increase of computing resource price ρ , the computing cost of AOAS, full offloading and random offloading increases, and the computing cost



(a) Consumption of the MD with application data b



(b) Consumption of the MD with cloud resource charge ρ

Fig. 4. The impact of application data and cloud resource charge on the MEC system.

of AOAS offloading algorithm is lower than that of the other three offloading methods. With the increase of computing resource price, users prefer all-local computing.

5 Conclusions

At present, there are still challenges for resource constrained 5G MD to implement real-time interactive or computing intensive power applications. Therefore, it is particularly important to reduce the energy consumption of MD and ensure the delay constraint of power applications. In view of this situation, this paper proposes a optimizes strategy of partial offloading, local computing speed and transmit power integration, which adjust the local computing speed by using the self-adaptive adjustment ability of DVFS, and minimize the response cost when the delay allows. Different from the related work, this paper considers the charging of cloud computing resources. The simulation results show that compared with all local computing, the energy consumption of mobile devices in AOAS is 66.67% less when the delay is limited.

Acknowledgment. This work is supported by State Grid Shandong Electric Power Company Science and Technology Project: “Research on Smart Grid 5G Edge Business Orchestration and Secondary Authentication Technology” (No. 520614220002).

References

1. Cisco’s latest VNI forecast: in 2017–2022: https://www.cisco.com/c/zh_cn/about/press/2019/02-22.html
2. Baktir, A.C., Ozgovde, A., Ersoy, C.: How can edge computing benefit from software-defined networking: a survey, use cases, and future directions. *IEEE Commun. Surv. Tutor.* **19**(4), 2359–2391 (2017)
3. Sheng, M., Wang, Y., Wang, X., Li, J.: Energy-efficient multiuser partial computation offloading with collaboration of terminals, radio access network, and edge server. *IEEE Trans. Commun.* **68**(3), 1524–1537 (2020)

4. Khan, A.U.R., Othman, M., Madani, S.A., Khan, S.U.: A survey of mobile cloud computing application models. In: *IEEE Communications Surveys and Tutorials*, vol. 16, no. 1, pp. 393–413 (2014)
5. Abbas, N., Zhang, Y., Taherkordi, A., Skeie, T.: Mobile edge computing: a survey. *IEEE Internet Things J.* **5**(1), 450–465 (2018)
6. Mouradian, C., et al.: A comprehensive survey on fog computing: state-of-the-art and research challenges. *IEEE Commun. Surveys Tuts.* **20**(1), 416–464 (2018)
7. “Mobile-edge computing—Introductory technical white paper,” White Paper, ETSI, Sophia Antipolis, France, Sep 2014. [Online]. Available: https://portal.etsi.org/portals/0/tbpages/mec/docs/mobile-edge_computing_-_introductory_technical_white_paper_v1%2018-09-14.pdf
8. Liu, J., Mao, Y., Zhang, J., Letaief, K.B.: Delay-optimal computation task scheduling for mobile-edge computing systems. In: *2016 IEEE International Symposium on Information Theory (ISIT)*, Barcelona (2016)
9. Qu, Y., Dai, H., Wu, F., et al.: Robust offloading scheduling for mobile edge computing. *IEEE Trans. Mobile Comput.* **PP**(99), 1–1 (2020)
10. Yang, T., Chai, R., Zhang, L.: Latency optimization-based joint task offloading and scheduling for multi-user MEC system. In: *2020 29th Wireless and Optical Communications Conference (WOCC)*, Newark, NJ, USA, pp. 1–6 (2020)
11. Alameddine, H.A., Sharafeddine, S., Sebbah, S., Ayoubi, S., Assi, C.: Dynamic task offloading and scheduling for low-latency IoT services in multi-access edge computing. *IEEE J. Sel. Areas Commun.* **37**(3), 668–682 (2019)
12. Zhang, W., Wen, Y., Guan, K., Kilper, D., Luo, H., Wu, D.O.: Energy-optimal mobile cloud computing under stochastic wireless channel. *IEEE Trans. Wireless Commun.* **12**(9), 4569–4581 (2013)
13. You, C., Zeng, Y., Zhang, R., Huang, K.: Asynchronous mobile-edge computation offloading: energy-efficient resource management. *IEEE Trans. Wireless Commun.* **17**(11), 7590–7605 (2018)
14. Wang, J., Peng, J., Wei, Y., Liu, D., Fu, J.: Adaptive application offloading decision and transmission scheduling for mobile cloud computing. In: *2016 IEEE International Conference on Communications (ICC)*, Kuala Lumpur, pp. 1–7 (2016)
15. Lin, X., Wang, Y., Xie, Q., Pedram, M.: Task scheduling with dynamic voltage and frequency scaling for energy minimization in the mobile cloud computing environment. *IEEE Trans. Serv. Comput.* **8**(2), 175–186 (2015)
16. Qu, G.: What is the limit of energy saving by dynamic voltage scaling? In: *Proceedings of the IEEE/ACM ICCAD*, San Jose, CA, USA, pp. 560–563 (2001)
17. Li, K.: Energy efficient scheduling of parallel tasks on multiprocessor computers. *J. Supercomput.* **60**(2), 223–247 (2012)
18. Yu, H., Wang, Q., Guo, S.: Energy-efficient task offloading and resource scheduling for mobile edge computing. In: *2018 IEEE International Conference on Networking, Architecture and Storage (NAS)*, Chongqing, pp. 1–4 (2018)
19. Wang, Y., Sheng, M., Wang, X., Wang, L., Li, J.: Mobile-edge computing: partial computation offloading using dynamic voltage scaling. *IEEE Trans. Commun.* **64**(10), 4268–4282 (2016)
20. Chen, S., Zheng, Y., Lu, W., Varadarajan, V., Wang, K.: Energy-optimal dynamic computation offloading for industrial IoT in fog computing. *IEEE Trans. Green Commun. Netw.* **4**(2), 566–576 (2020)
21. Li, F., Yao, H., Du, J., Jiang, C., Qian, Y.: Stackelberg game-based computation offloading in social and cognitive industrial internet of things. *IEEE Trans. Industr. Inf.* **16**(8), 5444–5455 (2020)

22. Wang, Q., Guo, S., Wang, Y., Yang, Y.: Incentive mechanism for edge cloud profit maximization in mobile edge computing. In: ICC 2019—2019 IEEE International Conference on Communications (ICC), Shanghai, China, pp. 1–6 (2019)
23. Wang, Q., Guo, S., Liu, J., Pan, C., Yang, L.: Profit maximization incentive mechanism for resource providers in mobile edge computing. *IEEE Trans. Serv. Comput.* **15**, 138–149 (2019)



Efficient Multi-dimensional Edge Resources Allocation for 5G Power MEC

Baichao Ma, Tianyu Wang, Xiaomin Xie, Dan Chen, Kai Huang, Falei Ji, and Shuang Yang^(✉)

State Grid Heze Power Supply Company, Heze, China
winnie.ys@163.com

Abstract. With the rapid development of smart grid technology, the demand for computing resources by 5G power terminals has sharply increased. In order to meet the services, power MEC technology is appearing. However, due to the limited computing resources, multi-dimensional resource allocation has always been one of the key problems to be solved in the power edge computing environment. This article allocates computing resources reasonably under limited resources of 5G power MEC and power consumption to meet the service quality and improve the maximum utility of the new power system. Aiming at the problem, a resource allocation model is proposed. By introducing the resource request emergency factor, resources are allocated to terminals that can maximize the new power system utility by taking the system utility as the optimization objective. This paper allocates transmission power reasonably through terminal request emergency factor, and allocates more transmission power to terminals with large emergency factor. An optimization scheme is proposed based on Polyblock algorithm and simulations show that the algorithm can indeed obtain the optimal solution under constraints.

Keywords: Smart grid · 5G power MEC · Multi-dimensional resource allocation · Polyblock algorithm

1 Introduction

In recent years, with the continuous development of smart grid and the Internet of Things, massive applications such as distributed energy resources and intelligent transportation have emerged, and the number of mobile internet terminals has sharply increased [1]. This has put forward higher requirements for 5G power services such as computing power, network quality, transmission rate, and response delay. The explosive growth of traffic has brought unprecedented pressure to the smart grid, greatly affecting the quality of user experience. In order to address this issue, 5G power cloud computing technology has been proposed, and people have begun to offload some or all tasks of terminals to cloud servers to complete. However, due to the geographical location of cloud servers being generally far away, despite their powerful computing power, they are far away from end users, resulting in increased transmission energy consumption and particularly high response latency. In order to effectively alleviate the challenges of high load, high bandwidth, high mobility, low latency and other aspects faced by the new power system, the concept of 5G power mobile edge computing (MEC) came into being.

Unlike cloud computing, 5G power MEC allows terminals to offload computing tasks to servers deployed at the edge of the network, localizing business, greatly reducing remote data transmission, network latency, and transmission costs. Although offloading computing tasks to edge servers can alleviate the demand of terminals for network performance services to some extent, the resources of edge servers are also limited, and a reasonable resource allocation model and task scheduling algorithm need to be introduced to coordinate and manage edge resources of the new power system. Reference [2] proposes a framework based on Stackelberg games, which decomposes multi resource allocation and pricing problems into a set of sub-problems, where each sub-problem only considers a single resource type. By determining the Stackelberg equilibrium algorithm for each resource type, terminals can obtain resources with maximum utility under constraints. Reference [3] deeply analyzed the network resource scheduling problem from two aspects: user experience and mobile operator resource allocation. The task scheduling and resource allocation problem were described as a non-convex mixed integer problem, and then a heuristic solution was used to solve the original problem, obtaining an approximate optimal solution with low complexity. Literature [4] studied a distributed mobile edge computing scenario, described the task allocation problem as a strategy game by making full use of the computing resources in the entire distributed system, and proposed a task unloading and allocation algorithm of game theory to solve this multiple optimization problem in a short time. Reference [5] studied the issue of fair aware task offloading and resource allocation in WMAN of MEC servers, and proposed a two-level algorithm to search for the optimal offloading solution, making full use of server resources fairly. Literature [6] designed an efficient approximation and online algorithm with demonstrable performance guarantee to improve users' satisfaction with the service provided by MEC. The experimental results show that the algorithm has good application prospects in reducing service delay and improving user satisfaction. Meanwhile, in order to solve the problem of large-scale mobile devices processing tasks simultaneously, reference [7] proposes an auxiliary mechanism for MEC systems. When the main MEC server cannot meet the latency requirements of mobile devices in its coverage area, some tasks can be offloaded to the auxiliary MEC server to obtain additional processing resources.

The MEC framework effectively reduces the computational and communication burden of the main MEC server, and improves the resource utilization of the auxiliary MEC server. In the face of the serious pressure on MEC servers caused by the complex and changeable edge computing environment, how to reasonably allocate computing resources and network resources under the changeable MEC conditions to meet the needs of mobile devices. Reference [8] proposed an intelligent, deep reinforcement learning based resource allocation (DRLRA) scheme, which can adaptively allocate computing and network resources under different MEC environments to reduce the average service time, Balance the use of resources. In addition, considering that edge servers will incur additional processing delays due to low energy. In order to solve this problem, [9] introduced renewable energy into mobile edge computing, used wireless power transmission technology to realize energy transmission between MEC servers, minimized the total delay of the system by optimizing unloading and wireless resource allocation, and used Lagrange multiplier method to obtain the optimal allocation of computing resources.

At the same time, an effective unloading exclusion algorithm (OEA) was proposed to determine the optimal unloading decision. Reference [10] describes the joint optimization problem of task offloading and heterogeneous resource allocation as a mixed integer nonlinear problem. Through the coupling relationship between resource allocation and task offloading, stable convergence solutions can be obtained through multiple iterations to fully utilize resources and maximize the average utility of the system.

It can be seen that the introduction of resource allocation models and task scheduling algorithms for overall management of edge resources can indeed allocate edge resources reasonably. This article provides a new interpretation of the rationality of edge resource allocation from the perspective of maximum system utility. We propose a resource allocation mechanism based on the “emergency factor”, which divides resource requests from terminals into “hot and cold” processing according to the emergency factor. With the goal of maximizing system utility, we allocate resources from various dimensions to terminals and provide corresponding transmission power consumption.

2 System Model and Problem Formulation

The edge resource allocation system consists of power terminals, transmission nodes and edge servers. Power terminals are the senders of the edge resource request and are responsible for receiving the calculation results of the edge servers. The transmission nodes realize the centralized communication, cache and computing functions of the system by means of optical fiber direct connection. Computer resources on edge servers are managed in a unified manner through virtualization. The power for system calculation and communication is delivered by the grid. Its model structure is shown in Fig. 1.

In this model, the resources of the edge server are mainly the basic hardware resources, including CPU (computing resources), hard disk (storage resources), network card (network resources), etc. The server has a main control board and a baseband board. The main control board is responsible for processing signals from terminals and transmission nodes and interconnecting with them. The baseband board is responsible for calculating, encoding, modulating, and other baseband processing data, and sending the processed pending data to terminals through the transmission nodes, thereby achieving real-time interaction between terminals and edge resource platforms, and ultimately achieving the beautiful vision of “terminal number, edge computing”.

2.1 Edge Server Model

The edge server model consists of several edge servers, and these physical resources are managed in a “virtualization” manner. This model divides these resources into D dimensions, denoted as $\mathbf{S} = \{S_1, S_2, \dots, S_D\}$, and the upper limit of each dimension resources is $S_d \forall d \in D$. The task resource request of the terminal is $\alpha_m = \{\alpha_{m1}, \alpha_{m2}, \dots, \alpha_{mD}\}$, and the total number of resource requests for each dimension of all terminals cannot exceed the upper limit of edge resources, that is:

$$\sum_{m \in M} \alpha_{md} \leq S_d \quad \forall d \in D \quad (1)$$

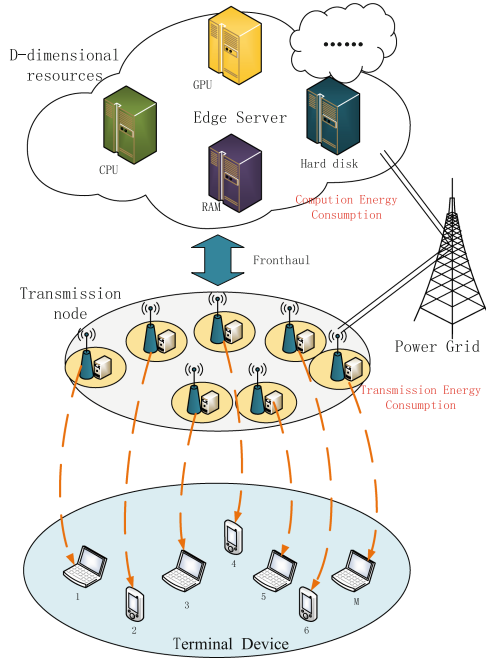


Fig. 1. Model structure

Among them, the Unit cost price of the d -th dimension resource of the edge resource is c_d , and the unit price of the d -th dimension resource sold to the terminal is, so the income of the edge resource end can be obtained as follows:

$$U_{MEC}(\alpha) = \sum_{m \in M} \sum_{d \in D} (p_d - c_d) \alpha_{md} \tag{2}$$

2.2 Transmission Node Model

The downlink transmission part of the transmission node model is only related to the allocated power consumption. The allocated power consumption is higher, the transmission effect is better and the profit is higher. Therefore, a transmission power vector $\mathbf{P} = \{p_1, p_2, \dots, p_M\}$ is introduced to reflect this situation. Where, the Unit cost price of transmission power consumption is c_t , and the unit price of transmission power consumption is p_t , so the benefits of transmission node end can be obtained as follows:

$$U_T(\mathbf{P}) = \sum_{m \in M} (p_t - c_t) P_m \tag{3}$$

2.3 Terminal Device Model

There are many types of resource requirements for terminal devices. After considering the urgency of events in real life, the emergency factors of resource requests from various

terminals ω_m and r_{md} dimensions are introduced. The larger the value, the greater the benefits brought by the response. The revenue of the terminal can be obtained as follows:

$$U_m(\boldsymbol{\alpha}_m, \mathbf{P}) = \sum_{d \in D} \omega_m r_{md} \ln(1 + \alpha_{md}) - \sum_{d \in D} p_d \alpha_{md} + \omega_m v_{mp} \ln(1 + P_m) - p_t P_m \quad (4)$$

$$U_{TER}(\boldsymbol{\alpha}, \mathbf{P}) = \sum_{m \in M} U_m \quad (5)$$

3 Constraints and Optimization Problems

Condition 1: Different dimensions of resources have resource limits, i.e.

$$\sum_{m \in M} \alpha_{md} \leq S_d \quad \forall d \in D \quad (6)$$

Condition 2: The power consumption resources provided by the power grid are limited and mainly used for calculation and communication. In terms of calculation, the unit energy consumption consumed by the introduction of the second dimension resources is mainly the transmission loss, and the total energy consumption needs to meet the following conditions:

$$\sum_{m \in M} \sum_{d \in D} \phi_d \alpha_{md} + \sum_{m \in M} P_m \leq P_{\max} \quad (7)$$

The ultimate goal of this model is to maximize the overall benefits of the system while meeting the constraints, namely:

$$\begin{aligned} U(\boldsymbol{\alpha}, \mathbf{P}) &= \max_{\boldsymbol{\alpha}, \mathbf{P}} U_{MEC}(\boldsymbol{\alpha}) + U_T(\mathbf{P}) + U_{TER}(\boldsymbol{\alpha}, \mathbf{P}) \\ &= \max_{\boldsymbol{\alpha}, \mathbf{P}} \sum_{m \in M} \sum_{d \in D} (p_d - c_d) \alpha_{md} + \sum_{m \in M} (p_t - c_t) P_m \\ &\quad + \sum_{m \in M} \sum_{d \in D} \omega_m r_{md} \ln(1 + \alpha_{md}) - \sum_{m \in M} \sum_{d \in D} p_d \alpha_{md} \\ &\quad + \sum_{m \in M} \omega_m v_{mp} \ln(1 + P_m) - \sum_{m \in M} p_t P_m \\ &= \max_{\boldsymbol{\alpha}, \mathbf{P}} \sum_{m \in M} \sum_{d \in D} [\omega_m r_{md} \ln(1 + \alpha_{md}) - c_d \alpha_{md}] \\ &\quad + \sum_{m \in M} [\omega_m v_{mp} \ln(1 + P_m) - c_t P_m] \end{aligned} \quad (8)$$

In summary, we can obtain the following optimization problems:

$$\begin{aligned}
 P1 : \max \quad & \sum_{m \in M} \sum_{d \in D} [\omega_m r_{md} \ln(1 + \alpha_{md}) - c_d \alpha_{md}] \\
 & + \sum_{m \in M} [\omega_m v_{mp} \ln(1 + P_m) - c_t P_m] \\
 \text{s.t.} \quad & \sum_{m \in M} \sum_{d \in D} \phi_d \alpha_{md} + \sum_{m \in M} P_m \leq P_{\max} \\
 & \sum_{m \in M} \alpha_{md} \leq S_d \quad \forall d \in D
 \end{aligned} \tag{9}$$

4 Problem Solving

The Polyblock outer approximation method is often used to solve monotonic optimization problems. Firstly, we need to prove that P1 is monotonically increasing in the feasible domain.

Prove: Let $\mathbf{U} = U1 + U2 + U3 + \dots + UM * (D + 1)$, where:

$$\begin{aligned}
 U1 &= \omega_1 r_{11} \ln(1 + \alpha_{11}) - c_1 \alpha_{11} \\
 &\vdots \\
 UM * (D + 1) &= \omega_M v_{Mp} \ln(1 + P_M) - c_D P_M
 \end{aligned} \tag{9}$$

It can be seen that the structure of the analytical formula $U1 \dots UM * (D + 1)$ is similar, where $U_i = \omega r \cdot \ln(1 + x) - cx$, here the defined domain is $[0, +\infty)$, then

$$\frac{dU_i}{dx} = \frac{\omega r}{1 + x} - c \tag{11}$$

Let $\frac{dU_i}{dx} = 0$, and the solution is:

$$x^* = \frac{\omega r}{c} - 1 \tag{12}$$

Because of

$$\frac{d^2 U_i}{dx^2} = -\frac{\omega r}{(1 + x)^2} < 0 \tag{13}$$

is constant. Therefore, $U1 \dots UM * (D + 1)$ obtains the maximum point (maximum point) at $x_1^*, x_1^*, x_1^*, \dots, x_{M*(D+1)}^*$, denoted as $\mathbf{X} = [x_1^*, x_1^*, x_1^*, \dots, x_{M*(D+1)}^*]$.

When $x_i < x_i^*$, $\frac{dU_i}{dx} > 0$, indicates that at $[0, x_i^*]$, the function monotonically increases. When $x_i > x_i^*$, $\frac{dU_i}{dx} < 0$ indicates that at $[x_i^*, +\infty)$, the function monotonically decreases. And \mathbf{U} is a function of $M * (D + 1)$ variables, so \mathbf{U} reaches its maximum value at \mathbf{X} . From this, it can be seen that P1 increases monotonically in $[0, \mathbf{X}]$, so this problem belongs to monotonic optimization problems.

Polyblock has an important property: the maximum value of the strictly increasing function defined on Polyblock is always obtained at a vertex of Polyblock. Therefore, the maximum value of the strictly increasing function can be effectively obtained by traversing the vertices of the Polyblock.

Firstly, establish an initial block, and based on the relationship between the extreme point and the boundary of the feasible region, there are two situations:

- (1) The point is within or on the boundary of the feasible region. As shown in Fig. 2, since the function reaches its maximum value at the extreme point and satisfies constraints 1 and 2, this point is the optimal solution.
- (2) The point is outside the boundary of the feasible domain.

Scenario 1: When the block formed by the extreme points completely includes the feasible region, as shown in Fig. 3. Obviously, the function satisfies monotonic conditions in the feasible domain, so reducing the block boundary makes

$$X_1 = [S_1 \cdots S_1, \cdots \cdots S_D \cdots S_D, P_{\max} \cdots P_{\max}]$$

Then this point is the initial block vertex.

Scenario 2: When the block formed by the extreme points contains some feasible regions, as shown in Fig. 4.

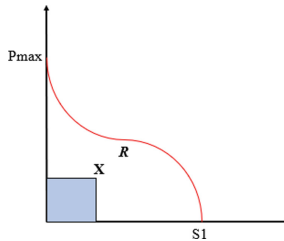


Fig. 2.

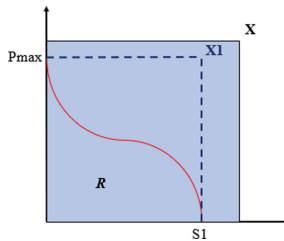


Fig. 3.

From the properties of the extreme points, it can be seen that the function inside the block formed by the extreme point \mathbf{X} monotonically increases, while the area outside the block monotonically decreases. Let any point in the feasible region outside the block be

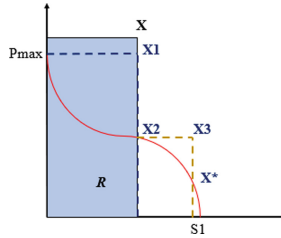


Fig. 4. .

X^* , and the function outside the block monotonically decreases on the S_1 axis. Therefore, $X_2 > X_3$, while the P_{\max} axis is in the block region, the function monotonically increases, so $X_3 > X^*$. Therefore, any point $X_2 > X^*$ outside the block remains constant, that is, there is no optimal solution outside the block, so let X_1 be the initial block vertex.

Next is the process of solving by updating the blocks. Firstly, construct a “0-X” straight line through the “two point formula”:

$$\frac{x_1}{x_1^*} = \frac{x_2}{x_2^*} = \frac{x_3}{x_3^*} = \dots = \frac{x_{M*(D+1)}}{x_{M*(D+1)}^*} = k \tag{14}$$

Namely:

$$\begin{aligned} x_1 &= k * x_1^* \\ x_2 &= k * x_2^* \\ &\vdots \\ x_{M*(D+1)} &= k * x_{M*(D+1)}^* \end{aligned} \tag{15}$$

Then, constraint conditions 1 and 2 form an $M^*(D+1)$ dimensional feasible domain boundary:

$$\begin{aligned} \phi_1 x_1 + \phi_2 x_2 + \dots + \phi_{M^*D} x_{M^*D} + x_{M^*D+1} + \dots + x_{M^*(D+1)} &\leq P_{\max} \\ x_1 + x_2 + \dots + x_M &\leq S_1 \\ x_{M+1} + x_{M+2} + \dots + x_{M+M} &\leq S_2 \\ &\vdots \end{aligned} \tag{16}$$

By substituting the “0-X” line into the feasible domain boundary, the intersection point of the two can be obtained:

$$\begin{aligned} \left[\begin{aligned} \phi_1 k_1 * x_1^* + \phi_2 k_1 * x_2^* + \dots + \phi_{M^*D} k_1 * x_{M^*D}^* \\ + k_1 * x_{M^*D+1}^* + \dots + k_1 * x_{M^*(D+1)}^* \end{aligned} \right] &\leq P_{\max} \\ k_2 * x_1^* + k_2 * x_2^* + \dots + k_2 * x_M^* &\leq S_1 \\ k_3 * x_{M+1}^* + k_3 * x_{M+2}^* + \dots + k_3 * x_{M+M}^* &\leq S_2 \\ &\vdots \end{aligned} \tag{17}$$

Here, we first calculate the scaling factor k :

$$\begin{aligned} & \left[\begin{array}{l} \phi_1 x_1^* + \phi_2 x_2^* + \dots + \phi_{M \cdot D} x_{M \cdot D}^* \\ + x_{M \cdot D + 1}^* + \dots + x_{M \cdot (D+1)}^* \end{array} \right] \leq P_{\max} / k_1 \\ & x_1^* + x_2^* + \dots + x_M^* \leq S_1 / k_2 \\ & x_{M+1}^* + x_{M+2}^* + \dots + x_{M+M}^* \leq S_2 / k_3 \\ & \vdots \end{aligned} \quad (18)$$

In order to simultaneously satisfy the constraints of the above equation $D + 1$, we select a common solution, which is:

$$k = \min(k_1, k_1, k_1 \dots k_{D+1}) \quad (19)$$

Substitute the “0-X” line to find the intersection point:

$$\mathbf{R} = [x_1, x_1, x_1, \dots, x_{M \cdot (D+1)}] \quad (20)$$

Finally, calculate the function values at the vertex and intersection. If the utility value at the vertex is infinitely close to the utility value at the intersection, then the point is the optimal solution. End the algorithm, otherwise, as shown in Fig. 5, generate a new vertex system. Select a new vertex by comparing the utility value of the function, and so on until the optimal solution is found.

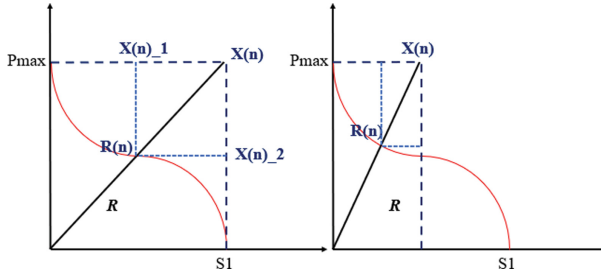


Fig. 5. .

5 Simulation Analysis

Through simulation, we have obtained the optimal solution under constraint conditions, that is, the system achieves maximum utility under the upper limit of power consumption and revenue.

In this model, we introduce the emergency factor r_{md} for resource requests in various dimensions. Terminals can dynamically adjust the emergency factor r_{md} based on their urgency of resource requirements and the benefits they can obtain. Based on the actual usage of CPU, RAM, and hard drives in daily life, we set the resource emergency factors

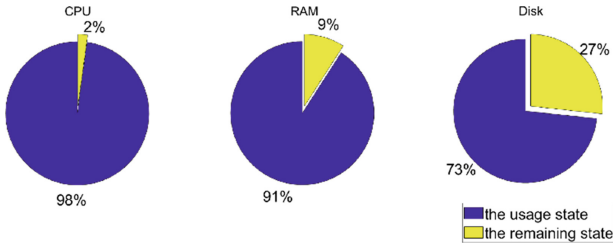


Fig. 6. Schematic diagram of resource usage in various dimensions

for the three dimensions to $r_{m1} = [0.5, 0.7]$, $r_{m2} = [0.4, 0.6]$, and $r_{m3} = [0.3, 0.5]$, respectively.

As shown in Fig. 6, it can be seen that in the case of maximum system utility, terminals have different resource requirements for different dimensions, which better reflects the actual demand situation in the environment.

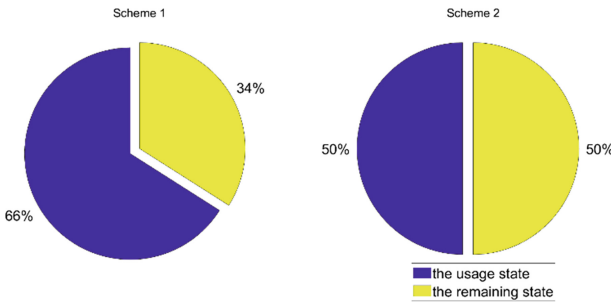


Fig. 7. Average resource utilization of different schemes

According to the resource utilization of each dimension shown in Fig. 7, we compared it with reference [4] and found that the average resource utilization rate of this model (Scheme 1) is significantly higher than that of reference [4] (Scheme 2).

In this model, we allocate transmission power by adjusting the resource request urgency factor ω_m of each terminal, so that ω_m is distributed in the following intervals: $\omega_m = [0.1, 0.2]$, $\omega_m = [0.3, 0.4]$, $\omega_m = [0.5, 0.6]$. As shown in Fig. 8, it can be seen that the transmission power consumption is closely related to the emergency factor ω_m of each terminal resource request, and the transmission power consumption allocated to each terminal by the emergency factor ω_m in different intervals is different. If the terminal has an urgent demand for resources, it can allocate more transmission power to provide services by increasing the terminal's emergency factor ω_m . The system then finds a balance point for resource requests of different dimensions under the constraints of power consumption and benefits obtained, in order to achieve the maximum utility of the system.

In this model, we introduce ω_m and r_{md} to dynamically adjust the resource requests of each terminal for different dimensions. With a fixed edge resource S_d and total power consumption P_{max} , we provide four schemes to compare system utility.

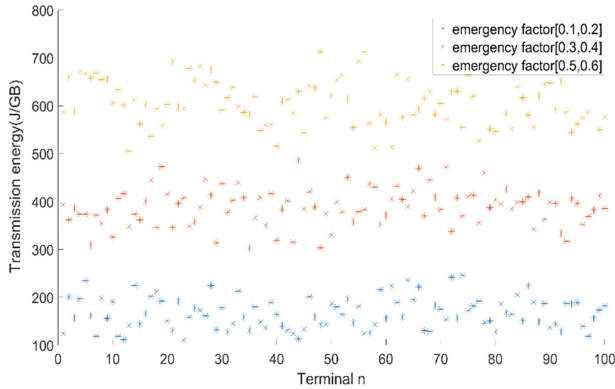


Fig. 8. Relationship between transmission energy consumption and emergency factor

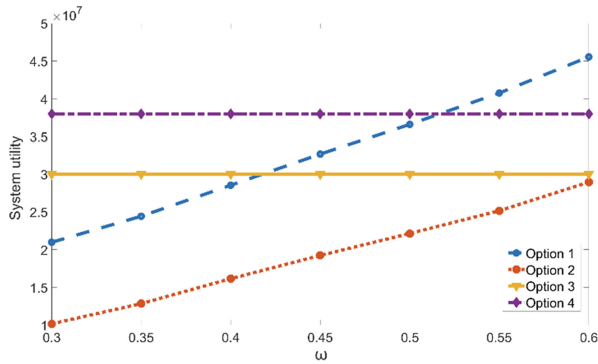


Fig. 9. System utility comparison

Option 1: Use this model architecture to dynamically allocate resource requests from terminals based on emergency factors;

Option 2: Use this model architecture to divide edge resources equally among terminals.

Option 3: Do not use this model, directly evaluate edge resources and sell them directly to end users.

Option 4: Evaluate the system utility based on the model scheme adopted in reference [2].

As shown in Fig. 9, in situations where the emergency factor is relatively small, terminals are not in a hurry about resource requirements, and the utility created by responding to resource requests is also relatively limited. This model does not have any advantages, and the system utility of Scheme 4 is also high. But as the urgent factor of resource demand continues to increase, responding to these resource requests and providing them with greater transmission power consumption will achieve greater utility, ultimately surpassing the system utility of other solutions, and the advantages of this model will also be reflected.

6 Conclusion

This paper uses an edge resource allocation model to allocate computing resources on 5G power edge servers, in order to improve the overall effectiveness of the system. We proposed a Polyblock based algorithm to solve optimization problems, and verified the effectiveness of our system model and algorithm through simulations. The comparison shows that the proposed model can indeed improve the overall utility of the new power system.


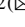

Acknowledgements. This work is supported by State Grid Shandong Electric Power Company Science and Technology Project: “Research on Smart Grid 5G Edge Business Orchestration and Secondary Authentication Technology” (No. 520614220002).

References

1. IMT-2020 (5G) Promotion Group 5G Vision and Requirements White Paper V1.0[R]. 2014. IMT-2020. 5G Vision and demand white paper V1.0[R] (2014)
2. Chen, Y., Li, Z., Yang, B., et al.: A Stackelberg game approach to multiple resources allocation and pricing in mobile edge computing [J]. *Futur. Gener. Comput. Syst.* **108**, 273–287 (2020)
3. Liao, Y., Shou, L., Yu, Q., et al.: Joint offloading decision and resource allocation for mobile edge computing enabled networks. *Comput. Commun.* **154**, 361–369 (2020)
4. Li, Z., Qin, J., Wen, W.: Delay-guaranteed task allocation in mobile edge computing with balanced resource utilization. In: *Proceedings of the 2020 4th International Conference on High Performance Compilation, Computing and Communications*, pp. 35–41 (2020)
5. Zhou, J., Zhang, X.: Fairness-aware task offloading and resource allocation in cooperative mobile edge computing. *IEEE Internet Things J.* (2021)
6. Li, J., Liang, W., Xu, W., et al.: Maximizing user service satisfaction for delay-sensitive IoT applications in edge computing. *IEEE Trans. Parallel Distrib. Syst.* **33**(5), 1199–1212 (2021)
7. Wang, H., Peng, Z., Pei, Y.: Offloading schemes in mobile edge computing with an assisted mechanism. *IEEE Access* **8**, 50721–50732 (2020)
8. Wang, J., Zhao, L., Liu, J., et al.: Smart resource allocation for mobile edge computing: a deep reinforcement learning approach. *IEEE Trans. Emerg. Top. Comput.* **9**(3), 1529–1541 (2019)
9. Xue, J., Wu, S., Wang, Z., et al.: Research on energy transmission strategy based on MEC in green communication. *Multimedia Tools Appl.*, 1–21 (2022)
10. Zhang, H., Liu, Z., Hasan, S., et al.: Joint optimization strategy of heterogeneous resources in multi-MEC-server vehicular network. *Wireless Netw.*, 1–14 (2022)
11. Xie, K., Wang, X., Xie, G., et al.: Distributed multi-dimensional pricing for efficient application offloading in mobile cloud computing. *IEEE Trans. Serv. Comput.*, 1–1 (2019)
12. Ai, Z.: *Research on Key Technologies for Trusted Edge Control in Smart Identity Networks*. Beijing Jiaotong University (2021)
13. Lan, Y.: *Research on Task Unloading and Resource Optimization of Edge Computing*. Beijing University of Posts and Telecommunications (2020)
14. Yang, L.: *Research on Resource Management Technology in Mobile Edge Networks*. Beijing University of Posts and Telecommunications (2021)



Medical Image Segmentation Based on Improved Hunter Prey Optimization

Shujing Li¹ , Qinghe Li¹, Mingyu Zhang¹, and Linguo Li^{1,2}  

¹ School of Computer and Information Engineering, Fuyang Normal University, Fuyang 236041, China
llg-1212@163.com

² School of Computer, Nanjing University of Posts and Telecommunications, Nanjing 210003, China

Abstract. Effective segmentation of medical images is the key to diagnosing diseases and evaluating treatment outcomes. At the same time, efficient medical image segmentation can not only reduce the time and cost of disease diagnosis, but also help doctors and patients implement diagnosis and treatment measures faster and better. However, due to the irregular shape of medical image targets, differences in imaging methods, and inherent differences in patient organ structures, medical images face significant challenges in segmentation accuracy and efficiency. This paper applies the Hunter Prey Optimization (HPO) to the field of medical image segmentation for the first time, and uses chaotic logistic mapping to improve and optimize population initialization. Taking fuzzy entropy as the objective function, combined with fuzzy median aggregation, a fuzzy improved Hunter Prey Optimization (FIHPO) is formed. Medical images are segmented under different threshold values by FIHPO, and compared with the original HPO, the improved Coyote Optimization Algorithm (FICOA) and the fuzzy Artificial Bee Colony and aggregation algorithm (FABCA). Finally, using Peak Signal to Noise Ratio (PSNR), Feature Similarity Index Measure (FSIM), and Structural Similarity Index Measure (SSIM) as evaluation criteria, a detailed data analysis was conducted on FIHPO, HPO, FICOA and FABCA. Through experimental analysis and comparison, it is found that the FIHPO can achieve better segmentation results in medical image thresholding.

Keywords: Hunter prey optimization · Medical image segmentation · Multi-level thresholding · Logistic chaotic mapping

1 Introduction

Image segmentation is a key task in computer vision and image preprocessing. Image segmentation technology is widely used in optical text recognition [1], medicine [2], agriculture [3], and other fields. Compared to other segmentation methods, thresholding segmentation is considered one of the most popular and promising segmentation methods due to its advantages of speed, simplicity, ease of implementation, and high computational efficiency [4]. Because the quality of segmented image is closely related to the

selection of thresholds, it is not easy to select a set of optimal thresholds in multi-level image thresholding. The introduction of swarm intelligence optimization algorithms in thresholding segmentation effectively solves this problem [5, 6].

Hao et al. [7] proposed ILSSA by combining iterative mapping (IM) and local escape operator (LEO) with the Salp Swarm algorithm (SSA). The ILSSA is applied to the segmentation of dermoscopic images of skin cancer. Abdel Baset et al. [8] combined Slime Mold algorithm (SMA) with Whale Optimization algorithm (WOA) and applied it to thresholding segmentation of chest X-ray images. However, during global exploration, this method is based on WOA. Vijh et al. [9] used a hybrid algorithm (H-LOA-CSO) of Lion Optimization Algorithm (LOA) and Cat Swarm Optimization (CSO) to combine the Otsu and Yager entropy as the fitness function. The H-LOA-CSO was successfully applied to thresholding of breast and lung histopathological images. Zhao et al. [10] proposed an improved Crow Search algorithm (CSA) based on variable neighborhood descent (VND) and information exchange mutation (IEM) strategies, called VMCSA, to apply it to multi-level image segmentation of COVID-19 X-ray images. Zhang et al. [11] proposed a Kernelized Fuzzy C-Means (KFCM) algorithm that is more robust than the original Fuzzy C-Means (FCM), that is, the Euclidean distance in FCM is replaced by the kernel induced distance. Then, spatial penalty is added to the objective function of KFCM. However, this method brings computational problems, modifying the objective function while changing most of the equations, and losing the continuity of the FCM. Lai [12] applied the Hierarchical Evolutionary algorithm (HEA) to image segmentation for the first time, using HEA to automatically classify into appropriate categories. In the segmentation experiments on head CT images, abdominal, brain, and knee joint MRI images, However, the author ignores the possibility that the algorithm may fall into local optimization. El Khatib et al. [13] proposed an improved Particle Swarm Optimization (PSO) algorithm, namely, elite exponential PSO (EEPSO). The authors applied it to medical image segmentation, and analyzed and compared the actual time complexity of it with the theoretical time complexity. Reboucas et al. [14] proposed a new Optimum Path Snakes (OPS), which has the characteristics of a new adaptive and nonparametric method for determining total energy. However, literature [15] indicates that this method cannot be well applied to ground glass opacity (GGO) nodules and para pleural nodules. Zhang et al. [16] proposed an improved Biogeography-Based Optimization (WRBBO) by using worst position learning and random scaled differential mutation. The feasibility of the WRBBO was verified by segmenting the CT images of liver tumors. Ali et al. [17] used a hybrid Differential Evolution (DE) algorithm to fit Gaussian curves for segmentation of MRI medical images. Liu et al. [18] proposed an improved DE based on the foraging behavior of slime molds, which realized the segmentation of breast cancer images.

Since Naruei et al. [19] proposed the HPO in 2022, Ma et al. [20] has been applied to bearing fault diagnosis problems. Wang et al. [21] used HPO for short-term wind power generation forecasting. Xiang et al. used the [22] HPO for structural damage identification. However, up to now, there is no application of HPO in the field of medical image thresholding.

This paper mainly studies the application of thresholding segmentation in the field of medical images. However, medical images are different from natural images. Due to

the irregular shape of the target in medical image segmentation, differences in imaging methods, and inherent differences in the structure of patient organs, medical images generally have uneven gray levels, blurred boundaries, and artifacts [23]. In order to improve segmentation accuracy, Li et al. [24, 25] combined the standard Kapur with the trapezoidal membership function to form a fuzzy Kapur. At the same time, in [26], they verified the feasibility of thresholding medical images using a swarm intelligence optimization algorithm based on fuzzy median aggregation and fuzzy Kapur. To sum up, this paper proposes an improved HPO (FIHPO) based on fuzzy median aggregation, fuzzy Kapur and the chaotic logic initialization.

The rest of this paper is organized as follows, Sect. 2 describes the principle of the HPO and the proposed improved HPO using chaotic Logistic. Section 3 analyzes and discusses the experimental results. We summarize the work of this article and describes the future research directions in Sect. 4.

2 The Principle of HPO Algorithm

2.1 The Initialization of HPO Population

The positions of population are randomly generated in the search space, as shown in Eq. (1).

$$x_i = rand(1, d) * (ub - lb) + lb \quad (1)$$

where x_i represents the location of the predator or prey.

Population initialization has a significant impact on the convergence speed and final solution of swarm intelligence optimization algorithms. However, using Eq. (1) for population initialization can easily lead to insufficient global search ability and easy to fall into local optimal solutions. Literature [7] shows that using chaotic sequences can make the population uniformly distributed in space as much as possible, which helps to enhance the global exploration ability of the algorithm and reduce the possibility of falling into local optimization. Therefore, this paper introduces a chaotic logistic map. The population initialization of the FIHPO is performed using chaotic logistic mapping, as in Eq. (2):

$$y(i + 1) = a * y(i) * (1 - y(i)) \quad (2)$$

Research shows that when $3.5699456 < a \leq 4$, the Logistic map starts to enter a chaotic state, obtaining good random distribution characteristics. When $a = 4$, the Logistic map is completely in a chaotic state, and the map has excellent random distribution characteristics. To obtain the optimal solution, this experiment takes $a = 4$. Combining with the HPO population initialization Eq. (1), Finally, the formula for initializing the population of the HPO using chaotic logic can be obtained as Eq. (3).

$$x_i = y(i + 1) * (ub - lb) + lb \quad (3)$$

2.2 The Location of Predators

The search mechanism for swarm intelligence optimization algorithms usually includes two steps: exploration and development. According to the mechanism, the predator position is Eq. (4):

$$x_{i,j}(t + 1) = x_{i,j}(t) + 0.5[(2CZP_{pos(j)} - x_{i,j}(t)) + (2(1 - C)Z\mu_{(j)} - x_{i,j}(t))] \quad (4)$$

where $x_{i,j}(t)$ is the current position of the predator, and Z is the adjustment parameter calculated by Eqs. (5) and (6):

$$P = \vec{R}_1 < C; IDX = (P == 0) \quad (5)$$

$$Z = R_2 \otimes IDX + \vec{R}_3 \otimes (\sim IDX) \quad (6)$$

Let C be a balance parameter used to balance the exploration and development mentioned above, expressed as Eq. (7):

$$C = 1 - it \left(\frac{0.98}{MaxIt} \right) \quad (7)$$

In order to balance exploration and development, the C value will decrease from 1 to 0.02 as the number of iterations increases.

2.3 The Location of Prey

According to HPO, if a prey is far from the group location, the predator will attack it. The group position is the average of all positions. The average value is calculated using the μ express, as in Eq. (8):

$$\mu = \frac{1}{n} \sum_{i=1}^n \vec{x}_i \quad (8)$$

Then use the Euclidean distance calculation formula to calculate the distance between the position of each prey and the average position, as in Eq. (9):

$$D_{euc(i)} = \left(\sum_{j=1}^d (x_{i,j} - \mu_j)^2 \right)^{\frac{1}{2}} \quad (9)$$

In order not to allow the HPO to converge too late, according to the predatory scenario in the biological world, the algorithm introduces a descending mechanism, as in Eq. (10):

$$K = round(C \times N) \quad (10)$$

The resulting prey position formula is Eq. (11), \vec{P}_{pos} is the location of the prey.

$$\vec{P}_{pos} = \vec{x}|i \text{ is sorted } D_{euc}(K) \quad (11)$$

2.4 The Location Update of Prey

According to the law of survival, when a prey is attacked, the prey tries to escape to a safe place to avoid attack. Here, it is assumed that the optimal global location is the optimal survival location for the prey. This position will improve the survival chances of the prey, and the predator has a probability of moving towards the position of other prey. Update the prey position using Eq. (12).

$$x_{i,j}(t + 1) = T_{pos(j)} + CZ\cos(2\pi R_4) \times (T_{pos} - x_{i,j}(t)) \tag{12}$$

T_{pos} is the global optimal position. To sum up, we can summarize the formula for updating the position of predators and prey into Eq. (13).

$$x_i t + 1 = \begin{cases} x_i(t) + 0.5[(2CZP_{pos} - x_i(t)) + (2(1 - C)Z\mu - x_i(t))] & R_5 < \beta \tag{13a} \\ T_{pos} + CZ \cos(2\pi R_4) \times (T_{pos} - x_i(t)) & else \tag{13b} \end{cases} \tag{13}$$

When R_5 less than β , x_i is the position of the predator, and the formula for updating the position of the predator is Eq. (13a), otherwise x_i is the position of the prey, and the formula for updating the position of the prey is Eq. (13b).

3 The Discussion of Medical Image Segmentation

3.1 Selection of Experimental Parameters and Aggregation Methods

This paper selected 5 medical images (Brain, Lesion, Colon, Tumor tissue and Hand X-ray) to test the FIHPO, and compared it with HPO, FICOA, and FABCA. The threshold number (nTH) was set to 2, 3, 4, and 5. The parameter settings are shown in Table 1. This experiment was conducted under the experimental environment of Windows 10 system, Intel Core i5 processor, running memory of 16 GB, and programming software of MATLAB 2019a.

Table 1. Parameter selection of LWHO

Parameter	nPOP	nTH	No. of iterations
Value	30	2, 3, 4, 5	1000

In order to obtain better segmentation results, a comparative experiment was conducted using t Hand X-ray in Figs. 1 and 2. According to the three fuzzy aggregation methods proposed in literature [24, 25], the experiment result is shown in Table 2.

Figures 1 and 2 show the segmentation results based on HPO and FIHPO. Similarly, in order to more intuitively demonstrate the performance differences between FIHPO and comparable algorithms in medical image segmentation, the experimental FSIM, and SSIM values are given in Sect. 3.2, and the experimental data are analyzed in detail.

From Table 2, it can be concluded that using fuzzy median aggregation can achieve higher PSNR values and better segmentation accuracy at the same threshold level.

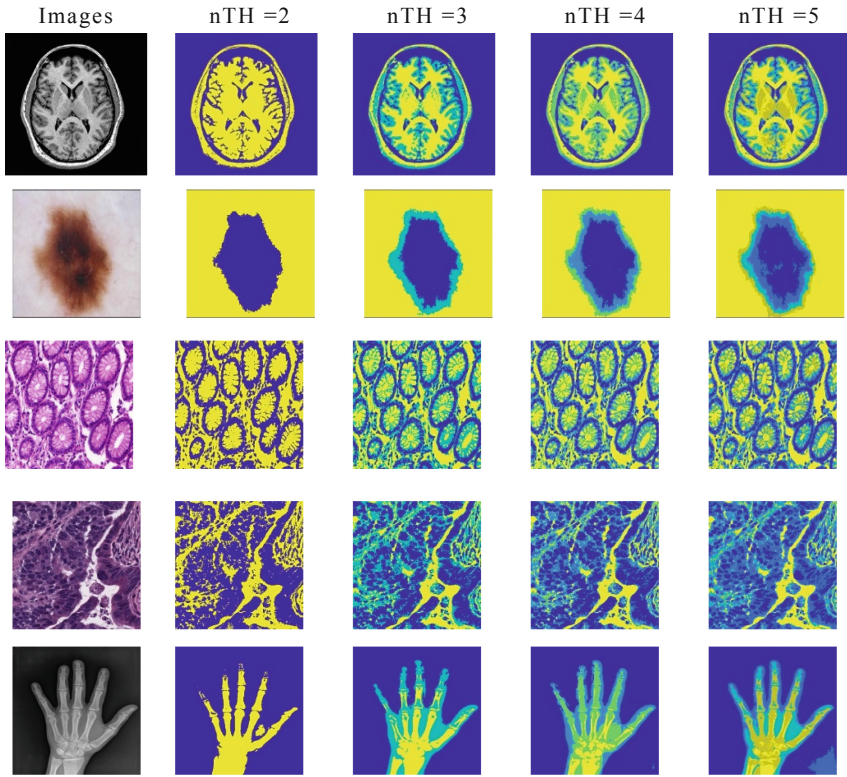


Fig. 1. The segmentation results of HPO

3.2 Comparison of Different Similar Algorithms

By comparing the results in Table 3, FIHPO obtained higher FSIM values in most test cases, while FABCA, which ranked second, HPO ranks third, FICOA ranks fourth. As can be seen from Table 3, FIHPO has the highest FSIM at all threshold levels for Lesion and Colon. For both Brain and Tumor issue images, FIHPO obtained optimal values with a threshold number of 2 and 4. In summary, FIHPO can obtain higher PSNR at most threshold levels for all test images.

Table 4 shows the SSIM values, it can be concluded that FMHPO achieved the optimal SSIM value in most test cases, and achieved significant segmentation results in all test images except for the image Brain. In addition, HPO and FABCA achieved the optimal SSIM values in 6 test cases. FICOA achieved the optimal SSIM value in only one test cases. Overall, FMHPO performs better in SSIM compared to the compared algorithms.

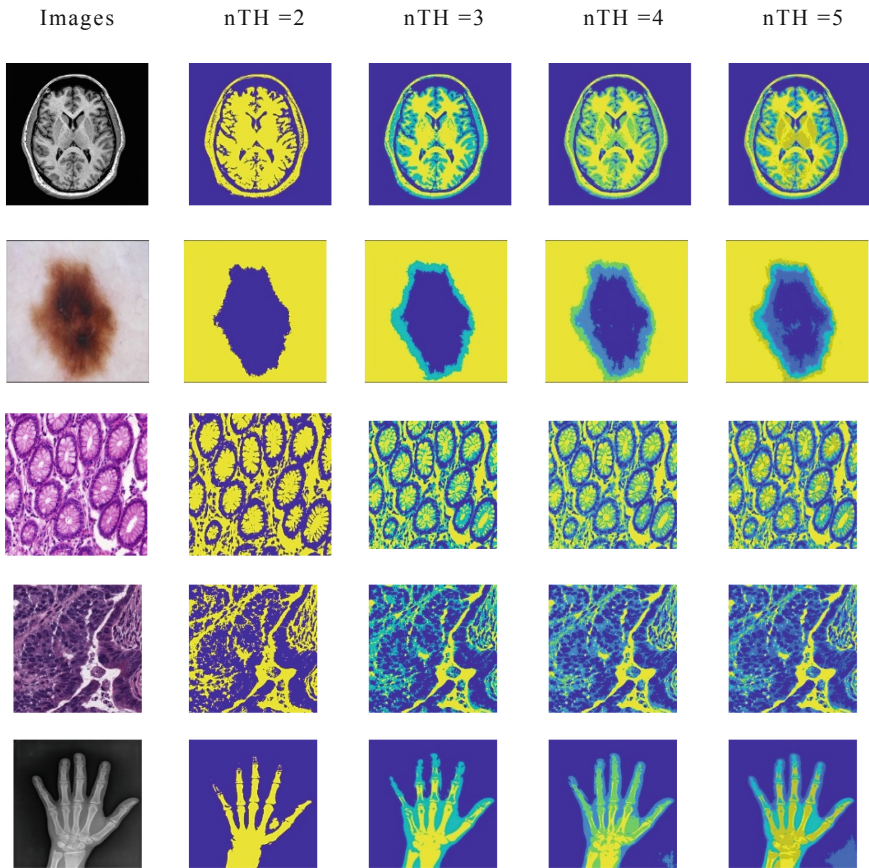


Fig. 2. The segmentation results of FIHPO

Table 2. Comparison of segmentation quality with different thresholds and aggregation

nTH	2	3	4	5
Median (M)	19.5649	23.7701	25.2147	26.4550
Average (A)	19.5365	23.6643	25.0808	25.4159
Iterative (I)	19.5365	23.7177	25.1944	26.0109

The bold data represents the optimal value for the current row, also this to compare the advantages and disadvantages of the results more prominently

Table 3. Comparison according to the FSIM

Images	nTH	HPO	FICOA	FABCA	FIHPO
Brain	2	0.6299	0.6281	0.6214	0.6286
	3	0.7788	0.7794	0.7795	0.7801
	4	0.8378	0.8245	0.8506	0.8359
	5	0.8850	0.8825	0.8754	0.8850
Lesion	2	0.7396	0.7422	0.7401	0.7396
	3	0.7561	0.7563	0.7576	0.7578
	4	0.7787	0.7878	0.7893	0.7912
	5	0.8133	0.8071	0.8147	0.8151
Colon	2	0.5772	0.5834	0.5772	0.5772
	3	0.7349	0.7509	0.7361	0.7275
	4	0.7396	0.8213	0.8097	0.8147
	5	0.8278	0.7989	0.8434	0.8485
Tumor tissue	2	0.6673	0.6673	0.6692	0.6673
	3	0.8103	0.8164	0.8095	0.8068
	4	0.8494	0.8700	0.8714	0.8634
	5	0.9068	0.8916	0.8968	0.8921
Hand X-ray	2	0.6787	0.6741	0.6772	0.6787
	3	0.7230	0.7166	0.7158	0.7247
	4	0.7570	0.7448	0.7506	0.7707
	5	0.7963	0.7700	0.7726	0.7963

The bold data represents the optimal value for the current row, also this to compare the advantages and disadvantages of the results more prominently

Table 4. Comparison according to the SSIM

Images	nTh	HPO	FICOA	FABCA	FIHPO
Brain	2	0.2990	0.2898	0.2675	0.2980
	3	0.5913	0.5935	0.5943	0.5919
	4	0.6368	0.6326	0.6399	0.6362
	5	0.7290	0.6670	0.7354	0.7288
Lesion	2	0.8825	0.8775	0.8824	0.8823
	3	0.8833	0.8804	0.8826	0.8825
	4	0.8839	0.8833	0.8832	0.8844
	5	0.8850	0.8838	0.8848	0.8854
Colony	2	0.4365	0.4244	0.4365	0.4365
	3	0.5922	0.5901	0.5899	0.5922
	4	0.6612	0.6336	0.6658	0.6648
	5	0.6952	0.6758	0.6977	0.7019
Tumor tissue	2	0.5282	0.5282	0.5290	0.5282
	3	0.6093	0.6040	0.6083	0.6098
	4	0.6617	0.6473	0.6445	0.6635
	5	0.6971	0.6798	0.6883	0.7015
Hand X-ray	2	0.6945	0.7024	0.6964	0.6945
	3	0.7636	0.7537	0.7513	0.7654
	4	0.7959	0.7814	0.7859	0.7980
	5	0.8209	0.7970	0.8083	0.8209

The bold data represents the optimal value for the current row, also this to compare the advantages and disadvantages of the results more prominently

4 Conclusion

In order to obtain a more efficient optimization algorithm, an improved HPO based on fuzzy median aggregation and fuzzy Kapur, using chaotic logistic mapping, was proposed to overcome the shortcomings of HPO, such as insufficient global exploration ability and easy to fall into local optimization. Compared to HPO, FIHPO can achieve higher optimization accuracy. Compared with FICOA, and FABCA, experimental results show that FIHPO has better segmentation effects in medical image segmentation. The following research can combine the excellent strategies of other optimization algorithms with the HPO, and can also apply the algorithm to other fields to solve more practical problems and improve the value of the FIHPO.

Funding. This paper is supported by Natural Science Foundation of Anhui under Grant KJ2020A1215, KJ2021A1251, 2022AH051325 and 2023AH052856, the Excellent Youth Talent

Support Foundation of Anhui under Grant gxyqZD2021142 and the Quality Engineering Project of Anhui under Grant 2021jyxm1117, 2021kcszsfkc307, 2022xsxx158 and 2022jcbs043.




References

1. Srivastava, S., Priyadarshini, J., Gopal, S., et al.: Optical character recognition on bank cheques using 2D convolution neural network. In: Applications of Artificial Intelligence Techniques in Engineering: SIGMA 2018, pp. 589–596. Springer, Singapore (2019)
2. Elaziz, M., Ewees, A.A., Yousri, D., et al.: An improved marine predators algorithm with fuzzy entro-py for multi-level thresholding: real world example of COVID-19 CT image segmentation. *IEEE Access* **8**, 125306–125330 (2020)
3. Singh, V., Misra, A.K.: Detection of plant leaf diseases using image segmentation and soft computing techniques. *Inf. Process. Agric.* **4**(1), 41–49 (2017)
4. Masood, S., Sharif, M., Masood, A., et al.: A survey on medical image segmentation. *Curr. Med. Imaging* **11**(1), 3–14 (2015)
5. Houssein, E.H., Helmy, B.E.D., Elngar, A.A., et al.: An improved tunicate swarm algorithm for global optimization and image segmentation. *IEEE Access* **9**, 56066–56092 (2021)
6. Oliva, D., Elaziz, M., Hinojosa, S., et al.: Multilevel thresholding for image segmentation based on metaheuristic algorithms. In: Metaheuristic Algorithms for Image Segmentation: Theory and Applications, pp. 59–69 (2019)
7. Hao, S., Huang, C., Heidari, A.A., et al.: Salp swarm algorithm with iterative mapping and local escaping for multi-level threshold image segmentation: a skin cancer dermoscopic case study. *J. Comput. Des. Eng.* **10**(2), 655–693 (2023)
8. Abdel-Basset, M., Chang, V., Mohamed, R.: HSMA_WOA: a hybrid novel Slime mould algorithm with whale optimization algorithm for tackling the image segmentation problem of chest X-ray images. *Appl. Soft Comput.* **95**, 106642 (2020)
9. Vijh, S., Saraswat, M., Kumar, S.: Automatic multilevel image thresholding segmentation using hybrid bio-inspired algorithm and artificial neural network for histopathology images. *Multimed. Tools Appl.* **82**(4), 4979–5010 (2023)
10. Zhao, S., Wang, P., Heidari, A.A., et al.: Boosted crow search algorithm for handling multi-threshold image problems with application to X-ray images of COVID-19. *Expert Syst. Appl.* **213**, 119095 (2023)
11. Zhang, D., Chen, S.: A novel kernelized fuzzy c-means algorithm with application in medical image segmentation. *Artif. Intell. Med.* **32**(1), 37–50 (2004)
12. Lai, C., Chang, C.: A hierarchical evolutionary algorithm for automatic medical image segmentation. *Expert Syst. Appl.* **36**(1), 248–259 (2009)
13. El-Khatib, S., Skobtsov, Y., Rodzin, S.: Improved particle swarm medical image segmentation algorithm for decision making. In: Intelligent Distributed Computing XIII, pp.437–442. Springer International Publishing (2020)
14. Reboucas, P.P., Silva A.C., Almeida, J.S, et al.: A new effective and powerful medical image segmentation algorithm based on optimum path snakes. *Appl. Soft Comput.* **76**, 649–670 (2019)
15. Cao, H., Liu, H., Song, E., et al.: Dual-branch residual network for lung nodule segmentation. *Appl. Soft Comput.* **86**, 105934 (2020)
16. Zhang, X., Wang, D., Chen, H.: Improved biogeography-based optimization algorithm and its application to clustering optimization and medical image segmentation. *IEEE Access* **7**, 28810–28825 (2019)
17. Ali, M., Siarry, P., Pant, M.: Multi-level image thresholding based on hybrid differential evolution algorithm. Application on medical images. In: Metaheuristics for Medicine and Biology, pp. 23–36 (2017)

18. Liu, L., Zhao, D., Yu, F., et al.: Performance optimization of differential evolution with slime mould algorithm for multilevel breast cancer image segmentation. *Comput. Biol. Med.* **138**, 104910 (2021)
19. Naruei, I., Keynia, F., Sabbagh, M.A.: Hunter–prey optimization: algorithm and applications. *Soft. Comput.* **26**(3), 1279–1314 (2022)
20. Ma, J., Liu, F.: Bearing fault diagnosis with variable speed based on fractional hierarchical range entropy and hunter-prey optimization algorithm-optimized random forest. *Machines* **10**(9), 763 (2022)
21. Wang, X., Li, J., Shao, L., et al.: Short-term wind power prediction by an extreme learning machine based on an improved hunter–prey optimization algorithm. *Sustainability* **15**(2), 991 (2023)
22. Xiang, C., Gu, J., Luo, J., et al.: Structural damage identification based on convolutional neural networks and improved hunter–prey optimization algorithm. *Buildings* **12**(9), 1324 (2022)
23. Yang, Y., Tian, D., Wu, B.: A fast and reliable noise-resistant medical image segmentation and bias field correction model. *Magn. Reson. Imaging* **54**, 15–31 (2018)
24. Li, L., Sun, L., Guo, J., et al.: Fuzzy multilevel image thresholding based on modified quick artificial bee colony algorithm and local information aggregation. *Math. Probl. Eng.* **2016**, 1–15 (2016)
25. Li, L., Sun, L., Kang, W., et al.: Fuzzy multilevel image thresholding based on modified discrete grey wolf optimizer and local information aggregation. *IEEE Access* **4**, 6438–6450 (2016)
26. Li, L., Sun, L., Xue, Y., et al.: Fuzzy multilevel image thresholding based on improved coyote optimization algorithm. *IEEE Access* **9**, 33595–33607 (2021)



Application of Improved Wild Horse Optimizer Based on Chaos Initialization in Medical Image Segmentation

Linguo Li^{1,2} , Mingyu Zhang¹, Qinghe Li¹, and Shujing Li¹  

¹ School of Computer and Information Engineering, Fuyang Normal University, Fuyang 236041, China

lsjing1981@163.com

² School of Computer, Nanjing University of Posts and Telecommunications, Nanjing 210003, China

Abstract. In the field of auxiliary medicine, medical image segmentation is an effective diagnostic measure, but there is still room for improvement in the accuracy and efficiency of medical image segmentation. Therefore, this paper analyzes a new swarm intelligence optimization algorithm—Wild Horse optimization algorithm (WHO), which has been improved and applied in medical image segmentation. The WHO is mainly optimized by simulating the life behavior of the wild horse population, and it has the characteristics of strong optimization ability and fast convergence speed, but the WHO is easy to fall into local optimization in medical image segmentation. Therefore, this paper uses the initialization method of Logistic chaotic map to replace the random initialization scheme in the original WHO, and compares the image segmentation results with Fuzzy Wild Horse optimization algorithm (FWHO), Fuzzy Improved Fast Artificial Bee Colony and its Aggregation Algorithm (FMQABCA) and Coyote Algorithm (COA). The results show that the improved WHO has better segmentation effect and efficiency.

Keywords: Logistic chaotic map · Wild horse optimization · Image segmentation · Kapur entropy

1 Introduction

Image segmentation is an important component of image processing, and plays a crucial role in medical image assisted therapy. Medical segmentation uses data features collected from medical images to separate human tissues or organs from the original medical images, thereby achieving the role of adjuvant therapy [1–3]. In recent years, various swarm intelligence optimization algorithms have been applied to thresholding medical images, and their corresponding thresholding segmentation methods have also developed from Bi-level thresholding to multi-level thresholding [4]. However, whether it is Bi-level thresholding or multi-level thresholding, their calculation methods can be divided into two categories: parametric methods and nonparametric methods. Due to the need to estimate a large number of statistical parameters, parametric methods not

only require a large amount of computation, but also have a strong dependence on initial parameters for segmentation, so its practical application is becoming less. On the contrary, nonparametric methods have gained more and more recognition [5].

Non parametric methods select thresholds by calculating certain specific criteria, such as information entropy (Kapur), maximum inter-class variance (Otsu), and so on. Ji [6] and others implemented the Moth flame optimization (MFO) based on Kapur entropy, and select the target value of Kapur to maximize. They used evaluation indicators to compare the segmentation effect and optimization performance with other algorithms. The experimental results show that the MFO has better stability and segmentation effect. Xing et al. [7] used Kapur entropy as an objective function to verify the higher segmentation accuracy and operational efficiency of the EPO (Imperial Penguin Optimization), and it has better time efficiency. He and Huang [8] tested the segmentation performance of the KH (Krill Herd) using three objective functions, Kapur entropy, Otsu method, and Tsallis entropy, respectively. The experimental results show that Kapur entropy has better segmentation accuracy and robustness at multi-level thresholding.

Based on the analysis of commonly used thresholding segmentation methods in the field of segmentation in recent years, it can be seen that Otsu and Kapur are currently two popular methods. However, in order to improve computational efficiency, it is still necessary to choose the algorithm that is more suitable for image segmentation. Yang and Wu [9] validated the NRQPSO (Non revisioning Quantum-behaved Particle Swarm Optimization), using Kapur as an objective function, to test the application of multiple thresholding segmentation to grayscale images. The experimental results show that the NRQPSO has significant advantages in segmentation efficiency and stability. Shen [10] combined GA (Genetic Algorithm) with Otsu to form IGA, and conducted experimental comparisons on segmentation accuracy and efficiency. The experimental results show that IGA has better segmentation accuracy and operational efficiency. Abdul [11] and others tested the efficiency of Grey Wolf Optimizer (GWO) in multi-level thresholding segmentation using Kapur entropy and Otsu as objective functions, respectively. Compared with BFO (Background Foraging Optimization) and PSO (Particle Swarm Optimization), the results show that this method is more excellent in segmentation quality and efficiency. Compared with BFO and PSO, it is also more stable.

Although current multi-level thresholding methods have greatly improved the segmentation efficiency and accuracy, most algorithms still have problems such as edge blurring and some isolated points. Based on the above shortcomings, the literature [12, 13] proposed the application of fuzzy objective function and fuzzy aggregation method in image thresholding, and achieved excellent segmentation accuracy and segmentation effect. The WHO is a new meta heuristic algorithm proposed by Iraj Naruei and Farshid Keynia in 2021. Li et al. [14] improved the WHO to form HMSWHO (Hybrid Multi Strategy Improved Wild Horse Optimizer) and applied it in the mechanical field, which improved the operational efficiency of the WHO. Marzouk et al. [15] applied the WHO to the field of multi-agent path finding in the Internet of Things system, achieving a better model framework. However, up to now, no application of WHO has been seen in the field of image segmentation. Therefore, this paper will use WHO to explore the field of image segmentation, and make some optimization improvements to it in the hope of achieving better segmentation results.

The rest of this paper is organized as follows, in the second part, we introduce the principle of the improved WHO. The selection of the objective function and parameter setting is discussed in third part. The fourth part compares the proposed algorithm with other most advanced algorithms in image thresholding and verifies the efficiency of this algorithm. Finally, the fifth part concludes this work.

2 The Improving of Wild Horse Optimizer

2.1 The Framework of WHO

The behavior of the wild horse consists of the following five main steps: 1) Create an initial population randomly, form a herd of horses, and select a leader. 2) The mating of grazing and wild horses. 3) Leaders (stallions) lead the population to find the best habitat. 4) leader competition and selection of the best leader. 5) Save the optimal solution.

2.1.1 Population Initialization

In the original algorithm, two types of horse herds were initially created, the leader (stallion) herd and the horse herd, and then different groups were formed based on the leader. Assuming that N is the total number of members of wild horses, the population size is $G = N * PS$, which is considered as a control parameter in the WHO. During the WHO iteration process, the optimal combination is performed based on the fitness (the best objective function) of the team members, and the best leader is selected. Then determine the grouping based on G (stallion), and the remaining members ($g = N - G$) are evenly distributed within the group. The specific formula is:

$$g_j = lb_j + rand_j(ub_j - lb_j) \quad (1)$$

$$G_j = lb_j + rand_j(ub_j - lb_j) \quad (2)$$

where, G_j and g_j represent the position of the population (leader) and the number of ordinary wild horses.

2.1.2 Grazing Behavior

The grazing behavior is simulated using Eq. (3), in which each team member moves within different radii and searches for leaders, namely:

$$X_{i,G}^j = 2 * Z * \cos(2\pi * R * Z) * (Stallion^j - X_{i,G}^j) + Stallion^j \quad (3)$$

where, $X_{i,G}^j$ is the current position of the group member, and $Stallion^j$ is the position of the stallion (leader). Z is an adaptive value calculated by Eq. (4), and its calculation method is as follows:

$$Z = R_2 \odot IDX + \vec{R}_3 \odot (\sim IDX) \quad (4)$$

$$IDX = (P == 0), P = \vec{R}_1 < TDR \quad (5)$$

where P is a vector composed of 0 or 1, R_1 , R_2 and R_3 are uniformly distributed random vectors within the range of [0, 1]. TDR's calculation formula is:

$$TDR = 1 - iter * \left(\frac{1}{maxiter} \right) \quad (6)$$

2.1.3 Mating Behavior of Wild Horses

One of the unique behaviors of horses is to separate the foal from the group and perform mating behavior. The foals leave the corresponding group before entering puberty, the male foals join the single herd group, and the female foals join another family group and seek partners after entering puberty. This behavior not only avoids inbreeding of the population, but also improves the reproductive quality of the population. The formula for the mating behavior of wild horses is as follows:

$$X_{G,K}^P = Crossover(X_{G,i}^q, X_{G,j}^z), \quad i \neq j \neq k, \quad p = q = end \quad (7)$$

$$Crossover = Mean \quad (8)$$

where, $X_{G,K}^P$ represents the individual position of group d in population k where individuals p leaving the group and enter population k again, $X_{G,i}^q$ indicates the individual position where the individual p in the population ki leaves the population and enters the population q again, $X_{G,j}^z$ indicates the individual position in population j where the individual z leaves the population and enters population q again.

2.1.4 Team Leader

In nature, wild horse leaders lead populations to explore suitable habitats. Assuming that the suitable habitat is a puddle, the population needs to move towards this puddle. Equation (9) calculates the next position of the leader in each population relative to the habitat, and the formula is:

$$Stallion_{G_i} = \begin{cases} 2 * Z * \cos(2\pi * R * Z) * (WH - Stallion_{G_i}) + WH, & \text{if } R_3 > 0.5 \\ 2 * Z * \cos(2\pi * R * Z) * (WH - Stallion_{G_i}) - WH, & \text{else} \end{cases} \quad (9)$$

In the formula, WH is the location of the habitat (i.e., the current optimal individual location), and the definitions of R and Z are the same as those described earlier. During the population initialization phase, it was introduced that if one of the team members has a fitness value that is better than the leader, their identities are exchanged, as shown in Eq. (10):

$$Stallion_{G_i} = \begin{cases} X_{G,i}, & \text{if } cost(X_{G,i}) < cost(Stallion_{G_i}) \\ Stallion_{G_i}, & \text{else} \end{cases} \quad (10)$$

Here, cost is the fitness function. $X_{G,i}$ is the position in the current group member, $Stallion_{G_i}$ is the leader's position.

2.2 Logistic Chaotic Mapping and Improved WHO

By introducing the initial value of the chaotic state into the optimization variables, and using the ergodicity of chaotic motion to make the initial value of the algorithm more scattered, the algorithm has the ability to avoid falling into local optimization [16]. Therefore, chaos initialization can be used to optimize the initialization of the Mustang algorithm to improve the convergence quality of the algorithm. In this paper, the Logistic chaotic map in the chaotic algorithm is used, and its formula is:

$$Z_i = x_{i+1} = \mu(1 - x_i) \quad (11)$$

where, x_i is the i th chaotic variable (x_i belongs to an interval $(0, 1)$), μ is the chaos control parameter, and its value directly affects the chaotic degree of the Logistic mapping equation, the higher μ (belongs to an interval $(0, 4)$), the higher degree of chaos, the better discrete type of the variable. In this paper, $\mu = 4$ as the control parameter.

The chaotic number Z_j obtained by Eq. (11) to replace the random number $rand_j$ in the original Eq. (1) and (2) in this paper. Thereby improving the optimization accuracy of the WHO and forming an improved WHO (LWHO). The improved initialization formula is:

$$g_j = lb_j + Z_j(ub_j - lb_j) \quad (12)$$

$$G_j = lb_j + Z_j(ub_j - lb_j) \quad (13)$$

3 Selection of the Objective Function and Parameter Setting

In order to apply LWHO to medical image segmentation, this paper uses fuzzy Kapur to get the optimal thresholds by maximizing the fitness function.

3.1 Selection the Objective Function of LWHO

As can be seen from the previous introduction, the most widely used objective functions for image thresholding are Kapur and Otsu. And the Kapur has the advantages of easy implementation, better segmentation effect, and can be applied to multi-level image thresholding. In this paper, the Kapur is selected, and membership functions are introduced to blur the division of pixels in different regions, transforming Kapur into fuzzy Kapur finally [17].

3.2 Parameter Selection of LWHO

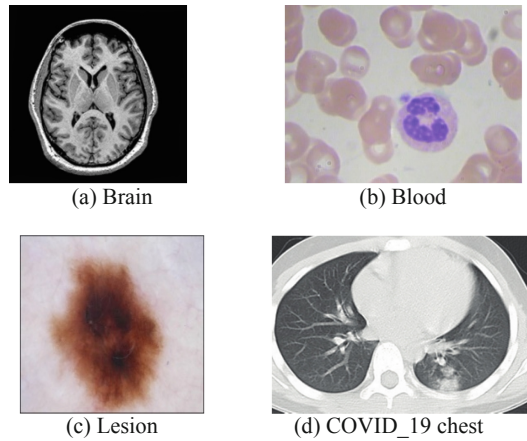
In the original WHO, the authors have discussed the performance of the algorithm under different parameters and provided relatively excellent algorithm parameters, such as setting the total number of wild horse members (N) to 30, and setting the percentage of stallions (G) in the total number of wild horses (PS) to 20%. However, on the premise of combining the application background of image segmentation, through experimental

Table 1. Parameter selection of LWHO

Parameters	N	PS	MT	Max_iter
Value	20	0.2	2, 3, 4, 5	1000

comparison, it is found that setting the parameters to the data in Table 1 can obtain better experimental results in image thresholding, where MT is the preset threshold number. Figure 1 shows the medical images used for testing in this paper.

Table 2 shows the PSNR and FSIM values under the condition that the objective function is fuzzy Kapur when the MT of COVID-19 chest image in Fig. 1 is 5 and the number of wild horses is 20 and 30 respectively.

**Fig. 1.** Original medical image**Table 2.** Result with different number of wild horses and iteration number

Parameters	Wild horses' number	150	500	1000	2000
PSNR	20	25.1429	25.1874	25.2179	25.1641
	30	25.1533	25.1813	25.1624	25.0981
FSIM	20	0.6889	0.7025	0.6953	0.6961
	30	0.7005	0.6972	0.6899	0.6835

The bold data represents the optimal value for the current row, also this to compare the advantages and disadvantages of the results more prominently

From the parameter comparison in Table 2, It can be seen that PSNR and FSIM with a number of 20 are superior to those with a number of 30 wild horses, only slightly lower when the number of iterations is 150. When the number of iterations is 500 and 1000, both FSIM and PSNR obtain relatively optimal data.

4 Analysis and Discussion of Medical Image Segmentation Results

4.1 The Visual Results of Medical Image Segmentation

This paper selects four different medical images to test the LWHO as show in Fig. 1. It includes brain image, blood cell image, infectious skin image and COVID-19 chest infection image. With fuzzy Kapur as the objective function, the test data were compared with FWHO, FMQABCA, and COA. In this paper, the maximum number of iterations was set to 1000, with the total number of wild horses $N = 20$, and the percentage of stallions in the total number of wild horses $PS = 0.2$.

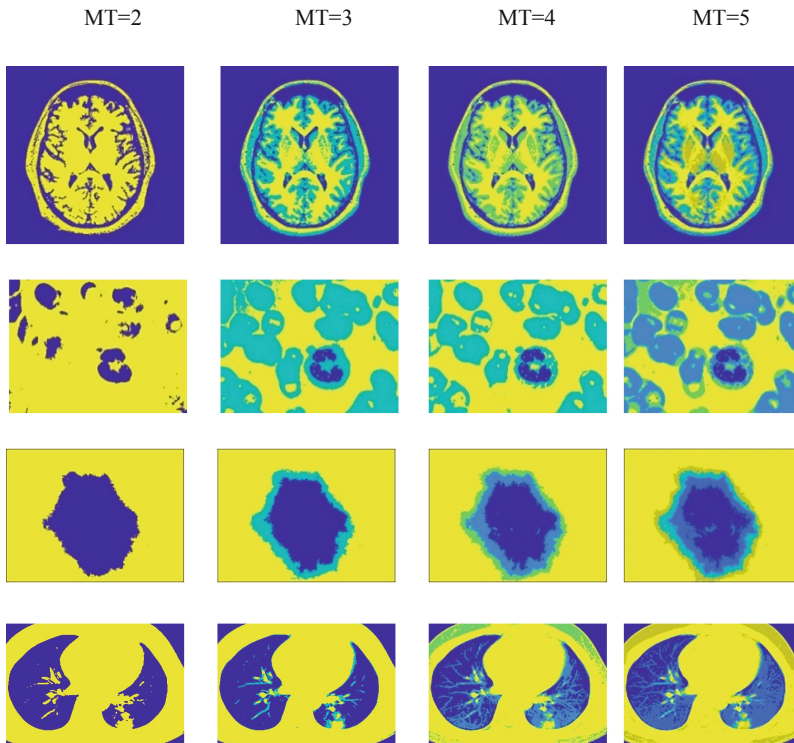


Fig. 2. Image segmentation results based on LWHO

Figure 2 is the visual result of the LWHO for multi-level thresholding of the original image in Fig. 1. From these figures, it can be seen that as the number of thresholds increases, the segmentation results of the image become increasingly refined.

4.2 Comparison of Different Similar Algorithm

The advantages and disadvantages of the LWHO cannot be accurately explained only from the visual results shown in Fig. 2. Therefore, the experimental data of LWHO in medical image segmentation are listed in Table 3.

As shown in Table 3, as the number of thresholds increases, the values of PSNR and FSIM gradually increase, indicating that the quality of image segmentation is continuously improving. However, only experimental data of LWHO in medical image segmentation are listed in Table 3. In order to fully illustrate the performance of LWHO, comparative data with other algorithms (COA, FMQABCA, FWHO) are listed in Table 4.

Table 3. Results of LWHO using fuzzy Kapur entropy

Image	MT	Thresholds					PSNR	FSIM
Brain	2	58.0000	156.5000				18.0098	0.6269
	3	27.8886	95.5282	197.0207			22.7553	0.7848
	4	16.9821	64.5000	116.5095	194.5000		24.2989	0.8317
	5	20.8805	59.0000	109.5274	155.4894	212.0000	25.9168	0.8948
Blood	2	89.1936	216.6936				22.6858	0.7601
	3	101.2154	163.9251	210.0936			24.9378	0.8378
	4	102.8631	162.9820	185.4250	230.2831		25.405	0.8538
	5	101.0577	161.6154	180.0009	198.4021	228.9423	26.1246	0.8975
Lesion	2	78.4891	183.2744				18.4777	0.7382
	3	65.5000	132.9194	173.5956			19.1663	0.7556
	4	47.0001	115.3710	149.6543	184.9728		19.4265	0.7875
	5	48.0644	94.8265	126.6440	164.2111	190.9391	19.5932	0.815
COVID_19chest	2	95.7952	199.0585				21.405	0.5388
	3	75.0000	149.0000	190.0000			22.7016	0.6144
	4	58.7500	140.7500	179.2500	224.7500		24.5451	0.6798
	5	57.2517	119.2529	148.7547	183.5030	224.2500	25.2179	0.6953

By comparing the experimental data in Table 4, it can be seen that the PSNR result of the LWHO in brain image does not reach a maximum of 18.0098 when the threshold value is 2, which is 0.2466 lower than that of the FWHO. In the segmentation results of infectious skin image and COVID-19 chest infection image, only when the threshold is 3, the PSNR is slightly lower than 0.0021 for FMQABCA and 0.0943 for FWHO respectively. Compared to FWHO, the PSNR increased by 0.1527 on average for all images and all thresholds conditions, with the highest single image increasing by 0.2412 on average, and the lowest increasing by 0.0825. Compared with FMQABCA, the average improvement is 0.3282, the highest single image improvement is 0.6099, and the lowest improvement is 0.1363. Compared with COA, the average improvement is 0.1461, the highest single image improvement is 0.1978, and the lowest improvement is 0.0983. From the above data comparison, it can be seen that the experimental data of LWHO are superior to those of COA, FMQABCA, and FWHO. Therefore, LWHO has relatively excellent segmentation results.

Table 4. PSNR comparison of image segmentation results with different algorithms

Image	MT	PSNR			
		COA	FMQABCA	FWHO	LWHO
Brain	2	18.2038	17.5314	18.2564	18.0098
	3	22.5291	21.4522	22.4991	22.7553
	4	23.7345	24.0853	23.8728	24.2989
	5	25.7222	25.4724	25.7751	25.9168
Blood	2	22.6858	22.6509	22.6858	22.6858
	3	24.8512	24.8461	24.1457	24.9378
	4	25.2573	25.166	25.2995	25.405
	5	25.9658	25.7603	26.0574	26.1246
Lesion	2	18.1418	18.046	18.0921	18.4777
	3	19.1324	19.1684	19.0438	19.1663
	4	19.3948	19.339	19.426	19.4265
	5	19.5502	19.5653	19.5313	19.5932
COVID_19chest	2	21.405	21.281	21.3522	21.405
	3	22.6428	22.1349	22.7959	22.7016
	4	24.3516	24.193	24.4593	24.5451
	5	24.7611	24.7242	24.9321	25.2179

The bold data represents the optimal value for the current row, also this to compare the advantages and disadvantages of the results more prominently

5 Conclusion

In this paper, the WHO’s traditional random initialization population method is improved to chaotic initialization population, which increases the randomness and ergodicity of initialization. Fuzzy Kapur is used as the objective function to perform multiple threshold segmentation for medical images. From the experimental results, it can be seen that when LWHO performs medical image segmentation, its segmentation effect is also continuously improving as the number of thresholds continues to increase. Compared with other algorithms, LWHO can also be found to have better segmentation effects in medical image segmentation.

In modern medical detection methods, medical image data accounts for 90% of medical information, which is the most important source of information for disease screening and diagnosis and treatment, as well as an important means to assist in clinical disease diagnosis and treatment. Image segmentation technology perfectly fits the gap in medical imaging. Therefore, in the future development of medicine, detecting pathology based on medical images should become the main diagnostic method of mainstream medicine.


Funding. This paper is supported by Natural Science Foundation of Anhui under Grant KJ2020A1215, KJ2021A1251, 2022AH051325 and 2023AH052856, the Excellent Youth Talent Support Foundation of Anhui under Grant gxyqZD2021142 and the Quality Engineering Project of Anhui under Grant 2021jyxm1117, 2021kcszsfkc307, 2022xsxx158 and 2022jcbx043.

References

1. Liu, S., Wang, H., Li, Y., et al.: AHU-MultiNet: adaptive loss balancing based on homoscedastic uncertainty in multi-task medical image segmentation network. *Comput. Biol. Med.* **150**, 1–12 (2022)
2. Singh, V.K., Kalafi, E.Y., Wang, S., et al.: Prior wavelet knowledge for multi-modal medical image segmentation using a lightweight neural network with attention guided features. *Expert Syst. Appl.* **209**, 1–13 (2022)
3. Wan, J., Yue, S., Ma, J., et al.: A coarse-to-fine full attention guided capsule network for medical image segmentation. *Biomed. Signal Process. Control* **76**, 1–11 (2022)
4. Khehra, B.S., Singh, A., Kaur, L.M.: Masi entropy and grey wolf optimizer based multilevel thresholding approach for image segmentation. *J. Inst. Eng. (India): Ser. B* **103**(5), 1619–1642 (2022)
5. Elaziz, M.A., Bhattacharyya, S., Lu, S.: Swarm selection method for multilevel thresholding image segmentation. *Expert Syst. Appl.* **138**, 1–24 (2019)
6. Ji, W., He, X.: Kapur's entropy for multilevel thresholding image segmentation based on moth-flame optimization. *Math. Biosci. Eng.* **18**(6), 7110–7142 (2021)
7. Xing, Z.: An improved emperor penguin optimization based multilevel thresholding for color image segmentation. *Knowl.-Based Syst.* **194**, 105570–105570 (2020)
8. He, L., Huang, S.: An efficient krill herd algorithm for color image multilevel thresholding segmentation problem. *Appl. Soft Comput.* **89**, 106063 (2020)
9. Yang, Z., Wu, A.: A non-revisiting quantum-behaved particle swarm optimization based multilevel thresholding for image segmentation. *Neural Comput. Appl.* **32**(16), 12011–12031 (2020)
10. Shen, L.: Implementation of CT image segmentation based on an image segmentation algorithm. *Appl. Bionics Biomech.* **2022**, 2047537 (2022)
11. Abdul, K., Khairuzzaman, M., Saurabh, C.: Multilevel thresholding using grey wolf optimizer for image segmentation. *Expert Syst. Appl.* **86**, 64–76 (2017)
12. Li, L., Sun, L., Guo, J., et al.: Fuzzy multilevel image thresholding based on modified quick artificial bee colony algorithm and local information aggregation. *Math. Probl. Eng.* **2016**, 1–18 (2016)
13. Li, L., Sun, L., Kang, W., et al.: Fuzzy multilevel image thresholding based on modified discrete grey wolf optimizer and local information aggregation. *IEEE Access* **4**, 6438–6450 (2016)
14. Li, Y., Yuan, Q., Han, M., et al.: Hybrid multi-strategy improved wild horse optimizer. *Adv. Intell. Syst.* **4**(10), 1–15 (2022)
15. Marzouk, R., Alzahrani, J., Alrowais, F., et al.: Quasi-oppositional wild horse optimization based multi-agent path finding scheme for real time IoT systems. *Expert. Syst.* **39**(10), 1–15 (2022)
16. Li, L., Huang, X., Qian, S., et al.: Fuzzy hybrid coyote optimization algorithm for image thresholding. *Comput. Mater. Continua* **72**(2), 3073–3090 (2022)
17. Upadhyay, P., Kumar, J.: Kapur's entropy based optimal multilevel image segmentation using Crow Search Algorithm. *Appl. Soft Comput. J.* **97**, 105522 (2020)



Improved Northern Goshawk Optimization Algorithm for Medical Image Segmentation

Tuo Zhou¹, Shunqiang Qian¹, Mingyu Zhang¹, and Linguo Li^{1,2}(✉) 

¹ School of Computer and Information Engineering, Fuyang Normal University,
Fuyang 236041, China
11g-1212@163.com

² School of Computer, Nanjing University of Posts and Telecommunications, Nanjing 210003,
China

Abstract. The computational complexity of multi-level medical image segmentation will continue to increase with the increase of the number of thresholds. Therefore, in this paper, we propose improved Northern Goshawk Optimization based on Levy and Simulated Annealing (SA) to Northern Goshawk Optimization (LSANGO) and optimize the fuzzy Kapur objective function for medical image segmentation. In the improvement of the LSANGO, the Levy flight strategy was firstly added in the exploration stage, and its global search ability was enhanced by using the random jump characteristics of the step size of this strategy, thereby obtaining a faster convergence speed. Then, in the update position stage, the SA mechanism is introduced, which effectively solves the problem that the Northern Goshawk Optimization (NGO) tends to fall into local optimum during the optimization process. To better evaluate the performance of the improved algorithm, the LSANGO is compared with NGO, Fuzzy Coyote Optimization Algorithm (FCOA), Whale Optimization Algorithm (WOA) and Altruistic Harris Hawks' Optimization Algorithm (HHO_Altruism). Finally, the superiority of LSANGO is verified by quantitative analysis of peak signal-to-noise ratio (PSNR) and feature similarity (FSIM) performance indicators.

Keywords: Northern Goshawk Optimization Algorithm · Medical image segmentation · Fuzzy Kapur · Levy flight · Simulated annealing

1 Introduction

Image segmentation [1, 2] technology occupies an important role in the fields of image processing [3, 4] and computer vision [5, 6]. Image segmentation, as the name implies, is to divide an image into regions with different features, that is, through the pixel features in the image, pixels with similarity criteria will be divided together, so as to achieve the purpose of segmentation by different regions. Nowadays, image segmentation has been widely used in many fields such as medicine [7–9], plant diseases and insect pests [10, 11] and satellite image processing [12, 13], among which medical image segmentation is the focus of researchers in recent years.

According to different principles, traditional image segmentation methods can be divided into thresholding method [14–16], region growing method [17, 18] and edge detection method [19, 20], among which the thresholding method is widely adopted because of its simplicity and efficiency. Thresholding image segmentation can be divided into two categories: single threshold (bi-level) and multi-level thresholds (multi-level). Bi-level [21] is the simplest form of thresholding segmentation which divided the original image into foreground and background, thus outputting a binarized image. However, grayscale images and color images more often appear in life, so single-threshold segmentation is not suitable. Multi-level thresholds [21] segmentation can solve this problem better, which divides the color image or grayscale image into multiple regions through multiple thresholds to obtain the desired region of interest. However, with the increase of the number of thresholds, the computational complexity of image segmentation will also increase significantly, so many optimization algorithms are applied to the field of thresholding image segmentation.

According to the inspiration of different things in nature and society, optimization algorithms can be divided into: swarm algorithm [22–24], evolutionary algorithm [25, 26], physical algorithm [27, 28] and game algorithm [29]. Among them, the Swarm Intelligence Optimization Algorithm (SIOA) has a significant effect on reducing the computational complexity. In order to solve the problem that the algorithm is easy to fall into local optimum, Li et al. [30] proposed the application of the improved Coyote algorithm (FICOA) in image segmentation, and used the Otsu and fuzzy Kapur for comparison, then perform median aggregation of domain information during image segmentation, which improves the accuracy of segmentation results. In order to improve the population diversity and find the global optimal solution faster, Zhao et al. [31] introduced a diffusion mechanism (DM) and an association strategy (AS) into the original slime mold optimization algorithm (Slime Mould Algorithm, SMA), resulting in an improved Slime Mould Algorithm (DASMA). Experiments were performed on CT images of BSD and chronic obstructive pulmonary disease (COPD), and the remaining eight popular algorithms were compared, and the results showed that DASMA has better competitiveness. Yan et al. [32] proposed a whale optimization algorithm (WOA) to solve the multi-level image segmentation problem. WOA can effectively balance the global search ability and local search ability. Zhao et al. [33] are committed to speeding up the segmentation of lung CT images. By reducing the threshold search range of the two-dimensional Otsu algorithm, the calculation amount is reduced and the calculation speed is improved. In order to effectively solve the image segmentation of brain MRI, Bandyopadhyay et al. [34] proposed an improved Harris Hawks' Optimization Algorithm (HHOA) which introduced chaotic initialization in the original HHO and altruism mechanism. The author selected 18 images from the Brainweb dataset and the Harvard Medical School WBA database to compare with several other advanced algorithms, and proved that HHOA has certain advantages.

The swarm intelligence algorithms proposed in the previous literatures have optimized the computational complexity of medical image thresholding to varying degrees. Similarly, in order to improve the segmentation efficiency of medical images, this paper proposes an improved Levy and SA to Northern Goshawk Optimization (LSANGO) based on NGO [35].

The rest structure of this paper is as follows: Sect. 2 briefly describes the original NGO. The third section describes the improvement points completed on the basis of NGO: Levy flight strategy and Simulated Annealing mechanism. The fourth section introduces the experimental results of LSANGO in medical image segmentation and its comparison with other algorithms. Finally, the article is summarized in the fifth section.

2 The Core Contents of NGO

2.1 Population Initialization

The NGO initialize the population matrix randomly in the search space, as shown in the following Eq. (1):

$$X = \begin{bmatrix} X_1 \\ \vdots \\ X_i \\ \vdots \\ X_N \end{bmatrix}_{N \times m} = \begin{bmatrix} x_{1,1} \cdots x_{1,j} \cdots x_{1,m} \\ \vdots \quad \ddots \quad \vdots \quad \ddots \quad \vdots \\ x_{i,1} \cdots x_{i,j} \cdots x_{i,m} \\ \vdots \quad \ddots \quad \vdots \quad \ddots \quad \vdots \\ x_{N,1} \cdots x_{N,j} \cdots x_{N,m} \end{bmatrix}_{N \times m} \tag{1}$$

where X_i represents the position of the i th northern goshawk, N represents the population number, M represents the population dimension.

After the population initialization is completed, the objective function value of the initialized population needs to be calculated, which can be expressed as the following Eq. (2):

$$F = \begin{bmatrix} F_1 \\ \vdots \\ F_i \\ \vdots \\ F_N \end{bmatrix}_{N \times 1} = \begin{bmatrix} F(X_1) \\ \vdots \\ F(X_i) \\ \vdots \\ F(X_N) \end{bmatrix}_{N \times 1} \tag{2}$$

where F_i is the objective function value of the i th northern goshawk.

2.2 Northern Goshawk Looks for and Finds Prey

The northern goshawk search for prey randomly in the search space, that is, determine the optimal area according to the global search ability of the algorithm, and prepare for the subsequent pursuit behavior. This behavior can be expressed by mathematical model as follows (3)–(5):

$$P_i = X_k, \quad i = 1, 2, \dots, N, \quad k = 1, 2, \dots, i - 1, i + 1, \dots, N \tag{3}$$

$$x_{i,j}^{new,P1} = \begin{cases} x_{i,j} + r(p_{i,j} - Ix_{i,j}), & F_{P_i} < F_i \\ x_{i,j} + r(x_{i,j} - p_{i,j}), & F_{P_i} \geq F_i \end{cases} \tag{4}$$

$$X_i = \begin{cases} X_i^{new,P1}, & F_i^{new,P1} < F_i \\ X_i, & F_i^{new,P1} \geq F_i \end{cases} \quad (5)$$

where P_i and $p_{i,j}$ are the prey position and the j th dimension position of the i th northern goshawk respectively, $x_{i,j}^{new,P1}$ and $X_i^{new,P1}$ is the new position of the i th northern goshawk in the j th dimension and the new position of the i th northern goshawk respectively.

2.3 Chasing and Fleeing of Prey

Because the prey will escape when it finds the attack of the northern goshawk, the northern goshawk will continue to chase the prey until catches it. That is, it reflects the local search ability of the algorithm. This hunting behavior can be expressed as follows (6)–(8):

$$x_{i,j}^{new,P2} = x_{i,j} + R(2r - 1)x_{i,j} \quad (6)$$

$$R = 0.02 \left(1 - \frac{t}{T} \right) \quad (7)$$

$$X_i = \begin{cases} X_i^{new,P2}, & F_i^{new,P2} < F_i \\ X_i, & F_i^{new,P2} \geq F_i \end{cases} \quad (8)$$

where $x_{i,j}^{new,P2}$ and $x_{i,j}^{new,P2}$ is the new position of the i th northern goshawk in the second stage and its corresponding new position in the j th dimension.

3 Improved Northern Goshawk Optimization (LSANGO)

In order to avoid the NGO falling into local optimum and improve its efficiency, the main improvement points of LSANGO are Levy flight and SA mechanism.

3.1 Levy Flight Strategy

Levy flight [36] is a special random step strategy which has the characteristics of short distance high-frequency search and long distance low-frequency search. The formula of Levy flight step size proposed in Mantegna algorithm is as follows (9):

$$s = \frac{u}{|v|^{1/\beta}} \quad (9)$$

In (9), s is the Levy flight step, meanwhile σ_u and σ_v can be expressed as the following Eq. (10):

$$\begin{cases} \sigma_u = \left\{ \frac{\Gamma(1+\beta)\sin(\pi\beta/2)}{\Gamma[(1+\beta)/2]\beta 2^{(\beta-1)/2}} \right\}^{1/\beta} \\ \sigma_v = 1 \end{cases} \quad (10)$$

where, $\beta = 1.5$.

3.2 Simulated Annealing (SA) Mechanism

The original NGO always determines whether to retain the new location by greedy selection strategy after the individual completes the location update operation, that is, by calculating the fitness value of the new location and the old location to compare, select the location with high fitness value to retain. This selection and elimination method seems reasonable, but it will reduce the diversity of the population and make the algorithm easy to fall into local optimization. SA [37] is a probability-based method, which can enhance the ability of the algorithm to jump out of the local optimum due to its sudden jump in probability.

Assumption X_i^t and X_i^{t+1} is the old position and updated position of the i th northern goshawk respectively, and $f(X_i^t)$ and $f(X_i^{t+1})$ are their corresponding fitness values respectively. If $f(X_i^{t+1}) > f(X_i^t)$, keep the updated position. At the same time, if the following Eq. (11) holds, the new position is also reserved.

$$\exp\left(\left(f(X_i^{t+1}) - f(X_i^t)\right) / T\right) > \text{rand} \quad (11)$$

T is the current temperature, which will decrease with the corresponding cooling coefficient.

4 Experimental Results and Comparative Analysis of Medical Images

4.1 Experiment Preparation and Parameter Setting

In order to verify the effectiveness of LSANGO, this paper selects four medical images under ISIC2019 dataset as experimental sample, as shown in Fig. 1, and compares them with FCOA in [30], WOA in [32] and HHO_Altruism in [34].

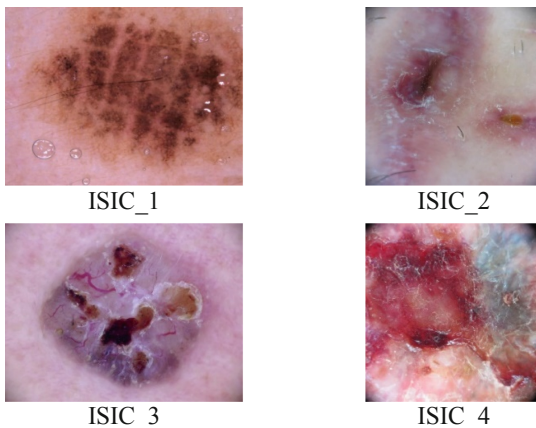


Fig. 1. Original medical image

Table 1. Experimental parameters

Parameters	Values
Search_agents	30
Max_iterations	1000
T	1000
Alpha	0.98

The experimental environment of this paper is Windows 10–64 bit system and AMD processor, Other experimental parameters are shown in Table 1.

4.2 Comparison of LSANGO and NGO in Medical Image Segmentation

This section shows the medical image segmentation effect of LSANGO as shown in Fig. 2 and NGO under the objective function fuzzy Kapur. In order to evaluate the advantages of the LSANGO more intuitively, the experimental data of LSANGO and NGO are listed for quantitative analysis, as shown in Tables 2 and 3.

It can be seen from Tables 2 and 3 that LSANGO has obtained higher PSNR than NGO in all cases. In detail, the PSNR of LSANGO has increased by 0.1132 on average. Among them, when the NT of ISIC_3 is 5, LSANGO achieves the largest improvement, the PSNR has increased by 0.2597. When the NT is 2 in ISIC_2 image, the lowest PSNR is also increased by 0.0148.

Similarly, in terms of FSIM, LSANGO's FSIM is slightly lower than that of NGO, except when NT is 5 in ISIC_1, NT is 2 in ISIC_2, and NT is 2 and 3 in ISIC_3. In most other cases, LSANGO shows obvious advantages. For specific data, the FSIM of LSANGO is 0.0079 higher than that of NGO on average. When the NT is 5 in ISIC_3, the highest increase is 0.0174. When the FSIM of LSANGO is lower than that of NGO, the highest FSIM of LSANGO is only 0.0057 lower.

4.3 Comparison and Analysis of LSANGO and Other Different Algorithms

This section compares LSANGO with FCOA, WOA and HHO_Altruism for medical image segmentation, as shown in Table 4.

It can be seen from Table 4 that, compared with FCOA, in all cases, the PSNR of LSANGO is higher. When the NT is 5 in ISIC_3, the PSNR increases the highest (0.503). When the NT is 2 in ISIC_2, the PSNR also increases 0.0153. Compared with WOA, LSANGO obtained a lower PSNR under the only condition that the NT is 2 in ISIC_4, but it is only 0.1309 lower. In other medical images, LSANGO's PSNR increased by 0.9068 on average. When NT is 2 in ISIC_3, the PSNR increased by 2.7764. Finally, compared with HHO_Altruism, LSANGO has obtained the same PSNR value when the NT is 2 in ISIC_2, and it is better in other cases.

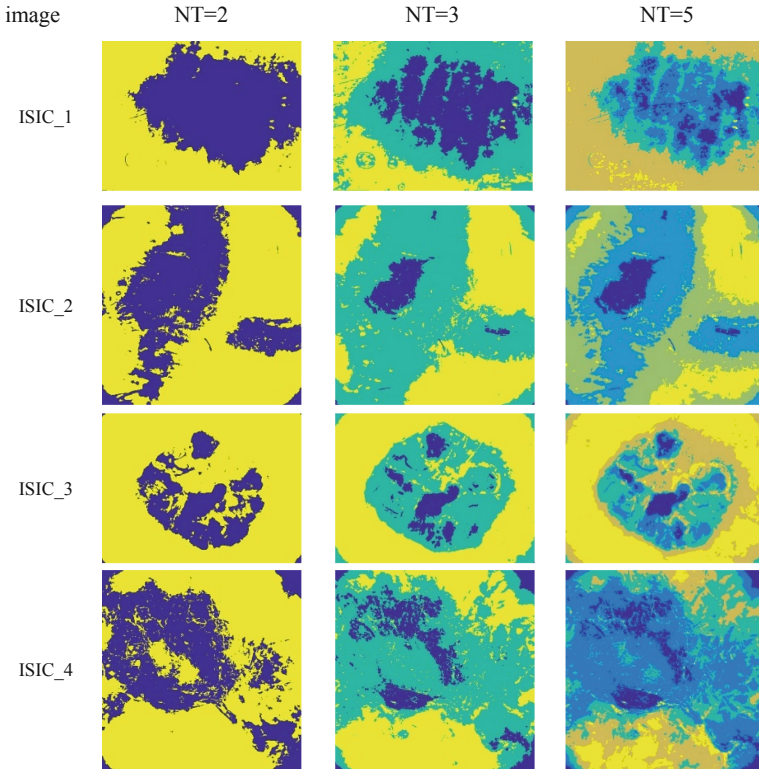


Fig. 2. Visual segmentation effect based on LSANGO

Table 2. Experimental data of LSANGO

Image	NT	Thresholds	PSNR	FSIM
ISIC_1	2	70.5 198.5	14.6026	0.6025
	3	73.5 136.5 198.5	14.8005	0.6677
	5	38.5 90.5 111 165.5 205	15.0859	0.7445
ISIC_2	2	75 201	20.5476	0.7822
	3	55.5 127 185.5	21.3509	0.7907
	5	54.5 130.5 155.5 185.5 231.5	22.0883	0.8169
ISIC_3	2	59 182	18.0066	0.6924
	3	55.5 117.5 188	19.3083	0.7349
	5	37.5 80.5 122.5 145 187.5	19.9841	0.793
ISIC_4	2	53 180	14.534	0.6435
	3	48 118.5 200	15.3067	0.6828
	5	41.5 110 156 189.5 226.5	15.7449	0.7698

Table 3. Experimental data of NGO

Image	NT	Thresholds	PSNR	FSIM
ISIC_1	2	68.5 196	14.5698	0.6023
	3	74.5 145 200	14.7643	0.6571
	5	59 103.5 137 166 215.5	15.0591	0.7489
ISIC_2	2	73.5 201	20.5328	0.7845
	3	62.5 134.5 199.5	21.1044	0.7774
	5	58.5 125 157 191 226	21.9179	0.8089
ISIC_3	2	60 174	17.8314	0.695
	3	52 109.5 173.5	19.16	0.7406
	5	40.5 82.5 123.5 170 214.5	19.7244	0.7756
ISIC_4	2	46.5 174	14.3601	0.6374
	3	46 122 204	15.2855	0.6769
	5	41 98.5 140 176 221	15.6929	0.7682

Table 4. Comparison data of different algorithms

Image	NT	PSNR			
		LSANGO	FCOA	WOA	HHO_Altruism
ISIC_1	2	14.6026	14.5002	14.4746	14.3485
	3	14.8005	14.6141	14.3501	14.5418
	5	15.0859	14.9672	14.8814	15.0628
ISIC_2	2	20.5476	20.5323	18.0228	20.5476
	3	21.3509	20.9909	19.6081	20.881
	5	22.0883	21.8133	21.6013	21.479
ISIC_3	2	18.0066	17.933	15.2302	15.2302
	3	19.3083	19.083	18.2254	19.1224
	5	19.9841	19.4811	19.7915	19.7439
ISIC_4	2	14.534	14.4577	14.6649	14.4633
	3	15.3067	15.2812	15.0883	15.3039
	5	15.7449	15.6697	15.5775	15.4842

5 Conclusion

In order to solve the problem of high computational complexity in medical image segmentation, this paper proposes a multilevel medical image thresholding method based on the improved Northern Goshawk Optimization Algorithm (LSANGO). The Levy flight strategy is added to enhance the global search ability of NGO, and the SA is introduced to redefine the position selection strategy, so that the LSANGO can more easily jump out of the local optimal, and then the improved algorithm (LSANGO) is used to optimize the objective function fuzzy Kapur to complete medical image segmentation. Finally, in order to verify the efficiency of LSANGO in medical image segmentation, LSANGO is compared with NGO, FCOA, WOA and HHO_Altruism. Through the quantitative analysis of PSNR and FSIM evaluation indicators, the results show that LSANGO can well complete the task of medical image segmentation, and shows better performance.

Funding. This paper is supported by the Natural Science Foundation of Anhui under Grant KJ2020A1215, KJ2020A1216, KJ2021A1251 and 2023AH052856, the Excellent Youth Talent Support Foundation of Anhui under Grant gxyqZD2019097 and gxyqZD2021142, the Postdoctoral Foundation of Jiangsu under Grant 2018K009B, the Foundation of Fuyang Normal University under Grant TDJC2021008 and the Quality Engineering Project of Anhui under Grant 2021jyxm1117, 2021kcszsfkc307 and 2019sjjd81.

References

1. Shirly, S., Ramesh, K.: Review on 2D and 3D MRI image segmentation techniques. *Curr. Med. Imaging Rev.* **15**(2), 150–160 (2019)

2. Abdel-Basset, M., Mohamed, R., Abouhawwash, M., et al.: An improved jellyfish algorithm for multilevel thresholding of magnetic resonance brain image segmentations. *Comput. Mater. Continua* **68**(3), 2961–2977 (2021)
3. Herrera-Pereda, R., Crispi, A.T., Babin, D., et al.: A Review on digital image processing techniques for in-Vivo confocal images of the cornea. *Med. Image Anal.* **73**, 1–28 (2021)
4. Abumalloh, R.A., Nilashi, M., Ismail, M.Y., et al.: Medical image processing and COVID-19: a literature review and bibliometric analysis. *J. Infect. Public Health* **15**(1), 75–93 (2021)
5. Chadebecq, F., Vasconcelos, F., Mazomenos, E., et al.: Computer vision in the surgical operating room. *Visceral Med.* **36**(6), 456–462 (2020)
6. Antoni, F., Russo, F., Ambrosio, L., et al.: Artificial intelligence and computer vision in low back pain: a systematic review. *Int. J. Environ. Res. Public Health* **18**(20), 1–12 (2021)
7. Chen, Y., Wang, M., Heidari, A. A., et al.: Multi-threshold image segmentation using a multi-strategy shuffled frog leaping algorithm. *Expert Syst. Appl.* **194**, 116511.1–116511.25 (2022)
8. Tamal, M.: Intensity threshold based solid tumour segmentation method for positron emission tomography (PET) images: a review. *Heliyon* **6**(10), 1–15 (2020)
9. Zhao, S., Wang, P., Asghar, H.A., et al.: Performance optimization of salp swarm algorithm for multi-threshold image segmentation: comprehensive study of breast cancer microscopy. *Comput. Biol. Med.* **139**, 1–11 (2021)
10. Castillo-Martínez, M.N., Funes, F., Carvajal-Gámez, B.E., et al.: Color index based thresholding method for background and foreground segmentation of plant images. *Comput. Electron. Agric.* **178**, 1–14 (2020)
11. Riehle, D., Reiser, D., Griepentrog, H.W.: Robust index-based semantic plant/ background segmentation for RGB-images. *Comput. Electron. Agric.* **169**, 1–12 (2020)
12. Babu, A.A., Rajam, V.: Water-body segmentation from satellite images using Kapur’s entropy-based thresholding method. *Comput. Intell.* **36**(3), 1242–1260 (2020)
13. Swain, M., Tripathy, T.T., Panda, R., et al.: Differential exponential entropy-based multilevel threshold selection methodology for colour satellite images using equilibrium-cuckoo search optimizer. *Eng. Appl. Artif. Intell.* **109**, 1–27 (2022)
14. Siri, S.K., Kumar, S.P., Latte, M.V.: Threshold-based new segmentation model to separate the liver from CT scan images. *IETE J. Res.* **4**, 1–8 (2020)
15. Gao, J., Wang, B., Wang, Z., et al.: A wavelet transform-based image segmentation method. *Optik* **208**, 1–11 (2019)
16. Xiao, L., Ouyang, H., Fan, C., et al.: Gesture image segmentation with Otsu’s method based on noise adaptive angle threshold. *Multimed. Tools Appl.* **79**, 35619–35640 (2020)
17. Mazouzi, S., Guessoum, Z.: A fast and fully distributed method for region-based image segmentation. *J. Real-Time Image Proc.* **18**(3), 793–806 (2020)
18. Wang, X., Wang, L., Li, G., Xie, X.: A robust and fast method for sidescan sonar image segmentation based on region growing. *Sensors* **21**, 1–13 (2021)
19. Wang, X., Wang, S., Guo, Y., et al.: Coal gangue image segmentation method based on edge detection theory of star algorithm. *Int. J. Coal Prep. Util.* **43**, 119–134 (2023)
20. Shang, R., Lin, J., Jiao, L., et al.: Superpixel boundary-based edge description algorithm for SAR image segmentation. *IEEE J. Select. Top. Appl. Earth Obs. Remote Sens.* **13**, 1972–1985 (2020)
21. Tan, Z., Zhang, D.: A fuzzy adaptive gravitational search algorithm for two-dimensional multilevel thresholding image segmentation. *J. Ambient. Intell. Humaniz. Comput.* **11**, 4983–4994 (2020)
22. Rodríguez, A., Camarena, O., Cuevas, E., et al.: Group-based synchronous-asynchronous grey wolf optimizer. *Appl. Math. Model.* **93**, 226–243 (2021)
23. Zhang, Y., Liu, Y., Li, J., et al.: WOCDA: a whale optimization based community detection algorithm. *Physical A* **539**, 1–16 (2020)

24. Gao, S., Gao, Y., Zhang, Y., et al.: Adaptive cuckoo algorithm with multiple search strategies. *Appl. Soft Comput.* **106**, 1–15 (2021)
25. Muoz, A., Rubio F.: Evaluating genetic algorithms through the approximability hierarchy. *J. Comput. Sci.* **53**, 101388.1–101388.7 (2021)
26. Zeng, Z., Zhang, M., Chen, T., et al.: A new selection operator for differential evolution algorithm. *Knowl. Based Syst.* **226**, 107150.1–107150.13 (2021)
27. Vesga-Ramírez, A., Sanabria-Gómez, J.D., Sierra-Porta, D., et al.: Simulated annealing for volcano muography. *J. S. Am. Earth Sci.* **109**, 103248.1–103248.12 (2021)
28. Boucekara, H.: Solution of the optimal power flow problem considering security constraints using an improved chaotic electromagnetic field optimization algorithm. *Neural Comput. Appl.* **32**(7), 2683–2703 (2019). <https://doi.org/10.1007/s00521-019-04298-3>
29. Moghdani, R., Elaziz, M.A., Mohammadi, D., et al.: An improved volleyball premier league algorithm based on sine cosine algorithm for global optimization problem. *Eng. Comput.* **37**(4), 2633–2662 (2020)
30. Li, L., Sun, L., Xue, Y., et al.: Fuzzy multilevel image thresholding based on improved coyote optimization algorithm. *IEEE Access* **9**, 33595–33607 (2021)
31. Zhao, S., Wang, P., Heidari, A.A., et al.: Multilevel threshold image segmentation with diffusion association slime mould algorithm and Renyi's entropy for chronic obstructive pulmonary disease. *Comput. Biol. Med.* **134**, 1–25 (2021)
32. Yan, Z., Zhang, J., Yang, Z., et al.: Kapur's entropy for underwater multilevel thresholding image segmentation based on whale optimization algorithm. *IEEE Access* **99**, 41294–41319 (2021)
33. Zhao, Y., Yu, X., Wu, H., et al.: A Fast 2-D Otsu lung tissue image segmentation algorithm based on improved PSO. *Microprocessors Microsyst.* **80**, 103527.1–103527.8 (2021)
34. Bandyopadhyay, R., Kundu, R., Oliva, D., et al.: Segmentation of brain MRI using an altruistic Harris Hawks' Optimization Algorithm. *Knowl. Based Syst.* **232**, 1–21 (2021)
35. Dehghani, M., Hubalovsky, S., Trojovsky, P.: Northern goshawk optimization: a new swarm-based algorithm for solving optimization problems. *IEEE Access* **9**, 162059–162080 (2021)
36. Xing, Z.: An improved emperor penguin optimization based multilevel thresholding for color image segmentation. *Knowl. Based Syst.* **194**, 105570.1–105570.20 (2020)
37. Ghatak, S., Rup, S., Majhi, B., et al.: An improved surveillance video synopsis framework: a HSATLBO optimization approach. *Multimed. Tools Appl.* **79**, 4429–4461 (2020)



Smart Home Camera Fall Detection System

Ziqi Ding^{1,2}, Hanwei Qian^{1,2}(✉), Zechen Wu^{1,2}, and Wei Liu³

¹ Department of Computer Information and Network Security, Jiangsu Police Institute, Nanjing, China

1401588211@qq.com, qianhanwei@gmail.com

² Engineering Research Center of Electronic Data Forensics Analysis, Nanjing, Jiangsu Province, China

³ City University of Macau, Macau, China

Abstract. As China's population ages, the issue of population aging has become increasingly severe. By the end of 2022, the population aged 60 and above in China has already reached 280 million, with an estimated 25 million falls occurring annually. Falls pose a serious threat to the health and well-being of the elderly. To address this problem, this article presents the design of an intelligent home camera fall detection system aimed at detecting falls and providing immediate assistance. The design incorporates streaming technology and image processing techniques, utilizing a Raspberry Pi camera placed in the home to collect data and stream it via RTMP. A remote server then pulls the video stream and performs fall detection using a combination of the Tiny-YOLOv3, AlphaPose, and ST-GCN algorithms. Upon detecting a fall, the system sends an immediate alert to designated individuals via the PushPlus platform, ensuring timely warnings and effectively safeguarding the safety of the elderly.

Keywords: Fall · Plug flow · Fall detection · PushPlus

1 Introduction

1.1 Research Background and Research Significance

China's population aging problem is becoming more and more serious [9]. The proportion of the elderly population continues to rise, and the pressure on providing for the elderly will increase in the future. At the same time, with the rapid development of the current society, the traditional family structure will also change accordingly, and the number of elderly people living alone will increase. Small things in life, such as turning on lights, boiling water, and taking things, may bring danger to the elderly with limited mobility. In my country, nearly 40 million elderly people fall every year, and 40–70% of the fall injuries require medical treatment, which in turn shortens the life expectancy of the elderly by 5–10 years.

Therefore, based on the above background, this paper designs a smart home camera fall detection system, aiming at real-time video monitoring of the daily life scenes of the elderly. Whether it is in a falling state, whether it is necessary to send an alarm and notification, realize the function of real-time monitoring of the elderly, and send a notification in time when the elderly fall is detected, and automatically remotely push it to the smart terminal of the elderly's children and community workers [2].

1.2 Research Content and Innovation Points of the Paper

This design mainly integrates and improves the traditional fall detection, collects data with the Raspberry Pi camera, and then communicates with the Ubuntu server through the RTMP protocol to perform streaming services, and then the fall detection program pulls the stream from the RTMP address. The obtained video stream is detected and processed subsequently [8]. This paper mainly conducts detailed research on fall recognition based on computer vision, and develops a smart home camera fall detection system. The innovations of this design mainly include the following three.

- (1) The system can build an efficient and stable live broadcast service through the combination of FFmpeg and Nginx.
- (2) The system combines target detection and pose estimation. By combining the two algorithms Tiny-YOLOv3 and AlphaPose, the detection and pose estimation of falling behavior can be realized.
- (3) The system can feed back the running results of the algorithm to the user in real time by calling the interface of PushPlus.

2 Overall Scheme Design of Smart Home Camera Fall Detection System

In order to reduce the health and economic losses caused by falls, this paper aims to design a smart home camera fall detection system, which will give an alarm at the first time of the fall. According to the functional requirements of the system, the hardware and software development platform and the overall design scheme are determined [6]. The main functions of the smart home camera fall detection system designed this time are: data collection and forwarding module, data receiving module, fall detection module, push notification alarm module, and selection of related operating systems. The functions of each module will be described below [4].

2.1 Arrangement of Chapters in this Article

Through the analysis and design of the functions of each module, the overall design topology of the smart home camera fall detection system is determined [5]. The system can collect video information through the camera, and then

encode and format the captured video raw data through FFmpeg, push the stream to the server through the RTMP protocol, and the server's fall detection program will start fall detection after reading the video data by pulling the stream Analysis, through the combined use of Tiny-YOLOv3, AlphaPose and ST-GCN, when a fall is detected, an alarm is pushed through the push module, and the user starts rescue after receiving the alarm message [1].

2.2 Data Acquisition and Forwarding Module

The data acquisition and forwarding module can collect video information through the camera, then transcode the original YUV data of the video into H.264, and then encapsulate the format through FFmpeg, convert the H.264 encoded video data into FLV format, and forward it through the RTMP protocol Go to the Nginx server (Fig. 1).

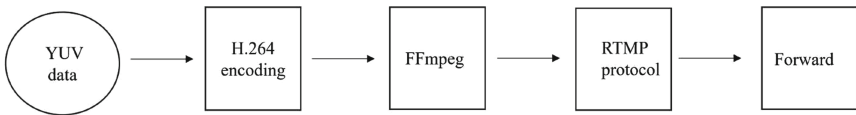


Fig. 1. Flow chart of data collection and forwarding

Get Camera Data The raw data acquired by the camera is the unprocessed image data captured by the image sensor. An image sensor is typically a semiconductor device that converts light signals into electrical signals to produce digital image data. This raw data is usually a series of numeric or pixel values that describe the brightness and color information of each pixel of the image.

H.264 encoding H.264 encoding is a new generation of digital video compression format following MPEG4 jointly proposed by the International Organization for Standardization (ISO) and the International Telecommunication Union (ITU). It mainly focuses on enhancing the speed of the encoding and decoding process, the accuracy of video data and the stability of transmission on the Internet, and has a longer-term design idea and design concept [7]. Compared with the previous MPEG-2 and MPEG-4 encoding, H.264 can reduce the video file size with the same video quality and reduce the bandwidth required for network transmission.

RTMP protocol RTMP (Real Time Messaging Protocol) is a communication protocol for streaming audio, video, and data over the Internet, and is a data transmission protocol based on TCP. RTMP can achieve the purpose of content distribution and shorten the transmission path by forwarding the data stream from one server to another. This process is called RTMP forwarding or RTMP streaming [3].

FFmpeg Video Processing Technology FFmpeg is a complete set of open source source code, which provides a complete technical framework for audio

and video data processing, has a very strong ability to process audio and video, and supports most audio and video coding standards FFmpeg is used to solve audio and video recording, format conversion, and open source audio and video data processing.

2.3 Data Receiving Module

Nginx is a high-performance web server software. Nginx is designed as a lightweight, scalable, and high-performance server. It can handle a large number of concurrent connections at the same time, and supports functions such as reverse proxy, load balancing, and HTTP caching. It adopts an event-driven asynchronous non-blocking architecture, which can efficiently handle a large number of concurrent requests while occupying very few resources. This makes Nginx one of the go-to options for handling high-traffic websites. It can be used as a reverse proxy server to forward requests to multiple backend servers to achieve load balancing and high availability. At the same time, Nginx also supports a variety of modules and plug-ins, which can be customized according to specific needs, meeting the customization requirements of this design.

2.4 Fall Detection Module

This module combines the three algorithms of Tiny-YOLOv3, AlphaPose and ST-GCN to realize an integrated target detection and human pose estimation model. First, use Tiny-YOLOv3 for target detection to obtain the position and category information of the target object in the image. Then, the detected human body target area is passed to AlphaPose for human body pose estimation, and the coordinate positions of the key points of the human body skeleton are obtained. Then, ST-GCN is used to model the key points of the human skeleton in time and space to obtain more accurate action features. Finally, use these features for human action classification or other applications.

2.5 Push Notification Alarm Module

The push notification alarm module is a common information transmission method, which is usually used to push important notifications, reminders, alarms and other information to the people in need in a timely manner. With the popularity of the Internet and mobile devices, push notifications have become an indispensable part of people's lives and work. Among them, PushPlus is a free push service based on the HTTP protocol. Users can use the API interface provided by it to quickly push the messages that need to be pushed to themselves or other members of the team to achieve timely, accurate and convenient push notification effects.

2.6 Summary of this Chapter

This chapter designs the overall scheme of the smart home camera fall detection system, analyzes and designs each functional module one by one, determines the overall system architecture diagram, fall detection flow chart, etc., and describes the specific functions that each functional module needs to achieve. In the design, the way to realize each functional module is selected from the perspectives of realizability, cost performance, convenience, etc., and the overall design scheme of the system is determined.

3 Hardware Environment of Fall Detection System

3.1 Hardware System

The hardware system is mainly composed of an image acquisition system, a video transponder, and a video stream receiver and processor. The image acquisition system acquires a real-time video stream, the video transponder forwards the video stream, and the video stream receiver and processor receive and process the captured video flow.

3.2 Video Capture Device

The video acquisition device adopts the binocular SH200 camera module for image acquisition, which is a very good camera module with many advantages. First of all, the binocular camera can acquire images from two perspectives, thereby calculating the distance and depth information of the object, which can be used in applications such as depth perception and distance measurement, and has the advantage of high-precision depth perception. Secondly, the binocular SH200 camera module adopts a low-power design, and the power consumption is very low, which is very suitable for use in embedded systems. In addition, the module is small in size and light in weight, and can be easily installed in various embedded devices. The binocular SH200 camera module can be used in human-computer interaction, machine vision, intelligent monitoring, virtual reality, automatic driving and other fields, and has a very broad application prospect. Finally, this module is easy to integrate and develop, and has realized the integration of hardware and software, and users can use it for development and application very conveniently. At the same time, this module also provides a wealth of API and SDK, which is convenient for users to carry out secondary development and customization. In conclusion, the binocular SH200 camera module is a very good camera module with many advantages, suitable for various embedded computing applications.

3.3 Video Repeater

The hardware platform used for video forwarding is Raspberry Pi (Raspberry Pi [4]), a small computer based on ARM architecture, developed and designed by the

Raspberry Pi Foundation in the UK. It is small in size and cheap, but powerful in performance, can run an operating system similar to a desktop computer, supports multiple programming languages, and can run artificial intelligence algorithms. The Raspberry Pi itself was originally designed for the education sector to enable students to learn computer programming and electrical engineering, but it has now been widely used in various fields such as home entertainment, Internet of Things, automation control, machine learning, etc. At present, the Raspberry Pi Foundation has launched several models of Raspberry Pi, including Raspberry Pi Zero, Raspberry Pi 1, Raspberry Pi 2, Raspberry Pi 3, Raspberry Pi 4, etc. Among them, Raspberry Pi 4 is the latest models, with 4GB and 8GB memory versions. The standard interfaces of Raspberry Pi include HDMI, USB, Ethernet, etc., and GPIO (General Purpose Input and Output Port) can also be used to connect and control electronic circuits. This design uses Raspberry Pi 3 Generation B, Raspberry Pi 3B is a single-board computer based on ARM architecture, using Broadcom BCM2837B0 quad-core processor, memory is 1GB LPDDR2 SDRAM, storage uses MicroSD card, supports Gigabit Ethernet network, dual-band wireless network and Bluetooth 4.2 and other network connection methods. In addition, the Raspberry Pi 3B is also equipped with 4 USB 2.0 ports, a complete HDMI port and a 3.5mm audio output port, which can be connected to peripherals and displays. It also has 40 GPIO pins, which can be used to connect sensors, control device etc. Raspberry Pi 3B supports multiple operating systems, including Raspbian, Ubuntu Mate, Windows 10 IoT, etc. It also supports multiple programming languages, such as Python, C, C++, Java, etc. Users can choose according to their needs. The GPU module of Raspberry Pi 3B is Broadcom VideoCore IV 3D graphics processor, which supports OpenGL ES 2.0, OpenVG and 1080p 30fps H.264 hardware decoder, etc. It has powerful functions in image processing. At the same time, the Raspberry Pi 3B is small in size and light in weight, only $88 \times 56 \times 19.5$ mm in size, which is very suitable for education, home entertainment, Internet of Things, robotics and other fields.

3.4 Video Stream Receiver and Processor

This system selects Ubuntu server as the video stream receiver and processor. Ubuntu is a server based on Linux operating system, which has many advantages. First, it's free, so you save yourself the cost of buying an operating system. Second, Ubuntu Server is relatively simple to install and configure because of its extensive documentation and community support. In addition, Ubuntu server has good security performance and can provide a variety of security options and tools, including firewall, encryption and access control. In addition, Ubuntu server also supports a large number of software and development tools, making it easier and more flexible to develop and deploy applications on the server. Finally, the update and maintenance of Ubuntu server is also very convenient, it can be operated through command line or graphical interface, and updates and security patches can be obtained regularly. These advantages make Ubuntu server a widely used server operating system, and also meet the development hardware requirements of this system

3.5 Summary

This chapter mainly introduces the hardware environment of the smart home camera fall detection system, respectively expounds the video acquisition device, video transponder, video stream receiver and processor, especially the detailed data introduction of the Raspberry Pi model selection and functional advantages, so that Complete the selection of all hardware environments of the entire smart home system.

4 System Experiment Test and Result Analysis

After completing the design of the smart home camera fall detection system, it is necessary to debug the system to ensure the normal and stable operation of the system. Specifically, the hardware and software parts need to be tested and debugged separately to find and solve problems, and optimize and improve the entire system in time. Finally, unit testing, integration testing and system testing are required to verify whether the system meets the design requirements.

4.1 System Experimental Test

In order to ensure the normal operation and stability of the system, the entire smart home camera fall detection system needs to be detected. There are many testing methods, the common ones are static testing and dynamic testing, black box testing, white box testing and gray box testing, manual testing and automated testing. This experimental test is mainly to carry out unit test and integration test according to different stages.

Unit testing The unit test mainly checks whether the Raspberry Pi operation, camera connection, FFmpeg push and pull stream, Nginx program operation, and PushPlus program call are normal.

Integration testing Test whether the communication between each module can be connected. Considering that FFmpeg pushes the data by calling the camera, and then transmits the video to the specified channel on the server through the RTMP protocol after video processing. You can use VLC software to test whether the specified channel can receive the data. The video stream information proves that there is no problem with the integration between modules (Fig. 2).

4.2 Analysis of Test Results

In this test, the entire system was tested for each stage to test whether it can identify the fall situation, and push the early warning through PushPlus to verify the effectiveness of the system. Under the unit test, the Raspberry Pi, camera, FFmpeg, Ubuntu, and Nginx are tested respectively. When the Raspberry Pi is tested, it is tested by checking whether it has a Python environment, and it is displayed as version 3.9. When testing the camera, it is displayed through



Fig. 2. Fall detection preview

a simple Python camera call, and the function of the camera is found to be normal. When testing Ubuntu, in order to facilitate subsequent login, the remote connection test is normal by installing the sunflower software. Test whether Nginx is running normally, and find that Nginx is running normally by checking the system process. During the system test, push the stream to the server through FFmpeg, and check the specified address through VLC software, and the channel can be viewed normally. during system testing. After a real person fell, the test found that the system can judge the situation of the fall, and push it to WeChat through PushPlus for early warning.

4.3 Summary

This chapter shows the implementation results of the entire smart home camera fall detection system, tests the hardware and software, and unit testing, integration testing at different stages of testing. The test results show that the smart home camera fall detection system designed this time meets the expected design requirements, can normally detect the expected action category, and send a message when it falls, and the PushPlus message is received normally, and the current fall situation can be received. The overall system run smoothly.

5 Conclusion and Outlook

This paper completes the smart home camera fall detection system, which can realize fall detection and early warning. Raspberry Pi's camera acquires video stream, after video encoding and other operations, FFmpeg software is applied, and the stream is pushed to the server through RTMP protocol, and the fall recognition program on the server detects it. When a fall occurs, call PushPlus to send a message push warning.

The main work done in this paper is as follows:

- (1) Introduced the research background and research significance of fall detection by consulting materials and reading literature. In addition, by further understanding the development status of fall detection at home and abroad, and analyzing the research status, the design direction of this project is determined.
- (2) First design the overall scheme of the smart home camera fall detection system according to the requirements, and then design the data collection and forwarding module, server data receiving module, fall detection module, and push notification alarm module according to the overall framework of the system to provide the overall system Design gives direction.
- (3) The hardware environment part of the system is based on the characteristics of the hardware, and the actual effect is considered comprehensively, and the selection and connection of the hardware are carried out.
- (4) In the system implementation part, Python is given priority as the development programming language, and the Raspberry Pi and Ubuntu server are both initialized and designed. The structure of the live website is built through the combination of FFmpeg and Nginx, and the specific fall detection is comprehensively applied. The advantages of the three algorithms Tiny-YOLOv3, AlphaPose, and ST-GCN, and the convenience of PushPlus application form a fall detection model.

Finally, after testing, the entire smart home camera fall detection system runs stably and functions normally. It can recognize when a person falls and send a push warning.

References

1. Aloman, A., Ispas, A., Ciotirnae, P., Sanchez-Iborra, R., Cano, M.D.: Performance evaluation of video streaming using MPEG DASH, RTSP, and RTMP in mobile networks. In: 2015 8th IFIP Wireless and Mobile Networking Conference (WMNC), pp. 144–151. IEEE (2015)
2. Cao, X., Kudo, W., Ito, C., Shuzo, M., Maeda, E.: Activity recognition using ST-GCN with 3D motion data. In: Adjunct Proceedings of the 2019 ACM International Joint Conference on Pervasive and Ubiquitous Computing and Proceedings of the 2019 ACM International Symposium on Wearable Computers, pp. 689–692 (2019)
3. Chang, Q., Yang, Z., Song, Y.: A scalable mobile live video streaming system based on RTMP and HTTP transmissions. In: Advanced Research on Computer Science and Information Engineering: International Conference, CSIE 2011, Zhengzhou, China, 21–22 May 2011. Proceedings, Part I, pp. 113–118. Springer (2011)
4. Jolles, J.W.: Broad-scale applications of the raspberry pi: a review and guide for biologists. *Methods Ecol. Evol.* **12**(9), 1562–1579 (2021)
5. Pattaranantakul, M., Sanguannam, K., Sangwongngam, P., Vorakulpipat, C.: Efficient key management protocol for secure RTMP video streaming toward trusted quantum network. *ETRI J.* **37**(4), 696–706 (2015)
6. Somkunwar, R.K., Thorat, N., Pimple, J., Dhupal, R., Choudhari, Y.: A novel based human fall detection system using hybrid approach. *J. Data Acquisition Process.* **38**(2), 3985 (2023)

7. Zhao, P., Li, J., Xi, J., Gou, X.: A mobile real-time video system using RTMP. In: 2012 Fourth International Conference on Computational Intelligence and Communication Networks, pp. 61–64. IEEE (2012)
8. Zheng, H., Liu, Y.: Lightweight fall detection algorithm based on AlphaPose optimization model and ST-GCN. In: Mathematical Problems in Engineering, vol. 2022 (2022)
9. Zhu, X., Zhao, H.: Experimentalist governance with interactive central-local relations: making new pension policies in China. *Policy Stud. J.* **49**(1), 13–36 (2021)



Design and Implementation of an Automated APK Analysis System for Practical Forensics

Yicheng Li¹, Guangjun Liang^{1,2,3}(✉), Keyan Tang¹, Yijia Teng¹, Haoran Ruan¹,
and Zixi Mo¹

¹ Department of Computer Information and Cyber Security, Jiangsu Police Institute, Nanjing, China

lianggjuni@126.com

² Engineering Research Center of Electronic Data Forensics Analysis, Nanjing, China

³ Key Laboratory of Digital Forensics, Department of Public Security of Jiangsu Province, Nanjing, China

Abstract. In order to cope with the widespread emergence of malicious APK in the application market and the increasingly rampant situation of mobile malware, as well as to meet the needs of the actual forensics work, this paper, based on the analysis of Android security mechanisms and their security problems, analyses and summarises the methodological principles, main technologies and functional flaws of existing APK automated analysis tools, and proposes an APK automated analysis system for actual forensics. Compared with traditional systems, the system is easy to operate and has a higher recognition accuracy rate. Besides, it will perform machine learning on the analysis results and calculate the similarity through the model to effectively assist the forensic work and fill the demand for APK analysis in the field of combat.

Keywords: APK · Forensics · Automated systems

1 Introduction

In recent years, smartphones have become rapidly popular, and the vast majority of smartphones on the market use the operating system Android or a deeply customised system based on Android. In this article, such phones are collectively referred to as Android smartphones. According to the latest mobile operating system market survey report released by International Data Corporation (IDC) in 2019, the market share of Android smartphones has increased year on year, and it has slightly increased from 85.1% in 2018 to 86.7% in 2019, and its shipments are expected to grow at a five-year compound rate of 2.1%, and the shipments will reach 1.32 billion units. This has become a major target for malicious code on mobile, and mobile internet security has become one of the mainstream security threats. According to statistics, in FY2022, 360 Security Brain intercepted a total of about 240.779 million new malicious program samples on mobile, an increase of 155.3% compared to 2021 (943.1), with an average of about 66,000 new mobile malicious program samples intercepted every day. The main types of malicious programs are bill-consuming, privacy theft, etc.

With the growing prevalence of mobile malware, forensics based on automated APK analysis is playing an increasingly important role in real-world applications. APK is an abbreviation for Android application package, which is an application package file format used by the Android operating system to distribute and install mobile applications and middleware. APK automatic analysis refers to a series of automated operations such as automatic deshelling, unpacking and analysis of Android application packages. Compared to traditional APK analysis which relies on manual experience, the advantage of automated analysis lies in its technical friendliness and the availability of services for users who have never been exposed to Android security.

For example, Wang Xingang [1] proposed a behavioural sequence-based malware detection technique for mobile smart terminals. The software function call graph is first analysed using key permissions so as to construct a sequence of function calls characterising the key behaviour of the software, and then a hierarchical attention network is used to achieve the detection and classification of malware. However, as the Deepwalk algorithm is only applicable to unprivileged graph structures and the probability of function node jumps in the function call graph varies, the learning process for the representation of the function call graph needs further research and improvement are needed for the representation learning process of function call graphs.

The study of a multi-feature-based approach for hybrid analysis and detection of Android malware proposed by Kai-Meng Zhang [2] uses a combination of static and dynamic analysis. In the dynamic analysis stage, the execution process of dynamic analysis is greatly simplified by writing scripts, and the detection efficiency of dynamic analysis is improved. In the dynamic analysis stage, the execution process of dynamic analysis is greatly simplified by writing scripts, which improves the efficiency of dynamic analysis detection. The detection model aging is effectively avoided while the detection accuracy is guaranteed. However, the method uses a Genymotion-based Android virtual environment rather than a real machine for feature extraction in the process of dynamic detection, so there is still considerable room for improvement in feature extraction under real machines.

In addition, Eddie Lu [3] proposed the use of more semantically complete application security vulnerabilities as feature supplements based on the traditional static features and Dalvik operations used by previous authors as features, expanding the feature types in the Android malicious application detection domain. In terms of feature selection, the innovative TF-IDF algorithm TIOE based on heterogeneous environment suitable for supervised classification tasks and the dynamic integration selection combined with Stacking integration model are proposed to effectively improve the type differentiation of the selected malicious APK application detection features. However, this method is not the best distance measure for the feature Hamming distance used in the distance measure between samples; at the same time, dynamic integration selection requires each base classifier to detect all the nearest neighbour points, which will bring a notable time overhead and still leaves much room for improvement.

William [4] designed an Android app detection system called TaintDroid. Radoniaina [5] used the open source tool Androblare to extract the sensitive data information flow of App runtime, and then constructed an information flow graph to achieve the detection of Android malware. Mehedee [6] proposed a malware detection technique based on

network traffic analysis by recording URL data in malware runtime logs to build a malicious communication DNS domain database, which can be combined with behavior-based detection techniques to improve detection accuracy.

The main work of this paper is to analyse and summarise the methodological principles, main techniques and functional flaws of existing APK automated analysis tools based on the analysis of Android security mechanisms and their existing security issues, to propose a design of an APK automated analysis system for real-world forensics, and to validate the system in real-world situations. The innovation of the system is to expand the analysis module, which enhances the information targeting and will perform machine learning on the analysis results, compare them with previous cases and calculate the similarity through the model to better assist in forensic real-world scenarios.

2 Overall Design of the APK Automated Analysis System

2.1 System Framework Design

2.1.1 System Architecture Framework

The structural framework of the system consists of four major modules, namely uploading and unpacking module, static analysis module, malicious APK classification module and analysis report display module. The system design framework is shown in Fig. 1.

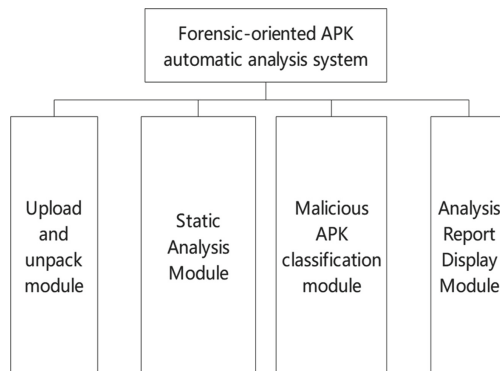


Fig. 1. System framework design diagram

2.1.2 System Operation Process

The system is designed to enable automated analysis, and the four modules in the system are layered so that only data is passed from module to module and do not interfere with each other's work. The general flow of the system operation is as follows:

1. The user uploads an APK file to the system in the upload and unpack module.
2. The upload and unpack module automatically unpacks the uploaded APK file.

3. The unpacked APK file enters the system and is statically analysed in the static analysis module.
4. The static analysis module passes the analysed data to the malicious APK classification module.
5. The malicious APK classification module classifies and predicts APKs according to the data passed in.
6. The analysis results from the static analysis module and the malicious APK classification module are passed to the report display module.
7. The report display module generates the final report and returns it to the user in the form of a web page.

The system flow design diagram is shown in Fig. 2.

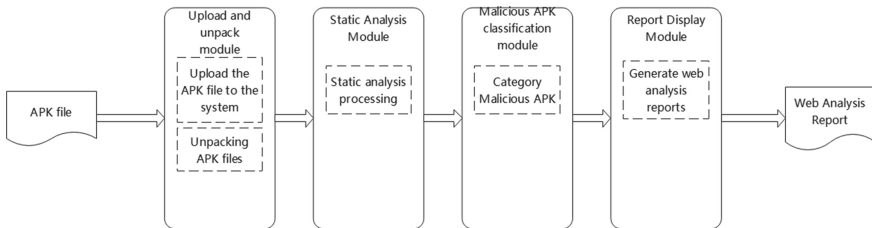


Fig. 2. System flow design diagram

2.2 System Implementation Design

The system adopts the design strategy of separating the front and back ends in the concrete implementation scheme. The front-end is responsible for the presentation of the pages, while the back-end is where the main functional modules of the system run. The front-end is developed using Vue technology, with the front-end application running independently on port 8080, providing an intuitive visualisation of the system pages and a convenient user interaction portal. On the back-end, the system is developed using the Flask framework, which runs independently on port 5000 and provides parameter data and API interfaces for each module, thus enabling data transfer and interconnection communication between modules. The front-end asynchronously requests the back-end API interface via axios, and the back-end returns the results to the front-end in the form of json data. In addition, the separation of the front-end and back-end implementations effectively avoids conflicts between the two ports, further guaranteeing the stability of the system's data and operation, ensuring that the system can run smoothly, while also providing the system developer with more possibilities for expansion and maintenance. The system implementation scheme is shown in Fig. 3.

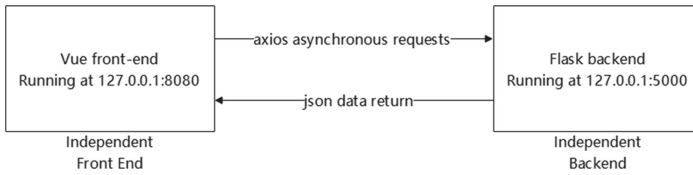


Fig. 3. System implementation plan

3 APK Automated Analysis System Module Design

3.1 Upload and Unpack Module

The uploading and unpacking module is responsible for the uploading of APK files and the unpacking of APK files. The structure of the uploading and unpacking module is shown in Fig. 4.

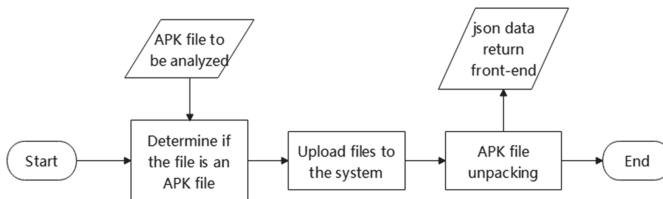


Fig. 4. Upload and unpack module structure diagram

3.2 Static Analysis Module

The APK static analysis module in this system consists of two sub-modules, the decompiling sub-module and the information extraction sub-module. The decompiler sub-module is the module that performs the basic work of decapsulating, unpacking and decompiling the APK file. The information extraction sub-module is the module that extracts and analyses the data from the processed APK file. These two modules finally pass the analysis result results into the malicious APK classification module and report display module to complete the whole module. The structure diagram of the static analysis module is shown in Fig. 5.

3.2.1 Decompiling Sub-module

The decompiling sub-module completes the decompilation process of the APK file in preparation for the subsequent specific analysis. APK decompilation refers to the reduction of the APK file to readable source code, XML resource files and other components. The ApkTool tool provided by Google is integrated in this module for decompiling. The ApkTool tool can view the xml files, AndroidManifest.xml and images under the res file [7]. Since the ApkTool tool runs at the command line, you need to open a new system

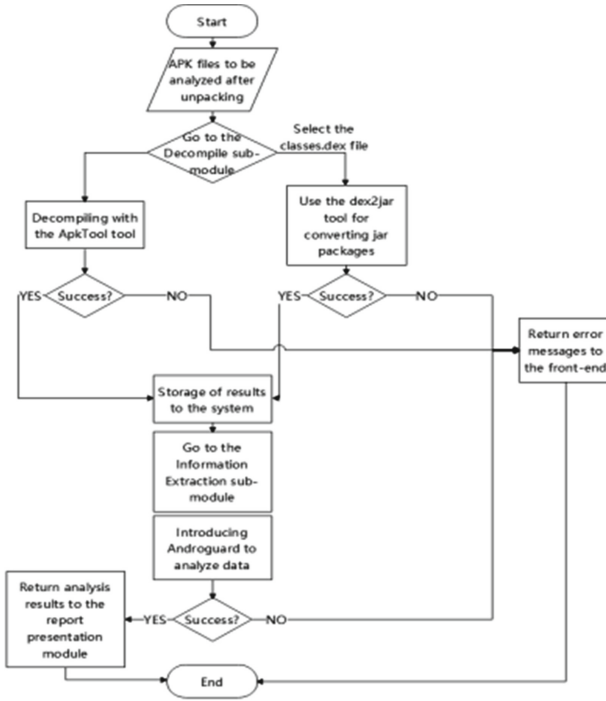


Fig. 5. Static analysis module structure diagram

process using the subprocess.Popen() function, then execute the “apktool d apkName” command in the new process with the exec() system call, and after the execution Close the process.

The dex2jar tool is also integrated in this module to convert the obtained classes.dex file into a jar package file, i.e. a package of java source code, for subsequent analysis. As the dex2jar tool runs from the command line, it is necessary to open a new system process using the subprocess.Popen() function on the system and then execute the “d2j-dex2jar-force classes.dex” command in the new process via the “exec() system call.” command, close the process after execution, and then unpack the jar package.

3.2.2 Information Extraction Sub-module

The information extraction sub-module completes the work of extracting information from APK files, including extracting the package name, sdk version, main activity, app name, permission information, detailed permission information, icon, Android version name and other information of the APK. This is achieved with the integration of the Androguard [8] tool, an open source tool written in Python for analysing Android applications and malware. It provides a range of tools that can help security researchers analyse and detect security vulnerabilities and malicious behaviour in Android applications, as well as help analysts analyse various components and structures in APK files, such as Dex files, Manifest files, resource files, code and decompile results.

We import Androguard in the module, according to the location of the APK file to create a new AnalyzeAPK object, AnalyzeAPK object is also a well-defined object in Androguard, through the array can export his three sub-objects, respectively apk object, abstract apk object, you can get some information about the apk, such as version number, package name, Activity, etc.; DalvikVMFormat, the array, an element that actually corresponds to class.dex, which can get classes, methods or strings from the DEX file; Analysis, the analysis object, because it contains special classes that link information about classes.dex. We name these three sub-objects with a, d, dx respectively.

3.3 Malicious APK Classification Module

3.3.1 n-Gram Feature Extraction Sub-module

n-gram is an important concept in natural language processing, referring to a statistical analysis method of text, which is to divide the text into segments consisting of n words or characters and calculate the frequency and probability of occurrence of each segment. The features extracted in this module are the n-gram features of the opcode in the Smali code after the decompilation of the APK file, using the number of n-gram features of the opcode to construct a model has a higher accuracy rate compared to other features and models. Smali file is an interpretation of bytecode, which is composed of Dalvik instructions, and in this system the APK static analysis module of the extraction of Smali source code has been done in the decompilation sub-module of APK static analysis module in this system. Dalvik instructions are divided into seven instruction set descriptions M, R, G, I, T, P, V, which represent seven types of instructions of move, return, jump, judge, fetch data, store data, and call method, respectively, and the instructions included in each instruction set description are shown in Exhibit 2. By traversing the Smali code, the core Dalvik instructions in the Smali code are extracted, and after adding the data set. The dataset is extracted and counted using the binary Bi-gram method, and finally the results are generated.

The structure of the n-gram feature extraction sub-module is shown in Fig. 6.

3.3.2 KNN Classification Model Sub-module

This module adopts the KNN classification model to classify the n-gram feature set extracted from the previous sub-module. The KNN model works by categorizing a new data point into its nearest neighbors, i.e., finding the K nearest points to the data point in the training data set, and then categorizing the data point into the category with the most occurrences among the K points. This module first obtains the learning sample set needed to build the model by performing binary Bi-gram feature extraction on 500 benign APKs and 683 malignant APKs. The KNN model is then built and the model is trained with the learning sample set. Finally, the trained model is used to predict the binary Bi-gram features extracted from the currently analyzed APKs, and the predicted result is either benign or malignant APKs. The structure of the KNN classification sub-module is shown in Fig. 7.

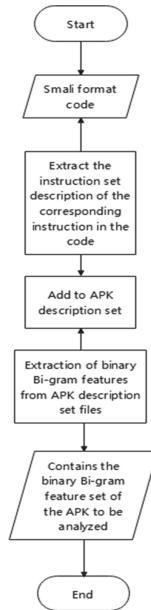


Fig. 6. Structure of n-gram feature extraction sub-module

3.4 Report Display Module

This module displays the analysis results of the system in the form of web pages. The result data of the static analysis module and the malicious APK classification module are passed to the external API set by the report display module in the form of json, and after the report display module receives the data, it forms a report in the form of web pages and returns it to the user for viewing. The structure of the report display module is shown in Fig. 8.

4 System Effect Implementation and Verification

4.1 System Interface Appearance Implementation

The system interface is realized by the design scheme of Vue framework and elementui. The appearance of the system interface is shown in Figs. 9 and 10. It is mainly divided into APK upload page and APK analysis report page. The user uploads the APK file to be analyzed in the APK upload page, and the system can automatically analyze it and display the analysis result on the report page. The report results are displayed in the form of web pages, and the results are displayed concisely and clearly.

4.2 Module Functional Test Verification

The two main functional modules of this system were tested to verify the effectiveness of the system method.

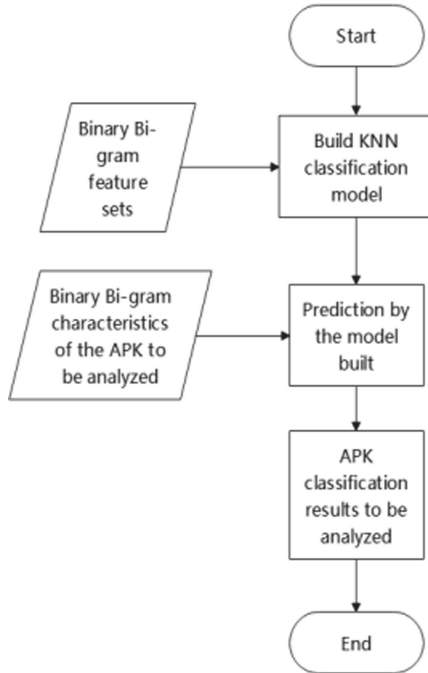


Fig. 7. Structure of KNN classification sub-module

4.3 Static Analysis Module Test Results

Download the “memory booster” APK and the “Best Wallpaper” APK from the Android App Store and analyse them with the system’s static analysis module. The system successfully performed static analysis on the two APKs and output the results, which are clearly visible and prove the feasibility of the static analysis module, as shown in Figs. 11 and 12.

4.4 Classification Module Implementation Results

150 benign APK samples and 150 malignant APK samples were extracted from the dataset and divided into two sample sets for predictive classification by the system. Sample set 1 was 150 benign APKs, of which 130 APKs were classified as benign APKs and 20 APKs were classified as malignant APKs, with an accuracy rate of 86.67%. Sample set 2 was 150 malignant APKs, 141 APKs were classified as malignant APKs and 9 APKs were classified as benign APKs, with an accuracy rate of 94.00%. In total, 271 APKs were correctly classified out of 300 samples, with an accuracy rate of 90.33%. The results are shown in Fig. 13.

The detection results can be compared to show that the experiment successfully classified malignant APK and benign APK with an overall accuracy of 90.33%, which basically completed the classification task and proved the effectiveness of the classification module.

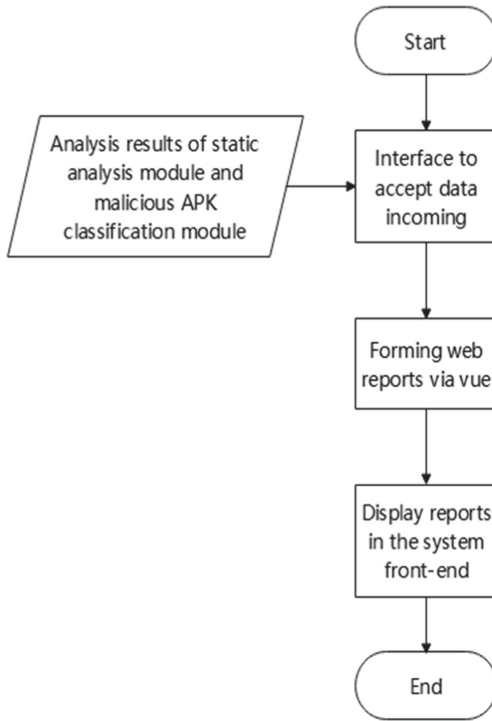


Fig.8. Structure of report display module



upload

Fig. 9. APK upload page



Fig. 12. Classification module test

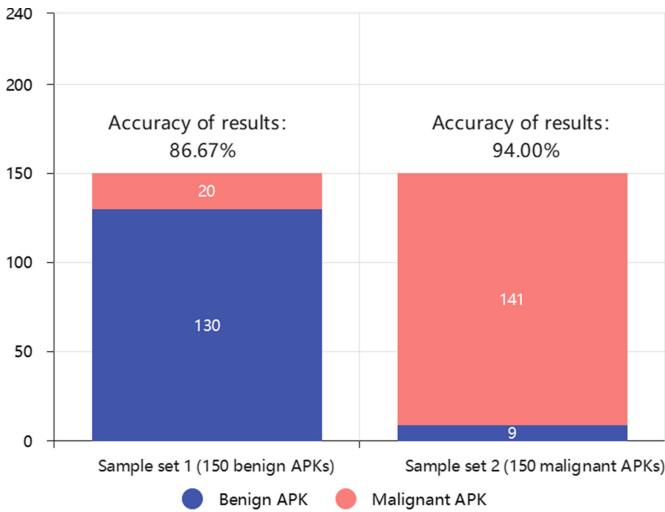


Fig. 13. Classification module implementation results

5 Conclusion

The proposed APK automated analysis system can perform rapid information extraction, information analysis and classification prediction of APK applications, which can effectively assist forensic work and fill the demand for APK analysis in the field of combat. The system needs to be further improved in terms of classification, such as for the multiple classification of malicious APK types in the malicious APK classification module, further optimization research is needed.

References

1. Wang, X.: Research on Malware Detection Technology for Mobile Smart Terminals Based on Behavioral Sequences. Guangzhou University (2022). <https://doi.org/10.27040/d.cnki.ggzdu.2022.0011-22>
2. Zhang, K.: Research on Multi-features Based Approach for Android Malware Hybrid Analysis and Detection. University of Electronic Science and Technology (2021). <https://doi.org/10.27005/d.cnki.gdzku.2021.002850>
3. Lu, J.: Research and Implementation of Automatic Detection Method for Android Malicious Applications. Beijing University of Posts and Telecommunications (2021). <https://doi.org/10.26969/d.cnki.gbydu.2021.001458>
4. Enck, W., Gilbert, P., Han, S., et al.: TaintDroid. *ACM Trans. Comput. Syst.* **32**(2), 1–29 (2014)
5. Andriatsimandefitra, R., Tong, V.V.T.: Detection and identification of android malware based on information flow monitoring. In: 2015 IEEE 2nd International Conference on Cyber Security and Cloud Computing (CSCloud), pp. 200–203. IEEE (2015)
6. Zaman, M., Siddiqui, T., Amin, M.R., et al.: Malware detection in Android by network traffic analysis. In: 2015 International Conference on Networking Systems and Security (NSysS), pp. 1–5. IEEE (2015)
7. Fen, D., Hongwei, L., Jie, F., et al.: Reverse analysis of APK program forensics on Android phones. *Criminal Technol.* **46**(04), 349–353 (2021). <https://doi.org/10.16467/j.1008-3650.2021.0090>
8. Google Project Hosting. Androguard. [9 Dec 2013]. <https://code.google.com/p/andro-guard>



A Police UAV System Based on Target Recognition

Zhenyu Qiu¹, Guangjun Liang^{1,2,3}(✉), Hongtian Du¹, Bohan Yan¹, Jiahao Peng¹,
and Zexin Ju¹

¹ Department of Computer Information and Cyber Security, Jiangsu Police Institute, Nanjing, China

lianggjun@126.com

² Engineering Research Center of Electronic Data Forensics Analysis, Nanjing, China

³ Key Laboratory of Digital Forensics, Department of Public Security of Jiangsu Province, Nanjing, China

Abstract. The As a kind of aircraft without carrying operators, unmanned aerial vehicle (UAV) has been rapidly developed in the civil field. It is widely used in police, urban management, agriculture, geology, meteorology, electric power, disaster relief and other industries. However, the current police UAV still has shortcomings in specific target recognition and tracking. Therefore, the police UAV equipped with target recognition technology is designed in this project to enhance its performance. The project also investigates the materials and structure of police UAV, and focuses on target recognition systems which use sensors and algorithms to identify, classify and track targets, providing support for autonomous navigation and surveillance of UAV.

Keywords: DJI Cellular · YOLO object detection · PID control algorithm · DroneKit-Python · UAV

1 Introduction

Unmanned aerial vehicle (UAV) is an aircraft that does not carry operators, is driven by power, can be reused, uses aerodynamic bearing to fly, can carry payloads, and can complete specified tasks under remote control or autonomous planning. In recent years, the civil UAV industry has developed rapidly [1, 2]. In the police, urban management, agriculture, geology, meteorology, electricity, emergency relief, video shooting and other industries has a wide range of applications. The associated members of the French LIST lab combine drones with smart cities, using the mobility, accessibility, autonomy, and many other advantages of drones to integrate them into tasks that allow difficult and complex tasks that cannot be accomplished by humans or other entities; Object detection and human pose recognition usually require high computing power and energy supply [3, 4]. UAV-assisted edge servers developed by the University of Ulsan in South Korea can be deployed near UAV scouts to provide computing services. Federal University of Maranean proposes a Multi-agent System Collaborative control collision Avoidance

Method Based on centralization and decentralization effects. A matrix called inverse Laplacian is proposed to control the agent when the UAV is on the collision path. Matrix adjustment occurs through the proportion relationship with the Laplacian matrix in the interaction graph between the agents. To avoid collisions [5].

Although unmanned aerial vehicle (UAV) has a wide range of applications, it is also distorted in various fields. Although there are many researches on UAV, and the current technology is becoming more and more mature, there are still huge shortcomings in the police use, and the related researches are relatively few. The police UAV design of this project is equipped with target recognition technology, which greatly improves the performance of the police UAV and plays a huge role in the identification and tracking of specific targets [6].

This project studies the material and structure of the body of the police UAV, discusses the more suitable material and structure of the police UAV, but the most in-depth research is in the target recognition of the police UAV. The UAV target recognition system can use a variety of sensors and algorithms to identify, classify and track the target. It provides support for autonomous navigation, target search, surveillance and strike of UAV, mainly including sensor systems, image processing algorithms and control systems.

2 Basic Architecture of Police UAV

2.1 The Composition of the Police UAV

Unmanned aerial vehicles (UAV) are unmanned aircraft in which the pilot does not fly on the aircraft like traditional aircraft, but transmits the flight segments and various operating procedures and equipment from a distance. The original purpose of studying UAV is to perform difficult tasks in war and reduce casualties. With the progress of science and technology, the application scenarios of police UAV are more and more extensive, and a variety of police UAV have played a huge role in solving cases [7, 8].

Generally speaking, the current UAV system on the market mainly includes the aircraft body, flight control system, power system, power system and so on. However, this component alone cannot realize some advanced functions required by the police. To achieve these functions, we need to rely on target recognition systems, holographic projection facilities, police loudspeakers, 4G image transmission module DJI Cellular and ground command center. In short, as shown in Fig. 1, the police UAV is composed of the UAV body, power system, 4G image transmission module DJI Cellular, sensor module, target recognition system and ground command center, that is, a police UAV system composed of hardware and software [9, 10].

2.1.1 Police Drone Fuselage

The fuselage of the UAV refers to the main body structure of the UAV. It is one of the important parts of the UAV and undertakes the function of fixing various equipment, loads and power systems.

There are many kinds of materials for UAV fuselage, common materials are carbon fiber composite, aluminum alloy, plastic, glass reinforced plastic, etc. Different materials have different characteristics, advantages and disadvantages, and the selection of

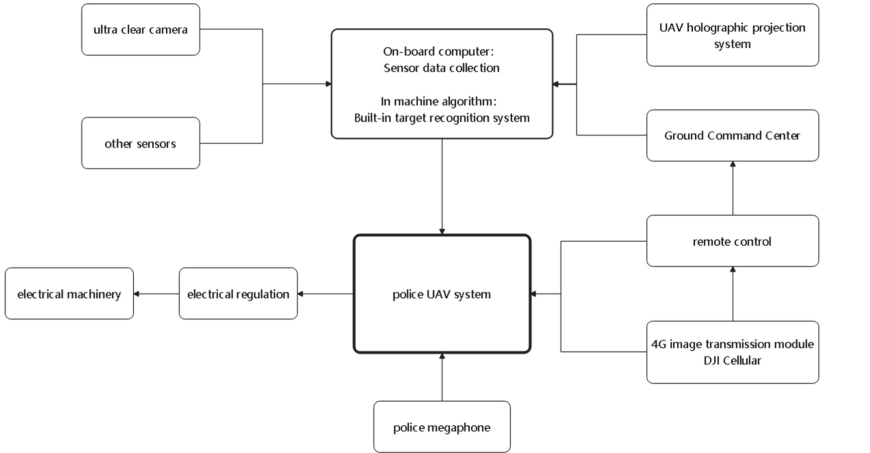


Fig. 1. The composition of the UAV

fuselage materials has an important impact on the performance, stability and durability of the UAV.

The size and weight of the UAV body are also very important factors. The size and weight of the fuselage will directly affect the flight performance, load capacity and flight time of the UAV. If the body weight is too heavy, it will affect the hovering ability and flight stability of the UAV, and if the body weight is too light, it may affect the carrying capacity and flight stability of the UAV.

2.1.2 Dynamical System

Including UAV flight control controller, battery, motor and electric regulation. UAV flight control system refers to the flight control system of UAV, which is mainly composed of hardware and software. The hardware part includes components such as sensors and actuators, while the software part includes algorithms such as attitude control, navigation control, and flight control. The UAV flight control system can communicate with the ground control station in real time through wireless communication and data link, and realize the functions of remote control and autonomous flight. The UAV on the market mainly use lithium polymer batteries as the main power, which have poor endurance and slow charging speed. To solve the above problems, we need to develop new UAV batteries with fast charging speed and strong endurance.

2.1.3 4G Image Transfer Module DJI Cellular

The traditional UAV connection control basically relies on the wireless network signal between the remote control and the UAV for control. The longer the distance is, the greater the possibility of signal loss. With the 4G module, the UAV can use the 4G network to fly freely in the area covered by the 4G network, and the mobile phone app can be used to control the UAV. At the same time, it can perform live video broadcast, or send back monitoring graphic information, and can realize UAV delivery within the

coverage of 4G network. As long as there is a 4G network, it can effectively control the UAV.

2.2 Sensor Module

It is mainly used to sense the environment around the UAV, but also can sense the UAV's own state.

- **Vision sensors:** cameras, infrared cameras, etc., for target recognition, drone navigation and shooting, etc.
- **Positioning sensors:** GPS, Inertial navigation systems (INS), etc., for positioning and navigation.
- **Environmental sensors:** barometers, thermometers, etc., for monitoring environmental changes and meteorological conditions, etc.

2.2.1 Target Recognition System

UAV target recognition system refers to a technical system carried on the UAV for identifying targets. UAV target recognition system can use a variety of sensors and algorithms to identify, classify and track targets, and provide support for autonomous navigation, target search, surveillance and strike of UAV.

The main components of UAV target recognition system include the following aspects:

– Sensor system

Sensor system is the core component of UAV target recognition system, which mainly includes infrared sensor, radar, optical sensor, etc. The sensor system can recognize, classify and track the target by obtaining the target's heat, electromagnetic wave, optical signal and other information.

Two, image processing algorithm.

Image processing algorithm refers to the realization of target recognition and tracking functions by processing and analyzing the image, signal and other information acquired by the sensor system. Image processing algorithms mainly include feature extraction, target detection, target tracking and other aspects, which need to have the characteristics of high speed and high precision to achieve fast and accurate target recognition and tracking.

– Control system

The control system refers to the control equipment on the UAV, which controls and manages the UAV target recognition system through software and hardware equipment. The control system needs to have the characteristics of high precision and high reliability to ensure that the UAV target recognition system can achieve high quality target recognition and tracking effect.

In general, UAV target recognition system is an advanced target recognition technology, which can quickly and accurately identify and track multiple types of targets, and provides important support and guarantee for UAV applications. In the future, with

the continuous development of technology and the expansion of application scenarios, UAV target recognition system will become an important direction and field in the field of UAV technology.

2.2.2 Round Command Center

Police UAV ground command center refers to a command center set up by the police for coordinating, managing and directing the use and operation of UAV in UAV monitoring and emergency response tasks. The ground command center of police UAV usually consists of a control room and related equipment, which is fast, efficient and safe.

2.3 Design of Target Recognition System for Police UAV

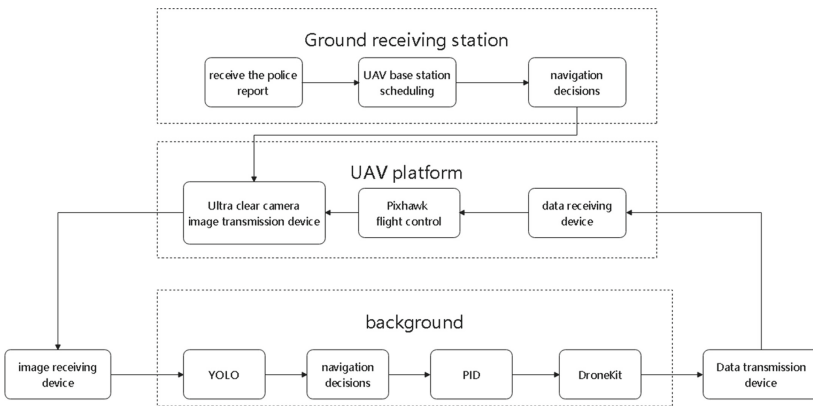


Fig. 2. The specific process of UAV target recognition

According to the above structure, we set up the following target recognition system for police UAV (Fig. 2):

- After receiving the police information, the ground receiving station decides the type and number of the UAV to be sent to the UAV base station for UAV scheduling according to the specific situation of the police information.
- Provide information according to the police situation, provide information for the UAV by navigation decision, and command the UAV to fly to the scene of the crime.
- Take a panoramic picture of the scene through the machine vision lens of the UAV, and then the picture is transmitted to the image collection device of the ground receiving station by the image transmission device.
- After the ground station obtains the picture, through the YOLO target detection algorithm, the regression problem of classification and target localization is combined by using anchor box, and a single CNN model is used to achieve end-to-end target detection, and the whole image is used as the input of the network. We directly regressed the position of the bounding box and its class in the output layer.

- According to the information identified by the YOLO algorithm, the ground receiving station makes decisions through GPS positioning, Beidou positioning, or the HD camera of the UAV to guide the UAV where to go next, or track a identified target.
- PID control algorithm is the most mature technology and the most widely used control algorithm in continuous system. According to the navigation decision, the ground receiving station uses PID control algorithm to accurately control the flight distance of the UAV or the distance between the UAV and the tracking target through three calculation methods: proportion, integral and differential.
- DroneKit-Python is a Python library for controlling drones. DroneKit provides an API for controlling the UAV. The code is independent of the flight controller, running on the onboard Companion Computer or other devices, and communicating with the flight control board via the MAVLink protocol via a serial port or wirelessly. The output results of navigation decision and PID control algorithm are converted into UAV control language through DroneKit, and transmitted to the UAV through the data transmission device.
- The UAV receives the control information from DroneKit through the data receiving device, and controls the position of the UAV through the Pixhawk flight control technology.
- The HD camera continues to take new photos, and continues to go through the above steps to constantly update the position information of the UAV, so that it can work more accurately and conveniently.

3 Specific Experimental Verification

This test uses cv2 module, numpy module, yolo v4 algorithm, and object-detection source code for experimental verification of target recognition, aiming to achieve continuous target recognition and tracking. Combined with the attached drawings and specific implementation methods, the target recognition function of this product is further explained in detail:

In order to realize the target recognition in the video, we first need to load the video clip, and obtain consecutive frames from the given video, so as to facilitate the subsequent processing of each frame of the image. In this step, we need to check whether there is a frame, if not, then exit the execution of this program. See Fig. 3 for the detailed code.

```
cap = cv2.VideoCapture("test.mp4")
od=ObjectDetection()
while True:
    ret, frame = cap.read()
    if not ret:
        break
```

Fig. 3. The video loading section demonstrates the code

At this point, you need to import the Python cv2 module and use the cvcapture function in the cv2 module to obtain the video.

If the above code can be realized (Fig. 3), it means that the video playback source can be successfully obtained. At this time, the next step is to obtain the image of each frame in the video. We first need to use the frame to display each frame of the video, and then we need to play the video frame by frame. In this test, we use a delay of 1ms for each frame. When the video is played frame by frame, we release the video file and close the window. See Fig. 4 for the detailed code.

```
cap = cv2.VideoCapture("los_angeles.mp4")

while True:
    ret, frame = cap.read()
    if not ret:
        break

    cv2.imshow("Frame", frame)

    key = cv2.waitKey(1)
    if key == 27:
        break

cap.release()
cv2.destroyAllWindows()
```

Fig. 4. The video is pulled out frame by frame

After testing, we were able to produce frames to render images from each Frame of the video source we tested on (Fig. 5).

Then, in order to realize the identification of ground vehicles, we need to use a rectangular box for each target to be identified. Now call the object detection function detect in object_detection.py, which is used to detect the information in the Frame to obtain the target information contained in each frame. When the information in the target is successfully obtained, we need to draw a rectangular box for the ground vehicle. (x, y, w, h) is used to identify the plane coordinates, width and height of the target, and then the rectangle method in the cv2 module is used to draw a matrix according to the box in the frame to identify the identified vehicle information. The specific code is shown in Fig. 6. Now the experiment is conducted to see whether the scheme is feasible.

After verification, we can observe in the Frame framework and conclude that this code successfully gets the object information contained in each frame and can use the rectangle to select the object. And it can keep tracking and positioning in the case of video. See Fig. 7 for details.

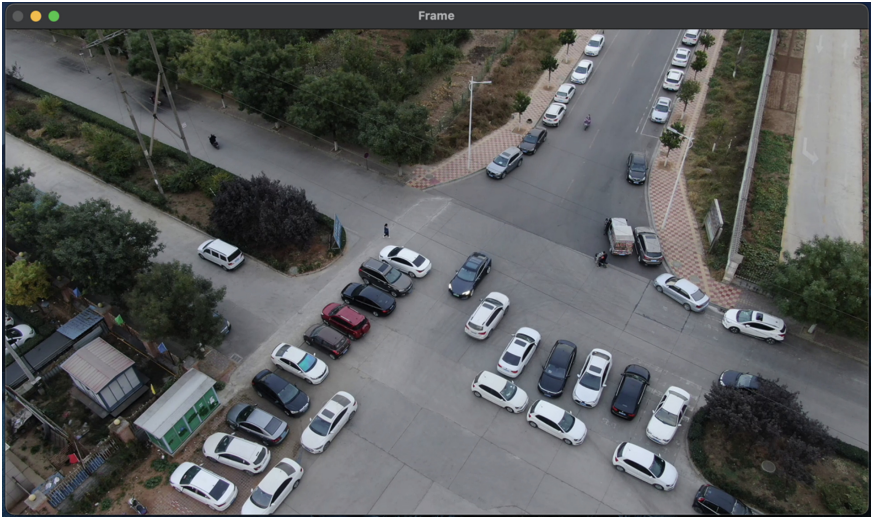


Fig. 5. The original scene

```
cap = cv2.VideoCapture("test.mp4")
od=ObjectDetection()
while True:
    ret, frame = cap.read()
    if not ret:
        break

    (class_ids, scores, boxes) = od.detect(frame)
    # class_id: what object is (car / track / person)
    # score: how confident is about the detection and
    # box: bounding box of the location of each object

    for box in boxes:
        print(box)
        (x, y, w, h) = box
        cv2.rectangle(frame, (x, y), (x + w, y + h), (0, 255, 0), 2)

    cv2.imshow("Frame", frame)

    key = cv2.waitKey(1)
    if key == 27:
        break
```

Fig. 6. Rectangle labeling for object recognition

After verification, we can observe in the Frame framework and conclude that this code successfully gets the object information contained in each frame and can use the rectangle to select the object. And it can keep tracking and positioning in the case of video. See Fig. 8 for details.



Fig. 7. Effect of rectangle labeling

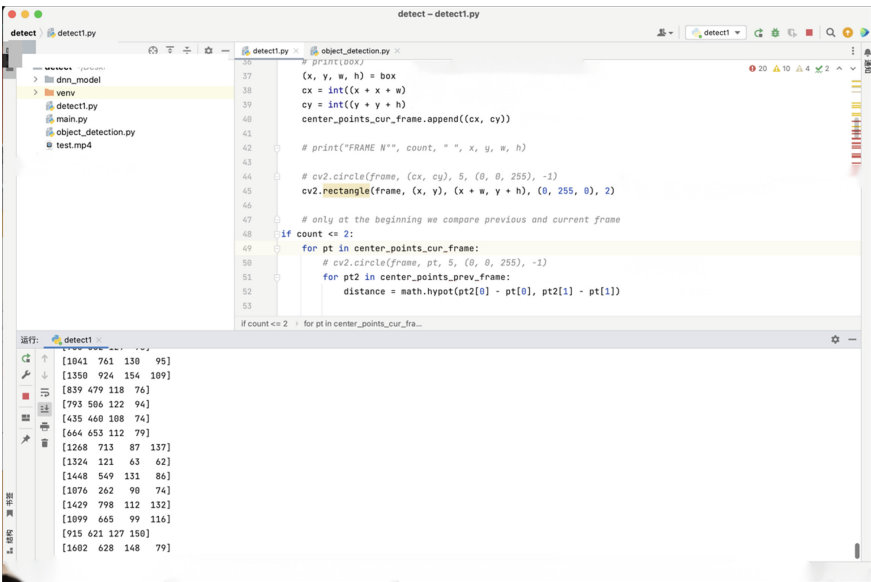


Fig. 8. Overall code presentation

4 Conclusion

The design of the police UAV improves the shortcomings of the current UAV application in the police, and the target recognition technology equipped with it can greatly improve the performance of the police UAV. It has a huge role in the identification of specific

targets and the tracking of specific targets. However, with the progress of society, there will be a variety of new security problems. How to use the police UAV to solve these security problems, and how to improve the accuracy of target recognition, and provide a continuous and stable endurance for the police UAV are all problems we need to consider in the future.

References

1. Chen, W., Jia, X., Zhu, X., et al.: Target detection in UAV aerial images based on DSM-YOLO v5. *Comput. Eng. Appl.*, 1–11 (2023)
2. Cheng, X., Cao, Y., Hu, Y., et al.: Small target detection method for UAV aerial images based on improved YOLO V5. *Flight Control and Detection* **6**(01), 80–85 (2023)
3. Bi, X.J.: Research on UAV identification algorithm based on YOLO in airport clearance area
4. Wu, J., Li, D.: UAV cluster formation control method research review. *Radio Commun. Technol.*, 1–7 (2023)
5. Ma, D., Chen, Y., Zhu, Z.: Multiple unmanned aerial vehicle (UAV) cooperative path planning for river inspection. *Control Eng.*, 1–8 (2023)
6. Huang, H., Fu, S.: YOLOv5 target recognition based wireless video tracking voice alarm system. *J. Mod. Inf. Technol.* **7**(9), 18–21 (2023)
7. Zhang, L.B.: Reliability analysis of UAV Measurement control and transmission system. *Wirel. Interconnection Technol.* **08**, 26–28 (2023)
8. Gao, L., Meng, H.-W., Wang, C., Guo, S.: Image data transmission technology for electric UAV swarm based on queue management. *Inf. Technol.* **01**, 56 + 52–61 (2023)
9. Wei, Y., Zhang, W.: Unmanned aerial vehicle (UAV) long life technology present situation and prospect. *J. New Ind.* **12**(11), 203–207 (2022)
10. Shi, X.: Unmanned Aerial Vehicle (UAV) Data Transmission Problem Research. Inner Mongolia University of Science and Technology (2022)



Design and Implementation of Public Opinion Safety Monitoring System from the Perspective of Rumor Tracing Governance

Wenjie Tang (✉), Lei Hong, Meng Yuan, and Yuyang Zheng

Jiangsu Police Institute, Nanjing 210000, China
1785660154@qq.com

Abstract. At present, with its special user anonymity mechanism and almost unlimited freedom of speech, Weibo has rapidly grown into a representative of mainstream social media platforms, but at the same time, it also gives criminals the opportunity to spread rumors. When some rumors aimed at inciting public emotions, selling anxiety and creating panic spread wildly on Weibo, it is easy to expand public opinion unprecedentedly, thus damaging the order of Internet environment and threatening national ideological security. Therefore, in view of this reality, on the basis of topic tracing, this paper establishes a rumor source tracing mechanism based on user influence and time label, so as to achieve rumor source suppression and root rumor refuting. This mechanism helps to stick to the important position of network information space created by emerging media, and guarantee the security of public opinion and ideology in the current vision of new media.

Keywords: Rumor tracing · User influence · PageRank · Sina Weibo

1 Introduction

WHO Director-General Tedros Adhanom Ghebreyesus said at a gathering of foreign policy and security experts in Munich, Germany, that “the one thing that spreads faster and easier than the virus” is the rumors. In response, the WHO has formed a “Myth-busters” team, which has teamed up with major social media platforms at home and abroad, including Facebook, Google, Tencent, Twitter, Tiktok, YouTube and so on, to combat COVID-19 rumors [1]. It can be seen from this that academic research on how to achieve timely guidance of public opinion and efficient response to public emergencies and comprehensive management of public opinion have gradually become a new hot spot.

This system trace the rumor originators based on the user node propagation chain in a timely manner, in order to effectively crack down on the source of rumors, block the spreading process, and help relevant departments to improve the way of handling public opinions of major events, thus dealing with the risks of online public opinions more efficiently and calmly.

2 Research Summary

Currently, the research field of online public opinion is mainly social science, which focuses on how the government improves control strategies. With the recent frequent occurrence of major public opinion events in China, the research on online public opinion monitoring has shown an increasing trend year by year. As the key to public opinion monitoring, tracing the source of transmission can timely lock the initial disseminators of rumors and give him severe punishment, which has great practical significance.

In view of the traceability technology, Yang Jing et al. [2] obtained the cascade set based on the forwarding relationship and topic correlation of Weibo, and determined the possible initiator of Weibo information by combining the user network and information cascade network. Then, the influence index and conformity index of nodes are iteratively calculated through text sentiment analysis and information cascade relation, and important participants in early Weibo information are extracted. Finally, the information source can be determined by combining the results of two traceability. In another article [3], he proposed a method of tracing the topic source of Weibo based on topic influence. By analyzing the correlation between user behavior and topic popularity change, quantitatively calculating the comprehensive influence of topic based on Weibo content and opinion leaders, and then the topic source set was found through the backtracking of similar topic sets. It solves the problem that Weibo hashtags are inconsistent with text content in actual situation. Although the above methods are based on practical problems and trace the source of the topic from multiple dimensions such as emotion analysis, user behavior and text content, the above two methods do not consider the characteristics of rumors themselves that are different from general information, and the key factor of the time label of Weibo publication has not been well reflected.

2.1 Characteristics of Rumor Originators

Zeng Ziming et al. [4] pointed out in their article that the total number of fans and followers of rumor spreaders is less. Similarly, the statistical results of Weibo rumors of Wuyue et al. [9] also clearly indicated that, compared with people who refute rumors, rumor originators often have a lower probability of being verified by Weibo and are often blocked users. In order to explore the reasons behind this phenomenon, this paper refers to the opinions put forward by Zhu Mengdie et al. [5] Since Weibo and other social media platforms adopt the anonymous mechanism, users do not need real-name authentication for posting, forwarding and commenting, which potentially increases the difficulty in tracing rumor information and gives rumormongers an opportunity to take advantage of this mechanism. In reality, rumor originators are different from the sources of general information transmission, influential users such as official certification tend not to publish false information at will, while rumor originators often present themselves as new users in order to avoid legal sanctions. This type of users are specifically manifested as less total number of fans and followers, less historical publication, high recent daily activity rate but low overall activity.

2.2 Time Label of Weibo Post

The specific posts of different users under the same topic have relatively specific time labels on Weibo and other social media platforms. Although in practical practice, the topic label of the source node may be inconsistent with the topic label presented in the actual transmission process, the time label is still an important influencing factor for rumor tracing after the source topic label of the Weibo is confirmed.

3 Research Methods

The tracing of rumors will be divided into two steps: source topic tracing and source user tracing (see Fig. 1 for details). The main purpose of source topic tracing is to solve the problem of inconsistency between Weibo content and topic labels in reality. In the process of spreading rumors, some illegal users often label the rumors as hot topics in order to attract attention, thereby increasing the exposure and browsing volume of this Weibo post. In addition, another common situation is that the initial topic tag of this rumor is not consistent with the version that has evolved and spread widely. Therefore, adopting a traceability method based on topic influence can effectively avoid the impact of this reality and achieve effective traceability of the initial topic tag.

On the basis of confirming the source topic, user traceability integrates PageRank algorithm and Hacker News sorting algorithm, and innovatively considers two key factors: user influence and specific time stamp. The PageRank algorithm model is essentially a node level computing technique for directed graphs, which is compatible with the communication relationship between Weibo users. However, in the actual traceability process, people subconsciously believe that the earlier the content is posted, the more likely it is to be the source node. In order to address the issue of the inability to integrate timestamp elements in the PageRank algorithm, this paper utilizes the improved Hacker News algorithm to effectively integrate and balance the impact of two key factors, Weibo posting time and Weibo user influence. This achieves the traceability of rumor originators under topic tracing.

3.1 Rumor Hashtag Traceability

Topic Influence Calculation The topic in this article refers to a seed event in the Weibo network and events directly related to it, which is specifically expressed as “#+event summary” on the platform. Topic influence is identified as the ability to trigger interactions (reposts, likes, and comments) from others. At present, the indicators to measure the popularity of topics are usually the number of reposts, likes, and comments. However, in actual situations, invalid comments, habitual reposts, and even hiring a large number of trolls to like can increase the value of the above indicators. Therefore, this article will quantitatively analyze the influence of topic content by using the attributes of forwarding number, reply number, content aggregation degree and topic category.

This algorithm first aims at the current rumor topic tag tp_0 , and uses the query expansion algorithm based on user query logs in the information retrieval field provided by Zhu Kunpeng et al. [10] to obtain the previous n topic tp_0 participants' respective historical

participation topics, and use TF-IDF distance to calculate the correlation between the topic tp_0 and the text content of each historical topic, and selects k related topics from it. For these k specific related topics tp , calculate the influence $In(tp)$ of the topic. The influence of the topic is mainly determined by the average influence of all microblogs in the topic, so the calculation formula is as follows:

$$In(tp) = \frac{1}{blg_{tp}} \sum_{j=1}^{blg_{tp}} \log \delta_j \times T(tp) \quad (3.1)$$

$$\delta_j = \alpha_j \times \beta_j \times \gamma_j \quad (3.2)$$

$$\gamma = \frac{\beta_e}{\beta} \quad (3.3)$$

Among them, blg_{tp} is the total number of microblogs under the topic, α_j is the number of reposts of the j th microblog tp under the topic, β_j is the number of replies to the j th microblog under the topic tp , and γ_j is the number of j th microblogs under the topic tp . Content aggregation, $T(tp)$ is the topic category impact index. The number of valid replies β_e is calculated using the TF-IDF distance, and the cosine function is used as a similarity function, and the number of replies with a correlation degree greater than 0.5 with the original topic is selected as the number of valid replies. In the existing research [2], the topic category impact index $T(tp)$ is calculated as follows:

$$T(tp) = \log \frac{\varepsilon}{\varepsilon_{tp}} \times \lambda_0(tp) \quad (3.4)$$

Among them, ε is the total number of posts on all microblogs in the network within one hour. By using the API interface of Sina Weibo, we can obtain the posting traffic of microblogs in some time periods, and realize the sample estimation of the total number of posts on microblogs in one hour. ε_{tp} is the total number of microblogs under the topic, and the initial weight of the $\lambda_0(tp)$ topic $\lambda_0(tp)$ depends on the category of the topic tp . Research [1] has shown that there are roughly six types of microblog topics: social hotspots, entertainment gossip, help mobilization, and marketing information, Leisure life, and health preservation, the corresponding relationship between each topic category and the initial weight is shown in Table 1.

Table 1. Correspondence table of topic category initial weight

Category	Topic initial weight
Leisure life/social hot spots	0.6
Entertainment gossip/help mobilization	0.3
Marketing information/health preservation	0.1

Through the above formula, the topic influence $In(tp)$ is comprehensively calculated. Literature [6] constructs a system dynamics model based on multiple realistic factors

such as government guidance and official news transparency, and conducts in-depth research on the trend of Internet public opinion dissemination, which is highly consistent with the actual spread of Weibo rumors. According to the research results, it can be inferred that the topics in the Weibo network, especially the hot topics, will experience a process of influence from small to large and then small, and the topic traceability research is actually under the condition of high popularity (Near the peak of the topic's influence) along the propagation path of the topic reverse upward search. Therefore, considering the actual dissemination trend of the topic, this paper selects the topic with the least influence among the related topics as the source topic, and repeats the above steps to realize the layer-by-layer backtracking of the topic.

Retrospective termination condition confirmation The Weibo network is a scale-free network. One literature [3] has proposed the concept of topic propagation threshold θ_c . Only when the effective propagation rate in the network is $\theta \geq \theta_c$ can the topic be effectively propagated in the Weibo. Based on the above research, this paper composes the topic propagation network of Weibo nodes and user nodes participating in the topic tp and their associated relationships, calculates the conditional probability of connections between nodes with different degrees and forms a probability matrix C_{kk} , and uses the reciprocal of the largest eigenvalue of the matrix as the propagation critical value θ_c . In the process of topic backtracking in the previous article, until the termination condition of the traceability recursion is met, that is, $\theta_k = \theta_c$, where θ_k is the effective propagation efficiency of the topic tp_c (taking the average degree of users in the network at this time), at this time topic of Weibo in the network The topic is the target source topic for source tracing.

3.2 The Source Tracing of the First Weibo Post of the Rumor

Measurement of User Influence The influence of Weibo users can usually be reflected by specific indicators such as the number of fans, the number of followers, and the number of works. However, simply considering the number of fans and the number of works without considering the quality of fans and works often cannot fully reflect a user's true Influence. Some users may not have a large fan audience, but they are in the follow-list of many officially certified Weibo accounts. The number of their works is not many, but each Weibo post has a very high fan interaction rate, so its real environment The user influence in is also extremely impressive. Considering the above practical problems comprehensively, this paper adopts the following formula:

$$P(i) = 0.5 \times S(i) + 0.5 \times F(i) \quad (3.5)$$

Among them, $P(i)$ is the comprehensive influence of user i , $S(i)$ is the influence of user i itself, which is mainly composed of user i 's daily activity rate $d(i)$, official certification degree $g(i)$ and user average interaction rate $h(i)$. $d(i)$ is used to calculate the average Weibo usage rate of user i in the past 30 days (used as posting, likes or comments, etc.), and $g(i)$ is whether user i is officially certified. To simplify the model calculation, the official certification is regarded as the result of this item is 1, otherwise it is 0. $h(i)$ is the ratio of user i 's average number of dynamic likes per Weibo posts to

the total number of Weibo users, and the calculation results of each user are normalized and processed into a unified measure. The final user's own influence $S(i)$ is the average of the three.

$F(i)$ is the influence of user i 's fans, which is mainly calculated based on the following PageRank algorithm:

$$PR(A) = (1 - d) + d \sum_{i=1}^n \frac{PR(P_i)}{C(P_i)} \quad (3.6)$$

Assume that the target user of the calculation is A , P_i is a certain fan who follows A , and $PR(A)$ represents the fan influence of user A . In the formula, N represents all fans of user A , $PR(P_i)$ represents the influence value of fan P_i linked to the requested user A , and $C(P_i)$ represents the number of outbound links of fan P_i . In order to simplify the calculation, this project regards $C(P_i)$ as the number of followers of P_i . In the actual development of the algorithm, in order to avoid the situation that the steady-state probability cannot be converged due to the dangling links between web pages, a damping coefficient $d(0 < d < 1)$ is introduced. This parameter is retained in this paper, and the value of d is 0.15. In the case of this paper, d represents the probability that a visitor sees the Weibo sent by user A through fan P_i . $1 - d$ represents the probability that a user randomly visits other users' web pages from the fan P_i 's Weibo web page. The calculated $PR(A)$ value is the required fan influence $F(i)$ of user A .

Source Node Possibility Calculation For the source topic obtained through source tracing, all Weibo information under this label is obtained. This part is based on the Hacker News sorting algorithm [8], and integrates time and user influence factors to achieve precise locking of rumor first-time users. Therefore, the source node often occupies the priority in time, so its corresponding time label is smaller than that of the forwarding node. In addition, based on the characteristics of first-time users in the context of rumors described earlier, this paper believes that compared with rumor reposters, users who spread rumors at the source usually appear to have lower user influence. The improved algorithm formula is as follows:

$$Score = \frac{\frac{1000}{P(A)^{0.1}} - 1}{(T + 2)^G} \quad (3.7)$$

Among them, $Score$ is the possibility that each Weibo under the source topic is the source node, T is the time interval between the posting time of this Weibo and the posting time of the first tweet of this topic, and G is the gravity factor, which is the power to pull down the ranking, according to Relevant literature is available in [6], and the value of G is 1.8. $P(A)$ is the comprehensive influence index of user A who posted the microblog calculated based on the PageRank algorithm. Among them, in order to make the calculation result more concise and clear, and balance the influence weight of user influence and time label on the final result, this paper multiplies the user's comprehensive influence $P(A)$ by 0.1 and then takes the inverse, and multiplies the result of this step by 1000, effectively making the final result The comprehensive influence calculation result is in the appropriate size range.

4 Experiment and Result Analysis

4.1 Experiment Procedure

This experiment uses the Sina Weibo platform as the source of experimental data. The research object is the entertainment news rumor “Jia Ling and Fan Cheng Cheng have a baby”, which was recently presented on Weibo hot search. This article monitors the entire process of the event from its start to end, and records the progress of related propagation through real-time crawlers. The data spans from 18:02 on March 13, 2023 to 00:00 on May 1, 2023. The data is manually annotated as a basis for later experimental verification. In the specific implementation, this article first selected the topic tags of the event in a highly discussed situation, and conducted three topic tracing based on this. The data involves a total of 16 topics (5 related topics/9 non related topics), obtaining 1154 original Weibo posts, 6857 forwarded Weibo posts, and 15562 Weibo comment responses. Based on the results of topic tracing, an impact analysis was conducted on 287 potential the first rumormonger under the source topic, ultimately confirming the source node of the rumor spreading under the tracing mechanism in this article. The specific process can be seen in Fig. 2.

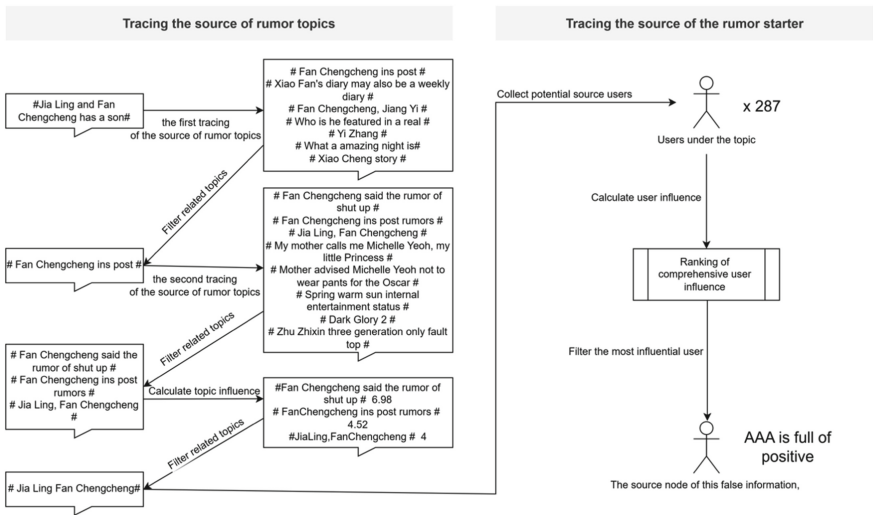


Fig. 2. Flow chart of rumor tracing experiment

4.2 Experimental Results and Analysis

Tracing the source of rumor topics This experiment selects the most popular related topic “# Fan Chengcheng ins #” of “Jia Ling and Fan Chengcheng have a baby” on Weibo as the starting point of topic tracing. According to the rumor topic traceability

mechanism proposed in this paper, a total of 332 Weibo data from March 14, 2023 to May 15, 2022, 7023) will be taken as the supporting data for the first traceability.

This topic is based on the 7 topics viewed by the top 3 posters under the time tag (Table 1 below), and select the related topic “#Fan Chengcheng ins post#”. Because the related topic is unique, there is no need to calculate the topic influence to confirm the source topic. Repeat the above operation, climb the topic discussion with the first post time under the topic “#Fan Chengcheng ins post#”, and screen the relevant Weibo topic tags, you can get 8 initial topic tags (Table 2 below), and further select 3 related topics. The results of this topic point to three possible source topics: “#Fan Chengcheng ins#” and “#Jia Ling Fan Chengcheng#”. Since the related topics are not unique, it is necessary to further calculate the topic influence of this result. The following calculation results (Table 3 below) can be obtained to confirm that “#Jia Ling Fan Chengcheng#” is the source topic of the second topic tracing. According to relevant calculation, it can be seen that the topic “#Jia Ling Fan Chengcheng#” has reached the condition for ending the topic traceability. Therefore, this article considers “#Jia Ling Fan Chengcheng#” as the final topic traceability result.

Table 2. Statistical table of topic traceability successively

Traceability meter	Topic name	Association
The first topic traceability results	#Fan Chengcheng ins post#	Related
	#Xiao Fan’s diary may also be a weekly diary#	Non-related
	#Fan Chengcheng, Jiang Yi#	Non-related
	#Who is he featured in a real#	Non-related
	#Yi Zhang#	Non-related
	#What a amazing night is#	Non-related
	#Xiao Cheng story#	Non-related
	The second topic traceability results	#Fan Chengcheng said the rumor of shut up#
#Fan Chengcheng ins post rumors#		Related
#Jia Ling Fan Chengcheng#		Related
#My mother calls me Michelle Yeoh, my little Princess#		Non-related
#Mother advised Michelle Yeoh not to wear pants for the Oscar#		Non-related
#Spring warm sun internal entertainment status#		Non-related
#Dark Glory 2#		Non-related
#Zhu Zhixin three generation only fault top#		Non-related

Table 3. Topic influence calculation results

Original posts	Retweets	Like	Total comments	Valid comments	Topic influence
#Fan Chengcheng said the rumor of shut up#	467	17334	3402	2975	6.98
#FanChengcheng ins post rumors#	28	1780	286	233	4.52
#Jia Ling Fan Chengcheng#	319	11033	1894	1567	4

Tracing the source of the rumor starter In the last part of the source topic labeled as “#Jia Ling Fan Chengcheng”, on the basis of the topic under 287 potential source user necessary data collection, according to each user weibo account information and specific post time, combined with the data into the previous formula, can get user comprehensive influence ranking (below Table 4), Although the user “AAA is full of positive” and the user “why what nickname” have the same comprehensive score, but the former is earlier, so the former is ranked as the first and the latter as the second. Accordingly, it can be confirmed that under the traceability mechanism of this paper, the user “AAA is full of positive” at 18:17 on March 13 is the source node of this rumor, which is highly consistent with the results of manual labeling and tracing mentioned above.

4.3 Model Evaluation and Validation

This paper repeats the above process, using the model of “#Dou Xiao and Xi Mengyao will become a family” 50 artificial annotation rumor source of sample test, and using the accuracy (see formula 4.1), to evaluate the model accuracy and reliability. blg_t is traceability results consistent with the number of results, blg_{ex} is the total number of test samples, part of the representative model traceability verification results in the following Table 5.

$$Precision = \frac{blg_t}{blg_{ex}} \quad (4.1)$$

In the total test samples, 36 sample traceability results are consistent with the annotation results, and the accuracy rate is about 0.72. Later, the study on the samples that failed to trace the source found that the main reason for the failure of the model was that the Weibo platform would delete the rumor source in time, so that the source could not be traced to the source node in the later stage. Apart from such cases, the accuracy rate of the model could be increased to 0.82.

5 Summary

The Cyberspace Administration of China said that the country will establish a good rumor traceability mechanism in the later stage [11]. The article aims to address the real weibo rumors frequency situation and national reality demand. Through the establishment of

Table 4. Calculation results of user influence under the topic “#Jia Ling Fan Chengcheng#”

User	Posting time	Retweet	Comment	Like	Certification	Followings	Followers	IP address	Total scoring	Ranking
AAA is full of positive	March 13, 18:17	0	12	5	No	224	48	Other	122.41	1
Why what nickname	March 13, 18:37	0	1	5	No	140	48	Jinan, Shandong	122.41	2
Ernest Soda water	March 13,19:58	0	1	2	No	11	4	Wuhan, Hubei	64.71	3
Why not ban mammoth	March 13, 19:11	0	1	2	No	101	31	Tianjin	64.63	4
Don't be lazy anymore	March 13, 19:45	0	1	0	No	736	3149	Shenzhen, Guangdong	61.85	5
There is shredded meat in the bowl	March 13, 18:02	36	426	5544	Yes	583	17946	Shanghai	60.76	6
= -Grain crisp	March 13, 20:10	0	3	0	No	117	84	Other	52.95	7
A new chapter forever	March 13, 20:22	0	1	0	No	384	110	Other	51.54	8
Not today 1	March 13, 21:49	0	1	0	No	569	2	Beijing	51.49	9
Electronic bug bug machine _	March 13, 20:41	0	1	0	No	305	133	Other	50.57	10

effective topic back and user back mechanism, this paper innovatively considering the user influence and the time tag of source node identification, a public opinion safety monitoring system for rumors tracing and governance on the Sina Weibo platform is designed. The platform can achieve effective rumors starting users, and punish criminals from the source rumors. At present, the system has been able to meet the current practical needs, but there is still room for progress. The overall function of the system is simple, and it is not possible to fully realize powerful rumors by rumors traceability solely. As a result, it is worth exploring how to turn rumor governance mode from later back to prior prevention, effectively inhibit increment, and clear stock and form the rumors collaborative prevention mechanism on the basis of multiple punishment source subject participation.

Table 5. Table of the validation results of the model test set

Subject	Source user from algorithm	Source user from manual	Consistence
# Dou Xiao and Xi Mengyao will eventually become a family #	Sweet bean variety	Sweet bean variety	Yes
#Positive students in two primary and secondary schools in Hangzhou#	Haifeng is here 2333	Haifeng is here 2333	Yes
#14 year old girl gets married#	Guinea pig video	Thousand orange spirit show	No
#Dig and dig Huang teacher close the studio reward#	Tarot constellation lucky Mun Meng	Tarot constellation lucky Mun Meng	Yes
#Net spread male star Hong Kong accompany birth#	Idle talk about fun	Idle talk about fun	Yes

Funding Statement. This study has been supported by The Innovation and Entrepreneurship Project Fund for College Students of Jiangsu Police Academy (Grant No. 202310329055Y). Jiangsu Provincial Public Security Department Project (Grant No. 2021KX010Z). The “qinglan Project” of Jiangsu Universities.

Conflicts of Interest. The authors declare that they have no conflicts of interest to report regarding the present study.

References

1. UN tackles ‘infodemic’ of misinformation and cybercrime in COVID-19 crisis. <https://www.un.org/en/un-coronavirus-communications-team/un-tackling-%E2%80%98infodemic%E2%80%99-misinformation-and-cybercrime-covid-19>
2. Yang, J., Zhou, X., Lin, Z., et al.: A-based control method for false information propagation. *J. Harbin Eng. Univ.* **37**(12), 1691–1697 (2016)
3. Jing, Y., Yuan, D., Jianpei, Z.: A method of Weibo topic traceability based on topic influence. *Small Microcomput. Syst.* **36**(09), 1939–1942 (2015)
4. Zeng, Z., Zhang, Y., Li, T.: Identification of potential rumor readers of public health emergencies with multi-feature fusion. *Lib. Inf. Work* **66**(13), 80–90. <https://doi.org/10.13266/j.issn.0252-3116.2022.13.008>
5. Zhu, M., Fu, S., Zheng, D., Li, Y.: Research on social media health rumors from the perspective of literature: characteristics, communication and governance. *Lib. Inf. Knowl.* **39**(05), 131–143. <https://doi.org/10.13366/j.dik.2022.05.131>
6. Deng, J., Zhang, X., Fu, Z., Wei, Q.: Research on emergency network public opinion communication based on system dynamics: take “Xiangshui explosion accident in Jiangsu province” as an example. *Data Anal. Knowl. Discov.* **4**(Z1), 110–121 (2020)

7. Liu, Y., Wang, L., Jia, Y., Li, Z., Gao, H.: Dynamic influence ranking algorithm based on musicians' social and personal information network. *Mathematics* **9**(20)
8. Stoddard, G.: Popularity and quality in social news aggregators: a study of Reddit and hacker news. *CoRR*,2015,abs/1501.07860
9. Wu, Y., Deng, M., Wen, X., Wang, M., Xiong, X.: Statistical analysis of dispelling rumors on Sina Weibo. *Complexity* **2020** (2020)
10. Kungpeng, Z., Fang, W.: Query extension method based on user log mining. *Comput. Appl. Softw.* **29**(06), 113–117 (2012)
11. CAC: A rumor traceability mechanism will be established. *Economic Guide* **03**, 7 (2022)



Design of Opinion Leader Identification System for Hot Public Opinion

Xinrong Cai^(✉), Lei Hong, Chengda Pan, and Yuxuan Han

Jiangsu Police Institute, Nanjing 210000, China
malenix@163.com

Abstract. Opinion leaders are key figures in the development of public opinion. Their published content and emotions often affect other users and dominate the development trend of the entire hot public opinion. The opinion leader identification system designed in this paper can automatically discover potential opinion leaders and predict hot public opinion. The system automatically acquires real-time hotspot public opinion data, uses the K-means++ algorithm to cluster users, finds existing opinion leaders, and then transfers the knowledge of opinion leader nodes to ordinary user nodes by constructing KTGNN, enriching the node representation of ordinary users, mining Identify potential opinion leaders among them. In the actual public opinion data test, the system can effectively discover potential opinion leaders and help predict hot public opinion trends.

Keywords: Internet public opinion · Opinion leader · Out-of-distribution learning · Graph neural network

1 Introduction

With the rapid development of the Internet, the influence of Internet hotspots and public opinion is increasing day by day. After many incidents have been fermented by online social platforms or forums, against the background of irrational Internet users, a relatively unified public opinion orientation will often be formed, which is somewhat instructive and deceptive to Internet users.

There is a class of key figures in the development of public opinion events, who often promote the development of events through their existing influence or highly provocative content. Such people are called opinion leaders. The content released by opinion leaders and the emotions they express are likely to lead a large number of audiences to participate in the fermentation of public opinion. Therefore, how to identify potential opinion leaders becomes the key to predicting the direction of public opinion.

In order to better predict the trend of public opinion and detect potential opinion leaders in hot public opinion in advance, this paper designs an opinion leader identification system for hot public opinion based on clustering algorithm and graph neural network. The system obtains hot public opinion on social media platforms in real time and digs out potential opinion leaders among them to build an opinion leader database.

2 Research Overview

The main methods of mining opinion leaders in social networks include index system construction, social network analysis, communication analysis, and data mining. This paper uses data mining methods to identify opinion leaders.

Scholar Xu Rui et al. proposed the identification of opinion leaders based on K-means and its derivative models. Identify by selecting the central node combined with the spatial distance [1]. In addition to K-means, Chen also proposed the OLMiner algorithm [2, 3] based on community detection, which selects more important communities by detecting communities and assigning indicators to identify opinion leaders. Some scholars also use machine learning methods to train opinion leader recognition models. Bizid et al. used supervised machine learning methods to train opinion leader recognition models in specific event topics [4]. Aiming at the multidimensional characteristics of users and the multimodal characteristics of user content in social networks, Liu et al. proposed a modal consistent MCHDE model to identify opinion leaders on social media platforms [5].

This paper explores potential opinion leaders in social networks, and mainly studies the graph learning task of OOD nodes on graphs. OOD graph learning was first proposed in OpenWGL [6] proposed by M. Wu, S. Pan and X. Zhu. In OOD graph learning, the most classic method is the unsupervised ODIN [7] proposed by Hsu Y C et al., which needs to train an additional model specially designed for OOD detection. Yu Song and Donglin Wang proposed OODGAT [8], which improved the accuracy of classification results, but lost its good classification effect when the distribution of graph data is too large.

3 The Main Design Concept and Technology of the System

As shown in Fig. 1, the system designed in this paper has four modules. The data acquisition module deploys regular crawlers on the server to obtain real-time data to ensure data effectiveness; the personnel relationship network module uses K-means++ to determine personnel categories; potential opinion leaders The mining module uses KTGNN to transfer the knowledge of opinion leaders to silent users, and discovers potential opinion leaders according to user characteristics; finally, the opinion leaders and their characteristics are stored in the database and displayed through the front end.

3.1 Real-Time Acquisition of Public Opinion Information

Among the major public opinion platforms, Twitter has become an important platform for hot public opinion brewing and dissemination due to its large number of users, high user activity, and strong user interaction. Therefore, the system designed in this paper takes the data of the Twitter platform as an example to discover potential opinion leaders in hot public opinion.

The system deploys the Twitter crawler program based on the Twint framework on the server, sets a fixed running time, obtains real-time hot public opinion, and performs

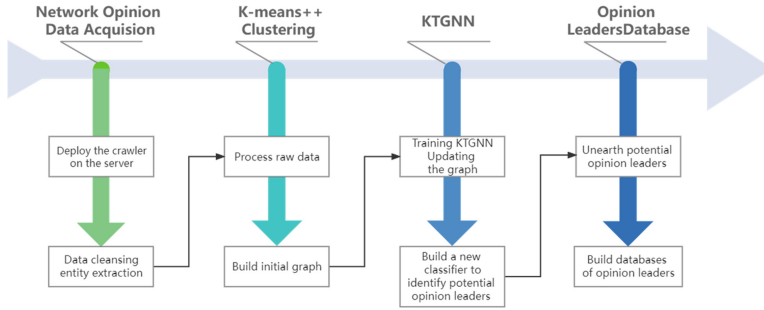


Fig. 1. System technical architecture diagram

necessary data cleaning after crawling, imports the data into the database, and realizes the acquisition of hot public opinion data [9].

The Twint framework is a framework that can use Twitter's search syntax to obtain relevant tweet data and user information through keywords and specific users. Due to the change of the Twitter framework, the Twitter API is facing a large-scale shutdown, and the data collection based on the Twint framework can not call the Twitter data through the Twitter API to ensure the stability of data acquisition.

3.2 Construction of Public Opinion Personnel Relationship Graph Based on K-Means++

In real life, among the user groups who follow the same public opinion, some users play a leading role in the development of public opinion and belong to opinion leaders, while some users are silent users. When dividing users, this paper finds that there is a high degree of similarity among user groups who follow the same public opinion. They all pay attention to similar topics and users, publish and repost similar tweets, have small behavioral differences, concentrated features, and high feature dimensions [10]. Under the high-latitude feature, it is difficult for ordinary classification models to find the boundary between the two types of nodes, but the K-means++ algorithm can efficiently cluster the two types of users through the calculation of the spatial distance [11]. Therefore, this paper uses the K-means++ algorithm to classify the users.

Choice of Distance Measure Formula

In terms of feature selection, this article selects features such as whether there is official certification, number of fans, recent activity, and whether the basic information is complete or not as K-means++ reference features. Since the Euclidean distance simply considers the numerical distance and ignores the dependence between data features, and there is a strong correlation and dependence between the features selected in this paper, this paper chooses the Mahalanobis distance to calculate the sample distance [12].

The Mahalanobis distance considers that there is a connection between features and introduces covariance. For a multivariate vector $x = (x_1, x_2, \dots, x_p)^T$, Let its mean be $\mu = (\mu_1, \mu_2, \dots, \mu_p)^T$, The Mahalanobis distance is defined as [13]:

$$D_M(x) = \sqrt{(x - \mu)^T \Sigma^{-1} (x - \mu)} \quad (1)$$

Selection of the Initial Centroid

Since there is a clear distinction between opinion leaders and ordinary users in the data of public opinion personnel, this paper selects the initial centroid by calculating the probability [14], and the overall process is as follows:

The collection of public opinion users is $S = \{X_1, X_2, \dots, X_n\}$.

1. Randomly pick an object from the set as the initial centroid.
2. Calculate the shortest distance between each object in the sample and the existing cluster center $D(X_i)$, namely

$$D(X_i) = \min\{dis(X_i, c_k)\} \quad (2)$$

3. Calculate the probability that each object in the sample becomes the next cluster center $P(x)$, and select the one with the highest probability as the next centroid.

$$P(x) = \frac{D(X_i)^2}{\sum_{X \in S} D(X_i)^2} \quad (3)$$

3.3 Identification of Potential Opinion Leaders Based on KTGNN

In the personnel relationship diagram, nodes V_S represent ordinary users, and nodes V_L represent opinion leaders. In order to better model the personnel relationship graph, the system constructs KTGNN [15]. The model learns more effective node representations for V_S nodes by transferring the rich knowledge in V_L nodes to V_S nodes, and completes the node labels of V_S nodes. The key modules of KTGNN are as follows.

Cross-domain Node Feature Completion Module

In the personnel relationship diagram, compared with V_L nodes, V_S nodes may have some unobservable dimensional features. Considering that the model needs to transmit messages between V_L and V_S nodes, the missing features of V_S nodes should be completed first. In this paper, a cross-domain feature completion module is designed. Considering the difference in the feature distribution of V_L and V_S nodes, the features based on V_L nodes are diffused in the graph, and the missing attributes of V_S nodes are iteratively completed.

First, the system divides the nodes in the personnel relationship graph into two parts V_S and V_L . At first V_L is the same as the V_L and V_S is the same as the V_S . The domain adaptive node feature completion module uses the complete attribute feature completion of V_L to perform multiple iterations to complete the knowledge transfer to

V_S . The unobservable feature \widehat{f}_i^u that V_S node i supplements with respect to V_L node j is shown in formula (4):

$$\widehat{f}_i^u = \sum_{v_j \in \{V_L \cap N(v_i)\}} \widehat{f}_j^u \cdot (f_i^o M^S, f_j^o M^L) \tag{4}$$

Among them, f is the feature matrix of the node, f^o is the observable feature, and f^u is the unobservable feature. \widehat{f}_j^u is to calibrate the variable of \widehat{f}_i^u by eliminating the effect of domain differences, as shown in formula (5):

$$\widehat{f}_j^u = f_j^u - (L - S) \cdot M^{ou} \cdot \text{Tanh}([f_j^u || (L - S) \cdot M^{ou}] \cdot M^S) \tag{5}$$

Among them, M^{ou} is the product of the observable feature and the unobservable feature parameter matrix, and M^S is the self-multiplication of the observable feature parameter matrix. $L - S$ is to represent the domain difference between V_L nodes and V_S nodes according to their observable attributes, which is used to learn unobservable domain differences. L and S are the expectations of observable features for V_L nodes, and V_S nodes, respectively.

Domain Adaptive Graph Messaging Module

On the personnel relationship graph, this paper divides the direction of message transfer into two types: intra-domain message transfer and inter-domain message transfer. This step also considers the difference in domain distribution between V_L nodes and V_S nodes, and designs a domain-adaptive graph message transfer module, correct the characteristics of the source node into the domain distribution of the target node and then pass it to the target node. The domain-adaptive graph messaging module considers two factors: adaptive domain discriminative features and neighbor importance.

Given edge $e_{i,j} = (i, j)$, the function of the a layer KTGNN to update the node representation is shown in (6):

$$h_i^a = U(h_i^{a-1}, MP(h_i^{a-1}, h_j^{a-1})) \tag{6}$$

The message passing function is shown in formula (7):

$$MP_{i \rightarrow j} = \widetilde{h}_i \cdot N(\widetilde{h}_i, h_j) \tag{7}$$

where \widetilde{h}_i is the source node feature calibrated by the domain difference factor, and N is the neighbor importance function, as shown in formulas (8) and (9).

$$N(\widetilde{h}_i, h_j) = ELU([\widetilde{h}_i \cdot M^j || h_j \cdot M^j]) \tag{8}$$

$$\widetilde{h}_i = h_i + \Delta_{i,j} \tag{9}$$

$\Delta_{i,j}$ is a distribution offset variable, which is only used for cross-domain message transmission, and the value of $\Delta_{i,j}$ in the domain is 0. The value of $\Delta_{i,j}$ outside the field is shown in formula (10):

$$\Delta_{i,j} = (-1)^{\psi(j)} \cdot \text{Tanh}(h_i || L - S) \cdot (L - S) \tag{10}$$

$$\psi(i) = \begin{cases} 1 & i \in VL \\ 0 & i \in VS \end{cases} \quad (11)$$

Using this module, the source node is calibrated to the domain of the target node at the time of message passing, thus attenuating the noisy information caused by nodes distributed outside the domain.

Domain Transferable Classifier

Since all the operations of the previous model were carried out while retaining the domain differences between V_L nodes and V_S nodes, the vector representations of different nodes still belong to two very different feature distributions, and V_S nodes only have a small number of training labels. In order to solve the underfitting problem caused by cheap domain and the overfitting problem caused by the scarcity of V_S node labels, the system designs a new domain transferable classifier which reclassifies V_S nodes by transferring knowledge from V_L nodes.

The new domain transferable classifier aims to transfer model parameters so that optimized source domain classifier parameters can be transferred onto target domain classifiers. It consists of three modules, which are source domain classifier CLF^{src} , target domain classifier CLF^{tgt} and cross-domain transformation module $Trans^{src \rightarrow tgt}$.

To predict V_S nodes which are the majority of nodes, the source domain classifier is trained with a V_L node set and the target domain classifier is trained with a V_S node set. The cross-domain conversion module is used to convert the original source domain classifier to the newly generated target domain classifier. The cross-domain transfer module takes the parameters of the source domain classifier as input and generates the parameters of the new target domain classifier.

Both source domain classifier $CLF^{src} = \text{sigmoid}(M^{src})$ and target domain classifier $CLF^{tgt} = \text{sigmoid}(M^{tgt})$ are fully connected layers activated by the Sigmoid function.

The cross-domain conversion module $Trans^{src \rightarrow tgt}(M^{src}) = MLP(M^{src})$ is implemented by a multi-layer perceptron with multi-layer nonlinear transformation, which can change the shape of the classification boundary of the classifier and generate a new classifier \widehat{CLF}^{tgt} .

The loss function for optimizing \widehat{CLF}^{tgt} and the whole model can be divided into two parts: KL divergence loss \mathcal{L}^{KL} and classification loss \mathcal{L}^{CLF} .

\mathcal{L}^{KL} is proposed to enable knowledge transfer between source and target domains by constraining the discriminant boundary of newly generated CLF^{tgt} to positions between CLF^{src} and CLF^{tgt} :

$$\mathcal{L}^{KL} = KL(\mathcal{P}^{src}, \widehat{\mathcal{P}}^{src}) + KL(\mathcal{P}^{tgt}, \widehat{\mathcal{P}}^{tgt}) \quad (12)$$

where \mathcal{P}^{src} is the output probability of CLF^{src} , \mathcal{P}^{tgt} is the output probability of CLF^{tgt} , and both $\widehat{\mathcal{P}}^{src} \in W^L$ and $\widehat{\mathcal{P}}^{tgt} \in W^S$ are the output probability of \widehat{CLF}^{tgt} . Classification loss \mathcal{L}^{CLF} is shown in formula (13):

$$\mathcal{L}^{CLF} = BCE(Lb^L, \widehat{Lb}_{CLS^{src}}^L) + BCE(Lb^S, \widehat{Lb}_{CLS^{tgt}}^S) + BCE(Lb^S, \widehat{Lb}_{CLS^{tgt}}^S) \quad (13)$$

Among them, Lb is the label of the node, and BCE is the binary cross entropy loss function, as shown in the formula (14):

$$BCE(Lb, \widehat{Lb}, N) = \frac{1}{N} \sum_{i=1}^N Lb_i \cdot \log \widehat{Lb}_i + (1 - Lb) \cdot \log(1 - \widehat{Lb}_i) \quad (14)$$

Combined with the adjustment of hyperparameters, the final loss function \mathcal{L} is shown in formula (15):

$$\mathcal{L}^{CLF} = 1.06 \cdot \mathcal{L}^{KL} + 0.97 \mathcal{L}^{dist} \quad (15)$$

4 System Function Design and Implementation

4.1 Construction and Analysis Module of Public Opinion Personnel Relationship Graph

Construction of Personnel Relationship Diagram

After the system uses K-means++ to group users into opinion leaders and ordinary users, it constructs a personnel relationship graph through the attention relationship among users, providing a data basis for the subsequent discovery of potential opinion leaders.

Node Feature Completion

In the first iteration, the module transmits the attribute characteristics of V_L nodes to V_S nodes with incomplete attribute characteristics, making them V_S nodes with complete attributes, and removes them from the V_S set. In the second round of iteration, the V_S nodes with complete attributes transmit messages to other V_S nodes directly connected with incomplete attributes to generate new V_S nodes with complete attributes, and the iterative process continues until the algorithm converges. The process is shown in Fig. 2.

The system finally obtains V_L nodes and V_S nodes that retain domain differences and have complete attribute characteristics, forming new graph data.

Node Classification Based on Transferable Classifiers

The system classifies the graph data nodes with node feature completion by constructing a transferable classifier, and its good fitting results are proved by experiments. The expected effect of domain transferable classifiers on graph data is shown in Fig. 3.

The system stores the classified results into the opinion leader database and records the relevant features after completion.

4.2 Local Interactive Module

Based on the B/S architecture, the local interaction module realizes the analysis function of opinion leaders and provides an interactive interface for users. The website uses Vue and SpringBoot to establish a front-end and back-end separation architecture, set up the back-end service and database on one server, and deploy the front-end web page on

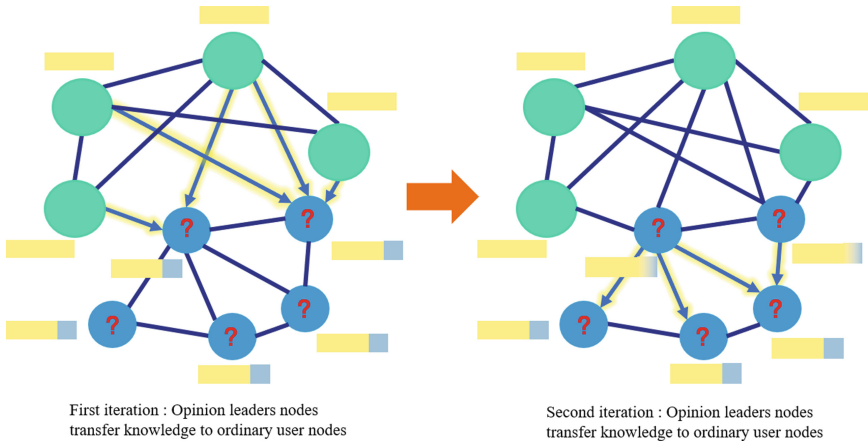


Fig. 2. Iterative process of domain adaptive node feature completion module

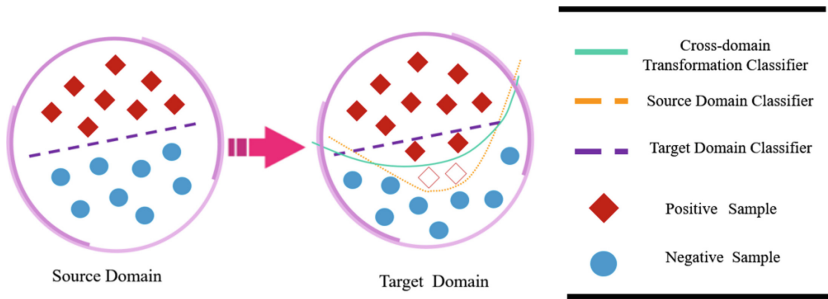


Fig. 3. Expected effect of domain transferable classifier

another server to achieve partial performance improvement. Due to the separation of the front and back ends and the characteristics of only transmitting data through the interface, most of the front-end pages have no loopholes, which greatly improves the security of the system and data. The front end of the system uses the Vue framework, which mainly processes and renders data through JS, and the back end uses the SpringBoot framework to implement the API interface of data and functions for the front end to call. The algorithm model used by the system is deployed on the back-end server to realize the function of identifying opinion leaders. The front-end page is mainly implemented using the Element UI component library. In the drop-down box at the top of the page, you can select some key events that have been automatically analyzed by the system. After clicking to select an event, the results will be displayed in the three tables below, that is, the characteristics of opinion leaders and opinion leader accounts related to the main event based on the analysis of a large number of existing events and people.

5 Experiments and Analysis

5.1 K-Means++ Clustering Experiment

This paper uses traditional K-means, hierarchical clustering, DBSCAN and other algorithms to conduct comparative experiments with K-means++ algorithm, uses the same data set of public opinion personnel for clustering experiment, and uses the silhouette coefficient to judge the accuracy of the algorithm.

5.2 KTGNN Experiment

The experiment divides the data set into training set/validation set/test set at a ratio of 60%/20%/20%, trains the model through the data of the training set, uses the validation set to evaluate the trained model, and evaluates the trained model according to the validation set. The effect obtained by adjusting the model. The project team finally selects the model with the best effect on the verification set and uses the test set to experiment and confirm the final effect.

The experiment takes F1-Score and AUC, two classic evaluation model indicators as the final evaluation standard of the experiment.

Four representative graph learning models were selected for the experiment as reference models, namely GCN, GAT, PinSAGE, and OODGAT. Considering that other models cannot directly handle graphs with incomplete feature nodes, in order to make a fair comparison with the method used by KTGNN, we tested these baseline models with some heuristic feature completion strategies and selected the best effect for each comparison model complement strategy. Based on the above criteria, each model is tested 10 times, and different random number seeds are selected each time, and the average value and standard deviation of each model experiment result are obtained, and this is used as a basis to measure the experimental effect of the KTGNN model.

5.3 Analysis of Experiment Results

Cluster Experiment Results

Table 1. Comparison of clustering experiments

Clustering algorithm	Silhouette coefficient
K-means++	0.312
K-means	0.258
DBSCAN	0.234
Hierarchical clustering	0.272

It can be seen from Table 1 that in the public opinion personnel data with a high degree of correlation between features, the clustering result of K-means++ has the highest

silhouette coefficient, and the clustering effect is the best, and because the initial centroid selection is more reasonable, K-means++ The algorithm is superior to other algorithms in convergence speed and is suitable for fast clustering in the system.

Graph Data Classification Experiment Results

Table 2. Experiment results of different models

Model evaluation standard	GCN	GAT	PinSAGE	ODDGAT	KTGNN
F1-score	68.28 ± 0.84%	71.93 ± 1.65%	73.29 ± 0.98%	75.73 ± 1.91%	82.79 ± 1.14%
AUC	57.54 ± 1.61%	64.22 ± 1.41%	80.04 ± 1.64%	82.31 ± 1.73%	84.21 ± 0.90%

The experimental results are shown in Table 2. Since most of the heuristic completion strategies ignore the problem of large differences in data distribution, KTGNN has achieved better results on the two classic indicators and can better solve the problem. The impact of the significant difference in the distribution of system data and the sparseness of small node labels is analyzed.

Funding Statement. This study has been supported by The Innovation and Entrepreneurship Project Fund for College Students of Jiangsu Police Academy (Grant No. 202310329015Z). Jiangsu Provincial Public Security Department Project (Grant No. 2021KX010Z).The “qinglan Project” of Jiangsu Universities.

Conflicts of Interest. The authors declare that they have no conflicts of interest to report regarding the present study.

References

1. Xu, R., Li, Y., Zi, Q., et al.: Research on opinion leader identification model in virtual learning community. *Comput. Technol. Dev.* **30**(05), 56–60 (2020)
2. Chen, Y.C., Chen, Y.H., Hsu, C.H., et al.: Mining opinion leaders in big social network. In: 2017 IEEE 31st International Conference on Advanced Information Networking and Applications (AINA), pp. 1012–1018. IEEE (2017)
3. Chen, Y.-C.: A novel algorithm for mining opinion leaders in social networks. *World Wide Web* **22**(3), 1279–1295 (2018). <https://doi.org/10.1007/s11280-018-0586-x>
4. Bizid, I., Nayef, N., Boursier, P., Faiz, S., Morcos, J.: Prominent users detection during specific events by learning on- and off-topic features of user activities. In: Proceedings of the 2015 IEEE/ACM International Conference on Advances in Social Networks Analysis and Mining 2015 (ASONAM'15), pp. 500–503. Association for Computing Machinery, New York, NY, USA (2015). <https://doi.org/10.1145/2808797.2809411>
5. Liu, Y., et al.: Identifying key opinion leaders in social media via modality-consistent harmonized discriminant embedding. *IEEE Trans. Cybern.* **50**, 717–728 (2020)

6. Wu, M., Pan, S., Zhu, X.: OpenWGL: Open-world graph learning. In: 2020 IEEE International Conference on Data Mining (ICDM), Sorrento, Italy, pp. 681–690. <https://doi.org/10.1109/ICDM50108.2020.00077>
7. Hsu, Y.C., Shen, Y., Jin, H., et al.: Generalized odin: detecting out-of-distribution image without learning from out-of-distribution data. In: Proceedings of the IEEE/CVF Conference on Computer Vision and Pattern Recognition, pp. 10951–10960 (2020)
8. Yu, S., Donglin, W.: Learning on graphs with out-of-distribution nodes. In: Proceedings of the 28th ACM SIGKDD Conference on Knowledge Discovery and Data Mining (KDD'22), pp. 1635–1645. Association for Computing Machinery, New York, NY, USA (2022). <https://doi.org/10.1145/3534678.3539457>
9. Liu, B.: Design and implementation of overseas public opinion analysis system based on Twitter big data processing. *Comput. Knowl. Technol.* **16**(27), 30–33+42. <https://doi.org/10.14004/j.cnki.ckt.2020.2859>
10. Yang, G., Kou, J., Yan, S., et al.: User classification based on improved kmeans++ algorithm and impact analysis of electricity price policy. *Electr. Power Demand Side Manage.* **22**(03), 57–62 (2020)
11. Feiyan, G.: Personalized classification of online learning users based on K-means clustering. *Digital Media Res.* **38**(12), 35–39 (2021)
12. Mao, J.: Research on classification of mobile 5G mobile phone users based on improved K-means clustering algorithm. *Netw. Secur. Technol. Appl.* **242**(02), 40–41 (2021)
13. Wang, X., Jia, R., Sun, Y.: Research on the construction of data-driven social network public opinion polarized group portraits. *Inf. Documentation Serv.* **42**(06), 21–30 (2021)
14. Liu, H., Liu, X., Yao, S., et al.: Statistical analysis of information dissemination characteristics of online social users based on public opinion portraits. *Mod. Inf.* **39**(09), 64–73 (2019)
15. Bi, W., Xu, B., Sun, X., Xu, L., Shen, H., Cheng, X.: Predicting the silent majority on graphs: knowledge transferable graph neural network (2023). <https://doi.org/10.48550/arXiv.2302.00873>



Research on Deep Clustering Based on Image Data

Xuanyu Li^{1,2}, Houqun Yang^{1,2(✉)}, Xiaoying Zhang^{1,2}, Dangui Yang^{1,2},
Jianqiang Huang³, and Lin Gan⁴

¹ College of Computer Science and Technology, Hainan University, Haikou 570228, Hainan, China

yhq@hainanu.edu.cn

² Haikou Key Laboratory of Deep Learning and Big Data Application Technology, Hainan University, Haikou 570228, Hainan, China

³ China Telecom (Hainan Branch), Haikou, Hainan, China

⁴ Elmore Family School of Computer and Electrical Engineering, Purdue University, West Lafayette, USA

Abstract. Clustering is an important branch of unsupervised tasks, aiming at mining deeper relationships and patterns in data. The quality of feature representation based on image datasets often determines the upper limit of clustering tasks. In recent years, the application of deep learning in deep clustering representation learning module has learned better feature representation, which gradually overcomes the limitation of traditional shallow clustering facing high-dimensional unstructured data. Deep clustering has become a popular research direction in the unsupervised field in recent years, and high clustering performance has been obtained in the continuous deepening research. The existing deep clustering research is mainly oriented to various fields of artificial intelligence, including natural language processing (NLP), speech recognition (ASR), computer vision (CV), etc. We take the field of computer vision as the entry point, analyze and study the research progress of deep clustering in computer vision (CV), and deconstruct the deep clustering model into two parts: a detailed classification of the feature extraction module from the perspective of network model architecture, while the data space of clustering is used as the entry point to divide the clustering module, and discuss the deep clustering. Finally, we analyze the datasets and evaluation metrics commonly used in experiments to study deep clustering architectures in computer vision.

Keywords: Deep clustering · Computer vision (CV) · Image data · Feature extraction

1 Introduction

Clustering is a fundamental topic in data mining and its main purpose is to mine the hidden valuable information in data. The essence of clustering is to divide a large amount of unlabeled data into multiple clusters, each containing similar instances of data samples,

while different instances are divided into different clusters [1]. The feature representation capability of the original data largely determines the upper limit of the clustering performance, and obtaining more robust feature representations from the original data is a key part of improving the clustering performance. With the continuous research and development of deep learning, deep learning shows the potential to obtain potential feature representations from the original data space, realizing the mapping of the original nonlinear samples to the low-dimensional representations, deep learning combined with the traditional clustering task, deep clustering has gradually evolved into an important branch of deep clustering in unsupervised domains.

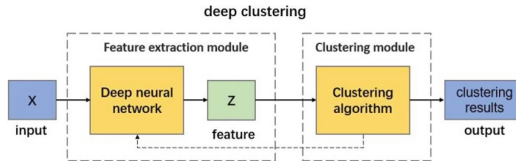


Fig. 1. General flow chart of deep clustering

Deep clustering can be divided into a feature extraction module and a clustering module according to the overall architecture, see Fig. 1. The feature extraction module performs nonlinear mapping on the original image data samples through deep neural networks to mine the hidden dependencies and obtain features with robustness. The clustering module then processes the clustering algorithm on the low-dimensional feature representations, divides the data samples of different categories into different clusters, and obtains the final clustering results. Some deep clustering models use the clustering results obtained from the pre-training as the supervised information, and iteratively optimize and train the model parameters in a self-supervised form.

Our study will take the feature extraction module and clustering module as the entry point to explore the research progress of deep clustering from the perspectives of model training strategy, clustering space of data, etc. See Fig. 2. In this paper, we take the deep neural network used in the feature extraction module as the starting point and broadly divide it into four branches: Based on AutoEncoder (AE), Based on Generative Adversarial Networks (GAN), Based on Contrastive Learning, and Based on Deep Neural Networks(DNN). According to the clustering space where the clustering task is located, this paper divides and analyzes the global data structure and local data structure respectively, and divides the deep clustering into three perspectives: model-based clustering methods, similarity-based clustering methods and subspace clustering.

2 Network Model of Feature Extraction Module

The feature extraction module of deep neural networks is introduced in deep clustering, aiming at pre-processing the original data to learn better features implicitly oriented to the clustering task, not only to overcome the limitations of manual feature extraction at the same time, but also to achieve the mapping of the original nonlinear samples into a low-dimensional representation.

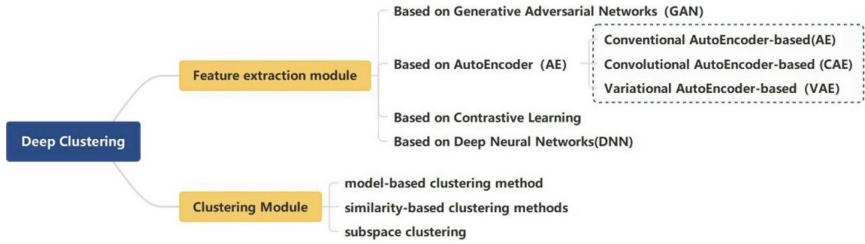


Fig. 2. Various architectures of current deep clustering

2.1 Based on Auto-Encoder (AE)

AutoEncoder is an important branch of neural networks, which consists of two parts: encoder and decoder, where the input of the encoder and the output of the decoder are the same, and its purpose is to perform representation learning in reconstructing the input data. We classify the deep clustering based on AutoEncoder into three categories: Conventional AutoEncoder-based, Convolutional AutoEncoder-based, and Variational AutoEncoder-based.

Conventional AutoEncoder-based (AE) DEC [2] acts as a deep embedded clustering using Student's t distribution to measure the similarity between the embedded points in the embedded feature space obtained by AutoEncoder and the initialized cluster centers. The KL scatter is used as a loss function to measure the soft assignment results from the target distribution, and finally using momentum stochastic gradient descent (SGD) to optimize the neural network parameters and the k -means clustering centers of AutoEncoder. IDEC [3] introduces undercomplete AutoEncoder, integrating the reconstruction loss and clustering loss of the selfencoder, thus improving the mechanism to improve the preservation of the local feature structure. DEC-DA [4], on the other hand, introduces data augmentation based on the DEC architecture.

Convolutional AutoEncoder-based (CAE) Convolutional AutoEncoder introduces convolutional layer and pooling operation on the basis of Conventional AutoEncoder, and replaces the fully connected layer in Conventional AutoEncoder with the convolutional layer in convolutional neural network, and the introduced convolutional layer can further preserve the local special features of the data, i.e., it improves the invariance of keeping features. Instead of DEC [2], DCEC [5] used SAE with a convolutional self-encoder, where the encoder uses a convolutional layer for special extraction and a convolutional transposition layer in the decoder for data reconstruction, preserving more localized features in the data-generating space, and [6] showed that the representation learning of the convolutional self-encoder is well suited for subspace clustering tasks. Subsequently.

Variational AutoEncoder-based (VAE) based Variational AutoEncoder is essentially a generative model that adds variance and mean computation while retaining the basic architecture of encoder and decoder, and complex high-dimensional image data are processed by the encoder to generate the hidden variable Z , which needs to be as close to the prior distribution (Gaussian distribution) as possible, and the decoder then maps the hidden variable of simple distribution to the image of complex distribution space. VaDE [7] uses KL scatter to further fit the GMM prior and posterior distributions, and the decoder will reconstruct the hidden variables obtained by randomly selecting in

each of the posterior distributions, and select stochastic gradient variational Bayesian and re-parameterization techniques for co-optimization. DC-VAE [8] introduces mutual information maximization on the feature representation learned by the variational self-encoder, in order to avoid soft clustering assignment errors that lead to representation learning.

The different classes of AutoEncoder in the feature extraction module each have their own advantages and limitations. The conventional AutoEncoder-based deep clustering has the strongest generalization ability and the widest application scenarios, but the clustering performance on high-dimensional unstructured data needs to be further enhanced, the convolutional AutoEncoder-based deep clustering retains more local feature information structure in the original data space, but the application scenarios have relative limitations, and the robustness of variational AutoEncoder-based deep clustering for extracting potential features is strong, but the computational effort of time complexity and space complexity is larger and more suitable for large-scale data scenarios. The performance of AutoEncoder deep clustering architecture cannot be further improved because it does not take much account of the potential dependencies between the data and decouples its original data structure inefficiently.

2.2 Based on Generative Adversarial Networks (GAN)

Deep clustering based on Generative Adversarial Networks (GAN) belongs to the unsupervised field of generative methods, Generative Adversarial Networks GAN contains two main components - the generator G and its nature as a binary classification model of the discriminator D , the generator and the discriminator alternately training process in order to achieve the purpose of constantly improving the training accuracy.

ClusterGAN [9] used GAN for the first time to accomplish clustering in a mapped latent feature space, and DASC introduces a generative DSC architecture based on Adversarial Network GANs, which performs adversarial learning on the raw data to produce better similarity matrices and feature representations for subspace clustering. Deep Subspace Clustering for Dual Adversarial Generative Networks DSC-DAG [10] is a model consisting of an encoder, two decoders, a fully connected layer and two discriminators. Its main task is to perform deep subspace clustering, Self-supervised Deep Subspace Clustering for Adversarial Generative Networks S2DSC-AG model [10] uses classifiers in the original input space and antagonistically trains the decoders of the generator to explore the self-supervised information using collaborative learning between the binary indicator matrix A_c and the subspace assignment indicator matrix γ_p . [11] is based on deep clustering with CGAN and is applied in remote sensing.

Deep clustering based on Generative Adversarial Networks can be better fitted to the distribution of the original data space by adversarial learning, and a more robust feature representation oriented to clustering is learned in the feature extraction phase.

2.3 Based on Contrastive Learning

Contrastive learning is one of the representative methods in the field of self-supervised learning, where higher-order feature representations are learned by constructing pairs of positive and negative samples. The basic paradigm of contrast learning consists of an

agent task and an objective function, which is essentially an artificially set rule defining positive and negative samples as supervised signals to train the model.

The end-to-end online clustering architecture CC [12], which proposes instance-level and cluster-level comparative learning, i.e., instance-level comparative learning (i.e., in the row space) and cluster-level comparative learning (i.e., in the column space) in the obtained feature subspace, GCC [13] retains the instance and cluster levels of the instance and cluster spaces in CC [12], introduces a graph structure based on graph structure, and proposes graph-based comparative learning and comparative loss of the graph Laplacian operator. [14] proposed contrast multi-view clustering where low-level features, high-level features and semantic labels of each view are learned in a fusion-free manner for contrast learning to learn a common semantics for all views. [15] proposed Graph Embedded Contrastive Multimodal Clustering Network (GECMC) to learn multimodal representations through graph structure, and pseudo-label guided contrast loss.

Compared to the AutoEncoder, the contrastive learning in the feature representation module improves the accuracy of feature representation by comparing the similarity between samples. Contrastive learning is also better for the clustering task in terms of its generalization ability, which reduces the problem of overfitting to some extent, but its generalization ability is affected by the data distribution. Deep clustering based on contrastive learning is computationally intensive when training models, and its time and space complexity is high especially when facing large-scale datasets or complex models.

2.4 Based on Deep Neural Networks (DNN)

Deep neural networks are algorithms derived from simulated neural systems, deep neural networks have good adaptability and portability, strong learning ability, and are commonly used for dimensionality reduction or clustering, but when the parameters of the neural network are increased in large numbers, it is easy to overfitting, falling into local optimization and other problems. In this section, from the perspective of deep clustering model training, deep clustering based on deep neural networks is divided into alternating training model and synchronous training model.

Alternating training. The essence of the alternating training strategy in deep clustering models is that the clustering information (e.g., pseudo-labels) generated by the model in pre-training the clustering results at the same time is transformed into an iterative update of the deep network in a self-supervised manner. JULE [16] iteratively optimizes the convolutional neural network weight parameters with the category labels obtained in the clustering task and performs the clustering task performed forward and the feature learning performed backward in a recursive manner. However, deep clustering models based on deep neural networks using the alternating training strategy are sensitive to network initialization and prone to error transmission, which needs to be solved by applying specific schemes (e.g., pre-training), and the model is constrained in large-scale data scenarios due to its alternating mechanism.

Simultaneous training. Representation learning and clustering tasks are performed simultaneously. SCAN [17] decouples the representation learning and clustering tasks, and the two-stage decoupling strategy used overcomes the limitation of relying on network initialization and thus learning low-level features in the end-to-end model. IIC [18] uses the invariant information of the mutual information to complete the clustering

task and prevents clustering degradation. Deep clustering based on deep neural networks using simultaneous training mechanism performs the representation learning task and clustering task simultaneously, which overcomes the limitation of alternating mechanism in large-scale data sets and can simultaneously perform deep clustering tasks in large-scale data application scenarios, but requires a global guidance scheme to improve the confidence of the task.

3 Clustering Module

Clustering is one of the extremely important researches in the field of unsupervised learning, and in the field of computer vision, processing unlabeled image data shows great potential. Deep clustering is accomplished by deep learning (e.g., self-encoder, generative adversarial networks, etc.) to learn feature representations, which are combined with downstream traditional clustering tasks such as K-means, spectral clustering, subspace clustering, and other clustering tasks to collaborate on deep clustering. We take the perspective of data space for clustering as the entry point, and introduce three perspectives from model-based clustering methods, similarity-based clustering methods and subspace clustering.

3.1 Model-Based Clustering Method

Model-based approaches fit the data through specific models to analyze the embedded structure, patterns or distributional features of the data, focusing on the global spatial structure of the data for learning, Gaussian mixture models, K-means, etc. are representative of model-based approaches. In [19], the deep clustering architecture based on dimensionality reduction (DR) and K-means, the dimensionality reduction phase uses DNN to nonlinearly map the original high-dimensional data into a feature space suitable for K-means execution, and then completes K-means clustering, the framework focuses on “K-means-friendly” The global data space structure is also experimentally verified the effectiveness of the algorithm.

3.2 Similarity-Based Clustering Methods

Similarity-based methods judge whether data samples belong to the same class by judging the similarity between them, usually based on the similarity between data samples, and similarity-based methods focus on the local structure of the data. Spectral clustering is a representative method based on similarity, which essentially decomposes features from the similarity matrix constructed from the original data, determines the similarity through the similarity matrix, and then performs dimensionality reduction after removing redundant features. [20] proposed a similarity-based deep clustering method for supervised optimization clustering task, which uses deep nonlinearity and hierarchical structure for representation learning to reflect the similarity relationship between samples in a better way, thus can make the similarity-based clustering task on generalization ability.

Similarity-based clustering algorithms can be divided into distance measure and non-distance similarity measure, where the distance between samples is used as a criterion to evaluate the similarity between samples, and non-distance similarity metrics are used to measure the similarity between samples using non-distance evaluation metrics.

Distance similarity measure In the calculation of distance similarity, the data are often transformed into the form of vectors and the distance between two vectors is calculated using the formula, where a smaller distance represents a higher similarity between the two samples and a larger distance represents a lower similarity between the two samples. The distance similarity measure is often used as Minkowski distance, Manhattan distance, Euclidean distance, Chebyshev distance, and Marxian distance.

The distance similarity measure is the most common method to measure the similarity in clustered samples, but there are limitations in using the distance measure to measure the similarity between samples, because the distribution of data points in the original data space where high-dimensional data is located is often sparse, so the distance measure cannot build clusters in high-dimensional data samples.

Non-distance similarity measure use criteria other than distance to measure the similarity between data samples, and the commonly used criteria for non-distance similarity measures are the cosine of the angle, jaccard similarity, and Pearson correlation coefficient.

3.3 Subspace Clustering

Subspace clustering is an effective clustering method for high-dimensional data, and the premise of subspace clustering tasks is based on the assumption that the data are located in the concatenation of all subspaces, and find the characteristic subspaces for all data to which they belong. The clustering process of subspace clustering can be roughly divided into two steps, the first step is to calculate the affinity between data points using the similarity measure strategy, and the affinity obtained is constructed into an affinity matrix, and the second step is to perform normalized cut or spectral clustering based on the affinity matrix, see Fig. 3.

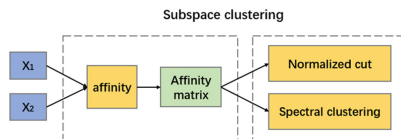


Fig. 3. Subspace clustering process

An important branch of research in depth-based subspace clustering is the study of deep subspace clustering based on DSC [21], O DSC [22], DASC [23], S2ConvSCN [24], TDSC-net [6, 25] and other models are the entry point for further research on DSC, see Table 1, DSC. The self-expression property (any data can be represented linearly by all other data in the same subspace to which it belongs) is introduced after the encoder of AE by using a self-expression layer that maps the original data nonlinearly to a potential

nonlinear subspace, and the network parameters are constructed as affinity matrices to complete the spectral clustering.

Model-based clustering methods have better generalization ability than similarity-based methods, and are easier to deal with out-of-sample data, but model-based clustering methods also have the limitation of being able to deal with complex and high-dimensional unstructured data. Similarity-based clustering methods have relatively high computational complexity and are difficult to handle for large data sets, but their scalability performance is better. Deep subspace clustering can discover different levels of clusters through different subspaces, and its architecture often adopts self-expression layer which leads to secondary temporal complexity and spatial complexity, and often cannot be well understood in the face of the original data structure and its feature expression will be affected accordingly.

Table 1. Summary of DSC-based methods

Methods	Base DSC	Characteristics
DSC [21]		Introduce the self-expression property, introduce the self-expression layer between the encoding and decoding layers of the self-encoder, and construct the affinity matrix using the weight parameters of the self-expression layer
O DSC [22]	Yes	Introduction of overcomplete network based on DSC
DASC [23]	Yes	Introducing generative adversarial networks on top of DSC
S2ConvSCN [24]	Yes	Introducing a dual self-monitoring mechanism supervision model on the basis of DSC
TDSC-net [25]	Yes	Introducing a triple mechanism based on the DSC
DLSC [6]	Yes	Introducing a fully connected layer and its transposition in the self-expression layer based on the DSC

4 Experiments and Data Sets

The selection of deep clustering models in computer vision varies for different scale types of datasets, and experiments based on different scale types of deep clustering can demonstrate the superiority of their clustering performance and their research value. We focus on the analysis of experimental datasets and experimental evaluation metrics for deep clustering in the field of computer vision (CV) and discuss possible implications.

4.1 Dataset

The commonly used image datasets for deep clustering models in computer vision roughly contain MNIST, STL10, USPS, Fashion, COIL-20, COIL-100, Yale B, ORL, CIFAR-10. In recent years, deep clustering models have shown good performance in small and medium-sized datasets, and some research has been focused on deep However, it is still challenging to improve the performance of deep clustering on large datasets.

4.2 Evaluation Indicators

Four evaluation metrics are commonly used in deep clustering experiments in computer vision: contrast clustering accuracy (ACC), standard mutual information (NMI), purity (PUR), and adjusted Rand index (ARI). Contrastive clustering accuracy (ACC) is used to indicate percentage of the overall sample that is assigned to the correct clustering label; The standard mutual information (NMI) is used to indicate the degree of association between two random data samples; The purity (PUR) is used to indicate the percentage of samples correctly predicted as that cluster within a cluster; The adjusted Rand index (ARI) is used to indicate the similarity between the sample clustering categories and the true categories.

5 Conclusion

We analyze in detail the research progress of deep clustering based on the field of computer vision (CV). In this paper, we divide deep clustering as a whole into two modules: feature extraction and clustering, introduce the feature extraction module from the perspectives of network architecture, constraints, and training strategies, respectively, and classify and introduce the deep clustering task from the perspective of the spatial structure of the data. In recent years, the research of deep clustering has achieved great success, in the future work, the improvement of generalization ability and scalability of deep clustering model is one of the concerns, how deep clustering model should be handled when facing the data beyond the training samples as well as large-scale data clusters. When deep clustering models are oriented to real-world clustering scenarios, especially large-scale image data scenarios, the applicability of the models and their temporal and spatial complexity often yield unsatisfactory training results, and how to get better clustering performance is still a non-negligible issue.

Acknowledgment. This research was funded by Hainan Province Science and Technology Special Fund (Grant No. ZDYF2022GXJS228; ZDYF2021GXJS006); Haikou Science and Technology Plan Project (2022-007;2022-015;2020-056).

References

1. Moses, C., et al.: Clustering with qualitative information. *J. Comput. Syst. Sci.* (2005)
2. Xie, J., Girshick, R., Farhadi, A.: Unsupervised deep embedding for clustering analysis. *Comput. Sci.* (2015)
3. Guo, X., Long, G., Liu, X., et al.: Improved deep embedded clustering with local structure preservation (2017)
4. Guo, X., Zhu, E., Liu, X., et al.: Deep Embedded Clustering with Data Augmentation. *ACM* (2018)
5. Guo, X., Liu, X., Zhu, E., et al.: Deep clustering with convolutional autoencoders. In: *International Conference on Neural Information Processing*. Springer, Cham (2017)
6. Kheirandishfard, M., Zohrizadeh, F., Kamangar, F.: Deep low-rank subspace clustering. In: *2020 IEEE/CVF Conference on Computer Vision and Pattern Recognition Workshops (CVPRW)*. IEEE (2020)

7. Jiang, Z., Zheng, Y., Tan, H., et al.: Variational Deep Embedding: An Unsupervised and Generative Approach to Clustering (2016)
8. Xu, C., Dai, Y., Lin, R., et al.: Deep clustering by maximizing mutual information in variational auto-encoder. *Knowl.-Based Syst.* **205**, 106260 (2020)
9. Mukherjee, S., Asnani, H., Lin, E., et al.: ClusterGAN: Latent Space Clustering in Generative Adversarial Networks. *arXiv* (2018)
10. Lin, Y., Fan, W., Bouguila, N.: Clustering analysis via deep generative models with mixture models. *IEEE Trans. Neural Netw. Learn. Syst.* (2020)
11. Hu, J., et al.: A robust deep learning approach for the quantitative characterization and clustering of peach tree crowns based on UAV images. *IEEE Trans. Geosci. Remote Sens.* **60**, 1–13, Art no. 4408613 (2022). <https://doi.org/10.1109/TGRS.2022.3142288>
12. Peng, D., Zhou, J.T., Hu, P., et al.: Contrastive Clustering (2020)
13. Zhong, H., et al.: Graph contrastive clustering. In: 2021 IEEE/CVF International Conference on Computer Vision (ICCV), Montreal, QC, Canada, pp. 9204–9213. <https://doi.org/10.1109/ICCV48922.2021.00909>
14. Xu, J., Tang, H., Ren, Y., Peng, L., Zhu, X., He, L.: Multi-level feature learning for contrastive multi-view clustering. In: 2022 IEEE/CVF Conference on Computer Vision and Pattern Recognition (CVPR), New Orleans, LA, USA, pp. 16030–16039 (2022). <https://doi.org/10.1109/CVPR52688.2022.01558>
15. Xia, W., Wang, T., Gao, Q., Yang, M., Gao, X.: Graph embedding contrastive multi-modal representation learning for clustering. *IEEE Trans. Image Process.* **32**, 1170–1183 (2023). <https://doi.org/10.1109/TIP.2023.3240863>
16. Yang, J., Parikh, D., Batra, D.: Joint unsuper-vised learning of deep representations and image clusters. In: Proceedings of the IEEE Conference on Computer Vision and Pattern Recognition (CVPR), pp. 5147–5156 (2016)
17. Van Gansbeke, W., Vandenhende, S., Georgoulis, S., Proesmans, M., Van Gool, L.: Learning to classify images without labels. *arXiv preprint arXiv:2005.12320* (2020)
18. Ji, X., Henriques, J.F., Vedaldi, A.: Invariant Information Clustering for Unsupervised Image Classification and Segmentation (2018)
19. Yang, B., Fu, X., Sidiropoulos, N.D., et al.: Towards K-means-friendly spaces: simultaneous deep learning and clustering (2016)
20. Li, X., Chen, Z., Poon, L.K.M., et al.: Learning latent superstructures in variational autoencoders for deep multidimensional clustering. In: Proceedings of the 7th International Conference on Learning Representations (ICLR) (2019)
21. Pan, J., Tong, Z., Li, H., et al.: Deep Subspace Clustering Networks (2017)
22. Valanarasu, J., Patel, V.: Overcomplete Deep Subspace Clustering Networks. *arXiv preprint arXiv:2011.08306* (2020)
23. Zhou, P., Hou, Y., Feng, J.: Deep adversarial subspace clustering. In: 2018 IEEE/CVF Conference on Computer Vision and Pattern Recognition. IEEE (2018)
24. Zhang, J., Li, C., You, C., Qi, X., Zhang, H., Guo, J., Lin, Z.: Self-supervised convolutional subspace clustering network. In: Proceedings of IEEE Conference on Computer Vision and Pattern Recognition, pp. 5473–5482 (2019)
25. Zhang, Z., Li, X., Zhang, H., Yang, Y., Yan, S., Wang, M.: Triplet deep subspace clustering via self-supervised data augmentation. In: 2021 IEEE International Conference on Data Mining (ICDM), Auckland, New Zealand, pp. 946–955 (2021). <https://doi.org/10.1109/ICDM51629.2021.00106>



Exploring Cross-Chain Mechanisms and Projects in Blockchain: A Comprehensive Summary

Yong Zhou¹, Yirui Bai¹, Zixuan Liu¹, Haoyu Gao^{1,2}, Chao Liu³, and Hong Lei^{1,4}(✉)

¹ School of Cyberspace Security, Hainan University, Haikou 570228, China
zixuan@hainanu.edu.cn, leiluono1@163.com

² Oxford-Hainan Blockchain Research Institute, Chengmai 571924, China

³ The Blockhouse Technology Limited, Oxford OX2 6XJ, UK
liuchao@tbtl.com

⁴ SSC Holding Company Ltd, Chengmai 571924, China

Abstract. The blockchain world is getting more and more complicated in other fields besides supply chain, finance and judicial evidence as a result of the technology's rapid development, making "communication" between various blockchains crucial. However, there are obvious differences between various blockchains in terms of the storage structure, security mechanism, and consensus mechanism. The lack of an interconnection mechanism between inter-blockchain results in high barriers to communication between blockchains, which is detrimental to the healthy development of blockchain technology and the blockchain application ecology. The utilization of cross-chain technology in blockchain is a significant technical approach to achieving blockchain interconnectivity, enhancing blockchain interoperability, and scalability. The paper examines the present state of cross-chain technology development and applications. In the context of the present state of blockchain cross-chain technology research, the five cross-chain mechanisms are analyzed and compared, along with the mainstream cross-chain projects, which are described and compared. This article's comparative study reveals that cross-chain technology still has some weaknesses, including execution efficiency, security, and interoperability. Additionally this paper presents two primary challenges, the validation and reversal of cross-chain transaction and security in cross-chain. Further technical advancements and standardization may be required to secure the cross-chain ecosystem. Lastly, this paper summarizes blockchain cross-chain technology and points out future directions.

Keywords: Cross-chain · Interoperability · Blockchain

1 Introduction

Blockchain technology has come a long way since the middle of 2008, when Satoshi Nakamoto proposed the concept of Bitcoin [1] in his publication. Since then, Ethereum [2] has been created by Vitalik, followed by NFT [3], DeFi [4], Metaverse [5], and

other cryptocurrencies. As blockchain technology has matured, it is also becoming more complicated across a range of industries. The application of blockchain technology has led to an increase in high throughput, low latency, and other performance requirements, but single-chain architecture technology is constrained by consensus speed, low throughput, and other restrictions, making it unfriendly to the commercial scenario of blockchain. Additionally, blockchain is presently in a closed state due to the different storage structures and consensus mechanisms. The absence of an interconnection mechanism has severely affected the healthy growth of blockchain technology and blockchain application ecology.

Some asset exchanges on some relatively secluded blockchains depend on neutralized exchanges, putting such asset transactions at risk of centralization. Cross-chain technology can interact between various blockchains in order to exchange assets, sync information, share applications, and carry out additional functions. This can amplify the influence of a single chain on the blockchain system and maximize individual interconnection [6], opening up more possibilities for blockchain technology. Currently, the mainstream cross-chain mechanisms are notary mechanisms, sidechain, relay, hash lock, and distributed key control. These mechanisms have been implemented in many cross-chain platforms, including the Lightning Network [7], Wecross [8], Bitxhub [9], and other projects.

The sections of this article are arranged as follows: The first section discusses the necessity and feasibility of cross-chains. The five cross-chain mechanisms are discussed and compared in Sect. 2. Section 3 describes several mainstream cross-chain projects, analyzing their respective principles and application scenarios, and comparing their performance. In Sect. 4, validation and reversal of cross-chain transactions and security are presented as the primary challenges, along with some ideas for where the effort might lead in the future. Finally the summary of the research content of the full text has been completed in Sect. 5.

2 Cross-Chain Mechanisms

2.1 The Development of Cross-Chain Technology

Cross-chain technology has gone through the phases of single-chain development, single-chain expansion, relay, and cross-chain platform and interconnection in four stages [10, 11]. When blockchain technology first emerged in 2008, it was primarily concerned with the study and optimization of single chains as shown in Fig. 1, which attracted a lot of academic research [12]. At the BitcoinTalk forum in 2013, Herliby proposed the atomic exchange [13], which states that cross-chain transactions only have two possible outcomes—success or failure—and that there is no third possible intermediate state. The cross-chain prototype then materialized, and the following year, the Block-Stream team proposed the sidechain that transfers assets using anchoring technology [14].

The hash-locked cross-chain mechanism used by the Lightning Network eliminates the single-chain bottleneck, makes it possible for the exchange of assets between different blockchains and maintains the atomicity of transactions. Cross-chain technology has gradually advanced into the stage of succeeding platforms due to the advancement

of blockchain technology. Gavin Wood and Vitalik have both proposed the idea of cross-chain technology and have cited products like Polkadot [15] and Ethereum 2.0 as examples. Currently, cross-chain platforms like Wecross add decentralized identity [16, 17] and other technologies, improve the security of user authentication, realize cross-chain interoperability, and increase the efficiency of the blockchain. These platforms realize the interconnection between chains, breaking information island between them.

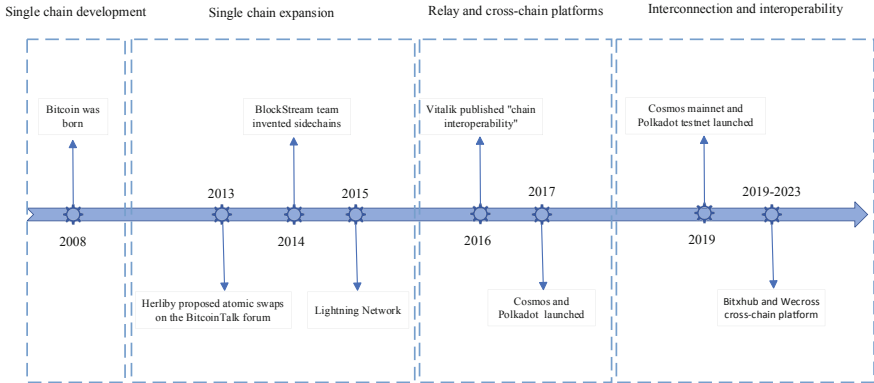


Fig. 1. The timeline of cross-chain technology development

2.2 Notary Mechanism

The notary mechanism emerged from the Interledger technology, in which the mutual distrust of participants was overcome through both parties trusting an asset exchange, similar to a real-world intermediary, through an “intermediary”. In the single signature mechanism, only one notary or a notary group undertakes data collection, transaction confirmation, and verification simultaneously [18]. This type of mechanism is relatively simple to implement, but it is vulnerable to centralized risks like a single failure. Each notary has a key that is accountable for signing its own book in the multi-signed notary, which enables cross-chain transactions to be completed by reaching consensus [19]. A multi-signature notary is more secure than a single-signature notary because it spreads out concentrated risk among several notaries, partially resolving the centralization issue. The distributed signature notary mechanisms combine cryptographic technologies to fragment key processing, disperse power to multiple nodes, perform transactions and produce signatures [20].

2.3 Sidechain/Relay

A fully independent blockchain system that can understand information from the main chain and react appropriately is known as the sidechain. It is a scalable cross-chain technology. Compared to the notary mechanism, it provides a more decentralized solution [21]. Sidechain is a concept related to mainchain that transfers equivalent assets in both

mainchain and sidechain using two-way peg technology. It is worth noting that the asset is briefly locked on the assets in the mainchain and releases equal value in the sidechain along with the same lock and release, rather than actually moving from the mainchain to the sidechain [10]. The two-way peg technologies include Simplified Payment Verification (SPV), single-hosted mode, alliance mode, drive chain mode, and hybrid mode [23], and this article will focus on the SPV-based two-way peg technology. Between the mainchains and sidechains, two-way peg technology is used to facilitate cross-chain transfers of assets.

Relay is a mechanism for transferring data between various blockchains that creates bridges between them and permits information to communicate throughout the network. Transactions typically involve the transmission and validation of transmissions [21]. Relay is a middle platform that allows users to send assets through various blockchains to perform cross-chain transactions. The relay node gets transaction information, confirms the transaction [22], and then transmits it to the entire network. From a formal point of view, the sidechain is focused on expressing the main relationship between the cross-chain, while the relay chain has no dependency relationship and is the technology and solution to realize the cross-chain, focusing on the transmission of cross-chain data. While the specific roles and functions of sidechain and relay are different, they are all developed to expand, optimize, and scale the operational efficiency of the blockchain network.

2.4 Hash Locking

Hash locking allows for cross-chain operations and information exchange by executing particular smart contracts on two chains [24]. There are two main types of smart contracts: the Revocable Sequence Maturity Contract (RSMC) and the Hashed Time Lock Contract (HTLC).

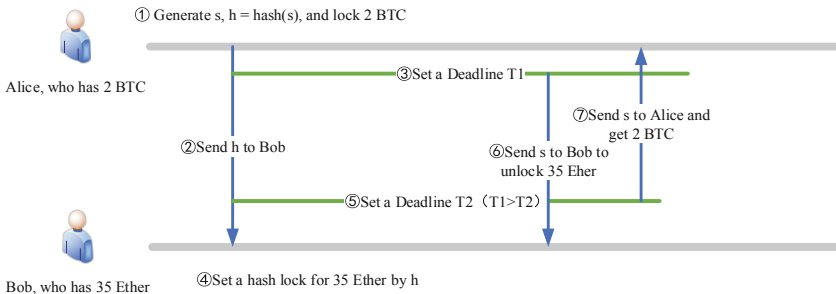


Fig. 2. The application scenario for hash-time lock

In order to address the issue of excessive fees in high-frequency small transactions, HTLC makes the assumption that there is a “micro-payment channel” among the participants in the transaction. Each time a payment is made, these off-chain transactions are simply updated, and when one party wants to submit, they only need to publish the most recent transaction on chain to receive the bitcoin they are due. In the hash-time

lock mechanism, there are these two locks, the time lock and the hash lock [25], the former being the duration of the transaction time and the latter using the hash function because of one-way and low collision, and only those who submit the hash image in smart contract of the locked asset within the specified time can extract the asset. The trading scenario for a hash time lock is shown in Fig. 2 below.

2.5 Distributed Private Key Control

Distributed private key control, as the name suggests, is the use of distributed nodes to control the private keys of various assets in the blockchain system. The use and ownership of digital assets are separated, so that the control of the assets on the chain is safely transferred to the decentralized system, while mapping the assets on the original chain to the cross-chain, realizing asset circulation and value transfer between different blockchain systems. In the implementation process, distributed private key control uses a built-in asset template based on a blockchain protocol and then deploys new smart contracts based on cross-chain transaction information to create new cryptocurrency assets [27].

Analogous to the distributed signature notary mechanism, the distributed private key control utilizes multi-party secure computing and key splitting technology, and the two parties participating in the cross-chain asset exchange transfer to the distributed public key in the distributed network. It offers a secure and dependable way to safeguard private data, and it may be tailored to meet the requirements of the application.

Table 1. Comparative analysis of cross-chain mechanisms

Projects for comparison	Notary mechanism	Hash-lock	Sidechain	Relay	Distributed private key control
Interoperability	All	Cross-dependence	All	All	All
Number of participating chains	Multi-chain	Double-chain	Double-chain	Multi-chain	Multil-chain
Transaction speed	Slow	Medium	Slow	Slow	Medium
Resistance to replay	Medium	Medium	Medium	Medium	Medium
Difficulty to achieve	Medium	Easy	Difficulty	Difficulty	Medium
Cross-chain asset transfer	Support	Not support	Support	Support	Support
Typical project	Interledger	Lightning Network	RootStock	Bitxhub	Fusion

2.6 Comparative Analysis of Cross-Chain Mechanisms

The five common cross-chain techniques have all been discussed above, and while they all show some efficiency improvement, their utilization is constrained by a variety of application circumstances and implementation principles. The paper examines and evaluates interoperability, number of chains involved, transaction speed, difficulty of achieving, and whether they enable cross-chain asset exchanges in order to provide a more intuitive understanding of the current five existing cross-chains in Table 1.

There is presently no cross-chain mechanism that can be used in any scenario, and the mechanisms that are available have varying degrees of flaws. The implementation of cross-chain mechanisms takes into account both the synchronization of data across chains as well as the results of transactions and how the results of transactions are consistent with different consensus algorithms. Furthermore, due to some blockchains' inherent conditions, such as the six confirmation rules in the Bitcoin system, cross-chain transactions may only succeed temporarily before a rollback occurs, which we immediately have to deal with.

3 Cross-Chain Projects

An overview of mainstream cross-chain projects is covered in this section, along with comparative studies of different cross-chain technology projects that represent examples of the cross-chain mechanisms discussed in Sect. 2.

3.1 Interledger

The Interledger Protocol [27], a technology protocol for cross-chain value transfer that permits cross-account transactions, was developed by Ripple in 2015. Interledger is a typical representative of the notary mechanism in its early stages, and has also integrated the hash locking mechanism in the project development process due to the fact that hash locking can enable atomic transactions without the involvement of trusted entities.

By sending value in the form of tiny packets rather than relying on a single payment network, Interledger ensures that value transactions are quick, secure, and comparatively economical [28]. The Interledger Protocol (ILPv4), a collection of guidelines used to describe how nodes send value through the interledger network, is the core of Interledger. The three package categories in ILPv4—Prepare, Fulfill, and Reject [29]—represent the three primary Interledger operating processes. When the sender receives the completed package, it can be confirmed that the package has been successfully delivered to the recipient [29]. Subsequently, the sender can continue to send the remaining prepared packets until all of the data has been safely transmitted. Interledger is trustworthy, not creating a unified ledger but achieving cross-chain asset transfers through the aforementioned agreement, and once the transaction is completed, the parties will reach a consensus.

3.2 Wecross

Wecross is a blockchain cross-chain platform that was separately created and is entirely open source. It supports application and multi-chain interaction as well as synchronous chain and heterogeneous chain interaction. The cross-chain platform begins with the underlying platform architecture design and seamlessly connects to the Wecross cross-chain platform without alterations to the original blockchain bottom platform.

Wecross bases four key technologies—the Universal Blockchain Interface (UBI), the Heterological Chain Interconnection Protocol (HIP), the Trusted Transaction Mechanism (TTM), and the Multilateral Cross-Domain Governance (MIG)—on this design approach [18]. A cross-chain division of unified business classes In the Wecross system design shown in Fig. 3, can identify and handle both its own internal blockchain resources and this cross-chain division itself. The collection and settlement business expenses chain C of the deposit business chain A and chain B, correspondingly, represent the deposit partitions and settlement partitions in the diagram.

By requiring interactive response messages providing both data and proof, all cross-chain interaction data can be self-certified in Wecross, ensuring the project’s practicality and reliability and making it applicable to an extensive variety of cross-chain scenarios.

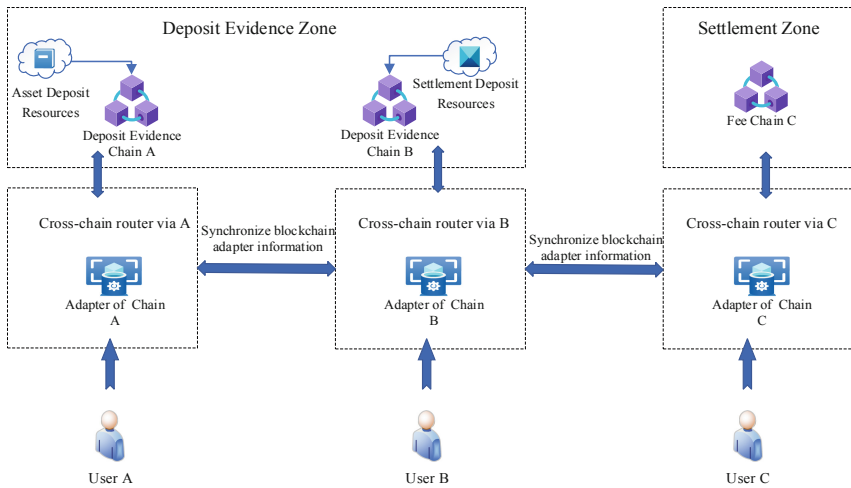


Fig. 3. Cross-chain division chart in Wecross

3.3 Bitxhub

Bitxhub is a cross-chain platform to implement the relay chain architecture, which consists of a relay chain, cross-chain peers, and application chains, independently created by Hangzhou Qulian Technology Co., Ltd.

The Bitxhub cross-chain transaction process is shown in the following Fig. 4. When a user initiates cross-chain transactions from the application chain A to the application

chain B, the user first makes a request to its own chain A and sends the transaction to it. Then chain A signs the transaction and throws the cross-chain event to pier A; pier A will first gather these with the signature cross-chain transaction and then arrange the packaging for the relay chain; the relay chain then confirms the transaction’s validity and then delivers it to pier B corresponding application chain B. Pier B will send the transaction to application chain B after receiving it. Eventually, chain B will perform this transaction and return the return receipt. This cross-chain platform’s entire process uses the Inter-Blockchain Transfer Protocol (IBTP), which is comparable to TCP/IP and supports relay chains for routing and verification.

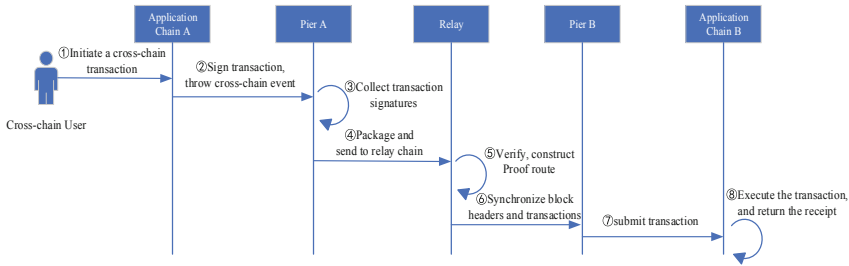


Fig. 4. The Bitxhub cross-chain transaction process

3.4 Comparative Analysis of Cross-Chain Projects

Several typical cross-chain projects are introduced in the front section, which use different mechanisms and has different ideologies and characteristics. Following that, they will be analyzed and compared with the following factors: mechanism, asset exchange, simplicity of implementation, centralization risk, interoperability, and atomicity.

Table 2. Comparative analysis of cross-chain projects

Cross-chain projects	Methods	Asset exchange	Realization	Centralization risk	Interoperability	Atomicity
Interledger	Notary/Hash-lock	Support	Easy	High	All	Yes
Wecross	Communication protocol suite	Support	Medium	Low	All	Yes
Bitxhub	Sidechains/Relays	Support	Difficulty	Low	Chain with relay	Yes

As shown in Table 2, Interledger, Wecross and Bitxhub all support asset exchange; however Bitxhub is the most difficult to implement than other projects; in addition to Interledger, there is centralized risk, while the rest is decentralized; in the pre-Interledger development period, it did not support atomic exchange, and the latter incorporated hash-locked support; Interledger and Wecross support the interaction between different blockchains, while Bitxhub is connected to the blockchain through a relay chain. In

other words, there are some flaws in some of the current cross-chain projects. However, cross-chain technology has been the focus of recent studies, and efforts in this area are also constantly advancing and breaking through. These technologies can not only make it possible for various blockchains to communicate with each other, but they can also enhance the safety and scalability of the entire blockchain system.

4 Challenges and Future Directions

Cross-chain provides asset exchange, performance broadening, and information sharing within the blockchain system, which is the inevitable choice that makes sense for the advancement of blockchain technology. The verification and reversal of cross-chain transactions, security performance challenges, and future directions for cross-chain research are all included in this section.

4.1 Challenges

Verification and Reversal of Cross-chain Transaction. Blockchain transactions are only deemed successful in cross-chain when the blockchains involved successfully verify the transaction and reach consensus. However, because heterogeneous blockchains in particular have incoherent consensus algorithms, consensus results cannot be insured. Additionally, each blockchain has its own confirmation processes such as the six confirmation processes used by the Bitcoin network, which only considered the transaction is valid if it has been confirmed by six consecutive blocks. It should also require an analogous approach to return to their starting point if the transaction rolls back within this process. Therefore, while executing cross-chain transactions, it is also important to take into account both the transaction's reliability and the processing once a rollback has been executed.

Security. The attack surface has risen slightly as a result of the introduction of cross-chain features like cross-chain smart contracts, side chains, relays, etc. The interaction of smart contracts or cross-chain scripts is comparatively vulnerable within the hash time lock. Attackers are also interested in the cross-chain nodes used for data and transaction transfer and authentication, and the efficiency of cross-chain transaction processing is limited. Cross-chain bridge hacking attacks, including the Chainswap attack, the Wormhole attack, and others, have been widely reported recently. The safeguards in place are insufficient to completely defeat them. Blockchain research has always concentrated on figuring out how to incorporate cross-chain data and transactions in a secure manner.

4.2 Future Directions

The requirements of blockchain applications have not been satisfied by single-chain performance, storage, etc., despite blockchain technology's rapid development and category's gradual sophistication. The field of blockchain research is focusing heavily on how to scale blockchain performance, and cross-chain technology can effectively address issues with single-chain architecture's performance storage and other challenges.

Although there are some bottlenecks in existing cross-chain technologies, cross-chain technology is currently evolving and developing in reality through a number of cross-chain projects, and it will continue to mature. The standardization and interoperability [31] of cross-chain technology, as well as the secure transfer of data across the chain, will be thoroughly investigated in the future. The technology bottleneck will be broken by blockchain technology, which will also promote cross-chain interaction and a more dynamic business strategy.

5 Conclusion

This paper first discussed the cross-chain mechanisms and cross-chain projects, and then conducted a comparison in terms of the inability to synchronize and secure information across chains, ensure an atomic transaction, and efficiently exchange information. There are some bottlenecks in existing cross-chain technologies. Third, this paper presents challenges and future directions according to existing cross-chain schemes in the literature. Verification and reversal of cross-chain transactions and security in cross-chain are still defective. The safeguards in place are insufficient to completely defeat them. This paper will guide future research to a certain extent to secure the sustainable future of the cross-chain ecosystem.

Acknowledgments. This work was supported in part by the National Key R&D Program of China (No. 2021YFB2700600); in part by the Finance Science and Technology Project of Hainan Province (No. ZDKJ2020009); in part by the National Natural Science Foundation of China (No. 62163011); in part by the Research Startup Fund of Hainan University under Grant KYQD(ZR)-21071.

References

1. Nakamoto S.: Bitcoin: a peer-to-peer electronic cash system. *Decent. Bus. Rev.* 21260 (2008)
2. Buterin V.: A next-generation smart contract and decentralized application platform. *J.* 3(37), 2–1 (2014)
3. Wang, Q., Li, R., Wang, Q., Chen, S.: Non-fungible token (NFT): overview, evaluation, opportunities and challenges. *J. arXiv preprint [arXiv:2105.07447](https://arxiv.org/abs/2105.07447)* (2021)
4. DA Zetzsche DW Arner RP Buckley 2020 Decentralized finance *J. Financial Regulation.* 6 2 172 203
5. S Mystakidis 2022 Metaverse *J. Encyclopedia.* 2 1 486 497
6. W Ou S Huang J Zheng QL Zhang G Zeng 2022 An overview on cross-chain: mechanism, platforms, challenges and advances *J. Comput. Netw.* 218 109378
7. Poon, J., Dryja, T.: The bitcoin lightning network: scalable off-chain instant payments (2016)
8. WeCross Technical White Paper Blockchain cross-chain collaboration platform, <http://www.d-long.com/eWebEditor/uploadfile/2020041616163616557031.pdf> (2020)
9. S Ye X Wang C Xu J Sun 2020 BitXHub: side-relay chain based heterogeneous blockchain interoperable platform *J. Comput. Sci.* 47 6 294 302
10. Kotey, S.D., Tchao, E.T., Ahmed, A.R., et al.: Blockchain interoperability: the state of heterogenous blockchain-to-blockchain communication. *J. IET Commun.* (2023)

11. Guo, Z., Liu, L., Liang, Z., et al.: Blockchain cross-chain technology research. In: 2022 IEEE 5th Advanced Information Management, Communicates, Electronic and Automation Control Conference (IMCEC), vol. 5, pp. 1064–1070. IEEE (2022)
12. Z Guo SY Guo SL Zhang 2020 Analysis of blockchain cross chain technology J. Internet Things. 4 2 36 49
13. Herlihy, M.: Atomic cross-chain swaps. In: Proceedings of the 2018 ACM Symposium on Principles of Distributed Computing, pp. 245–254 (2018)
14. K Lindorff-Larsen S Piana K Palmo 2010 Improved side-chain torsion potentials for the Amber ff99SB protein force field J. Proteins: Struct. Func. Bioinf. 78 8 1950 1958
15. Wood, G.: Polkadot: Vision for a heterogeneous multi-chain framework. J. **21**(2327), 4662 (2016)
16. Bai, Y., Lei, H., Li, S., Gao, H., Li, J., Li, L.: Decentralized and self-sovereign identity in the era of Blockchain: a survey. In: 2022 IEEE International Conference on Blockchain (Blockchain), pp. 500–507. IEEE (2022)
17. Salleras, X.: Citadel: self-sovereign identities on dusk network. J. arXiv preprint [arXiv:2301.09378](https://arxiv.org/abs/2301.09378) (2023)
18. S Hao M Hanyu Z Yanfeng 2022 Development and application of blockchain cross-chain technology J. Comput. Sci. 49 05 287 295
19. Rivest, R., Shamir, A., Adleman.: A method for obtaining digital signatures and public-key cryptosystems. Commun. ACM **21**(2), 120–126 (1978)
20. Haimerl, N.: Cross-Chain Traceability in Decentralized Finance. Doctoral dissertation, Wien (2023)
21. Back, A., Corallo, M., Dashjr, L., et al.: Enabling blockchain innovations with pegged sidechains. J. **72**, 201–224 (2014)
22. Lys, L., Micoulet, A., Potop-Butucaru, M.: Atomic cross chain swaps via relays and adapters. In: Proceedings of the 3rd Workshop on Cryptocurrencies and Blockchains for Distributed Systems, pp. 59–64
23. Dilley, J., Poelstra, A., Wilkins, J., et al.: Strong federations: an interoperable blockchain solution to centralized third-party risks. J. arXiv preprint [arXiv:1612.05491](https://arxiv.org/abs/1612.05491) (2016)
24. F Li Z Li H Zhao 2019 Research on the progress of blockchain cross-chain technology J. Softw. 30 6 1649 1660
25. Li, T., Yang, C., Yang, Q., et al.: MetaOpera: a cross-metaverse interoperability protocol. J. arXiv preprint [arXiv:2302.01600](https://arxiv.org/abs/2302.01600) (2023)
26. Zhao, L., Zhang, Q., Zhao, H., Wang.: Across block chain consensus transation model based on cluster center. PeerJ. Comput. Sci., **46**(S2), 557–561 (2019)
27. H Shuai H Xiangnian C Xiaoliang 2021 A review of the development and application of blockchain cross-chain technology J. Xihua Univ. (Natl. Sci. Edn.) 40 3 1 14
28. Hope-Bailie, A., Thomas, S.: Interledger: creating a standard for payments. In: Proceedings of the 25th International Conference Companion on World Wide Web, pp. 281–282 (2016)
29. Qasse, I.A., Talib, M.A., Nasir, Q.: Inter blockchain communication: a survey. In: Proceedings of the ArabWIC 6th Annual International Conference Research Track, pp. 1–6 (2019)
30. VA Siris P Nikander S Voulgaris 2019 Interledger approaches J. IEEE Access 7 89948 89966
31. Wang, G., Wang, Q., Chen, S.: Exploring blockchains interoperability: a systematic survey. J. ACM Comput. Surv., (2023)



A Data Processing and Analysis System for Fourier Transform Infrared Spectrometer

Wanjie Ren^{1,2}(✉), Qi Liu¹, Liang Li², Peng Wang², and Rui Tuo²

¹ Nanjing University of Information Science and Technology, Nanjing 210044, China
renwanjie66@126.com

² Shandong Institute of Non-Metallic Materials, Jinan 250031, China

Abstract. Existing Fourier transform infrared spectrometers have problems such as noise interference, baseline drift, low accuracy and stability of spectrum acquisition, and lack of corresponding analysis models. In this paper, by improving the technical defects of existing Fourier transform infrared spectrometers, a design The spectral information processing and analysis system used for Fourier transform infrared spectrometer test data enables users to make custom choices among multiple comprehensive and effective functional modules, and realize personalized spectral processing and analysis while collecting spectra, solving The problems existing in the existing Fourier transform infrared spectrometer are solved.

Keywords: Fourier transform infrared spectrometer · Noise interference · Baseline drift

1 Introduction

Fourier transform infrared spectrometer can perform qualitative and quantitative analysis of samples, and is widely used in petroleum, chemical, medical and other fields. Since the emission and absorption spectra of a substance are uniquely determined by its own structural characteristics and corresponding physical mechanisms, the type and content of a substance can be identified through the spectrum.

When the spectrometer is working, the light emitted by the light source is divided into two beams by the beam splitter, which are respectively reflected by the fixed mirror and the moving mirror to form an optical path difference, thereby causing interference. By performing Fourier transform and other processing on the interference optical signal, the infrared absorption spectrum is finally obtained, and the processing and analysis technology of the original spectrum will directly affect the accuracy of the spectrometer for qualitative and quantitative analysis of samples.

The traditional Fourier transform infrared spectrometer has the following technical defects: (1) Only simple processing of the original spectrum requires the user to use other software or tools for further processing of the spectrum. (2) In the process of infrared spectrum signal collection, it may be affected by factors such as the state of the spectroscopic instrument, collection background, and detection conditions, resulting in interference in the measured spectrum, such as noise interference. At the same time, since

the background is collected every time a sample spectrum is collected, the change of the background makes the spectrum baseline drift. In addition, factors such as abnormal sample interference and light scattering will also reduce the accuracy and stability of spectral acquisition. Therefore, preprocessing infrared spectral data is a key step to ensure the quality of follow-up work. (3) Since the characteristic frequency region and fingerprint region of the infrared spectrum play an important role in distinguishing compounds with similar structures, the positioning accuracy of the spectral peak directly affects the performance of subsequent sample analysis. The existing Fourier transform infrared spectrometer can locate the spectral peak. The accuracy needs to be further improved. (4) In addition, when conducting qualitative and quantitative research on infrared spectroscopy, it is sometimes necessary to establish a stable and reliable analysis model, and the existing Fourier transform infrared spectrometer lacks a corresponding analysis model.

In this paper, by improving the above-mentioned technical defects of the existing Fourier transform infrared spectrometer, a spectral information processing and analysis system for the test data of the Fourier transform infrared spectrometer is designed, so that users can customize among multiple comprehensive and effective functional modules choose to realize personalized spectral processing and analysis while collecting spectra.

2 Main Text

This paper adopts a data processing and analysis system of Fourier transform infrared spectrometer. The analysis system includes: data preprocessing module, curve transformation and peak positioning module, feature extraction module and human-computer interaction module, data preprocessing module, curve transformation and The peak positioning module and feature extraction module are electrically connected with the Fourier infrared spectrometer to realize data interaction and receive the test data of the Fourier infrared spectrometer; through the data preprocessing module, basic spectral transformation, spectral filtering and denoising, multiple scattering correction and Elimination of abnormal data; through the curve transformation and peak positioning module, polynomial fitting of the infrared spectrum, automatic peak positioning and coordinate transformation are realized according to the spectral data; through the feature extraction module, the continuous projection method and genetic algorithm are used to screen the wavelengths carrying relevant information, Calculate the characteristic variables of the spectrum, effectively extract and optimize the spectral information; use the human-computer interaction module to realize the automatic processing and analysis of the infrared spectrum according to the user's custom requirements.

2.1 Data Preprocessing Module

The data preprocessing module can realize basic transformations such as derivation, centering, and normalization of the infrared spectrum of the Fourier transform infrared spectrometer, as well as processing such as baseline drift correction and abnormal sample detection. Users can choose specific preprocessing operations and its sequence.

2.1.1 Infrared Spectrum Filtering and Denoising Sub-module

(a) Wavelet packet filter denoising.

The spectral information is decomposed into background information, component information and noise by wavelet packet transform, and the wavelet packet threshold denoising is realized:

- ① Wavelet packet decomposition of the signal. Select the appropriate wavelet function and decomposition scale according to the signal, and calculate the best wavelet basis given the entropy standard;
- ② Threshold quantization of wavelet packet decomposition coefficients. Select the appropriate threshold rule based on experience, select the appropriate threshold, and process the decomposed wavelet packet coefficients;
- ③ Wavelet packet reconstruction. The original spectral signal is reconstructed from the Nth layer wavelet packet decomposition coefficients and the processed coefficients.

The threshold calculation formula is as follows:

$$Tr = \sqrt{2 * \log(length(s))} \tag{1}$$

(b) Mobile smoothing filtering.

Effectively reduce spectral noise by averaging or weighting redistribution of data points and their neighbors to obtain a smoother curve. Take the average of odd data points in the window, use this average to replace the center point of the data in the window, and move the window to get new data.

$$y(t) = \sum_{i=t-\frac{n-1}{2}}^{t+\frac{n-1}{2}} x(t - i) \tag{2}$$

The window width is n, the data value of the window center wavelength point t is x(t), and the new data point after smoothing is y(t).

(c) Savitzky-Golay convolutional smoothing filter

Improve the simple mean calculation to a polynomial least squares fit to the data in a moving window by the polynomial. The width of the smoothing window is n = 2m + 1, and the original data points in the window are fitted with a polynomial of degree k-1, namely:

$$y_i = a_0 + a_1i + a_2i^2 + \dots + a_{k-1}i^{k-1} \tag{3}$$

In: $i = (-m, -m + 1, \dots, 0, 1, \dots, m-1, m)$. Solve an overdetermined system of equations:

$$Y_{(2m+1) \times 1} = X_{(2m+1) \times k} \cdot A_{k \times 1} + E_{(2m+1) \times 1} \tag{4}$$

The formula for calculating the filtered value Y is as follows:

$$\hat{Y} = XA = X(X^T X)^{-1} X^T Y = BY \tag{5}$$

In: $B = X(X^T X)^{-1} X^T$ is the filter coefficient matrix, which is determined by and only by the X matrix, and the B matrix is a $(2m + 1) \times (2m + 1)$ order matrix, and the S-G smooth fitting equation can be obtained according to the coefficient matrix. The $Mn_3Al_2(SiO_4)_3$ infrared spectrum was preprocessed according to the aforementioned S-G smoothing filtering method, and the filtering result is shown in Fig. 1, and the burrs of the original spectrum were filtered out.

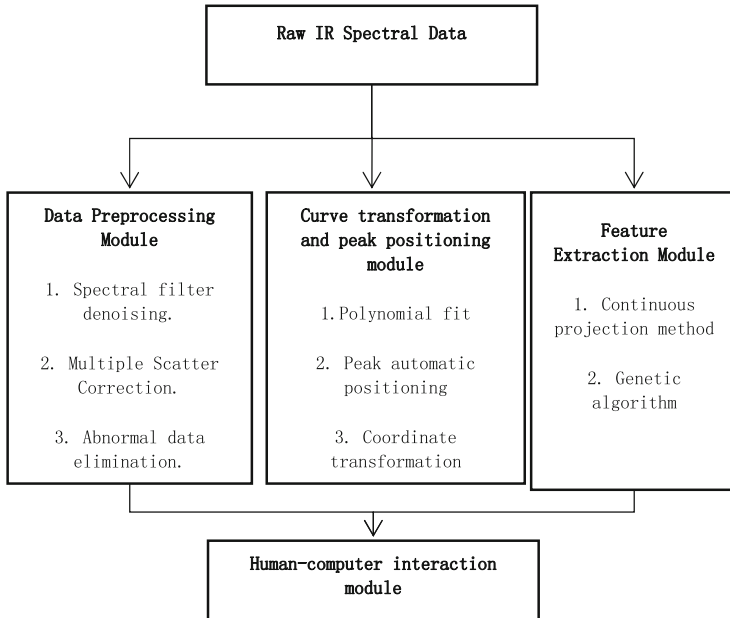


Fig. 1. Schematic diagram of the principle of Fourier transform infrared spectrometer

2.1.2 Multivariate Scattering Correction Submodule

The original spectrum of each sample is based on the average spectrum as a reference, and the regression constant and regression coefficient are calculated to correct the drift and offset of the spectrum.

Find the average spectrum of all sample spectra, in: \mathbf{A} is n -dimensional spectral matrix. That is, there are n groups of sample spectra, and each spectrum contains p wavelength data.

$$\overline{\mathbf{A}}_{i,j} = \frac{\sum_{i=1}^n \mathbf{A}_{i,j}}{n} \quad (6)$$

The regression coefficient of each spectrum relative to the standard spectrum is obtained by unary linear regression operation m_i and regression constant b_i , The

calculation formula is:

$$\mathbf{A}_i = m_i \bar{\mathbf{A}} + b_i \quad (7)$$

Make the difference between the original spectrum of the sample and its tilt translation, and divide it by its linear offset to correct the baseline translation and offset of the spectrum

$$\mathbf{A}_{i(MSC)} = \frac{(\mathbf{A}_i - b_i)}{m_i} \quad (8)$$

2.1.3 Abnormal Sample Elimination Sub-module

Combining principal component analysis with data compression capabilities and Mahalanobis distance to detect outlier samples. Calculate the principal component of each sample, the principal component of the sample replaces the spectral data of the sample, calculate the Mahalanobis distance, in: \mathbf{X} is sample data, \mathbf{C}_X is covariance of sample data, $\bar{\mathbf{X}}$ is mean of the data.

$$D^2(i) = (\mathbf{X}_i - \bar{\mathbf{X}}) \mathbf{C}_X^{-1} (\mathbf{X}_i - \bar{\mathbf{X}})^T \quad (9)$$

Set the threshold to distinguish abnormal samples. The threshold is set as follows:

$$D_t = \bar{D} + e\delta_D \quad (10)$$

2.2 Curve Transformation and Peak Positioning Module

The curve transformation and peak positioning module can realize the functions of polynomial fitting, peak positioning and coordinate transformation of infrared spectral curves, and users can choose from them according to their needs to process the original spectrum or the preprocessed spectrum.

2.2.1 Given a Sequence of $n + 1$ Spectral Data (t_i, p_i) , $i = 0, \dots, n$, Interpolate Using a Piecewise Quintic Polynomial Such That the Piecewise Polynomial Passes Through All Point Sequences

- ① Estimate the first derivative at the starting point, end point and intermediate point;
- ② Estimate the second derivative at the starting point, end point and intermediate point;

For each segment of quintic polynomial, the coefficients of the fitted polynomial are obtained using the constraints at its endpoints. The piecewise polynomial fitting results of the $\text{Mn}_3\text{Al}_2(\text{SiO}_4)_3$ infrared spectrum are shown in Fig. 2. The method in this paper can effectively achieve the fitting of the spectral curve.

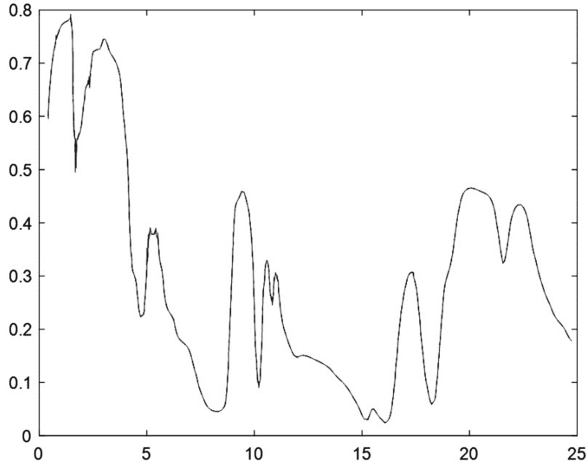


Fig. 2. Mn₃Al₂(SiO₄)₃ Schematic diagram of spectral preprocessing (S-G smoothing filter)

2.2.2 Infrared Spectrum Peak Positioning and Marking Sub-module

The specific steps of peak positioning are as follows:

- ① Obtain the first-order difference dy of the original spectrum, and the subscript position zeros where the difference is 0;
- ② Differentiate the zeros to determine whether the current waveform is horizontal, and group the subscripts in the zeros;
- ③ Process each horizontal wave so that there is only one peak turning point in each horizontal wave;
- ④ When detecting the peak point, each point in the horizontal wave behaves the same, so the median point in the horizontal wave is selected as the only peak point, thereby correcting dy ;

If a certain horizontal wave is at the starting position of the signal, dy will be filled forward at the starting position of the signal;

If a horizontal wave is at the signal end position, then dy is filled backward at the signal end position;

If a certain horizontal wave is in the middle of the signal, then dy is bounded by the median value and filled forward and backward;

The specific steps of peak positioning are as follows:

- ① Obtain the first-order difference dy of the original spectrum, and the subscript position zeros where the difference is 0;
- ② Differentiate the zeros to determine whether the current waveform is horizontal, and group the subscripts in the zeros;
- ③ Process each horizontal wave so that there is only one peak turning point in each horizontal wave;

- ④ When detecting the peak point, each point in the horizontal wave behaves the same, so the median point in the horizontal wave is selected as the only peak point, and dy is modified accordingly;
- ⑤ to obtain the peak point that meets the peak detection;
- ⑥ Use the peak detection distance to filter out invalid peak points. For the above peak points, extract the peak point point by point according to its amplitude from high to low, and take it as the center, the positive and negative minimum distance is the interval, and all points in this interval are regarded as non-peak points;
- ⑦ Finally output the indicator matrix of the peak point.

Figure 3 shows the peak positioning results of the infrared spectrum of $\text{Mn}_3\text{Al}_2(\text{SiO}_4)_3$, according to the minimum peak distance set by the user, the peak positioning and marking are realized.

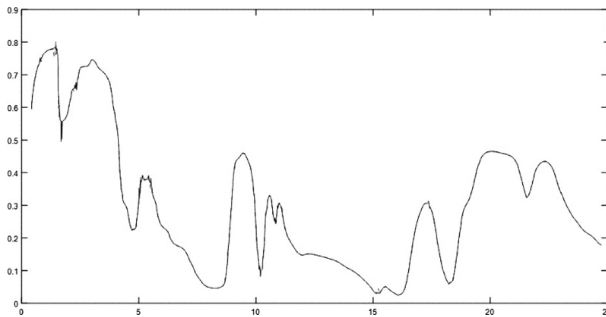


Fig. 3. Schematic diagram of piecewise polynomial fitting of infrared spectrum of $\text{Mn}_3\text{Al}_2(\text{SiO}_4)_3$

The feature extraction of $\text{Mn}_3\text{Al}_2(\text{SiO}_4)_3$ infrared spectrum is carried out by genetic algorithm, and the result is shown in Fig. 4. Where the selection result is 1, it means that the corresponding wavelength is selected as the characteristic wavelength.

The feature extraction of $\text{Mn}_3\text{Al}_2(\text{SiO}_4)_3$ infrared spectrum is carried out by genetic algorithm, and the result is shown in Fig. 4. Where the selection result is 1, it means that the corresponding wavelength is selected as the characteristic wavelength.

3 Paper Summarize

Based on the basic functions of the traditional Fourier transform infrared spectrometer, this paper sets up the spectral information processing and analysis system. Complete functions such as spectral information preprocessing, peak positioning, and feature extraction according to individual requirements.



A Method for Identifying Meat Quality Based on CNN-SVM

Peiyong Zhao¹, Yuhua Zhang², and Jianxi Zhang²(✉)

¹ Computational Sciences, School of Statistics and Mathematics, Shandong University of Finance and Economics, Ji'nan, Shandong, China

² Computational Sciences, Shandong Institute of Commerce and Technology, Ji'nan, Shandong, China

xer8290@163.com

Abstract. To identify the quality variation in meat during storage and transportation, and improve the efficiency of rapid detection of meat quality changes, a meat quality change recognition method based on an improved CNN-SVM model is proposed. Firstly, a CNN model is constructed using meat images as input samples. Replacing the fully connected layer of traditional CNN models with a global average pooling layer to reduce the number of model parameters while extracting image features. The data enhancement and batch normalization techniques are used to improve the model generalization ability and reduce the model overfitting. Secondly, nonlinear support vector machine SVM is used to replace the Softmax classifier in traditional CNN models to improve the accuracy of image change recognition. Finally, an example verification was conducted on the proposed model. The results show that compared with traditional CNN models, the improved CNN-SVM model has stronger recognition ability for changes in meat quality.

Keywords: Quality variation · CNN · SVM

1 Introduction

With the development of machine vision and artificial intelligence technology, automatic detection of agricultural product quality has always been a research hotspot in the field of agricultural engineering [1]. The application of deep learning technology to achieve fast and accurate meat detection [2] can not only provide a fast and non-destructive identification method different from physical and chemical detection, but also provide a reliable basis for the quality control of meat storage and transportation process.

Convolutional neural networks (CNN) are a typical deep learning model [3, 4], which plays an important role in the field of image recognition. However, the number of neurons in the full connection layer of the traditional CNN model will increase exponentially when the degree of functional nonlinearity is high, which will increase too many training parameters and easily weaken the generalization ability of the model. This paper proposes an improved CNN SVM hybrid model to address the problems of

traditional CNN models. Firstly, a Global average Pooling (GAP) layer is adopted to replace the fully connected layer of traditional CNN models, in order to effectively reduce the number of parameters while extracting features. Secondly, data augmentation and Batch Normalization (BN) techniques are introduced into the model to optimize and improve the model. Finally, a nonlinear support vector machine (SVM) was used to replace the Softmax function of traditional CNN models for classification [5], in order to further improve the accuracy of image recognition.

2 Traditional Convolutional Neural Networks

Convolutional neural networks are a special type of artificial neural networks [6–8], whose main feature is convolutional operation, which performs well in many fields, especially in image recognition. The traditional CNN model consists of an input layer, convolutional layer, pooling layer, fully connected layer, and output layer. The model structure is shown in Fig. 1. The input layer inputs sample data, the convolutional layer extracts features from the input samples, the pooling layer down-sampling the extracted features, the fully connected layer integrates the output of the pooling layer, and the output layer generally uses the Softmax function for multi classification output.

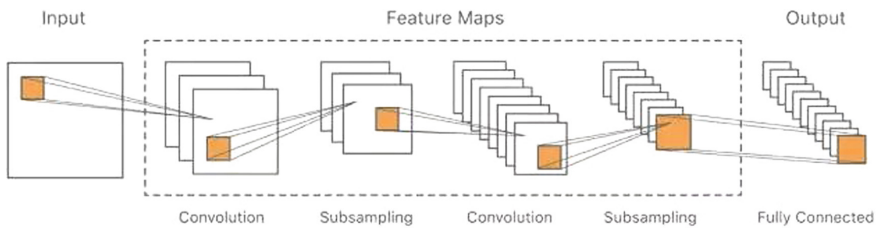


Fig. 1. Typical CNN architecture

The traditional CNN model uses the full connection layer for feature integration before the output layer. When the function is highly nonlinear, the number of neurons will increase exponentially, which is easy to cause overfitting, and is not conducive to improving the generalization ability of the model [9, 10]. Moreover, using the Softmax function as a classifier in traditional CNN models only transforms the output results of the fully connected layer into a simple transformation that conforms to the probability distribution, which has little help in improving model recognition performance [11–13].

3 A Method for Identifying Meat Quality Based on CNN-SVM Model

3.1 CNN-SVM Model

In response to the shortcomings of traditional CNN models, this paper proposes an improved CNN SVM model to identify the degree of quality changes in meat images. The improvements include:

- (1) Replacing the fully connected layer of traditional CNN models with GAP layer [14]. The GAP layer can adaptively extract features from each feature map, significantly reducing model parameters.
- (2) Data enhancement and batch normalization techniques are applied in the model to improve the generalization ability of the model, reduce overfitting, and accelerate the convergence speed of the model.
- (3) A nonlinear SVM was designed to replace the Softmax classifier in traditional CNN to distinguish the degree of changes in meat image, in order to improve the accuracy of quality change recognition.

The meat image is input into the model, and after convolution, batch normalization, and activation operations, it enters the pooling layer. After two consecutive operations, it is transmitted to the GAP layer for global average pooling. Finally, the GAP layer features are transmitted to SVM for quality recognition. The specific recognition principle is as follows:

- (1) The convolutional layer extracts features from the input image samples. Shallow convolution is used to extract low-level basic features such as image edges and shapes, while deep convolution is used to extract high-level abstract features in the image. The convolution operation formula is as follows:

$$X_i^k = \sum_{j \in N_{k-1}} W_{ij}^k \otimes X_j^{k-1} + b_i^k \quad (1)$$

where X_i^k represents the i -th feature map of the k -th layer output, W_{ij}^k is the weight value of the i -th convolution in the k -th layer, \otimes represents convolution operator, X_j^{k-1} represents the j -th feature map output from the $k-1$ layer, N_{k-1} is the set of output feature maps for the $k-1$ st layer, b_i^k is the bias term of the i -th convolution in the k -th layer.

- (2) The image feature data extracted from the convolution layer is batch normalized to avoid gradient dispersion, improve the model generalization ability and reduce overfitting.
- (3) Nonlinear activation is carried out by using the Rectified Linear Unit (ReLU) with good unsaturated characteristics and unilateral suppression [14] to improve the expression ability of the network. The activation function is as follows:

$$x_i^{k+1} = \text{ReLU}(X_i^k) = \begin{cases} 0, & x_i^k < 0 \\ x_i^k, & x_i^k > 0 \end{cases} \quad (2)$$

where x_i^k is the value of each pixel in X_i^k .

- (4) Input the activated feature data into the pooling layer, and use the maximum pooling method for down-sampling. Reduce the feature size while maintaining the same feature dimension, and reduce the number of parameters while retaining effective features. The maximum pooling formula is:

$$x_i^{k+2}(m, n) = \max_{\substack{1+(m-1)P \leq s \leq mP \\ 1+(n-1)Q \leq t \leq nQ}} \{x_i^{k+1}(s, t)\} \quad (3)$$

where $x_i^{k+1}(s, t)$ is the pixel value of the s -th row and t -th column of the i -th feature map input to the pooling layer, P and Q are the height and width of the pooling window, $x_i^{k+2}(m, n)$ is the pixel value of the m -th row and n -th column of the i -th feature map output after pooling operation.

- (5) After two convolutions of the image into pooling operations, c feature maps with size $M \times N$ are input into the GAP layer. The GAP layer automatically adjusts the size of the pooling kernel to $M \times N$, and performs global average pooling on each feature map to obtain the feature vector $X_r = \{x_1, x_2, \dots, x_i, \dots, x_c\}$. Where

$$x_i = \frac{1}{MN} \sum_{m=1}^M \sum_{n=1}^N x_i^{k+2}(m, n) \tag{4}$$

- (6) Feed the feature vectors output by the GAP layer into the SVM classifier. SVM is commonly used to solve binary classification problems [15], and the mathematical model of SVM is:

$$\begin{cases} \min \frac{1}{2} \|w\|^2 + \rho \sum_{r=1}^L \xi_r \\ s.t. \quad y_r(wX_r + g) + \xi_r \geq 1, r = 1, 2, \dots, L \end{cases} \tag{5}$$

where w is the hyperplane normal vector, g is the classification threshold, $\rho > 0$ is the penalty factor, $\xi \geq 0$ is the relaxation variable, X_r is the feature vector of the r -th sample, y_r is the category label, and L is the number of samples.

Equation (5) model is only applicable to the linearly separable problem of sample data. Due to the linear indivisibility of image sample data, when using SVM for classification, this paper uses Gaussian radial basis function to map the sample data from low dimensional space to high dimensional space, and obtains its classification decision function in high dimensional space as follows:

$$f(X) = \text{sgn}\left(\sum_{r=1}^L a_r^* y_r \exp\left(-\frac{\|X_r - X\|^2}{2\sigma^2}\right) + g^*\right) \tag{6}$$

where sgn is a signed function, a_r^* is the Lagrange multiplier, σ is the width parameter, g^* is the optimal threshold, X is the feature vector of the sample to be tested.

When using SVM for multi classification, every two classes of samples can be trained to obtain a sub classifier, and $1(1-1)/2$ sub classifiers can be trained for l class samples. When conducting quality recognition for new samples, each sub classifier is used to distinguish and vote on them, and the category with the highest number of votes is selected as the final result of quality recognition.

3.2 Meat Quality Identification Process

The meat quality recognition process based on CNN-SVM model is mainly divided into three stages: data processing stage, model training stage, and quality recognition stage.

- (1) Divide the image dataset into training, validation, and testing sets, and perform data normalization processing.

- (2) Initialize CNN-SVM model parameters.
- (3) Input the training set samples into the improved CNN model for model training.
- (4) Transfer the saved parameters to the CNN-SVM model and train the SVM using the output features and sample labels of the GAP layer.
- (5) Input the test set into the trained CNN SVM model and output the results.

4 Experiment and Result Analysis

4.1 Preparation of Test Samples

Take photos of normally slaughtered, unfrozen pork and save them as fresh pork sample images. Grouping fresh pork samples for storage at $-20\text{ }^{\circ}\text{C}$. Each group of samples is taken out and placed in a $0\text{ }^{\circ}\text{C}-4\text{ }^{\circ}\text{C}$ environment for another day to detect their volatile base nitrogen [16, 17]. All samples were tested for 7 days. Before each detection of basic nitrogen in pork samples, high-definition cameras are used to capture the tested samples, and the captured images are saved in JPG or PNG format.

4.2 Freshness Classification Criteria

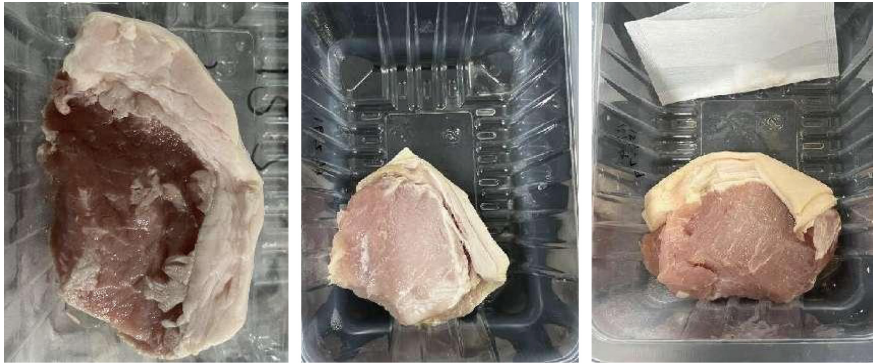
After the sample preparation, according to the volatile base nitrogen value and the classification criteria in Table 1, the pork sample images were labeled respectively and classified into the corresponding categories of 5 categories. As shown in Fig. 2.

Table 1. Freshness classification

Sample	TVB-N(mg/100g)
Fresh	≤ 15
Vice-fresh-1	15 ~ 16
Vice-fresh-2	16 ~ 18
Spoilage-1	18 ~ 20
Spoilage-2	≥ 20

4.3 Data Set

Crop the sample image to 224 pixels \times 224 pixels using the minimum bounding rectangle. Each sample is approximately 11 KB. The samples are augmented by affine transformation, perspective transformation and rotation. Obtain 6000 initial images and 11800 augmented images. Randomly allocate training and testing sets in a 4:1 ratio, and allocate training and validation sets in a 9:1 ratio (Table 2).



Fresh

Vice-fresh-1

Vice-fresh-2



Spoilage-1

Spoilage-2

Fig. 2. Pictures for pork freshness samples

Table 2. Number of initial and extended images

Category	Initial number	Initial and augmented number	Number of verified images
Fresh	1200	3600	360
Vice-fresh-1	2400	7200	720
Vice-fresh-2	800	2000	200
Spoilage-1	400	1000	100
Spoilage-2	1200	4000	400

4.4 Experimental Results of CNN SVM Model

The training of CNN models involves traditional data augmentation of samples through the Image Data Generator module. When the iteration reaches 100 times, the accuracy of the validation set no longer significantly changes, and the CNN model training is completed. Migrate CNN model parameters to CNN-SVM model, use the features extracted from the GAP layer and sample labels for SVM training, and ultimately use SVM for fault classification.

Use the confusion matrix to quantitatively evaluate the degree of confusion between various categories. The rows and columns of the matrix represent real and predicted situations. The diagonal element value represents the accuracy of identifying the freshness of various types of pork, while other positions represent the misclassification rate. According to the analysis of confusion matrix Table 3, fresh pork has the best recognition effect, with an accuracy rate of 89%, while corruption level has the worst recognition accuracy, with an accuracy rate of 81%; The overall accuracy of identifying the freshness of various types of pork is 84.8%. It can be seen that the CNN-SVM model has a high accuracy in identifying the freshness of pork.

Table 3. Confusion matrix

	Fresh	Vice-fresh-1	Vice-fresh-2	Spoilage-1	Spoilage-2
Fresh	89%	1%	0	0	0
Vice-fresh-1	0	88%	0	1%	0
Vice-fresh-2	4%	0	82%	0	0
Spoilage-1	0	0	0	81%	3%
Spoilage-2	0	0	0	2%	84%

To verify the superiority of the model, this paper applies the CNN-SVM model to simulate and compare with traditional CNN models and Artificial Neural Network (ANN) models. The final recognition accuracy of each model is shown in Table 4.

Table 4. Comparison of diagnostic results of different models

Models	Recognition accuracy (%)
CNN-SVM	82.85
CNN	78.55
ANN	67.69

From Table 4, it can be seen that the recognition accuracy of the CNN-SVM model in this paper is 82.85%, while the traditional CNN model has a recognition accuracy of 78.55%, which has improved the recognition accuracy by 4.3%. Compared to the

ANN model, the recognition accuracy of the CNN-SVM model has been improved by 15.16%. The experimental results show that the recognition method proposed in this paper performs better.

5 Conclusion

This paper proposes a CNN-SVM model for identifying quality changes in meat images. Using meat images as input samples, the improved CNN model was used to extract image features. The model was optimized using data augmentation and batch normalization techniques, and SVM was used to effectively recognize 5 types of pork images. Finally, this paper verifies the effectiveness of the model by comparing it with other methods.

References

1. Guangli, C., Wei, Z., et al.: A method of fruit picking robot target identification based on machine vision[J]. *J. Chin. Agricult. Mechaniza* **39**(2), 83–88 (2018)
2. Shen, D.G., Wu, G.R., Suk, H.I.: Deep learning in medical image analysis [J]. *Ann. Rev. Biol. Eng.* **19**, 221–248 (2017)
3. He, K., Gkioxari, G., Dollár, P., et al.: Mask-RCNN[C]. In: *Proceedings of the IEEE International Conference on Computer Vision*, pp. 2961–2969 (2017)
4. Moeskops, P., Viergever, M.A., Mendrik, A.M., de Vries, L.S., Benders, M.J., Išgum, I.: Automatic segmentation of MR brain images with a convolutional neural network. *IEEE Trans. Med. Imaging* **35**, 1252–1261 (2016)
5. Saunders, C., Stitson, M.O., Weston, J., et al.: *Support vector machine-reference manual* (2000)
6. Middleton, I., Damper, R.I.: Segmentation of magnetic resonance images using a combination of neural networks and active contour models. *Med. Eng. Phys.* **26**, 71–86 (2004)
7. Zhao, L., Jia, K.: Multiscale CNNs for brain tumor segmentation and diagnosis[J]. *Comput. Math. Methods Med.* **5**, 1–7 (2016)
8. Dolz, J., Desrosiers, C., Ayed, B.: 3D fully convolutional networks for subcortical segmentation in MRI: a large-scale study. *Neuroimage* **S1053–8119** (17) 30332 (2017)
9. Wu, G., Kim, M.J., Wang, Q., et al.: Scalable high performance image registration framework by unsupervised deep feature representations learning. *IEEE Trans. Biomed. Eng.*, **63**(7), 1505–1516
10. Miao, S., Wang, Z.J., Liao, R.: A CNN regression approach for real-time 2D/3D registration. *IEEE Trans. Med. Imaging* **35**, 1352–1363 (2016)
11. Ghesu, F.C., Georgescu, B., Mansi, T., et al.: An artificial agent for anatomical landmark detection in medical images. In: *International Conference on Medical Image Computing and Computer-Assisted Intervention*, pp. 229–237 (2016)
12. Hua, K.L., Hsu, C.H., Hidayati, S.C., Cheng, W.H., Chen, Y.J.: Computer-aided classification of lung nodules on computed tomography images via deep learning technique. *Onco. Targets. Ther.* **8**, 2015–2022 (2015)
13. Huynh, B.Q., Li, H., Giger, M.L.: Digital mammographic tumor classification using transfer learning from deep convolutional neural networks. *J. Med. Imaging* **3**(3), 034501 (2016)
14. Nair, V., Hinton, G.E.: Rectified linear units improve restricted boltzmann machines[C]. In: *International Conference on Machine Learning* (2010)
15. Cortes, C., Vapnik, V.: Support-vector networks[J]. *Mach. Learn.* **20**(5), 273–297 (1995)

16. Liu, D., Pu, H., Wang, L., et al.: Combination of spectra and texture data of hyperspectral imaging for prediction of p H in salted meat[J]. *Food Chem.* **160**, 330–337 (2014)
17. Girolam, A., Napolitano, F., Faraone, D., et al.: Measurement of meat color using a computer vision system[J]. *Meat Sci.* **93**(1), 111–118 (2013)



Research on Asphalt Pavement Disease Detection Based on Object Detection Algorithms

Wendang Cheng¹, Ke Hou¹, Wenjiang Liu^{2(✉)}, and Feng Liu³

¹ School of Rail Transportation, Shandong Jiaotong University, Jinan 250357, Shandong, China

² School of Aeronautics, Shandong Jiaotong University, Jinan 250357, Shandong, China
574523006@qq.com

³ Jinan Urban Construction Group, Jinan 250031, Shandong, China

Abstract. The present manuscript endeavors to furnish a comprehensive scrutiny of the model framework implemented by YOLOv5s for object detection, with a particular emphasis on its enhancements for detecting irregularities on asphalt road surfaces. The evaluation of the model encompasses precision and recall metrics, with mAP serving as the principal performance indicator. In order to augment the precision of the model, the backbone network has been fortified by integrating the ResNet18 residual network and the ECA attention mechanism. This augmentation has significantly enhanced the model's capacity to detect cracks and potholes, resulting in a notable 6.0% increase in mAP compared to the original YOLOv5s model. The integration of the ResNet18 network and ECA attention mechanism has considerably amplified the model's ability to discern intricate features. Simultaneously, this integration has also facilitated in curtailing computational costs, thus rendering the model more efficient. The experimental analysis conducted in this context provides explicit evidence of the superiority of the YOLOv5s-RD model over the original YOLOv5s model in identifying and localizing road imperfections. The findings underscore the potential of this enhanced model framework to make a significant contribution to the domain of road maintenance and safety.

Keywords: Pavement distress · Object detection · YOLOv5s · ResNet · ECA attention mechanism

1 Introduction

Highways are of utmost importance to our national infrastructure, and their efficient preservation is a crucial factor in ensuring seamless and secure operations. As of the conclusion of 2021 [1], the total length of roadways in the nation has reached an impressive 5.28 million kilometers, with road maintenance accounting for nearly 99.0% of this mileage. This serves as an indication that our nation's highway maintenance has entered the stage of "comprehensive maintenance", with the size of road maintenance continuously expanding. At present, the identification of asphalt pavement defects primarily relies on visual inspection and simple instrument measurements. However, these techniques are subjective and vulnerable to a variety of factors, such as on-site environmental conditions. However, the aforementioned approaches are prone to subjectivity and

vulnerability to diverse influences including on-site environmental conditions. Therefore, regions exhibiting pre-existing anomalies may witness a considerable amount of both false positives and false negatives. To optimize detection efficacy and mitigate the occurrence of false positives and false negatives, it is imperative to delve into more scientific and precise detection methodologies. These approaches must curtail the impact of subjective factors, thereby elevating objectivity and accuracy during the detection process.

In recent years, the domain of defect detection has witnessed substantial progress owing to the advancements in deep learning technology. These advancements have led to the development of defect detection techniques that rely on deep learning. These techniques can be broadly classified into two categories, which are differentiated by their network architectures. The first category encompasses two-stage detection algorithms that include notable instances such as the Region-based Convolutional Neural Network [2] (R-CNN), Fast R-CNN [3], and Faster R-CNN [4], among others. R-CNN utilizes sliding windows to generate candidate regions for detection. However, this approach is intricate and computationally demanding. Recognizing the necessity to address the laborious selective search process in R-CNN, Faster R-CNN introduces region proposal networks as a substitute for selective search. Alzraiee et al. [5] have exemplified an application of Faster R-CNN to road surface damage detection. These two-stage detection algorithms have exhibited potential in enhancing defect detection accuracy, and their incorporation of deep learning techniques proffers valuable insights for augmenting the detection process. Research has evinced that two-stage detection methodologies can be employed for the detection of surface defects on roads and other surfaces. Nevertheless, the intermediate processes are intricate, encompassing a considerable number of iterative experiments, which result in inefficiency and complexity in fulfilling on-site detection requisites.

The second classification pertains to detection algorithms that are single-stage, typified by CenterNet [6] and YOLO [7]. These algorithms manifest a significant advantage, whereby the need for prior knowledge of candidate bounding boxes is eliminated. Instead, they integrate object image feature extraction and box prediction to estimate image categories and evaluate region coordinates. This methodology leads to a substantial improvement in detection efficiency by streamlining the process and removing the requirement for manual bounding box annotations. Through the utilization of these integrated techniques, these algorithms achieve enhanced accuracy and efficiency in defect detection. Nonetheless, the CenterNet algorithm displays evident drawbacks, such as poor performance in the presence of small objects and imbalanced aspect ratios, as well as slower speed. Furthermore, handling targets with imbalanced aspect ratios may pose challenges. On the contrary, the family of algorithms known as YOLO, comprising YOLOv3 [8], YOLOv4 [9], and YOLOv5, bring about remarkable advantages in both the speed and accuracy of detection. Xue et al. [10] proposed a technique of detecting defects in asphalt pavement based on YOLOv3, which enables the precise detection and localization of road cracks. Additionally, Rahman et al. [11] introduced a method for detecting defects in asphalt pavement based on YOLOv4, that is capable of simultaneously detecting and localizing various types of road surface defects, such as

cracks, potholes, and surface damages. These approaches, which employ YOLO, exhibit excellent performance in the detection of defects in asphalt pavement.

Existing methodologies for the detection and recognition of road defects based on YOLOv3 and YOLOv4 present certain limitations with regard to real-time detection requirements and the handling of complex data features associated with such defects. Conversely, the YOLOv5 series of algorithms surpass YOLOv3 and YOLOv4 in both detection accuracy and speed. As such, the objective of this study is to investigate enhancements of the YOLOv5s algorithm and assess its applicability in detecting asphalt pavement defects. Through the improvement in the YOLOv5s algorithm, we aim to enhance its detection capabilities in the presence of complex data features.

2 YOLOv5s Model Framework

The YOLOv5s methodology represents an advanced single-stage detection approach that incorporates both feature extraction and box prediction for object classification and evaluation. Notably, YOLOv5s distinguishes itself from other algorithms through its smaller model size, faster detection speed, and heightened accuracy. This outcome is achieved by means of a staged training strategy that partitions the network into three distinct phases: backbone, neck, and head. The model architecture is shown in Fig. 1. Importantly, YOLOv5s offers a more compact model size, quicker detection speed, and superior accuracy than other algorithms. In the backbone phase, the CSPDarknet53 network architecture is implemented to extract feature information from images. This architecture ensures both accuracy and resolves the issue of gradient repetition during information propagation. The neck phase incorporates PANet and FPN approaches to fuse and enhance contextual information within the features. Lastly, the head phase represents the core component of the object detection network, utilizing the YOLOv5 architecture for object detection and localization.

Furthermore, YOLOv5s incorporates a variety of techniques for preprocessing image data, including Mosaic data augmentation, adaptive anchor box algorithms, and adaptive image scaling. These methods are instrumental in enhancing the detection performance of YOLOv5s, particularly for small objects, while also diminishing computational complexity. Additionally, these preprocessing techniques contribute to the model's robustness and generalization capabilities, enabling it to excel in a diverse array of defect detection scenarios.

3 Improving the Detection Model for Asphalt Pavement Defects

This investigation principally incorporates an enhanced ResNet18 residual network into the foundational network to augment the profundity of convolutional layers. Moreover, a mechanism of attention known as Efficient Channel Attention (ECA) is implemented into the foundational network. Consequently, a fresh network for the detection of asphalt defects, named YOLOv5s of Road Detection (YOLOv5s-RD), is put forward.

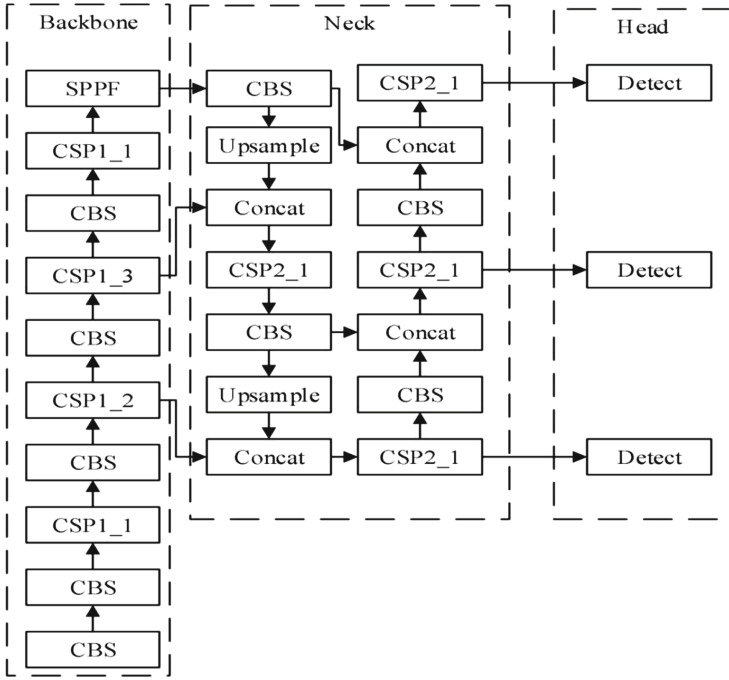


Fig. 1. Structure of YOLOv5s

3.1 ResNet18 Residual Network

ResNet18 is a profound residual network that comprises numerous residual blocks. The ResNet18 residual network’s structure and fundamental residual block are depicted in Fig. 2.

In the network architecture, each residual block is composed of two convolutional layers and a skip connection. The convolutional layers utilize 3×3 kernels with an output channel of 64 that matches the input channel. The skip connection facilitates the direct addition of the input to the convolutional layers’ output, resulting in seamless information flow to the subsequent layer. To increase the network’s depth, multiple stacks of residual blocks are utilized, with each stack having a varying number of residual blocks. This design choice enables the network to learn more intricate and nuanced feature representations. ResNet18 incorporates global average pooling after the stack of residual blocks, which aggregates the feature maps of each channel into a scalar value, aiding in summarizing the learned features. This design allows the network to learn more complex feature representations. Finally, the resultant of the global average pooling is linked to a fully connected layer, thereby facilitating the mapping of features to the ultimate class predictions. ResNet18 employs residual connections to effectively enable information propagation within the network. This particular architecture empowers ResNet18 to showcase remarkable performance in the realm of asphalt pavement disease detection. Consequently, ResNet18 holds considerable advantages in tackling the issue of asphalt pavement disease image classification.

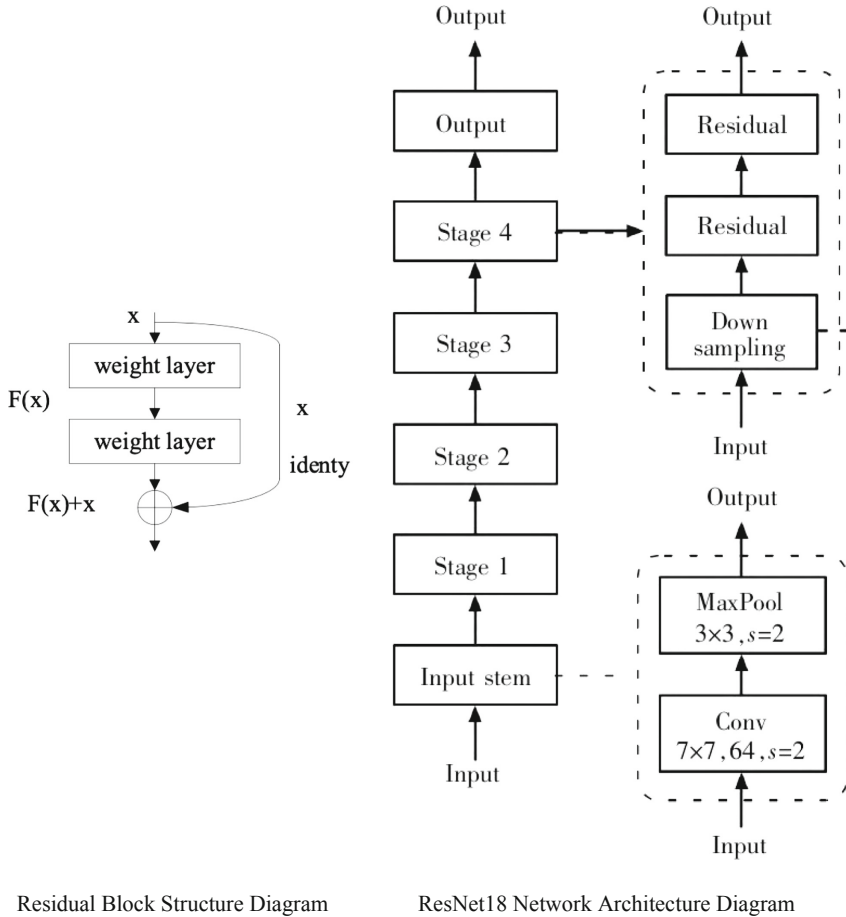


Fig. 2. Shows the network architecture diagram.

3.2 ECA Attention Mechanism

The ECA mechanism has been developed with the specific goal of augmenting networks' representational capacity. Its primary objective is to reduce parameters and computational complexity while also mitigating the redundancy of attention mechanisms. ECA, akin to the SE (Squeeze-and-Excitation) attention mechanism, predominantly focuses on modeling inter-channel dependencies. Nevertheless, it accomplishes this with improved computational efficiency. The integration of the ECA mechanism into the network architecture model leads to a more effective and efficient approach to capturing inter-channel dependencies, ultimately resulting in enhanced performance. Figure 3 exhibits a visual representation of the ECA network architecture model.

The ECA operates in the following manner: Initially, the input feature map is subjected to global average pooling, which transforms the feature map of each channel into a scalar value. This scalar value represents the global importance of the features of that

channel. Subsequently, a one-dimensional convolution operation is executed on the outcome of the global average pooling using a window size of k . This convolution operation captures the inter-channel dependencies by convolving the features of the preceding and succeeding channels at each position, generating a new channel-wise representation. To ensure that the attention weights are confined within the range of 0 and 1, the output of the one-dimensional convolution is activated by a sigmoid function. This results in attention weights for each channel, which are then employed to weigh the original feature map. Finally, the attention weights are multiplied by the original feature map, leading to a feature map that is weighted by the ECA attention mechanism.

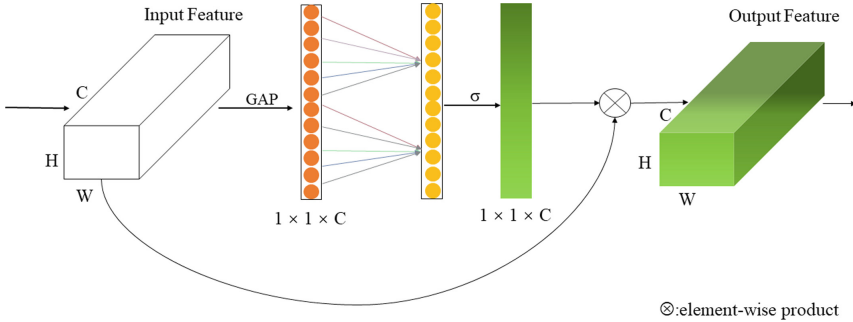


Fig. 3. Shows the model diagram of the ECA network structure.

4 Experiment

4.1 Experimental Environment and Dataset

The experimental procedure was carried out within a Windows operating system milieu, utilizing the NVIDIA RTX A5000 GPU that possessed an 8GB memory. The training phase encompassed 200 epochs, with a batch size of 8 and AdamW optimization algorithm for parameter optimization. An initial learning rate of 0.01 was employed during the training. In addition, the input image resolution was set to 640×640 .

To detect defects on roads, the dataset utilized in this particular study was made publicly available by the Roboflow website in the year 2023. The dataset comprised 1797 validated images of road defects, encompassing two distinct categories of defects, namely cracks, and potholes. To overcome the limitation of a relatively small number of samples, data augmentation techniques were employed to substantially increase the dataset size. These techniques encompassed the application of various operations such as random rotation, shear transformation, position translation, and random scaling to generate a substantial number of additional validated images of defects. Consequently, the dataset was augmented to a total of 8160 validated images of defects. To enable the training and validation procedures, the augmented dataset underwent a randomized division into two distinct subsets, namely the training set and the validation set, in an 8:2 proportion. This partitioning strategy ensured an adequate volume of data for model

training and at the same time allowed for an objective assessment of its performance on novel data during the validation phase.

4.2 Evaluation Metrics

In the domain of detecting defects in asphalt pavement, conventional precision metrics are inadequate to effectively account for the presence of multiple labels. To appraise the efficacy of the model, we resorted to a binary classification confusion matrix. This matrix comprises various categories including true positives (TP), false positives (FP), true negatives (TN), and false negatives (FN). A sample confusion matrix is depicted in Table 1.

Table 1. Confusion matrix for binary classification

Confusion Matrix		Real Value	
		Positive	Negative
Predicted value	Positive	TP	FP
	Negative	FN	TN

The formulas for precision and recall are as follows:

$$P = \frac{TP}{TP + FP} \tag{1}$$

$$R = \frac{TP}{TP + FN} \tag{2}$$

To thoroughly evaluate the efficacy of the model, this investigation utilizes mAP(mean Average Precision) as the assessment criterion. mAP is deduced from the precision and recall of the model’s predictions. The equations employed to determine AP (Average Precision) and mAP are as follows:

$$AP = \frac{\sum_{i=1}^N P_i}{N} \tag{3}$$

$$mAP = \frac{\sum_{j=1}^M AP_j}{M} \tag{4}$$

In the equation: M represents the total number of classes used for detection, and N represents the number of images tested.

4.3 Experimental Results and Analysis

To corroborate the efficacy of the algorithm proposed, a sequence of five experiments were executed to scrutinize the influence of network architecture variations on algorithmic performance. Diverse models were utilized to detect defects in the aforementioned

experiments. Specifically, the native YOLOv5s model, YOLOv5s-CBAM model, which integrates the CBAM attention module, YOLOv5s-ECA model, which integrates the ECA attention module, YOLOv5s-ResNet model, which integrates ResNet18 residual network, and the YOLOv5s-RD model, as proposed in this paper, were all trained and assessed in the five experiments.

From Table 2, it is apparent that the improved YOLOv5s-RD manifests superior detection capabilities for both categories of defects in comparison with the native YOLOv5s model. Specifically, YOLOv5s-ResNet exhibits a noteworthy mAP enhancement of 1% for mAP50 and 0.9% for mAP95 relative to the original model. On the other hand, YOLOv5s-ECA demonstrates a mAP50 improvement of 1.8% and a mAP95 improvement of 1.1% in contrast to the original model. By integrating these techniques, YOLOv5s-RD achieves a remarkable mAP50 improvement of 6.0% and a mAP95 improvement of 5.2% compared to the original model.

Table 2. Presents the experimental performance of the improved YOLOv5s and the original YOLOv5s.

Model	Precision	Recall	mAP50			mAP50–95
			Crack	Pothole	All	
YOLOv5s	0.702	0.678	0.542	0.844	0.693	0.362
YOLOv5s-CBAM	0.679	0.676	0.53	0.836	0.683	0.349
YOLOv5s-ResNet	0.714	0.682	0.545	0.862	0.703	0.371
YOLOv5s-ECA	0.715	0.685	0.555	0.867	0.711	0.373
YOLOv5s-RD	0.761	0.717	0.614	0.892	0.753	0.414

Random sampling was conducted on the validation set's samples, and Fig. 4 displays the outcomes for road defect detection. The images from left to right present the ground truth labels, the native YOLOv5s model's detection outcomes, and the improved YOLOv5s-RD model's detection results, which were proposed in this research. It can be observed that within this dataset, the native YOLOv5s model exhibits relatively inferior detection performance, indicating issues like false positives and false negatives. In contrast, the enhanced model showcases elevated precision, diminished false positive rate, and reduced false negative rate.

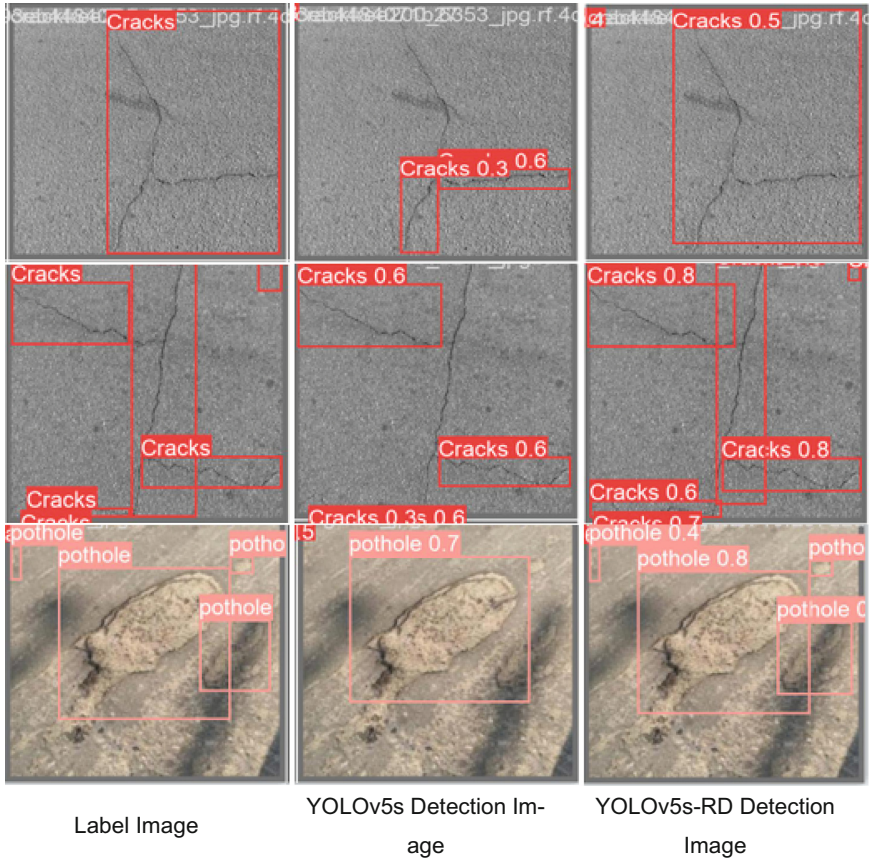


Fig. 4. Illustrates the detection results of road surface defects.

5 Conclusion

The present investigation endeavors to enhance the performance of the YOLOv5s model employed for the detection of asphalt road defects. Various modifications, namely, the integration of ResNet18 and ECA attention mechanisms in the backbone network, have been suggested. The experimental findings reveal that the proposed YOLOv5s-RD model surpasses the original YOLOv5s model in terms of precision, recall, mAP50, and mAP50–95. The efficacy of utilizing mAP as an evaluation metric for multi-label image classification tasks has also been demonstrated. Future research will concentrate on broadening the detection capabilities to other kinds of road defects, such as cracks, ruts, and patches. In summary, these modifications to the YOLOv5s model furnish a more precise and efficient solution for detecting asphalt road defects.

Project. Key Technological Project in the Transportation Industry, Project Number: 2022-ZD4–066.

References

1. Ministry of Transport. Statistical Bulletin on the Development of the Transportation Industry in 2021 [N]. China Transportation News, 2022–05–25(002)
2. Girshick, R., Donahue, J., Darrell, T., et al.: Rich feature hierarchies for accurate object detection and semantic segmentation[C]. In: 2014 IEEE Conference on Computer Vision and Pattern Recognition(CVPR), pp. 580–587. Columbus, OH, USA, IEEE (2014)
3. Girshick, R.: Fast R-CNN[C]. In: 2015 IEEE International Conference on Computer Vision (ICCV), pp. 1440–1448. Santiago, Chile, IEEE (2015)
4. Ren, S., He, K., Girshick, R., et al.: Faster R-CNN: towards real-time object detection with region proposal networks[J]. *Adv. Neural Inf. Process. Syst.*, **28** (2015)
5. Alzraiee, H., Leal Ruiz, A., Sprotte, R.: Detecting of pavement marking defects using faster R-CNN[J]. *J. Perform. Constr. Facil.* **35**(4), 04021035 (2021)
6. Duan, K., Bai, S., Xie, L., et al.: Centernet: keypoint triplets for object detection[C]. In: Proceedings of the IEEE/CVF International Conference on COMPUTER vision, pp. 6569–6578 (2019)
7. Redmon, J., Divvala, S., Girshick, R., et al.: You only look once: unified, real-time object detection[C]. In: 2016 IEEE Conference on Computer Vision and Pattern Recognition (CVPR), pp. 779–788. Las Vegas, NV, USA, IEEE (2016)
8. Redmon, J., Farhadi, A.: YOLOv3: an incremental improvement[EB/OL]. 2018–04–08[2022–08–12]. <https://arxiv.org/abs/1804.02767>
9. Bochkovskiy, A., Wang, C.Y., Liao, H.Y.M.: YOLOv4: optimal speed and accuracy of object detection [EB/OL]. 2020–04–23[2022–08–12]. <https://arxiv.org/abs/2004.10934>
10. Xue, Y., et al.: YOLONG: a YOLO-based approach for road crack detection. *IEEE Access* **8**, 133235–133245 (2020)
11. Rahman, S.M.M., et al.: Deep learning-based asphalt pavement disease detection using YOLOv4. *IET Intel. Transp. Syst.* **15**(2), 229–236 (2021)



Research on Deep Learning-Based Concrete Bridge Crack Detection

Ke Hou¹, Wendang Cheng¹, Wenjiang Liu^{2(✉)}, and Feng Liu³

¹ School of Rail Transportation, Shandong Jiaotong University, Jinan 250357, Shandong, China

² School of Aeronautics, Shandong Jiaotong University, Jinan 250357, Shandong, China
317012753@qq.com

³ Jinan Urban Construction Group, Jinan 250031, Shandong, China

Abstract. Cracks are prevalent structural defects in concrete bridges. Presently, cracks detection heavily relies on manual inspection, which is inefficient and inaccurate. The industry has been focusing on research into automated and intelligent methods of crack detection. In this paper, we propose an enhanced deep learning technique based on YOLOv5 that addresses the issues of high false detection rates and poor real-time performance in detecting concrete bridge cracks. To begin with, we replace the C3 module in YOLOv5 with the C2f module from YOLOv8, which expands the network's perception range and the capability to represent features. Secondly, we introduce the SE attention mechanism, which adaptively adjusts the channel weights of feature maps, enhancing the focus on important features. Finally, we adopt a DyHead object detection head based on the attention mechanism, which performs excellently in capturing the details and boundary information on bridge cracks. Experiments have demonstrated that this method can rapidly and accurately detect cracks with a low false detection rate. The average precision (mAP, Mean Average Precision) reaches 94.2%, showing a significant improvement of 9.7% compared to the original network. These results showcase the outstanding performance of the proposed method in concrete bridge crack detection tasks.

Keywords: Cracks in bridges · Object detection · YOLO v5 · C2f module · SE attention mechanism · DyHead

1 Introduction

In the realm of transportation, bridges are a vital component of infrastructure, which is crucial for ensuring traffic safety and driving economic development. Nevertheless, prolonged usage and environmental factors can cause cracking issues in concrete bridges, and data indicates that cracks are a significant contributor to bridge damage [1, 2]. This has a significant impact on bridge stability and longevity. Traditional methods of detecting cracks in concrete bridges rely primarily on manual inspection and visual detection, which are plagued by high labor costs, low efficiency, and subjectivity issues. Thus, proposing a method that can rapidly and accurately detect and identify cracks in concrete bridges is essential, considering the future demand for detecting a large number of concrete bridges.

In recent years, there have been remarkable advances in deep learning-based image processing techniques across multiple fields. These innovative solutions have proven superior to traditional algorithms, leading to the widespread implementation of deep learning-related algorithms in the industrial sector [3]. The concept of deep learning was first introduced by Hinton et al. [4] in 2006. This approach involves multiple hidden layers and perceptual layers, providing a better representation of abstract and deep-level information. Its application to bridge crack detection enables automated and real-time detection of cracks, reducing the workload of bridge maintenance departments. Given the real-time requirements of bridge crack detection, object detection algorithms with faster detection speeds are necessary. YOLO (You Only Look Once) is a single-stage detection algorithm known for its faster speed [5]. The YOLO series algorithms, including YOLO v3 [6], YOLO v4 [7], and YOLO v5, have demonstrated significant advantages in detection speed and accuracy, and have been widely applied to intelligent identification of structural cracks. Zhang et al. [8] proposed an improved YOLO v3 model for bridge disease detection. They successfully improved the accuracy of disease recognition by introducing the Focal Loss function and a new transfer learning method. Jang et al. [9] presented a deep learning network called HDCB-Net based on a hybrid extended convolutional block, combined with YOLO v4 for pixel-level crack detection. The YOLO v5 series algorithms, with their significant improvements in recognition accuracy and detection efficiency, have enabled real-time and precise detection of bridge cracks [10].

In this manuscript, the YOLOv5s object detection model was subject to modification through the development of module programs utilizing Python 3.8. A total of 2164 and 538 images comprising annotated information were allocated to serve as the training and validation datasets for the modified model and the original model, respectively, which were employed in the execution of detection comparative experiments. The results of the comparative analyses indicated a substantial enhancement in the detection performance of the modified model, thereby signifying its wider scope of applicability and value.

2 YOLOv5 Model

The YOLOv5 framework functions as a deep learning-based model for detecting objects. The fundamental concept of the YOLO (You Only Look Once) sequence of models involves transforming object detection tasks into a solitary forward pass predicament, which allows for the detection of objects in real time. The YOLOv5 framework is divided into four versions, specifically s, m, l, and x, which are based on the network's depth and width. YOLOv5s has the smallest network depth in the YOLO series algorithms and is the fastest in terms of detection speed. This consequently fulfills the requirement for real-time detection.

The network architecture of YOLOv5 comprises three primary components: the backbone network, the feature pyramid network (FPN), and the prediction head.

1. Backbone: The backbone network functions as the feature extractor in YOLOv5, with its main responsibility being to derive features from the input image. CSP-Darknet53 is the backbone network for YOLOv5, a convolutional neural network structure featuring numerous convolutional layers, batch normalization layers, and

activation function layers. This structure is equipped with CSP (Cross Stage Partial) connections, which facilitate the reduction of parameters alongside the improvement of feature representation capacity. CSPDarknet53 is capable of extracting semantic features from the input image, which are subsequently utilized in object detection tasks.

2. **Feature Pyramid Network (FPN):** The Feature Pyramid Network addresses the challenge of detecting objects on different scales. It incorporates additional convolutional layers and upsampling operations into the backbone network to merge features of different levels, resulting in feature maps with multi-scale information. The FPN utilized in YOLOv5 is known as PANet (Path Aggregation Network). PANet performs feature fusion through both bottom-up and top-down pathways. The bottom-up pathway extracts semantic information from the lower-level feature maps of the backbone network and performs upsampling. The top-down pathway combines the feature maps from the previous level with the feature maps from the bottom-up pathway. Through this fusion operation, PANet generates feature maps with multi-scale information, enabling the detection of objects of different sizes.
3. **Prediction Head:** The Prediction Head is responsible for predicting the position and class of objects in YOLOv5. It performs predictions on feature maps on different scales and generates bounding box coordinates and class confidences. It comprises convolutional layers and fully connected layers. For each scale of feature maps, the Prediction Head generates a set of bounding boxes and class confidences. These bounding boxes contain the positional information of the objects, while the class confidences indicate the probability of the object being present within the bounding box. The Prediction Head has the ability to adapt to various object detection tasks, modifying its predictions based on the number and size of the targets.

3 Algorithm Improvement

3.1 Improvement on Backbone and Feature Pyramid Network Structure

The C2f module comprises several Residual Blocks, each of which involves two convolutional layers. The input to the C2f module is the feature map from the previous layer, and the output feature map is achieved after the feature map passes through multiple Residual Blocks. These feature maps are subsequently fused with feature maps from lower layers to generate the final feature representation.

The C2f module performs multi-scale feature fusion by introducing multiple Residual Blocks and utilizing feature maps from different levels. The fusion of features from different levels allows the C2f module to leverage contextual information on the image, thereby enhancing object detection accuracy and robustness. The use of skip connections and residual connections in each Residual Block effectively transfers low-level features to higher-level features, which helps alleviate information loss during feature transmission while preserving their richness and diversity. The convolutional layers within each Residual Block extract more informative features, which are then fused into the final feature representation through residual connections. This improves the model's discriminative ability for objects and backgrounds, thereby increasing the accuracy of object

detection. The C2f module may have better multi-scale feature fusion capabilities compared to the C3 module. Incorporating the C2f module into the YOLO v5 model can enhance the detection capability for objects on different scales, thus improving accuracy and robustness in object detection. Figure 1 shows the structure diagram of the C2f module.

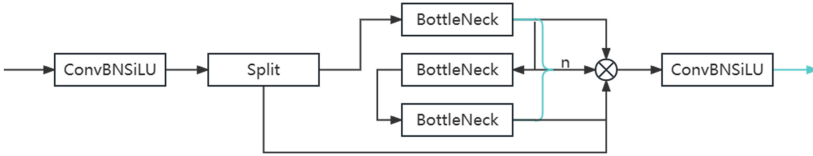


Fig. 1. Structure diagram of the C2f module

3.2 SE Attention Mechanism

The Squeeze-and-Excitation (SE) attention mechanism operates on the principle of compressing spatial dimensions into a feature vector and then learning channel weights to adaptively weight the feature map. The mechanism consists of three stages, namely, the squeeze phase, excitation phase, and re-excitation phase. In the squeeze phase, the input feature map is globally average-pooled to obtain a feature vector that represents the statistical information about the entire feature map. Subsequently, a fully connected layer is applied at the excitation phase to learn channel weights. The weights obtained in the re-excitation phase represent the importance or weight distribution of each corresponding channel. The original feature map is adaptively weighted channel-wise, and element-wise multiplication is performed with the weights obtained in the re-excitation phase. The SE attention mechanism can learn the importance of each channel and weight the feature map accordingly, thereby improving the detection accuracy of small targets. The SE network is illustrated in Fig. 2.

3.3 DyHead

DyHead comprises numerous attention modules, encompassing scale-aware attention, spatial attention, and channel attention. Each attention module is composed of an attention generation module and a feature fusion module. The former is accountable for generating dynamic weights, whereas the latter applies these dynamic weights to effectuate feature fusion on the feature maps. The network structure of DyHead is formed by hierarchically stacking these multiple attention modules in accordance with the levels of the feature maps.

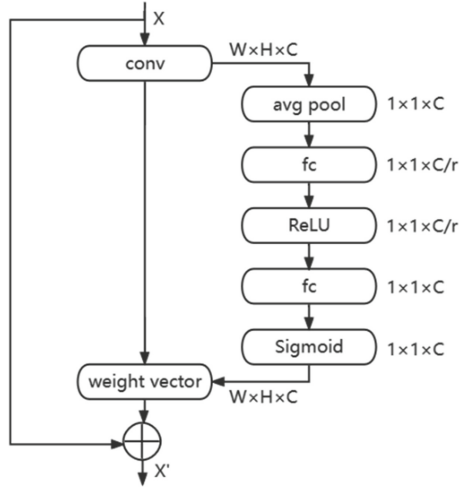


Fig. 2. SE network diagram

In particular, the scale-aware attention mechanism is introduced to dynamically integrate features from varied scales based on their respective semantic significance.

$$\pi_L(F) \cdot F = \sigma \left(f \left(\frac{1}{SC} \sum_{S,C} F \right) \right) \cdot F \quad (1)$$

where $f(\cdot)$ represents a linear approximation implemented by a 1×1 convolutional layer, and $\sigma(x) = \max(0, \min(1, \frac{x+1}{2}))$ is a hard-sigmoid function.

The attention module that is spatial-aware is centered on differentiating regions between spatial positions and feature levels, with a focus on maintaining a consistent coexistence within these regions. Given the high-dimensional nature of this module, it is broken down into two distinct steps. Firstly, deformable convolutions are employed to enable attention learning for regions that are discriminative, subsequently leading to the aggregation of features across levels at the same spatial positions.

$$\pi_S(F) \cdot F = \frac{1}{L} \sum_{l=1}^L \sum_{k=1}^K w_{l,k} \cdot F(l; p_k + \Delta p_k; c) \cdot \Delta m_k \quad (2)$$

Among them, K represents the number of positions in coefficient sampling, $p_k + \Delta p_k$ represents the shifted position, and Δm_k represents the importance level of position p_k .

The deployment of channel attention is ultimately realized to facilitate the dynamic switching of channel activation and deactivation to meet the needs of various tasks.

$$\pi_C(F) \cdot F = \max \left(\alpha^1(F) \cdot F_c + \beta^1(F), \alpha^2(F) \cdot F_c + \beta^2(F) \right) \quad (3)$$

In the passage, F_c represents a slice of features in the c -th channel. $[\alpha^1, \alpha^2, \beta^1, \beta^2] = \theta(\cdot)$ is a function that learns to control the activation threshold. Initially, $\theta(\cdot)$ performs

global average pooling on an $L \times S$ dimension to reduce the dimensionality. Then, it utilizes two fully connected layers and a normalization layer, followed by applying a shifted sigmoid function to normalize the output to the range $[-1, 1]$.

The above three attention mechanisms are applied sequentially and can be nested multiple times to effectively stack multiple π_L , π_S , and π_C blocks together. The DyHead module is illustrated in Fig. 3.

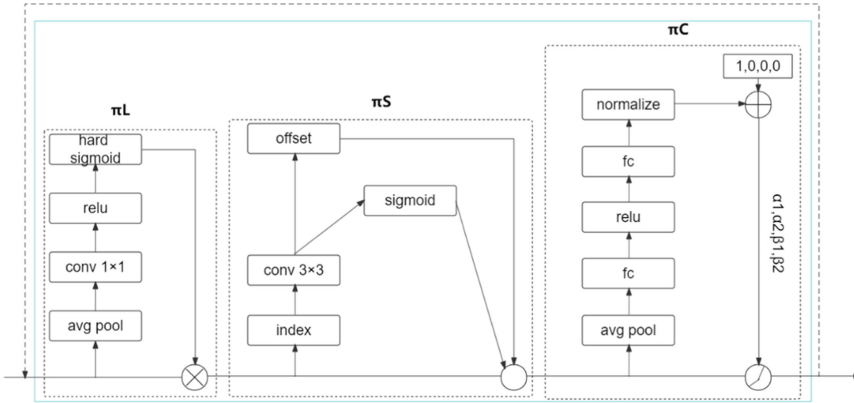


Fig. 3. Diagram of the DyHead module structure

4 Experiments

4.1 Data Source and Model Training

The experimental dataset utilized in this investigation is a publicly available dataset procured from the Roboflow platform, which serves as an AI image recognition model training data annotation platform. The dataset comprises 2702 images of cracks detected in concrete bridges. Subsequently, the dataset was arbitrarily divided into a training set and a validation set, in an 8:2 ratio.

To conduct the model training, my personal computer was utilized, which was equipped with an AMD Ryzen7 5800H CPU, 16GB RAM, and an RTX 3060 Laptop GPU with 6GB VRAM. The PyTorch deep learning framework was employed. The entire training process was scheduled for 156 epochs, and the batch size was established to be 2, based on the dataset and model size. The AdamW optimization algorithm was employed for parameter optimization, with an initial learning rate of 0.01. The input image resolution was set to 640×640 .

4.2 Experimental Results and Analysis

In order to authenticate the efficacy of the model method proposed within this article and accommodate the real-time necessities of detecting concrete bridge cracks, the

YOLO v5s model was implemented as the original model. This model was subsequently juxtaposed with YOLO v5s-MNV2, which incorporates a MobileNet V2 attention mechanism, YOLO v5s-SE, which includes an SE attention mechanism, and YOLO v5s-SE with MobileNet V2 attention mechanism. Additionally, YOLO v5s-SEDH, which integrates an SE attention mechanism and attention-based object detection head DyHead, as well as YOLO v5s-BCD, which comprises an SE attention mechanism and attention-based object detection head DyHead proposed in this paper, and replaces the C3 module with the C2f module in the model. These models were experimentally analyzed on the same dataset.

Table 1. Experimental results of YOLO v5s model and its improved variants.

Model	mAP50	Map50–95	Precision	Recall
YOLOv5s	0.845	0.37	0.897	0.746
YOLOv5s-MNV2	0.809	0.377	0.766	0.749
YOLOv5s-SE	0.913	0.494	0.888	0.854
YOLOv5s-SEDH	0.908	0.541	0.861	0.883
YOLOv5s-CBD	0.942	0.587	0.888	0.879

According to the findings presented in Table 1, it is evident that the enhanced YOLO v5s-CBD model exhibits a significant advancement over the original YOLO v5s model. By incorporating attention mechanisms to augment the extraction of crucial features relating to cracks, it is observed that the integration of the SE attention mechanism leads to superior outcomes. Specifically, the average precision (mAP) at IoU threshold 0.5 (mAP50) experiences a 6.8% increase, and the mAP from IoU 0.5 to 0.95 (mAP50-95) is enhanced by 12.4%. Moreover, the replacement of the detection head with DyHead while incorporating the SE attention mechanism results in further progress. The mAP50 climbs by 6.3%, and the mAP50-95 is boosted by 17.1%. Given the challenge posed by larger receptive fields and the loss of local detailed information when employing larger convolutional layers in the original model's C3 module, this study proposes replacing the C3 module with the C2f module in the YOLO v5s-SEDH model. This modification enhances the feature representation capability, reduces the number of parameters, improves computational efficiency, and adapts well to handling small-sized images. The mAP50 demonstrates a 9.7% increase, and the mAP50-95 experiences a 21.7% improvement.

From Fig. 4, it can be observed that the proposed model in this paper shows significant improvement in the localization and identification of cracks compared to the native model. The improved model is able to easily detect and accurately locate bridge cracks, meeting the requirements for routine concrete bridge crack detection.

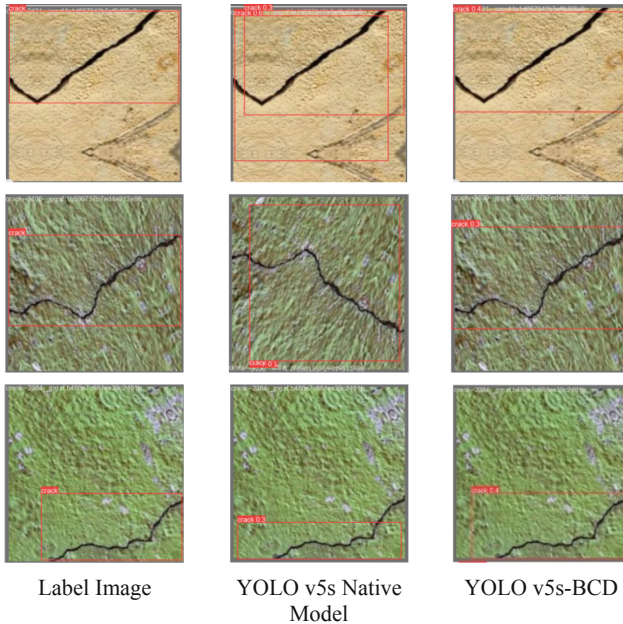


Fig. 4. Comparison of detection results

5 Conclusion

In the present investigation, the focus of attention was directed towards the detection of concrete bridge cracks using a deep learning approach. Our study involved the optimization and refinement of the YOLOv5s model. The c3 module was replaced with the c2f module from YOLOv8, the SE attention mechanism was incorporated, and the detection head was substituted with DyHead. These modifications led to a notable improvement in detection accuracy and performance. In order to compare the efficacy of the improved model with the native YOLOv5s model, comparative experiments were conducted using the same dataset. The results of the experiments demonstrated a 9.7% improvement in mAP (mean Average Precision) with the improved model. This outcome attests to the effectiveness and superiority of the introduced improvement strategies. Through the incorporation of attention mechanisms and optimization of network structure, we have successfully enhanced the accuracy and efficiency of concrete bridge crack detection. The findings of this study may provide valuable guidance for research and practical applications in related fields.

Nonetheless, despite the significant improvement in mAP achieved by our improved model, there remain certain challenges and areas that require further improvement. For instance, our model may still encounter false detections and missed detections in complex scenarios, thereby necessitating further research and enhancement. Additionally, the generalization capability and adaptability of the model need to be explored and improved for larger-scale datasets and the detection of cracks in more categories.

In summary, our study has presented a novel improved model for deep learning-based concrete bridge crack detection and has validated its effectiveness through rigorous experimentation. We are of firm conviction that these findings can provide valuable technical support for bridge safety and maintenance in the field of transportation. Furthermore, they serve as a source of inspiration and reference for future research and applications.

Project. Key Technological Project in the Transportation Industry, Project Number: 2022-ZD4-066.

References

1. Bu, G.P., Chanda, S., Guan, H., et al.: Crack detection using a texture analysis-based technique for visual bridge inspection. *Electron. J. Struct. Eng.* **14**(1), 41–48 (2015)
2. Ruan, X.L., Wang, B., Jing, G.Q., Ji, D.J., Wang, Y.L.: Research on automatic identification technology for surface cracks in bridge concrete structures. *World Bridges* **45**(6), 55–59 (2017)
3. Sun, Z.J., Xue, L., Xu, Y.M., et al.: A survey of deep learning research. *J. Comput. Appl. Res.* **29**(8), 2806–2810 (2012)
4. Hinton, G.E., Salakhutdinov, R.R.: Reducing the dimensionality of data with neural networks. *Science* **313**(5786), 504–507 (2006)
5. Du, Y.C., Pan, N., Xu, Z.H., et al.: Pavement distress detection and classification based on yolo network. *Int. J. Pavement Eng.* **22**(13), 1659–1672 (2021)
6. Redmon, J., Farhadi, A.: YOLOv3: An Incremental Improvement. 2018-04-08 [2022-08-12]. <https://arxiv.org/abs/1804.02767>
7. Bochkovskiy, A., Wang, C.Y., Liao, H.Y.M.: YOLOv4: Optimal Speed and Accuracy of Object Detection. 2020-04-23 [2022-08-12]. <https://arxiv.org/abs/2004.10934>
8. Zhang, C.B., Chang, C.C., Jamshidi, M.: Concrete bridge surface damage detection using a single-stage detector. *Comput.-Aided Civ. Infrastruct. Eng.* **35**(4), 389–409 (2020)
9. Jiang, W., Liu, M., Peng, Y., et al.: HDCB-net: a neural network with the hybrid dilated convolution for pixel-level crack detection on concrete bridges. *IEEE Trans. Industr. Inf. Industr. Inf.* **17**(8), 5485–5494 (2020)
10. Shu, Z.K., Yan, Z.Y., Xu, X.H., et al.: Pavement crack detection method of street view images based on deep learning. *J. Phys. Conf. Ser.* **1952**(2), 022–043 (2021)



Design of Automatic Brick Laying Machine Based on TRIZ Theory

Jinyang Zhao, Hongli Zhang^(✉), and Pengcheng Zhang

Shandong Jiaotong University, No. 5001 Haitang Road Changqing University Science and
Technology Park, Jinan, China
63027776@qq.com

Abstract. The manual tiling method is inefficient and of poor quality. In order to improve the efficiency and quality of tiling, this paper designs an automatic tiling machine based on TRIZ theory. Using product analysis, the main functions of the product as well as its construction were identified; using problem analysis, the key problems to be solved in the design process were identified, including three aspects of laying ash, walking, and tile placement; conflict and contradiction analysis was conducted on the identified key problems, and the 39 engineering parameters and 40 invention principles of TRIZ theory were used to find the possible original understanding. Combined with the original understanding found, the design of three key mechanisms in the product, namely, the ash laying mechanism, the traveling mechanism and the tile laying mechanism, was completed, and the selection of the drive motor was completed. Finally, the advantages and shortcomings of the design are analyzed and improvement directions are proposed.

Keywords: TRIZ theory · Automatic brick laying machine · Structural design · Motor selection

1 Preface

Traditional tiling work is labor-intensive and time-consuming, and poses certain safety hazards. The use of automated brick-laying devices for brick-laying tasks helps to improve the efficiency, quality and safety of brick-laying work. At present, with the rapid development of automation technology, in foreign countries, some large construction companies and logistics companies have widely used this equipment, achieving important economic and social benefits [1]. In China, automatic brick-laying machines have also started to gain wide attention and application. Therefore, it is of great research importance to design an automatic brick-laying machine with high reliability and automation [2–4].

2 Product Design Process Based on TRIZ Theory

TRIZ theory is a method for problem solving and product design that is not limited to a specific field and is universal. Currently, it is widely used in product design and other fields [5, 6], and the overall product design process can be summarized into four levels:

analysis level, problem level, solution level, and design level. According to this product design process, a product design process model based on TRIZ theory is established, as shown in Fig. 1. Firstly, we start from the analysis of the product, summarize the problems that need to be solved in the design process, identify the contradictions and conflicts in the problems, and then determine the principles of problem solving through the contradiction matrix, and finally form the final feasible solution. The model is highly targeted and efficient in solving problems, avoiding the blindness of the traditional design process [7, 8].

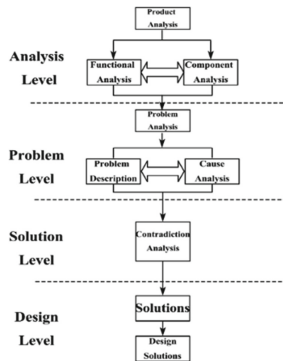


Fig. 1. Product design process based on TRIZ theory

3 Automatic Brick Laying Machine Design Analysis

3.1 Product Analysis

Analyze the product to be designed, determine the primary and secondary functions of the product to be designed, and focus on the mechanism to achieve the primary function, with the aim of improving the efficiency of the product design.

(1) Functional analysis

The purpose of functional analysis is to clarify the main function of the designed product. The main function of the automatic tile laying machine is that it can complete the whole tile laying process independently, including the task of laying ash, automatically carrying bricks, placing bricks, with mobility, and can complete independent walking; the secondary function is that it can pass its own compensation control system, and can accurately calibrate the size and shape of the bricks, and can according to different patterns can be laid as needed. The overall function tree of the product is shown in Fig. 2.

(2) Component analysis

According to the main functions determined by the functional analysis link, the main designed mechanism of the product includes three major parts: the ash laying mechanism,

the tile laying mechanism and the traveling mechanism, among which the tile laying mechanism includes the tile moving mechanism and the tile grabbing mechanism, as shown in Fig. 3.

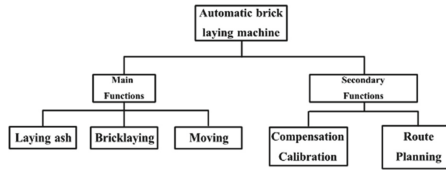


Fig. 2. Function tree of automatic brick laying machine

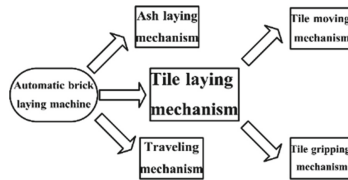


Fig. 3. The main mechanism of automatic tile laying machine

3.2 Problem Analysis

After the main mechanism to be designed has been defined through the product analysis session, it is necessary to identify the key issues to be solved in the design process through problem analysis.

(1) Problem description

Combined with the product analysis and market research, the design of this product needs to address the following issues:

- (1) What kind of mechanism can be used to make laying ash efficient.
- (2) what kind of mechanism design can make the tile moving process reliable.
- (3) what kind of gripping method is used to design the gripping mechanism to produce a large gripping force.
- (4) how to design the traveling mechanism to ensure that the walking operation can be achieved in different ground environments.

(2) Cause analysis

The following analysis of the causes of the above problems is made:

- (1) When automatic brick laying machines are operating on construction sites, construction time is tight and therefore there is a need to increase the efficiency of laying ash as much as possible to reduce wasted time.

- (2) The tile moving process is a basic operation in the construction of automatic brick laying machines. The quality of tile moving directly affects the quality of the project, so ensuring its reliability is the primary prerequisite for improving production efficiency and meeting production needs.
- (3) Has a large gripping force, can ensure that the tiles can be firmly fixed on the gripping device, to avoid loose tiles, shaking, misalignment, falling and other problems in the process of moving, to ensure the stability of tile laying work, so the gripping mechanism needs to produce a large gripping force.
- (4) Construction site ground environment is usually diverse, can walk in different ground environment, can adapt to a variety of construction sites, so as to meet a variety of different work needs, improve the versatility and adaptability of construction, more efficient completion of construction tasks, so the traveling mechanism needs to have good adaptability.

3.3 Conflict Identification and Resolution Ideas

The problem analysis session identifies the key requirements when designing each mechanism. The TRIZ theory is applied to convert the design requirements of each mechanism into 39 common engineering parameters, determine the contradiction conflicts among them, bring them into the contradiction matrix, and obtain the corresponding design principle solutions to guide the product design [9].

(1) Conflict Identification

The ash laying mechanism is designed with its high efficiency as the primary consideration. The simple structure of the ash laying mechanism cannot meet the high efficiency requirements of the brick laying operation, then the high efficiency requirements of the brick laying operation and the complexity of the mechanism constitute a contradictory conflict, when the efficiency of the mechanism is improved, it means that the complexity of the mechanism will deteriorate accordingly. Converting them according to 39 generic engineering parameters gives the improvement parameter number 39 (productivity) and the deterioration parameter number 36 (complexity of the equipment). Bringing them into the contradiction matrix, the design principles obtained are the 12th principle (equipotential), the 17th principle (dimensional excess), the 28th principle (mechanical substitution), and the 24th principle (intermediation).

The primary consideration in the design of the tile moving mechanism is reliability. When performing moving operations, the tile moving mechanism should follow a simple and straightforward established operation to place the tiles in the designated position, without the need for complex operations of human intervention in the moving process, reducing the operability of the mechanism and reducing the probability of problems in the operation of the mechanism. At this point, the reliability of the mechanism and the operability of the mechanism constitute a contradictory conflict, and when the reliability of the mechanism is improved, the operability of the mechanism will deteriorate accordingly. Converting them according to 39 general engineering parameters gives the improvement parameter number 27 (reliability) and the deterioration parameter number

33 (ease of operation). Bringing them into the contradiction matrix, the design principles obtained are the 27th principle (cheap substitution), the 17th principle (excessive dimensionality), and the 40th principle (use of mixed materials).

The primary consideration in the design of the tile gripping mechanism is the magnitude of the gripping force. When performing gripping operations, it is desirable to generate a large gripping force by using multiple parts working together in the mechanism, and this is difficult to achieve if the number of parts comprising the mechanism is small. At this point the magnitude of the gripping force of the mechanism and the number of components that make up the mechanism form a contradictory conflict, and when the gripping force generated by the mechanism is improved, the number of components that make up the mechanism deteriorates accordingly. Converting them according to 39 general engineering parameters yields an improvement parameter numbered 10 (force) and a deterioration parameter numbered 26 (number of substances). Bringing them into the contradiction matrix, the design principles obtained are the 14th principle (spherical), the 29th principle (pneumatic-hydraulic structure), the 18th principle (mechanical vibration), and the 36th principle (system complexity).

The primary consideration in the design of the travel mechanism is adaptability. Automatic brick laying machine needs to face the slope, uneven road and other diverse operating scenarios, requiring the ability to quickly move to the operating range in a diverse environment, that is, to complete the task of tile laying, without too precise requirements for movement accuracy. At this point the adaptability of the travel mechanism and the accuracy of the travel mechanism operation constitute a contradictory conflict, and when the adaptability of the mechanism is improved, the accuracy of the mechanism movement deteriorates accordingly. Converting them according to 39 general engineering parameters yields an improvement parameter numbered 35 (adaptability and diversity) and a deterioration parameter numbered 28 (measurement accuracy). Bringing them into the contradiction matrix, the design principles obtained are: principle 35 (change of the state of aggregation of objects), principle 5 (union), principle 1 (division), and principle 10 (pre-action). Bringing them into the contradiction matrix, the design principles obtained are: the 35th principle (change of the state of aggregation of objects), the 5th principle (union), the 1st principle (division), and the 10th principle (pre-action).

Combined with the determined invention principle, the design principle of Article 24 was selected for the ash laying mechanism, Article 17 was selected for the tile moving mechanism, Article 29 was selected for the tile gripping mechanism, and Article 5 was selected for the traveling mechanism. Combining the above, the corresponding table of TRIZ principle contradiction analysis of automatic brick-laying machine is shown in Table 1.

(2) Solution Ideas

The Intermediation Principle is applied to the design of the ash laying mechanism. According to the principle, it is desired to use one of the intermediate detachable parts in the mechanism to carry out the ash removal operation, so the mechanism is designed in the way of stirring ash removal, and the ash removal operation is completed by rotating the detachable roller with blades driven by a motor.

Table 1. Automatic brick-laying machine TRIZ principle contradiction analysis correspondence table.

Mechanism Name	Improved parameter serial number	Deteriorated parameter serial number	The obtained design principle serial number	Selected principle serial number
Ash laying mechanism	39	36	12, 17, 28, 24	24
Tile moving mechanism	27	33	27, 17, 40	17
Tile gripping mechanism	10	26	14, 29, 18, 36	29
Traveling mechanism	35	28	35, 5, 1, 10	5

Application of the dimensional excess principle to the design of a tile moving mechanism. According to the principle content, tile movement should not only consider linear motion in two-dimensional plane, but should be considered in the direction that can realize three-dimensional space linear movement, so a truss-type mechanical structure that can realize linear motion in X, Y and Z directions is used to perform tile movement operation.

Application of pneumatic-hydraulic structure principle to the design of tile gripping mechanism. According to the principle content, tile grasping can be considered to use pneumatic or hydraulic system to achieve, so the pneumatic suction cup driven by pneumatic system is used to achieve tile grasping operation.

Application of the union principle to the design of the travel mechanism. According to the principle content, the automatic brick laying machine should combine all parts when moving, so the traveling mechanism is designed as a one-piece structure.

3.4 Program Design

According to the selected design principle, the specific scheme design of the ash laying mechanism, the tile moving mechanism, the tile grasping mechanism and the traveling mechanism are carried out separately, and the model drawing is drawn.

(1) Ash laying mechanism

According to the intermediary principle instruction of TRIZ theory, the roller which realizes the function of mixing down the ash as a key intermediate part should satisfy that it can be disassembled and replaced. Therefore, when designing the ash laying mechanism, the rollers are connected to the silo with detachable shafts. This design can realize the ash laying requirement when laying bricks, but also make the ash laying mechanism can be disassembled and replaced with different sizes of rollers at any time to meet the ash laying task of different ash materials according to the different sizes of concrete ash particles. The designed ash laying mechanism consists of four parts: silo,

removable roller, pressure roller, and laying funnel. When laying tiles, the concrete is put into the silo and crushed by the roller blades rotating and then spilled through the downcomer funnel, the gray material is not smooth when it falls to the ground, so it needs to use the pressure roller to compact the road. Considering that the actual mixing action does not need to drop too much material, otherwise it will cause the accumulation of concrete on the ground, the design of the drop funnel in the form of a huddle is used to reduce the amount of falling concrete. The overall model of the ash laying mechanism is shown in Fig. 4.

(2) Tile moving mechanism

According to the TRIZ theory of dimensional excess principle instruction, the tile moving mechanism as a whole should meet the truss type structure to realize the movement of tile plane and vertical direction. Therefore, when designing the tile moving mechanism, the support arm bars are arranged in X, Y and Z directions to form a simple truss structure. The drive wheel is attached to the arm bar to realize the movement in the plane direction, and the motor is placed on the upper part of the vertical bar, and the ball screw is used to convert the rotation of the motor into the linear movement in the vertical direction to realize the movement of the tiles in the vertical direction. This design can ensure the stability of the tile moving process by achieving the vertical movement while keeping the truss structure unchanged. The designed tile moving mechanism consists of four parts: arm bar, drive wheel, ball screw, motor and gearbox. The arm bar is connected to form a truss type mechanism, and the ball screw mechanism is installed on the arm bar in vertical direction. The arm bar is connected with each other as a whole to form a truss type mechanism, and the ball screw mechanism is installed on the arm bar in vertical direction. After the tiles are grasped, the horizontal movement of the overall mechanism is realized by the drive wheel, and the vertical movement is realized by the ball screw mechanism driven by motor plus reducer. The overall model of the tile moving mechanism is shown in Fig. 5.

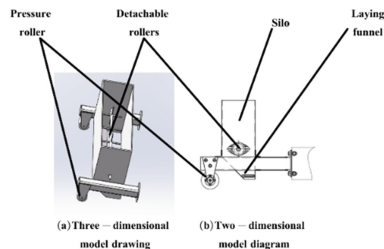


Fig. 4. Ash laying mechanism model drawing

(3) Tile gripping mechanism

According to the pneumatic-hydraulic structure principle instruction of TRIZ theory, the tile gripping mechanism should use pneumatic or hydraulic device to realize the tile

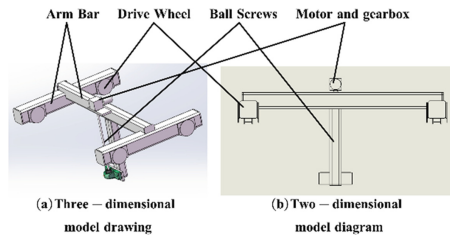


Fig. 5. Tile moving mechanism model drawing

gripping. The pneumatic device is quicker to execute than the hydraulic device and can improve the efficiency when gripping tiles. Therefore, when designing the tile gripping mechanism, multiple sets of removable pneumatic suction cups are used for gripping. This design ensures that the gripping force is large enough for tile gripping, and the number of pneumatic suction cups can be adjusted to achieve the gripping of different sizes of tiles. The designed tile gripping mechanism consists of four parts: fixed plate, upper connecting plate, pneumatic suction cup and air tube, and the air pressure station is connected to the suction cup through the air tube, which is stuck between the fixed plate and the upper connecting plate, considering the different sizes of the tiles to be gripped, there is a gap between the fixed plate and the upper connecting plate, so that the distance between the suction cups can be adjusted according to the size of the tiles. The overall model of the tile gripping mechanism is shown in Fig. 6.

(4) **Traveling mechanism**

According to the union principle instruction of TRIZ theory, the traveling mechanism should be of one-piece design. Therefore, in the design of the traveling mechanism, the frame and the tile placement bar are connected as a whole, the driving wheel and the driven wheel are placed under the frame, and the upper part of the frame is set up with a slide rail, and the tile moving mechanism can be placed on the slide rail. This design allows the automatic brick laying machine to travel as a whole while ensuring independent operation of the truss-type tile moving mechanism. The designed traveling mechanism consists of four parts: driving wheel, driven wheel, carriage, and tile placement bar, the frame is directly connected with the tile placing rod, the whole traveling mechanism is driven by double motors, the motor drives the driving wheel to rotate, the driven wheel follows the rotation, when moving, the tiles can be placed on the rod between the frame to achieve the overall rapid movement of tiles. The overall model diagram of the travel mechanism is shown in Fig. 7.

Combining the design of the laying ash mechanism, tile moving mechanism, tile grasping mechanism, and traveling mechanism, the overall model diagram of the automatic tile laying machine is obtained as shown in Fig. 8.

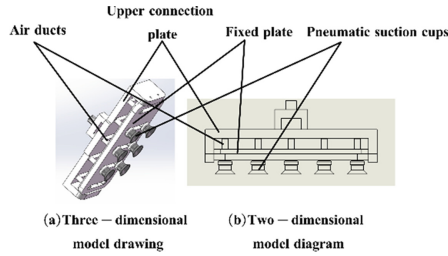


Fig. 6. Model drawing model drawing

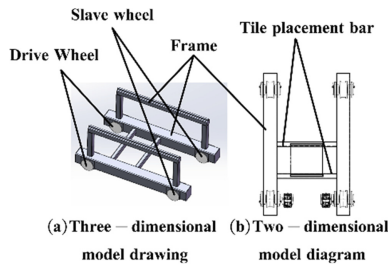


Fig. 7. Traveling mechanism of tile gripping mechanism

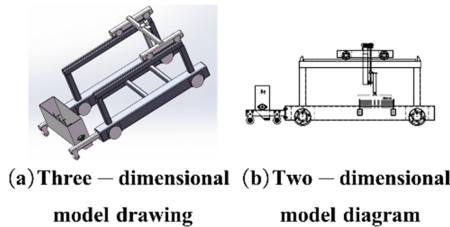


Fig. 8. Overall model drawing of automatic brick laying machine

4 Drive Motor Selection Calculation

After the overall design of each mechanism is determined, in order to realize the automatic operation of the product, it is necessary to combine the design of the traveling mechanism, tile moving mechanism for the selection of drive motor and reducer calculation.

4.1 Traveling Mechanism Drive Motor and Reducer Selection

When carrying out the task of laying tiles, it is required that the traveling mechanism should be smooth enough when carrying tiles to move, and the speed should not be too fast, so the maximum speed (v) design for uniform and stable operation is 0.5 m/s. The maximum overall mass (m) when fully loaded with tiles is 400 kg. Drive wheel diameter

(ϕ) is 160 mm. The coefficient (μ) of friction between the driving wheel and the ground is 0.5. g is 9.8 N/kg.

Motor power is:

$$P = \mu mgv = 0.5 \times 400 \times 9.8 \times 0.5 = 980 \text{ W} \quad (1)$$

Considering the motor power margin and other issues, the selected motor power size is 1.5 KW, and its rated output speed is 1500 r/min.

Drive wheel speed is:

$$n = \frac{60v}{\pi\phi} = \frac{60 \times 0.5}{\pi \times 0.16} = 60 \text{ r/min} \quad (2)$$

The reduction ratio of the reducer is:

$$i = \frac{1500}{60} = 25 \quad (3)$$

Therefore, the motor and reducer integrated reducer is chosen, and its model is YZP1.5-KA37-25.

4.2 Tile Moving Mechanism Drive Motor and Reducer Selection

When carrying out the task of tiling, in order to meet the requirements of efficient operation, the tile moving mechanism should move the tiles to the designated position quickly, so the maximum speed (v') of the mechanism when running uniformly and steadily is designed to 1 m/s. The mass (m') of the overall mechanism when the mechanism carries the tiles to move is 100 kg. Guide rails are laid between the mechanism and the frame, and the mechanism drive wheel diameter (ϕ') is 80 mm. The coefficient (μ') of friction between the drive wheel and the rail is 0.1. g is 9.8 N/kg.

Motor power is:

$$P' = \mu' m' g v' = 0.1 \times 100 \times 9.8 \times 1 = 98 \text{ W} \quad (4)$$

Considering the motor power margin and other issues, the selected motor power size is 0.25 KW, and its rated output speed is 1500 r/min.

Drive wheel speed is:

$$n' = \frac{60v'}{\pi\phi'} = \frac{60 \times 1}{\pi \cdot 0.08} = 239 \text{ r/min} \quad (5)$$

The reduction ratio of the reducer is:

$$i' = \frac{1500}{239} = 6.2 \quad (6)$$

Therefore, the motor and reducer integrated reducer is chosen, and its model is YZP0.25-KA37-7.

5 Conclusion

This paper completes the design of the main mechanism of the automatic brick laying machine based on TRIZ theory. The automatic brick laying machine designed by this method meets the corresponding design requirements and can complete the brick-laying task automatically. However, this design is only a preliminary structure design according to TRIZ theory, and the motor and reducer selection work of the preliminary design has been completed. There is still room to improve the efficiency of the designed ash laying mechanism, traveling mechanism, tile moving mechanism and tile gripping mechanism. The next step is to use TRIZ theory to improve the efficiency of the automatic brick laying machine, to study and optimize the design of each component of the designed mechanism, and to continue to improve the mechanical structure of each mechanism. Through continuous optimization design to get more efficient mechanism, so as to get better performance of automatic brick laying machine.

Acknowledgements. This work is supported by Shandong Jiaotong University Research Fund (2023YK045).

References

1. Vidovszky, I., Pém, A.: Analyses of automated bricklaying workflow regarding time and arrangement. *IOP Conf. Ser. Mater. Sci. Eng.* **1218**(1) (2022)
2. Qiao, Y., Wang, L., Jiao, L., Zhou, X., Zhu, H., Niu, Z.: Research on the design of a multifunctional brick laying machine. *Mech. Eng. Autom.* **3**, 89–90+93 (2020)
3. Yong, H., Gang, Z.: A control system design of an indoor split type automatic brick laying machine. *Henan Sci. Technol.* **21**, 65–66 (2016)
4. Yanli, Z., Ke, C., Wang Guang, L., Peng, C.W., Guo, X., Wei, Z.: Design of automatic brick laying machine based on image processing. *J. Xi'an College Arts Sci. (Natural Science Edition)* **21**(04), 25–29 (2018)
5. Liu, X., Cao, H., Chen, G.: *TRIZ Theory and Application*. Peking University Press, Beijing (2015)
6. Ai, X., Hu, K., Zhou, H., et al.: Research on industrial design innovation process based on TRIZ. *Mach. Des.* **32**(11), 105–109 (2015)
7. Le, Z., Zhixue, S., et al.: Research on the application of TRIZ theory in the design of shopping carts for the elderly. *Mach. Des.* **12**, 126–128 (2017)
8. Tang, R., Zhang, R.: TRIZ-based product innovation design. *J. Hebei Univ. Technol.* **33**(2), 91–95 (2004)
9. Sun, Y.W.: *The Golden Key of TRIZ to Open the Door of Innovation*. Science Press, Beijing (2021)



Design of Fuzzy Super-Twisting Sliding Mode Controller for Underwater Fishing Manipulator

Shanshan Yin¹, Zhiguang Guan¹(✉), Chao Wang¹, and Mingxing Lin²

¹ Shandong Provincial Engineering Lab of Traffic Construction Equipment and Intelligent Control, Shandong Jiaotong University, Jinan 250357, China
guanzhiguang@sdjtu.edu.cn

² School of Mechanical Engineering, Shandong University, Jinan 250061, China
mxlin@sdu.edu.cn

Abstract. Using underwater fishing manipulator instead of artificial fishing are less risky and productive, but the working environment of underwater fishing by manipulator is complex and changeable, and the stability is poor. Therefore, this paper uses the dynamics equation of underwater manipulator as the manipulator motion control system's control model, and proposes a motion control algorithm that depends on fuzzy superspiral sliding mode, which is able to overcome the difficulty of manipulator trajectory tracking and increase the stability and precision of the underwater fishing manipulator's control. The underwater manipulator's dynamics equation is used as the control model of the motion system, it illustrates the stability of the underwater manipulator control system using the Lyapunov stability theory. Combined with MATLAB and SIMULINK software co-simulation, the control effect of the underwater manipulator is analyzed, and the proposed control method's accuracy is confirmed, which provides a more accurate and effective control mode for the underwater manipulator.

Keywords: Underwater fishing manipulator · Fuzzy super-twisting sliding mode control · Sliding mode

1 Introduction

The motion system of the underwater manipulator is high nonlinearity and high-coupled, the influence of hydrodynamic interaction and complex underwater environment noise coming from the underwater manipulator's motion control system is relatively large. For the above problems, Xiao [1] applied sliding mode control to the servo control of underwater manipulator. However, the control stability is insufficient, and large errors are easy to occur when the motor has high speed and large load. Dong [2] proposed a neural network sliding mode controller for trajectory tracking of multi-joint underwater manipulators, but the response speed is slow and the adjustment time of controller and tracking error is long.

To address the issues of high-frequency oscillation and sensitivity of controller parameters in traditional sliding mode control in nonlinear system, in this paper, to

address the issues of low control accuracy and sluggish response time, sliding mode control and fuzzy control are coupled to create a fuzzy super-twisting sliding mode control system. The sliding mode controller replaces the sliding surface with a fuzzy controller. The dynamic equation of the underwater manipulator is analyzed. The Lyapunov function is used to examine the stability of the controller. The simulation is composed of MATLAB and SIMULINK to prove the validity of the control system. The control system has good nonlinear characteristics and robustness.

2 Fuzzy Control and Sliding Mode Control

2.1 Fuzzy Control

Fuzzy control is a control law described by fuzzy mathematics language to operate the system. The fuzzy controller [3] describes and quantifies the practical experience in language, and obtains qualitative and inaccurate regulation rules.

(1) Fuzzy controller structure

The fuzzy controller is constituted of fuzzifier [4], fuzzy rule base [5], fuzzy inference engine and defuzzifier [6], The fundamental structure of the fuzzy controller is shown in Fig. 1.

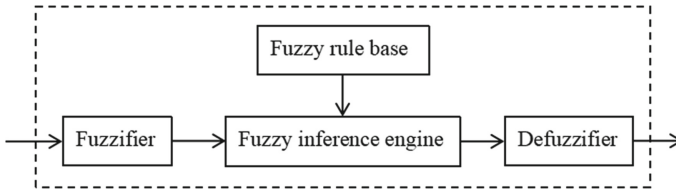


Fig. 1. Structure of fuzzy controller

(2) Fuzzy algorithm

Fuzzy algorithm is a kind of calculation method based on fuzzy logic theory, by dealing with fuzzy information, the problem which is challenging to handle by traditional accurate algorithm is solved. The general steps of its design are as follows: (1) Determine the fuzzy system’s input, output, and value ranges. (2) Determine the type and parameters of membership function: this paper uses the Gaussian membership function, and determine the mean and standard deviation of each membership function. (3) Determine the rule base. (4) Design a fuzzy inference engine. (5) Design paste machine.

2.2 Sliding Mode Control

Sliding mode control regards the state of the control system as the trajectory of the point in the state space, and controls the system’s state by introducing a sliding mode surface

to limit the state trajectory to slide on this surface. The sliding mode refers to the rapid and stable sliding of the system state on a preset hyperplane. A sliding control law must be established to prevent the system state from sliding to achieve the sliding mode. The following is an expression for the system:

$$\dot{x} = f(x), x \in \mathbb{R}^N \tag{1}$$

In the state space, it is assumed that there exists a switching surface:

$$S(X) = s(X_1, X_2, X_3, X_4, \dots, X_n) = 0 \tag{2}$$

The state space is bisected by the switching surfaces $s > 0$ and $s < 0$. On the switching surface, three different motion types pass through three different point. As shown in Fig. 2:

- (1) A is the usual point. When the system passes through the switching surface $s = 0$, it leaves point A directly.
- (2) B is the starting point, and the system is separated from both sides of the switching surface $s = 0$, leaving point B.
- (3) C is the termination point, and the system gradually approaches this point from both sides of the switching surface $s = 0$.

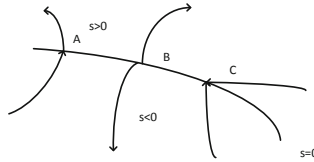


Fig. 2. Motion mode on sliding mode switching surface

The requirement that the motion point in the sliding mode region is the termination point can be expressed by the following formula:

$$\lim_{s \rightarrow 0^+} \dot{s} \leq 0 \text{ 及 } \lim_{s \rightarrow 0^-} \dot{s} \geq 0$$

Based to the second theorem of Lyapunov stability, the constructable function:

$$v(x_1, x_2, x_3, \dots, x_n) = [s(x_1, x_2, x_3, \dots, x_n)]^T [s(x_1, x_2, x_3, \dots, x_n)] \tag{3}$$

3 Design of Fuzzy Superspiral Sliding Mode Controller

3.1 Sliding Mode Controller Design

Dynamics equation of underwater manipulator:

$$M(\theta)\ddot{\theta} + C(\theta, \dot{\theta})\dot{\theta} + D(\theta, \dot{\theta})\dot{\theta} + G'(\theta) + \tau_d + F_f = \tau \tag{4}$$

where $\tau_d = F_d + F_f$, F_d is external disturbance, which is continuous bounded, and $\dot{F}_d \approx 0$. F_f is friction.

(1) Sliding mode controller design:

The ideal Angle of the joint is θ_d , Take tracking error $e = \theta - \theta_d$, Define the sliding mode function as:

$$s = \dot{e} + \Lambda e e \tag{5}$$

where $\Lambda = \begin{bmatrix} \lambda_1 & 0 & 0 & 0 \\ 0 & \lambda_2 & 0 & 0 \\ 0 & 0 & \lambda_3 & 0 \\ 0 & 0 & 0 & \lambda_4 \end{bmatrix}$, $\lambda_i > 0, u = \tau, i = 1, 2, 3, 4$.

$$\dot{s} = \ddot{\theta} - \ddot{\theta}_d + \Lambda \dot{e} = M^{-1}(u - (C + D)\dot{\theta} - G' - \tau_d) - \ddot{\theta}_d + \Lambda \dot{e} \tag{6}$$

(2) The design controller is:

$$u = M(\ddot{\theta}_d - ks) + (C + D)\dot{\theta} + G' \tag{7}$$

Design the following Lyapunov functions:

$$V(s) = \frac{1}{2}s^T s \tag{8}$$

The derivative of formula (8) can be obtained:

$$\begin{aligned} \dot{V}(s) &= s^T \dot{s} = s^T (-ks - M^{-1}\tau_d + \Lambda \dot{e}) \\ &= \sum_{i=1}^4 \left(-|s_i|k_i|s_i| - |s_i|(M^{-1}\tau_{d_i} - \lambda_i \dot{e}_i) \right) \\ &\leq \sum_{i=1}^4 \left(-|s_i|k_i|s_i| - |s_i|(M^{-1}\bar{\tau}_{d_i} - \lambda_i \dot{e}_i) \right) \end{aligned}$$

where $\bar{\tau}_d$ is the upper bound on τ_d , M^{-1} is the module of the inertial matrix M^{-1} . Choose the appropriate value of Λ , enable $M^{-1}\bar{\tau}_d - \Lambda \dot{e} > 0$, that is $\dot{V}(s) < 0$, Then the system is stable.

3.2 Design of Fuzzy Super-Twisting Sliding Mode Controller

Super-twisting sliding mode control is normally utilized to resolve the nonlinear uncertain systems control problem [7, 8]. It has the benefits of outstanding robustness and excellent anti-interference ability. A super-twisting function is introduced on the sliding surface to make the control system trajectory converge to the sliding surface quickly under certain conditions, at the same time, some chattering phenomena in conventional

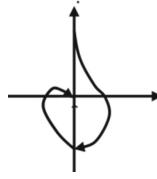


Fig. 3. Super-twisting algorithm phase trajectory

sliding mode control are eliminated. The phase trajectory of the super-twisting algorithm is shown in Fig. 3.

The design controller is:

$$u = M(\ddot{\theta}_d - ks) + (C + D)\dot{\theta} + G' + u_{sw} \tag{9}$$

where:

$$\begin{cases} u_{sw} = -K_1 |s|^{\frac{1}{2}} \text{sign}(s) + v \\ \dot{v} = -K_2 \text{sign}(s) \end{cases} \tag{10}$$

where K_1 ,

where $\text{sign}(s)$ is a sign function,

$$\begin{cases} s > 0, \text{sign}(s) = 1 \\ s < 0, \text{sign}(s) = -1 \\ s = 0, \text{sign}(s) = 0 \end{cases}$$

To demonstrate the super-twisting sliding mode controller's stability, the following Lyapunov function is designed.

$$V(s) = \frac{1}{2} s^T s \tag{11}$$

The derivative of formula (11) can be obtained:

$$\begin{aligned} \dot{V}(s) &= s^T \dot{s} = s^T (-ks - M^{-1} \tau_d + \Lambda \dot{e} - K_1 |s|^{\frac{1}{2}} \text{sign}(s) - K_2 f \text{sign}(s) dt) \\ &= \sum_{i=1}^4 \left(-|s_i| k_i |s_i| - k_{1i} |s_i|^{\frac{3}{2}} - |s_i| f (k_{2i} + M^{-1} \bar{\tau}_{d_i} - \lambda_i \dot{e}_i) dt \right) \\ &\leq \sum_{i=1}^4 \left(-|s_i| k_i |s_i| - k_{1i} |s_i|^{\frac{3}{2}} - |s_i| f (k_{2i} + M^{-1} \bar{\tau}_{d_i} - \lambda_i \dot{e}_i) dt \right) \end{aligned}$$

where $\bar{\tau}_{d_i}$ denotes the interference term and the upper bound of friction derivative of the joint i . Because sign is not differentiable at 0, take the derivative of friction force as 0, M^{-1} is the module of the inertial matrix M^{-1} , take the applicable values of K_2 and Λ , make $K_2 + M^{-1} \bar{\tau}_{d_i} - \Lambda \dot{e} > 0$, that is $\dot{V}(s) < 0$, Then the system is stable.

With the goal to enhance the sliding mode controller’s functionality and lessen chattering, a fuzzy control system can be designed. The fuzzy super-twisting sliding mode controller is:

$$u = M (\ddot{\theta}_d - ks - \beta F) + (C + D)\dot{\theta} + G' + u_{sw} \tag{12}$$

Define fuzzy sets as:

$$A^m = \{NZP\} \tag{13}$$

$$B^m = \{NZP\} \tag{14}$$

where N, Z and P represent negative, zero and positive respectively. Take $x_i = \{\theta_1\theta_2\theta_3\theta_4\dot{\theta}_1\dot{\theta}_2\dot{\theta}_3\dot{\theta}_4\}$ as the input to the rule. Take f_i as the output to the rule. Fuzzy rules can take the following forms:

$$\text{IF } x_i \text{ is } A_j^m \text{ THEN } f_i \text{ is } B_j^m;$$

where A_j^m and B_j^m are fuzzy subsets of fuzzy set A^m and B^m respectively. Specific fuzzy adjustment rules can be summed up using the sliding mode motion and control experience information:

Rule 1: IF x_i is NB THEN f_i is PB;

Rule 2: IF x_i is Z THEN f_i is Z;

Rule 3: IF x_i is PB THEN f_i is PB.

Among them, the product inference machine, single value fuzzifier, and central average defuzzifier are used in the design of the fuzzy system, and Gaussian membership functions is used, it is expressed as follows:

$$\mu(x_i) = \exp \left[- \left(\frac{x_i - \alpha}{\sigma} \right)^2 \right] \tag{15}$$

x stands for the fuzzy variable’s value, c is the membership function’s center, σ is the parameter to controls the width of the membership function. The result is as follows:

$$f_i = \vartheta_{f_i}^T \phi_{f_i}(x_i) \tag{16}$$

where,

$$\vartheta_{f_i}^T = \left[\theta_{f_i}^1, \dots, \theta_{f_i}^m, \dots, \theta_{f_i}^M \right]^T \tag{17}$$

$$\phi_{f_i}(x_i) = \left[\varphi_{f_i}^1(x_i), \dots, \varphi_{f_i}^m(x_i), \dots, \varphi_{f_i}^M(x_i) \right]^T \tag{18}$$

where M is the number of fuzzy rules, N is the number of fuzzy subsets in the input fuzzy set, x_i is the fuzzy input, the fuzzy set’s center and height are represented by the vectors ϑ_{f_i} and $\phi_{f_i}(x_i)$ of the fuzzy system output f_i , The sliding mode controller can be created as follows when used with the fuzzy control system mentioned above:

$$f_i = \vartheta_{f_i}^T \phi_{f_i}(x_i) \tag{19}$$

$$F = \begin{bmatrix} f_1 & 0 & 0 & 0 \\ 0 & f_2 & 0 & 0 \\ 0 & 0 & f_3 & 0 \\ 0 & 0 & 0 & f_4 \end{bmatrix} \tag{20}$$

Combined with the formula (19), the parameters are fuzzified. The super-twisting fuzzy sliding mode controller's block diagram is displayed in Fig. 4.

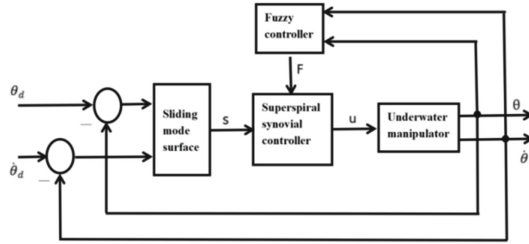


Fig. 4. Block diagram of fuzzy super-twisting sliding mode controller

4 Simulation Experiment

The dynamic equation of the manipulator is:

$$M(\theta)\ddot{\theta} + C(\theta, \dot{\theta})\dot{\theta} + D(\theta, \dot{\theta})\dot{\theta} + G'(\theta) + \tau_d = \tau \tag{21}$$

External interference is τ_d , $\tau_d = F_d + F_f$, where:

$$F_d = \begin{bmatrix} 0.1 \sin t \\ 0.1 \sin t \\ 0.1 \sin t \\ 0.1 \sin t \end{bmatrix} \tag{22}$$

F_f is for friction, where:

$$F_f = \begin{bmatrix} 0.1 \text{sign}(\theta_1) \\ 0.1 \text{sign}(\theta_2) \\ 0.1 \text{sign}(\theta_3) \\ 0.1 \text{sign}(\theta_4) \end{bmatrix} \tag{23}$$

Take the expected Angle as:

$$\theta_d = \begin{bmatrix} \sin t \\ \sin t \\ \sin t \\ \sin t \end{bmatrix} \tag{24}$$

The super-twisting sliding mode controller takes parameters K_1, K_2, k, β, F .

$$K_1 = 10, K_2 = 1000 \times \begin{bmatrix} 1 & 0 & 0 & 0 \\ 0 & 1 & 0 & 0 \\ 0 & 0 & 1 & 0 \\ 0 & 0 & 0 & 1 \end{bmatrix}$$

$$k = 500 \times \begin{bmatrix} 1 & 0 & 0 & 0 \\ 0 & 1 & 0 & 0 \\ 0 & 0 & 1 & 0 \\ 0 & 0 & 0 & 1 \end{bmatrix}, \beta = 300 \times \begin{bmatrix} 50 & 0 & 0 & 0 \\ 0 & 1 & 0 & 0 \\ 0 & 0 & 0.001 & 0 \\ 0 & 0 & 0 & 20 \end{bmatrix}$$

The fuzzy controller adjusts the parameter F in real time.

Then the joint angle tracking effect and error of super-twisting sliding mode control are shown in Figs. 5, 6, 7, 8, 9, 10, 11 and 12.

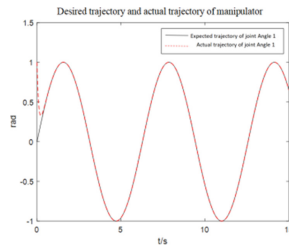


Fig. 5. Joint angle 1 tracking effect

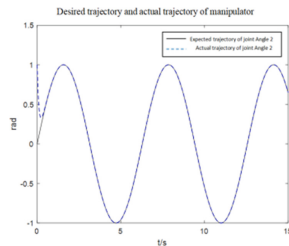


Fig. 6. Joint angle 2 tracking effect

The joint angle tracking effect and error of fuzzy super-twisting sliding mode control are shown in Figs. 13, 14, 15, 16, 17, 18, 19 and 20.

Tables 1 and 2 show the performance parameters of the control system.

The data analysis depicted in Tables 1 and 2 allows for the conclusion that the mean square error and mean absolute error of fuzzy super-twisting sliding mode control are lesser than those of super-twisting sliding mode control. To sum up, the fuzzy super-twisting sliding mode controller created in this paper provides superior control outcomes.

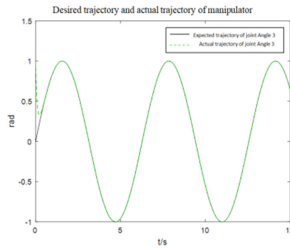


Fig. 7. Joint angle 3 tracking effect

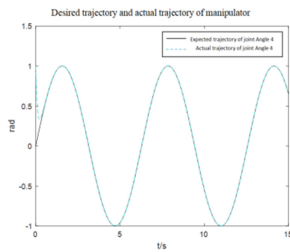


Fig. 8. Joint angle 4 tracking effect

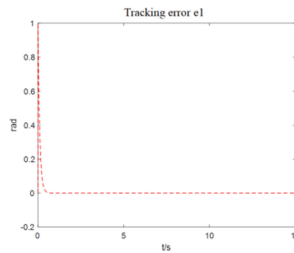


Fig. 9. Joint angle 1 tracking error

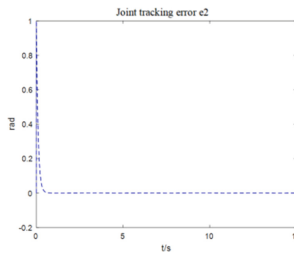


Fig. 10. Joint angle 2 tracking error

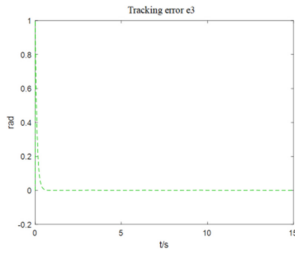


Fig. 11. Joint angle 3 tracking error

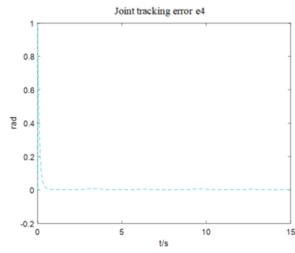


Fig. 12. Joint angle 4 tracking error

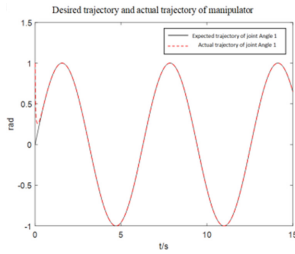


Fig. 13. Joint angle 1 tracking effect

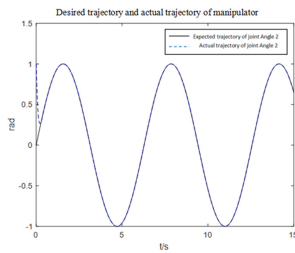


Fig. 14. Joint angle 2 tracking effect

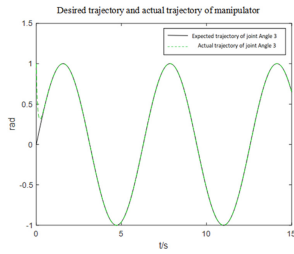


Fig. 15. Joint angle 3 tracking effect

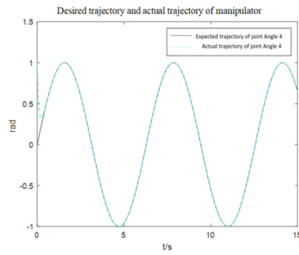


Fig. 16. Joint angle 1 tracking effect

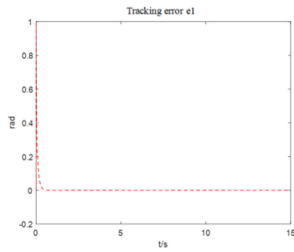


Fig. 17. Joint angle 1 tracking error

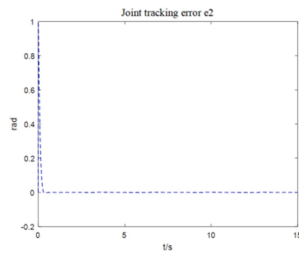


Fig. 18. Joint angle 2 tracking error

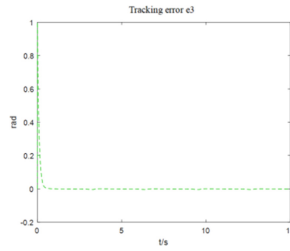


Fig. 19. Joint angle 3 tracking error

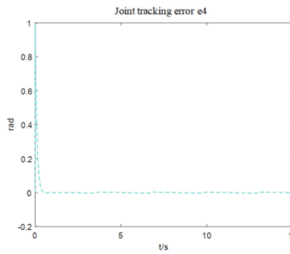


Fig. 20. Joint angle 4 tracking error

Table 1. Performance parameter table of super-twisting sliding mode control system

Joint	Mean square error	Mean absolute error
Joint 1	0.003374	0.006810
Joint 2	0.003461	0.007056
Joint 3	0.003379	0.007308
Joint 4	0.003397	0.009496

Table 2. Performance parameter table of fuzzy super-twisting sliding mode control system

Joint	Mean square error	Mean absolute error
Joint 1	0.001577	0.003989
Joint 2	0.003167	0.005804
Joint 3	0.002853	0.006714
Joint 4	0.003238	0.007871

5 Conclusion

Aiming at the high frequency oscillation of conventional sliding mode and the sensitivity of controller parameters in the motion control system of underwater fishing manipulator, it is suggested to use a control method based on fuzzy super-twisting sliding mode in this work. By uniting the benefits of fuzzy control and sliding mode control, a fuzzy super-twisting sliding mode controller is created, the Lyapunov function demonstrates the stability of the underwater fishing manipulator control system. Finally, MATLAB/SIMULINK is used to carry out the simulation analysis. The simulation results indicate that the mean square error and mean absolute error of the fuzzy super-twisting sliding mode controller are smaller and the control is more effective. The algorithm's reliability is confirmed.

Acknowledgements. This work is supported by Natural Science Foundation of Shandong Province (ZR2020ME267, ZR2023MF077), Science and technology plan project of Shandong Provincial Department of Transportation (2023B93), Science and Technology Support Plan for Youth Innovation in Universities of Shandong Province Colleges and Universities (2019KJB014).

References

1. Xiao, Z.: Research on dynamic characteristics and autonomous operation of deep-water manipulator. Huazhong University of Science and Technology(2011)
2. Dong, Y.: Dynamic analysis and trajectory tracking sliding mode control of underwater manipulator. Dalian University of Technology(2018)
3. Liu, Y., Han, J., Zhang, S., et al.: Adaptive fuzzy control for quadrotor with parameter uncertainties. *Int. J. Control. Autom. Syst.* **19**(6), 2292–2301 (2021)
4. Liu, Y., Zhang, Y., Li, Y.: A hybridized fuzzy clustering algorithm based on feature selection for customer churn prediction. *Expert Syst. Appl.* **159**, 113525 (2020)
5. Wang, B., Fan, W., Tan, Y., et al.: Adaptive optimization method of fuzzy rule base based on deep learning. *Control. Eng.* **27**(3), 468–476 (2020)
6. Wang, Y., Wang, B.: Fuzzy clustering defuzzification based on improved dynamic window method. *Control and Decision.* **34**(10), 2364–2371 (2019)
7. Jia, C., Jin, C.: New superspiral sliding mode control strategy based on extended state observer. *Automation and Instrumentation in Chemical Industry.* **49**(02), 133–143 (2022)
8. Chu, R., Liu, Z., Chu, Z.: Improved super-twisting sliding mode control for ship heading with sideslip angle compensation. *Ocean Engineering.*260(2022)



Research on Remote Control System of Excavator Based on Industrial Internet of Things

Ran Liu, Zhenyuan Zhao, and Zhiguang Guan^(✉)

Shandong Provincial Engineering Lab of Traffic Construction Equipment and Intelligent Control, Shandong Jiaotong University, Jinan 250357, China
guanzhiguang@sdjtu.edu.cn

Abstract. With the rapid development of the times, the construction of various industries require the use of excavators for on-site construction, as well as various rescue and disaster relief activities. These belong to the excavator's high-risk operations, the operator's personal safety can not be guaranteed. Therefore, in order to overcome the safety hazards of modern excavators in high-risk operations, this paper will develop a remote control system based on industrial Internet of Things to control remote excavators. Reduce the operator's time and risk in the dangerous operation area, reduce the operator's labor intensity and ensure personal safety. First, the design scheme of the wireless communication system and the overall scheme of the remote control system were determined by analyzing the basic requirements of the remote control system. Next, complete the hardware selection and write the program and configure the hardware parameters. Finally, we tested the remote control system, and the test data showed that the transmission rate delay is low and can effectively receive commands from the remote control terminal with good reliability, which basically meets the requirements of the remote control system.

Keywords: Excavator · Remote control · Industrial Internet of Things

1 Introduction

Remote control of excavators can effectively increase operational efficiency, reduce operational risk and be applied to complex environments and different types of tasks. At present, the technology of remote control of excavators is developing, not only to achieve remote control, but also to be able to combine with artificial intelligence, big data and other technologies to better serve various work scenarios and needs [1]. However, when performing remote control of excavators, attention still needs to be paid to its safety and reliability issues to ensure that it works properly and safeguards the safety of the operator and the operating environment. The remote control excavator based on industrial Internet is a kind of intelligent equipment based on computer control technology. The industrial Internet-based remote control system is an intelligent device based on computer control technology, which enables efficient operation and management of excavators through

remote monitoring and control of industrial automation systems and equipment [2]. Its main feature is that it can integrate a variety of sensors and controllers to obtain mechanical, electrical and hydraulic data in real time, and process and analyze them to ensure safe operation while achieving efficient work. The system supports a variety of network transmission protocols [3], remote control and monitoring, and can realize remote fault detection, historical record query, running status analysis and other functions of the device, effectively improving the reliability and stability of the device operation [4]. In addition, the system can better match the human-computer interaction interface, which can display the operation data and status of the equipment in real time and provide real-time decision support for operators, greatly improving work efficiency and accuracy. In short, the remote control of excavator with the support of industrial Internet has various advantages such as intelligence, efficiency, safety and reliability, and will become one of the mainstream directions of excavator control in the future.

2 Overall Design and Analysis of Remote Control System

2.1 Requirement Analysis of Remote Control System

In order to realize the design of the excavator remote control system, a requirement analysis of the system is needed. This can be done by analyzing four points: reliability, operational flexibility, communication efficiency and ease of operation of the system. The detailed analysis results are shown below.

- (1) Reliability: The remote control system of excavator needs to maintain reliability and be able to respond to instructions at any time. Therefore, the system should be stable and highly available.
- (2) Operational flexibility: when controlling the excavator remotely, the operator needs to know the excavator status and environmental conditions in real time, so the system should provide the corresponding sensor and display screen and other auxiliary equipment.
- (3) Communication efficiency: in the process of remote control of excavator, communication efficiency should be ensured to reduce communication delay and loss. Therefore, the communication protocol or mechanism needs to select a reasonable packet size, retransmission frequency, fragmentation rate and other channel parameters.
- (4) Ease of operation: Remote operation should be as quick and convenient as possible for the operator. Therefore, the system operation interface should be designed to be simple and clear and easy to operate.

2.2 Overall Design of Remote Control System

The excavator remote control system is a kind of intelligent control system for industrial equipment realized based on remote communication technology. The overall scheme should include system architecture design: selecting the control architecture and communication network mode suitable for excavators, determining the system reliability requirements and supporting hardware facilities. As well as the control module design, determine what functions the control module includes and select the appropriate sensors and actuators according to the actual application scenario. Communication module

design: select appropriate wireless communication technology (e.g. 4G, 5G, LoRa, etc.), determine the communication protocol and data transmission format, and realize remote communication [4]. The software development writes the control program and communication program to realize the effective connection and data interaction between the control module and communication module to realize the remote control of excavator. This paper for the excavator remote control system design scheme is shown in Fig. 1, mainly including SIMATIC S7-1200 controller, Tianqi IOT gateway, cloud server, DTU and operation device composition. After successful testing of the direct connection of the two controllers through the S7 communication protocol, the two SIMATIC S7-1200 controllers are connected to the IOT gateway. The IOT gateway enables data exchange and off-site control of the two SIMATIC S7-1200 controllers through the same cloud server, and the data of the off-site controllers can be detected in real time from the local area, and the values of the analog output ports of the SIMATIC S7-1200 controllers can be controlled in real time through off-site control to realize the control of the excavator.

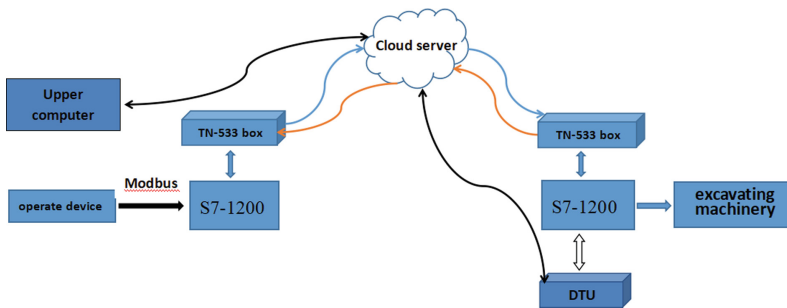


Fig. 1. Remote control system schematic

2.3 Communication Protocol Design

As the data needs to be transmitted remotely, the S7 communication protocol, which is a proprietary protocol of Siemens, was finally used after a practicality analysis, and is one of the Siemens S7 communication protocol clusters [5]. The TCP/IP implementation of the S7 protocol relies on block-oriented ISO transport services, and the S7 protocol is encapsulated in the TPKT and ISO-COTP protocols, which enable PDUs (protocol data units) to be transmitted over TCP. It is used for PLC programming, exchanging data between PLCs, accessing PLC data from SCADA (Supervisory Control and Data Acquisition) systems and for diagnostic purposes. This protocol is divided into seven layers, layers 1–4 will be done by the computer itself (the underlying driver), layer 5 TPKT, the application layer data transfer protocol, between TCP and COTP protocol. This is a transport service protocol, mainly used to build a bridge between COTP and TCP, layer 6 COTP, COTP is the OSI 7-layer protocol defined on top of TCP. Layer 7, S7 communication, this layer is related to user data, where the reading of PLC data messages is done. Table 1 shows that the S7 protocol is based on the OSI model.

Table 1. The S7 protocol is based on the OSI model.

OSI layer	Protocol
7. Application layer	S7 communication
6. Presentation layer	S7 communication (COTP)
5. Session layer	S7 communication (TPKT)
4. Transport layer	ISO-on-TCP(RFC 1006)
3. Network layer	IP
2. Data link layer	Ethernet
1. Physical layer	Ethernet

2.4 System Hardware Design

In this paper, for the selection of hardware devices, according to the analysis for remote control system, SIMATIC S7-1200 controller is used as the control core of the whole control system, and its CPU is 1215C. This PLC is one of the core products introduced by Siemens, which realizes modular and compact design and is powerful and suitable for a wide range of applications in many places. And the largest CPU is scalable up to eight signal modules to support additional digital and analog I/O [6].

The product CloudBOX TN-533 was adopted as the IOT gateway. TN-533 is designed for industrial PLC products with industrial grade design. It provides remote program download and remote data acquisition for PLC products with RJ-45 network port, RS232 and RS485, such as PLCs of Siemens, Mitsubishi, Omron, Panasonic, Delta, and Yonghong, etc. Through high-speed 4G, WAN and WIFI networks, combined with PLC supporting software or Tianqi IOT cloud platform, it can realize remote program download and data acquisition. It can be quickly connected to PLCs, industrial control machines and other devices, and data from user devices connected to TN-533 can be transmitted to the server through 4G network to achieve transparent data transmission remotely. On the left side of Fig. 2 is CloudBOX TN-533.

The DTU uses USR-G780 V2, a second generation 4G DTU product developed with embedded Linux. It supports 4G high-speed access for mobile, Unicom and telecom, with “transparent transmission” as the core function, and is highly easy to use, so users can easily and quickly integrate it into their own systems. The DTU software is fully functional and covers most of the conventional application scenarios. It can achieve transparent bi-directional data transmission from serial port to network with simple settings. And support protocol pass-through mode, custom registration packet, heartbeat packet function, support 2-way Socket connection, support TCP Server, and support pass-through cloud access. It has high speed and low latency, and supports FTP upgrade and FOTA self-upgrade. On the right side of Fig. 2 is USR-G780 V2.

2.5 System Software Design

After hardware selection, TIA Portal V16 was used as the final development tool to write the software program, which mainly included the input and output of switching quantity



Fig. 2. Cloud BOX TN-533 (left) and USR-G780 V2 (right)

and analog quantity as well as the program writing of S7 communication protocol and Modbus communication protocol. The communication protocol between the handle and PLC adopts Modbus protocol. Firstly, the handle will be configured with baud rate of 9600, data bits of 1 start bit, 8 data bits, 1 stop bit, no validity bit, communication interface of RS485, data format of Modbus, the working mode will be set as master mode, and the PLC will be configured as slave mode through the configuration software [7]. Receive the data sent by the handle through the data stream and store it in the DB block. The remote communication protocol used is the S7 protocol, and this protocol transfers the data in its DB block to the cloud service through the cloud BOX TN-533, and sends the data down to the receiving end through the cloud server to realize the remote transmission of data. The analog output module outputs the analog quantity and thus controls the excavator action [8].

2.6 Hardware Parameter Configuration

The above steps have done a good job of local communication settings, the next virtual network port tool for the cloud server and the cloud BOX TN-533 parameters configuration, remote access IP address and remote access mask configured to the same address. Table 2 shows the cloud server parameters configuration.

Parameter configuration of DTU We use USR-G780 V2.1.3 DTU supporting software to configure, connect DTU with computer using serial port, so that the computer can read the parameters of DTU. By configuring the IP address and port number of the remote access server, the DTU is connected to the cloud server, and the registration package is enabled, so that the DTU can send the login message to the cloud server after getting power. Figure 3 shows the DTU configuration parameters.

Table 2. Cloud server parameters.

Project name	Configuration parameter
Data center ports	9000
Transport protocol	UDP
Remote access IP	192.168.168.1
Remote access mask	255.255.255.0
Data center IP	mcn.ecsiot.com

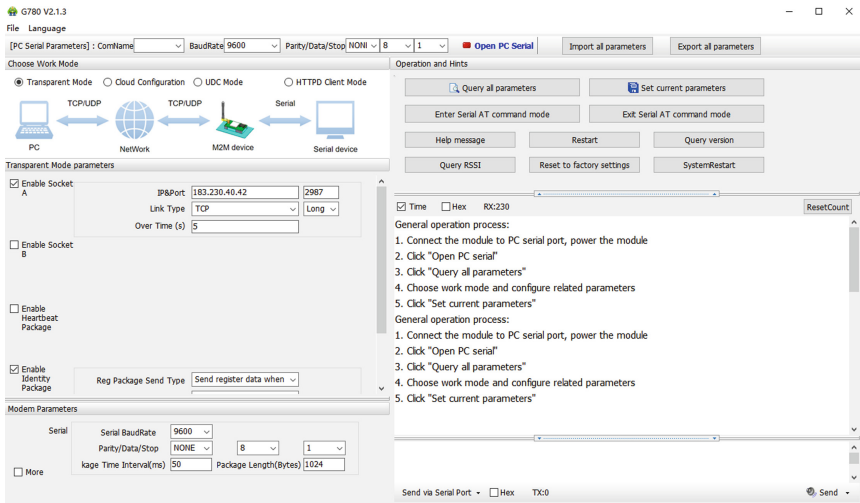


Fig. 3. DTU parameter settings

3 Upper Computer APP Design

3.1 Sliding Mode Controller Design

Based on the requirement analysis of the excavator remote control system, a good upper computer interface is needed for human-computer interaction between the excavator and the operator. The programming software vendor of choice was MIT APP Inventor from the MIT Center for Mobile Learning, which allows the creation of mobile apps through a browser-based editing tool [9]. Its App can be deployed to run on a cell phone through a connection cable between a computer and a cell phone. The login interface, as well as the data collection module and remote control module are designed on this software. Figure 4 shows the login design interface.

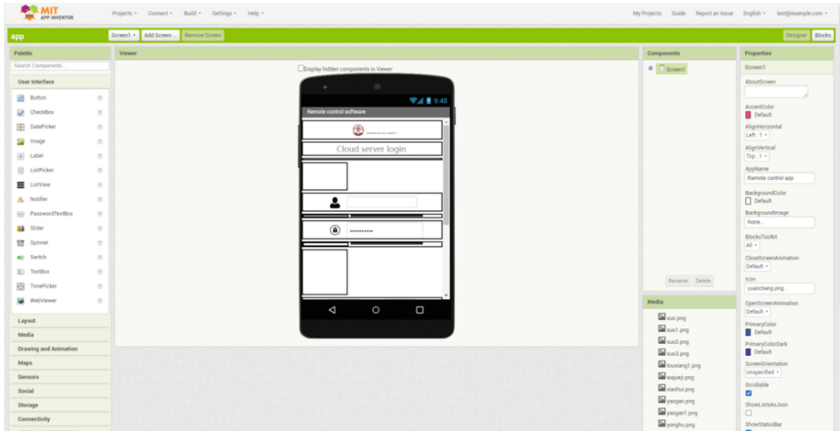


Fig. 4. Login design interface

4 Communication Delay Test

According to the previous analysis and configuration, the construction of the entire communication link and the design of the hardware and software system were completed. The communication capability of the remote control system will be tested in the following. Because of the specificity of the remote control system, the delay value becomes one of the most important key indicators for the whole communication system. It will directly affect the comfort and safety of the operation of the whole communication system as well as the reliability, so the time delay of the whole communication system will be tested several times. The Ping command, which comes with the Windows operating system, is actually an application developed based on the ICMP protocol request-response message. In order to test the communication effect between the on-board side of the system and the remote control side, a request message is sent to the IP address 192.168.168.1 using the Ping command after the local PC is connected to the PLC and the Cloud BOX TN-533, and when the message is received at that address, a 32-byte response message is returned immediately. To ensure the reliability of the experimental test results, several experiments will be conducted and the results will be analyzed. The results of several experiments show that the delay time is basically kept within 10–50 ms, so that the communication delay in the remote control system designed in this paper can basically meet the requirements. Figure 5 shows the partial delay test results.

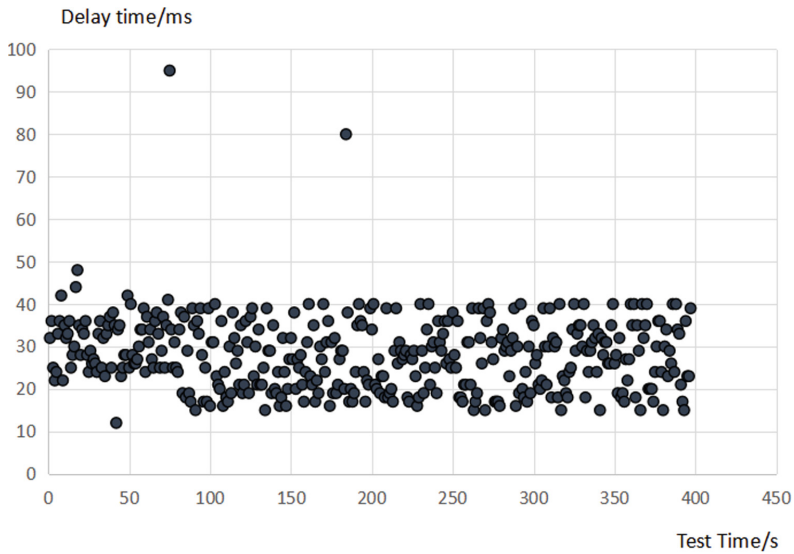


Fig. 5. Partial delay test

5 Conclusion

Aiming at the risk of excavators operating in hazardous places and the dependence on operators, this paper designs a remote control system for excavators based on industrial Internet of Things. Through the combination of industrial Internet of Things and cloud server, the excavator can be remotely controlled with low latency and high reliability. It completes the basic functions of walking, steering, slewing and telescoping of the moving arm, bucket bar and bucket. The system has good application value, which can improve the efficiency and safety of mechanized operations, reduce the reliance on operators and reduce the risk of their operation in hazardous places.

Acknowledgements. This work is supported by Shandong SME Innovation Capacity Enhancement Project (2022TSGC1379).

References

1. Shao, Y.: Research on Remote Control System of Electric Excavator Based on 5G Wireless Communication. The Overseas Chinese University (2022)
2. Pan, S., Pan, M.: Explore the application of wireless network technology in Industrial Internet of Things. *Internet Weekly* **09**, 85–87 (2023)
3. Wang, Y., Dai, Y., Liu, D., et al.: Research and application of reliable data transmission technology based on UDP. *Comput. Eng. Appl.* **03** (2010)
4. Wen, S.: Design of Remote Control and Monitoring System for Electric Excavator Based on Wireless Communication. Huaqiao University (2020)
5. Zheng, Y.: Implementation of S7-1200 control system in TIA Botu software S7 communication. *Digit. World* **5**, 62 (2019)

6. Chen, K., Gu, X.: Application of modbus TCP communication protocol in PLC course. *Autom. Appl.* **64**(06), 222–224 (2023)
7. Guan, T., Han, M., Chen, G., et al.: Design and research of general control system based on Modbus protocol. *Sci. Technol. Innov.* **08**, 92–95 (2023)
8. Wang, J.: Research on Siemens S7–1200PLC communication. *Southern Agric. Mach.* **52**(18), 146–149 (2021)
9. Yang, D.: Multi-touch implementation of canvas components in app inventor. *Comput. Knowl. Technol.* **17**(17), 61–63 (2022)



Research on Underwater Positioning Based on Binocular Vision

Siqi Zhou¹, Yang Li¹, Zhiguang Guan¹(✉), and Mingxing Lin²

¹ Shandong Provincial Engineering Lab of Traffic Construction Equipment and Intelligent Control, Shandong Jiaotong University, Jinan 250357, China

guanzhiguang@sdjtu.edu.cn

² School of Mechanical Engineering, Shandong University, Jinan 250061, China

mxlin@sdu.edu.cn

Abstract. Due to the different refractive indexes of air and water, the propagation paths of light in air and water are different. The traditional matching principle is not suitable for underwater feature point matching, which increases the difficulty of binocular positioning of machine vision. In view of the above problems, the three-dimensional coordinates of the target point are derived by transforming the three main visual space coordinate systems. Combined with Snell refraction theorem and similar triangle theorem, the binocular underwater refraction model is established, and the underwater polar line corresponding to a point on the left image in the right image is determined. According to the light propagation characteristics, the corresponding point trajectory is obtained, and the underwater stereo matching is completed, which lays a foundation for achieving high-precision underwater binocular positioning.

Keywords: Underwater · Binocular vision · Machine vision · Target location

1 Introduction

The development of underwater resources such as oceans and lakes is getting faster and faster, and the amount of underwater exploration activities is gradually increasing [1]. Due to the complex underwater environment, hypoxia, high water pressure, light and other problems, underwater exploration is limited, which increases the difficulty of research [2], and also covers the mysterious veil for the underwater environment. Early underwater exploration mainly relies on sonar technology [3]. This technology has made outstanding contributions to underwater exploration and is still widely used today. Nowadays, with the development of machine vision and artificial intelligence, visual sensors are increasingly entering the field of underwater exploration. It is more and more practical in underwater biological monitoring, seabed engineering operations, and underwater welding [4–6]. Therefore, it is necessary to study underwater vision.

Compared with monocular vision and multi-view vision, binocular vision technology is closer to the principle of human eye imaging. The operation process is simple, the result is accurate, and the calculation amount is small. When binocular vision is used

in underwater environment, the light refraction in water is quite different from that in land air, which leads to the camera imaging model in air is no longer suitable. In view of the above problems, Xu [7] proposed a method of binocular vision guided positioning, which uses four-point light source to guide the navigation of binocular camera, and adds a false light source elimination algorithm, so that the binocular camera can determine the position and direction by judging and guiding the distance of the light source, which is suitable for close and clear waters. Liu [8] established a mathematical model starting from the propagation of light in the water, proposed a four-dimensional parametric model of underwater light to calibrate the image, and found the most suitable objective function for nonlinear optimization. The three-dimensional reconstruction relies on the point cloud to reduce the error and improve the reprojection accuracy to improve the accuracy of underwater binocular measurement, but the image quality requirements are high, the water quality requirements are relatively high, and the application range is narrow. Huang [9] proposed a nonlinear mathematical model suitable for unstructured environment, which is suitable for underwater binocular positioning algorithm when the camera glass is too thick to produce refraction error, which simplifies the problem of non-intersection of straight lines on different planes. Li [10] established a nonlinear mathematical model according to the distortion parameters of binocular camera, and then used focal length normalization to determine the spatial straight line of the target point and the optical axis of the camera. Finally, the midpoint of the common vertical line of the binocular camera was solved by orthogonal projection method, and the non-intersection of the projection line of the binocular camera was solved by introducing the straight line on different planes. These two positioning methods are highly innovative, with poor accuracy and cumbersome process.

Underwater binocular positioning uses known image information to establish a three-dimensional space to obtain the target pose [11]. The establishment of the light refraction model is the key to underwater binocular positioning technology. The process of underwater binocular positioning is shown in Fig. 1.

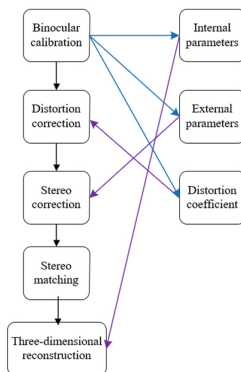


Fig. 1. Underwater binocular positioning process

2 The Principle of Binocular Positioning

The visual positioning system mainly includes world coordinates, camera coordinates and image coordinates. The conversion relationship of these three coordinate systems is shown in Fig. 2.

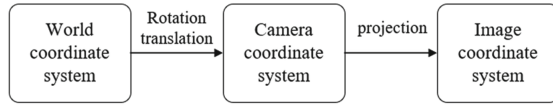


Fig. 2. Coordinate system conversion relationships

World coordinate system: is the reference frame of the target object position. In addition to infinity, the world coordinates can be placed freely according to the convenience of operation. In binocular vision, the world coordinate system has three main uses: (1) determining the position of the calibration object during calibration; (2) It is a reference coordinate system, which acts as a benchmark. The relative position of the left and right cameras can be obtained through the world coordinate system. (3) As a container for reconstructing the three-dimensional coordinates. The object after three-dimensional reconstruction is in it. The world coordinate system is the first station to incorporate the visible objects into the operation.

Camera coordinate system: It is a coordinate system that measures the object from the camera angle. The origin of the camera coordinate system is on the optical center of the camera, and the Z axis is parallel to the optical axis of the camera. It is the key to connect with the target object. The object is converted to the camera coordinate system by projection transformation in the three-dimensional world coordinate system, and then converted to the camera coordinate system by camera shooting. It is the medium of world coordinate system and image coordinate system transformation.

Image coordinate system: Establish a two-dimensional coordinate system in the photos taken by the camera. The camera to specify the position of the target object in the image.

The process of positioning is the transformation calculation between the three coordinate systems to derive the coordinates of the target in the image in the three-dimensional world. The world coordinate system is (X_W, Y_W, Z_W) , the image coordinate system is (u, v) , the optical axis focus on the image is (u_0, v_0) , the camera coordinate system is (X_C, Y_C, Z_C) , the camera focal length is f , a pixel width in the positive direction of the X-axis is d_x , a pixel width in the positive direction of the Y-axis is d_y , and the pixel size deviation is γ . The camera external parameter rotation matrix and the translation matrix are R and T respectively. The final three-dimensional coordinates obtained after the coordinate system transformation are:

$$Z_c \begin{bmatrix} u \\ v \\ 1 \end{bmatrix} = \begin{bmatrix} \frac{1}{d_x} & \gamma & u_0 \\ 0 & \frac{1}{d_y} & v_0 \\ 0 & 0 & 1 \end{bmatrix} * \begin{bmatrix} f & 0 & 0 \\ 0 & f & 0 \\ 0 & 0 & 1 \end{bmatrix} * [R \ T] * \begin{bmatrix} X_W \\ Y_W \\ Z_W \\ 1 \end{bmatrix} \tag{2.1}$$

For the binocular camera, in order to make the positioning more accurate, it is necessary to calculate the parallax of the two cameras. The principle of binocular vision is shown in Fig. 3.

The target is imaged at two positions simultaneously by the left and right cameras. The target position will generate coordinates in the two imaging planes, and the difference between the two is the parallax value. By calculating the parallax value, the actual coordinates of the position of the measured object in the world coordinate system can be obtained based on the basic theorem of similar triangles. After obtaining the coordinate data, the actual relative position of the camera and the target can be calculated using Formulas (2.2) and (2.3):

$$\frac{d - (x^l - x^r)}{Z - f} = \frac{d}{Z} \tag{2.2}$$

$$Z = \frac{df}{x^l - x^r} \tag{2.3}$$

In the formula: x^l, x^r are the horizontal axis coordinates of the measured object on both sides of the imaging plane;
 d is the baseline length of the two cameras;
 Z is the relative distance calculated based on this formula.

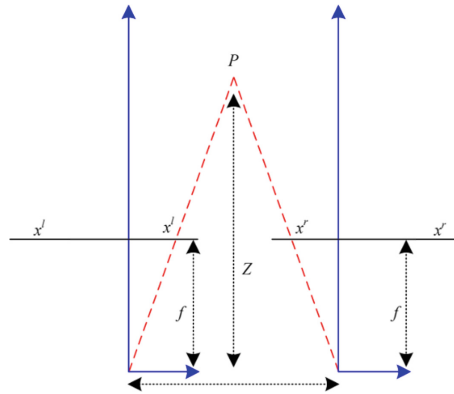


Fig. 3. Principle diagram of binocular vision

The distance measurement of underwater binocular vision is different from the distance measurement in the air. Due to the refraction of the liquid, the incident light will change the direction of propagation before being taken into the binocular camera in the closed waterproof cover, so the visual imaging model in the air cannot be directly applied underwater [12]. After obtaining the internal and external parameters of the camera by land calibration, combined with the underwater refractive polar line model, the distance after refraction through the water medium is calculated.

3 Underwater Refraction Model

The existing underwater binocular positioning technology has a lot of inventions and research improvements. Different methods have certain advantages in their corresponding underwater environment positioning. For underwater binocular positioning in more complex environments, such as positioning and ranging in dynamic environments, or in dark and noisy dusty underwater environments, the above positioning technology is difficult to play a role. Therefore, by promoting the integration of various underwater optical models, the research of underwater detection in high-dimensional, dynamic, complex and changeable environments will become the mainstream direction of underwater binocular positioning research [13].

The refraction of the underwater line structured light sensor is shown in Fig. 4. The camera is installed in a waterproof shell sealed with a high-transmittance acrylic plate. Considering that the thickness of the acrylic plate is small and the two sides are parallel, the refraction of the acrylic plate is neglected here to simplify the optical path.

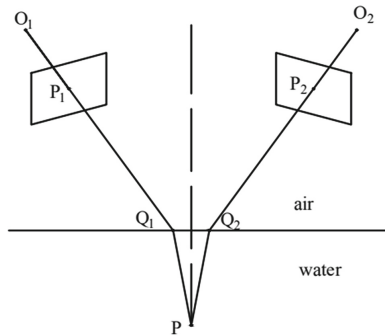


Fig. 4. Refraction diagram of the underwater line structured light sensor

The optical center of the camera is set as the optical center of the left camera O_1 and the optical center of the right camera O_2 , respectively. The focal length of the camera is f , the distance from the optical center to the refractive surface is h , the baseline length is d , and the angle between the camera and the ground is θ . The intersection point of the optical center of the left camera to the left image is $P_1(x_1, y_1, z_1)$, and the intersection point of the optical center of the right camera to the right image is $P_2(x_2, y_2, z_2)$. The refractive index of air and water is set to n_1, n_2 , and the target point $P(x_0, y_0, z_0)$. The straight line O_1P_1 intersects the refracting surface at $Q_1(x_3, y_3, z_3)$ and the straight line O_2P_2 intersects the refracting surface at $Q_2(x_4, y_4, z_4)$.

The plane equation of the left image:

$$x \sin \theta + z \cos \theta = f$$

From the similar triangle theorem, the O_1Q_1 equation can be obtained as follows:

$$\frac{x}{x_1} = \frac{y}{y_1} = \frac{z}{z_1}$$

Then, from the similar triangle theorem, we can obtain:

$$\frac{x_3}{x_1} = \frac{y_3}{y_1} = \frac{z_3}{z_1}$$

The light is incident from the air, the left incident angle is θ_1 , the refraction angle is θ_2 , and the incident equation is:

$$\frac{x}{x_3} = \frac{y}{y_3} = \frac{z}{z_3}$$

Normal equation:

$$\begin{cases} x = x_3 \\ y = y_3 \end{cases}$$

According to Snell's law of refraction:

$$n_1 \theta_1 = n_2 \theta_2$$

Substituting into the trigonometric function, the above equation can be transformed into:

$$n_1^2 - \frac{n_1^2}{1 + \tan^2 \theta_1} = n_2^2 - \frac{n_2^2}{1 + \tan^2 \theta_2}$$

From the geometric relationship:

$$\begin{cases} \tan^2 \theta_1 = \frac{x_3^2 + y_3^2}{z_3^2} \\ \tan^2 \theta_2 = \frac{(x_0 - x_3)^2 + (y_0 - y_3)^2}{(z_0 - z_3)^2} \end{cases}$$

According to the similar triangle theorem:

$$\begin{cases} x_0 y - y_0 x = 0 \\ x y_3 - y x_3 = 0 \end{cases}$$

Similarly, the plane equation of the right, right image is derived:

$$(d - x) \sin \theta + z \cos \theta = f$$

The linear O_2Q_2 equation is:

$$\frac{x - d}{x_4 - d} = \frac{y - d}{y_4 - d} = \frac{z - d}{z_4 - d}$$

The incident light equation:

$$\frac{x - x_0}{x_3 - x_0} = \frac{y - y_0}{y_3 - y_0} = \frac{z - z_0}{z_3 - z_0}$$

Normal equation:

$$\begin{cases} x = x_4 \\ y = y_4 \end{cases}$$

According to the similar triangle theorem:

$$\frac{x_2 - d}{x_4 - d} = \frac{y_2}{y_4} = \frac{z_2}{z_4}$$

Let the right incidence angle be θ_3 and the refraction angle be θ_4 . According to Snell's law of refraction, we can obtain:

$$n_1\theta_3 = n_2\theta_4$$

Further derivation, from the geometric relationship, can be obtained:

$$\begin{cases} (d - x_2)\sin\theta + z_2\cos\theta = f \\ d(y_4 - y_0) + y_0x_4 - x_0y_4 = 0 \\ x(y_4 - y_0) - y(x_4 - x_0) + x_4y_0 - x_0y_4 = 0 \end{cases}$$

It can be seen that when the matching point is extracted by stereo matching, a series of corresponding left and right poles can be obtained by changing the coordinates of P points, that is, the corresponding poles of any point on the left image on the right image can be obtained.

The epipolar constraint theory is the premise of the stereo matching algorithm. In the underwater environment, due to the different refractive indexes of different media, the epipolar line is no longer a straight line, and bending deformation occurs. This paper discusses the imaging model of the binocular camera sharing the refractive surface, which makes the binocular stereo matching more accurate.

In addition, the non-coplanar imaging model and the calculation of intermediate medium error are also one of the development directions of underwater binocular positioning. Artificial intelligence, which can make positioning more accurate, reduce errors, and track targets in real time, is also one of the development directions of machine vision. Identifying and quickly locating the target position, combined with real-time positioning of the recognition algorithm, is a hot topic in future research.

4 Conclusion

Firstly, this paper expounds the current research status, advantages and problems of underwater binocular positioning. Secondly, the principle of binocular positioning is introduced in detail, and the constraint of stereo matching epipolar line in underwater environment is deduced. Finally, the expression formula of stereo matching corresponding epipolar line is calculated from the perspective of optical refraction, and other problems to be solved in underwater binocular positioning are discussed. The future research directions of binocular positioning are proposed: (1) The positioning speed is efficient and accurate; (2) Real-time tracking mark target position.

Acknowledgements. This work is supported by Natural Science Foundation of Shandong Province (ZR2020ME267, ZR2023MF077), Science and technology plan project of Shandong Provincial Department of Transportation (2023B93), Science and Technology Support Plan for Youth Innovation in Universities of Shandong Province Colleges and Universities (2019KJB014).

References

1. Zhou, J., Zhang, D., Zhang, W.: Cross-view enhancement network for underwater images. *Eng. Appl. Artif. Intell. Artif. Intell.* **121**, 105952 (2023)
2. Li, X., Zhang, M.: Target segmentation and target positioning of underwater binocular vision system. *Huazhong Univ. Sci. Tech. (Nat. Sci. Ed.)* **45**(12), 53–59 (2017)
3. Ren, C., Huang, Y., Xia, Z.: Modeling of spatial correlation characteristics of broadband ocean ambient noise vector field. *Acta Phys. Sin.* **71**(02), 131–141 (2022)
4. Xu, Y., Du, J., Lei, Z.: Review: applications status and key technologies of underwater robots in fishery. *Robot.* **45**(01), 110–128 (2023)
5. Zhang, G., Bu, T., Ge, Y.: Design of automatic control system of underwater vehicle based on machine vision. *Ship Sci. Technol.* **42**(10), 49–51 (2020)
6. Liu, S., Zhong, J., Wang, G.: Edge detection on arc image of underwater wet welding. *Electr. Weld. Mach.* **4**, 14–17 (2000)
7. Xu, S., Jiang, Y., Li, Y.: A stereo vision localization method for autonomous recovery of autonomous underwater vehicle. *J. Harbin Eng. Univ.* **43**(08), 1084–1090 (2022)
8. Liu, J., Zhuang, S., Tu, D.: Underwater modeling and calibration method of binocular stereo vision imaging system. *Acta Photonica Sinica* **51**(12), 1211002 (2022)
9. Huang, W., Xu, X., Wu, F.: Research of underwater binocular vision stereo positioning technology in nuclear condition. *Opto-Electron. Eng.* **43**(12), 28–33 (2016)
10. Li, G., Xie, X.: High precision positioning method for underwater moving binocular vision. *China Measur. Test.* **41**(S1), 37–39 (2015)
11. Yang, H., Wan, T.: Research on binocular positioning and grasping accuracy of grape picking manipulator. *J. Agric. Mechanization Res.* **44**(12), 49–54 (2022)
12. Xie, Z., Shao, W., Gao, X.: Underwater multiple line-structured light binocular measuring method based on discrete epipolar curve model. *Chin. J. Lasers* **48**(13), 108–118 (2021)
13. Zhang, Q., Dong, Y., Hai, B.: Underwater curve constraint model based on non-parallel binocular vision. *Acta Optica Sinica.* **36**(03), 141–147 (2016)



Simulation of Remote Control of Excavator Bucket Rod Hydraulic System Based on AMESim

Zhenyuan Zhao¹, Qin Sun¹, Baoping Wang¹(✉), and Nan Zhang²

¹ Shandong Jiaotong University, Jinan 250357, China
wangbaoping@sdjtu.edu.cn

² Jinan Special Equipment Inspection and Research Institute, Jinan, China

Abstract. With the vigorous promotion of artificial intelligence and the advancement of robotics, construction machinery has also continued to evolve in the direction of digitalization and intelligence. Hydraulic excavators have an important role in engineering construction, however, excavator operators encounter problems such as landslides and bad weather, which bring great challenges to drivers and industrial production, so remote control and unmanned driving of excavators gradually become the focus of research. For the realization of remote control of hydraulic excavator, this paper applies electro-hydraulic proportional control technology to the hydraulic system of a model of excavator, and designs the operating lever control system as an electro-hydraulic proportional control hydraulic system to realize the control of electrical signals without changing the original function of excavator. Simulation was performed by AMESim to create a solenoid proportional reversing valve model according to the selected model, and the flow control characteristics of the system were analyzed to determine the hydraulic system stability.

Keywords: Excavator hydraulic system · Solenoid proportional reversing valve · AMESim simulation

1 Introduction

Automation and intelligent technology continues to develop, and intelligent construction has become the mainstream of development. And the remote control of hydraulic excavator can guarantee the operational efficiency in harsh environment and ensure the safety of personnel to reduce driving fatigue. According to WY1.5 excavator, Cui Guohua et al. proposed a design scheme for the intelligent excavator electronic control hydraulic system [1]. Ronghua Liu used RS232 wireless communication module to design a remote controller for wireless remote control of excavator [2]. In recent years many researchers have applied electronic control to excavator motor and pump control to achieve energy saving, and Xuan Wu et al. targeted the pump displacement control by electrical signals to prevent sudden speed changes and improve the coordination of the action when the excavator is operated in compound [3]. Solenoid proportional reversing valve as a pilot

valve is the key to achieve electro-hydraulic control of hydraulic excavator, and the speed of hydraulic rod extension is controlled by the magnitude of the given electrical signal instead of the manual operation, to achieve the purpose of wireless remote control.

2 Bucket Rod Hydraulic Cylinder Control Principle

In this paper, the hydraulic circuit of bucket rod hydraulic cylinder of a model excavator is simplified, and the principle is shown in Fig. 1 a is a manual control circuit, and b is an electronically controlled hydraulic circuit. The manual valve is replaced by a solenoid proportional valve to realize the electric signal control, and the control signal input port is A1, A2. The main oil circuit has high pressure and large hydraulic force, which is not suitable for direct commutation by solenoid proportional valve. In order to ensure the timely response of the system, a pilot oil circuit is led from the main oil circuit through the pressure reducing valve to control the commutation of the liquid-controlled directional valve. Two sets of liquid-controlled check valves form a locking circuit to avoid the bucket rod from falling back due to stoppage when it is extended.

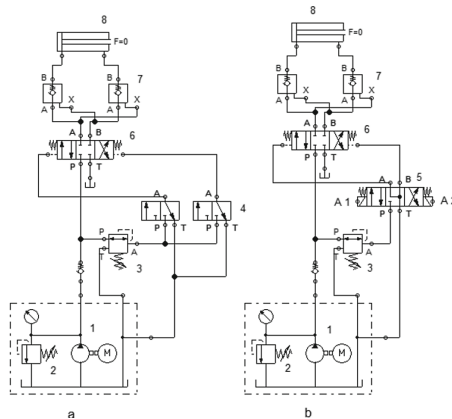


Fig. 1. Bucket rod hydraulic cylinder control circuit 1. Hydraulic pump 2. Relief valve 3. Pressure reducing valve 4. Manual pilot reversing valve 5. Solenoid proportional reversing valve 6. Hydraulic control reversing valve 7. Hydraulic control check valve 8. Bucket rod hydraulic cylinder

3 Modeling and Simulation of the System

In this paper, two major parts of the electro-hydraulic system of the bucket rod cylinder are tested for static and dynamic characteristics. The static characteristics test includes the steady-state flow characteristics test (output flow-control signal signal characteristics test), and the dynamic characteristics test includes the system response characteristics test (control signal-hydraulic extension speed) [4], and the effective speed range of the system is determined according to the system response (Table 1).

Table 1. Bucket rod cylinder parameters

Parameter name	Numerical value
Displacement of bucket rod cylinder supply pump (cc/rev)	28
Pump pressure (MPa)	23
Displacement of the pilot pump (cc/rev)	4.5
Pilot pump pressure (MPa)	3.9
Inner diameter of hydraulic cylinder (mm)	85
Piston rod diameter (mm)	55

3.1 Calculation of Bucket Rod Cylinder

(1) Pump flow calculation

$$Q = \frac{q_1 n \eta_{vb}}{1000} \quad (1)$$

q_1 —Displacement of bucket rod cylinder supply pump (cc/rev);

n —Engine speed (rev/min, $n = 2200$ rev/min);

η_{vb} —Pump volumetric efficiency;

The calculation gives $Q = 55.4$ L/min.

(2) The force of the rodless chamber of the bucket rod hydraulic cylinder

$$F_1 = \frac{PD_1^2 \pi \eta_{mg}}{4} \quad (2)$$

P —Pump pressure (Pa);

D_1 —Inner diameter of hydraulic cylinder (m);

η_{mg} —Mechanical efficiency of hydraulic cylinders;

The calculation gives $F_1 = 127903.3$ N.

(3) Bucket rod hydraulic cylinder has the force of the rod cavity

$$F_2 = \frac{P(D_1^2 - d_1^2) \pi \eta_{mg}}{4} \quad (3)$$

d_1 —Piston rod diameter (m)

The calculation gives $F_2 = 74352.1$ N.

(4) Bucket rod hydraulic cylinder extension speed

$$v_1 = \frac{4Q\eta_{vg}}{60,000\pi D_1^2} \quad (4)$$

The calculation gives $v_1 = 0.155$ m/s.

(5) Bucket rod hydraulic cylinder retraction speed

$$v_2 = \frac{4Q\eta_{vg}}{60,000\pi(D_1^2 - d_1^2)} \tag{5}$$

The calculation gives $v_2 = 0.266$ m/s.

3.2 Selection of Solenoid Proportional Reversing Valve

(1) Calculation of pilot oil circuit

$$Q_x = \frac{q_2 n \eta_{vbx}}{1000} \tag{6}$$

q_2 —Displacement of the pilot pump (cc/rev);

η_{vbx} —Volumetric efficiency of the pilot pump (0.88);

The calculation gives $Q_x = 8.7$ L/min.

(2) Calculation of valve passage diameter

The flow rate calculated in combination with the mechanical design manual is used to determine the passage diameter of the solenoid proportional reversing valve [5]:

$$Q_x = \mu A_1 \sqrt{\frac{2\Delta P}{\rho}} \tag{7}$$

ΔP —Differential pressure before and after the valve port (Pa);

A_1 —Valve port area;

ρ —The density of the fluid;

μ —Flow coefficient;

As shown in the schematic diagram, the pilot reversing valve is a three position four way valve, the neutral function is Y type, the diameter is 6 mm. After checking the mechanical design manual to determine the choice of 4WRA6W5-10BZ4M. Its flow characteristics are shown in Fig. 2.

3.3 AMESim Modeling Simulation

AMESim (Advance Modeling Environment for Simulation of engineering systems) is the most famous international platform for advanced modeling and simulation of engineering systems, which was successfully developed by the French state company in 1995. It is a powerful software for modeling, simulation and dynamics analysis of hydraulic and mechanical systems, and it is specialized in solving complex systems of hydraulics, mechanics, pneumatics, electromagnetism and control, etc. It has excellent expertise and design experience not only in the mechanical and hydraulic fields, but also in the aerospace industry, automotive manufacturing and traditional hydraulic industry [6].

AMESim software consists of five parts: graphical modeling AMESim, simulation and analysis tools, sub-model editing tool AMESet, customization, packaging and encryption platform AMECustom, runtime tool AMERun, and database management administration AMEDesk. They have their own characteristics and applications. The simulation steps are as follows:

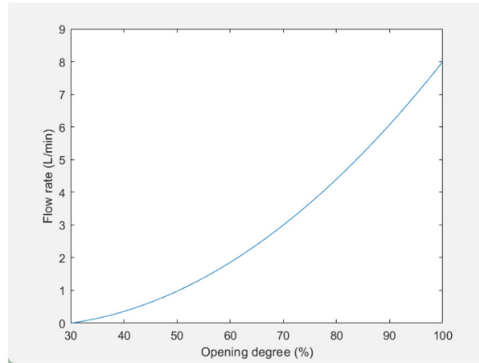


Fig. 2. Solenoid proportional valve open flow relationship

- (1) In the sketch mode, the simulation model is built, and the appropriate model is selected or created from the library according to the physical quantities input and output of each component and the required functions.
- (2) After building the sketch, in the sub-model mode, select the components according to the scenario they are used in and the physical quantities to be considered.
- (3) In the parameter mode, input the parameters of each component, such as dimensions, weight, control signals and various forces and other physical quantities.
- (4) The run mode is to perform simulation calculations for the whole system, set up batch processing, and complete the analysis of the results.

System simulation model

The hydraulic components library, mechanical library and signal library in AMESim are modeled by referring to the schematic diagram as shown in Fig. 3 below. The whole simulation model mainly has main pump, pilot pump, check valve, hydraulic control reversing valve, solenoid proportional reversing valve, hydraulic control check valve, relief valve, hydraulic cylinder, control signal and piping model. This is not marked in the diagram. The dimensionless control signal is used instead of the electric control signal of the solenoid proportional valve and the load force applied to the hydraulic cylinder. The load force on the hydraulic cylinder is simulated as the maximum force applied to the hydraulic rod extension and retraction of the excavator. A quantitative pump is used instead of a variable pump under full load, and the model is built according to the pressure-flow characteristics of the selected model of the solenoid proportional reversing valve.

(1) Main pump and pilot pump modeling

The main pump and the pilot pump are directly modeled from the library, and their parameters are set as shown in Fig. 4.

(2) Solenoid proportional valve simulation model

The valve creation module in the hydraulic components library is used to import the open flow data of the selected model into a 2D table to set the open flow relationship of

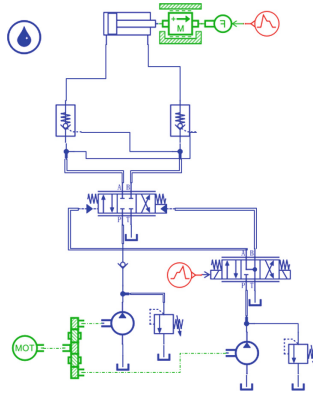


Fig. 3. Hydraulic system model

Title	Value	Unit	Tags	Name
index of hydraulic fluid	0			indexf
pump displacement	28	cc/rev		displ
typical pump speed	2500	rev/min		wtyp

Title	Value	Unit	Tags	Name
index of hydraulic fluid	0			indexf
pump displacement	4.5	cc/rev		displ
typical pump speed	2000	rev/min		wtyp

Fig. 4. Main pump and pilot pump parameters

the model. The model and the opening flow relationship are shown in Fig. 5 and are the same as for the selected model.

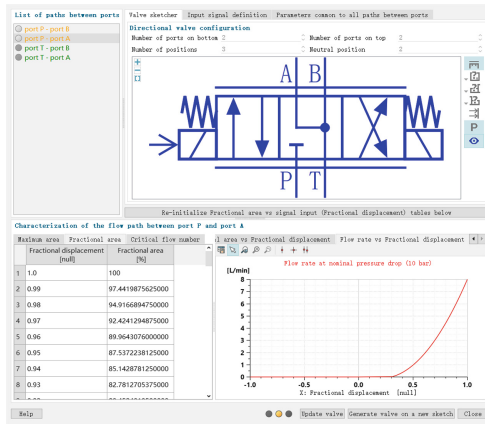


Fig. 5. Solenoid proportional directional valve model and open flow relationships

(3) Setting of load force

The pressure signal is “+”, the tension signal is “-”, and the simulation time is 10 s. The hydraulic cylinder is subjected to a force of 120,000 N when it is extended and 70,000 N when it is retracted (Fig. 6).

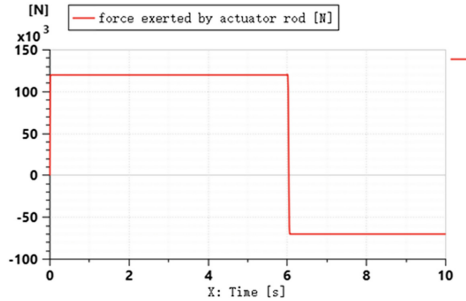


Fig. 6. Load of the system

(4) Setting of the switching signal of the solenoid proportional reversing valve

Because of the dead zone, the pilot reversing valve has a right position operating signal interval of 0.3 to 1 and a left position operating signal interval of -0.3 to -1 . The direction of the control signal is changed according to the given load force. If the characteristics of the reversing valve do not meet this system, the system will have drastic pressure flow fluctuations during reversing (Fig. 7).

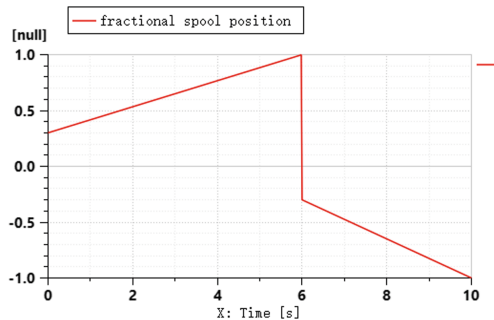


Fig. 7. Solenoid proportional directional valve control signal

(5) Analysis of simulation results

From the displacement of the hydraulic rod and the movement speed of the hydraulic rod in Fig. 8, it is concluded that the extension and retraction speed and displacement are steadily increasing with the increase of time, which is consistent with the calculated

values and the set requirements, indicating that the system model is very stable. Simplifying the simulation, the simulation time is changed to 6 s, and only the hydraulic rod extension is observed. Figure 9 shows that the controllable interval of the solenoid valve is small, it opens at 0.3, and the flow rate reaches the maximum value at about 0.46. Figure 10 shows the hydraulic rod extension speed corresponding to different given signals, so the effective control interval of the bucket rod hydraulic cylinder speed is 0.3 ~ 0.45. After changing the control signal, as in Fig. 11, the control signal increases linearly from 0.3 to 0.45 in 6 s, and the hydraulic rod extension speed also. The control signal increases linearly from 0.3 to 0.45 within 6 s, and the hydraulic rod extension speed also increases to 0.18 m/s, which can better meet the actual demand.

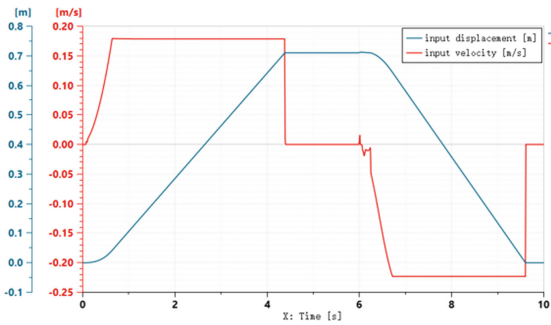


Fig. 8. Displacement and movement speed of the hydraulic rod

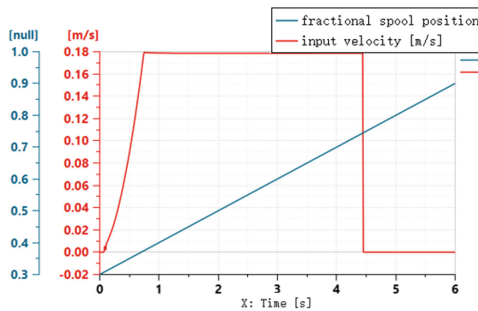


Fig. 9. Control signal and bucket rod cylinder extension speed

The load force of the hydraulic cylinder is increased linearly from 90,000 N to 120,000 N in 6 s. The pressure-flow characteristic curve of the load in Fig. 12 shows that the pressure in the rodless chamber increases as the load force rises, and the flow rate reaches the maximum when the liquid-controlled reversing valve reaches a certain opening. This is in line with the characteristics of the bucket rod hydraulic cylinder rod work.

With the opening of the liquid-controlled reversing valve, the pressure of the pilot valve A port gradually reaches the maximum, and the flow rate of the A port increases with the displacement of the spool of the liquid-controlled reversing valve and then

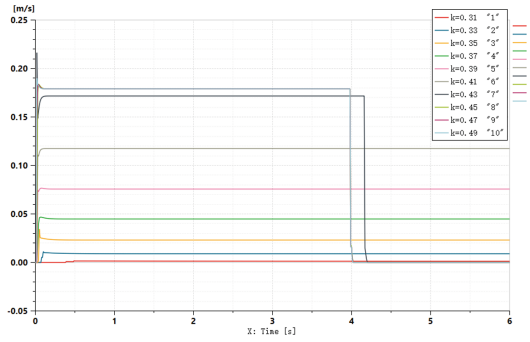


Fig. 10. Hydraulic rod extension speed for different given signals

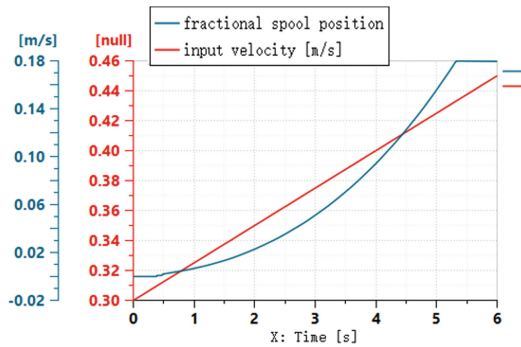


Fig. 11. Hydraulic rod extension speed at 0.3 ~ 0.45 control signal

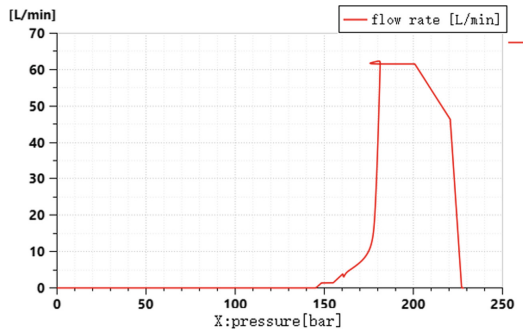


Fig. 12. Pressure flow characteristic curve of the load

decreases to zero, at which time the spool no longer moves. The flow and pressure curve of the pilot valve A port does not show any violent jitter, which meets the stable control type (Fig. 13).

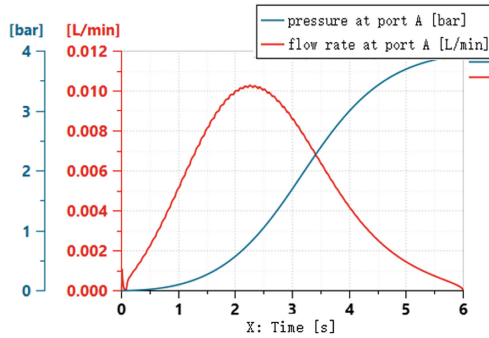


Fig. 13. Solenoid proportional reversing valve A port pressure flow

4 Conclusion

In this paper, using AMESim software, the model design and simulation analysis of the bucket rod hydraulic cylinder control circuit of a type of excavator incorporating a solenoid proportional reversing valve are carried out, and the conclusions are as follows:

- (1) Applying the solenoid proportional reversing valve for the reversing of the pilot oil circuit, the outstretched and retracted speed of the bucket rod hydraulic cylinder is stable and meets the calculated requirements. The selected solenoid proportional reversing valve has a control dead zone, which can be eliminated by adjusting the given signal through the controller, and the speed adjustment interval can be expanded to achieve more accurate infinitely variable speed regulation. Through calculation and simulation, reference data is provided for the improvement of the hydraulic part of the electronically controlled excavator.
- (2) This paper describes the design of hydraulic excavator working device and hydraulic system based on AMESim software platform, taking the bucket bar control circuit of an excavator as the research object to verify the accuracy of hydraulic system simulation model design.

Acknowledgements. This work is supported by Shandong Province Small and Medium Enterprises Innovation Capability Improvement Project (2021TSGC1441); Construction Machinery Intelligent Equipment Innovation & Entrepreneurship Community (GTT20220211); Shandong SME Innovation Capacity Enhancement Project (2022TSGC1379).

References

1. Cui, G., Han, Y., Lv, C.: Design of intelligent excavator electric control hydraulic system. *Road Mach. Constr. Mechanization* (02), 50–51+54 (2007)
2. Liu, R.: Research on electro-hydraulic control system of wireless remote control excavator. *Mach. Tools Hydraulics* **44**(16), 124–127 (2016)
3. Wu, X., Chen, J., Yin, S.: Study on the coordination of composite action of fully electronically controlled positive flow hydraulic excavator. *Hydraulics Pneumatics* **47**(2), 146–154 (2023)

4. Liao, Y., Wang, S.: Simulation and experimental study on the test system of AMESim-based electromagnetic proportional reversing valve. *J. Hubei Coll. Nationalities (Nat. Sci. Ed.)* **35**(2), 209–211, 215 (2017)
5. Li, H., Wang, S., Qi, J., Wang, G., Sun, B., Yang, S., Zhang, Y.: Selection and application of pilot-operated two-position three-way solenoid valves. *Valve* **2022**(5), 393–396 (2022)
6. Shang, X.: Analysis and simulation study of hydraulic system of WY60 excavator. Shandong University of Science and Technology (2011)



Kinematics Study of Six-Axis Industrial Robots Based on Virtual Simulation Technology

Yuchen Liu, Lingyan Zhao^(✉), Maofei Liang, and Fayong Wang

Shandong Jiaotong University, Jinan 250357, China
206082@sdjtu.edu.cn

Abstract. Manufacturing industry is an important basic part of China's economic development. With the rapid development of Internet of Things, big data, virtual simulation, sensors and other technologies, the rapid transformation of manufacturing industry to digitalization and intelligence is promoted. Industrial virtual simulation technology can realize the purpose of mirroring the physical space of the physical equipment in the digital virtual space, so as to realize the virtual debugging and parameter optimization of the physical equipment. In this paper, a robot kinematic modeling and simulation analysis method based on virtual simulation technology is proposed. Taking the six-axis industrial robot as the research object, the mathematical model of robot forward and reverse kinematics is established by the D-H parameter method; taking the automated production line of flange bearing as an example, the SimReal industrial simulation software is used for virtual modeling of the robot body and PLC virtual commissioning simulation of the production line, and the end parameters and six-joint motion parameters are collected based on the trajectory teaching method. The accuracy and rationality of the theory and research method are verified by comparing the theoretical results of the mathematical model with the simulation results.

Keywords: Virtual simulation · Six-axis industrial robot · SimReal · Robot kinematics

1 Introduction

With the rapid economic and social development, the world is transitioning to the middle of "Industry 4.0" development, which means that China should accelerate the integration of industrialization and information technology in the strategy of simultaneous development of both [1]. Virtual simulation is a technology that creates virtual environments on a computer and interacts with them. With the development of science and technology and the increase of application demand, virtual simulation technology has been rapidly developed and widely used both at home and abroad [2].

Industrial robots are an important part of high-tech equipment and are of great importance for important future industrial production and social development as well as for strengthening military defense strength, which is expected to be another strategic emerging industry after automobiles, aircraft, and computers [3].

In this paper, a robot kinematic modeling and simulation analysis method based on virtual simulation technology is proposed for the study of a six-axis industrial robot. The accuracy of the kinematic model is verified by error analysis of theoretical and simulation parameters.

2 Six-Axis Robot Kinematic Model Study

2.1 Research Subjects

The object of this paper is the SV2-6045 vertical multi-joint six-axis robot from APE. The robot body is shown in Fig. 1. The robot is small enough to replace light physical operations of less than 3 kg, and its body is internally aligned and the joints are modularly designed and assembled. The specific dimensions between the various axes are shown in Fig. 2. The working space is shown in Fig. 3.

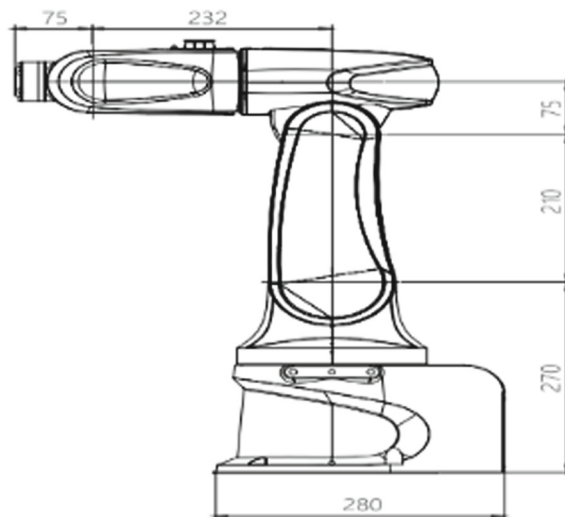


Fig. 1. Robot size diagram

2.2 Robot Kinematic Equations

2.2.1 Establishment of D-H Coordinate System

Typically, a robot coordinate system is composed of a reference coordinate system and the robot's workspace. The robot datum coordinate system is a fixed coordinate system defined in the robot control system to describe the robot's motion state and position information. When two rods are connected by rotating joints, as shown in Fig. 4, the lower joint of rod $i-1$ is numbered $i-1$, while the upper joint is numbered i . Define the rod length and the rod turning angle. The relative motion is angular displacement



Fig. 2. Robot body

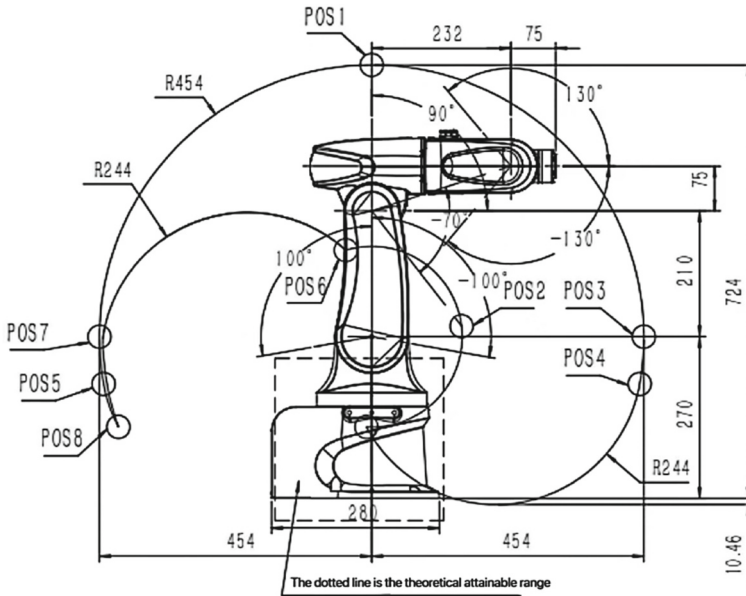


Fig. 3. Robot work space

and is denoted by. When the two joints are connected by moving joints, the relative displacement is a line displacement, denoted by. For a rotating joint, it is a variable and a constant. Similarly, for a moving joint, it is a variable and a constant.

The robot D-H parameter table is established through the linkage coordinate system model in Fig. 5, as shown in Table 1.

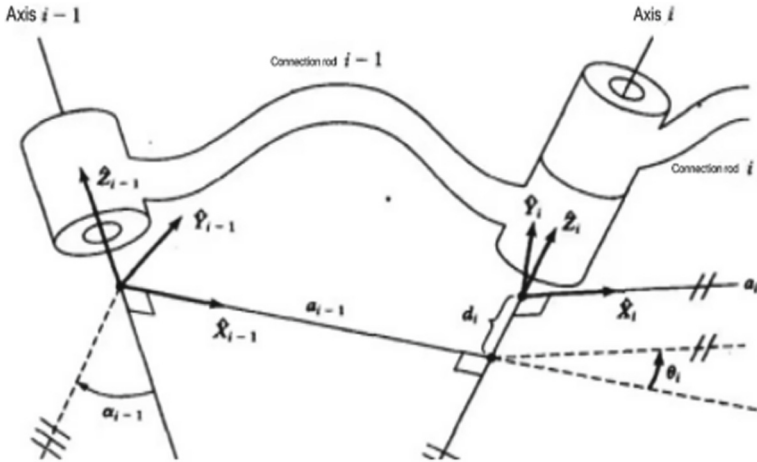


Fig. 4. Determination of linkage parameters

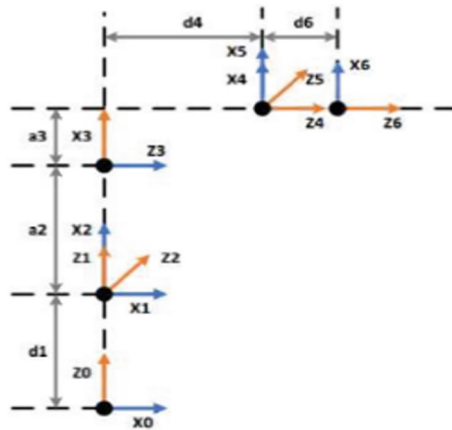


Fig. 5. Robot linkage coordinate system

2.2.2 Robot Positive Kinematics Analysis

The forward kinematic analysis of the robot means that the structural parameters and joint variables of each joint are known, and the spatial position of the robot end linkage coordinate system in a fixed coordinate system is determined. The transformation equation for the transformation of $\{i-1\}$ system to $\{i\}$ system is expressed as:

$${}^{i-1}A = \text{Rot}(x_{i-1}, a_{i-1})\text{Trans}(x_{i-1}, a_{i-1})\text{Rot}(z_i, \theta_i)\text{Trans}(z_i, d_i)$$

$$= \begin{bmatrix} \cos\theta_i & -\sin\theta_i & 0 & a_{i-1} \\ \sin\theta_i \cos a_{i-1} & \cos\theta_i \cos a_{i-1} & -\sin a_{i-1} & -d_i \sin a_{i-1} \\ \sin\theta_i \sin a_{i-1} & \cos\theta_i \sin a_{i-1} & \cos a_{i-1} & d_i \cos a_{i-1} \\ 0 & 0 & 0 & 1 \end{bmatrix}$$

Table 1. D-H parameter table

i	$a_{i-1}/(^\circ)$	a_{i-1}/mm	d_i/mm	$\theta/(^\circ)$	Rotation range/ $(^\circ)$
1	0	0	270	θ_1	[165, +165]
2	-90	0	0	θ_2-90	[100, +100]
3	0	210	0	θ_3	[-70, +90]
4	-90	75	232	θ_4	[160, +160]
5	90	0	0	θ_5	[-130, +130]
6	-90	0	75	θ_6	[-360, +360]

$$s_i = \sin\theta_i, c_i = \cos\theta_i, s_{ij} = \sin(\theta_i + \theta_j), c_{ij} = \cos(\theta_i + \theta_j) \tag{1}$$

From Table 1 D-H parameter table and Eq. (1), the flush transformation array between adjacent connecting rods can be obtained as:

$$\begin{aligned}
 {}^0_1A &= \begin{bmatrix} c_1 & s_1 & 0 & 0 \\ s_1 & c_1 & 0 & 0 \\ 0 & 0 & 1 & 270 \\ 0 & 0 & 0 & 1 \end{bmatrix} & {}^1_2A &= \begin{bmatrix} s_2 & c_2 & 0 & 0 \\ 0 & 0 & 1 & 0 \\ c_2 & -s_2 & 0 & 0 \\ 0 & 0 & 0 & 1 \end{bmatrix} & (2) \\
 {}^2_3A &= \begin{bmatrix} c_3 & -s_3 & 0 & 210 \\ s_3 & c_3 & 0 & 0 \\ 0 & 0 & 1 & 0 \\ 0 & 0 & 0 & 1 \end{bmatrix} & {}^3_4A &= \begin{bmatrix} c_4 & -s_4 & 0 & 75 \\ 0 & 0 & 1 & 232 \\ -s_4 & -c_4 & 0 & 0 \\ 0 & 0 & 0 & 1 \end{bmatrix} \\
 {}^4_5A &= \begin{bmatrix} c_5 & -s_5 & 0 & 0 \\ 0 & 0 & -1 & 0 \\ s_5 & c_5 & 0 & 0 \\ 0 & 0 & 0 & 1 \end{bmatrix} & {}^5_6A &= \begin{bmatrix} c_6 & -s_6 & 0 & 0 \\ 0 & 0 & 1 & 75 \\ -s_6 & -c_6 & 0 & 0 \\ 0 & 0 & 0 & 1 \end{bmatrix}
 \end{aligned}$$

The relationship between the robot base coordinate system and the end-effector coordinate system can be obtained by multiplying the flush transformation matrices of the adjacent connecting rods in sequence:

$${}^0_6A = {}^0_1A {}^1_2A {}^2_3A {}^3_4A {}^4_5A {}^5_6A = \begin{bmatrix} a_{11} & a_{12} & a_{13} & p_x \\ a_{21} & a_{22} & a_{23} & p_y \\ a_{31} & a_{32} & a_{33} & p_z \\ 0 & 0 & 0 & 1 \end{bmatrix} \tag{3}$$

The elements in the formula are as follows:

$$\begin{aligned}
 a_{11} &= s_6(c_4s_1 - s_4c_1s_{23}) + c_6[c_5(c_4c_1s_{23} + s_1s_4) + s_5c_1c_{23}] \\
 a_{21} &= -s_6(s_4s_1s_{23} + c_1c_4) - c_6[-s_5s_1c_{23} + c_5(c_1s_4 - c_4s_1s_{23})] \\
 a_{31} &= c_6(-s_5s_{23} + c_4c_5c_{23}) - s_4s_6c_{23}
 \end{aligned}$$

$$\begin{aligned}
a_{12} &= c_6(c_4s_1 - s_4c_1s_{23}) - s_6[c_5(c_4c_1s_{23} + s_1s_4) + s_5c_1c_{23}] \\
a_{22} &= s_6[-s_5s_1c_{23} + c_5(c_1s_4 - c_4s_1s_{23})] - c_6(s_4s_1s_{23} + c_1c_4) \\
a_{32} &= -c_6s_4c_{23} - s_6(c_4c_5c_{23} - s_5s_{23}) \\
a_{13} &= -s_5(c_4c_1s_{23} + s_1s_4) + c_5c_1c_{23} \\
a_{23} &= s_5(c_1s_4 - c_4s_1s_{23}) + c_5s_1s_{23} \\
a_{33} &= -c_5s_{23} - c_4s_5c_{23}
\end{aligned} \tag{4}$$

$$\begin{aligned}
p_x &= 210c_1s_2 + 75c_5c_1c_{23} - 75s_5(c_4c_1s_{23} + s_1s_4) + 75c_1s_{23} + 232c_1c_{23} \\
p_y &= 75s_5(c_1s_4 - c_4s_1s_{23}) + 210s_2s_1 + 75c_5s_1c_{23} + 75s_1s_{23} + 232s_1c_{23} \\
p_z &= -232s_{23} + 210c_2 - 75c_5s_{23} + 75c_{23} - 75c_4s_5c_{23} + 270
\end{aligned}$$

2.2.3 Robot Inverse Kinematics Analysis

Robot inverse kinematics is the process of finding the joint angles of the robot arm to reach the desired position satisfying the desired position given the desired position and attitude of the end-effector of the robot arm relative to the reference coordinate system. Usually when the position and attitude of the end-effector are given, the solution is not unique when one wants to inverse solve the variable problem of displacement and rotation of each joint for the given conditions. Setting the origin of the three coordinate systems fixed at the wrist of the robot arm as the wrist point A, the wrist point with respect to the base coordinate system is:

$$\begin{cases} p_{ax} = p_x - d_6a_x \\ p_{ay} = p_y - d_6a_y \\ p_{az} = p_z - d_6a_z \end{cases} \tag{5}$$

From Eqs. (3) and (5), the position of the wrist when $d_6 = 0$ is:

$$\begin{bmatrix} p_{ax} \\ p_{ay} \\ p_{az} \end{bmatrix} = \begin{bmatrix} 75c_1s_{23} + 232c_1c_{23} + 210c_1s_2 \\ 75s_1s_{23} + 232s_1c_{23} + 210s_2s_1 \\ 75c_{23} - 232s_{23} + 210c_2 + 270 \end{bmatrix} \tag{6}$$

The transformation from Eq. (6) yields:

$$p_{ay}c_1 - p_{ax}s_1 = 0 \tag{7}$$

$$\theta_1 = \text{atan2}(p_{ay}, p_{ax}) \tag{8}$$

The transformation from Eq. (6) yields:

$$Ac_2 + Bs_2 = C \tag{9}$$

Among them $A = p_{az} - 270$, $B = p_{ax}c_1 + p_{ay}s_1$, $C = \frac{(A^2 + B^2 - 15349)}{420}$.

From Eq. (9) we get θ_2 as:

$$\begin{aligned}\theta_2 &= \text{atan2}\left(C, \pm \sqrt{A^2 + B^2 - C^2}\right) - \text{atan2}(A, B) \\ \theta_3 &= \text{atan2}\left(75(p_{ax}c_1 + p_{ay}s_1) - 232(p_{az} - 210c_2 - 270), \right. \\ &\quad \left. 75(p_{az} - 210c_2 - 270) + 232(p_{ax}c_1 + p_{ay}s_1)\right) - \theta_2\end{aligned}$$

According to Eq. (3), the attitude transformation matrix between the linkage coordinate system {3} to the linkage coordinate system {6} is obtained as

$${}^3R_6 = \begin{bmatrix} r_{11} & r_{12} & r_{13} \\ r_{21} & r_{22} & r_{23} \\ r_{31} & r_{32} & r_{33} \end{bmatrix} = \begin{bmatrix} c_4c_5c_6 - s_4s_6 & -c_6s_4 - c_4c_5s_6 & -c_4s_5 \\ c_6s_5 & -s_6s_5 & c_5 \\ -c_4s_6 - c_5c_6s_4 & c_5s_4s_6 - c_4c_6 & s_4s_5 \end{bmatrix} \quad (10)$$

$$\begin{cases} \Theta_5 = \text{atan2}\left(\pm \sqrt{r_{13}^2 + r_{33}^2}, r_{23}\right) \\ \theta_4 = \left(r_{33}/s_5, -r_{12}/s_5\right) \\ \theta_6 = \left(-r_{22}/s_5, r_{21}/s_5\right) \end{cases} \quad (11)$$

The joint angles of the robot arm interact with each other and there are eight final solutions. In general, the optimal set of solutions is selected according to the “minimum travel rule” for the motion of the arm.

3 SimReal-Based Virtual Commissioning of PLC for Production Lines

In this paper, the virtual modeling and simulation of the welding process of the SV2-6045 six-axis industrial robot on the production line is developed. The welding line is first modeled in general by SimReal, as shown in Fig. 6. The production line control logic is shown in Fig. 7. The motor supplies power to run the conveyor, and once the sensor is activated, the motor will stop the conveyor and the six-axis robot senses the signal to perform the welding action. The program consists of three sensor input switches, a timer and a motor output coil, and 12 robot joint variable addresses. The PLC simulation variable table is shown in Fig. 8, and the virtual simulation process is shown in Fig. 9.

4 Kinematics Simulation Analysis Based on SimReal

4.1 Forward Kinematics Simulation Analysis

The above welding trajectory is a circular trajectory with a diameter of 105 mm. Therefore, the robot end trajectory was first taught to the SimReal virtual debugger. To verify the accuracy of the above robot kinematic equations, the virtual robot motion was set to manual mode and the robot end-effector was captured to six sampling points on the trajectory path to obtain six sets of joint axis angles.

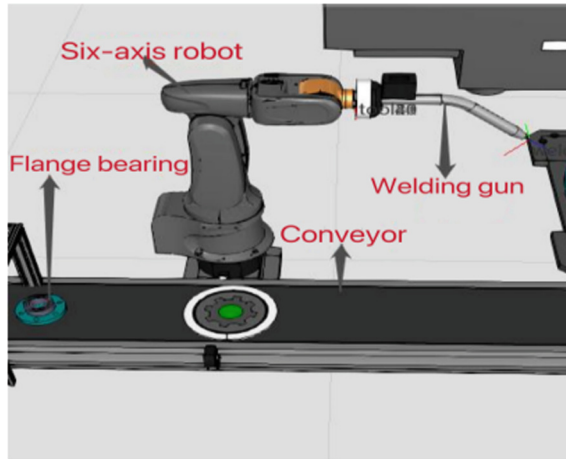


Fig. 6. Overall layout of welding

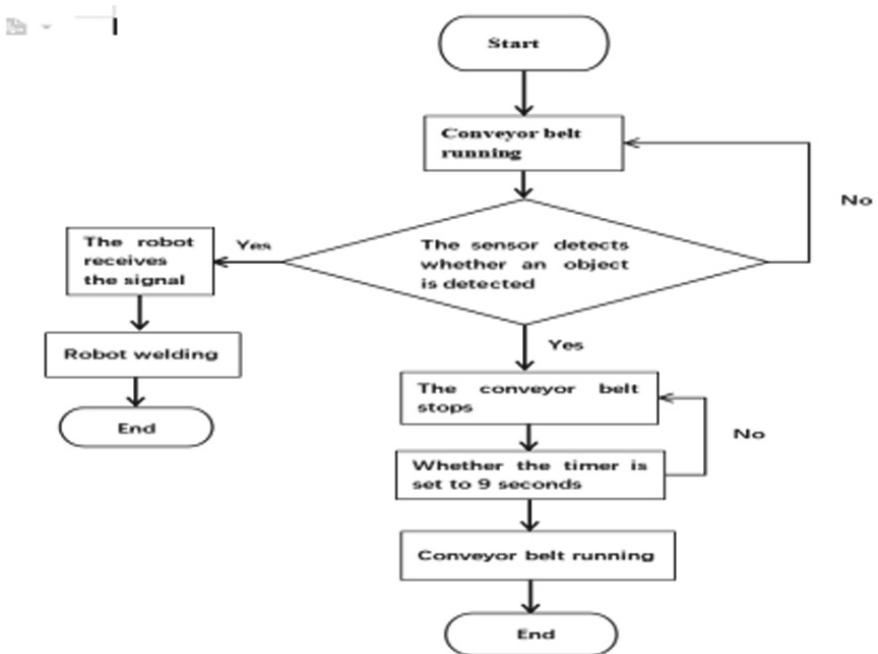


Fig. 7. PLC program flow chart

The data were brought into the above positive kinematic mathematical model, and the equation solving procedure was written by C language to obtain the robot end position parameters, and the obtained theoretical analysis results were compared with the simulation data as shown in Table 2.

Default variable table

	Name	Data type	Address	Keep	H...	H...	H...	Monitor
1	J1	Real	%Q01	<input type="checkbox"/>	<input checked="" type="checkbox"/>	<input checked="" type="checkbox"/>	<input checked="" type="checkbox"/>	
2	J1.1	Real	%Q011	<input type="checkbox"/>	<input checked="" type="checkbox"/>	<input checked="" type="checkbox"/>	<input checked="" type="checkbox"/>	
3	Sensor	Bool	%I0.0	<input type="checkbox"/>	<input checked="" type="checkbox"/>	<input checked="" type="checkbox"/>	<input checked="" type="checkbox"/>	
4	Electric motors	Bool	%Q0.0	<input type="checkbox"/>	<input checked="" type="checkbox"/>	<input checked="" type="checkbox"/>	<input checked="" type="checkbox"/>	
5	J2	Real	%Q02	<input type="checkbox"/>	<input checked="" type="checkbox"/>	<input checked="" type="checkbox"/>	<input checked="" type="checkbox"/>	
6	J2.2	Real	%Q022	<input type="checkbox"/>	<input checked="" type="checkbox"/>	<input checked="" type="checkbox"/>	<input checked="" type="checkbox"/>	
7	J3	Real	%Q03	<input type="checkbox"/>	<input checked="" type="checkbox"/>	<input checked="" type="checkbox"/>	<input checked="" type="checkbox"/>	
8	J3.3	Real	%Q033	<input type="checkbox"/>	<input checked="" type="checkbox"/>	<input checked="" type="checkbox"/>	<input checked="" type="checkbox"/>	
9	J4	Real	%Q04	<input type="checkbox"/>	<input checked="" type="checkbox"/>	<input checked="" type="checkbox"/>	<input checked="" type="checkbox"/>	
10	J4.4	Real	%Q044	<input type="checkbox"/>	<input checked="" type="checkbox"/>	<input checked="" type="checkbox"/>	<input checked="" type="checkbox"/>	
11	J5	Real	%Q05	<input type="checkbox"/>	<input checked="" type="checkbox"/>	<input checked="" type="checkbox"/>	<input checked="" type="checkbox"/>	
12	J5.5	Real	%Q055	<input type="checkbox"/>	<input checked="" type="checkbox"/>	<input checked="" type="checkbox"/>	<input checked="" type="checkbox"/>	
13	J6	Real	%Q06	<input type="checkbox"/>	<input checked="" type="checkbox"/>	<input checked="" type="checkbox"/>	<input checked="" type="checkbox"/>	
14	J6.6	Real	%Q066	<input type="checkbox"/>	<input checked="" type="checkbox"/>	<input checked="" type="checkbox"/>	<input checked="" type="checkbox"/>	
15				<input type="checkbox"/>	<input checked="" type="checkbox"/>	<input checked="" type="checkbox"/>	<input checked="" type="checkbox"/>	

Fig. 8. PLC Variable Table

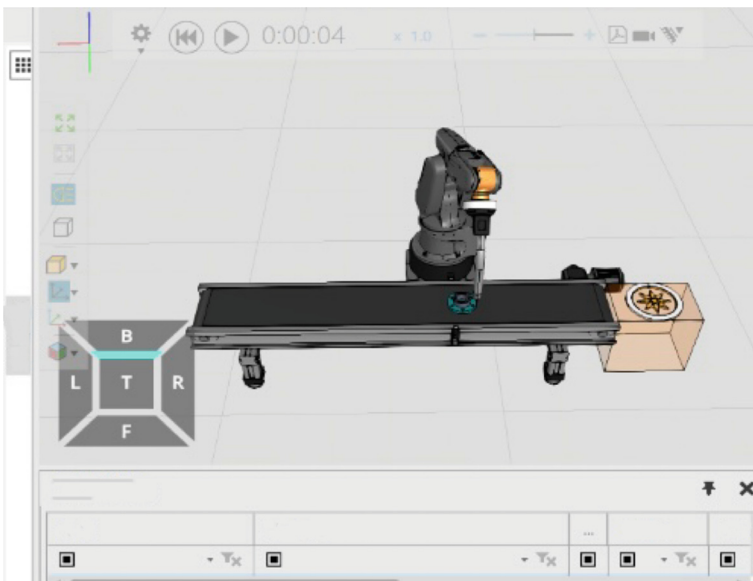


Fig. 9. Virtual Simulation

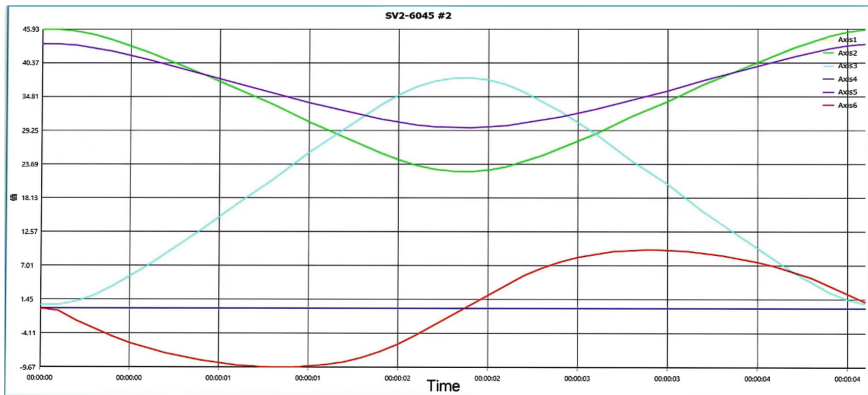
According to the comparison results in Table 3, it can be seen that the results obtained from the theoretical calculation and simulation are consistent, so the kinematic equations established by the D-H parameter method are correct and the robot simulation model is accurate.

Table 2. Comparison of formula calculation and simulation results

Joint angle	Access	x/mm	y/mm	z/mm
φ_1	Theory	365.002	0	224.479
	Simulation	365.002	0	224.479
φ_2	Theory	345.808	-40.583	224.479
	Simulation	345.808	-40.583	224.479
φ_3	Theory	297.262	-50.239	224.479
	Simulation	297.262	-50.239	224.479
φ_4	Theory	262.263	-15.24	224.479
	Simulation	262.263	-15.24	224.479
φ_5	Theory	271.919	33.306	224.479
	Simulation	271.919	33.306	224.479
φ_6	Theory	317.648	52.247	224.479
	Simulation	317.648	52.247	224.479

4.2 Inverse Kinematic Simulation Analysis

To solve the robot inverse kinematics, the robot end poses are input and the rotation angle variables of the robot rotation joints are solved inverse. The (365.002, 0, 224.479) point on the path is taken as the starting point, and the circular path is divided into 65 equal parts to obtain 65 sampling points. Using the SimReal statistics function, the angular displacement curves of each joint axis of the robot were obtained by simulation as shown in Fig. 10, and the trajectory was displayed using the trajectory tracking and observed whether it coincided with the circular path as shown in Fig. 11.

**Fig. 10.** Angular displacement curve of joint axis

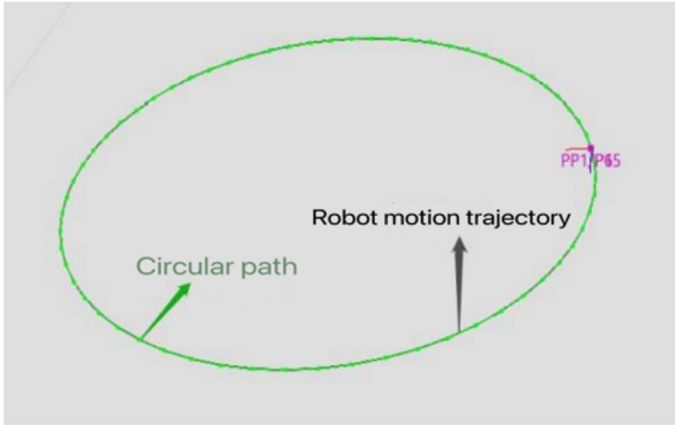


Fig. 11. Circular path and robot trajectory

The robot kinematic inverse solution program was written to calculate its rotation angle for each joint axis under the end trajectory (only the optimal solution of the inverse kinematic equation was calculated). The inverse kinematic solution is compared with the simulation results for the six sampling points in the above section, as shown in Table 3. In turn, the average error data is obtained as shown in Table 4.

Table 3. Comparison of formula calculation and simulation results

φ_i	Access	θ_1	θ_2	θ_3	θ_4	θ_5	θ_6
φ_1	Theory	0	45.923961	0.559810	0	43.516198	0
	Simulation	0	45.923950	0.559845	0	43.516174	0
φ_2	Theory	-6.693446	41.827972	7.478312	0	40.693715	-6.693447
	Simulation	-6.693450	41.827880	7.478485	0	40.693634	-6.693451
φ_3	Theory	-9.592673	31.326847	24.526701	0	34.146453	-9.592673
	Simulation	-9.592743	31.326874	24.526703	0	34.146423	-9.592743
φ_4	Theory	-3.325695	23.015045	37.107795	0	29.877160	-3.325695
	Simulation	-3.325684	23.014984	37.107941	0	29.877075	-3.325684
φ_5	Theory	6.983091	25.418495	33.568216	0	31.013291	6.983091
	Simulation	6.983032	25.418488	33.568269	0	31.013245	6.983032
φ_6	Theory	9.340424	35.810638	17.383228	0	36.806164	9.340424
	Simulation	9.340454	35.810638	17.383300	0	36.806091	9.340454

The robot joint axis angular displacement trajectory curve shown in Fig. 10 runs smoothly without protrusion, indicating smooth robot operation. The circle path shown by Fig. 11 coincides with the robot trajectory. From the error analysis, it can be seen

Table 4. Error data

Error	θ_1	θ_2	θ_3	θ_4	θ_5	θ_6
Average error	0.000029	0.000033	0.000080	0	0.000060	0.000029

that the theoretical value of the robot inverse kinematic model is highly similar to the simulation data, which shows that the robot inverse kinematic model is accurate.

5 Conclusion

Virtual simulation technology has become an important part of modern manufacturing industry. In this paper, the SV2-6045 six-axis industrial robot is used as a research object to apply virtual simulation technology to the kinematic modeling and development process of the robot. By establishing the mathematical models of the forward and inverse kinematics of the robot, as well as the SimReal-based virtual model and PLC virtual debugging, the kinematic theoretical model is quickly and efficiently simulated and verified, and the rationality and accuracy of the research content of this paper is proved by the error analysis of the theoretical and simulation results.

Acknowledgements. This work is supported by Shandong SME Innovation Capacity Enhancement Project (2022TSGC1379). Innovation and Entrepreneurship Training Program for University Students (National level: 202211510025).

References

1. Jianbao, H., Cao, Y., Tan, H., Lin, Z.: Application of virtual simulation technology in the design of robot production line [J]. *Guangdong Sci. Technol.* (02) (2021)
2. Yikun, Z.: Kinematic analysis of six-axis industrial robots[J]. *Sci. Technol. Innov. Appl.* **27**, 73–75 (2021)
3. Jiang, M.: Analysis of the application of industrial robotics in the field of intelligent manufacturing [J]. *Mod. Ind. Econ. Informatization* (09) (2022)
4. Zhang, L., Hu, Q., Luo, K., Peng, J.: Research on debugging method based on robot kinematics [J]. *Autom. Appl.* (05) (2017)
5. Zhao, L.: Research on the construction of digital twin model and virtual commissioning of logistics equipment [D]. *Gen. Res. Inst. Mach.* (2022)
6. Hui, L.: The application of immersive virtual simulation technology (IVR) in English audiovisual [J]. *Adv. Comput., Signals Syst.* **6**(4) (2022)
7. Qian, X., Meng, D.: Robot kinematics analysis and simulation research [J]. *Henan Sci. Technol.* (07) (2020)
8. Zhang, X.: Kinematics modeling and analysis of industrial robot [J]. *Agricultural Engineering and Equipment* (02) (2020)
9. Peng, G., Hongbo, D., Ma, B.: Comparison of robot kinematics modeling with two DH models [J]. *Mech. Res. Appl.* (06) (2019)



FES Cycling System in Rehabilitation Engineering: A Survey

Wenyuan Wang¹, Yan Yan², Min Liu³(✉), Mingxu Sun^{1,4,5}, Tao Shen^{1,6},
Yiming Zhu¹, and Fangqiang Guo¹

¹ University of Jinan, Jinan 250022, China

² Shandong Guohe Industrial Technology Research Institute Co., Ltd, Jinan 250000, China

³ Shandong Provincial Third Hospital, Jinan 250132, China
1770426982@qq.com

⁴ Shandong BetR Medical Ltd, Jinan 250101, China

⁵ Centre for Health Sciences Research, University of Salford, Salford, UK

⁶ HIT Robot Group Co. Ltd, Harbin 150060, China

Abstract. Functional electrical stimulation (FES) is widely used in rehabilitation therapy to restore motor function in patients with paralysis. FES cycling systems are used as one of the important applications of FES in rehabilitation engineering, and has been proven to be a safe and effective rehabilitation system. These systems regulate the current and pulse width of the FES according to the feedback signal. This paper surveys the current state of research on FES cycling systems. It covers FES control, signal feedback, and challenges and prospects of existing FES cycling systems. Particularly, the combination of FES with electromyography (EMG) and different sensors.

Keywords: Functional electrical stimulation · FES cycling system · Feedback signal; EMG · Sensors

1 Introduction

According to the World Health Organization, 16 million new stroke patients are diagnosed worldwide every year. It is estimated that by 2030, 18.4 million new stroke victims will be diagnosed each year [1]. Stroke is an acute cerebrovascular disease. The disease causes symptoms such as paralysis, sensory impairment, aphasia and memory loss. Moreover, the mortality and disability rates of stroke patients are relatively high [2]. Nowadays, with the improvement of medical level, the fatality rate of stroke patients has been greatly reduced, but there will still be many patients with sequelae such as varying degrees of paralysis. According to statistics, about 20% of patients have varying degrees of motor impairment after stroke [3–5].

The primary rehabilitation goal for patients with these movement disorders is to regain walking ability. For the patient, walking has a therapeutic effect by lengthening the joints and improving blood flow. However, because of the inherent instability of the body's posture during walking. Experts and scholars have proposed a multitude

of approaches to combat this challenge including the use of orthopedic devices [6], mechanical exoskeletons [7], and the FES cycling system [8–10] that can regulate muscle contraction. The patient is performing a passive form of rehabilitation with orthoses and mechanical exoskeletons; the paralyzed muscles do not achieve active contraction and the treatment is slow. In addition, the relatively large size of these devices limits the environment in which they can be used. With these factors in mind, the FES cycling system may be the best way to treat lower extremity movement disorders.

FES has been a research hotspot in the field of rehabilitation medicine since the 70s. After more than half a century, the development of FES technology from wired to wireless transmission of signals, from a single channel to multi-channel stimulation, its technology has become mature [11]. Researches have shown that application of FES is effective in improving muscle strength and motor control, decreasing spasticity, and improving range of motion [12, 13]. FES cycling system is an applied research of FES technology. FES combined with cycling has been studied for many years [14–16]. Compared with the standing and walking system, the FES cycling training system has a simple structure and is easy to use, which has a significant effect on improving the condition of patients with lower limb motor dysfunction and is beneficial to the physical and mental health of patients [17].

As the muscle response to FES is non-linear and time-varying, and varies with the degree of muscle fatigue, the FES cycling system uses EMG or sensors to supply feedback information about muscle motion or athletic biomechanics. By analyzing the feedback information, the current and pulse width magnitude of the FES required for rehabilitation training can be obtained, so that the selection of the type of signal feedback in the system has become essential. Currently, the four common ways to obtain feedback signals in FES cycling systems are: encoders, inertial sensors, electromyography and torque sensors. Next, training systems using different types of signal feedback methods will be analyzed and their advantages and disadvantages are summarized.

2 FES Cycling System Using Different Signal Feedback Types

2.1 Encoders

The stimulation in most FES cycling systems relies on a pre-set pattern where the encoder attached to the pedal crank acts as a sensor to detect the angular position [18–23].

The shaft encoder is connected by a chain and sprocket, which has the same dimensions as the crank, and the measured crank angle is differentiated to obtain the crank speed [24]. The shaft encoder is interfaced to the stimulus control program, which runs on a laptop with MATLAB/Simulink and a real-time toolbox to control the multichannel stimulator or, alternatively, can run within the multichannel stimulator itself. Surface electrodes are connected to the corresponding the hamstrings and right and left quadriceps. The crank angle measurement is used to open and close each muscle group during each cycle according to a pre-specified pattern. To simplify the control structure, T. Schauer et al. proposed to apply one pulse width variable to all muscles based on the above system, simplifying the control structure to a system with pulse width input and crank speed output. The patient can adjust the stimulation intensity autonomously via a throttle on the handle [25]. The simplified system is shown in Fig. 1.

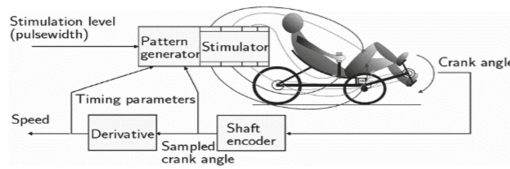


Fig. 1. Open loop system

The encoders used in the FES cycling system can perform the work of signal acquisition and transmission well by virtue of their small size, high resolution, low latency, and no contact and no wear, but they put forward high protection requirements for use in outdoor environments and can produce errors due to mechanical gaps, which can have an impact on the rehabilitation training of the whole system.

2.2 Inertial Sensors

In most cases, stimulation in the FES bicycle system relies on alternating stimuli sent to the popliteus, quadriceps and gluteus muscles based on the estimated crank angle of the encoder. It is important to notice that the stimulation pattern must be adjusted manually for each patient individually, depending on the sitting position and anthropometry of each patient, the number of muscles stimulated and the shape of the bike geometry [26]. Another aspect, the FES control for cycling rehabilitation training is dependent on the cycling system and it would not be convenient to use a commercially available bicycle with FES control if mechanical modifications to the bicycle with encoders were required in order to incorporate the FES control system.

IMUs are incorporated with magnetometers accelerometers and gyroscopes to compose a complete inertial sensor. They integrate multiple pieces of information by using an optimal sensor fusion algorithm, which allows estimating the orientation of body parts. Inertial sensors have been used in recent research for systems that control the angular position of joints via FES [27–30]. In addition to this, inertial sensors are used to measure the crank speed in FES cycling systems [31, 32].

Depending on the placement of the inertial measurement unit in the FES cycling system, two stimulation modes correspond to each: joint angle-based and crank angle-based stimulation modes.

Stimulation patterns based on crank angle

The inertial sensor is anchored in the center of the wheelchair-style cycling crank, and its measured acceleration and angular velocity signals are transmitted to a laptop computer via a transmission protocol such as Bluetooth.

The timing of the stimulation is decided by the crankshaft rotation angle calculated based on the measured acceleration of gravity [33]. The crank angle θ is calculated from the x and y axis acceleration components of the sensor. Besides the crank angle that can be solved using Eq. (1) below, the crank angle can also be expressed in the form of sine and cosine [34–37].

$$\theta = \tan^{-1} \frac{a_x}{a_y} \quad (1)$$

Although it is possible to calculate the cycling speed using the angular velocity signal measured by the gyroscope mounted in the IMU at the center of the crankshaft, the effects of backlash (vibration) can have an impact on the accuracy of the momentary cycling speed. To reduce the error, the researchers chose to improve the system using 2 IMUs, which are mounted on the horizontal frame near the crank and at the center of the crankshaft, respectively (See Fig. 2) [38]. First, the acceleration signal was measured using the IMU mounted on the horizontal frame near the crank, and the acceleration signal was integrated to obtain the riding speed, but there was a large integration error. At this time, the angular velocity signal measured by another IMU mounted at the center of the crankshaft is compensated for the integration error by Kalman filtering. When the cycling speed reaches the target value, the stimulation intensity is controlled by closed-loop control.

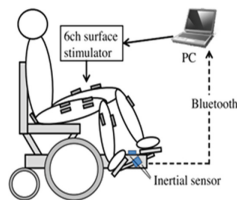


Fig. 2. FES control system for cycling wheelchair

The system of determining stimulus timing based on crank angle also has issues that need to be addressed. Because of the inconsistency in all aspects of data for each patient, each crank value associated with the patient needs to be manually adjusted when adjusting the crank angle [38].

Stimulation patterns based on joint angles.

Through using a joint angle-based stimulation pattern rather than a crank angle-based approach to FES riding, this new method provides a plug-and-play system that does not require initial calibration or manual adjustment [26].

The joint angles are first estimated and transformed for geometric parameterization independence before the stimulation pattern is determined. Multiple IMUs are placed on the patient's lower limb and acceleration and gyroscope data are transmitted wirelessly to a receiver connected to the control unit (See Fig. 3). The laptop computer performs joint angle estimation and generates stimulation timing based on the pattern. The required pulse width and current is transferred to the functional electrical stimulator and applied to the transcutaneous adhesive electrodes placed on the quadriceps and hamstrings.

Cycling simulation of the joint angle-based approach using different geometric parametric corrections (See Fig. 4). After some initial cycles, it is ensured that the joint angle estimation is working correctly before increasing the stimulation current. Increasing the stimulation current results in an acceleration of the cycling motion, which means that FES cycling using a simple joint angle driven stimulation pattern is possible without the need for manual adjustment [39].

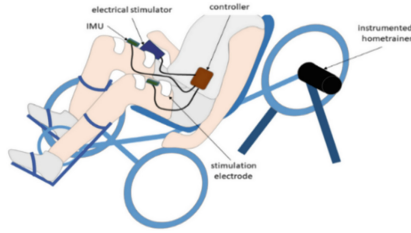


Fig. 3. Schematic diagram of FES cycling system based on joint angle

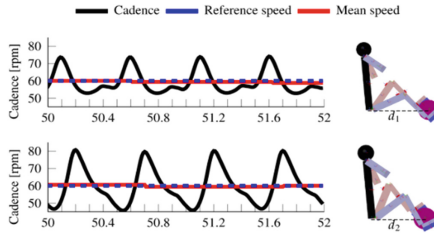


Fig. 4. Cycling simulation

Due to the independence of the bicycle and FES equipment, each patient can use the same settings and stimulation patterns in different cycling devices [26]. But further work is needed to validate this approach compared to the crank angle-based stimulus model.

2.3 Electromyography (EMG)

The use of electromyography (EMG) for FES applications is not a new approach in addition to the several sensors mentioned above. However, in contrast to the FES cycling system, which consists of encoders or inertial sensors, it is not suitable for all situations. For example, situations where the patient completely loses the ability to control muscles autonomously to produce movement. The range of FES cycling rehabilitation training in combination with EMG is limited [40].

In general, there are three conditions in which electromyography combined with FES cycling is more appropriate:

- (1) Patients with partial paralysis can weakly and actively drive a part of the muscle to produce a weak EMG [41].
- (2) Use of EMG signals from the healthy limb side for hemiplegic patients with symmetrical muscles on the opposite side of the paralysis controlled by FES [42].
- (3) To stimulate the paralyzed muscles on the ipsilateral side of the limb using the EMG of certain healthy muscles of the patient [43, 44]. For instance, modulating triceps stimulation based on the EMG of the biceps muscle [45].

When the FES cycling system is driven by real-time EMG, changes in hamstring strength are measured during training using two specialized metrics: average area under

torque (AUT), which is used to measure stroke performance in paralyzed limbs, and maximum EMG amplitude, used in further studies of muscle strength recovery in the paralyzed limb [46].

Before training, muscle electrodes and stimulation electrode pads are adhered to the corresponding muscles, and each muscle is exerted in the corresponding range. During training, the system generates electrical stimuli of different intensities based on the real-time EMG and runs at different cycling speeds. The EMG-assisted control-based system, EMG acquisition and stimulation output are synchronized in real time, and its stimulation intensity is adaptively adjusted and variable in real time. However, the real-time synchronization of EMG acquisition and stimulation output of this system is not perfect, and further research is still needed to solve it.

In addition to the real-time synchronization issues that need to be addressed above, when analyzing the collected EMG signals, it is important to note that they contain a variety of interfering signals [47]. Table 1 summarizes several common interference signal categories and suppression methods in EMG signals. Among them, the interfering signals, mainly stimulation artifacts, increase the difficulty of processing EMG signals due to their higher frequency and amplitude, which require the removal of artifacts and the use of pure EMG signals to detect the patient's intention during cycling [28].

Table 1. Interference signals in EMG acquisition and methods of suppression

Interference signal category	Common methods of inhibition
Radio frequency	Anti-radio networks, high frequency suppressors
Industrial frequency	Wave trap
Environmental noise	Noise reduction circuits, decoupling circuits, isolation methods
Bioelectricity	Filter networks, wavelet filtering
Artifacts	Blanking method, blocking method, non-linear negative feedback method

2.4 Torque Sensors

As a kind of kinetic sensor, the torque sensor can not only work with EMG to form a multi-sensor embedded FES bicycle system [48], but also be applied as a single sensor in the FES cycling system to collect and transmit the corresponding signal in real time [49], causing the system to produce stimulating actions.

When the FES cycling system is equipped with an auxiliary motor, the motor can be directly connected to the torque sensor mounted on the crank, which can assist in pedaling or fully drive the pedals and the patient's legs. As the pedals rotate at a constant speed, resistance torque is generated at the crank due to factors such as patient muscle fatigue and friction loss. The torque sensor picks up real-time torque values and transmits them to the controller, which achieves precise control of the motor to provide the right

torque to conquer resistance and ensure effective cycling rehabilitation training for the patient.

3 Discussion and Conclusion

The FES cycling system, as one of the applications of FES technology, is a system in which the feedback signals collected by the sensors or EMG achieve control of a functional electrical stimulator, which in turn improves the motor function of the patient and is more effective and has a wider range of applications than single-function electrical stimulation.

The method of using an encoder as a sensor to detect angular position, although used in most FES cycling systems, requires not only manual adjustment of the stimulation pattern according to the sitting position of each patient, the number of muscles being stimulated, and other factors, but also the reduction of errors caused by the mechanical gap of the encoder.

By mounting the inertial sensor on the crank, a complete FES cycling system can be quickly built and put into operation on a different bike, providing equipment flexibility. However, when dealing with different patients, the relevant crank values need to be manually adjusted. To solve this problem, it is proposed to place the inertial measurement unit in the patient's lower extremity without manual adjustment and determine the stimulation pattern based on the joint angle. In follow-up studies, muscle force response compensation should be improved to make the cycling experience smoother relative to the cadence trajectory.

For patients who are not completely incapacitated, the FES cycling system combined with EMG is a good option. Based on the patient's voluntary EMG signal, FES is autonomously generated to the target muscle to control the muscle to complete the pedaling action. In refining the real-time synchronization of EMG acquisition and stimulation output, attention also needs to be paid to the removal of artifacts when collecting EMG signals. Although lower limb EMG is being used more frequently in FES cycling systems, recent investigations have mainly used inertial sensors. As the muscle response induced by FES is non-linear and time-varying, non-linear control using inertial sensors is used to overcome the non-linear and time-varying effects of FES.

References

1. Mackay, J., Mensah, G.A., Mendis, S., et al.: The atlas of heart disease and stroke[J]. Switz.: World Health Organ. **19**(6), 505–505 (2005)
2. Suri, H., Dougherty, C.: Presentation and management of headache in pituitary apoplexy[J]. *Curr. Pain Headache Rep.* **23**, 1–4 (2019)
3. Winstein, C.J., Stein, J., Arena, R., et al.: Guidelines for adult stroke rehabilitation and recovery: a guideline for healthcare professionals from the american heart association/american stroke association[J]. *Stroke; J. Cereb. Circ.* **42**(7), e98 (2016)
4. Krishnamurthi, R.V., Moran, A.E., Feigin, V.L., et al.: Stroke prevalence, mortality and disability-adjusted life years in adults aged 20–64 years in 1990–2013: data from the global burden of disease 2013 study[J]. *Neuroepidemiology* **45**(3), 190–202 (2015)

5. Longde, W., Jianmin, L., Yi, Y., et al.: Summary of China stroke prevention and treatment report 2017[J]. *Chin. J. Cerebrovasc. Dis.* **15**(11), 611–616 (2018)
6. Jaeger, R.J., Yarkony, G.M., Roth, E.J.: Rehabilitation technology for standing and walking after spinal cord injury[J]. *Am. J. Phys. Med. Rehabil.* **68**(3), 128–133 (1989)
7. Ren, Y., Zhang, D.: Design and realization of knee rehabilitation device with functional electrical stimulation and mechanical exoskeleton fusion[J]. *Chin. J. Rehabil. Med.* **31**(03), 330–332 (2016)
8. MacIntosh, B.J., Baker, N., Mraz, R.: Improving functional magnetic resonance imaging motor studies through simultaneous electromyography recordings. *Hum. Brain Mapp.* **28**, 835–845 (2007)
9. Ganesh, G., Franklin, D.W., Gassert, R., Imamizu, H.: Accurate real-time feedback of surface EMG during fMRI. *Neurophysiol.* **97**, 912–920 (2007)
10. Moreno JC, Brunetti FJ, Pons JL (2004) An autonomous control and monitoring system for a lower limb orthosis: the gait project case. Conference Proceedings-26th Annual International Conference of the IEEE Engineering in Medicine and Biology Society, EMBC 2004, vol. 24. San Francisco, CA, United States, pp. 2125–2128
11. Popović, D.B.: Advances in functional electrical stimulation (FES)[J]. *J. Electromyogr. Kinesiol.* **24**(6), 795–802 (2014)
12. Daly, J.J., et al.: Recovery of coordinated gait: randomized controlled stroke trial of functional electrical stimulation (fes) versus no fes, with weight-supported treadmill and over-ground training. *Neurorehabil. Neural Repair.* **25**(7), 588–596 (2011)
13. Hara, Y.: Neurorehabilitation with new functional electrical stimulation for hemiparetic upper extremity in stroke patients. *J. Nippon Med. Sch.* **75**(1), 4–14 (2008)
14. Frotzler, A., Coupaud, S., Perret, C., Kakebeeke, T.H., Hunt, K.J., Donaldson, N.D.N., Eser, P.: High-volume fes-cycling partially reverses bone loss in people with chronic spinal cord injury. *Bone* **43**(1), 169–176 (2008)
15. Donaldson, N., Perkins, T., Fitzwater, R., Wood, D., Middleton, F.: Fes cycling may promote recovery of leg function after incomplete spinal cord injury. *Spinal Cord* **38**(11), 680 (2000)
16. Krause, P., Szecsi, J., Straube, A.: Fes cycling reduces spastic muscle tone in a patient with multiple sclerosis. *NeuroRehabilitation* **22**(4), 335–337 (2007)
17. Mulder, A.J., Hermens, H.J., Janssen, F., Zilvold, G.: A low-cost FES exercise bicycle for training paraplegics at home. *J. Med. Eng. Technol.* **13**, 90–92 (1989)
18. Kawai, H., Bellman, M.J., Downey, R.J., Dixon, W.E.: Closed-loop position and cadence tracking control for FES-cycling exploiting pedal force direction with antagonistic biarticular muscles. *IEEE Trans. Control Syst. Technol.* **27**, 730–742 (2017)
19. Rouse, C.A., Cousin, C.A., Allen, B.C., Dixon, W.E.: Shared control for switched motorized FES-cycling on a split-crank cycle accounting for muscle control input saturation. *Automatica* **123**, 109294 (2021)
20. Duenas, V.H., Cousin, C.A., Ghanbari, V., Fox, E.J., Dixon, W.E.: Torque and cadence tracking in functional electrical stimulation induced cycling using passivity-based spatial repetitive learning control. *Automatica* **115**, 108852 (2020)
21. Cousin, C.A., et al.: Closed-loop cadence and instantaneous power control on a motorized functional electrical stimulation cycle. *IEEE Trans. Control Syst. Technol.* **28**, 2276–2291 (2020)
22. Cousin, C.A., Duenas, V.H., Rouse, C.A., Dixon, W.E.: Admittance control of motorized functional electrical stimulation cycle. *IFAC Pap.* **51**, 272–277 (2019)
23. Allen, B.C., Stubbs, K.J., Dixon, W.E.: Position and cadence tracking of a motorized FES-cycle with an unknown time-varying input delay using saturated FES control. *Automatica* **139**, 110176 (2022)

24. Perkins, T.A., de Donaldson, N.N., Hatcher, N.A.C., Swain, I.D., Wood, D.E.: Control of leg-powered paraplegic cycling using stimulation of the lumbo-sacral anterior spinal nerve roots [J]. *IEEE Trans. Neural Syst. Rehabil. Eng.: Publ. IEEE Eng. Med. Biol. Soc.* **10**(3) (2002)
25. Hunt, K.J., Schauer, T., Negård, N.O., et al.: A pilot study of lower-limb FES cycling in paraplegia[C]. *Proceedings 7th Annals Conference International Functional Electrical Stimulation Society*. Ljubljana, Slovenia (2002)
26. Sijobert, B., Le Guillou, R., Fattal, C., et al.: FES-induced cycling in complete SCI: a simpler control method based on inertial sensors[J]. *Sensors* **19**(19), 4268 (2019)
27. Anaya-Reyes, F., Narayan, A., Aguirre-Ollinger, G., et al.: An omnidirectional assistive platform integrated with functional electrical stimulation for gait rehabilitation: a case study[J]. *IEEE Trans. Neural Syst. Rehabil. Eng. Rehabil. Eng.* **28**(3), 710–719 (2020)
28. Sanches, M.A.A., Gaino, R., Kozan, R.F., et al.: Digital controller design considering hardware constraints: application in a paraplegic patient[J]. *Rev. Bras. Engenharia Bioméd.* **30**, 232–241 (2014)
29. Valtin, M., Kociemba, K., Behling, C., Kuberski, B., Becker, S., Schauer, T.: RehaMovePro: a versatile mobile stimulation system for transcutaneous FES applications. *Eur. J. Transl. Myol.* **26**, 6076 (2016)
30. Sijobert, B., Azevedo, C., Pontier, J., et al.: A sensor-based multichannel FES system to control knee joint and reduce stance phase asymmetry in post-stroke gait[J]. *Sensors* **21**(6), 2134 (2021)
31. Chaikho, L., Clark, E., Raison, M.: Transcutaneous functional electrical stimulation controlled by a system of sensors for the lower limbs: a systematic review[J]. *Sensors* **22**(24), 9812 (2022)
32. Wiesener, C., Schauer, T.: The Cyathlon RehaBike: inertial-sensor-driven functional electrical stimulation cycling by team Hasomed. *IEEE Robot. Autom. Mag.* **24**, 49–57 (2017)
33. Watanabe, T., Murakami, T., Handa, Y.: Preliminary tests of a prototype FES control system for cycling wheelchair rehabilitation. 2013 IEEE 13th International Conference on Rehabilitation Robotics (ICORR). IEEE, (2013)
34. Wannawas, N., Faisal, A.A.: Towards AI-controlled FES-restoration of movements: learning cycling stimulation pattern with reinforcement learning[J]. *arXiv preprint arXiv:2303.09986* (2023)
35. Duenas, V.H., Cousin, C.A., Parikh, A., et al.: Motorized and functional electrical stimulation induced cycling via switched repetitive learning control[J]. *IEEE Trans. Control Syst. Technol.* **27**(4), 1468–1479 (2018)
36. Reichenfeller, W., Gföhler, M., Angeli, T.: Design of a test and training tricycle for subjects with paraplegia[J]. *Technol. Disabil. Disabil.* **17**(2), 93–101 (2005)
37. Ceroni, I.: Cycling induced by functional electrical stimulation: a case study inspired by the experience of CYBATHLON 2020[J] (2021)
38. Watanabe, T., Tadano, T.: Experimental tests of a prototype of IMU-based closed-loop fuzzy control system for mobile FES cycling with pedaling wheelchair[J]. *IEICE Trans. Inf. Syst.* **101**(7), 1906–1914 (2018)
39. Ruppini, S., Wiesener, C., Schauer, T.: Inertial sensor-based control of functional electrical stimulation in paraplegic cycling[J]. *Eur. J. Transl. Myology.* **26**(2) (2016)
40. Zhang, D., Guan, T.H., Widjaja, F., et al.: Functional electrical stimulation in rehabilitation engineering: a survey[C]. *Proceedings of the 1st International Convention on Rehabilitation Engineering and Assistive Technology: in Conjunction with 1st Tan Tock Seng Hospital Neurorehabilitation Meeting*, pp. 221–226
41. Futami, R., et al.: Application of local EMG-driven FES to incompletely paralyzed lower extremities. *Proceedings of the 10th Annual Conference of the International FES Society* (2005)

42. Yu, W., et al.: An adaptive FES switching system for hemiplegics. *Int. J. Smart Eng. Syst. Des.* **5**(4), 299–311 (2003)
43. Peckham, P.H., Marsolais, E.B., Mortimer, J.T.: Restoration of key grip and release in the C6 tetraplegic patient through functional electrical stimulation. *J. Hand Surg.* **5**(5), 462–469 (1980)
44. Saxena, S., Nikolic, S., Popovic, D.: An EMG-controlled grasping system for tetraplegics. *J. Rehabil. Res. Dev.* **32**, 17 (1995)
45. Giuffrida, J.P., Crago, P.E.: Reciprocal EMG control of elbow extension by FES. *IEEE Trans. Neural Syst. Rehabil. Eng.* **9**(4), 338–345 (2001)
46. Fang, Y., Chen, S., Wang, X., et al.: Real-time electromyography-driven functional electrical stimulation cycling system for chronic stroke rehabilitation[C]. 2018 40th Annual International Conference of the IEEE Engineering in Medicine and Biology Society (EMBC). IEEE, pp. 2515–2518 (2018)
47. Xie, C.: Design and Experimental Study of a Lower Limb Wearable Myoelectric Control Rehabilitation System for Stroke Patients [D]. Southeast University (2021)
48. Wang, X., Leung, K.W.C., Fang, Y., et al.: Design of functional electrical stimulation cycling system for lower-limb rehabilitation of stroke patients[C]. 2018 40th Annual International Conference of the IEEE Engineering in Medicine and Biology Society (EMBC). IEEE, pp. 2337–2340 (2018)
49. McRae, C.G.A., Johnston, T.E., Lauer, R.T., et al.: Cycling for children with neuromuscular impairments using electrical stimulation—development of tricycle-based systems[J]. *Med. Eng. Phys.* **31**(6), 650–659 (2009)



Cooling Performance Elevation of a 3T Animal Gradient Assembly with Hollow Pipe Axial Gradient Coil

Zhaokun Lu¹ and Yaohui Wang²(✉)

¹ University of Jinan, Jinan 250022, China

² Chinese Academy of Sciences, Beijing 100190, China
yhw@mail.iee.ac.cn

Abstract. The cooling performance of gradient coils is an important indicator of magnetic resonance imaging (MRI), which is closely related to the image resolution of MRI. This article uses COMSOL Multiphysics finite element software to conduct heat transfer simulation analysis on magnetic resonance imaging gradient coils, providing technical support for the design and finite element simulation of efficient heat dissipation gradient coils. Firstly, point data for the coil winding is obtained through the target field-based method. Then, a three-dimensional model is created using Solidworks. Finally, the three-dimensional model of the gradient coil is imported into COMSOL for multi-physical simulation coupling simulation and analysis, including magnetic field and solid heat transfer. In this paper, the temperature distribution of two groups of gradient coils with different cooling structures is simulated when the X coil current, Y coil current and Z coil current are separately supplied. Among them, one group is a gradient coil using a hollow water-cooled plastic pipe cooling structure, and the other group is a gradient coil using a hollow wire water-cooled structure. Comparing the heat transfer simulation results of two sets of gradient coils, it is found that gradient coils with hollow wire water-cooled structures have better heat dissipation performance, which is of great reference significance for the cooling structure design of actual gradient coils.

Keywords: Gradient coils · Finite element · Hollow wire

1 Introduction

In biomedical research and clinical experiments, small animals are often the most preferred experimental subjects. Magnetic resonance imaging (MRI) technology plays a crucial role in clinical experiments and biological research on small animals. People sometimes use small animals as experimental subjects to verify the image quality of MRI [1].

MRI was developed in the 1970s and possesses characteristics such as non-invasiveness, non-destructiveness, high soft tissue contrast, multiple imaging parameters, and rich image information. MRI images are created by encoding spatial information of

an object through the application of linear gradient fields and the frequency and phase encoding of acquired nuclear magnetic resonance signals [2]. Gradient coils form a major component of an MRI scanner and are responsible for providing spatial encoding of the magnetic resonance signals. The function of gradient coils is to induce linearly varying gradient magnetic fields in three orthogonal spatial directions, thereby identifying the source of the magnetic resonance signals and enabling spatial localization and output of structural information. The image resolution of MRI is directly related to the scan time and the strength and switching rate of the gradient magnetic field. Achieving ultra-high image resolution and ultra-fast imaging speed is an important development direction for MRI [3]. Currently, higher demands are placed on image resolution and imaging time in the diagnosis of complex diseases, detection of small lesions, brain functional neurocognition, and other localized high-resolution imaging applications. Therefore, improving the strength and switching rate of the gradient magnetic field is of paramount significance in enhancing MRI image resolution, reducing imaging time, and accelerating MRI image generation efficiency.

Increasing the power amplifier of the gradient coils and increasing the number of wires turns in the gradient coils are the main methods to enhance the strength of the gradient magnetic field. However, improvements in these two aspects can lead to excessive heat generation in the gradient coils, either locally or overall, which further results in issues such as image distortion and signal loss. In this case, addressing the heating problem becomes an urgent matter. Currently, there are two common cooling methods employed in MRI equipment. One approach involves cooling using cooling pipes, where cooling pipes are arranged around the gradient coils, and liquid nitrogen or cooling water is circulated inside them for cooling purposes. The other method involves using hollow conductors to construct Z-gradient coils, with cooling water flowing through the inside of the coils to achieve a reduction in the temperature of the gradient coils.

Using COMSOL software for thermal simulation of gradient coils can help engineers optimize the design of the coils to enhance their heat transfer performance. By performing simulation analysis on specific parameters, materials, and structures of the gradient coils, the impact of the design on temperature distribution, heat loss, and cooling effectiveness can be evaluated. This aids in guiding the practical manufacturing and improvement of gradient coils, thereby enhancing the performance and stability of MRI systems [4].

This study focuses on a set of gradient coils designed based on the target field method. Firstly, the generated two-dimensional coordinate data of the gradient coils is exported in MATLAB. Then, the two-dimensional coordinate data is converted to three-dimensional coordinate data using known formulas for coil radius and arc length, and imported into SolidWorks software for three-dimensional modeling. Finally, the constructed model is imported into COMSOL for finite element simulation and post-processing. The thermal models of two sets of gradient coils with different cooling methods are simulated, and the heat dissipation effects of the two cooling methods are compared, providing valuable insights for the design of practical cooling structures for gradient coils.

2 Obtaining Coil Coordinates Using the Target Field Method

The target field method is a design method for gradient coils developed by Turner. This method utilizes a Fourier-Bessel expansion of the magnetic field generated by currents flowing on a cylinder. By inverting the relationship between current and field, it becomes possible to evaluate the current density required to generate a specified target field B_z on the surface of a cylinder with a smaller radius [5].

Assuming that the current distribution $j(\varphi, z)$ on the surface of a cylinder of radius a with components j_φ and j_z , the axial component of the magnetic field can be represented by a Fourier-Bessel series.

$$B_z(\rho, \varphi, z) = -a \frac{\mu_0}{2\pi} \sum_{m=-\infty}^{+\infty} \int_{-\infty}^{+\infty} dk e^{im\varphi} e^{ikz} ka I_m(k\rho) K_m'(ka) J_\varphi^m(k) \quad (1)$$

for $r < a$, where.

$$J_\varphi^m(k) = \frac{1}{2\pi} \int_{-\infty}^{\infty} \int_{-\pi}^{\pi} j_\varphi(\varphi, z) e^{-im\varphi} e^{-ikz} d\varphi dz \quad (2)$$

and K_m, I_m , are the usual modified Bessel functions.

In particular, the current is generally concentrated on the surface of the cylinder, so the radial component is missing, and the φ - and z - components of the current density are related to the continuity equation, in which case $J_\varphi^m(k)$ can be reduced to.

$$J_\varphi^m(k) = -\frac{ka}{m} J_z^m(k) \quad (3)$$

Evaluating Eq. (1) on a second cylinder of radius $r = c < a$ and performing the inverse Fourier transform of both sides of the equation, yields [6].

$$J_\varphi^m(k) = -\frac{B_z^m(c, k)}{\mu_0 ka I_m(kc) K_m'(ka)} \quad (4)$$

where,

$$B_z^m(c, k) = \frac{1}{2\pi} \int_{-\pi}^{+\pi} d\varphi \int_{-\infty}^{+\infty} dz e^{-im\varphi} e^{-ikz} B_z(c, \varphi, z) \quad (5)$$

For coils of different radii, based on the approximation and convergence conditions of the modified Bessel function, the magnetic field inside the coil behaves like the target field.

Based on the principles of the target field method and the desired parameters of the gradient coil (as shown in Table.1), a program was written in MATLAB to generate a two-dimensional image of the gradient coil and export the corresponding two-dimensional coil coordinate data.

The two-dimensional coil coordinate data of the gradient coil was transformed into three-dimensional coordinate data using the known formulas for coil radius and arc length, and exported in Excel. Subsequently, the three-dimensional coil coordinate data was organized for the preparation of three-dimensional modeling in Solidworks.

Table 1. Design parameters of X, Y and Z gradient coils

	X coil	Y coil	Z coil
Coil radius (m)	P: 0.11070 S: 0.14305	P: 0.11330 S: 0.14565	P: 0.10708 S: 0.13943
DSV (m)	0.180	0.180	0.180
Gradient strength (mT/m)	200	200	200
Field deviation (%)	±5	±5	±5
Minimum wire spacing (mm)	4.2	4.4	6.6
Loop quantity	132	136	72

3 Three-Dimensional Modeling and Simulation Study

Solidworks is a leading, mainstream computer aided design (CAD) software solution known for its powerful features, ease of use, and technological innovation. It offers diverse design options, reduces errors in the design process, and enhances product quality. COMSOL Multiphysics, a multi-physics simulation software, utilizes the finite element method to simulate various problems described by partial differential equations in scientific research and engineering. Users can easily achieve direct coupling analysis of multiple physics fields by selecting or customizing different specialized partial differential equations, all within a user-friendly graphical interface. Additionally, it supports Solidworks import functionality, provides efficient computational performance, and possesses robust bidirectional coupling capabilities across multiple fields, enabling high-precision numerical simulations [7].

This article utilized Solidworks software to create highly realistic three-dimensional models of gradient coils, which were then imported into COMSOL software. The COMSOL software was used to analyze the magnetic field and temperature distribution of the gradient coils after applying current. In COMSOL, by constructing the imported models, adding the necessary material properties and physical fields, appropriately meshing the grids, and including relevant research parameters, the magnetic field and temperature distribution generated by the X, Y, and Z gradient coil configurations (with two cooling structures) were obtained. Post-processing techniques were employed to analyze and evaluate the thermal performance of the two different cooling methods for the gradient coils. Figure 1 illustrates the overall design and analysis workflow of this study.

3.1 Solidworks 3D Modeling

Segmenting the coil. After organizing the three-dimensional coordinate data of the gradient coil into a TXT file, a new Solidworks project is created. The “gb_part” option is selected, and under “Features,” “Curves” is chosen. In the “Curves” section, “Curve Through XYZ Points” is selected, and the TXT file containing the three-dimensional coordinates is imported. Upon import, Solidworks will display the three-dimensional outline of the gradient coil, including numerous tangled lines. Each coil needs to be

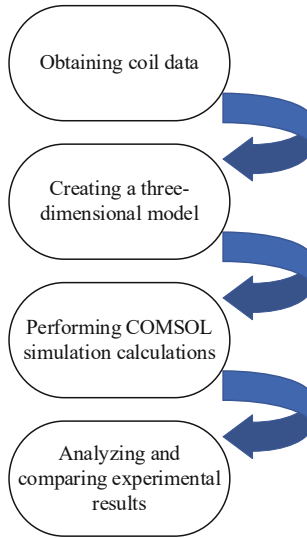


Fig. 1. Overall design flowchart

individually segmented. Partial coordinates are selected from the three-dimensional coordinate file and copied into a newly created TXT file. Then, the newly created TXT file is imported into Solidworks using "Curve Through XYZ Points." The individual coil is observed to check for large openings or obvious extensions that do not conform to the design. If any are present, corresponding three-dimensional coordinate points are added or removed accordingly. If there are no issues, the file is saved. These steps are repeated until each coil is separated. TXT files for each individual coil are organized to prevent confusion in subsequent work.

Adjusting the coil structure and interconnecting them. The individually segmented coils do not meet the final requirements and require some adjustments. First, the coil's opening direction is aligned with the Z-axis direction by removing or adding three-dimensional coordinate points. Then, some points are removed at the opening of the coil (typically, two coordinate points near the Z-axis). Finally, a new TXT file is created, and the three-dimensional coordinates of each individual coil are sequentially copied into this file. The newly created TXT file is imported into Solidworks to check if the generated coil profiles meet the requirements. It is important to note that not all coils are connected together. While in actual MRI devices, gradient coils are often connected by two electrical circuits, I have separately created three-dimensional models for the X, Y, and Z gradient coils. Moreover, when constructing the models for each set of gradient coils, I did not connect all parts. Although finite element simulations aim to be as realistic as possible, certain compromises need to be made during the model creation process due to objective conditions. For instance, the wires connecting different coil sections have irregular shapes and high levels of bending, making it challenging to generate high-quality meshes in COMSOL. This significantly affects the overall model simulation results and may even lead to convergence issues in the computation results.

Additionally, in COMSOL, it is essential to set up the physical fields appropriately to establish electrical connections between the disconnected parts of the gradient coils, thereby achieving the electrical circuit of the actual gradient coils in reality.

Creating a three-dimensional model of the gradient coils. Finally, generating a three-dimensional model by scanning over the established coil profiles.

Creating the X and Y coils. The specific steps are as follows: Select a point, preferably the initial point of the innermost coil; choose to insert, reference geometry, Plane. In Second Reference, select the top view reference plane; draw a sketch on the newly created reference plane. Click on center rectangle and select the initial point as the center point. Draw a rectangle with a length of 3.5 mm and a width of 3–4 mm (to avoid small thin faces at the corners during cutting); Select Swept. In Profile and Path, choose Sketch Profile and the corresponding curve in the two selection boxes below. In Options, select Follow Path for Profile Orientation. In Profile Twist, choose Specify Twist Value. In Direction 1, choose 41deg (the angle may vary for each coil section and needs to be adjusted until the generated coil matches the expectations); Create a sketch on the front view reference plane. Use Centrepoint Arc to draw two arcs on both sides of the coil profile, with 8mm from the center point. The length of the arcs should be greater than the coil profile. Connect the two arcs with straight lines to form a closed shape; Select Extruded Cut. Choose the Sketch Plane in From. In Direction 1, select Through All and check Flip side to cut; The model of the X coil is shown in Fig. 2a, and the model of the Y coil is shown in Fig. 2b.

Creating the Z coil. The coil modeling is relatively simple. Firstly, select “Swept” and choose “Circular Profile” in “Profile and Path”. Select the corresponding curve and set the diameter to 4mm. Repeat the steps with the same curve, but this time set the diameter to 3mm (to create a coil with hollow wire). The model of the Z coil is shown in Fig. 2c.

Creating the casing. Creating Sketch 1 on the front reference plane, selecting “Circle” and drawing two circles with the origin as the center. Selecting “Extruded Boss” with “Blind” chosen for both “Direction 1” and “Direction 2”, and a distance of 0.3 m. Creating Sketch 2 on the front reference plane, selecting “Centerpoint Arc” and drawing two short arcs with different radii centered at the origin, connecting them with straight lines. Selecting “Extruded Cut” with “Through All” chosen for both “Direction 1” and “Direction 2”. Using “Linear Pattern” and selecting “Circular Pattern” with “Equal spacing” chosen, an angle of 360deg, and a quantity of 16. The 3D modeling diagram of the gradient coil as a whole is shown in Fig. 3.

3.2 COMSOL Finite Element Simulation

Import and construct the model. In the COMSOL geometry options, import the pre-built 3D models of the X, Y, Z gradient coils, and the outer shell. Click on “Construct” to initiate the construction process. Right-click on the geometry and select “More Volumes” and then “Spiral” Add four spiral volumes, positioning them between the shield coils and the main coils, and aligning them closely with the two sets of coils. Add two difference operations and choose the option to retain the objects to be subtracted. This will transform the spirals into hollow tubes.

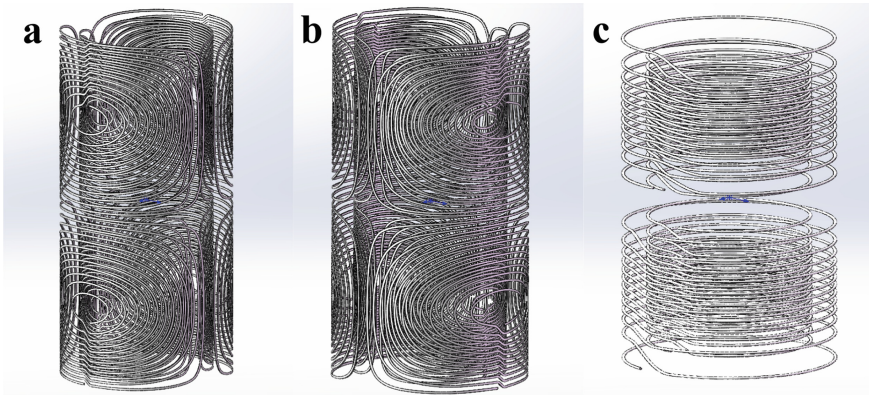


Fig. 2. (a) 3D modeling diagram of X Gradient Coil, (b) 3D modeling diagram of Y gradient coil, (c) 3D modeling diagram of Z gradient coil

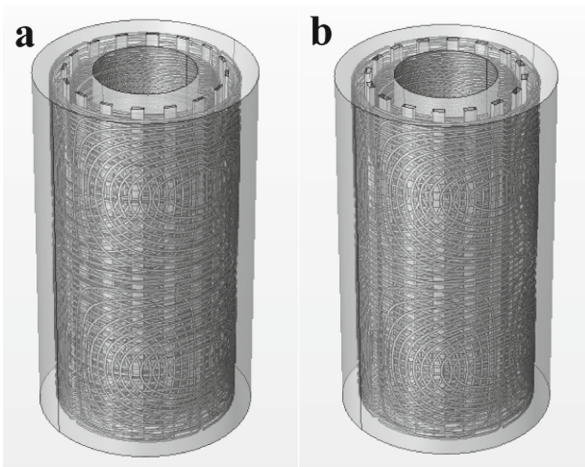


Fig. 3. (a) 3D modeling diagram of hollow water-cooled plastic pipes gradient coils, (b) 3D modeling diagram of hollow water-cooled wire gradient coils

Add and define material properties. Select materials from the built-in material library in COMSOL. Set the material of the coils as copper, the material of the hollow part of the Z coil and water cooling pipe as water, the material of the water cooling pipe as plastic, and the material of the casing as epoxy resin. Add relative magnetic permeability and relative dielectric constant in the material property details for water.

Add physical fields. Add physical fields. Choose Magnetic Field (mf) and Heat Transfer in Solid and Fluid (ht) in the physical fields' selection. In the Magnetic Field (mf), add eight coils (four coils for the Z coil), set the wire model as a single wire, select current as the coil excitation, and set the current magnitude to 50A. In the geometry analysis input, add the corresponding surfaces with default options for the remaining settings. In

the Heat Transfer in Solid and Fluid (ht), select fluid and add the domain with material properties for water. Add heat flux, select all boundaries for the boundary selection, choose convection heat flux as the flux type, select user-defined for the heat transfer coefficient type with a value of $1000 \text{ W/m}^2 \text{ K}$. Set the external temperature to 293.15 K . Add surface-to-environment radiation with a user-defined surface emissivity value of 0.8 , and leave the remaining options as default. Add multiphysics, and in the multiphysics selection, add Electromagnetic Heating. Couple the two physical fields together.

Mesh Partitioning. In the sequence type, select “Physics-controlled meshing,” and choose a finer mesh size. Due to the large size of the designed gradient coil in this study and the high level of realism in the established 3D model, the current model is not yet optimal and there is room for improvement. On the other hand, a finer mesh partitioning, although increasing computational load, also enhances the accuracy of the computed results. Given sufficient computational resources, this is a reasonable choice.

Study. Because the overall coil has an irregular circular shape, the study is divided into two steps: firstly, the geometric analysis of the coil is performed to obtain the current distribution in the coil. Therefore, the study consists of two steps: firstly, add Study Step 1 and include a Coil Geometry Analysis to obtain the current density distribution in the coil; then, select Step 2 and add a Steady-State Study to obtain the magnetic flux density and temperature distribution in the coil.

Post-processing. After the computation, the temperature distribution of the gradient coils can be obtained in the results of COMSOL. The temperature distributions of the X, Y, and Z gradient coils with individual excitations are shown in Figs. 4 and 5. Figure 5 depict the temperature distributions of the gradient coils cooled using the traditional hollow plastic tube cooling method. In the derived values, the maximum and average temperatures are calculated for the volume. The computed results for the coils with the traditional cooling structure are presented in Table.2, while the results for the coils using the hollow water-cooled conductor structure are shown in Table.3.

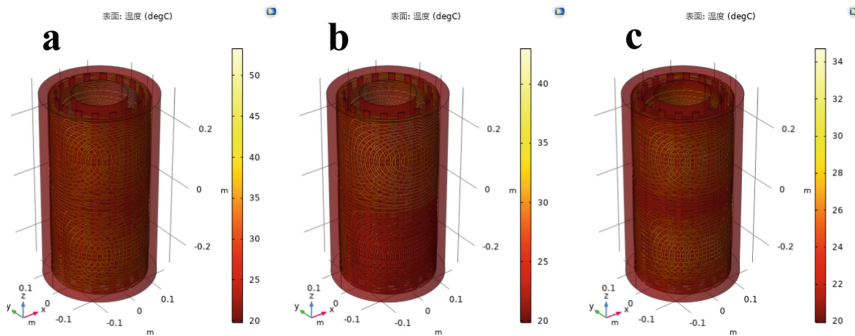


Fig. 4. (a) Temperature distribution of X coil with excitation using hollow water-cooled plastic pipes cooling structure, (b) Temperature distribution of Y coil with excitation using hollow water-cooled plastic pipes cooling structure, (c) Temperature distribution of Z coil with excitation using hollow water-cooled plastic pipes cooling structure

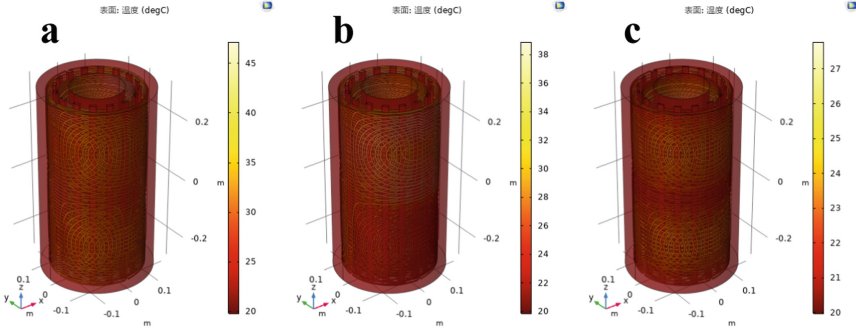


Fig. 5. (a) Temperature distribution of X coil with excitation using hollow water-cooled wire structure, (b) Temperature distribution of Y coil with excitation using hollow water-cooled wire structure, (c) Temperature distribution of Z coil with excitation using hollow water-cooled wire structure

Table 2. Hollow water-cooled plastic pipes cooling structure

	X coil	Y coil	Z coil
Average temperature (°C)	31.408	28.491	24.756
Maximum temperature (°C)	53.308	42.995	34.765

Table 3. Hollow water-cooled wire structure

	X coil	Y coil	Z coil
Average temperature (°C)	29.448	26.869	22.530
Maximum temperature (°C)	47.132	38.874	27.772

4 Conclusion

In this study, the contour plots of the gradient coils were obtained using the target field method. The two-dimensional contour plots of the coils were then converted into three-dimensional representations, and the corresponding three-dimensional coordinates were exported. The gradient coil’s three-dimensional coordinates were imported into Solidworks for 3D modeling. Finally, the constructed model was imported into COMSOL solid heat transfer simulations.

Based on the simulation results, it can be observed that the gradient coils with a hollow wire water-cooling structure exhibit a slight decrease in steady-state temperature compared to the gradient coils with hollow water-cooled plastic pipes cooling structure. Specifically, the highest temperature of the X coil decreased by 11.5%, and the average temperature decreased by 6.2%, the highest temperature of the Y coil decreased by 9.6%, and the average temperature decreased by 5.7%, the highest temperature of the Z coil decreased by 21.3%, and the average temperature decreased by 8.9%. These

findings indicate that the hollow conductor water-cooling structure offers improved heat dissipation performance for gradient coils, providing valuable insights for the design of cooling structures in practical gradient coil systems.

References

1. Lu, Z.: 3D Mouse Lung Cancer Phantom Development and MRI Performance Evaluation[D]. Wake Forest University, (2019)
2. Wang, S., Su, Z., Ying, L., et al.: Accelerating magnetic resonance imaging via deep learning[C]. 2016 IEEE 13th international symposium on biomedical imaging (ISBI). IEEE, pp. 514–517 (2016)
3. Doneva, M.: Mathematical models for magnetic resonance imaging reconstruction: an overview of the approaches, problems, and future research areas[J]. IEEE Signal Process. Mag. **37**(1), 24–32 (2020)
4. Vajdi, M., Moghanlou, F.S., Sharifianjazi, F., et al.: A review on the comsol multiphysics studies of heat transfer in advanced ceramics[J]. J. Compos. Compd. **2**(2), 35–43 (2020)
5. Sánchez, C.C.: Forward and Inverse Analysis of Electromagnetic Fields for MRI using Computational Techniques[D]. University of Nottingham, (2008)
6. Turner, R.: A target field approach to optimal coil design[J]. J. Phys. D Appl. Phys. **19**(8), L147 (1986)
7. Pepper, D.W., Heinrich, J.C.: The finite element method: basic concepts and applications with MATLAB, MAPLE, and COMSOL[M]. CRC press, (2017)



Adaptive One-Step Prediction Enhanced Kalman Filter Algorithm for INS/Vision Integrated Mobile Robot Localization

Ronghao Shang, Yide Zhang, Tonghui Zhou, Tai Cheng, Kun Liang,
Wuwen Zhang, Ting Wang, Zhongwei Shi, and Yuan Xu^(✉)

School of Electrical Engineering, University of Jinan, Jinan 250022, Shandong, China

xy_abric@126.com

Abstract. Localization accuracy is an important index for evaluating multi-sensor integrated system. For ensuring the high precision, usually more accuracy sensor is adopted for reducing the measurement error or better localization algorithms are used. This paper proposes an adaptive one-step prediction enhanced algorithm that combines kalman filter (KF) algorithm for INS/Computer Vision integrated localization system, to address the issue of some data in the inertial navigation system (INS) being unusable for data fusion. The process can be realized by determining whether one-step prediction is needed by the fast or slow motion of the robot. Based on that, the optimal estimation of the system state can be achieved by computer programming. Analysis of computer simulation experimental is done by comparing the proposed algorithm with INS/Computer Vision integrated KF and one-step prediction enhanced KF, the positioning accuracy can be enhanced and the positioning error can be minimized.

Keywords: INS · Computer vision · Kalman filter algorithm · Adaptive one-step prediction algorithm

1 Introduction

Since the 20th century, with the development of automation integration technology, data communication technology and sensor technology, mobile robots have been widely used in more and more industries. At the same time, the requirements for robot positioning accuracy have become higher and higher [1]. Traditional navigation and positioning technologies can be mainly classified as absolute positioning based on global navigation satellite systems and relative positioning based on inertial sensors and odometers [2]. In order to accomplish the robot's autonomous and high-precision positioning task, the combined positioning method of mobile robots with multi-sensor data fusion is usually chosen. INS/Vision integrated localization stands out among many positioning technologies because of its ability to fuse the advantages of visual navigation system

(VNS), which has no cumulative error [3], and inertial navigation system (INS), which is not subject to external interference.

The traditional Kalman filter (KF) in the current combinatorial localization algorithm has a large number of practical examples in the engineering field. The Kalman filter is a recursive prediction method that uses optimal estimation in the time domain [4]. The algorithm combines the system state estimation at the next moment and the feedback from the measurement to obtain a more accurate state estimate at that moment [5]. Most of the algorithms used in practical engineering for loose combinations as well as tight combinations are built on the Kalman filter for improvement. Therefore, the Kalman filter is adopted here for simulation studies. It should be noted that the sampling frequencies of the two subsystems in the INS/Vision integrated localization system are different [6], however, the vision and the filter usually have the same sampling time, which may cause the INS data to be excluded from data fusion, thereby lowering the accuracy of combined navigation [7]. For avoiding that, an adaptive one-step prediction enhanced Kalman filter method will be proposed. In details, the output of the Kalman filter is applied to improve the positioning error, which is realized by judging the Marschall distance between the measured value and the optimal estimate, and introducing adaptive one-step prediction to reduce the effect of sampling time on data loss.

The structure of this paper is as follows. In the second section, a robot localization scheme with vision and inertial fusion will be introduced. The third section improves the Kalman filter using an adaptive one-step prediction enhanced method. The fourth section introduces a simulation experiment, which validated the proposed method. The fifth section concludes the paper.

2 Robot Positioning Solution with Inertial and Vision Fusion

2.1 INS/Vision Integrated Localization Strategy

When the INS/Vision integrated localization system works properly, its basic architecture is shown in Fig. 1. In which, INS uses accelerometer, gyroscope and magnetometer to complete the computation of the target robots position information, the visual navigation system completes the measurement of the position of the target robot by acquiring the images between two adjacent frames. On this basis, the localization information of the binocular vision solution is used to observe the INS localization solution error, and the position information of the target robot measured by inertial and vision localization respectively is the difference is input into the adaptive one-step prediction enhanced filter to achieve the prediction of the inertial navigation localization solution error.

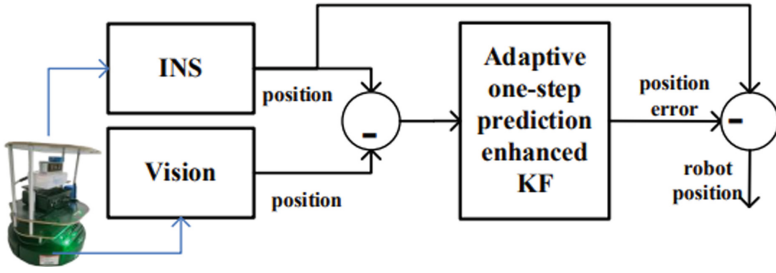


Fig. 1. Basic architecture of a INS/Vision integrated localization strategy.

2.2 State Space Model for Inertial/Vision Localization Systems

According to the INS/Vision integrated localization strategy, the data fusion model uses state equation with four state vectors [8], as shown in Eq. (1).

$$\underbrace{\begin{bmatrix} \delta x_t^I \\ \delta y_t^I \\ \delta vx_t^I \\ \delta vy_t^I \end{bmatrix}}_{s_{e,t}^I} = \underbrace{\begin{bmatrix} 1 & 0 & \Delta t & 0 \\ 0 & 1 & 0 & \Delta t \\ 0 & 0 & 1 & 0 \\ 0 & 0 & 0 & 1 \end{bmatrix}}_{F_e^I} \underbrace{\begin{bmatrix} \delta x_{t-1}^I \\ \delta y_{t-1}^I \\ \delta vx_{t-1}^I \\ \delta vy_{t-1}^I \end{bmatrix}}_{s_{e,t-1}^I} + w_t^I \tag{1}$$

where, $(\delta x_t^I, \delta y_t^I)$ indicates the position error of INS, $(\delta vx_t^I, \delta vy_t^I)$ indicates the velocity error of INS, Δt denotes the sampling time, $w_t^I \sim N(0, Q)$ expresses the system noise and Q is the covariance matrix of the system noise. t is the index time of INS. k is the index time of vision system.

Based on Eq. (1), the system observation equation will be obtained as Eq. (2).

$$\underbrace{\begin{bmatrix} \delta \tilde{x}_t^I \\ \delta \tilde{y}_t^I \end{bmatrix}}_{z_t} = \underbrace{\begin{bmatrix} x_t^I - x_k^V \\ y_t^I - y_k^V \end{bmatrix}}_G = \underbrace{\begin{bmatrix} 1 & 0 & 0 & 0 \\ 0 & 1 & 0 & 0 \end{bmatrix}}_{G} s_{e,t}^I + v_t^I \tag{2}$$

where, $v_t^I \sim N(0, R)$ is the measurement noise and R is the covariance matrix of the measurement noise.

3 Adaptive One-Step Prediction Enhanced KF

Kalman filter finally obtains the optimal state estimation at current moment by using a combination of the estimating state value at the previous moment and the derived feedback from the current measurement. Generally, KF consists of two phases based on the algorithm execution steps: time update and measurement update. The quantitative part is in charge of the feedback, including the calculation of the Kalman gain, the update of error covariance values and state variable.

For a linear system with a known state space expression as shown in Eq. (3), the optimal estimate of the state at the next moment is obtained by a recursive algorithm based on data fusion of the state estimation error with the measurement error at the next moment.

$$\begin{cases} x_{k+1} = Fx_k + w_k \\ z_k = Hx_k + v_k \end{cases} \tag{3}$$

where, k is discrete time, F is transfer matrix, H is observation matrix; x_k is the state quantity; z_k is observation; w_k and v_k are white noise.

The recursive formula of the KF algorithm can be obtained based on Eq. (3).

The first step of state prediction is performed as shown in Eq. (4), $\hat{x}_{k,k-1}$ is status one-step predicted value.

$$\hat{x}_{k,k-1} = F\hat{x}_{k-1} \tag{4}$$

The one-step prediction error variance array is calculated as Eq. (5).

$$P_{k,k-1} = FP_{k-1}F^T + Q \tag{5}$$

In which, P_{k-1} is state transfer covariance estimation at time $k-1$, the estimated error variance array P_k is obtained in Eq. (6).

$$P_k = [I - K_kH]P_{k,k-1} \tag{6}$$

K_k is the Kalman filtering gain, it can be obtained from Eq. (7).

$$K_k = P_{k,k-1}H^T[HP_{k,k-1}H^T + R]^{-1} \tag{7}$$

Then, the state estimation \hat{x}_k is got as shown in Eq. (8), which is the state optimal estimate at moment k .

$$\hat{x}_k = \hat{x}_{k,k-1} + K_k[z_k - H\hat{x}_{k,k-1}] \tag{8}$$

The covariance distance of data can be represented by Mahalanobis distance, which is an efficient method for calculating the similarity of two unknown sample sets. The algorithm calculates the Mahalanobis distance between the measured value and the optimal estimate, and a certain threshold is set to determine whether to make a one-step prediction. The basic calculation formula is given as Eq. (9).

$$D_M = (x - y)^T \Sigma^{-1} (x - y) \tag{9}$$

in which, x and y indicate two different data points. Σ is covariance matrix.

In summary, Pseudo code of adaptive one-step prediction enhanced KF is given as Algorithm 1.

Algorithm 1: Adaptive one-step prediction enhanced Kalman filter

Input: $\mathbf{z}_k, x_0, P_0, F, H, Q, R$

Output: $\hat{\mathbf{x}}_k$

```

1 for  $k = 1 : \text{number}$  do
2   if  $\text{mod}(k, \Delta t / \Delta t_{INS})$ 
3      $\hat{\mathbf{x}}_{k,k-1} = F\hat{\mathbf{x}}_{k-1}$ 
4      $P_{k,k-1} = FP_{k-1}F^T + Q$ 
5      $K_k = P_{k,k-1}H^T[HP_{k,k-1}H^T + R]^{-1}$ 
6      $\hat{\mathbf{x}}_k = \hat{\mathbf{x}}_{k,k-1} + K_k[z_k - H\hat{\mathbf{x}}_{k,k-1}]$ 
7      $P_k = [I - K_kH]P_{k,k-1}$ 
8      $M_k = (z_k - H\hat{\mathbf{x}}_{k,k-1})^T R^{-1} (z_k - H\hat{\mathbf{x}}_{k,k-1})$ 
9     if  $M_k > M_{ave}$  otherwise;
10    for  $h = 1 : \Delta t / \Delta t_{INS}$  do
11       $\hat{\mathbf{x}}_{h,h-1} = F\hat{\mathbf{x}}_{h-1}$ 
12       $P_{h,h-1} = FP_{h-1}F^T + Q$ 
13    end
14     $K_k = P_{k,k-1}H^T[HP_{k,k-1}H^T + R]^{-1}$ 
15     $\hat{\mathbf{x}}_k = \hat{\mathbf{x}}_{k,k-1} + K_k[z_k - H\hat{\mathbf{x}}_{k,k-1}]$ 
16     $P_k = [I - K_kH]P_{k,k-1}$ 
17 end
18  $M_{ave}$  is the mean of the Mahalanobis distance between the filter's
    measured value and the best estimate at each moment

```

4 Experimental Simulation Analysis

To show the performance of the proposed algorithm, a real test was carried out. The experimental platform used in this paper mainly consists of one Turtlebot2 mobile robot platform, as shown in Fig. 2, on which one binocular camera and one Inertial Measurement Unit (IMU) device based on Industrial Personal Computer (IPC) are mounted. Among them, the binocular camera and IMU device are responsible for measuring the current robot position information, and the position information solved by the subsystem is input to the IPC on the robot platform respectively; meanwhile, a computer device is arranged at the remote end to exchange data with the IPC on the mobile robot platform through wireless transmission.

This section will examine the localization error by contrasting the proposed algorithm with the INS/Vision integrated KF algorithm and the one-step predictive enhanced KF algorithm. The detailed trajectory, including the reference path, as well as the paths for INS, vision, INS/Vision integrated KF, one-step prediction enhanced KF and adaptive one-step predictive KF are demonstrated in Fig. 3 respectively. In the test, the sampling time is assigned as $\Delta t_{INS} = 0.05$ s, and $\Delta t / \Delta t_{INS} = 14$. To make the comparison more clear, Figs. 4 and 5 show

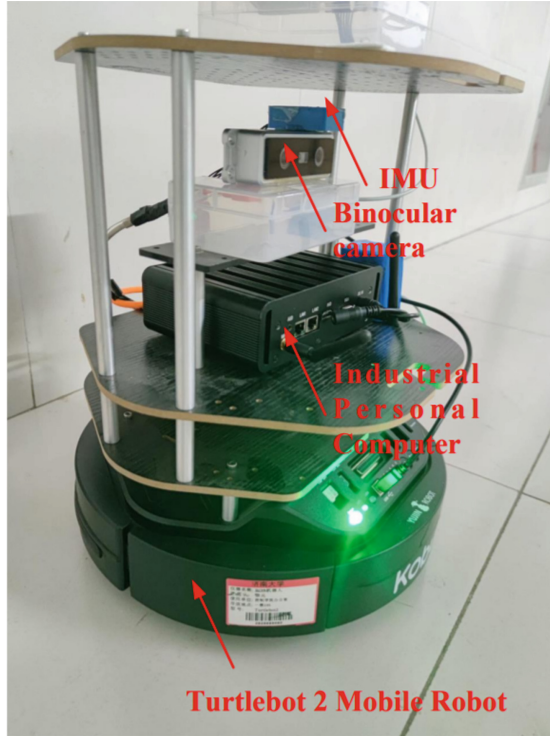


Fig. 2. The mobile robot used in the experiment.

the localization errors in the eastward and northward in the test estimated by the three algorithms. In addition, Fig. 6 presents the errors cumulative distribution function (CDF) chart of three algorithms. When CDF is 0.9, the three algorithm have positioning errors of 0.092 m, 0.075 m and 0.072 m, respectively.

Table 1 demonstrates the root mean square error (RMSE) of position for three algorithms. The proposed method has position RMSE in the east direction and north direction are 0.035788 m and 0.034246 m, respectively, and the average position RMSE of that is 0.035017 m. Comparing with other two methods, the proposed adaptive one-step predictive KF provides an decrease of position RMSE about 14.75% and 4.3% respectively. The proposed method fully shows its performance on enhancing the positioning accuracy.

5 Conclusion

In INS/Vision integrated system, some data in INS is unavailable for data fusion thus affecting the positioning accuracy. Aiming at solving the problem, an adaptive one-step predictive enhanced KF algorithm is presented in this article. It adaptively adopts one-step prediction to improve positioning error. The test

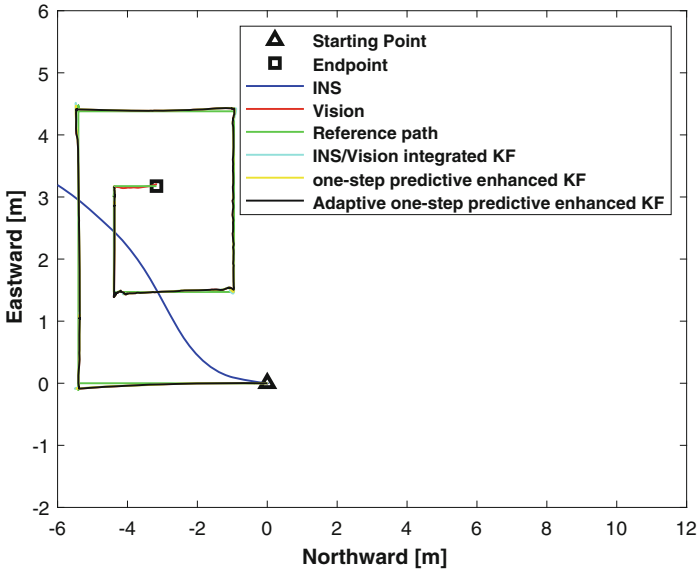


Fig. 3. Trajectory comparison chart.

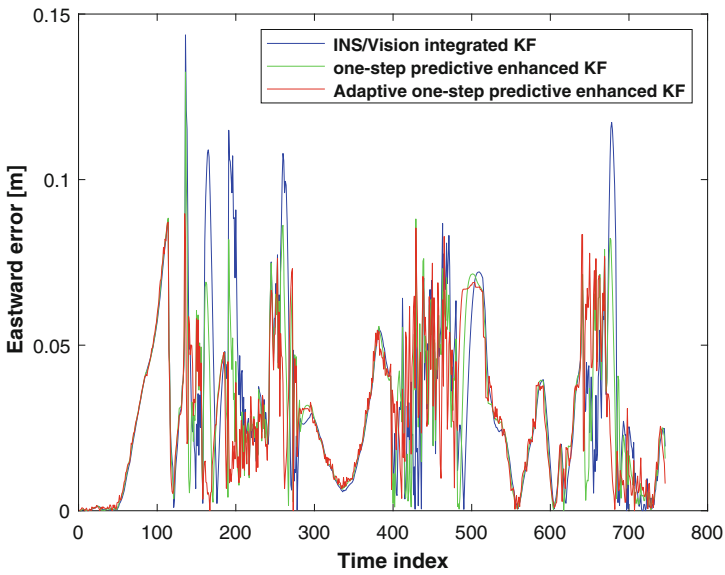


Fig. 4. Eastward error.

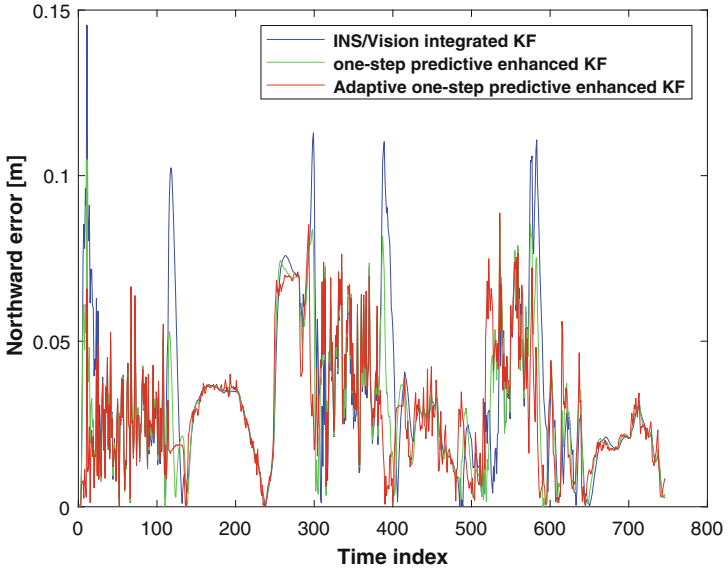


Fig. 5. Northward error.

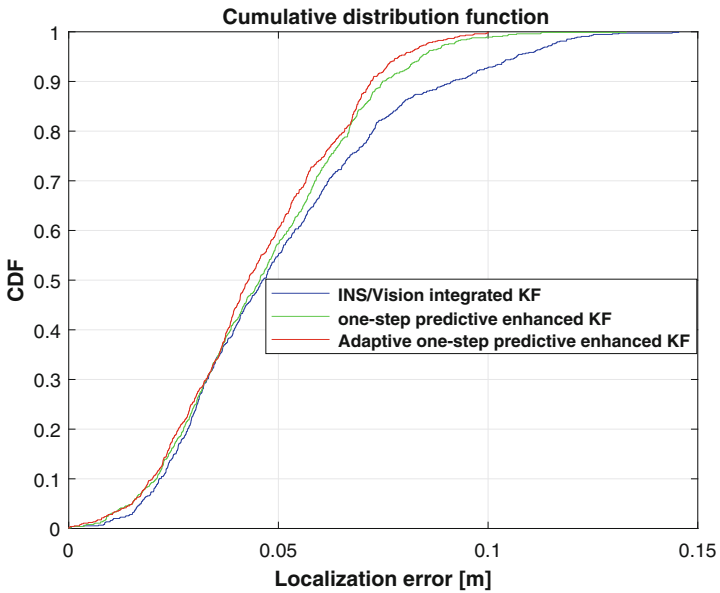


Fig. 6. CDFs of Adaptive one-step prediction enhanced KF, one-step prediction enhanced KF and INS/Vision integrated KF.

Table 1. The RMSE (m) generated by Adaptive KF, one-step prediction enhanced KF and INS/Vision integrated KF under different direction

Direction	RMSE		
	Integrated KF	One-step prediction enhanced KF	Adaptive KF
Northward	0.041196	0.0361	0.034246
Eastward	0.040955	0.037081	0.035788

results show that in contrast to INS/Vision integrated KF and one-step predictive enhanced KF, the proposed algorithm plays a positive role in improving the positioning accuracy.

References

1. Cui, Y., Liu, S., Liu, Q.: Navigation and positioning technology in underground coal mines and tunnels: a review. *Southern Afr. Inst. Min. Metallurgy* (6) (2021). <https://doi.org/10.17159/2411-9717/1065/2021>
2. Xu, Y., Liu, T., Sun, B., Zhang, Y., Khatibi, S., Sun, M.: Indoor vision/ins integrated mobile robot navigation using multimodel-based multifrequency kalman filter. *Math. Probl. Eng.* (2021). <https://doi.org/10.1155/2021/6694084>
3. Zhao, S.: Trial-and-error or avoiding a guess initialization of the Kalman filter. *Automatica* **121**(1), 109184 (2020)
4. Zhao, S., Shmaliy, Y.S., Shi, P., Ahn, C.K.: Fusion kalman/ufir filter for state estimation with uncertain parameters and noise statistics. *IEEE Trans. Industr. Electron.* (2017). <https://doi.org/10.1109/TIE.2016.2636814>
5. Zhu, F., Shen, Y., Wang, Y., Jia, J., Zhang, X.: Fusing GNSS/INS/vision with a priori feature map for high-precision and continuous navigation. *IEEE Sens. J.* **21**(20), 23370–23381 (2021). <https://doi.org/10.1109/JSEN.2021.3105110>
6. Xu, Y., Shmaliy, Y.S., Chen, X., Li, Y., Ma, W.: Robust inertial navigation system/ultra wide band integrated indoor quadrotor localization employing adaptive interacting multiple model-unbiased finite impulse response/Kalman filter estimator. *Aerosp. Sci. Technol.* **98**, 105683 (2020)
7. Chen, X., Yuan, X., Li, Q., Tang, J., Shen, C.: Improving ultrasonic-based seamless navigation for indoor mobile robots utilizing EKF and LS-SVM. *Measurement* **92**, 243–251 (2016)
8. Wu, Q., Feng, J., Gao, Y., Bi, S., Zhuang, Y., Xu, Y.: One-step prediction-enhanced fir filter and its application in ins/vision-integrated mobile robot localization. *IEEE Sens. J.* **23**(7), 7493–500 (2023). <https://doi.org/10.1109/JSEN.2023.3247897>



Analysis of Abnormal Transmission Synchronous Belt of Industrial Robot Based on Visual Inspection

Han Jiang, Lanzhu Ren, Gandong Chen, and Lingyan Zhao^(✉)

Shandong Jiaotong University, Jinan 250357, China
206082@sdjtu.edu.cn

Abstract. In view of the phenomenon that the synchronous belt of industrial robot will jump teeth and slip in use, an image acquisition system based on MATLAB is designed. The image collected by the macro camera is preprocessed to obtain the general contour boundary. In order to obtain the high accuracy synchronous belt tooth profile data, it is necessary to fit the data. Harris corner detection screen boundary feature points, through cubic spline interpolation, digital filtering algorithm to get the best contour curve. Comparing the tooth profiles of different synchronous belts can directly reflect the cause of abnormal transmission of synchronous belts. Compared with the traditional manual detection, avoid the secondary measurement error caused by contact. The tooth shape of the incoming synchronous belt is controlled by visual inspection, which is easy to operate, the measurement accuracy is controlled at the pixel level, and the data is reliable.

Keywords: MATLAB · Pretreatment · Harris corner detection · Curve fitting

1 Introduction

As an important power transmission component of industrial robot, the tooth profile parameters directly affect the reliability and smoothness of robot grasp. In the process of use, the phenomenon of skipping teeth and slipping is often caused by unqualified tooth shape parameters. It is obviously not suitable for industrial robots that need to meet high precision transmission.

Most of the synchronization belts used by industrial robots rely on imports, individuals can not control the quality of the products, and the synchronization belt failed to kill the problem products in the cradle before installation.

The detection technology of synchronous belt tooth profile in China is still in the developing stage, and compared with strength detection, tooth profile detection is more difficult [1]. Ensure that the detection accuracy is within 0.01mm. The more mature method of detection technology on the market is the use of ray projection imaging method for size detection, but it has high requirements for installation accuracy and is expensive.

As a flexible material, synchronous belt will cause secondary error when it is in contact with measuring instruments [2], and visual detection has gradually evolved into a

mainstream detection method. In this paper, a synchronization belt tooth profile detection technology based on MATLAB vision is proposed, and the contour of synchronization belt tooth profile is extracted by image processing method. The real profile parameters of the synchronous belt can be obtained by converting it into specific data and calibrating the proportional relationship between the acquired image pixels and the actual distance.

This visual detection method has the advantages of simple operation, pixel level accuracy, high speed and high efficiency. It can meet the quality requirements of mass sampling inspection.

2 Overall Scheme Design and Research

The project is divided into three parts:

Firstly, the image acquisition and preprocessing: The industrial camera plus macro lens is used for image acquisition, and the smaller field of view can reduce the interference of the external environment, and the universality is stronger. The image preprocessing method can better realize the separation of the measured object and the background.

Second, the contour fitting: The separated contour boundary is composed of many pixels, which contain various noises. The edge points were screened according to Harris corner detection method, and the contour data of synchronization belt was extracted by curve fitting and smoothing filtering.

Thirdly, data analysis: The tooth profile parameters of the belt before and after the use of the belt and the slip belt are analyzed comprehensively, and the characteristics of its contour curve are compared, and the reasons for the jump teeth and slip of the belt are analyzed.

2.1 Platform Construction

Components of vision measurement system: 35 mm industrial camera, macro lens, light source controller, point light source. The system is shown (see Fig. 1). The tension $F = 20\text{N}$ during the use of the synchronous belt is simulated by the tensiometer. The collected images are shown (see Fig. 2).

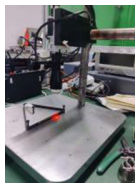


Fig. 1. Mechanical vision measurement system

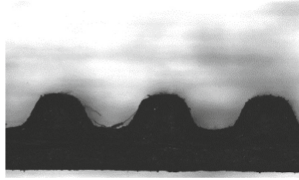


Fig. 2. Image acquisition

2.2 Camera Calibration

In macro range conditions, the camera field of view is only within 10 mm. Unable to meet the space for checkerboard calibration. This article uses a calibrated ruler (as see Fig. 3) to convert the relationship between pixels and actual distance, and create a scale. When measuring, it is only necessary to ensure that the magnification of the lens is consistent with the calibration time to achieve point to point and point to line distance measurement on the collected image.

This calibration method is not affected by the internal parameter matrix or calibration error. When it is necessary to collect synchronous belts with different tooth sizes, simply recalibrate the scale, making the operation more convenient.



Fig. 3. Calibration scale

2.3 Image Preprocessing

To improve the visual effect of the image, pixel contrast enhancement is performed on the image. By using gamma transformation, areas with lower grayscale values are stretched, while areas with higher grayscale levels are compressed, weakening the reflection effect caused by light in the synchronous belt and weakening the background. As shown (see Fig. 4).

$$S = cr^{\gamma} \quad (1)$$

Remap the grayscale values located in different ranges in the image, as shown (see Fig. 5). In the range of 0.2 to 0.4, the contour boundary of the synchronous belt is the clearest.

Binary operation is the most effective method for image segmentation, which uses the maximum inter class variance method to specify the grayscale threshold and achieve



Fig. 4. Enhancement of image

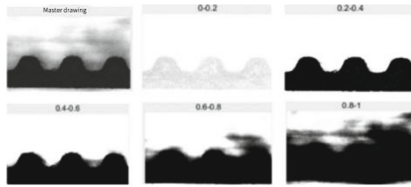


Fig. 5. Contrast enhancement

the separation of foreground and background. The bright area on the surface of the synchronous belt and the shaded part on the contour edge are not completely separated. It is particularly important to use black and white pixel swapping in the image to remove small objects and extract subsequent feature points (see Fig. 6):

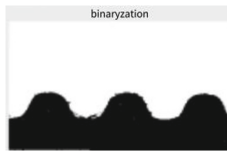


Fig. 6. Binarization of value

Morphological corrosion is used to extract contour boundaries, and structural element B is used to corrode the original image A (see Fig. 7). The principle is as follows:

$$\beta(A) = A - (A \odot B) \tag{2}$$

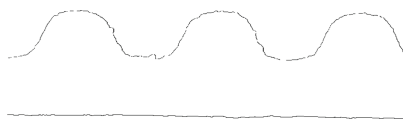


Fig. 7. Edge detection

2.4 Synchronous Belt Parameters

GATES, as a precise arc toothed synchronous belt, is widely used in automation control equipment due to its excellent transmission performance. The structural parameters are shown (see Fig. 8).

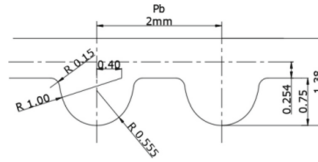


Fig. 8. Standard belt parameters

Synchronous belt transmission relies on the meshing of the synchronous belt teeth and the corresponding grooves of the pulley. To achieve the accuracy of the transmission ratio, it is necessary to ensure that there is no relative sliding between the two. During normal use, various factors such as transmission speed, tension, wear, etc. May affect the tooth shape of the synchronous belt and the pulley to not engage as expected. We need to compare the specifications and parameters of the synchronous belt product to see the cause of the problem.

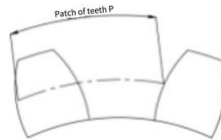


Fig. 9. Belt wheel tooth structure

Factors that affect the correct meshing of synchronous belt teeth and belt gear grooves:

- (1) The pitch P_b with teeth is equal to the pitch P of the gear teeth (see Fig. 9). The synchronous belt undergoes elastic deformation and changes in pitch.
- (2) The thickness of synchronous belt tooth root determines its shear and Flexural strength.
- (3) An appropriate root circle radius can reduce stress concentration, while an excessively large root circle radius can reduce the effective area when meshing with the pulley.
- (4) The radius of the tooth tip circle determines whether there will be interference during meshing [3].

3 Corner Detection

Corners are the points in an image where the maximum gradient change between pixels and the surrounding area, and the maximum curvature of the curve, objectively reflecting the local features of the image. This article adopts the corner detection method of image edge information detection, and extracts feature points using the image edge curve extracted (see Fig. 7).

3.1 Harris Corner Detection Principle

Establish a fixed window to slide in any direction on the original image. If there is a significant change in the grayscale value of the pixels before and after sliding, it is considered that there are corner points in the window.

$$E(\mu, \nu) = \sum_{x,y} \omega(x, y) [I(x + \mu, y + \nu) - I(x, y)]^2 \tag{2}$$

$\omega(x, y)$ as a window function, set it as a Gaussian weighting function, and when the corners are at the center of the window, the grayscale values will undergo drastic changes. The grayscale value of the moved pixel $I(x + \mu, y + \nu)$ Conducting Taylor expansion:

$$I(x + \mu, y + \nu) \approx I(x, y) + \mu I_x(x, y) + \nu I_y(x, y) \tag{3}$$

Bring in the original formula and simplify it:

$$M = \sum_{x,y} \omega(x, y) \begin{bmatrix} I_x^2 & I_x I_y \\ I_x I_y & I_y^2 \end{bmatrix} \tag{4}$$

I_x, I_y they are respectively the Partial derivative in the x and y directions. For images, they can be obtained by sobel operator, namely:

$$I_x = I \otimes (-1, 0, 1)$$

$$I_y = I \otimes (-1, 0, 1)'$$

Corner calculation formula (Fig. 10):

$$R = \det(M) - kTr^2(M) \tag{5}$$

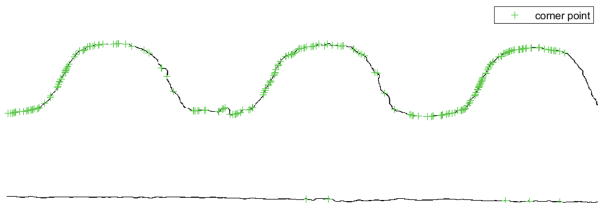


Fig. 10. Corner point extraction

4 Contour Fitting

An image is a matrix composed of two-dimensional discrete variables, which can reflect the contour information of the image through data fitting. Quantify data without changing the shape of the image contour.

4.1 Least-Squares Fit

The least squares method is the most commonly used method for data fitting, which is used to solve the optimal solution. The principle is that when the function relationship $y = f(x)$ is unknown, Extracting k -order polynomial approximation with $(k + 1)$ parameters from n sets of sampled data $(k + 1 < n)$.

$y = f(x) = a_0 + a_1x + a_2x^2 + \dots + a^kx_k$ When the fitting function satisfies the Eq. (6), It is called a least squares fitting polynomial.

$$I_{\min} = \sum_{i=0}^k [p(x_i) - y_i]^2 \quad (6)$$

The minimum sum of squares of the difference between the ordinates of the function model and the scatter value at the sampling point is considered the best fit, as shown in the following figure (Fig. 11):

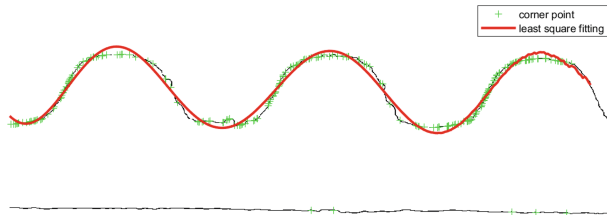


Fig. 11. The least square method was used to fit the curve

The characteristics of least squares fitting: (1) The fitting curve does not pass through all the sampling points, but the curve with the smallest Residual sum of squares of residuals passing through the sampling points is filtered among the sampling points. The sampling points will be inserted back and forth near the final fitting curve, which can only reflect the general curve trend of the sampling points. (2) Local fitting is not smooth.

4.2 Cubic Spline Interpolation Fitting

It is difficult to achieve good fitting accuracy and effect by directly fitting a large number of data points with a single curve. Although fitting accuracy can be improved by increasing the order, it is only possible within a suitable order range.

Cubic Spline interpolation uses Cubic function curve to replace the straight line of Linear interpolation, that is, every adjacent two points are Cubic function curves expressed as $ax^3 + bx^2 + cx + d$.

Assuming there are $[a, b]$ sample points on the interval $n + 1$, that is, the interval $[a, b]$ is divided into n intervals $[(x_0, x_1), (x_1, x_2), \dots, (x_{n-1}, x_n)]$, with two endpoints $x_0 = a$ and $x_n = b$, then there is the following:

On each segmented interval $[x_{i-1}, x_i]$, the interpolation function is a cubic polynomial;

Satisfy the interpolation condition, that is, each sample point is traversed by a certain interpolation function;

Smoothness of the curve refers to the continuity of the second-order and lower derivative functions of the interpolation function (Fig. 12).

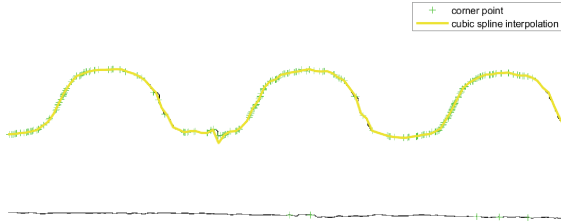


Fig. 12. Cubic interpolation fits the curve

When using cubic spline difference for fitting, it can ensure that the fitted curve passes through each sampling point. Compared with polynomial least squares fitting, it has fewer operations and is flexible. It can simulate any curve shape and the fitted curve has good convergence.

4.3 Smooth Filtering

In the process of data fitting, the influence of noise points can cause “flying points” on the image. The extracted contour boundaries can be regarded as signals, and specific frequency bands in the signal are removed through filtering to prevent noise interference.

The weighted moving average filter performs local weighted linear regression according to the influence of different distance data around the pixel on the prediction value, and the weight function is Gaussian function. Store the data into a filter array with a fixed length value of N , and use the average value of the entire array as the filtering result.

$$\bar{X} = \frac{1}{N} \sum_{i=1}^{N-1} X_{N-1} \tag{7}$$

The filtering results are shown (see Fig. 13):

Compare the contours of different fitted curves to visually reflect the size deviation of each position of the synchronous belt, as shown (see Fig. 14):

5 Data Comparison

The tooth profile parameters of synchronous belt were collected in three different use cases, namely standard, wear and slip, and were analyzed comprehensively from pitch, root thickness and tooth height.

Usually, the slip of synchronization belt is caused by the change of pitch. Compare the pitch parameters of wear synchronization belt and slip synchronization belt. It is

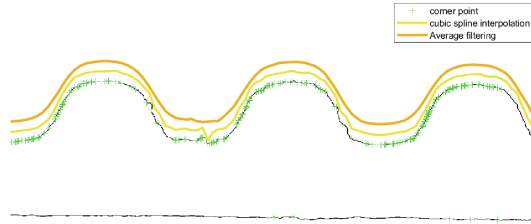


Fig. 13. Contour feature point sampling

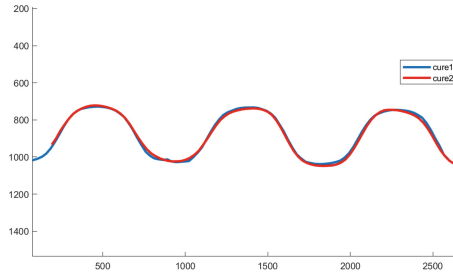


Fig. 14. Contrast of contour

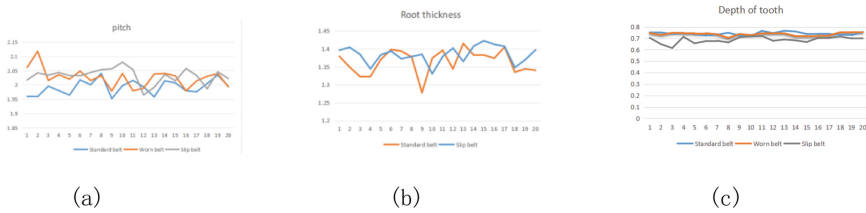


Fig. 15. Parameter line graph

found that the pitch of the synchronous belt as a flexible material becomes larger during use (see Fig. 15).

The problem of tooth profile parameters of synchronous belt mainly focuses on tooth height and root thickness. The tooth height of the slip synchronous belt is obviously lower than the normal level of the other two synchronous belts. This will cause the gear groove of the slip belt to preferentially contact the pulley during meshing. Under the action of larger root thickness, only the root of the synchronous belt is stressed.

There is a side gap between synchronous belt tooth and belt gear tooth slot, which can not reach the ideal meshing state. When the adjacent synchronous belt teeth are affected, there will be no force phenomenon, resulting in uneven load between different belt teeth and lower carrying capacity than normal level (see Fig. 16):

The larger the radius of the root circle and the thickness of the root of the synchronous belt, the more obvious the uneven phenomenon of load. When the sliding synchronous belt engages from the loose edge into the tight edge, the tension increases beyond the

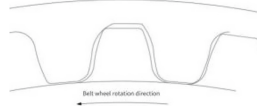


Fig. 16. Abnormal mesh diagram

load-bearing limit of the teeth of the synchronous belt currently being stressed, and the synchronous belt will slip.

From the point of view that the synchronization belt will change during use, the longer the use time, the smoother the surface of the synchronization belt and the larger the pitch. There is a large pitch error between the synchronous belt and the pulley. Under the action of thicker synchronous belt tooth root, the error is amplified, and each synchronous belt tooth accumulates between each other, and the belt tooth climbs to the top of the belt gear tooth, resulting in skid (Fig. 17).



Fig. 17. Creep teeth

When the synchronous belt is engaged normally, it can be measured by the tooth height of the synchronous belt and the thickness of the tooth root. When the tooth height is too low, the belt wheel is easier to push the tooth root of the synchronous belt. The contact part between the top of the gear and the belt is detected when the belt engages, so that the force part is concentrated on the tooth surface. The reliable contact area increases the force area while also reducing the wear of the synchronous belt and extending the service life.

When meshing, it is necessary to observe whether the tooth side gap is reserved on both sides of the synchronous belt teeth, in order to ensure that the tooth surface of the synchronous belt side teeth in the contact part of the belt wheel is stressed at the same time, so as to avoid uneven load on the synchronous belt teeth.

6 Conclusion

This paper presents a method based on MATLAB to detect the tooth profile of industrial robot transmission synchronous belt. In this method, γ -transform is used to enhance and re-map the image to obtain a clear synchro-band image. Then the outline information was extracted by morphology. Finally, the corner detection is used to fit the contour boundary. The synchronization band boundary can be approximated as sinusoidal signal and smoothed. The relevant measurement results show that the proposed method can effectively extract the contour information of the synchronous belt, obtain more accurate

dimensions, display the wear condition of the synchronous belt more intuitively, and can be widely used to measure various dimensions of the synchronous belt.

References

1. Li, J., Liu, Y., Li, H., Jiang, D., Wang, C., Gong, L.: Research on gear parameter measurement method based on vision principle [J]. *Tool Eng.* **56**(10), 147–151 (2022)
2. Cao, M.: Design of Synchronous Belt Tooth Profile Measurement System [D]. Changchun University of Science and Technology, (2020). <https://doi.org/10.26977/d.cnki.gccgc.2020.000122>
3. Haijiao, Y., Yang, X.: Low light image enhancement method combining adaptive Gamma transform and MSRCR algorithm[J]. *China Sciencepaper* **17**(11), 1245–1253 (2022). <https://doi.org/10.3969/j.issn.2095-2783.2022.11.011>
4. Xuan, D.: Research on Dimension Detection Technology of Bearing and Synchronous Pulley Based on Machine Vision[D]. Henan University of Technology, (2020). <https://doi.org/10.27791/d.cnki.ghegy.2020.000038>
5. Ji, Z.: DROPOUT optimization of neural network overfitting problem[J]. *J. Changzhi Univ.* **37**(02), 37–39 (2020)
6. Qi, Y., Wang, D.: Performance comparison of image edge detection methods[J]. *China Stand.* **14**, 141–144 (2022)
7. Yang, J., Li, Q., Yang, X., Zhu F., Deng, Z.: Research on digital image edge detection based on Matlab[J]. *Mod. Transm.* (03):54–56 (2022)
8. Zhao, H., Fan, L., Chang, J.: Fuzzy data interpolation based on cubic spline basis function[J]. *J. Hebei United Univ. Nat. Sci. Ed.* **44**(04), 68–79 (2022)
9. Peihe, Z., Tongde, Z., Keke, R., et al.: Application of high density electrical method based on least square regularization in 71502 face floor of Xiaogang Coal Mine[J]. *China Sciencepaper* **17**(1), 15–20 (2022). <https://doi.org/10.3969/j.issn.2095-2783.2022.01.003>
10. Cheng, Y., Zhang, H., Guo, Z.: Research on rivet hole detection technology of mine car based on least square fitting circle[J]. *Coal Mine Mach.* **42**(12):168–171 (2021). <https://doi.org/10.13436/j.mkjx.202112055>
11. Li, M., Kong, W.-W., Hu, Y., et al.: Adaptive multi-exposure image fusion based on weighted least squares[J]. *China Sciencepaper* **16**(7), 723–728 (2021). <https://doi.org/10.3969/j.issn.2095-2783.2021.07.006>
12. Zhang, Z., Pang, M., Teng, C.: Research on measurement of tooth profile parameters of synchronous belt based on point cloud data[J]. *Sensors* **22**(17) (2022)
13. Li, X., Sun, Y., Ma, J., Wang, B., Zhang, Z., Zhang, Z., Zou, J.: Design of AI online ecological picking system based on matlab visual recognition[J]. *Acad. J. Eng. Technol. Sci.* **4.0**(2.0) (2021)
14. Sun, R., Lei, T., Chen, Q., Wang, Z., Du, X., Zhao, W., Nandi, A.K.: Survey of image edge detection[J]. *Front. Signal Proc.* (2022)
15. Zhao, L., Han, Y., Chen, H., Song, Q.: MATLAB image processing in automatic control[J]. *J. Res. Sci. Eng.* **4**(7) (2022)

Author Index

B

Bai, Yirui 421
Bao, Fengbo 86
Bu, Jiayi 161

C

Cai, Xinrong 400
Cen, Dingjie 1
Chen, Bo 74
Chen, Cong 298
Chen, Dan 311
Chen, Dong-cheng 119
Chen, Gandong 561
Chen, Huiguang 170
Chen, Ke 237
Chen, Liuyuan 197
Chen, Yu 227
Chen, Yuanji 18
Chen, Zhiling 1
Cheng, Tai 552
Cheng, Wendang 449, 459
Cui, Dandan 247

D

Dai, Meiling 176, 187
Ding, Ziqi 355
Du, Hongtian 378
Du, Yibin 29
Duan, Chengyu 288
Duan, Ming 29

F

Feng, Lei 207, 217
Feng, Xiaonan 52
Feng, Zhichang 298
Fu, Xinqi 197

G

Gan, Lin 411
Gao, Haoyu 421

Gao, Zhipeng 258
Gong, Xingle 258
Guan, Zhiguang 479, 492, 501
Guangqiang, Yin 268
Guo, Fangqiang 532
Guo, Jingsong 86
Guo, Liang 52
Guo, Lulu 29
Guo, Shaoyong 227, 237
Guo, Sheng 29

H

Han, Jiaqi 197
Han, Jingqi 197
Han, Ming 197
Han, Yuxuan 400
He, Haoran 207
Hong, Lei 388, 400
Hou, Ke 449, 459
Hou, Xinqiao 137
Huang, Jianqiang 411
Huang, Kai 311

J

Ji, Falei 311
Ji, Yutong 288
Jia, Xiangyuan 197
Jiang, Han 561
Jiang, Zhiliang 197
Jiao, Ge 63
Ju, Zexin 378
Juanjuan, Zhou 268

L

Lei, Hong 421
Lei, Lei 1
Li, Aocheng 197
Li, Danfeng 18
Li, Dongdong 176, 187
Li, Haipo 247
Li, Jingwen 170

Li, Liang 432
 Li, Linguo 323, 334, 344
 Li, Qinghe 323, 334
 Li, Shujing 323, 334
 Li, Wenjing 207, 217
 Li, Xuanyu 411
 Li, Yang 501
 Li, Yicheng 365
 Li, Zhenghao 298
 Liang, Guangjun 365, 378
 Liang, Kun 552
 Liang, Maofei 520
 Lin, Fei 125
 Lin, Mingxing 479, 501
 Lin, Mugang 161
 Liu, Chao 421
 Liu, Feng 449, 459
 Liu, Lin 153
 Liu, Min 532
 Liu, Qi 432
 Liu, Ran 492
 Liu, Wei 355
 Liu, Wenjiang 449, 459
 Liu, Yibo 52
 Liu, Yuchen 520
 Liu, Yuxiao 237
 Liu, Zixuan 421
 Liu, Zuojian 1
 Lu, Jinjia 63
 Lu, Zhaokun 542

M

Ma, Baichao 311
 Ma, Qun 298
 Meng, Bingqian 137
 Meng, Fanping 125
 Mo, Zixi 365

P

Pan, Chengda 400
 Peng, Jiahao 378
 Peng, Jiansheng 86, 93, 105

Q

Qian, Hanwei 355
 Qian, Shunqiang 344
 Qian, Wei 93, 105
 Qin, Yong 1
 Qin, Zifu 52

Qiu, Zhenyu 378

R

Ren, Lanzhu 561
 Ren, Wanjie 432
 Ruan, Haoran 365
 Rui, Lanlan 258

S

Shang, Ronghao 552
 Shao, Wenyi 125
 Shen, Fang 288
 Shen, Tao 532
 Shi, Xiaohou 176, 187
 Shi, Zhongwei 552
 Song, Xinghui 41
 Sun, Mingxu 532
 Sun, Qin 509
 Sun, Yaqi 161
 Sun, Yating 247, 258

T

Tang, Keyan 365
 Tang, Peng 161
 Tang, Wenjie 388
 Tang, Yuna 18
 Teng, Yijia 365
 Tuo, Rui 432

W

Wang, Baoping 509
 Wang, Chao 479
 Wang, Fangyan 63
 Wang, Fayong 520
 Wang, Fengsi 52
 Wang, Haoran 125
 Wang, Peng 432
 Wang, Tianyu 311
 Wang, Ting 552
 Wang, Wei 29
 Wang, Wenyan 532
 Wang, Yaohui 542
 Wang, Zhen 288
 Wang, Zhiguo 278
 Wang, Ziyang 247
 Wu, Haiyan 137
 Wu, Yang 146
 Wu, Zechen 355

X

Xia, Yinxiang 52
Xiaohan, Huang 268
Xie, Xiaomin 311
Xiong, Ao 227, 237
Xu, Ren 125
Xu, Yong 1, 18
Xu, Yuan 552

Y

Yan, Bohan 378
Yan, Hui 74
Yan, Yan 532
Yang, Dangui 411
Yang, Houqun 411
Yang, Ke 237
Yang, Shaojie 227
Yang, Shuang 298, 311
Yang, Yang 247, 258
Yao, Hui 227
Yin, Kangning 278
Yin, Shanshan 479
Yu, Chen 278
Yuan, Fucai 197
Yuan, Meng 388
Yuan, Yiping 63

Z

Zebang, Qin 268
Zhang, Gaofeng 298
Zhang, Hongli 468
Zhang, Hongyu 93, 105
Zhang, Jiale 288

Zhang, Jian 153
Zhang, Jianxi 440
Zhang, Jinli 207, 217
Zhang, Mingyu 323, 334, 344
Zhang, Nan 237, 509
Zhang, Pengcheng 468
Zhang, Wuwen 552
Zhang, Xiaoying 411
Zhang, Yide 552
Zhang, Yuhua 440
Zhang, Zhiwei 298
Zhao, Jinyang 468
Zhao, Lingyan 520, 561
Zhao, Linxiang 146
Zhao, Longjun 247
Zhao, Pan 197
Zhao, Peiying 440
Zhao, Yikun 207, 217
Zhao, Zhenyuan 492, 509
Zheng, Sen 18
Zheng, Yuyang 388
Zhi, Cai 227
Zhou, Fanqin 207, 217
Zhou, Siqi 501
Zhou, Tonghui 552
Zhou, Tuo 344
Zhou, Yiting 153
Zhou, Yong 421
Zhu, Chuanming 170
Zhu, Meng 237
Zhu, Peipei 41
Zhu, Yiming 532
Zong, Teng 52